

High-pressure physical behavior of minerals and rocks: Mineralogy, petrology and geochemistry

Edited by

Lidong Dai, Xi Liu, Geeth Manthilake, Vassilios Saltas and Haiying Hu

Published in

Frontiers in Earth Science



FRONTIERS EBOOK COPYRIGHT STATEMENT

The copyright in the text of individual articles in this ebook is the property of their respective authors or their respective institutions or funders. The copyright in graphics and images within each article may be subject to copyright of other parties. In both cases this is subject to a license granted to Frontiers.

The compilation of articles constituting this ebook is the property of Frontiers.

Each article within this ebook, and the ebook itself, are published under the most recent version of the Creative Commons CC-BY licence. The version current at the date of publication of this ebook is CC-BY 4.0. If the CC-BY licence is updated, the licence granted by Frontiers is automatically updated to the new version.

When exercising any right under the CC-BY licence, Frontiers must be attributed as the original publisher of the article or ebook, as applicable.

Authors have the responsibility of ensuring that any graphics or other materials which are the property of others may be included in the CC-BY licence, but this should be checked before relying on the CC-BY licence to reproduce those materials. Any copyright notices relating to those materials must be complied with.

Copyright and source acknowledgement notices may not be removed and must be displayed in any copy, derivative work or partial copy which includes the elements in question.

All copyright, and all rights therein, are protected by national and international copyright laws. The above represents a summary only. For further information please read Frontiers' Conditions for Website Use and Copyright Statement, and the applicable CC-BY licence.

ISSN 1664-8714
ISBN 978-2-83251-395-8
DOI 10.3389/978-2-83251-395-8

About Frontiers

Frontiers is more than just an open access publisher of scholarly articles: it is a pioneering approach to the world of academia, radically improving the way scholarly research is managed. The grand vision of Frontiers is a world where all people have an equal opportunity to seek, share and generate knowledge. Frontiers provides immediate and permanent online open access to all its publications, but this alone is not enough to realize our grand goals.

Frontiers journal series

The Frontiers journal series is a multi-tier and interdisciplinary set of open-access, online journals, promising a paradigm shift from the current review, selection and dissemination processes in academic publishing. All Frontiers journals are driven by researchers for researchers; therefore, they constitute a service to the scholarly community. At the same time, the *Frontiers journal series* operates on a revolutionary invention, the tiered publishing system, initially addressing specific communities of scholars, and gradually climbing up to broader public understanding, thus serving the interests of the lay society, too.

Dedication to quality

Each Frontiers article is a landmark of the highest quality, thanks to genuinely collaborative interactions between authors and review editors, who include some of the world's best academicians. Research must be certified by peers before entering a stream of knowledge that may eventually reach the public - and shape society; therefore, Frontiers only applies the most rigorous and unbiased reviews. Frontiers revolutionizes research publishing by freely delivering the most outstanding research, evaluated with no bias from both the academic and social point of view. By applying the most advanced information technologies, Frontiers is catapulting scholarly publishing into a new generation.

What are Frontiers Research Topics?

Frontiers Research Topics are very popular trademarks of the *Frontiers journals series*: they are collections of at least ten articles, all centered on a particular subject. With their unique mix of varied contributions from Original Research to Review Articles, Frontiers Research Topics unify the most influential researchers, the latest key findings and historical advances in a hot research area.

Find out more on how to host your own Frontiers Research Topic or contribute to one as an author by contacting the Frontiers editorial office: frontiersin.org/about/contact

High-pressure physical behavior of minerals and rocks: Mineralogy, petrology and geochemistry

Topic editors

Lidong Dai — Institute of geochemistry, Chinese Academy of Sciences, China

Xi Liu — Peking University, China

Geeth Manthilake — UMR6524 Laboratoire Magmas et Volcans (LMV), France

Vassilios Saltas — Hellenic Mediterranean University, Greece

Haiying Hu — Institute of Geochemistry, Chinese Academy of Sciences, China

Citation

Dai, L., Liu, X., Manthilake, G., Saltas, V., Hu, H., eds. (2023). *High-pressure physical behavior of minerals and rocks: Mineralogy, petrology and geochemistry*.

Lausanne: Frontiers Media SA. doi: 10.3389/978-2-83251-395-8

Table of contents

- 05 **Editorial: High-pressure physical behavior of minerals and rocks: Mineralogy, petrology and geochemistry**
Lidong Dai, Haiying Hu, Xi Liu, Geeth Manthilake, Vassilios Saltas and Jianjun Jiang
- 08 **A Review of High-Temperature and High-Pressure Experimental Apparatus Capable of Generating Differential Stress**
Dongsheng Ren and Heping Li
- 14 **Lithologic Structure of the Anninghe Fault Zone: Constraints From High-Pressure Wave Velocity Experiments**
Sheqiang Miao, Yongsheng Zhou, Xi Ma and Jiaxiang Dang
- 21 **Elastic-Wave Radiation, Scattering, and Reception of a Dipole Acoustic Logging-While-Drilling Source in Unconsolidated Formations**
Zhen Li, Qiaomu Qi, Chuang Hei, Can Jiang and Xing-Jian Wang
- 32 **Zircon SHRIMP U-Pb Dating and Significance From Weathered Residual Kaolin Deposits on the Northern Margin of the Qinzhou-Hangzhou Suture Zone, China**
Chunhai Li, Qifa Sun, Zhonglin Sun, Xiaohua Zhou, Wei Zhang, Rong Chen and Tianshan Gao
- 42 **Experimental Research on Electrical Conductivity of the Olivine-Ilmenite System at High Temperatures and High Pressures**
Wenqing Sun, Lidong Dai, Haiying Hu, Mengqi Wang, Ziming Hu and Chenxin Jing
- 54 **Thermodynamic Properties of Fe-Bearing Wadsleyite and Determination of the Olivine-Wadsleyite Phase Transition Boundary in (Mg,Fe)₂SiO₄ System**
Chang Su, Yonggang Liu, Dawei Fan, Wei Song, Jiyi Jiang, Zhenjun Sun and Guang Yang
- 65 **High-Temperature and High-Pressure Phase Transition of Natural Barite Investigated by Raman Spectroscopy and Electrical Conductivity**
Meiling Hong, Lidong Dai, Haiying Hu, Xinyu Zhang and Chuang Li
- 79 **Acoustoelastic FD Simulation of Elastic Wave Propagation in Prestressed Media**
Haidi Yang, Li-Yun Fu, Bo-Ye Fu and Tobias M. Müller
- 97 **Geodynamics Based on Solidification of Liquid/Molten Substances in the Earth's Interior**
Xin Li, Mingjiang Tao and Duanwei He
- 105 **Stress-Strain-Sorption Behaviour of Smectites Upon Exposure to Dry and Wet CO₂**
Miao Zhang, Christopher James Spiers, Jinfeng Liu and Hongwei Zhou

- 126 **High P-T Calcite-Aragonite Phase Transitions Under Hydrous and Anhydrous Conditions**
Xia Zhao, Zhi Zheng, Jiangzhi Chen, Yue Gao, Jianhui Sun, Xue Hou, Mengjun Xiong and Shenghua Mei
- 134 **The Effect of Quartz Particle Size on the Frictional and Electrically Conductive Properties of Mixed Graphite–Quartz Gouges**
Jinyu Chen
- 146 **Processing Method of Soil Temperature Time Series and Its Application in Geothermal Heat Flow**
Liming Yang, Rongcai Song, Ben Dong, Likun Yin, Yifan Fan, Bo Zhang, Ziwei Wang, Yingchun Wang and Shuyi Dong
- 155 **Pseudotachylite-Mylonites Record of Transient Creep From Inter-Seismic Ductile to Co-Seismic Rupture**
Wenhao Dai, Yongsheng Zhou and Xi Ma
- 166 **Electrical conductivity of siderite and its implication for high conductivity anomaly in the slab-mantle wedge interface**
Haiying Hu, Chenxin Jing, Lidong Dai, Chuanyu Yin and Dongmei Chen



OPEN ACCESS

EDITED AND REVIEWED BY
Derek Keir,
University of Southampton,
United Kingdom

*CORRESPONDENCE

Lidong Dai,
✉ dailidong@vip.gyig.ac.cn
Haiying Hu,
✉ huhaiying@vip.gyig.ac.cn
Xi Liu,
✉ xi.liu@pku.edu.cn
Geeth Manthilake,
✉ geeth.manthilake@uca.fr
Vassilios Saltas,
✉ saltas@hmu.gr

SPECIALTY SECTION

This article was submitted to Solid Earth
Geophysics,
a section of the journal
Frontiers in Earth Science

RECEIVED 17 December 2022
ACCEPTED 29 December 2022
PUBLISHED 09 January 2023

CITATION

Dai L, Hu H, Liu X, Manthilake G, Saltas V
and Jiang J (2023), Editorial: High-
pressure physical behavior of minerals and
rocks: Mineralogy, petrology
and geochemistry.
Front. Earth Sci. 10:1126463.
doi: 10.3389/feart.2022.1126463

COPYRIGHT

© 2023 Dai, Hu, Liu, Manthilake, Saltas and
Jiang. This is an open-access article
distributed under the terms of the [Creative
Commons Attribution License \(CC BY\)](https://creativecommons.org/licenses/by/4.0/).
The use, distribution or reproduction in
other forums is permitted, provided the
original author(s) and the copyright
owner(s) are credited and that the original
publication in this journal is cited, in
accordance with accepted academic
practice. No use, distribution or
reproduction is permitted which does not
comply with these terms.

Editorial: High-pressure physical behavior of minerals and rocks: Mineralogy, petrology and geochemistry

Lidong Dai^{1*}, Haiying Hu^{1*}, Xi Liu^{2*}, Geeth Manthilake^{3*},
Vassilios Saltas^{4*} and Jianjun Jiang¹

¹Key Laboratory for High-Temperature and High-Pressure Study of the Earth's Interior, Institute of Geochemistry, Chinese Academy of Sciences, Guiyang, Guizhou, China, ²MOE Key Laboratory of Orogenic Belts and Crustal Evolution, School of Earth and Space Sciences, Peking University, Beijing, China, ³Laboratoire Magmas et Volcans, CNRS, IRD, OPGC, Université Clermont Auvergne, Clermont-Ferrand, France, ⁴Institute of Physics of Earth's Interior and Geohazards, Hellenic Mediterranean University Research and Innovation Center, Crete, Greece

KEYWORDS

electrical conductivity, ultrasonic elastic wave velocity, Raman spectroscopy, stress-strain-sorption property, structural phase transition, deformation, theoretical calculation, high pressure

Editorial on the Research Topic

High-pressure physical behavior of minerals and rocks: Mineralogy, petrology and geochemistry

The 8th “From Atom to Earth” Symposium on High-Pressure Science and Earth Science was held at the Institute of Geochemistry, Chinese Academy of Sciences (IGCAS), Guiyang, China between July 2nd and 5th, 2021. Professor Lidong Dai from the IGCAS Key Laboratory of High-temperature and High-pressure Study of the Earth's Interior (HTHPSEI) was the conference president. 156 prominent Chinese scholars, such as from Peking University, Chinese Academy of Sciences, etc. participated in the conference. Professors Xi Liu, Duanwei He, Lidong Dai, Chun-An Tang and Zizheng Gong delivered the specific conference speeches (Figure 1). As distinguished and invited delegates, professors Hongsen Xie and Heping Li attended this conference. CAS Key Laboratory of HTHPSEI, together with IGCAS and Chinese Society of Mineralogy, Petrology and Geochemistry, provided the conference service.

This Research Topic, hosted by Frontiers in Earth Science, is the accessory Volume II that follows the special Volume I entitled “Earth Deep Interior: High-pressure Experiments and Theoretical Calculations from the Atomic to the Global Scale” on the basis of the 8th “From Atom to Earth” Symposium on High-Pressure Science and Earth Science, held at the CAS Key Laboratory of HTHPSEI (Dai et al.). The volume contains fifteen papers, including original studies and a review article reporting on the high-pressure physical behavior of minerals and rocks, recently obtained by using experimental measurements and theoretical calculations under high-temperature and high-pressure conditions. High-*P* electrical transport characterizations, phase transition, ultrasonic elastic wave velocity, Raman spectroscopy, stress-strain-sorption properties and deformation on some representative minerals and rocks are presented in the light of experimental investigations. Some new progress based on theoretical calculations pay attention to the *P*–*T* phase boundary, thermal capacity, thermal



FIGURE 1

The 8th "From Atom to Earth" Symposium on High-Pressure Science and Earth Science held in IGCAS, Guiyang, China between July 2nd and 5th, 2021.

expansion coefficient, elastic moduli, rock physical parameters, and solidification of liquid/molten substance in the Earth's interior, etc.

Ren and Li present a comprehensive review on the development of high-temperature and high-pressure experimental apparatuses capable of generating differential stress, in order to accurately simulate the temperature field, the hydrostatic pressure environment and the differential stress distribution of deep Earth's interior, such as Griggs press, Paterson rheometer, D-DIA press, RDA press and torsional diamond anvil cell. By comparing the advantages and shortcomings for each corresponding high-pressure equipment in the measurement of sample size, accuracy, temperature range and stress distribution, the future development of high-*T* and high-*P* experimental apparatus with differential stress has good prospects.

Some new obtained high-*P* experimental results and theoretical calculations have been reported for a selection of minerals and rocks. Using Electrochemical Impedance Spectroscopy (EIS), Hu et al. investigated the electrical conductivity of natural siderite at conditions of 1–3 GPa and 100°C–700°C in YJ-3000t multi-anvil high-pressure apparatus. Their results indicate that the incipient decarbonation temperatures are considerably lower than the decomposition boundary of siderite determined by phase equilibrium experiments, implying that the initial decarbonation reaction in subducting oceanic crust occurs at a shallower depth. The 30 vol% of siderite is required to enhance the electrical conductivity of (Mg,Fe)CO₃ solid solutions. The recovered products of magnetite and graphite generated from the decarbonation reaction of the siderite component of Fe-bearing carbonate make a significant contribution to the high conductivity anomaly observed in the slab-mantle wedge interface. Similarly, Sun et al. determined electrical conductivities of the olivine-ilmenite systems with various contents of ilmenite ($V_{ilm} = 4, 7, 10, 11$ and 15 vol%) and pure ilmenite aggregates using EIS at 1.0–3.0 GPa and 773–1273 K. They proposed that the percolation threshold of the ilmenite grains in the dry olivine-ilmenite systems was about 11 vol% resulting in the interconnection of ilmenites, which can dramatically enhance the conductivities of the olivine-ilmenite systems. Hong et al. studied the structural phase transition and its corresponding *P*–*T* phase diagram in conjunction with high-*P* electrical conductivity and Raman spectroscopy experiments of natural barite under the

conditions of 298–873 K and 1.5–35.0 GPa, using a diamond anvil cell. They observed a positive correlation between pressure and temperature of phase transformation and proposed that the obtained phase diagram of natural barite can improve the knowledge of the structural and electrical properties for other barite-group minerals MSO₄ (M = Sr and Pb) under high-*T* and high-*P* conditions. Chen measured the electrical conductivity of synthetic carbon-bearing gouges along a fault-parallel direction under progressive fault slip, under conditions of a slip rate of 1 mm/s, a normal stress of 2 MPa, at ambient temperature, and a pure N₂ atmosphere using a rotary shear low to high-velocity friction high-pressure apparatus. They concluded that some representative carbonaceous minerals represented by the mixtures of identical 6 wt% graphite may complicate the frictional properties of fine-grained fault gouges in mature faults. Zhao et al. determined the high *P*–*T* calcite–aragonite phase transitions under hydrous and anhydrous conditions. Their results suggest the phase transition of calcite–aragonite in the subduction zone, where the solid recrystallization–reconstructive phase transition can exist in slabs under wide *P*–*T* conditions (1–2 GPa and 160°C–400°C) whereas, the dissolution–precipitation–dehydration process can only occur under lower *P*–*T* conditions (less than 1.5 GPa and 110°C). Miao et al. measured the ultrasonic elastic *P*–wave velocity of typical rocks (i.e., granite, granodiorite, granodiorite mylonite, anorthosite, diorite, mafic granulite, gabbro, diabase and pyroxenite) in the Anninghe fault zone under pressures of 50–600 MPa. They argue that the lithologic difference between the southern and northern sections of the Anninghe fault zone within the middle and upper crust at depths less than 25 km, is primarily that the rocks in the southern section (Xichang) are more felsic than those in the northern section (Shimian). Zhang et al. performed the multiple stepwise axial loading and unloading, oedometer-type experiments on ~1 mm thick discs of pre-pressed Na-SWy-1 and of Ca-SAZ-1 montmorillonite. Their results can provide a first step towards modelling stress-strain-sorption effects in smectite rich caprocks penetrated by CO₂, though further refinements are needed for broader application to the smectite-CO₂-H₂O system. Dai et al. analyzed the microstructures of samples for mylonites, pseudotachylite and cataclasite by the optical microscopic

observation, SEM and EBSD from the Red River fault in southwest China. Based on the analysis of the microstructures and deformation mechanism of fault rocks, they proposed the oscillation deformation model to explain transient creep of the brittle–plastic transition zone during the seismic cycle in the Red River fault.

On the other hand, some recently obtained theoretical modeling results on the P – T phase boundary, thermal capacity, thermal expansion coefficient, elastic moduli, rock physical parameters, and solidification of liquid/molten substance in the Earth's interior, etc. are displayed in this special topic. Li et al. investigate the characteristics of acoustic wavefields associated with logging-while-drilling (LWD) in an unconsolidated formation using the time–domain finite difference (FDTD) method to simulate the wavefields corresponding to a ring dipole source. These simulation results can provide a theoretical foundation for the borehole detection by LWD single-well acoustic imaging technique in unconsolidated formations. Yang et al. carry out numerical acoustoelasticity simulations for wave propagation in single- and double-layer models under four states of prestresses, confining, uniaxial, pure-shear, and simple-shear. Their theoretical calculations can display the significant impact of prestressed conditions on seismic responses in both phase and amplitude.

Applying the Clausius-Clapeyron equation in combination with molar volumes and entropies of both compositions, the phase transition boundary of Fe-bearing olivine and wadsleyite was estimated by Su et al. Their research results suggest that the existence of Fe might decrease the transition pressure from olivine to wadsleyite, which would consequently cause a higher temperature at the 410 km discontinuity. Li et al. investigated the geodynamic solidification of liquid/molten substances in the Earth's interior using three sets of observations including Global Positioning System data, length of day data, and the latent heat of Earth solidification. They put forward that the liquid solidification in the Earth's interior is the main source for the movement of plates.

In addition, Li et al. performed zircon SHRIMP (sensitive high resolution ion microprobe) dating in ore-forming veins of weathered residual Kaolin deposits from the northern the Qinzhou-Hangzhou Metallogenic belt margin within the Yangtze and Cathaysia plates. Their research results indicate that the ore-forming granite veins intruding into the Jiuling rock masses are Neoproterozoic in age (843 ± 10 Ma) and the ore-forming granite porphyry veins intruding

into Neoproterozoic Anlelin formation strata are late Jurassic (152.3 ± 1.8 Ma). Yang et al. developed a convenient and fast model for processing soil temperature time series, which can provide a crucial technical support for the comprehensive utilization of geothermal resources in highland areas or the assessment of the geothermal potential of the region. In this method, the soil thermal diffusion coefficients corresponding to different depths can be obtained, the temperature can be calculated at these different depths, and finally, the approximate soil temperature gradient of the measured area will be successfully obtained to apply in geothermal heat flow.

Author contributions

All authors listed have made a substantial, direct, and intellectual contribution to the work and approved it for publication.

Acknowledgments

The topic editors would like to thank all contributing authors to this Research Topic and the editorial staff of Frontiers in Earth Science for making this special collection possible.

Conflict of interest

The authors declare that the research was conducted in the absence of any commercial or financial relationships that could be construed as a potential conflict of interest.

Publisher's note

All claims expressed in this article are solely those of the authors and do not necessarily represent those of their affiliated organizations, or those of the publisher, the editors and the reviewers. Any product that may be evaluated in this article, or claim that may be made by its manufacturer, is not guaranteed or endorsed by the publisher.

Reference

L. Dai, H. Hu, J. Jiang, X. Liu, G. Manthilake, and V. Saltas (Editors) (2022). "Earth deep interior," *High-pressure experiments and theoretical calculations from the atomic to the*

global Scale (Lausanne, Switzerland: Frontiers Media SA), 1–121. doi:10.3389/978-2-88976-543-0



A Review of High-Temperature and High-Pressure Experimental Apparatus Capable of Generating Differential Stress

Dongsheng Ren^{1,2} and Heping Li^{2*}

¹State Key Laboratory of Earthquake Dynamics, Institute of Geology, China Earthquake Administration, Beijing, China, ²Key Laboratory of High-temperature and High-pressure Study of the Earth's Interior, Institute of Geochemistry Chinese Academy of Sciences, Guiyang, China

OPEN ACCESS

Edited by:

Vassilios Saltas,
Hellenic Mediterranean University,
Greece

Reviewed by:

Kai Luo,
Yunnan University, China
Desheng Li,
Shanghai Jiao Tong University, China

*Correspondence:

Heping Li
Liheping@vip.gyig.ac.cn

Specialty section:

This article was submitted to
Solid Earth Geophysics,
a section of the journal
Frontiers in Earth Science

Received: 11 January 2022

Accepted: 31 January 2022

Published: 07 March 2022

Citation:

Ren D and Li H (2022) A Review of
High-Temperature and High-Pressure
Experimental Apparatus Capable of
Generating Differential Stress.
Front. Earth Sci. 10:852403.
doi: 10.3389/feart.2022.852403

It has been demonstrated that the matters in the earth's interior are subjected to isotropic hydrostatic pressure and are also extensively superimposed by the differential stress. The differential stress contributes significantly to the free energy of matters and it is the determining factor controlling the composition, structure, configuration, properties, and interaction processes of the matter system. Hence, the differential stress is one of the most fundamental thermodynamic variables governing the earth's interior system along with the temperature and the hydrostatic pressure. Nevertheless, due to the limitations of high-temperature and high-pressure (HT-HP) setup and *in situ* measurement techniques as well as limited understanding of the differential stress, previous HT-HP experiments of the earth's interior didn't cover the role of the differential stress except for some special stress-strain mechanics experiments and piezolysis and kinetic metamorphism experiments. This makes many of the knowledge about the earth's interior obtained from HT-HP experiments generally questionable. Currently, HT-HP experimental apparatus that can be used to simulate the temperature, hydrostatic pressure, and differential stress in the earth's interior includes the Griggs press, the Paterson rheometer, the D-DIA press, the RDA press, and the torsional diamond anvil cell. The maximum hydrostatic pressure that can be simulated in the Griggs press at high temperatures is only about 2 GPa and there is large uncertainty in the calibration of the differential stress. The Paterson rheometer provides too low confining pressure. The D-DIA press and RDA press can simulate a wide range of temperature and pressure but the D-DIA press can achieve very small strain variables and the RDA press has very heterogeneous sample stresses. The torsional diamond anvil cell can only accept a small sample size and it is difficult to calibrate the differential stress. Also, these existing HT-HP experimental apparatus with the differential stress are not easily interfaced with *in situ* measurement systems for investigating the physical properties such as electrical, ultrasonic, and thermophysical properties. Hence, scholars need to invest more efforts in the research and development of HT-HP apparatus with the differential stress in the future to properly understand the composition, structure, configuration, properties, and interactions of the matter in the earth's interior.

Keywords: differential stress, differential stress generator, high temperature, high pressure, phase transition

INTRODUCTION

The composition, structure, constructions, properties, interaction processes, and formation and evolution law of the earth's interior are the most important research contents in the study on the earth's inner working mechanism. Field observations such as geological, geochemical, geophysical, costeaning, probing, and drilling as well as laboratory analysis tests, theoretical calculations, and HT-HP experiments are the main tools used today to explore the inner working mechanism of the earth. However, the conclusions obtained from field observations and laboratory analysis tests require HT-HP experiments for validation. Also, the inversion of field geophysical data and theoretical computational simulations require HT-HP experiments to provide various trait parameters for the earth's interior. The information on the earth's interior obtained by field surveys and laboratory analysis tests are relatively limited and theoretical computational simulations are usually unable to investigate the non-equilibrium thermodynamic system and the naturally complex HT-HP matter system in the earth's interior. In contrast, HT-HP experiments can reveal new phenomena and patterns that are difficult to reveal by field surveys, laboratory analysis tests, and theoretical computational simulations. Hence, HT-HP experiments of the earth's interior play an important role in the exploration of the earth's inner working mechanism (Karato, 2008, 2013).

In the stress analysis, the stress component also changes as the orientation of the stress unit body changes. There is an orientation of the stress unit body in which the shear stress component on the unit body surface is zero meaning that only the principal stress acts in the orthogonal section. When the stress values in the three principal stress directions are different, the object is subjected to the differential stress. Earth's magnetic field, mantle convection, mantle column, plate subduction, magma intrusion, volcanoes, earthquakes, faults, folding, dynamic metamorphism, and other geological phenomena all indicate that the earth's interior are subject to isotropic lithostatic pressure (equivalent to hydrostatic or quasi-hydrostatic pressure) or lithostatic pressure + pore/fracture fluid pressure, and there is also extensive superimposed differential stress on it (Kawamoto and Shimamoto, 1997; Niemeijer and Spiers, 2006; Imber et al., 2008; Toy et al., 2011; Rowe and Griffith, 2015). The differential stress acting on the earth's interior system, whether it produces elastic or plastic deformation, significantly contributes to the free energy of the matter. The differential stress is the decisive factor controlling the phase composition, structure, construction, properties, and interaction processes of the material system. Hence, the differential stress, like the temperature and hydrostatic pressure, is one of the most fundamental thermodynamic variables governing the earth's interior system. Nevertheless, previous HT-HP experiments of the earth's interior didn't cover the role of the differential stress except for some special stress-strain mechanics experiments and a few piezolysis and kinetic metamorphism experiments. As a result, much of what has been learned about the earth's interior from HT-HP experiments to date is generally questionable. Hence, a proper understanding of the

composition, structure, construction, properties, and interactions of the earth's interior requires knowledge of the physicochemical properties of the earth's interior under high temperatures, high pressures, or differential stresses.

In this study, the progress and problems in the study on the physical properties of the earth's interior under the differential stress are briefly reviewed. Also, the existing HT-HP apparatus that can generate the differential stress are reviewed and some future research trends in this field are presented.

LITERATURE REVIEW

The effects of the differential stress on the phase, structure, and properties of condensed matter are well known in many fields such as condensed matter physics, materials science, and microelectronics. For instance, Ma, *et al.* found using their invented torsional diamond anvil cell type high-pressure device that the addition of torsional stress can greatly reduce the pressure of the phase transition of the metallic iron from α to ϵ (Ma and Emre, 2006; Benjamin et al., 2012; Daniel et al., 2014). The mechanism of the cold working hardening of metallic materials is the process associated with the cold working of materials to generate point defects and dislocations, to form internal stress in the crystal lattice, and eventually to induce the hardening of materials. The effects of the external differential stress and the internal stress on the phonon spectra of condensed matter and the peak positions and peak widths of X-ray diffraction spectra have long been used to measure the stress state of various materials especially for thin films and semiconductor devices (Siakavellas et al., 1997; Cao et al., 2006). The differential stress has a significant effect on the structural phase transition and physical properties of semiconductor materials (Grave et al., 2014; Budnitski and Kuna, 2016), ferroelectric materials (Li et al., 2015; Zhu, 2014; Xu et al., 2016; Seyidov, 2016), superhard materials (Korotaev et al., 2016), and nonlinear optical materials (Mylvaganam et al., 2015). The differential stress significantly modulates the band structure of semiconductor materials and the magnetic properties and magnetic structure phase transition of ferromagnetic materials (Xu et al., 2008; Li et al., 2014; Coe et al., 2012).

In the field of HT-HP experimental studies on the composition, structure, construction, properties, and interactions of the earth's interior, the effect of the differential stress as a fundamental thermodynamic variable on the experimental results have not been taken into account due to the limited HT-HP experimental apparatus or *in situ* measurement techniques for simulating high-temperature and complex stress conditions. The only exceptions are some specialized stress-strain mechanics experiments as well as piezolysis and dynamic metamorphism experiments (Tullis and Yund, 1991; Demouchy and Mainprice, 2011; Anil et al., 2012; Niwa et al., 2012; Ken et al., 2012; Liu et al., 2013; Wassmann and Stöckhert, 2013; Miyakawa and Kawabe, 2014; Kausala and Zhang, 2015; Ben-Itzhak et al., 2016; Pavel et al., 2016) which had more reports on the effect of the differential stress. Even though there have been occasional sporadic reports,

the systematicity and completeness of these studies are still far from being applied to solve specific earth science problems. As a result, much of the knowledge on the earth's interior material obtained based on the HT-HP experimental results are questionable. For instance, the effects of the differential stress at high temperatures and high (quasi) hydrostatic pressures on the phase transformation of geological materials have been reported only in the following extremely sporadic cases for pyroxene and quartz.

- 1) It is known that the Clinopyroxene-Orthorhombic pyroxene phase transition boundaries obtained at high temperatures and high pressures were significantly different from each other. Based on the thermodynamic analysis of previous experimental details and results, Coe (1970) proposed the effect of the shear stress on the temperature and pressure of the Clinopyroxene-Orthorhombic pyroxene phase transition. However, unfortunately, no specific experimental verification and further systematic study of this hypothesis have been carried out since then.
- 2) Zhou et al. (2005) studied the phase transition of quartz at the temperature of 950–1,000°C, the confining pressure of 1.3 GPa, and the axial compressive stress of 1.5–1.67 GPa. The pressure of the phase transition from α quartz to coesite was found to be closely related to the differential stress and the presence of coesite at the interface between the indenter and the sample. However, it is also unfortunate that this work was not continued later. Richter (2016) found the formation of coesite by the shear experiments at 600–900°C and 1–1.5 GPa, but only qualitatively discussed that the formation of coesite is closely related to the differential stress.
- 3) Singh et al. (2012) used the laser-heated diamond anvil cell synchrotron X-ray diffraction to find a significant difference in the transition pressure of stishovite from tetragonal to oblique phases in the differential stress and hydrostatic pressure environments (about 40 and 60 GPa, respectively). However, this work only found such phenomena, and the relationship between the differential stress and the phase transition pressure for a given temperature and (quasi) hydrostatic pressure could not be measured accurately in the anvil cell. Also, the essential correlation between the (quasi) hydrostatic pressure and the differential stress in the anvil cell was not investigated. So no quantitative results were available.
- 4) Demouchy and Mainprice (2011) used a HT-HP second-stage WC anvil apparatus using a 45° waist-cut sample assembly of the sample column to find that the shear stress had an important effect on the phase transition kinetics of forsterite-wadsleyite. However, *in situ* measurement of the shear stress and the essential correlation between the shear stress and the confining pressure could not be achieved. So the quantitative relationship between the temperature and the pressure of the phase transition reaction and the shear stress could not be obtained.
- 5) Niwa et al. (2012) used laser heating of diamond anvil cells in combination with a high-fluorescence miniaturized X-ray machine and found that the differential stress inside the

diamond anvil cells could reduce the transition temperature of the silicate calixarene analog CaIrO_3 from calixarene to post-calixarene to room temperature. However, it was also impossible to accurately measure the differential stress in the anvil cell and the essential correlation between the (quasi) hydrostatic pressure and the differential stress in the anvil cell. Therefore, the quantitative relationship between the differential stress and the temperature and pressure of the phase transition could not be obtained. Experimental studies on partial melting of geomaterials at high temperatures, high (quasi-) hydrostatic pressures, and high differential stresses were reported. But they focused on the relationship between the differential stress and the partial melting kinetics, the spatial distribution of the melt and melt segregation, as well as the constitutive and rheological behavior of the partially melted samples (Tumarkina et al., 2011; Holtzman and Benjamin, 2012). So the quantitative relationship between the differential stress and the temperature/pressure of the melt phase transition of the solid sample has not been reported yet. The effects of the differential stress on the physical properties of geological materials at high temperatures and high (quasi) hydrostatic pressures have been reported only for the conductivity of magnetite-bearing serpentine (Kawano et al., 2012) and polycrystalline olivine (Caricchi et al., 2011; Zhang et al., 2014). However, the experimental reports focused on the mechanism of the differential stress-sample structure-sample conductivity. There are no experimental reports on the effect of the differential stress on the core factors that directly constrain the conductivity of samples such as the electronic band structure, the lattice defect types and concentrations, and the carrier migration activation energy of the constituent minerals.

In summary, there are very few existing reports for the effects of the differential stress on the physicochemical properties of geological materials. The majority of reports are missing quantitative results and only qualitatively discuss the contribution of the differential stress. This is mainly due to the slow research and development progress of differential stress generators.

HIGH-TEMPERATURE AND HIGH-PRESSURE EXPERIMENTAL APPARATUS CAPABLE OF GENERATING DIFFERENTIAL STRESS

The formation and evolution of various geological and tectonic phenomena in the earth is ultimately the result of the deformation of mineral rocks under complex physicochemical conditions. To better understand the deformation of the earth's interior under various physical conditions such as the temperature, confining pressure, differential stress, and strain rate, as well as chemical environments such as the oxygen fugacity and fluids in the real earth's interior, special HT-HP experimental apparatus are

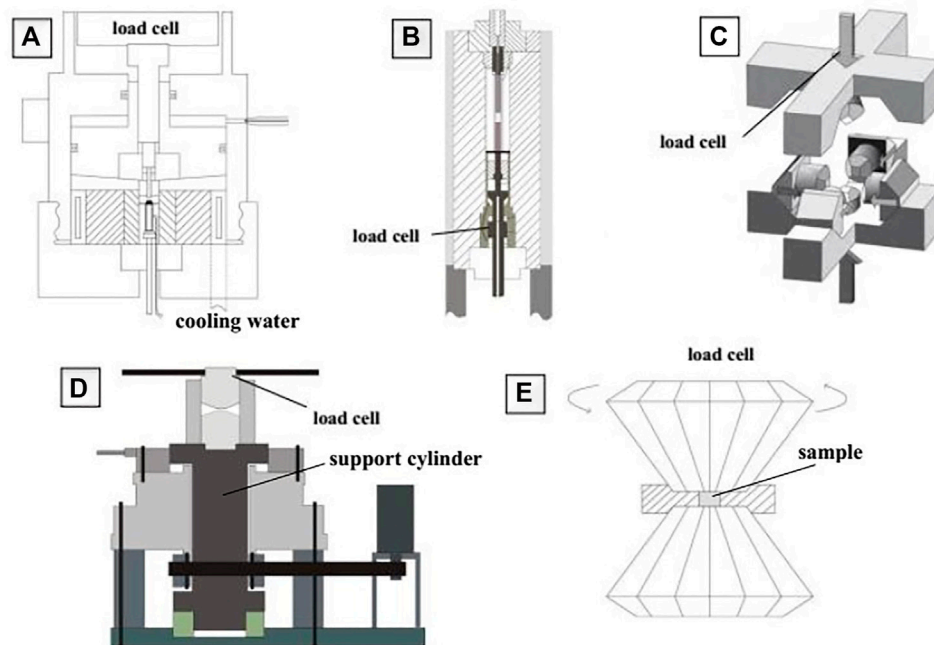


FIGURE 1 | Differential stress apparatus. **(A)** Griggs deformation apparatus (Griggs, 1967), **(B)** Paterson deformation apparatus (Paterson, 1970), **(C)** Deformation-DIA (Wang et al., 2003), **(D)** Rotational Deformation Apparatus (Yamazaki and Karato, 2001), **(E)** Diamond anvil cell (Niwa et al., 2012).

needed to test the mechanical properties of the earth's interior. In the 1960s, David Griggs, a pioneer in the field of international tectonics, developed a new high-temperature, high-pressure deformation device, the Griggs rheometer (Griggs, 1967), by modifying a piston-cylinder high-pressure device as shown in **Figure 1A**. This device can be used to determine the stress-strain properties of geological materials and also to qualitatively study the microstructural evolution of deformation. Based on the work of predecessors, scientists have developed a new generation of Griggs deformation apparatus, such as Ghaffari has reported on the development of an ultrasound probe array that allows us to monitor deforming samples in a high-pressure, high-temperature solid medium apparatus (Ghaffari and Pec, 2020). However, the Griggs rheometer employing a solid medium cannot obtain true isotropy of the confining pressure and the friction between the loading axis and the confining pressure medium makes the differential stress measurement quite inaccurate (Ji et al., 2008). To overcome these disadvantages of the Griggs rheometer, Paterson, *et al.* of the Australian National University designed the Paterson rheometer (Paterson, 1970) which is a deformation device employing a gas medium as shown in **Figure 1B**. However, because the Paterson rheometer uses a gaseous pressure medium, the confining pressure obtainable is very limited (≤ 700 MPa) and this method cannot be combined with other *in situ* measurement techniques. In the 21st century, Wang et al. (2003) developed the Deformation-DIA (**Figure 1C**) and Yamazaki and Karato (2001) developed the Rotational Deformation Apparatus (**Figure 1D**) for HT-HP deformation measurement. The D-DIA consists of four

peripheral wedges with a trapezoidal cross-section sliding on a 45° slope and a set of upper and lower symmetrical guide blocks. The upper and lower anvils can move independently of the four surrounding anvils, thus generating the differential stress. The most important feature of the RDA device is that the upper and lower anvils can rotate relative to each other. The rotation of the anvil will cause a large frictional force between the anvil surface and the sample, thus generating large shear stress in the sample. Both D-DIA and RDA can now reach a very high confining pressure of about 25 GPa and can be used in combination with the synchrotron X-ray diffraction. So they are greatly contributing to the development of solid-state geosciences. The diamond-to-top anvil pressure chamber (**Figure 1E**) is another important HT-HP device that can be easily combined with synchrotron radiation. The small size of the sample chamber (in the order of microns), the uneven heating of the sample, and the incomplete separation of pressure generation and plastic deformation in the DAC experiments make rheological studies with DAC difficult, especially because of the large errors in the stress-strain measurements (Niwa et al., 2012). The temperature and pressure range of the existing differential stress apparatus is shown in **Table 1**.

The prominent influence of the differential stress on the material properties and mineral phase transition is gaining more and more attention, while the current technically mature differential stress experimental apparatus has their own drawbacks and shortcomings. Hence, there is an urgent need to develop a HT-HP experimental apparatus that can accurately simulate the temperature, hydrostatic pressure, and differential

TABLE 1 | P-T ranges of some typical differential stress apparatus.

	P/GPa	T/K	Advantages	Shortages
Griggs	<2.0	<1,500	Large sample size	Small strain
Paterson	<0.5	<1,600	Accurate stress measurement	Low confining pressure
D-DIA	<25.0	<2000	High temperature and High confining pressure	Small strain
RDA	<28.0	<2,300	High temperature and High confining pressure	Uneven stress distribution

stress in the earth's interior and can be easily interfaced with various *in situ* measurement techniques to investigate the physical properties.

CONCLUSION AND OUTLOOK

With the rapid development and advancement of HT-HP experimental techniques, the effects of the differential stress on the physicochemical properties of rocks and minerals have been clarified. The results of these studies are of great importance for the deep understanding of geological processes in the earth's interior, deformation of the earth's internal circles, plate tectonics, geodynamics, and interpretation of geophysical observations. However, due to the limitation of the equipment, there are still many kinds of researches required regarding the effect of the differential stress on the physicochemical properties of matters such as the measurement of physical properties and experiments under the differential stress which is inseparable from the development of engineering techniques.

However, the confining pressure and produced stress that can be obtained by the existent differential stress experiments are

limited. With the development of synchrotron radiation technology and various large-chamber rheometer apparatus, it is hoped that this research field can be extended to the bottom of the lower mantle and even core conditions in the future. Synchrotron radiation technology should be combined with more *in situ* measurement techniques so that many new phenomena, new effects, and new properties of the earth's interior under high temperatures, high pressures, and differential stresses can be further discovered and applied.

AUTHOR CONTRIBUTIONS

All authors listed have made a substantial, direct, and intellectual contribution to the work and approved it for publication.

FUNDING

This project is supported by the National Natural Science Foundation of China, Project No. 42104176.

REFERENCES

- Anil, S. K., Andrault, D., and Bouvier, P. (2012). X-ray Diffraction from Stishovite under Nonhydrostatic Compression to 70 GPa: Strength and Elasticity across the Tetragonal-Orthorhombic Transition. *Phys. Earth Planet. Interiors* 208–209, 1. doi:10.1016/j.pepi.2012.07.003
- Benjamin, H. K., King, D. S. H., and Kohlstedt, D. L. (2012). Effects of Stress-Driven Melt Segregation on the Viscosity of Rocks. *Earth Planet. Sci. Lett.* 359–360, 184. doi:10.1016/j.epsl.2012.09.030
- Ben-Itzhak, L. L., Erez, J., and Aharonov, E., (2016). Precipitation of CaCO₃ in Pressure Solution Experiments: The Importance of Damage and Stress [J]. *Earth and Planetary Science Letters: A Letter Journal Devoted to the Development in Time of the Earth and Planetary System* 434, 30–41.
- Budnitzki, M., and Kuna, M. (2016). Stress Induced Phase Transitions in Silicon. *J. Mech. Phys. Sol.* 95 (1), 63–91. doi:10.1016/j.jmps.2016.03.017
- Cao, L. Z., Cheng, B. L., Wang, S. Y., Fu, W. Y., Ding, S., Sun, Z. H., et al. (2006). Influence of Stress on Raman Spectra in Ba_{1-x}Sr_xTiO₃ thin Films. *J. Phys. D: Appl. Phys.* 39, 2819–2823. doi:10.1088/0022-3727/39/13/027
- Caricchi, L., Gaillard, F., Mecklenburgh, J., and Le Trong, E. (2011). Experimental Determination of Electrical Conductivity during Deformation of Melt-Bearing Olivine Aggregates: Implications for Electrical Anisotropy in the Oceanic Low Velocity Zone. *Earth Planet. Sci. Lett.* 302, 81–94. doi:10.1016/j.epsl.2010.11.041
- Coe, R. S., Gilder, S. A., and Wright, J. P. (2012). The Thermodynamic Effect of Nonhydrostatic Stress on the Verwey Transition. *Earth Planet. Sci. Lett.* 319–320, 207–217. doi:10.1016/j.epsl.2011.11.021
- Coe, R. S. (1970). The Thermodynamic Effect of Shear Stress on the Ortho-Clinic Inversion in Enstatite and Other Coherent Phase Transitions Characterized by a Finite Simple Shear. *Contr. Mineral. Petrol.* 26, 247–264. doi:10.1007/bf00373203
- Daniel, G. A., Schmitt, M. P., Robinson, J. A., and Wolfe, D. E. (2014). Stress Induced Phase Transition in Gd₂O₃ Films by Ion Beam Assisted Reactive Electron Beam-Physical Vapor Deposition (EB-PVD). *Surf. Coat. Techn.* 242, 68. doi:10.1016/j.surfcoat.2014.01.020
- Demouchy, S., Mainprice, D., Tommasi, A., Couvy, H., Barou, F., Frost, D. J., et al. (2011). Forsterite to Wadsleyite Phase Transformation under Shear Stress and Consequences for the Earth's Mantle Transition Zone. *Phys. Earth Planet. Interiors* 184, 91–104. doi:10.1016/j.pepi.2010.11.001
- Ghaffari, H. O., and Pec, M. (2020). An Ultrasound Probe Array for a High-Pressure, High-Temperature Solid Medium Deformation Apparatus. *Rev. Scientific Instr.* 91 (8), 085117. doi:10.1063/5.0004035
- Grave, J. D., Glorie, S., and Buslov, M. M., (2014). Detrital Zircon Provenance of Early Palaeozoic Sediments at the Southwestern Margin of the Siberian Craton: Insights From U–Pb geochronology [J]. *J. Asian Earth Sci.* 82 (3), 115–123.
- Griggs, D. (1967). Hydrolytic Weakening of Quartz and Other Silicates. *Geophys. J. Int.* 14 (1–4), 19–31. doi:10.1126/science.152.3722.674-a
- Holtzman, K., and Benjamin, (2012). Effects of Stress-Driven Melt Segregation on the Viscosity of Rock [J]. *Earth Planet. Sci. Lett.* 2, 123–135.
- Imber, D., Faulkner, D. R., Mitchell, T. M., and Rutter, E. H., (2008). On the Structure and Mechanical Properties of Large Strike-Slip Faults [J]. *Geol. Soc. Spec. Publ.* 299 (1), 139–150.
- Ji, L. D., Shuwenand Zhang, (2008). Jurassic Tectonic Revolution in China and New Interpretation of the “Yanshan Movement” [J]. *Acta Geologica Sinica English Edition* 3 (2), 236–258.
- Karato, S. I. (2008). *Deformation of Earth Materials: An Introduction to the Rheology of Solid Earth*. Cambridge: Cambridge University Press, 1.
- Karato, S. I. (2013). *Physics and Chemistry of the Deep Earth*. New York: John Wiley & Sons, 1–402.
- Kausala, M., and Zhang, L. (2015). Stress-induced Phase and Structural Changes in KDP Crystals. *Comput. Mater. Sci.* 109, 359. doi:10.1016/j.commatsci.2015.07.044

- Kawano, S., and Yoshino, T. (2012). Electrical Conductivity of Magnetite-Bearing Serpentine during Shear Deformation. *Geophys. Res. Lett.* 39, L20313. doi:10.1029/2012gl053652
- Kawano, S., Yoshino, T., and Katayama, I. (2012). Electrical Conductivity of Magnetite-Bearing Serpentine during Shear Deformation. *Geophys. Res. Lett.* 39 (20), 20313. doi:10.1029/2012gl053652
- Kawamoto, E., and Shimamoto, T., (1997). The Strength Profile for Bimineralic Shear Zones: An Insight From High-Temperature Shearing Experiments on Calcite-Halite Mixtures [J]. *Tectonophysics* 295 (1), 1–14. doi:10.1016/S0040-1951(98)00112-7
- Ken, N., Nobuyoshi, M., Yusuke, S., Kenya, O., Hirotsada, G., and Takehiko, Y. (2012). *In Situ* observation of Shear Stress-Induced Perovskite to post-perovskite Phase Transition in CaIrO₃ and the Development of its Deformation Texture in a diamond-anvil Cell up to 30 GPa. *Phys. Earth Planet. Interiors* 194–195, 10. doi:10.1016/j.pepi.2012.01.007
- Korotayev, A. D., Ovchinnikov, S. V., and Pochivalov, Y. I., (2016). Structure-Phase States of the Metal Surface and Undersurface Layers After the Treatment by Powerful Ion Beams [J]. *Surf. Coat. Technol.* 105 (1–2), 84–90.
- Li, S., Ya, G., and Nan, C. (2014). Strain-induced Modulation of Magnetic Anisotropy in Co/BaTiO₃ Composite. *Chin. Sci. Bull.* 59, 5191–5193. doi:10.1007/s11434-014-0595-9
- Li, X., Xi, Z., Liu, P., Long, W., and Fang, P. (2015). Stress and Temperature-Induced Phase Transitions and thermal Expansion in (001)-cut PMN-31PT Single crystal. *J. Alloys Comp.* 652, 287–291. doi:10.1016/j.jallcom.2015.08.233
- Liu, M., Johnston, M. B., and Snaith, H. J., (2013). Efficient Planar Heterojunction Perovskite Solar Cells by Vapour Deposition [J]. *Nature* 501 (7467), 395.
- Ma, Y., Selvi, E., Levitas, V. I., and Hashemi, J. (2006). Effect of Shear Strain on the α - ϵ Phase Transition of Iron: a New Approach in the Rotational diamond Anvil Cell. *J. Phys. Condens. Matter* 18, S1075–S1082. doi:10.1088/0953-8984/18/25/s14
- Miyakawa, K., and Kawabe, I., (2014). Pressure Solution of Quartz Aggregates Under Low Effective Stress (0.42–0.61 MPa) at 25–45°C [J]. *Applied Geochemistry* 40, 61–69.
- MylvaganamKausalaand Zhang, (2015). Effect of Crystal Orientation on the Formation of Bct-5 Silicon [J]. *A. Materials science & processing* 10, 62–79.
- Niemeijer, A. R., and Spiers, C. J., (2006). Velocity Dependence of Strength and Healing Behaviour in Simulated Phyllosilicate-Bearing Fault Gouge [J]. *Tectonophysics* 1, 12–36. doi:10.1016/j.tecto.2006.03.048
- Niwa, K., Miyajima, N., Seto, Y., Ohgushi, K., Gotou, H., and Yagi, T. (2012). *In Situ* observation of Shear Stress-Induced Perovskite to post-perovskite Phase Transition in CaIrO₃ and the Development of its Deformation Texture in a diamond-anvil Cell up to 30GPa. *Phys. Earth Planet. Interiors* 194–195, 10–17. doi:10.1016/j.pepi.2012.01.007
- Paterson, M. S. (1970). A High-Pressure, High-Temperature Apparatus for Rock Deformation. *Int. J. Rock Mech. Mining Sci. Geomechanics Abstr.* 7 (5), 517–526. doi:10.1016/0148-9062(70)90004-5
- Pavel, K., Pavel, P., and Aleksey, Y. (2016). The Role of Non-hydrostatic Stresses in Phase Transitions in boron Carbide. *Comput. Mater. Sci.* 121, 106. doi:10.1016/j.commatsci.2016.04.041
- Richter, (2016). Stresses and Pressures at the Quartz-to-Coesite Phase Transformation in Shear Deformation Experiments [J]. *Journal of Geophysical Research Solid Earth Jgr* 1, 1312–1335.
- Rowe, C. D., and Griffith, W. A., (2015). Do Faults Preserve a Record of Seismic Slip: A Second Opinion [J]. *J. Struct. Geol.* 78, 1–26.
- Seyidov, M. Y., Mikailzade, F. A., Suleymanov, R. A., Bulut, N., and Salehli, F. (2016). The Influence of Uniaxial Compressive Stress on the Phase Transitions and Dielectric Properties of NaNO₂. *J. Phys. Chem. Sol.* 93, 22–26. doi:10.1016/j.jpcs.2016.02.004
- Siakavellas, M., Raptis, Y. S., Anastassakis, E., and Lockwood, D. J. (1997). Strain Effects on InSb Phonons in Bulk and Superlattice Layers. *J. Appl. Phys.* 82, 6235–6239. doi:10.1063/1.366509
- Singh, K. M., Ahir, V. B., and Tripathi, A. K., (2012). Metagenomic Analysis of Surti Buffalo (Bubalus Bubalis) Rumen: A Preliminary Study [J]. *Molecular Biology Reports* 39 (4), 4841–4848.
- Toy, M., French, A. L., Adeyemi, O. M., and Agniel, D. M., (2011). The Association of HIV Status With Bacterial Vaginosis and Vitamin D in the United States [J]. *J. Womens Health* 20 (10), 1497–1503.
- Tullis, J., and Yund, R. A., (1991). Diffusion Creep in Feldspar Aggregates: Experimental Evidence [J]. *J. Struct. Geol.* 13 (9), 987–1000.
- Tumarkina, E., Misra, S., Burlini, L., and Connolly, J. A. D. (2011). An Experimental Study of the Role of Shear Deformation on Partial Melting of a Synthetic Metapelite. *Tectonophysics* 503, 92–99. doi:10.1016/j.tecto.2010.12.004
- Wang, Y., Durham, W. B., Getting, I. C., and Weidner, D. J. (2003). The Deformation-DIA: A New Apparatus for High Temperature Triaxial Deformation to Pressures up to 15 GPa. *Rev. Scientific Instr.* 74 (6), 3002–3011. doi:10.1063/1.1570948
- Wassmann, D., and Stöckert, M., (2013). Seismic Visibility of a Deep Subduction Channel: Insights From Numerical Simulation of High-Frequency Seismic Waves Emitted From Intermediate Depth Earthquakes [J]. *Solid Earth Discussions*.
- Xu, H., Jian, A., Xue, C., Chen, Y., Zhang, B., and Zhang, W. (2008). Temperature Dependence of Biaxial Strain and its Influence on Phonon and Band gap of GaN Thin Film. *Chin. Phys. B* 17, 2245. doi:10.1088/1674-1056/17/6/051
- Xu, Y., Yan, Y., Eli Young, S., and Feng, Y. (2016). Influence of Perpendicular Compressive Stress on the Phase Transition Behavior in (Pb,Ln,Ba)₂(Zr,Sn,Ti)₂O₇ Antiferroelectric Ceramics. *Ceramics Int.* 42, 721–726. doi:10.1016/j.ceramint.2015.08.170
- Yamazaki, D., and Karato, S.-i. (2001). High-pressure Rotational Deformation Apparatus to 15 GPa. *Rev. Scientific Instr.* 72 (11), 4207–4211. doi:10.1063/1.1412858
- Zhang, B., Yoshino, T., Yamazaki, D., Manthilake, G., and Katsura, T. (2014). Electrical Conductivity Anisotropy in Partially Molten Peridotite under Shear Deformation. *Earth Planet. Sci. Lett.* 405, 98–109. doi:10.1016/j.epsl.2014.08.018
- Zhou, Y., He, C., Song, J., Ma, S., and Ma, J. (2005). An experiment Study of Quartz-Coesite Transition at Differential Stress. *Chin.Sci.Bull.* 50, 446–451. doi:10.1007/bf02897461
- Zhu, D., and Ma, W. (2014). Effect of Mechanical Stress on Phase Stability and Polarization States in Ferroelectric Barium Titanate and lead Titanate. *Ceramics Int.* 40, 6647–6654. doi:10.1016/j.ceramint.2013.11.123

Conflict of Interest: The authors declare that the research was conducted in the absence of any commercial or financial relationships that could be construed as a potential conflict of interest.

Publisher's Note: All claims expressed in this article are solely those of the authors and do not necessarily represent those of their affiliated organizations or those of the publisher, the editors, and the reviewers. Any product that may be evaluated in this article, or claim that may be made by its manufacturer, is not guaranteed or endorsed by the publisher.

Copyright © 2022 Ren and Li. This is an open-access article distributed under the terms of the Creative Commons Attribution License (CC BY). The use, distribution or reproduction in other forums is permitted, provided the original author(s) and the copyright owner(s) are credited and that the original publication in this journal is cited, in accordance with accepted academic practice. No use, distribution or reproduction is permitted which does not comply with these terms.



Lithologic Structure of the Anninghe Fault Zone: Constraints From High-Pressure Wave Velocity Experiments

Sheqiang Miao, Yongsheng Zhou*, Xi Ma and Jiaxiang Dang

State Key Laboratory of Earthquake Dynamics, Institute of Geology, China Earthquake Administration, Beijing, China

OPEN ACCESS

Edited by:

Lidong Dai,
Institute of geochemistry (CAS), China

Reviewed by:

Lin Wu,
Institute of Geology and Geophysics
(CAS), China
Yongbin Wang,
Yunnan University, China

*Correspondence:

Yongsheng Zhou
zhouysh@ies.ac.cn

Specialty section:

This article was submitted to
Solid Earth Geophysics,
a section of the journal
Frontiers in Earth Science

Received: 12 January 2022

Accepted: 31 January 2022

Published: 18 March 2022

Citation:

Miao S, Zhou Y, Ma X and Dang J
(2022) Lithologic Structure of the
Anninghe Fault Zone: Constraints
From High-Pressure Wave
Velocity Experiments.
Front. Earth Sci. 10:853474.
doi: 10.3389/feart.2022.853474

The P-wave velocities of typical rocks in the Anninghe fault zone under pressures of 50–600 MPa were systematically measured. The P-wave velocities of the felsic, intermediate, and mafic rock types under atmospheric pressure were 5.86, 6.06, and 6.50 km/s, respectively, with pressure coefficients of 2.19×10^{-4} , 3.80×10^{-4} , and 4.03×10^{-4} km/s/MPa, respectively. The results were combined with deep-imaging seismic data to establish crustal rock composition models at different depths in the study area. The composition of the Anninghe crust is very different in the horizontal and vertical directions. The most notable feature in the vertical direction is that the lithologic compositional change is gradual rather than abrupt with increasing depth. In the middle and upper crust, shallower than 25 km, the lithologic difference between the southern and northern sections of the Anninghe fault zone is primarily that the rocks in the southern section (Xichang) are more felsic than those in the northern section (Shimian).

Keywords: P-wave velocity, high-pressure experiment, lithologic structure, Anninghe fault zone, crust

INTRODUCTION

The Anninghe fault zone is located in Western Sichuan on the eastern edge of the Qinghai–Tibet Plateau. It has a total length of 150 km, starting from Shimian in the north and passing through Mianning to Xichang in the south, as shown in **Figure 1**. It inclines to the east, with an inclination ranging from 50° to 80°. The Anninghe fault zone forms the eastern boundary of the Sichuan–Yunnan block, together with three other sinistral strike-slip fault zones—Xianshuihe in the northwest and Zemuhe and Xiaojiang in the south. It is the fault zone with the most frequent seismic activity in Southwest China (Zhang, 2008). Previous studies suggested that the Anninghe fault was divided into two segments around Mianning, the northern segment of the fault is located from Shimian to Mianning and the southern segment of the fault is located from Mianning to Xichang. The observed fault activity indicates that the activity rates of the northern and southern sections are approximately 2.8–3.7 and 5–8 mm/a, respectively. Six of the eight recorded earthquakes with $M_s > 6.0$ occurred in the southern segment (Ran et al., 2008). The Anninghe fault zone is the main area of strain accumulation in the Sichuan–Yunnan region. There are some gaps or sparse sections of small earthquake activity along the fault zone, and attention should be paid to the potential for medium- and long-term strong earthquakes in this area (Wen et al., 2008).

Lithologic structure models of the fault zone form a basis for establishing the rheological structure and strength of the fault, which is significant for assessing and forecasting earthquake hazards (Christensen and Fountain, 1975; Sun et al., 2012).

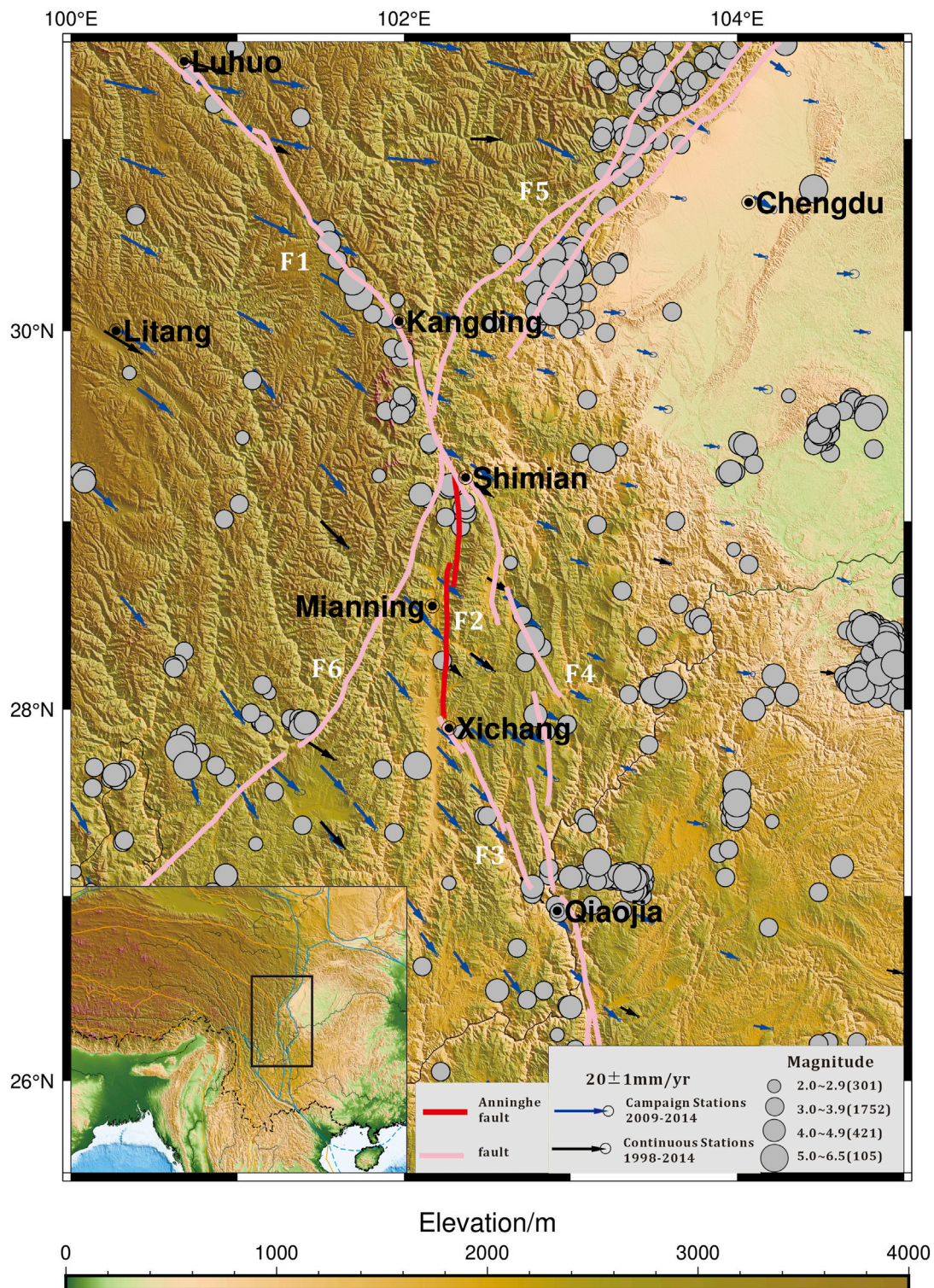


FIGURE 1 | Tectonic and topographic map of eastern margin of the Tibetan Plateau. F1: Xianshuihe fault, F2: Anninghe fault, F3: Zemuhe fault, F4: Daliangshan fault, F5: Longmenshan fault, F6: Lijiang-Xiaojinhe fault. Blue and black vectors show GPS velocity field of crustal motion in eastern margin of the Tibetan Plateau relative to the stable Eurasia. Gray small circles show epicenters of earlier documented historical earthquakes (2012–2021).

TABLE 1 | Chemical compositions and densities of the rock samples.

Sample#	SiO ₂	TiO ₂	Al ₂ O ₃	TFe ₂ O ₃	MnO	MgO	CaO	Na ₂ O	K ₂ O	P ₂ O ₅	LOI	Total	Density g/cm ⁻³
	(wt. %)												
05A	74.95	0.19	12.55	1.54	0.04	0.24	1.18	4.04	3.41	0.03	1.65	99.83	2.65
08A	76.00	0.10	11.58	1.16	0.03	0.10	1.26	4.32	3.52	0.01	1.43	99.51	2.63
11D	61.43	0.55	16.14	5.44	0.09	2.74	6.32	3.59	1.66	0.11	1.80	99.88	2.86
11E	39.35	3.74	14.79	23.97	0.23	4.40	8.92	2.23	0.43	0.32	1.52	99.89	3.22
11H	43.34	0.44	6.81	11.07	0.15	21.82	9.71	0.11	0.05	0.04	6.01	99.55	2.97
15B	59.84	0.62	15.33	6.59	0.11	3.58	6.56	3.03	1.65	0.14	2.00	99.45	2.86
16E	50.50	0.72	14.18	8.88	0.18	7.27	12.61	2.61	0.50	0.05	1.88	99.38	3.12
21G	77.26	0.05	11.97	1.13	0.03	0.10	0.45	3.55	4.58	0.01	0.80	99.93	2.61
27D	56.91	0.82	18.29	6.56	0.11	3.20	7.07	4.34	0.35	0.20	1.80	99.65	2.85
30D	52.83	0.86	18.52	8.92	0.15	4.70	7.93	3.88	0.43	0.22	0.97	99.41	2.83
38C	77.95	0.10	11.39	0.55	0.01	0.19	0.02	1.83	6.61	0.01	0.77	99.43	2.56
18G	68.29	0.34	15.09	3.49	0.09	0.65	2.62	5.18	2.45	0.08	1.20	99.48	2.65
19D	49.69	2.21	14.27	11.92	0.21	6.97	9.41	2.34	0.75	0.24	2.07	100.06	2.97
42D	45.01	1.56	11.77	11.66	0.13	14.46	9.82	1.96	0.28	0.02	2.68	99.35	3.04
45B	73.41	0.21	12.26	3.12	0.06	0.08	0.39	4.62	5.03	0.02	0.48	99.68	2.65
45C	73.15	0.35	10.58	4.92	0.13	0.18	0.67	4.43	4.52	0.01	0.70	99.64	2.65
NO.1	52.83	0.81	18.74	8.44	0.15	5.19	8.77	3.86	0.32	0.21	0.38	99.69	2.91

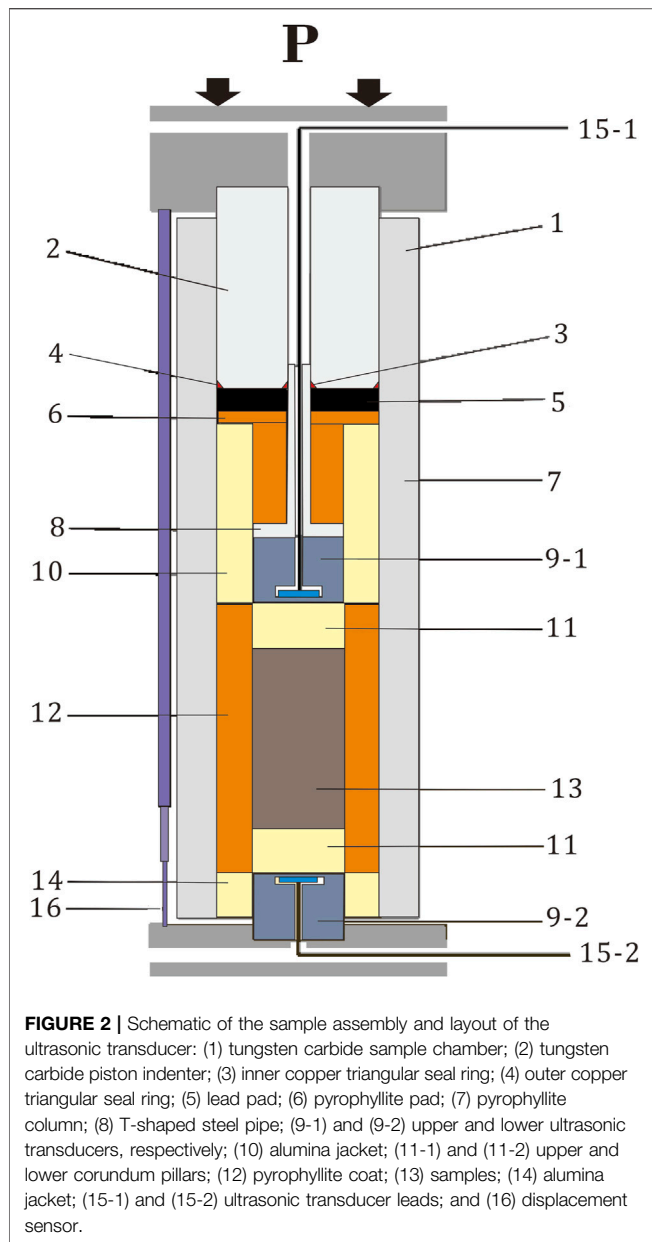


FIGURE 2 | Schematic of the sample assembly and layout of the ultrasonic transducer: (1) tungsten carbide sample chamber; (2) tungsten carbide piston indenter; (3) inner copper triangular seal ring; (4) outer copper triangular seal ring; (5) lead pad; (6) pyrophyllite pad; (7) pyrophyllite column; (8) T-shaped steel pipe; (9-1) and (9-2) upper and lower ultrasonic transducers, respectively; (10) alumina jacket; (11-1) and (11-2) upper and lower corundum pillars; (12) pyrophyllite coat; (13) samples; (14) alumina jacket; (15-1) and (15-2) ultrasonic transducer leads; and (16) displacement sensor.

Here, we report measurements of the P-wave velocities of various exposed rock types in the Anninghe fault zone up to pressures of 600 MPa. The data are compared with the crustal P-wave velocity to estimate the crustal mineral compositions and lithologic structures in Shimian, Mianning, and Xichang, which are important nodes in the study area.

SAMPLES AND METHODS

Representative samples of basement and intrusive rocks in the study area (Indosinian and Jinning granitoids, Indosinian diorites, Jinning and Hercynian mafic rocks, and Precambrian rocks) were systematically collected along the Anninghe fault zone and included granite, granodiorite, granodiorite mylonite,

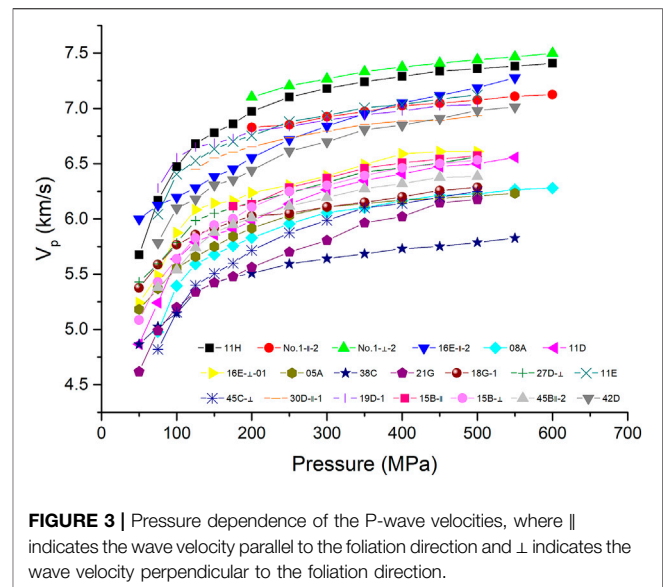


FIGURE 3 | Pressure dependence of the P-wave velocities, where \parallel indicates the wave velocity parallel to the foliation direction and \perp indicates the wave velocity perpendicular to the foliation direction.

anorthosite, diorite, mafic granulite, gabbro, diabase, and pyroxenite. The samples used in the experiments were fresh, complete, and dense, with porosities of less than 0.5%. The chemical compositions and densities of the samples are shown in **Table 1**. Principal element analyses were completed using X-ray fluorescence spectroscopy at the Institute of Geology and Geophysics, Chinese Academy of Sciences, and the densities were obtained using the immersion method.

The samples were cylinders with a diameter of 20 cm and a height of 40 cm. For the anisotropic samples, the wave velocities in the directions perpendicular and parallel to the foliation were measured. The high-pressure wave velocity experiments were completed at the State Key Laboratory of Earthquake Dynamics, Institute of Geology, China Earthquake Administration, using ultrasonic pulse transmission technology, as shown in **Figure 2** (Yang X et al., 2014). The ultrasonic transducer was 1.0-MHz LiNbO_3 , the ultrasonic sampling accuracy was 12 bits, the maximum sampling rate was 100 MHz, and the measurement accuracy was better than 1.0% ($p > 20$ MPa). The experiments were performed at room temperature and at pressures of 10–600 MPa. Because the wave velocity increased nonlinearly and rapidly with pressure under low pressures, the measurement interval was 25 MPa below 200 and 50 MPa above 200 MPa (Yang Y et al., 2014).

RESULTS AND DISCUSSION

Natural rocks may have elastic anisotropy resulting from compositional stratification, lattice-preferred orientations, and shape-preferred orientations. The arithmetic mean value of the wave velocities in different directions can be close to the wave velocity value of an isotropic rock (Ji et al., 2014; Kern et al., 2015). In this study, the P-wave velocities of 20 samples were measured. **Figure 3** summarizes the wave velocity measurement results. **Figure 4A** shows the dependence of the wave velocities of various rocks on the SiO_2 content at 500 MPa, and **Figure 4B**

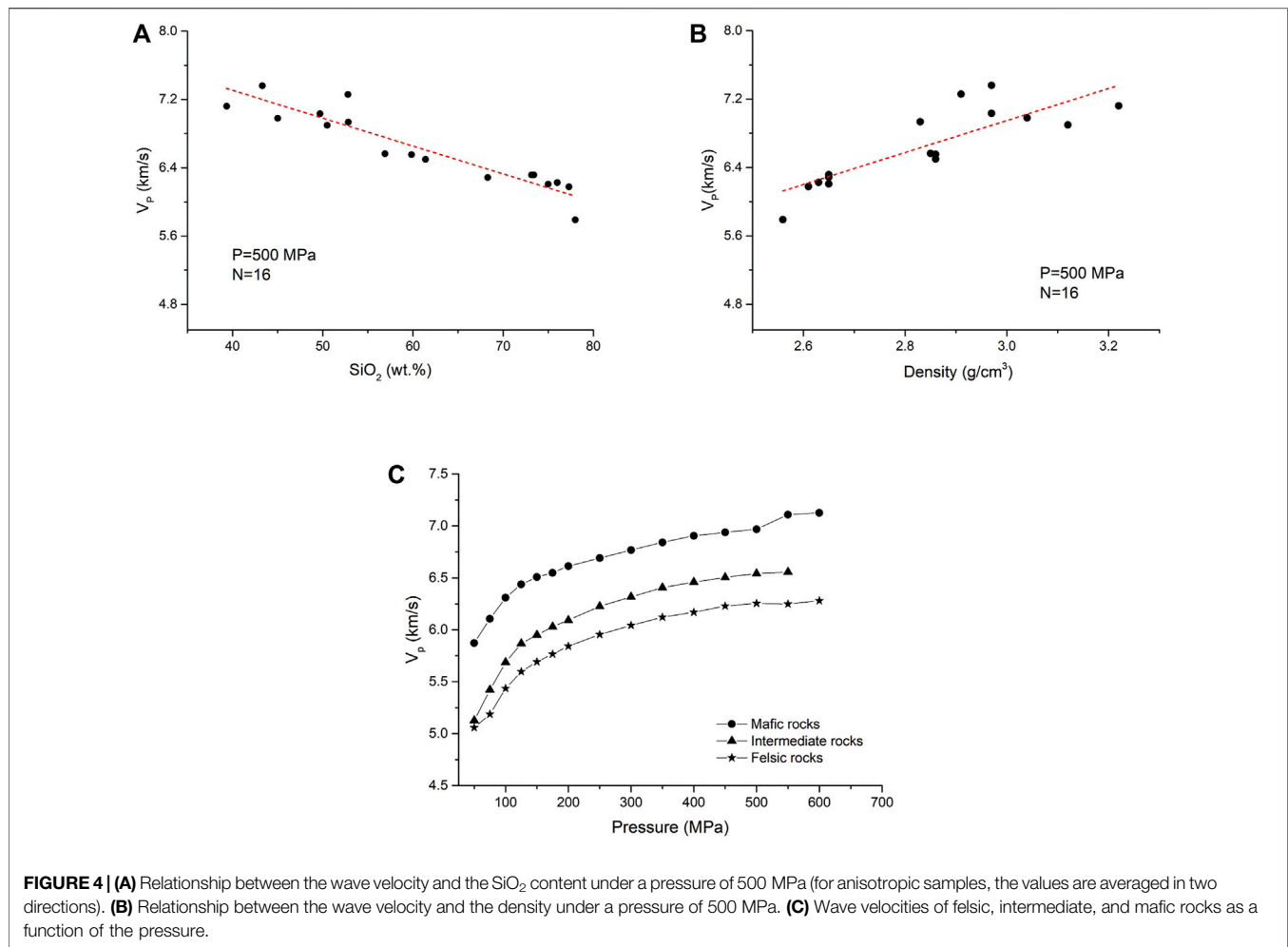


FIGURE 4 | (A) Relationship between the wave velocity and the SiO_2 content under a pressure of 500 MPa (for anisotropic samples, the values are averaged in two directions). **(B)** Relationship between the wave velocity and the density under a pressure of 500 MPa. **(C)** Wave velocities of felsic, intermediate, and mafic rocks as a function of the pressure.

shows the dependence of the wave velocities and densities of various rocks at 500 MPa. **Figure 4C** shows wave velocities of felsic, intermediate, and mafic rocks as a function of the pressure.

The experimental P-wave velocities of the rocks in the study area had the following characteristics. 1) With increasing pressure, the P-wave velocities of all rock types increased rapidly and nonlinearly in the range of 0–300 MPa. In the range of 300–600 MPa, even though the P-wave velocities increased, the increase rate slowed and the relationship between the P-wave velocity and the pressure was approximately linear. This indicates that the microcracks in the rocks were essentially closed at 300 MPa and that the P-wave velocity value in the range of 300–600 MPa reflects the intrinsic characteristics of the rocks. 2) The P-wave velocity of the rocks had an inverse correlation with the SiO_2 content and a positive correlation with the density. These laws are mafically consistent with the results obtained by multiple previous researchers (Christensen and Mooney, 1995; Ji et al., 2002). The P-wave velocities of the felsic, intermediate, and mafic rock types under atmospheric pressure were 5.86, 6.06, and 6.50 km/s, respectively, with pressure coefficients of 2.19×10^{-4} , 3.80×10^{-4} , and 4.03×10^{-4} km/s/MPa, respectively.

CRUSTAL ROCK COMPOSITION MODEL PREDICTION FOR THE ANNINGHE FAULT ZONE

Deep-imaging seismic data along the Anninghe fault are shown in **Figure 5A** (Wu Jianping, personal communication). The P-wave velocity experimental results for the basement rocks were corrected to the pressure (P) and temperature (T) conditions of the middle and lower crust using the following equation:

$$V(z) = V_0 + DP(z) + (dV/dT)[T(z) - 20] \quad (1)$$

where Z is the depth, V_0 is the extrapolated zero pressure wave velocity, D is the pressure derivative of the wave velocity, P is the lithostatic pressure, and dV/dT is the temperature reciprocal of the wave velocity, which is assumed to be 3.5×10^{-4} km/s/°C here. The temperature–depth profile for the Anninghe fault zone was calculated based on the surface heat flow of 55 mW/m² (Hu et al., 2001). The results are shown in **Figure 5B**.

In general, the crust along the Anninghe fault zone is divided into upper, middle, and lower layers. The thicknesses of the upper, middle, and lower crust are 20 km, 20 km, and approximately 10 km, respectively (Li et al., 2016; Zhu et al.,

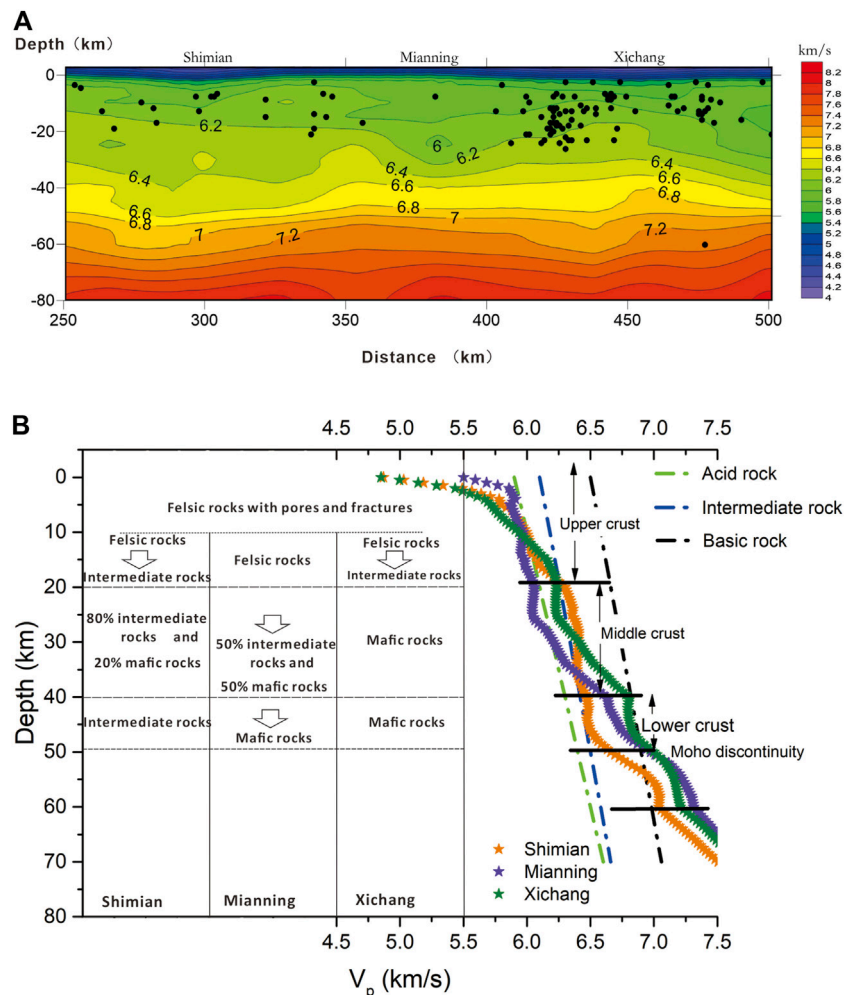


FIGURE 5 | (A) Deep-imaging seismic data along the Anninghe fault. Black small circles show hypocenters of earlier documented historical earthquakes (2008–2021). **(B)** Comparison between the experimental data and the deep-imaging seismic data shown alongside the crustal rock composition model.

2017). Comparing the experimental data with the deep-imaging seismic data indicates that the lithospheric composition in the study area is very different in the transverse and longitudinal directions and that the wave velocity of each layer does not correspond to a single felsic or mafic rock type because the wave velocity obviously falls between those of the two rock types. In this case, the proportion of each lithology was calculated according to the Voigt–Reuss–Hill model (Sun et al., 2012).

The estimations of the crustal lithologic compositions in Shimian, Mianning, and Xichang are shown in **Figure 5B**. At depths of 0–10 km, the wave velocity gradually increases from 5.5 to 6.0 km/s, corresponding to the gradual closure of the pores and fractures of the felsic rocks.

Within the middle crust, the change rate of the wave velocity with depth in Mianning and Xichang is significantly greater than those of the felsic or mafic rock types obtained in the laboratory; therefore, there is an obvious compositional change with depth. The most notable feature in the vertical direction is that the lithologic

compositional change is gradual rather than abrupt with increasing depth.

In the middle and upper crust, shallower than 25 km, that is, at the lower limit of the main seismogenic depth for earthquakes, the lithological difference between the southern and northern sections of the Anninghe fault zone is primarily that the rocks in the southern section (Xichang) are more felsic than those in the northern section (Shimian). Whether this lithologic difference leads to the rapid slip rate in the south section, where most of the large earthquakes above 6.0 occur, is worthy of further investigation.

CONCLUSION

The P-wave velocities of various rock types in the Anninghe fault zone under pressures of 0–600 MPa were systematically measured. The results were combined with deep-imaging seismic data to establish crustal rock composition models at different depths in the study area. At depths of 0–10 km, the wave velocity gradually

increases from 5.5 to 6.0 km/s, corresponding to the gradual closure of the pores and fractures in felsic rocks. With increasing depth, the composition changes significantly, with the lithology gradually changing from felsic rocks to a mixture of intermediate and mafic rocks at the bottom of the middle crust. In the middle and upper crust, shallower than 25 km, the rocks in the southern section (Xichang) of the Anninghe fault zone are more felsic than those in the northern section (Shimian).

DATA AVAILABILITY STATEMENT

The original contributions presented in the study are included in the article/supplementary material, further inquiries can be directed to the corresponding author.

AUTHOR CONTRIBUTIONS

ZY contributed to conception and design of this study. SM conducted the experiments and wrote the first draft of the

manuscript. All authors contributed to manuscript revision, read, and approved the submitted version.

FUNDING

This study was supported by the National Key Research and Development Program of China (Grant 2018YFC1503400) and the Basic Research Fund of the Institute of Geology, China Earthquake Administration (IGCEA1912).

ACKNOWLEDGMENTS

We thank Prof. Lidong Dai for his kind invitation, Prof. Xiaosong Yang and Wenbo Qi for their valuable technical support during the experimental phase, Prof. Jianping Wu for providing the deep-imaging seismic data, Wenming Yao for providing assistance with the sample preparation, and Tongbin Shao for his valuable suggestions which significantly improved the manuscript.

REFERENCES

- Christensen, N. I., and Fountain, D. M. (1975). Constitution of the Lower Continental Crust Based on Experimental Studies of Seismic Velocities in Granulite. *Geol. Soc. America Bull.* 86, 227–236. doi:10.1130/0016-7606(1975)86<227:cotlcc>2.0.co;2
- Christensen, N. I., and Mooney, W. D. (1995). Seismic Velocity Structure and Composition of the continental Crust: A Global View. *J. Geophys. Res.* 100, 9761–9788. doi:10.1029/95jb00259
- Hu, S. B., He, L. J., and Wang, J. Y. (2001). Compilation of Heat Flow Data in the China continental Area (3rd Edition). *Chin. J. Geophys.* 44 (5), 611–626. (in Chinese with English abstract). doi:10.1002/cjg2.180
- Ji, S., Shao, T., Salisbury, M. H., Sun, S., Michibayashi, K., Zhao, W., et al. (2014). Plagioclase Preferred Orientation and Induced Seismic Anisotropy in Mafic Igneous Rocks. *J. Geophys. Res. Solid Earth* 119, 8064–8088. doi:10.1002/2014jb011352
- Ji, S., Wang, Q., and Xia, B. (2002). *Handbook of Seismic Properties of Minerals, Rocks and Ores*. Presses inter Polytechnique.
- Kern, H., Lokajicek, T., Svitek, T., and Wenk, H. R. (2015). Seismic Anisotropy of Serpentine from Val Malenco, Italy. *J. Geophys. Res. Solid Earth* 120, 4113–4129. doi:10.1002/2015jb012030
- Li, M., Zhang, S., Wang, F., Wu, T., and Qin, W. (2016). Crustal and Upper-Mantle Structure of the southeastern Tibetan Plateau from Joint Analysis of Surface Wave Dispersion and Receiver Functions. *J. Asian Earth Sci.* 117, 52–63. doi:10.1016/j.jseas.2015.12.002
- Ran, Y., Chen, L., Cheng, J., and Gong, H. (2008). Late Quaternary Surface Deformation and Rupture Behavior of strong Earthquake on the Segment north of Mianing of the Anninghe Fault. *Sci. China Ser. D-earth Sci.* 51, 1224–1237. doi:10.1007/s11430-008-0104-6
- Sun, S., Ji, S., Wang, Q., Wang, H., Long, C., and Salisbury, M. (2012). Seismic Properties of the Longmen Shan Complex: Implications for the Moment Magnitude of the Great 2008 Wenchuan Earthquake in China. *Tectonophysics* 564–565, 68–82. doi:10.1016/j.tecto.2012.06.018
- Wen, X., Fan, J., Yi, G., Deng, Y., and Long, F. (2008). A Seismic gap on the Anninghe Fault in Western Sichuan, China. *Sci. China Ser. D-earth Sci.* 51, 1375–1387. doi:10.1007/s11430-008-0114-4
- Yang, X., Yang, Y., and Chen, J. (2014). Pressure Dependence of Density, Porosity, Compressional Wave Velocity of Fault Rocks from the Ruptures of the 2008 Wenchuan Earthquake, China. *Tectonophysics* 619–620, 133–142. doi:10.1016/j.tecto.2013.09.012
- Yang, Y., Chen, J. Y., and Yang, X. S. (2014). Experimental Studies on Relationship between P-Wave Velocity and Porosity of Fault Rocks from the Rupture of the 2008 Wenchuan Earthquake. *Chin. J. Geophys.* 57, 1883–1890. (in Chinese with English abstract).
- Zhang, P. Z. (2008). Present Tectonic Deformation, Strain Distribution and Deep Dynamic Process in Western Sichuan on the Eastern Margin of Qinghai–Tibet Plateau. *Sci. China: Earth Sci.*, 1041–1056.
- Zhu, J. S., Wang, X. B., Yang, Y. H., Fan, J., and Cheng, X. Q. (2017). The Crustal Flow beneath the Eastern Margin of the Tibetan Plateau and its Process of Dynamics. *Chin. J. Geophys.* 60, 2038–2057. (in Chinese with English abstract).

Conflict of Interest: The authors declare that the research was conducted in the absence of any commercial or financial relationships that could be construed as a potential conflict of interest.

Publisher's Note: All claims expressed in this article are solely those of the authors and do not necessarily represent those of their affiliated organizations, or those of the publisher, the editors and the reviewers. Any product that may be evaluated in this article, or claim that may be made by its manufacturer, is not guaranteed or endorsed by the publisher.

Copyright © 2022 Miao, Zhou, Ma and Dang. This is an open-access article distributed under the terms of the Creative Commons Attribution License (CC BY). The use, distribution or reproduction in other forums is permitted, provided the original author(s) and the copyright owner(s) are credited and that the original publication in this journal is cited, in accordance with accepted academic practice. No use, distribution or reproduction is permitted which does not comply with these terms.



Elastic-Wave Radiation, Scattering, and Reception of a Dipole Acoustic Logging-While-Drilling Source in Unconsolidated Formations

Zhen Li¹, Qiaomu Qi^{1,2*}, Chuang Hei³, Can Jiang⁴ and Xing-Jian Wang¹

¹State Key Laboratory of Oil and Gas Reservoir Geology and Exploitation, Chengdu University of Technology, Chengdu, China,

²College of Geophysics, Chengdu University of Technology, Chengdu, China, ³Electronics and Information College, Yangtze University, Jingzhou, China, ⁴Institute of Acoustics, Chinese Academy of Sciences, Beijing, China

OPEN ACCESS

Edited by:

Lidong Dai,
Institute of geochemistry (CAS), China

Reviewed by:

Zhengan Wu,
Southwest Petroleum University,
China
Tianyang Li,
Chongqing University, China

*Correspondence:

Qiaomu Qi
qiaomu_qi@163.com

Specialty section:

This article was submitted to
Solid Earth Geophysics,
a section of the journal
Frontiers in Earth Science

Received: 19 February 2022

Accepted: 10 March 2022

Published: 29 March 2022

Citation:

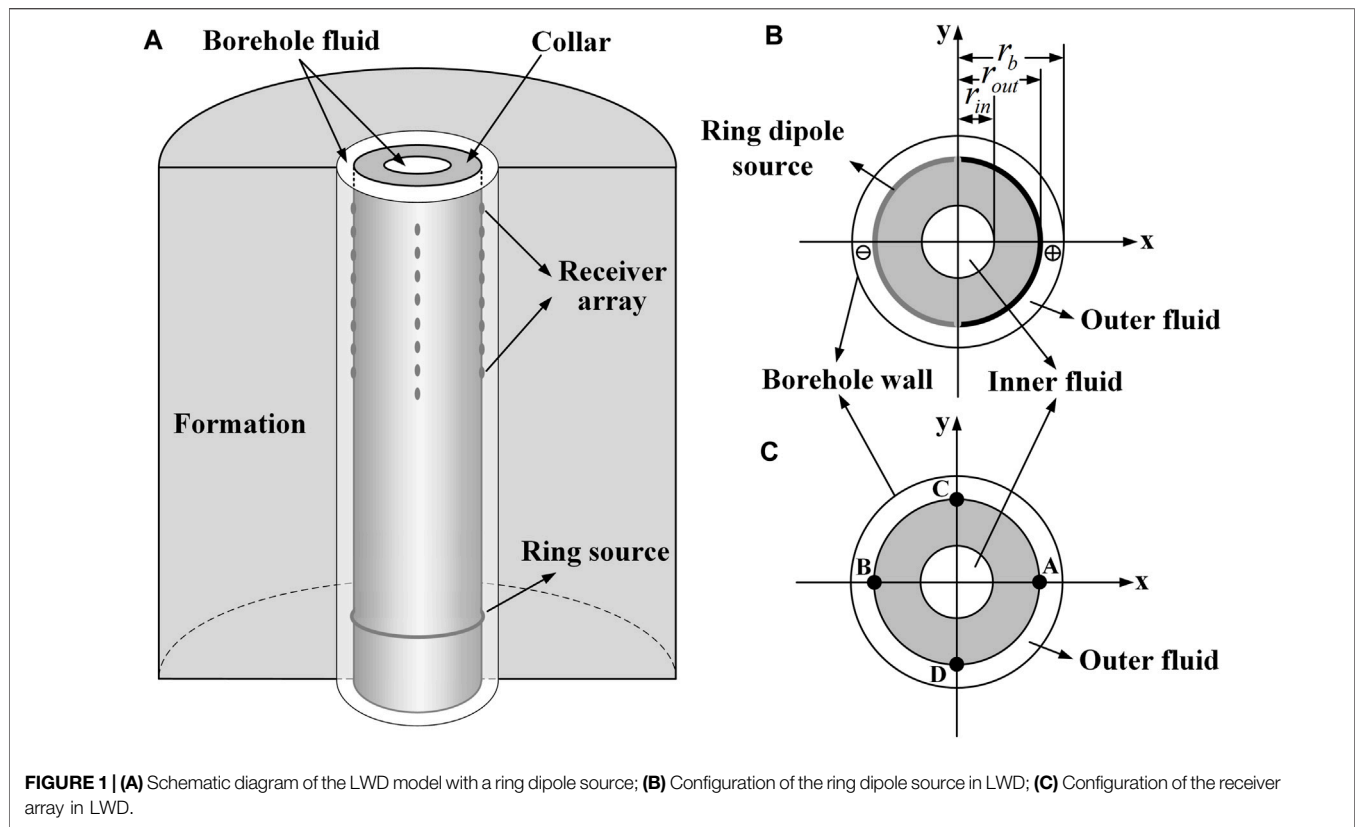
Li Z, Qi Q, Hei C, Jiang C and
Wang X-J (2022) Elastic-Wave
Radiation, Scattering, and Reception
of a Dipole Acoustic Logging-While-
Drilling Source in
Unconsolidated Formations.
Front. Earth Sci. 10:879345.
doi: 10.3389/feart.2022.879345

Single-well acoustic imaging in logging-while-drilling (LWD) has important application potential in evaluating cluster-well drilling safety as it can be applied to the real-time detection of an existing cased borehole from a new well during drilling. Forward modelling can help us understand the mechanism of elastic-wave radiation, scattering and reception. In this work, we investigate the characteristics of acoustic wavefields associated with LWD in an unconsolidated formation. We use the time-domain finite difference (FDTD) method to simulate the wavefields corresponding to a ring dipole source. The modeling results reveal the existence of a new Mach wave apart from the conventional P- and S-waves. The Mach waves are secondary waves resulting from the constructive interference of the collar waves. Such wave is often overlooked in the previous studies of single-well acoustic imaging in LWD. We found that not only P- and S-waves but also the Mach waves could be scattered by the nearby cased borehole and propagate back to the original borehole. The simulations indicate that both the scattered P-waves and the scattered Mach S-waves exhibit strong amplitudes. This study provides a theoretical foundation for the borehole detection by LWD single-well acoustic imaging technique in unconsolidated formations.

Keywords: single-well acoustic imaging, LWD, mach waves, nearby borehole detection, unconsolidated formation

INTRODUCTION

Single-well acoustic imaging has achieved rapid development in the last decades. Based on the elastic waves reflected or scattered back to the borehole, the technique could provide geological structures information located at tens of meters away from the borehole and plays an important role in oil and gas exploration process (Hornby, 1989; Tang, 2004; Haldorsen et al., 2006; Tang and Patterson, 2009; Hirabayashi et al., 2017; Hirabayashi, 2020). To verify the effectiveness of single-well acoustic imaging and provide a method for testing downhole acoustic imaging tools, Tang et al. (2016) conducted physical experiments with two test boreholes drilled with a distance of 10 m. The target hole can be well imaged from the measurement hole despite the size of the borehole is much smaller than the wavelength. Their pioneering work proved that the single-well acoustic imaging could be used for the detection of nearby boreholes, which is of great significance for drilling safety evaluation in densely drilled fields.

**TABLE 1 |** Model parameters of the LWD.

	P-Velocity (m/s)	S-Velocity (m/s)	Density (kg/m ³)	Outer Radius (m)
Inner fluid	1,500	--	1,000	0.035
Drill collar	5,860	3,130	7,850	0.14
Outer fluid	1,500	--	1,000	0.205
Formation	1800	460	2000	∞

In recent years, cluster-well drilling has been widely adopted especially in offshore exploration and development because the procedure can significantly reduce the drilling costs. The formations in shallow-water marine environments is usually very soft and unconsolidated. The borehole source radiation and propagation in such formations are quite different from in the consolidated fast formations. Gu et al. (2021) studied the elastic-wave radiation from a dipole source in an open borehole and its scattering occurs at a nearby cased borehole for an unconsolidated formation. The results show that compared to SH-waves, P-waves are more advantageous for the borehole detection in unconsolidated formations. Compared to the conventional wireline logging, logging-while-drilling (LWD) can provide real-time formation parameters, it is useful to apply single-well acoustic imaging among other LWD acquisitions. A number of theoretical and practical studies on single-well acoustic

imaging in LWD have been done in the past few years. Tang et al. (2007) achieved the first imaging of the formation interface using the LWD monopole waveform data. Cao et al. (2016), Wei et al. (2019) studied the radiation and reflection of the P- and S-waves with an LWD dipole source. Yang et al. (2019) simulated the acoustic fields excited by linear phased array acoustic transmitters to realize azimuth identification. Pan et al. (2020) investigated the wave reflection and scattering in a borehole with finite depth based on numerical simulation. Up to now, the radiation and scattering of a dipole source in unconsolidated slow formations has not yet been investigated. Meanwhile, the previous studies only focus on the P- and S-waves radiated directly from the source. Meredith et al. (1993) pointed out that the Mach waves will generate when the tube-wave velocity is greater than the formation S-wave velocity. In the context of LWD acquisition, as a result of the good coupling between the

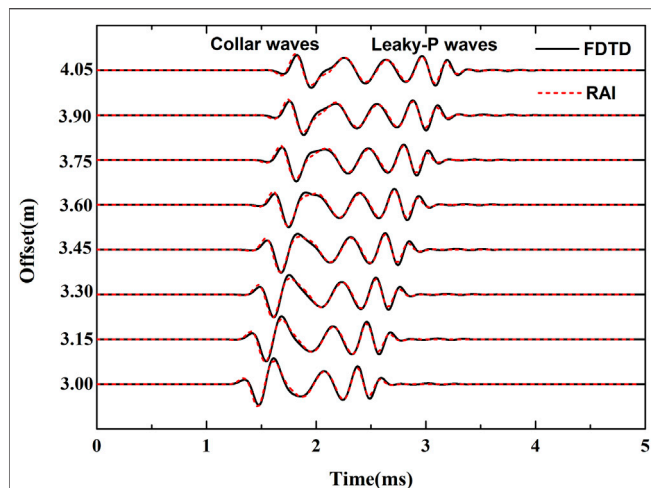


FIGURE 2 | Comparison between the modeling results of the numerical FDTD (black solid line) and semi-analytical RAI (red dot line) methods.

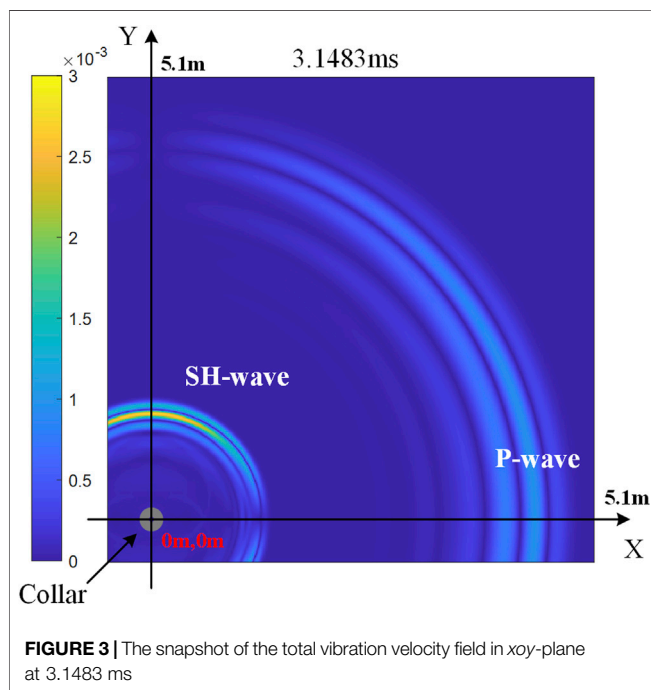


FIGURE 3 | The snapshot of the total vibration velocity field in xoy-plane at 3.1483 ms

drill collar and transmitters, strong collar waves will form. The collar-wave velocity is usually greater than the formation S-wave velocity, sometimes even greater than the formation P-wave velocity. Hence, Mach waves will exist in most acoustic measurements in LWD and its radiation from the borehole and scattering outside the borehole have not been fully understood.

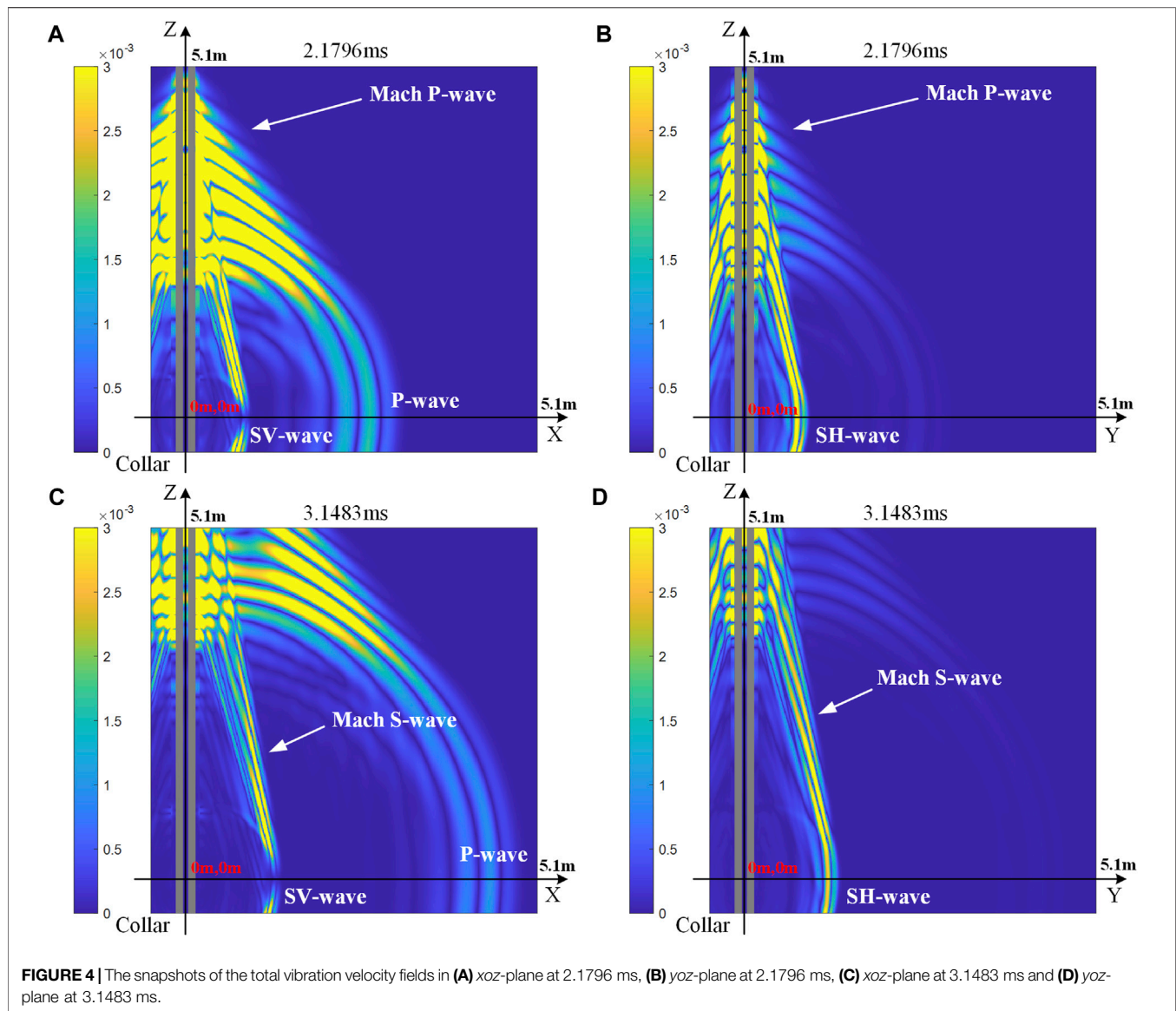
Understanding the elastic-wave radiation, scattering and reception characteristics in an LWD environment for an unconsolidated formation can help us evaluate the

performance of different types of waves for single-well acoustic imaging. In this paper, we first simulate the acoustic fields in an unconsolidated formation excited by a ring dipole LWD source and analyze the characteristics of the radiation of the P-, S- and Mach waves. Then, we model the scattering of the radiated waves occurred at a nearby cased borehole. Lastly, we analyze the received signal of the scattering waves from the cased borehole. We compare the arrival times and amplitudes between different types of scattered waves received in the measurement borehole. The synthetic study provides a theoretical foundation for the borehole detection by LWD single-well acoustic imaging technique, which is meaningful for the evaluation of cluster-well drilling safety in shallow-water marine environments.

DIPOLE LWD MODEL AND VALIDATION OF SIMULATION RESULTS

The schematic of the LWD model with a dipole source is illustrated in **Figure 1**. The drill collar is centered and occupies most of the space of the borehole. The borehole is surrounded by an unconsolidated formation with low P- and S-wave velocities. A ring dipole source is placed on the surface of the drill collar as shown in **Figures 1A,B**. The dipole source is composed of two half circular sources which can generate radial forces with same amplitudes but opposite phases. The polarization direction of the dipole source is in x -direction (see **Figure 1B**). The receiver array including four sub-arrays is also on the surface of the collar as shown in **Figures 1A,C**. The interval between two adjacent receivers is 0.15 m. The minimum offset, i.e., the distance between the source and first receiver, is 3.0 m. The outer radius of the inner fluid, drill collar and outer fluid is $r_{in} = 0.035$ m, $r_{out} = 0.14$ m and $r_b = 0.205$ m, respectively. The outer radius of the formation is infinite. The parameters of the borehole fluid, drill collar and formation used in the elastic modeling are shown in **Table 1**.

Numerical simulation is widely used in the theoretical study of the acoustic logging (Li et al., 2020). In this study, the three-dimensional finite-difference method in time-domain (FDTD) is used in the simulation of the elastic wave propagation (Cheng et al., 1995). The perfectly matched layer (PML) is usually used for removing the artificial wave reflection caused by the truncation of the computational zone in the numerical simulation of both electromagnetics and elastodynamics (Liu and Sinha, 2003; Zhang et al., 2019). We use the complex frequency-shifted perfectly matched layer (CFS-PML) method (Zhang and Shen, 2010) to remove the artificial reflection which is caused by the truncation of the computational domain. The source function is the standard Ricker source with 3 kHz center frequency which is the typical frequency used in real dipole acoustic logging. In the modeling, the grid size in FDTD is 5 mm and the thickness of the CFS-PML is 30 grid cells. To validate the accuracy of the modeling results, we



compare the synthetic waveforms modeled by FDTD and real-axis integration (RAI) methods (Tang and Cheng, 2004). The waveforms recorded here are fluid displacements which are taken as the difference between the positions of A and B in the subarrays (see **Figure 1C**) (Tang and Cheng, 2004). As shown in **Figure 2**, the modeling result of FDTD (black solid lines) agrees well with the modeling result of RAI (red dot lines). Strong collar waves and leaky-P waves can be observed. The leaky-P wave is a wave mode which is dispersive and attenuative. It travels along the borehole and radiates energy into the formation. Differently, the P- and S-wave radiated from the source directly are both body waves traveling in the formation. The Mach wave is secondary wave caused by constructive interference of the radiated collar wave.

RADIATION FROM A RING DIPOLE SOURCE IN LWD

To investigate the radiation characteristics of the ring dipole source, we first simulated the elastic wave propagation in a homogeneous unconsolidated formation in the context of LWD acquisition. The computational domain is from -0.5 to 5.1 m in all x -, y - and z -directions. The center of the ring dipole source is at the origin of the coordinate. The geometry and parameters for elastic modeling are given in **Table 1**. As the velocity-stress staggered grid is used in the FDTD simulation, the vibration velocity can be used to represent the radiation characteristics. The total vibration velocity can be calculated based on the velocity component, i.e., v_x , v_y and v_z in a Cartesian coordinate system.

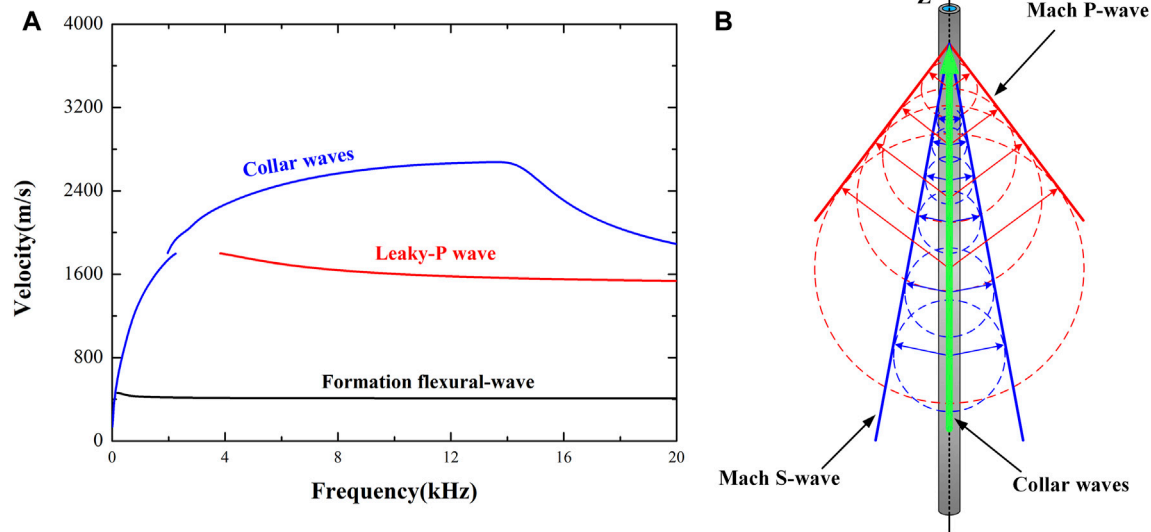


FIGURE 5 | (A) The phase velocity dispersion curves of the inner borehole wave modes; **(B)** Schematic diagram of the generation of the Mach P-wave and Mach S-wave.

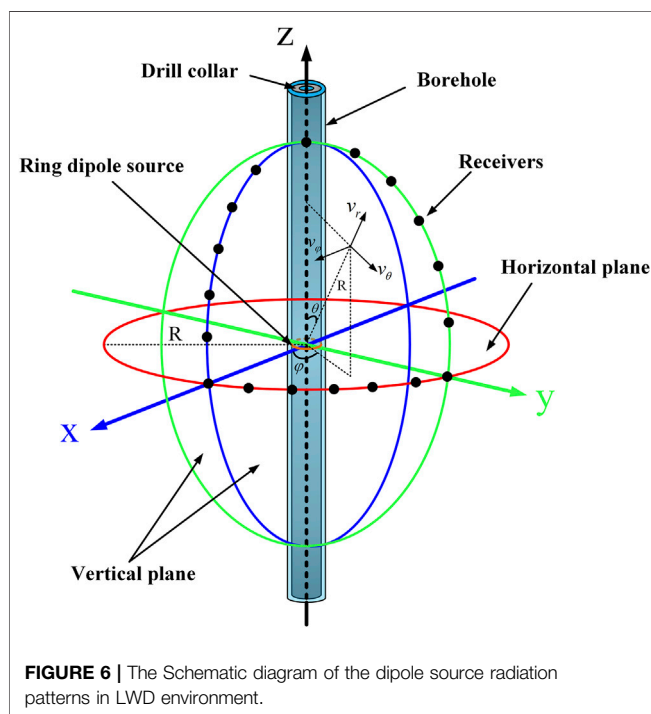
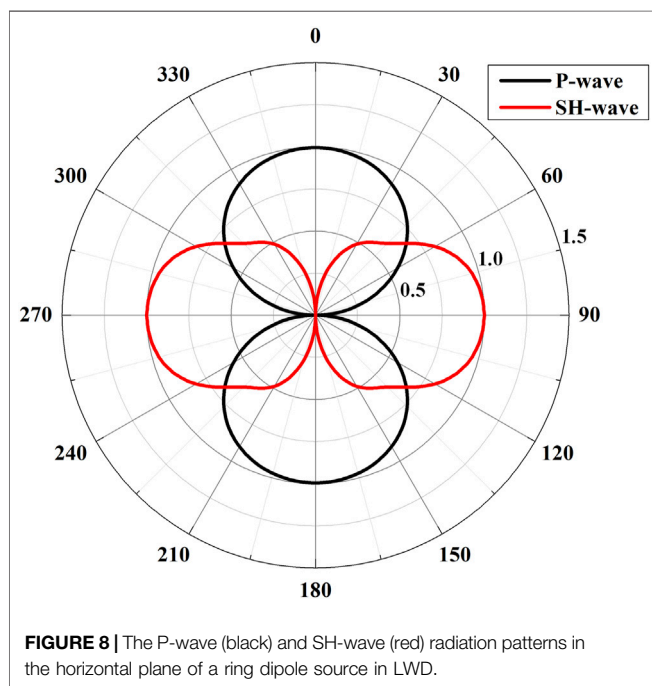
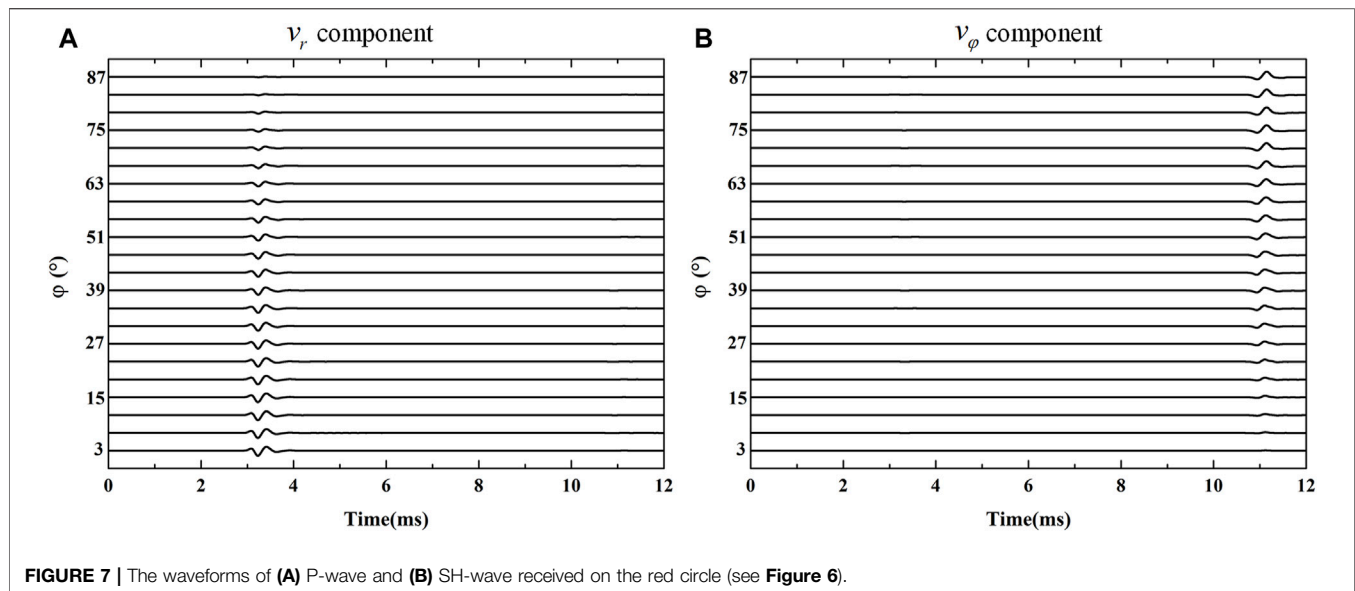


FIGURE 6 | The Schematic diagram of the dipole source radiation patterns in LWD environment.

Figure 3 shows the snapshot of total vibration velocity in the xoy -plane at 3.1483 ms. The wave propagation pattern in the horizontal plane in LWD context is similar to the results associated with an open borehole. The snapshot reveals the propagation P- and SH-waves which have different dominant radiation directions (Tang et al., 2014). The amplitude of the

P-wave in x -direction is larger than that of the S-wave. The snapshots of the total vibration velocity in the vertical planes are shown in Figure 4. Apart from the P- and S-waves radiated from the source directly, there also exists secondary P- and S-waves, which are closely related to the collar waves. These secondary waves are commonly known as Mach waves. As the transmitter is well coupled to the drill collar, strong collar waves are produced. The collar waves will radiate into the formation and form secondary waves. Figure 5A shows the phase velocity dispersion curves of collar waves (blue line), leaky-P waves (red) and formation flexural-waves (black) (Zheng and Hu, 2017). The propagation velocity of the collar waves is faster than the P- and S-waves in most frequency range. The collar waves will interfere constructively and this leads to the formation of the secondary Mach waves as shown in Figure 5B (Meredith et al., 1993). To distinguish the two secondary waves propagating at different velocities, here we name them as Mach P-wave and Mach S-wave, respectively. The sine of the propagation angle of Mach wave, which is the angle between the borehole axis and the wavefront of the Mach waves, is equal to the ratio of P-/S-wave velocity to collar-wave velocity. As the collar-wave is dispersive (see blue line in Figure 5A), the Mach wave also behaves as dispersive wave. The width of the wave package will increase as the collar wave propagates in z -direction. Interestingly, as the collar waves excited by a dipole source are directional, the corresponding Mach waves radiated into the formation by collar waves are also directional. Figures 4A,C show the snapshots in xoz -plane, while Figures 4B,D show the snapshot in yo -plane. Apparently, the amplitudes of Mach waves are different in different directions.

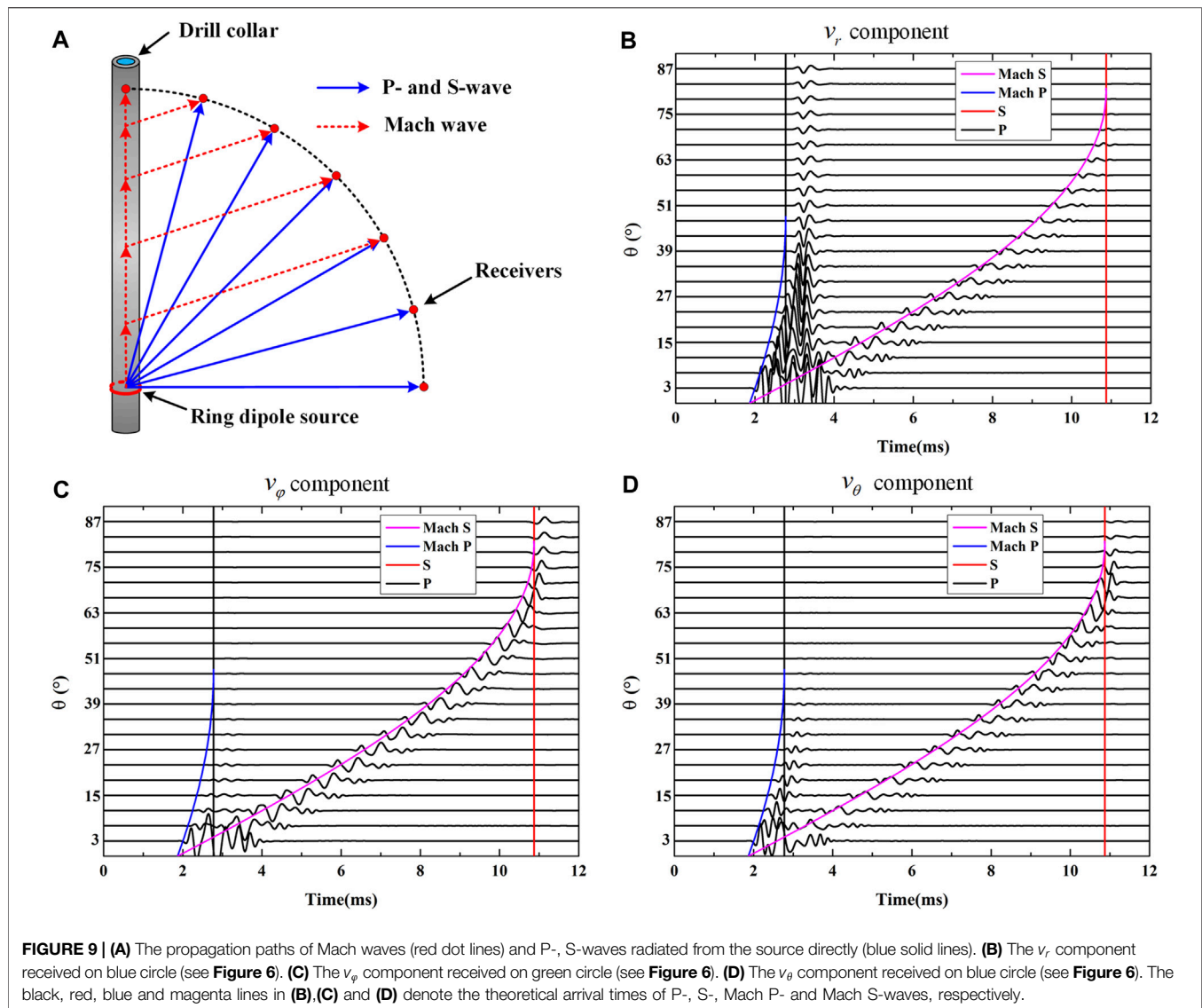
To further investigate the radiation characteristics, we recorded the transient waveforms on three circles



representing three orthogonal directions as shown in Figure 6. The centers of these circles are at the origin. The radii R of these circles are all 5.0 m. The red, blue and green circles are in xoy -, xoz -, and yoz -plane respectively. The small black spheres represent the receivers on the circles. The vibration velocities v_r , v_θ and v_ϕ in spherical coordinate were derived from v_x , v_y and v_z by coordinate transformation. According to the polarization direction of these waves, the v_r , v_θ and v_ϕ in Spherical coordinate correspond to P-, SV- and SH-waves, respectively. Figure 7 shows the v_r (P-wave) and v_ϕ components (SH-wave) received

on the red circle. The v_θ component is not shown here due to the fact that SV-wave is always zero in the xoy -plane. The vertical axis is the azimuth ϕ and the abscissa is time. Both P- and SH-waves consist of one wave packet. The arrival times of waves in different azimuths are the same because their propagation distances are equal. The radiation patterns of the P- and SH-waves can be obtained by plotting the maximum absolute values of the vibration velocities in the Polar coordinates. The amplitudes are normalized by the amplitude of SH-waves at $\phi = 90^\circ$. As shown in Figure 8, both the P- and SH-waves are directional, and the maximum amplitudes of the P- and SH-waves are comparable in the horizontal plane.

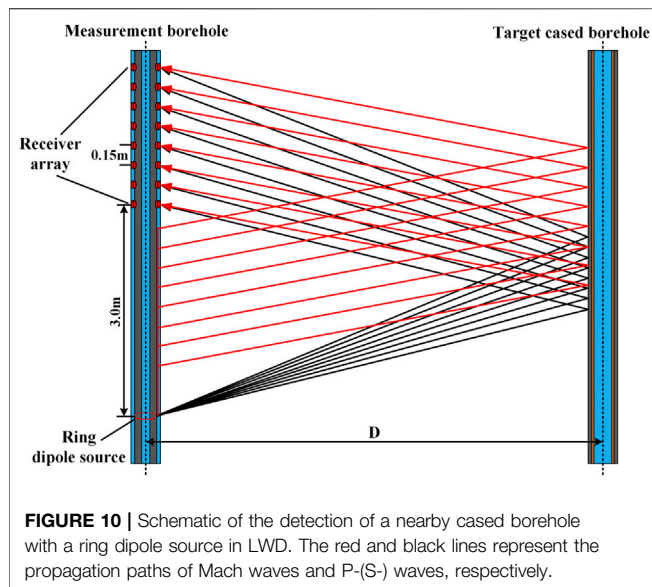
For the waves radiated from the borehole in the vertical planes, the wavefields are more complicated. As we discussed earlier, apart from the P- and S-waves radiated from the source directly, the Mach waves, which are secondary waves, play an important part in the wavefields. As shown in Figure 9A, the propagation paths of the Mach waves are different from the P- and S-waves. For the receivers in the vertical planes, the travel-path of the Mach waves is composed of two parts. The collar wave first travels along the drill collar with a much higher speed and then it radiates into the formation with the velocity of P-/S-wave of the formation (see red dot lines in Figure 9A). However, for the P- and S-waves radiated directly from the source, the propagation distances from the source to the receivers on the blue and green circle are all the same (blue solid lines in Figure 9A). As shown in Figures 9B–D, the arrival times of the P- or S-waves at different θ on the vertical circles are equal. This is the same with the results in xoy -plane. On the other hand, as shown in Figures 9B–D the arrival times of Mach waves changes with the angle θ because their propagation paths are different for different receivers. Figures 9B,D show the v_r and v_θ component in the xoz -



plane respectively. **Figure 9C** shows the v_ϕ component in the yoz -plane. As shown in **Figure 6**, when θ is small, the receivers are very close to the drill collar. In this case, the amplitudes of the waves close to the onset of P-waves are heavily influenced by the collar waves. These waves mainly propagate along the borehole and are not made use of for the detection of structures outside the borehole. The modeling results in **Figures 9B–D** show that the P-waves have much higher amplitudes than the S-waves, which is similar to the case of wireline logging in an open borehole in unconsolidated formations (Gu et al., 2021). However, the existence of the drill collar results in the generation of the Mach S-waves with high amplitudes. The Mach S-waves also exist in both x - and y -directions. Compared to the Mach S-waves, the influence of the Mach P-waves is relatively weak.

NEARBY CASED BOREHOLE SCATTERING AND RECEPTION IN LWD ACQUISITION

To investigate the wave scattering by a nearby cased borehole, we build a dual-borehole model to simulate the nearby borehole detection during the LWD acquisition. **Figure 10** shows the physical model for nearby borehole detection with a ring dipole source in an LWD measurement. The axes of the two boreholes are parallel to each other with a distance of D . The nearby cased borehole is assumed to be well cemented. The geometry and physical parameters of the nearby borehole are listed in **Table 2**. The parameters of the measurement borehole and drill collar are the same with the previous example (see **Table 1**). The black and red lines denote the propagation paths of P-(S-) waves and Mach waves respectively. The propagation



paths of Mach waves are also composed of two parts, which is similar to the case shown in **Figure 9A**.

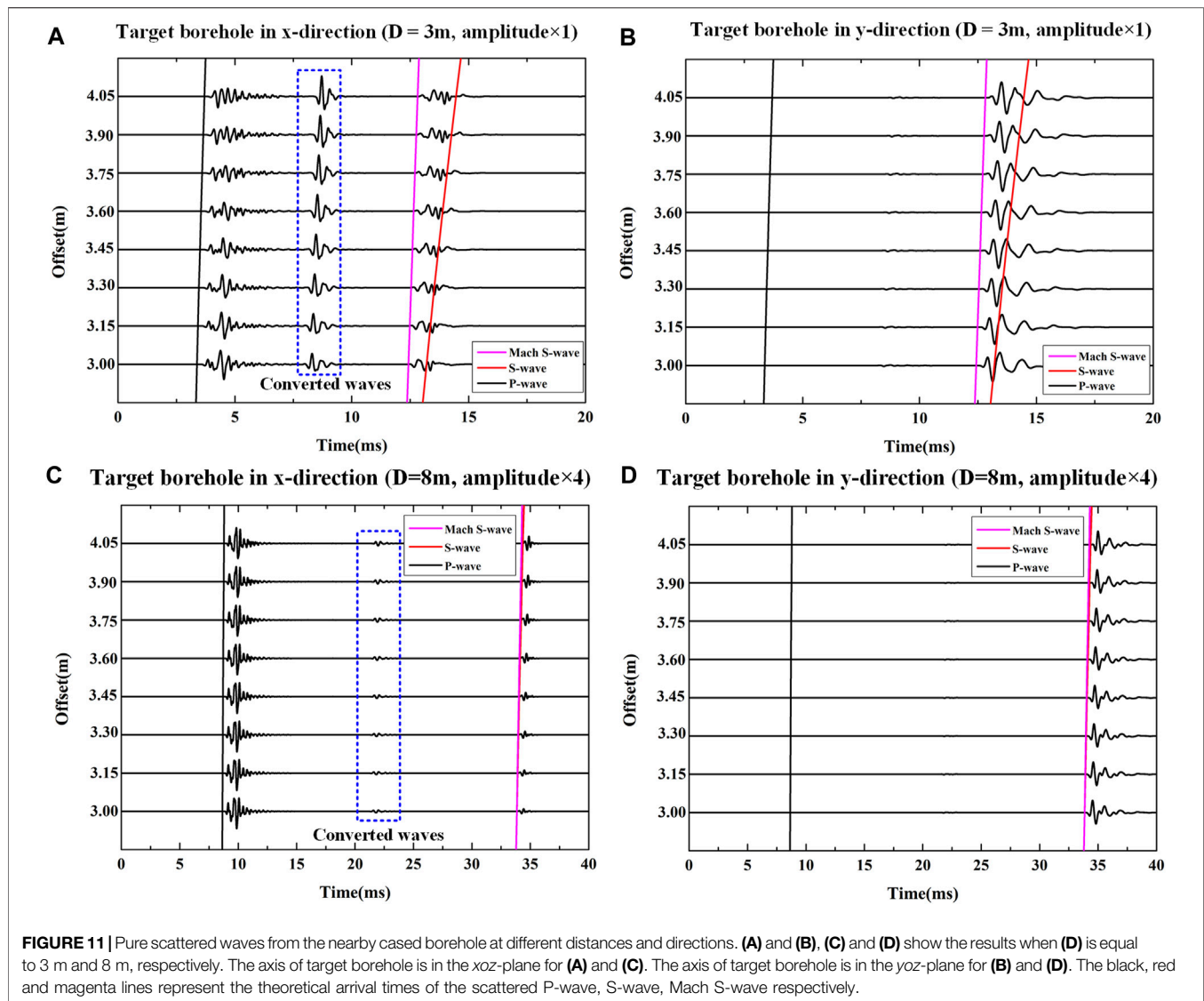
The fluid displacements received in the measurement borehole are plotted in **Figure 11**. To clearly show the scattered waves from the target cased borehole, we have removed the direct waves propagating along the drill collar and the measurement borehole (see **Figure 2**). The black, red and magenta lines represent the theoretical arrival times of P-, S- and Mach S-waves respectively. The arrival times of Mach P-waves are not shown because the Mach P-waves cannot be received in the receivers according to the ray theory. **Figures 11A,C** are the modeling results when the plane of the two boreholes is parallel to the x -direction. **Figures 11B,D** are the modeling results when the plane of the two boreholes is parallel to the y -direction. Note that the polarization of the dipole source is in x -direction, the characteristics of the received waveforms will depend on the position of the nearby target borehole.

When the target borehole is very close to the measurement borehole, for example $D = 3$ m as shown in **Figures 11A,B**, we can distinguish the Mach S-waves and the S-waves based on their arrivals. The scattered P- and Mach S-waves are much stronger than the scattered S-waves. Besides, remarkable converted waves occur when the target borehole is located on the x -direction (see blue dot outline box in **Figure 11A**). We plot the maximum absolute values of different types of

scattered waves in **Figure 13A**. As shown in **Figures 11A,B**, the S-S wave marked in **Figure 13A** is dominated by the scattered Mach S-waves. **Figure 13A** shows that the amplitudes of the scattered P-waves and converted waves change evidently with the offset. The scattered Mach S-waves have more stable and larger amplitudes when the orientation of the target borehole is perpendicular to the source polarization direction. The amplitudes of scattered Mach S-waves become smaller when the source polarization direction is parallel to the plane of the measurement and target boreholes. Therefore, the scattered Mach S-wave should be used for imaging the nearby boreholes as its stable, strong amplitudes and good orientation sensitivity. With increasing distance between the measurement and target boreholes, as waveforms shown in **Figures 11C,D** and normalized amplitudes shown **Figure 13B**, the relative amplitudes of different types of waves change markedly. The scattered waves become less sensitive to the offset and meanwhile, the amplitude of the converted wave shows apparent decrease compared with the results when $D = 3$ m. The scattered P-wave possess the maximal amplitude. As the arrival times of the scattered S-wave and scattered Mach S-wave are similar (see **Figures 11C,D**) when $D = 8$ m, we could not distinguish their amplitudes based on arrivals. As the scattered S-wave and the scattered Mach S-wave are mixed together in the waveform, we just call them scattered S-wave without distinction here. To identify the amplitudes of scattered S-wave caused by S-wave and Mach S-wave respectively, we build a new borehole detection model shown in **Figure 12A**. Part of the drill collar between the source and receiver array is removed to destroy the constructive interference of the collar wave. As the Mach S-wave is not excited, the influence on the scattered S-wave caused by the Mach S-wave is eliminated. The modeling result is shown in **Figure 12B** when the source orientation is perpendicular to the target borehole orientation. Comparing with scattered S-wave under the influence of the Mach S-wave (see **Figure 11D**), the amplitudes of the scattered S-wave caused by pure S-wave is smaller. That means the existence of Mach S-wave will enhance the scattered S-wave in this case. The scattered S-waves when the source polarization is perpendicular to the orientation of the target borehole still exhibit strong amplitude which is about 80% of the scattered P-wave. Hence, the scattered P-wave is the best choice for single-well acoustic imaging in LWD with an unconsolidated formation when the distance between the measurement and target boreholes.

TABLE 2 | Model parameters of the nearby cased borehole.

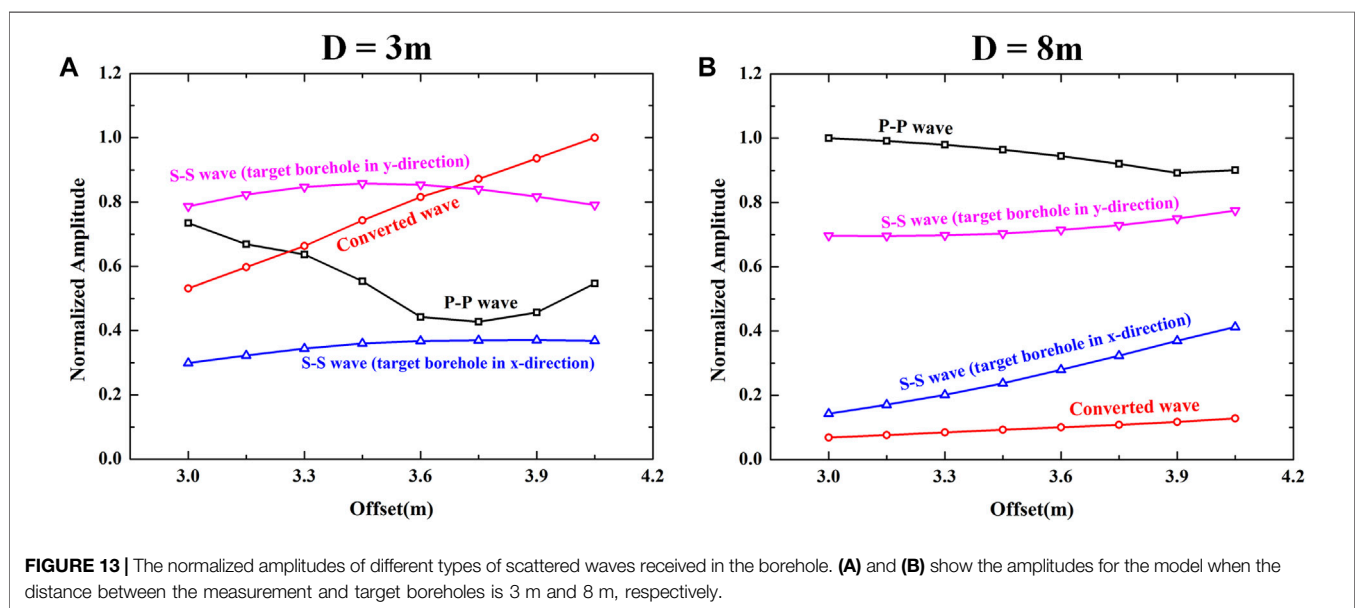
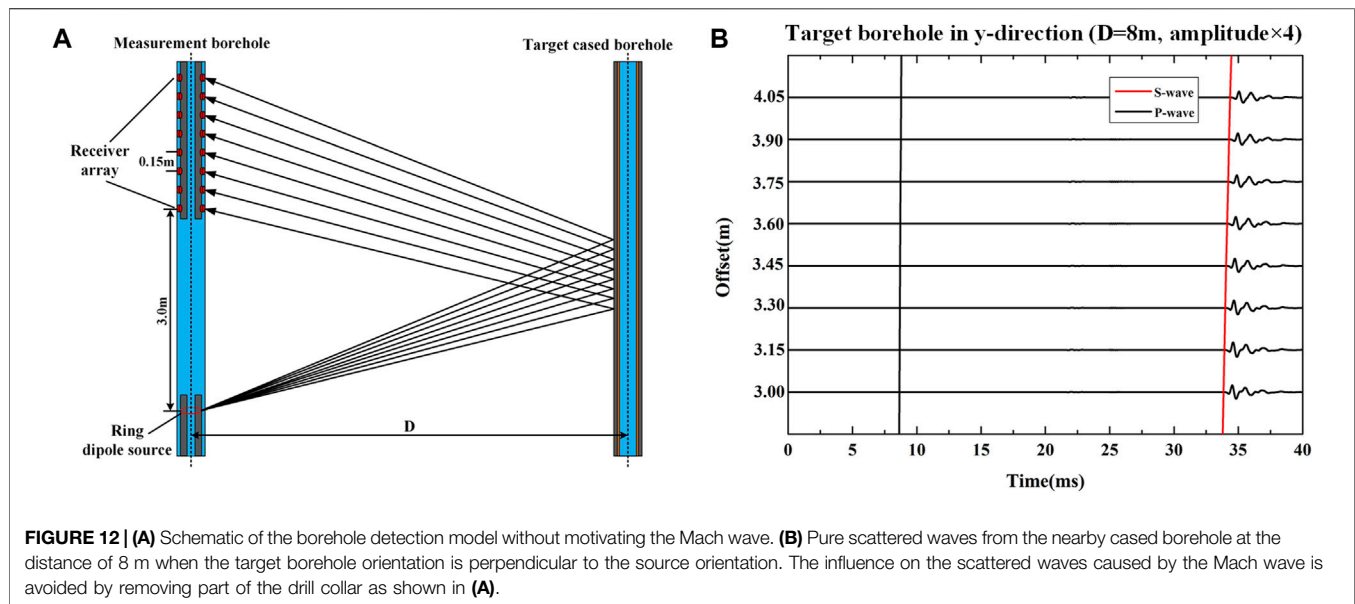
	P-Velocity (m/s)	S-Velocity (m/s)	Density (kg/m ³)	Outer Radius (m)
Fluid	1,500	--	1,000	0.16
Casing	6,098	3,354	7,500	0.17
Cement	2,823	1729	1920	0.22



DISCUSSIONS

In the application of borehole detection, the measurement and target boreholes can often be close to each other, especially when drilling toward the existing borehole in the case of drilling a relief well. As we shown in this work, the characteristics of the scattered waves change significantly when the distance between the measurement and target boreholes varies. This is due to the presence of the Mach S-waves. When the distance between two boreholes is large enough, we can simply use the scattered P-waves for imaging the trajectory of the nearby boreholes (see **Figures 11C,D**, **Figure 13B**). Because the arrival time of the scattered S-wave is late, it usually could not be recorded in LWD logging tools

and thus, will not influence the imaging results. For the case with a close distance between the two boreholes, as shown in **Figures 11A,B**, **Figure 13A**, the scattered Mach S-waves exhibit stable and strong amplitudes when the orientation of the target borehole is perpendicular to the source polarization direction. Although the amplitudes of scattered P-waves and converted waves change markedly, they also have strong amplitudes at certain offsets. Application of the different types of scattered waves indiscriminately can lead to erroneous borehole trajectories in the imaging results. Hence, pure scattered Mach S-waves should be extracted before imaging for the case of boreholes with close distance. On the other hand, different types of scattered waves bring different information



of the target borehole, so these waves can be jointly analyzed for LWD single well imaging for obtaining better imaging results.

CONCLUSION

When the drill collar and transmitters are well coupled, strong collar waves can be generated. Such wave will first propagate along the drill collar and meanwhile, part of the collar wave energy will radiate into the formation. Because the collar wave velocity is much faster than the velocity of the unconsolidated formation, the radiated collar waves will interfere constructively

in the formation and form secondary waves which is known as Mach waves. Apart from the P- and S-waves radiated from the source directly, the Mach wave also plays an important role in the outer borehole wavefields. The existence of a nearby cased borehole will generate significant scattered waves in the measurement borehole during LWD acquisition. The presence of Mach S-wave results in different characteristics of the scattered waves with different distances between the measurement and target boreholes. When the target borehole is close to the measurement borehole, the amplitudes of scattered P-waves and converted waves show apparent variation with the source-receiver offset. The scattered Mach S-wave should be used for imaging as its stable, strong amplitudes and good orientation

sensitivity. With increasing distance between the two boreholes, the scattered waves become less sensitive to the offset. The scattered P-wave possess the largest amplitude, which is most ideal for subsequent imaging purpose. This study provides a theoretical foundation for the borehole detection in LWD by single-well acoustic imaging in unconsolidated formations.

DATA AVAILABILITY STATEMENT

The original contributions presented in the study are included in the article/Supplementary Material, further inquiries can be directed to the corresponding author.

REFERENCES

- Cao, J. J., Tang, X. M., Su, Y. D., Wei, Z. T., and Zhuang, C. X. (2016). Radiation Characteristics of the Single-Well Imaging Field in While-Drilling Logging Using an Acoustic Dipole Source. *Chin. J. Geophys.* 59, 3503–3513. doi:10.6038/cjg20160932
- Cheng, N., Cheng, C. H., and Toksöz, M. N. (1995). Borehole Wave Propagation in Three Dimensions. *The J. Acoust. Soc. America* 97, 3483–3493. doi:10.1121/1.412996
- Gu, X.-H., Tang, X.-M., and Su, Y.-D. (2021). Delineating a Cased Borehole in Unconsolidated Formations Using Dipole Acoustic Data from a Nearby Well. *Geophysics* 86, D139–D147. doi:10.1190/GEO2020-0570.1
- Haldorsen, J., Voskamp, A., Thorsen, R., Vissapragada, B., Williams, S., and Fejerskov, M. (2006). *Borehole Acoustic Reflection Survey for High Resolution Imaging*. New Orleans, LA: Society of Exploration Geophysicists, 314–318.
- Hirabayashi, N. (2021). Beamform Processing for Sonic Imaging Using Monopole and Dipole Sources. *Geophysics* 86, D1–D14. doi:10.1190/geo2020-0235.1
- Hirabayashi, N., Sakiyama, N., and Ikegami, T. (2017). Characteristics of Waveforms Recorded by Azimuthally Spaced Hydrophones of Sonic Logging Tool for Incident Plane Waves. *Geophysics* 82, D353–D368. doi:10.1190/geo2017-0201.1
- Hornby, B. E. (1989). Imaging of Near-borehole Structure Using Full-waveform Sonic Data. *Geophysics* 54, 747–757. doi:10.1190/1.1442702
- Li, T., Wang, Z., Wang, R., and Yu, N. (2020a). Pore Type Identification in Carbonate Rocks Using Convolutional Neural Network Based on Acoustic Logging Data. *Neural Comput. Applic* 33, 4151–4163. doi:10.1007/s00521-020-05246-2
- Li, T., Wang, Z., Yu, N., Wang, R., and Wang, Y. (2020b). Numerical Study of Pore Structure Effects on Acoustic Logging Data in the Borehole Environment. *Fractals* 28, 2050049. doi:10.1142/S0218348X20500498
- Liu, Q. H., and Sinha, B. K. (2003). A 3D Cylindrical PML/FDTD Method for Elastic Waves in Fluid-filled Pressurized Boreholes in Triaxially Stressed Formations. *Geophysics* 68, 1731–1743. doi:10.1190/1.1620646
- Meredith, J. A., Toksöz, M. N., and Cheng, C. H. (1993). Secondary Shear Waves from Source Boreholes. *Geophys. Prospect.* 41, 287–312. doi:10.1111/j.1365-2478.1993.tb00571.x
- Pan, Y., He, X., Chen, H., and Wang, X. (2020). Reflection Signals and Wellbore Scattering Waves in Acoustic Logging while Drilling. *J. Geophys. Eng.* 17, 552–561. doi:10.1093/jge/gxaa014
- Tang, X.-M., Cao, J.-j., and Wei, Z.-t. (2014). Shear-wave Radiation, Reception, and Reciprocity of a Borehole Dipole Source: With Application to Modeling of Shear-Wave Reflection Survey. *Geophysics* 79, T43–T50. doi:10.1190/geo2013-0096.1
- Tang, X.-M., and Patterson, D. J. (2009). Single-well S-Wave Imaging Using Multicomponent Dipole Acoustic-Log Data. *Geophysics* 74, WCA211–WCA223. doi:10.1190/1.3227150

AUTHOR CONTRIBUTIONS

All authors listed have made a substantial, direct, and intellectual contribution to the work and approved it for submission.

FUNDING

This work is supported by the National Natural Science Foundation of China (Grant nos. 42104132, 41904113; 42074163). This work is also supported by Sichuan International Science and Technology Innovation Cooperation Program (Grant No: 2021YFH0050).

- Tang, X., Cao, J., Li, Z., and Su, Y. (2016). Detecting a Fluid-Filled Borehole Using Elastic Waves from a Remote Borehole. *J. Acoust. Soc. America* 140, EL211–EL217. doi:10.1121/1.4960143
- Tang, X. M., and Cheng, C. H. (2004). *Quantitative Borehole Acoustic Methods*. Amsterdam: Elsevier Science Publishing.
- Tang, X. M. (2004). Imaging Near-borehole Structure Using Directional Acoustic-wave Measurement. *Geophysics* 69, 1378–1386. doi:10.1190/1.1836812
- Tang, X. M., Zheng, Y., and Patterson, D. (2007). Processing Array Acoustic-Logging Data to Image Near-Borehole Geologic Structures. *Geophysics* 72, E87–E97. doi:10.1190/1.2435083
- Wei, Z., Tang, X., and Cao, J. (2019). Acoustic Radiation and Reflection of a Logging-While-Drilling Dipole Source. *Geophys. J. Int.* 219, 108–128. doi:10.1093/gji/ggz193
- Yang, S., Qiao, W., and Che, X. (2019). Numerical Simulation of Acoustic fields in Formation Generated by Linear Phased Array Acoustic Transmitters during Logging while Drilling. *J. Pet. Sci. Eng.* 182, 106184. doi:10.1016/j.petrol.2019.106184
- Zhang, R., Sun, Q., Zhuang, M., Huang, W.-F., Zhan, Q., Wang, D., et al. (2019). Optimization of the Periodic PML for SEM. *IEEE Trans. Electromagn. Compat.* 61, 1578–1585. doi:10.1109/TEM.2018.2866441
- Zhang, W., and Shen, Y. (2010). Unsplit Complex Frequency-Shifted PML Implementation Using Auxiliary Differential Equations for Seismic Wave Modeling. *Geophysics* 75, T141–T154. doi:10.1190/1.3463431
- Zheng, X., and Hu, H. (2017). A Theoretical Investigation of Acoustic Monopole Logging-While-Drilling Individual Waves with Emphasis on the Collar Wave and its Dependence on Formation. *Geophysics* 82, D1–D11. doi:10.1190/geo2016-0266.1–

Conflict of Interest: The authors declare that the research was conducted in the absence of any commercial or financial relationships that could be construed as a potential conflict of interest.

Publisher's Note: All claims expressed in this article are solely those of the authors and do not necessarily represent those of their affiliated organizations, or those of the publisher, the editors, and the reviewers. Any product that may be evaluated in this article, or claim that may be made by its manufacturer, is not guaranteed or endorsed by the publisher.

Copyright © 2022 Li, Qi, Hei, Jiang and Wang. This is an open-access article distributed under the terms of the Creative Commons Attribution License (CC BY). The use, distribution or reproduction in other forums is permitted, provided the original author(s) and the copyright owner(s) are credited and that the original publication in this journal is cited, in accordance with accepted academic practice. No use, distribution or reproduction is permitted which does not comply with these terms.



Zircon SHRIMP U-Pb Dating and Significance From Weathered Residual Kaolin Deposits on the Northern Margin of the Qinzhou-Hangzhou Suture Zone, China

Chunhai Li^{1,2,3*}, Qifa Sun¹, Zhonglin Sun¹, Xiaohua Zhou², Wei Zhang², Rong Chen² and Tianshan Gao²

OPEN ACCESS

Edited by:

Lidong Dai,
Institute of geochemistry (CAS), China

Reviewed by:

Mingliang Wang,
Suzhou University, China
Lv Zheng-Hang,
Institute of Geochemistry (CAS), China

*Correspondence:

Chunhai Li
lichunhai01@sina.com.cn

Specialty section:

This article was submitted to
Geochemistry,
a section of the journal
Frontiers in Earth Science

Received: 15 January 2022

Accepted: 07 February 2022

Published: 31 March 2022

Citation:

Li C, Sun Q, Sun Z, Zhou X, Zhang W,
Chen R and Gao T (2022) Zircon
SHRIMP U-Pb Dating and Significance
From Weathered Residual Kaolin
Deposits on the Northern Margin of the
Qinzhou-Hangzhou Suture
Zone, China.
Front. Earth Sci. 10:855459.
doi: 10.3389/feart.2022.855459

¹Harbin Natural Resources Comprehensive Investigation Center, China Geological Survey, Harbin, China, ²Nanjing Geological Survey Center, China Geological Survey, Nanjing, China, ³School of Earth Science and Engineering, Nanjing University, Nanjing, China

Weathered residual Kaolin deposits on the northern margin of the Qinzhou-Hangzhou Suture Zone are characterized by more feldspar-containing minerals and fewer dark minerals. These deposits have attracted increasing attention because of their high whiteness, low harmful impurity content, low depth of weathered mineralization, and ease for mining. The ore-forming rock masses mainly include granite (granite porphyry), quartz porphyry, euryte, haplite, and other acidic veins; the ore-bearing walls are mainly of Upper Proterozoic. Previous studies suggested that dyke rocks related to Kaolin deposits in this belt belong to the Mesozoic, but there is a lack of information regarding specific mineralization ages. In this study, two dyke wall-type weathered residual Kaolin deposits were selected from the northern margin of the Qinzhou-Hangzhou Suture Zone (Dongxicun and Yinbeidong, Jiangxi Province, China) for zircon SHRIMP dating. Two zircon U-Pb-based ages were obtained: 843 ± 10 Ma from Dongxicun granite veins that intrude into the Neoproterozoic Jiuling rock masses; 152.3 ± 1.8 Ma for Yinbeidong granite porphyry veins that intrude into the Neoproterozoic Anlelin Formation. We suggest that the dykes related to the Kaolin deposits were formed in the Neoproterozoic and late Jurassic. The Neoproterozoic dyke may be related to the convergence, formation, or pyrolysis of the Rodinia Supercontinent and the late Jurassic dyke may be related to the subduction of the Paleo-Pacific Plate. These results provide a chronological basis for the investigation and evaluation of weathered residual Kaolin deposits on the Qinzhou-Hangzhou Suture Zone.

Keywords: kaolin deposit, zircon U-Pb dating, weathered eluvial deposit, Jiangxi province, Qinzhou-Hangzhou suture zone

INTRODUCTION

The northern Jiangxi Province is geologically complex with frequent magmatic activity in the Proterozoic and Mesozoic. This region has relatively rich Kaolin resources and ranks among the top in China in terms of reserves. There are nearly 100 known Kaolin deposits and ore sites (Figure 1), among which the most representative is in the village of Gaoling (Ehu, Fuliang County) in northeastern Jiangxi (Li et al., 2017; Wang et al., 2018). The Kaolin deposits are divided into three types: weathered residual; volcanic hydrothermal alteration; sedimentary. Weathered residual Kaolin deposits are very important in terms of reserves and mining quantities. Their formation is mainly affected by the ore-forming parent rock masses, tectonic conditions, and water conditions; ore-forming parent rock masses mainly include granite, pegmatite, and other acidic veins.

I-Yangtze Plate, I1-Low Yangtze Tectonic Unit, I2-Jiugong Mountain Tectonic Unit, I3-Wuning-Xiushui Tectonic Unit, I4-Jiuling Mountain Tectonic Unit, I5-South Edge of Jiuling Mountain Tectonic Unit, I6-Zhanggong Mountain Tectonic Unit, I7-Leping Tectonic Unit, II-Qingzhou-Hangzhou Suture Zone, II1-Leping-Shexian Melange Subzone, II2-Wannian Tectonic Unit, II3-Ophiolite Melange Subzone of Northeast Jiangxi, II4-Huaiyu Mountain Tectonic Unit, II5-Dongxiang-Longyou Ophiolite Melange Subzone, III-Cathaysia Plate, III1-Wugong Mountain- North WuYi Mountain Tectonic Unit.

Yichun is located in northwestern Jiangxi Province, with its geotectonic position on the northern margin of the Qinzhou-Hangzhou Suture Zone (QHSZ) or the Qinzhou-Hangzhou

Metallogenic Belt (QHMB) between the Yangtze and Cathaysia plates (Figure 1), roughly equivalent to the Jiangnan Orogenic Belt. The known mineral resources mainly include copper, gold, tungsten, iron, coal, lithium, niobium-tantalum, Kaolin, cement, and groundwater. Among these, Kaolin deposits have attracted more and more attention due to their high whiteness, low content of harmful impurities, and ease of mining. The weathered residual Kaolin deposits in Yichun (Jiangxi Province) were formed through superficial weathering of aluminum-rich silicate. Hydrothermal alterations such as illitization and Kaolinization frequently occur, so Kaolin deposits are easily weathered. Acidic veins these form Kaolin deposits from weathered residualization are also controlled by regional faults and characterized by a zonal distribution. In general, the acidic veins include more feldspar-containing minerals, mainly Kaolinite, illite, feldspar, and sericite, but fewer dark minerals, such as biotite and hornblende. The minerals are rich in Al_2O_3 (more than 15%) and have a low content of harmful impurities, such as TiO_2 and Fe_2O_3 (more than 3% in total). Despite their small scale, the deposits are found in large quantities and at low weathered mineralization depths, and are often produced in groups and belts ranging from tens to hundreds of meters in length. A single vein has a width of one to 6 m and a single vein belt has a width of tens of meters, which makes the deposits mining targets. The ore-forming rock masses mainly include granite, granite porphyry, quartz porphyry, eurite, haplite, and other veins, and the intrusive wall rocks are mainly of Neoproterozoic age. Wang and Fang (1994) conducted a preliminary study of the characteristics and formation mechanisms of high-quality Kaolin deposits in Yichun using

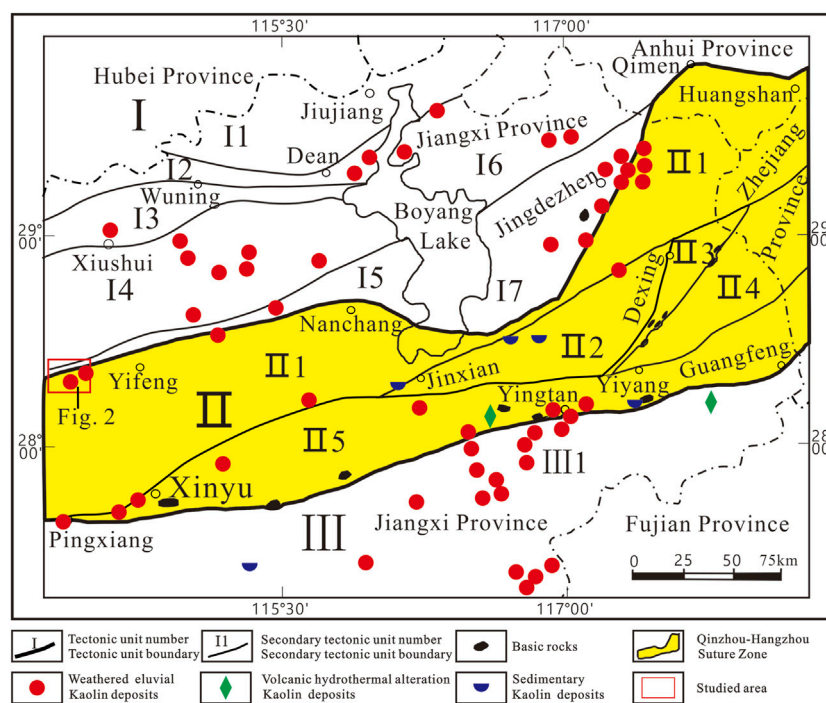


FIGURE 1 | Distribution of Kaolin deposits and the tectonic location in northern Jiangxi province (after Wang et al., 1986 and Jiang et al., 2015).

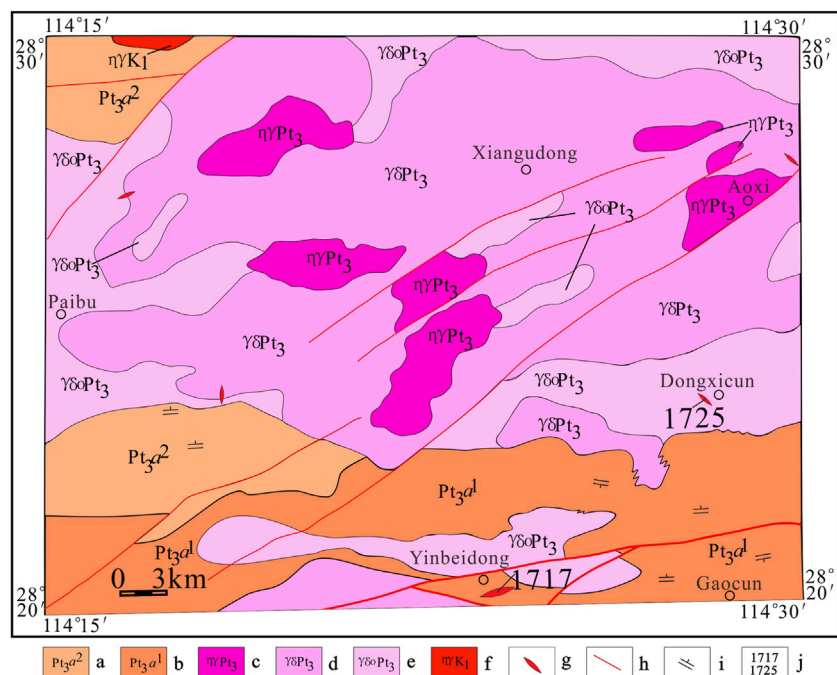


FIGURE 2 | Regional geological map in Yichun area of Jiangxi province and location of the samples (after the author participated in the 1:50,000 Gaocun, Daqiao and Xujiadu regional geological survey project). a-Middle member of Neoproterozoic Anlelin Formation, b-Lower member of Neoproterozoic Anlelin Formation, c-Neoproterozoic monzogranite, d-Neoproterozoic granodiorite, e-Neoproterozoic tonalite, f-Late Cretaceous monzogranite, g-Acid dykes, h-Fault, i-Attitude of schistosity, j-Sampling location and number.

microscopic identification and chemical composition analysis. They found that the Kaolin is mainly composed of Kaolinite minerals (largely scaly Kaolinite and tubular 7 Å halloysite), lepidolite (white mica), albite, quartz, and potash feldspar. Heavy minerals include apatite, topaz, microlite, and niobium-tantalite, but almost no iron oxide minerals, which may be related to the post-magmatic hydrothermal alteration of albite. These regional data suggested that most of the acidic veins that form Kaolin deposits occurred during the Mesozoic, but there is a lack of data for specific mineralization ages. In this study, we selected two weathered residual Kaolin deposits from Dongxicun and Yinbeidong in Yichun (northern QHMB margin) for zircon SHRIMP U-Pb dating and recorded two ages from veins in Kaolin deposits, 843 ± 10 Ma (granite veins in deposits intruding into Jiuling tonalite masses) and 152.3 ± 1.8 Ma (granite porphyry veins in deposits intruding into the Anlelin Formation). These two specific U-Pb ages could reveal a chronological basis for the investigation and evaluation of weathered residual Kaolin deposits on the Qinzhou-Hangzhou Suture Zone.

GEOLOGICAL BACKGROUND

In the region, Upper Proterozoic and Quaternary strata are distributed over a large area (Figure 2), and the Carboniferous–Triassic, Jurassic, and Cretaceous Systems are sporadically exposed. The Proterozoic Erathem in the region is

mainly composed of the Yifeng Formation Complex and the Anlelin Formation. Lithologically, the Yifeng Formation is mainly sericite (quartz) phyllite (partly schist) containing inter-layers (or lens) of metatuffaceous rocks, silty sand, and metaplasia-horn porphyry (metadiabase). The Carboniferous–Triassic System is mainly composed of carbonate deposits, with lesser deposits of mudstone. The Jurassic System is mainly composed of carbonate–clastic deposits. The Cretaceous System is mainly composed of red, mostly coarse, clastic rocks. The rock masses are mainly from the Neoproterozoic Jiuling terrane and the Mesozoic rock masses are mostly present in the form of rock strains or veins.

The QHSZ has undergone multiple periods of tectonic deformation. The tectonic traces are mainly NE-trending folds–faults and a NW-trending fault zone, followed by a near EW-trending fault zone. The near EW-trending tectonic zone formed earlier than the NW-trending fault zone and both are mostly filled by veins. The NE-trending fault zone was the latest formed (or had the longest active period), and features large scale and multiple periods. The exposed Anlelin Formation is mainly of Proterozoic age. The lower section is a thickly layered variable residual fine to medium-grained lithic sandstone intercalated with silty slate. The middle section is thin–medium layered variable residual siltstone and silty slate, containing variable residual fine-grained lithic sandstone and metastatic tuff inter-layers (or lens). The Neoproterozoic Jiuling compound rock masses are mainly exposed and are produced in the form of rock bases. Lithologically, from old to new, they are roughly

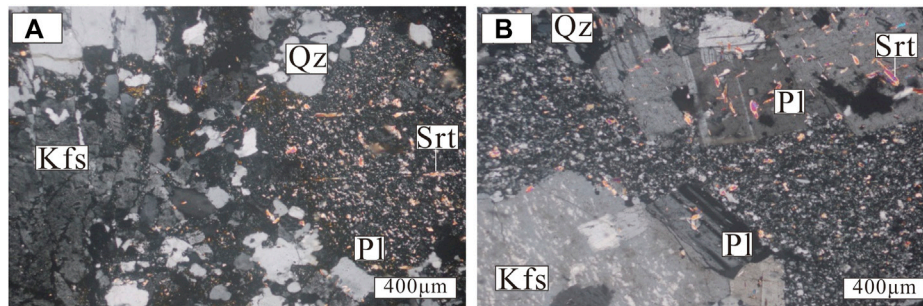


FIGURE 3 | Photomicrographs of the granite dyke (Sample 1725) **(A)** and the granitic porphyry dyke (Sample 1717) **(B)** Qz-quartz; Pl-plagioclase; Kfs-potash feldspar; Srt-sericite.

tonalite, granodiorite, and monzogranite. Previously reported ages of the Jiuling rock masses are mainly derived from samples on the northern margin and are generally 816 to 837 Ma (Zhong et al., 2005; Yuan et al., 2012; Duan et al., 2019). The Mesozoic rock masses have a small exposed area and are predominantly present in the form of rock strains and veins. They are mainly granites with some Kaolin deposits weathered from granite veins.

SAMPLING

Samples for this study were recovered from the newly mined village of Dongxicun and Yinbeidong Kaolin deposits in Yichun (Figure 2). The ore-forming granite vein (Sample 1725) of the Kaolin deposits in Dongxicun is distributed along the NW and intrudes into the Neoproterozoic Jiuling medium to fine-grained tonalite masses. The exposed width of the vein zone is 10–20 m, the current mining depth is over 6 m. Granite veins, which became yellow–white and fine to medium-grained structures upon weathering, are mainly composed of feldspar and quartz. The feldspars are yellowish-white, white, and earthy upon weathering, and mainly include plagioclase feldspar (35% abundance; 0.5–1.5 mm), mostly sericitized potassium feldspar (20%; 0.7–2.0 mm), and colorless quartz (35%; 0.3–1.5 mm) that features hypautomorphic-allotriomorphic filling (Figure 3A). Biotite has been altered by chlorite and limonite, with a content of less than 3%. Accessory minerals include trace amounts of apatite and magnetite.

Distributed in a near EW direction, the Yinbeidong Kaolin ore-forming granite porphyry vein (Sample 1717) roughly occurs at $345^{\circ} < 88^{\circ}$ and intrudes into the plate-like metasilstone of the Neoproterozoic Anlelin Formation. The exposed width of the vein is about 20 m, the current mining depth is over 4 m. Quartz veinlets have developed in veins and plate-like metasilstones. The veinlet density is 8–10 pieces/m, with single pieces 0.6–4 cm in width; the occurrence of the veinlets is similar to the granite porphyry intrusion surfaces. After weathering, the granite porphyry vein is white (slightly greenish-white when fresh) with a porphyritic structure. Phenocrysts (about 30%) are mainly feldspar and the matrix (about 70%) is mainly felsic rock and biotite ($< 0.5\%$) with a rust-colored surface upon

iron precipitation and weathering. Feldspar phenocrysts are mainly plagioclase feldspar, with polysynthetic twins and Carlsbad-albite compound twins. The surface is mostly sericitized, white and subhedral (1.5–2.5 mm). The potassium feldspar phenocrysts (1.5–3.0 mm) have a striped structure and are allotriomorphic. Quartz (0.3–1.5 mm) is allotriomorphic and mostly filled with other mineral particles, with obvious wavy extinction (Figure 3B). Local chloritization and ferritization occurs, with few iron mineral particles. The accessory minerals include trace amounts of apatite and magnetite. Plate-like metasilstone xenoliths of the Anlelin Formation are present in the veins, with sulfide aggregates such as pyrite and marcasite occasionally observed. Pyrite (0.5–2 mm) is light yellow and cube-shaped, while marcasite (0.5–2 mm) is light white and allotriomorphic.

METHODS

After sampling, the material was crushed and then subjected to gravitational force and magnetic separation. The zircons were selected under a binocular lens, and then the particles and several reference samples (TEM) were placed on an epoxy resin target. They were then ground and used for transmission, reflection, cathode luminescence (CL) imaging, and SHRIMP U-Pb measurements. The CL images were taken at Institute of Geology, Chinese Academy of Geological Sciences.

The zircon U-Pb age data were generated from the SHRIMP II instrument of the Beijing SHRIMP Center (Institute of Geology, Chinese Academy of Geological Sciences). For detailed analytical procedures and principles, refer to Compston et al. (1992). The programs Ludwig SQUID 1.0 and ISOPLOT were used for data processing. A value recommended by the International Union of Geological Sciences (1977) was used as the age calculation constant. The error of a single data point is 1σ and the weighted average age has a confidence level of 95%.

RESULTS

A total of 18 measuring points for 18 zircons in Sample 1725 were subjected to SHRIMP U-Pb dating. The results are shown in

TABLE 1 | SHRIMP Zircon U-Pb data of the granite dyke (Sample 1725) related to Dongxicun Kaolin deposit.

Spot	$^{206}\text{Pb}_c(\%)$	U (ppm)	Th (ppm)	$^{232}\text{Th}/^{238}\text{U}$	$^{206}\text{Pb}^*$ (ppm)	$^{207}\text{Pb}^*/^{206}\text{Pb}^*$	$\pm\%$	$^{207}\text{Pb}^*/^{235}\text{U}$	$\pm\%$	$^{206}\text{Pb}^*/^{238}\text{U}$	$\pm\%$	$^{206}\text{Pb}/^{238}\text{U}$ $\pm 1\sigma$ age (Ma)	$^{206}\text{Pb}/^{232}\text{Th}$ $\pm 1\sigma$ age (Ma)
1	--	374	91	0.25	45.7	0.0683	1.8	1.343	2.3	0.1426	1.4	859 ± 12	901 ± 38
2	--	300	38	0.13	35.8	0.0660	1.6	1.264	2.2	0.1390	1.5	839 ± 12	893 ± 38
3	--	382	64	0.17	47.8	0.06801	1.4	1.370	2.0	0.1461	1.5	879 ± 12	926 ± 30
4	1.68	1,193	132	0.11	155	0.0578	3.0	1.188	3.3	0.1490	1.4	895 ± 12	628 ± 130
5	0.14	589	51	0.09	74.8	0.0659	1.5	1.340	2.1	0.1475	1.4	887 ± 12	910 ± 73
6	0.05	291	40	0.14	35.1	0.0666	1.7	1.288	2.3	0.1403	1.5	846 ± 12	797 ± 45
7	--	285	38	0.14	34.4	0.0720	2.2	1.398	2.7	0.1407	1.5	849 ± 12	1,092 ± 72
8	--	370	60	0.17	45.6	0.0671	1.6	1.330	2.3	0.1437	1.7	866 ± 14	891 ± 38
9	--	324	47	0.15	40.6	0.0677	1.9	1.365	2.4	0.1461	1.5	879 ± 12	897 ± 55
10	--	420	62	0.15	56.8	0.06888	1.4	1.499	2.0	0.1578	1.4	945 ± 13	1,018 ± 40
11	0.45	439	54	0.13	64.5	0.0743	2.1	1.744	2.6	0.1702	1.4	1,013 ± 14	683 ± 85
12	0.55	296	51	0.18	40.5	0.0630	2.5	1.377	2.9	0.1586	1.5	949 ± 13	716 ± 65
13	0.04	665	127	0.20	79.6	0.06917	1.1	1.327	1.8	0.1392	1.4	840 ± 11	675 ± 17
14	1.16	891	221	0.26	112	0.0691	2.2	1.377	2.6	0.1445	1.4	870 ± 11	1,059 ± 49
15	0.87	701	121	0.18	92.4	0.0623	2.4	1.305	2.8	0.1521	1.4	913 ± 12	834 ± 66
16	0.07	326	52	0.16	39.1	0.0657	1.5	1.266	2.1	0.1398	1.5	844 ± 12	852 ± 33
17	--	405	196	0.50	51.3	0.0692	2.1	1.413	2.5	0.1482	1.4	891 ± 12	907 ± 24
18	--	215	262	1.26	28.7	0.0727	2.7	1.562	3.1	0.1559	1.6	934 ± 14	928 ± 21

Note: Pb_c and Pb^* represent common lead and radioactive lead, respectively. The measured ^{204}Pb is used to correct the common lead in zircons, and the age is $^{206}\text{Pb}/^{238}\text{U}$.

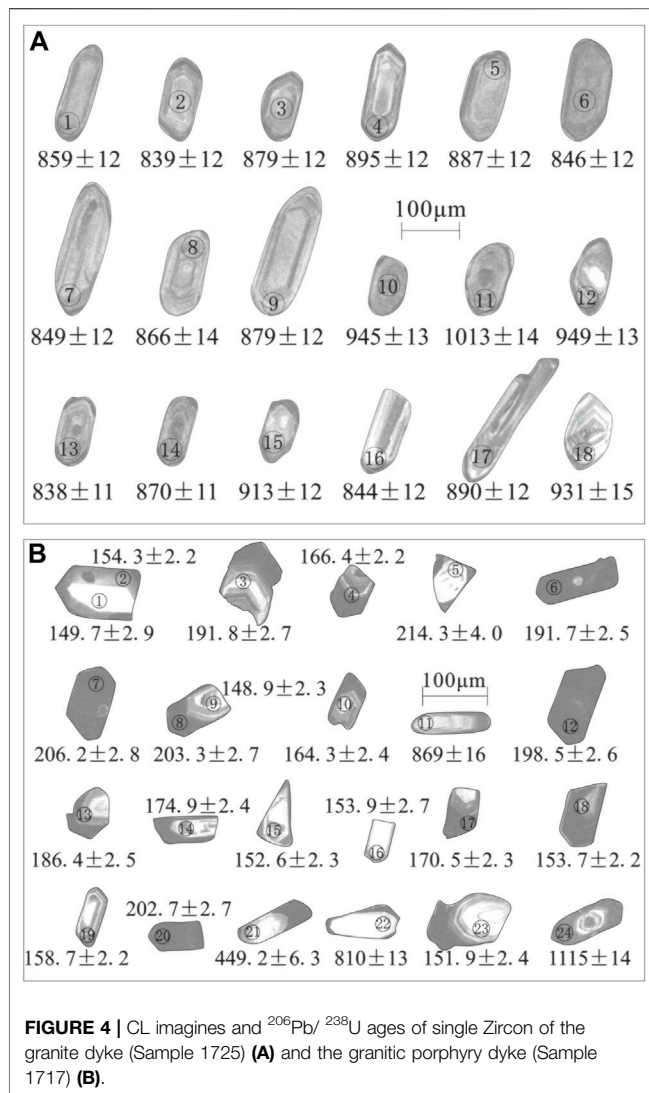
Table 1 and the corresponding CL images are shown in **Figure 4A**. In Sample 1717, a total of 24 measuring points for 22 zircons were subjected to SHRIMP U-Pb dating, with the results shown in **Table 2** and corresponding CL images in **Figure 4B**.

The points 1725-4, 1725-5 and 1725-10 do not lie on the harmonic curves, with an age range of 887 ± 12 Ma to 945 ± 13 Ma. The measuring points can be divided into two groups distributed on the U-Pb harmonic curves (**Figures 5A,B**), except for 1725-11, 1725-12, 1725-15, 1725-17, and 1725-18 because they are relatively old (891 ± 12 – $1,013 \pm 14$ Ma). For the group with younger ages, the $^{206}\text{Pb}/^{238}\text{U}$ age was weighted and averaged; an age of 843 ± 10 Ma was obtained (MSWD = 0.12, $n = 5$). The zircons are shaped like short columns and mostly have a ring structure, U contents of 285–665 ppm, and Th/U ratios of 0.13–0.20. They are magmatic zircons and represent the emplacement of the granite veins. The second group was characterized by relatively older $^{206}\text{Pb}/^{238}\text{U}$ ages (871 ± 11 Ma, MSWD = 0.51, $n = 5$), high U contents (324–889 ppm), and Th/U ratios of 0.15–0.26. The zircons are shaped like short to long columns and mostly have a ring structure; they could represent a record of the Jiuling tonalite wall rocks. The oldest zircons (891 ± 12 to $1,013 \pm 14$ Ma) are mostly ellipsoidal, except for 1725-17 that is shaped like long columns, and most have a ring structure. They may represent a record of the regional wall rocks from the magma source area or the magma influx area.

The measuring points from Sample 1717 can be divided into two groups and distributed on the U-Pb harmonic curves (**Figures 5C,D**), except for 1717-11, 1717-21, 1717-22, and 1717-24, which are relatively older. In the first group, the $^{206}\text{Pb}/^{238}\text{U}$ age was weighted and averaged and an age of 152.3 ± 1.8 Ma (MSWD = 0.77, $n = 7$) was obtained. The zircons are shaped like short columns (larger than the captured zircon particles) and most of them have a ring structure, U contents of 207–4,230 ppm, and Th/U ratios of 0.25–0.86. They are magmatic zircons and represent the

emplacement of granite porphyry veins. The second group has an $^{206}\text{Pb}/^{238}\text{U}$ age of 170.5–206.2 Ma, high U contents (1957–26,130 ppm), and Th/U ratios of 0.05–0.28 (except for 1717-5). The zircons are shaped like short columns and most of them have no annulus structure. They may represent a record of the magma source area or unclosed U-Pb isotopic system. Zircons aged 869–810 Ma (1717-11 and 1717-22) are mostly shaped like long columns with no annulus structure, U contents of 118–359 ppm, and Th/U ratios of 0.1–0.46; these may represent a record of the Anlelin Formation wall rocks and/or Jiuling rocks. The zircons aged $1,115 \pm 14$ Ma (1717-24) are shaped like long columns with a core-mantle structure, U contents of 1780 ppm, and Th/U ratio of 0.01, and may represent a basement record. The zircons aged 449.2 ± 6.3 Ma (1717-21) are shaped like long columns with a core-mantle structure, U content of 782 ppm, and Th/U ratio of 0.26; these may represent a Caledonian thermal event.

The older zircon ages (891 – $1,013$ Ma) captured in Sample 1725 are equivalent to the $^{40}\text{Ar}/^{39}\text{Ar}$ age (928 ± 19 Ma) of the Xiwan albite granite in Dexing, Jiangxi (928 ± 19 Ma) (Hu et al., 1998) or the zircon U-Pb age of amphibole granite mixed into ophiolite (about 968 Ma) (Li et al., 1994), which may reflect residual rock fragments of the South China Sea (Yang et al., 2012; Wu et al., 2016) or the convergence, formation, and disintegration of the Rodinia Supercontinent (Hao and Zhai, 2004; Lu et al., 2004; Pan et al., 2016). The age of another group of zircons captured by granite veins is 871 ± 11 Ma, which may be a record of the Jiuling tonalite wall rocks. This is slightly older than the SHRIMP zircon U-Pb age (855 ± 5 Ma) of the Cangxi schist tuff of Liuyang in the northeastern Hunan Province (Gao et al., 2011). The emplacement of the granite veins was dated to 843 ± 10 Ma, which is older than ages of the northern margin of the Jiuling rock masses (837–816 Ma) (Zhong et al., 2005; Yuan et al., 2012; Sun et al., 2017; Duan et al., 2019; Wu et al., 2019) and the Shuangqiaoshan Group on the northern margin of Jiuling (840–819 Ma) (Gao et al., 2011; Zhou et al., 2012). This could



suggest that the formation of the Neoproterozoic tonalite masses on the Jiuling southern margin and the Anlelin Formation was slightly earlier than the rock masses and strata on the northern margin. Duan et al. (2017) showed that during extension, after the collision of the Neoproterozoic Cathaysian and Yangtze plates, magma on the southeastern Jiuling rock masses in the QHMB had a deep origin and early formation age, and that it gradually migrated toward the northwestern Jiuling rock masses.

The oldest zircon age of Sample 1717 is $1,115 \pm 14$ Ma and may represent a basement record. It is consistent with the zircon U-Pb age for the volcanic rocks in the Tieshajie Formation complex ($1,119 \pm 6$ Ma) (Cheng et al., 1991). Another group of older zircons captured by granite porphyry veins reflected ages of 869 to 810 Ma, which may be a record of the Anlelin Formation wall rocks and/or Jiuling rock masses. The age captured by the granite porphyry veins (449.2 ± 6.3 Ma) is a record of a Caledonian thermal event and is slightly older than the granites intruded into the Xinyu Iron Ore Area in the northern part of the QHMB (~ 420 Ma) (Zhang et al., 2018),

but is similar to the formation age of the early Caledonian granites in the eastern part of South China ($440\text{--}460$ Ma) (Zhang F. R. et al., 2009) and the Wugongshan gneissic granite in Jiangxi (456.9 ± 2.6 Ma) (Lou et al., 2005). This suggests that at least one important tectonic magmatism event occurred in the late Early Paleozoic, which would be consistent with a lack of Lower Paleozoic strata in the Yichun area. The youngest age (152.3 ± 1.8 Ma, granite porphyry veins) represents the emplacement of the veins that become Kaolin deposits through weathered residualization. This is consistent with ages of the tungsten-tin-forming granites in southern Jiangxi ($150\text{--}155$ Ma), such as the Zhangtiantang (Feng et al., 2007a), Hongtaoling (Feng et al., 2007b), Piaotang (Zhang et al., 2009b), and Tianmenshan (Liu et al., 2007) rock masses. This similarity indicates that during the period of tungsten-tin mineralization caused by large-scale magmatic activity in the southern Jiangxi (Nanling area), medium acid veins mostly intruded along fault structures on the southern margin of the Jiuling rock masses and became, upon weathering, Kaolin deposits rather than tungsten-tin deposits, which reflects differences in tectonic structure or magma source. The tungsten-tin mineralization is located on the Cathaysia Plate and the Kaolin deposits in the QHSZ between the Cathaysia and Yangtze plates. Emplacement (152.3 ± 1.8 Ma) of the Yinbeidong ore-forming granite porphyry veins (Sample 1717) was earlier than the metallogenic age (about 124 Ma) (Li et al., 2017) of the Gaoling Kaolin ore field in the Ehu rock base of northeastern Jiangxi (Zhao et al., 2010). The Yinbeidong Kaolin deposit is located in the Leping-Shexian mélange sub-belt of the QHSZ and the Ehu Kaolin deposit in the Leping tectonic unit of the Yangtze Plate, suggesting that the acidic veins that form Kaolin deposits in the northern Jiangxi tend to migrate from south to north. Zircons captured by the granite porphyry veins were dated to $170.5\text{--}206.2$ Ma and may represent the age record of the magma source area, be caused by an unclosed zircon U-Pb isotopic system, or high U contents ($1957\text{--}26,130$ ppm). This can be seen in 1717–8 to 9, which are different parts of the same zircon. The age of the center with annulus structure is 148.9 ± 2.3 Ma and the edge with no annulus structure is 202.3 ± 2.7 Ma.

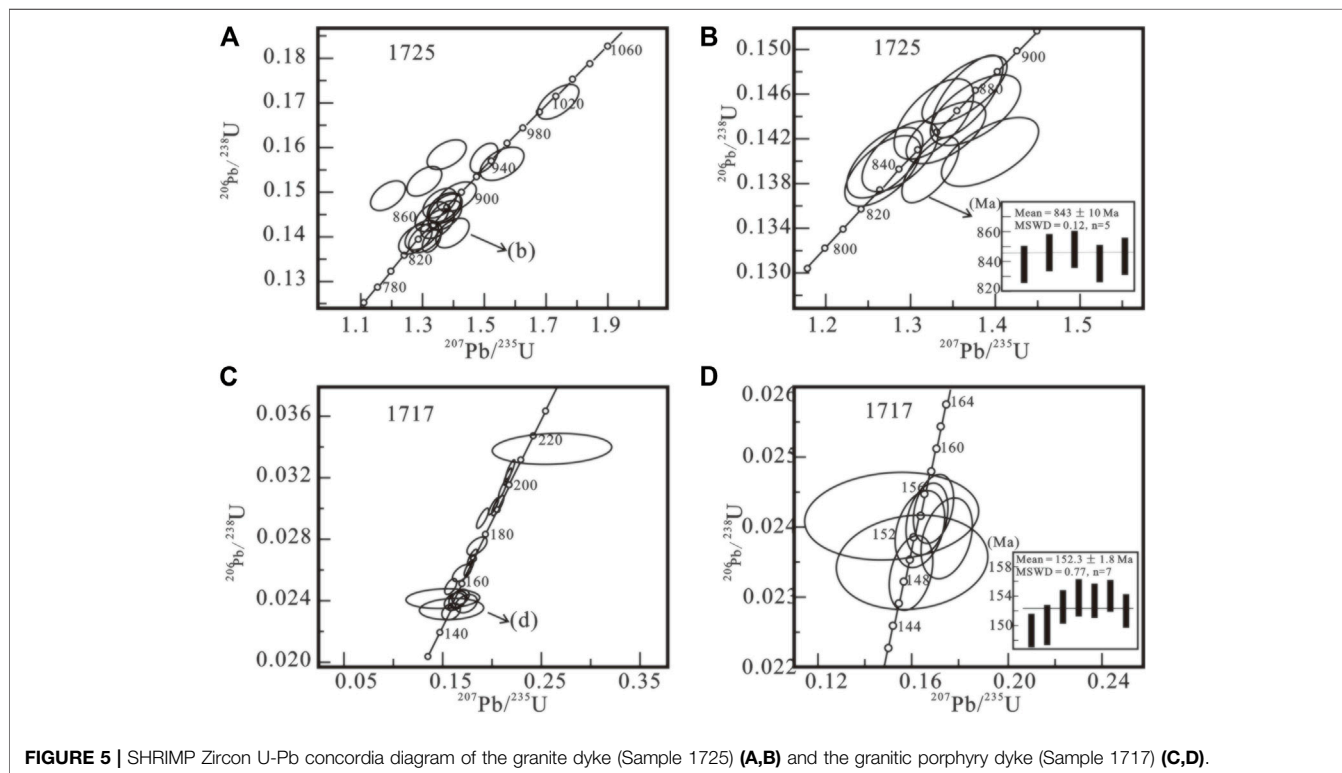
DISCUSSION

The early Neoproterozoic thermo-tectonic event of the QHMB was the product of orogeny and the result of the convergence of the Rodinia Supercontinent (Lu et al., 2004) during the transition from Rodinia to the Gondwana Supercontinent (Zhou et al., 2008). This is slightly later than the typical Neoproterozoic Grenville orogen globally (Wang et al., 2017). Zhang (2013) proposed that the Neoproterozoic orogenic event in the Jiangnan Orogenic Belt is characterized by multi-period accretion and collage, and that evolution stages occur at: 1) ~ 880 Ma, when the Shuangxiwu arc collided to Cathaysia Plate; 2) $860\text{--}838$ Ma, when the Jiangnan area was part of an arc-back-arc basin, with developed arc magmatism; 3) $835\text{--}825$ Ma, when the Jiangnan

TABLE 2 | SHRIMP Zircon U-Pb data of the granitic porphyry dyke (Sample 1717) related to Yinbeidong Kaolin deposit.

Spot	$^{206}\text{Pb}_c(\%)$	U (ppm)	Th (ppm)	$^{232}\text{Th}/^{238}\text{U}$	$^{206}\text{Pb}^*$ (ppm)	$^{207}\text{Pb}^*/^{206}\text{Pb}^*$	$\pm\%$	$^{207}\text{Pb}^*/^{235}\text{U}$	$\pm\%$	$^{206}\text{Pb}^*/^{238}\text{U}$	$\pm\%$	$^{206}\text{Pb}/^{238}\text{U} \pm 1\sigma$ age (Ma)	$^{206}\text{Pb}/^{232}\text{Th} \pm 1\sigma$ age (Ma)
1	0.20	207	133	0.67	4.19	0.0495	13	0.160	13	0.02350	1.9	149.7 ± 2.9	151 ± 13
2	--	1,210	292	0.25	25.2	0.0511	2.6	0.1706	3.0	0.02422	1.5	154.3 ± 2.2	155.9 ± 6.2
3	--	5,500	1,515	0.28	143	0.04959	1.3	0.2066	1.9	0.03021	1.4	191.8 ± 2.7	160.6 ± 3.4
4	0.02	4,230	2,366	0.58	95.1	0.04923	1.2	0.1775	1.8	0.02616	1.4	166.4 ± 2.2	160.6 ± 2.6
5	0.98	303	204	0.70	8.90	0.0561	15	0.262	16	0.03381	1.9	214.3 ± 4.0	203 ± 22
6	--	20,397	1,020	0.05	529	0.04876	0.51	0.2029	1.4	0.03019	1.3	191.7 ± 2.5	189.5 ± 4.5
7	0.00	21,091	1,001	0.05	589	0.04895	0.44	0.2194	1.4	0.03251	1.4	206.2 ± 2.8	191.2 ± 4.0
8	0.08	17,005	862	0.05	468	0.04889	0.60	0.2159	1.5	0.03203	1.3	203.3 ± 2.7	175.2 ± 6.5
9	--	579	448	0.80	11.6	0.0497	3.6	0.1599	3.9	0.02336	1.5	148.9 ± 2.3	144.1 ± 4.0
10	0.27	807	345	0.44	17.9	0.0479	3.3	0.1706	3.6	0.02581	1.5	164.3 ± 2.4	139.7 ± 4.9
11	0.93	359	34	0.10	44.9	0.0584	4.6	1.162	5.0	0.1443	2.0	869 ± 16	459 ± 190
12	--	26,130	1,387	0.05	702	0.04907	0.44	0.2116	1.4	0.03127	1.3	198.5 ± 2.6	198.6 ± 4.7
13	0.29	5,013	542	0.11	127	0.04742	1.6	0.1918	2.1	0.02933	1.4	186.4 ± 2.5	132.2 ± 8.9
14	0.45	1957	536	0.28	46.4	0.0489	3.3	0.1855	3.6	0.02750	1.4	174.9 ± 2.4	153.1 ± 8.1
15	--	593	342	0.60	12.2	0.0497	4.3	0.1643	4.5	0.02396	1.5	152.6 ± 2.3	148.7 ± 5.2
16	0.37	581	163	0.29	12.1	0.0454	16	0.151	16	0.02416	1.8	153.9 ± 2.7	146 ± 32
17	0.04	8,079	833	0.11	186	0.04889	1.1	0.1807	1.7	0.02681	1.4	170.5 ± 2.3	161.2 ± 5.6
18	--	1,187	413	0.36	24.6	0.0502	3.1	0.1670	3.4	0.02413	1.4	153.7 ± 2.2	157.5 ± 6.6
19	0.30	1,694	1,403	0.86	36.4	0.0465	2.2	0.1599	2.6	0.02493	1.4	158.7 ± 2.2	147.1 ± 2.9
20	0.03	23,396	1,250	0.06	642	0.04880	0.45	0.2149	1.4	0.03195	1.3	202.7 ± 2.7	177.4 ± 4.2
21	0.92	782	194	0.26	48.9	0.0586	4.2	0.583	4.5	0.0722	1.4	449.2 ± 6.3	273 ± 36
22	--	118	52	0.46	13.5	0.0693	6.6	1.280	6.8	0.1339	1.8	810 ± 13	864 ± 72
23	--	316	243	0.79	6.45	0.0533	3.8	0.1753	4.2	0.02384	1.6	151.9 ± 2.4	150.2 ± 4.6
24	0.42	1780	75	0.04	290	0.07869	0.92	2.049	1.6	0.1889	1.4	1,115 ± 14	

Note: Pb_c and Pb^* represent common lead and radioactive lead, respectively. The measured ^{204}Pb is used to correct the common lead in zircons, and the age is $^{206}\text{Pb}/^{238}\text{U}$.



area was in the co-collision–post-collision stage; 4) < 810 Ma, when the Jiangnan region entered the premature rift evolution environment.

The Neoproterozoic lithium deposits in South China are mostly produced in orogenic belts, and most ore bodies occur in late rock strains and altered granite and pegmatite veins of

compound rock masses (Shu et al., 2021). The Neoproterozoic massive sulfide polymetallic deposits in the QHMB are related to continental margin island arc volcanism. Neoproterozoic metamorphic Fe-Mn deposits are related to continental rifting volcanism and have experienced late transformation of regional metamorphism and thermal metamorphism (Xu et al., 2015).

In South China during the Mesozoic, the Tethyan Tectonic Domain was transformed into the Pacific Tectonic Domain because of the oblique subduction of the Izanagi Plate (Xie et al., 2005; Xu and Xie, 2005; Mao et al., 2008). Since the Jurassic, the Izanagi Plate has migrated to the NW and subducted under the Okhotsk Plate (Wan and Zhu, 2002). Wang and Shen (2003) suggested that early Mesozoic granite distributed east to west on the southern ridge of Jiangxi may be post-orogenic granite related to Indosinian movement. Together with associated bimodal volcanic rocks and A-type granite, they formed an extensional tectonic environment and homologous granitic intrusion-volcanic complex of South China in the late Mesozoic may be directly associated with the subduction of the Paleo-Pacific Plate under the Eurasian Plate. Li et al. (1999), Hu et al. (2004), and Peng et al. (2008) postulated that Mesozoic magmatic activity in South China was closed and correlated with lithospheric extension; low t_{MD} and high ϵNd belts are considered evidence for lithospheric extension and strong crust-mantle interactions (Hong et al., 2002). Previous studies investigated the relationship between Cretaceous granite magmatism and lithospheric extension in South China, and proposed five stages of granite emplacement events at 164–87 Ma (Li, 1999) or 180–80 Ma (Xie et al., 2005).

Mao et al. (2007) indicated that the large-scale tungsten-tin polymetallic mineralization in the middle and late Jurassic in the Nanling area is related to the subduction of the Paleo-Pacific Plate, with mineralization mostly occurring in the back-arc tectonic setting of the continental margin. Peng et al. (2008) indicated that the large-scale granite intrusion and explosive mineralization of tungsten, tin, and other metals in the middle section of Nanling were formed in a tectonic setting of lithospheric extension, thinning, and crustal extension that could be associated with the second Mesozoic lithospheric extension event in South China. Pei et al. (2008) demonstrated that the early tungsten-tin mineralization of Nanling strata in the Mesozoic was associated with deep tectonic-magmatic processes, crustal magma-tectonic power, and an intrusive contact tectonic system formed during the tectonic-magmatism of continental margin-intracontinental orogeny. Hua (2005) proposed that the mineralization of tungsten and tin was related to dynamic extension background, crust-mantle interactions, and the participation of deep heat fluids. Li et al. (2008) indicated that the middle-late Jurassic tungsten mineralization and multi-stage tungsten-tin mineralization in South China were the result of multi-stage subduction of oceanic plates (or ridges) during different periods. Lin et al. (2020) estimated the difference in basement depth between the QHSZ and the Cathaysian Plate through seismic sounding and calculated depths of 0.5–2.0 km (QHSZ) and 1.5–3.0 km (Cathaysian Plate), with the QHSZ extending at least 8 km deep. This led to the hypothesis that

differences in basement depth, fault properties, and deep magmatism cause differences in mineralization.

CONCLUSION

The SHRIMP U-Pb dating of zircons in ore-forming veins of weathered residual Kaolin deposits on the northern QHMB margin showed that the ore-forming granite veins intruding into the Jiuling rock masses are Neoproterozoic (843 ± 10 Ma) in age and the ore-forming granite porphyry veins intruding into Neoproterozoic Anlelin Formation strata are late Jurassic (152.3 ± 1.8 Ma). We suggest that there were two periods in the formation of ore-forming rock masses of Kaolin deposits on the northern QHMB margin. Neoproterozoic Kaolin-forming veins may be related to the convergence, formation, or disintegration of the Rodinia Supercontinent and the Jurassic Kaolin-forming veins may be related to the subduction of the Paleo-Pacific Plate. Therefore, subsequent investigations and evaluations of weathered residual Kaolin deposits on the QHMB need to strengthen the identification and evaluation of late Jurassic and, particularly, Neoproterozoic acidic veins.

DATA AVAILABILITY STATEMENT

The original contributions presented in the study are included in the article/Supplementary Material, further inquiries can be directed to the corresponding author.

AUTHOR CONTRIBUTIONS

CL wrote the initial draft of the work and the final paper. CL, XZ and WZ interpreted the experiments and scanning electron microscope images. CL, QS, ZS, RC and TG contributed in interpreting the results. All authors finally approve the manuscript and thus agree to be accountable for this work.

FUNDING

This research was financially supported by China Geological Survey (DD20211579, DD20160038) and the NSF of China (41102052).

ACKNOWLEDGMENTS

We acknowledge Liu Shoujie (National Science and Technology Infrastructure Platform Beijing SHRIMP Center) for his assistance in sample loading, instrument commissioning and monitoring, and data processing. We also thank Li Qiming from China University of Geosciences (Wuhan), Yang Haoran and Liu Meng from Chengdu University of Technology, and Xie Rongbo, from China University of Petroleum (Beijing) for their help in the field and with sample collection. Finally, we thank Sev Kender, PhD, from Liwen Bianji (Edanz) (www.liwenbianji.cn/), for editing the English text of a draft of this manuscript.

REFERENCES

- Cheng, H., Hu, S. L., and Tang, Z. H. (1991). New Recognition on the Isotopic Geochronology of the “Tieshajie Group” in the Southern Part of Northeastern Jiangxi. *Reg. Geology China* 2, 151–154.
- Compston, W., Williams, I. S., Kirschvink, J. L., Zichao, Z., and Guogan, M. A. (1992). Zircon U-Pb Ages for the Early Cambrian Time-Scale. *J. Geol. Soc.* 149, 171–184. doi:10.1144/gsjgs.149.2.0171
- Duan, Z., Liao, S. B., Chu, P. L., Huang, W. C., Zhu, Y. H., Shu, X. J., et al. (2019). Zircon U-Pb Ages of the Neoproterozoic Jiuling Complex Granitoid in the Eastern Segment of the Jiangnan Orogen and its Tectonic Significance. *Geology China* 3, 493–516. CNKI:SUN:DZL0.2019-03-006.
- Feng, C. Y., Feng, Y. D., Xu, J. X., Zeng, Z. L., She, H. Q., Zhang, D. Q., et al. (2007a). Isotope Chronological Evidence for Upper Jurassic Petrogenesis and Mineralization of Altered Granite-type Tungsten Deposits in the Zhangtiantang Area, Southern Jiangxi. *Geology China* 4, 642–650. doi:10.3969/j.issn.1000-3657.2007.04.013
- Feng, C. Y., Xu, J. X., Zeng, Z. L., Zhang, D. Q., Qu, W. J., She, H. Q., et al. (2007b). Zircon SHRIMP U-Pb and Molybdenite Re-os Dating in Tianmenshan-Hongtaoling Tungsten-Tin orefield, Southern Jiangxi Province, China, and its Geological Implication. *Acta Geologica Sinica* 7, 952–963. doi:10.3321/j.issn:0001-5717.2007.07.011
- Gao, L. Z., Chen, J., Ding, X. Z., LiuZhang, Y. R. C. H., Zhang, H., Liu, Y. X., et al. (2011). Zircon SHRIMP U-Pb Dating of the Tuff Bed of Lengjiaxi and Banxi Groups, Northeastern Hunan, Constraints on the Wuling Movement. *Geol. Bull. China* 7, 1001–1008. 1671-255207-1001-0.
- Hao, J., and Zhai, M. G. (2004). Jinning Movement and Sinian System in China, Their Relationship with Rodinia Supercontinent. *Chin. J. Geology* 1, 139–152. doi:10.3321/j.issn:0563-5020.2004.01.014
- Hong, D. W., Xie, X. L., and Zhang, J. S. (2002). Geological Significance of the Hangzhou-Zhuguangshan-Huashan High- ϵ Nd Granite belt. *Geol. Bull. China* 6, 348–354. doi:10.3969/j.issn.1671-2552.2002.06.012
- Hu, S. L., Hao, J., and Li, Y. J. (1998). $^{40}\text{Ar}/^{39}\text{Ar}$ Isochron Age of the Xiwan Albite Granite in Dexing, Jiangxi, Determined by the Laser Mass Spectrometry. *Reg. Geology China* 1, 66–68. doi:10.1088/0256-307X/15/11/025
- Hua, R. M. (2005). Differences between Rock-Forming and Related Ore-Forming Times for the Mesozoic Granitoids of Crust Remelting Types in the Nanling Range, South China, and its Geological Significance. *Geol. Rev.* 6, 633–639. CNKI:SUN:DZLP.0.2005-06-005.
- Jiang, S. Y., Peng, N. J., Huang, L. C., Xu, Y. M., Zhan, G. L., and Dan, X. H. (2015). Geological Characteristic and Ore Genesis of the Giant Tungsten Deposits from the Dahutang Ore-Concentrated District in Northern Jiangxi Province. *Acta Petrologica Sinica* 3, 639–655. CNKI:SUN:YSXB.0.2015-03-001.
- Li, N., Wu, X. L., Wu, D. X., Zhou, C., and Hu, F. L. (2017). Geological Features and Utilization prospect of Ehu Kaolin Deposit in Fuliang County, Jiangxi Province. *J. East China Univ. Technol. (Natural Sciences)* 2, 149–157. doi:10.3969/j.issn.1674-3504.2017.02.007
- Li, X. F., Watanabe, Y., Hua, R. M., and Mao, J. W. (2008). Mesozoic Cu-Mo-W-Sn Mineralization and ridge/Triples Subduction in South China. *Acta Geologica Sinica* 5, 625–640. doi:10.3321/j.issn:0001-5717.2008.05.006
- Li, X. H., Zhou, G. Q., and Zhao, X. J. (1994). SHRIMP Ion Microprobe Zircon U-Pb Age of the NE Jiangxi Ophiolite and its Tectonic Implications. *Geochimica* 2, 125–131. CNKI:SUN:DQHX.0.1994-02-002.
- Lin, J. Y., Tang, G. B., Xu, T., Cai, H. T., Lü, Q. T., Bai, Z. M., et al. (2020). P-wave Velocity Structure in Upper Crust and Crystalline Basement of the Qinhang and Wuyishan Metallogenic Belts, Constraint from the Wanzai-Hui'an Deep Seismic Sounding Profile. *Chin. J. Geophys.* 12, 4396–4409. doi:10.6038/cjg202000158
- Liu, S. B., Wang, D. H., Chen, Y. C., Xu, J. X., Zeng, Z. L., Ying, L. J., et al. (2007). SHRIMP Dating of Tianmenshan Granite Pluton and Granite-Porphry Dyke in Southern Jiangxi Province, Eastern Nanling Region and its Significance. *Acta Geologica Sinica* 7, 972–978. doi:10.3321/j.issn:0001-5717.2007.07.013
- Lou, F. S., Shen, W. Z., Wang, D. Z., Shu, L. S., Wu, F. J., Zhang, F. R., et al. (2005). Zircon U-Pb Isotopic Chronology of the Wugongshan Dome Compound Granite in Jiangxi Province. *Acta Geologica Sinica* 5, 636–644. doi:10.3321/j.issn:0001-5717.2005.05.008
- Lu, S. N., Li, H. K., Chen, Z. H., Yu, H. F., Jin, W., and Guo, K. Y. (2004). Relationship between Neoproterozoic Cratons of China and the Rodinia. *Earth Sci. Front.* 2, 515–523. doi:10.3321/j.issn:1005-2321.2004.02.021
- Mao, J. W., Xie, G. Q., Guo, C. L., and Chen, Y. C. (2007). Large-scale Tungsten-Tin Mineralization in the Nanling Region, South China, Metallogenic Ages and Corresponding Geodynamic Processes. *Acta Petrologica Sinica* 10, 2329–2338. doi:10.3969/j.issn.1000-0569.2007.10.002
- Mao, J. W., Xie, G. Q., Guo, C. L., Yuan, S. D., Cheng, Y. B., and Chen, Y. C. (2008). Spatial-temporal Distribution of Mesozoic Ore Deposits in South China and Their Metallogenic Settings. *Geol. J. China Universities* 4, 510–526. doi:10.3969/j.issn.1006-7493.2008.04.005
- Pan, G. T., Lu, S. Ni., Xiao, Q. H., Zhang, K. X., Yin, F. G., Hao, G. J., et al. (2016). Division of Tectonic Stages and Tectonic Evolution in China. *Earth Sci. Front.* 6, 1–23. doi:10.13745/j.esf.2016.06.00
- Pei, R. F., Wang, Y. L., Li, L., and Wang, H. L. (2008). South China Great Granite Province and its Metallogenic Series of Tungsten-Tin Poly-Metallics. *China Tungsten Industry* 1, 10–13. doi:10.3969/j.issn.1009-0622.2008.01.003
- Peng, J. T., Hu, R. Z., Yuan, S. D., Bi, X. W., and Shen, N. P. (2008). The Time Ranges of Granitoid Emplacement and Related Nonferrous Metallic Mineralization in Southern Hunan. *Geol. Rev.* 5, 617–625. doi:10.3321/j.issn:0371-5736.2008.05.006
- Shu, L. S., Zhu, W. B., and Xu, Z. Q. (2021). Geological Settings and Metallogenic Conditions of the Granite-type Lithium Ore Deposits in South China. *Acta Geologica Sinica* 10, 3099–3114. doi:10.7762/j.cnki.dizhixuebao.2021152
- Sun, K. K., Chen, B., Chen, J. S., and Xiang, X. K. (2017). The Petrogenesis of the Jiuling Granodiorite from the Dahutang deposit, Jiangxi Province and its Tectonic Implications. *Acta Petrologica Sinica* 3, 907–924. doi:10.00-0569/2017/033(03)-0907-24
- Wan, T. F., and Zhu, H. (2002). 2. Tectonics and Environment Change of Meso-Cenozoic in China Continent and its Adjacent Areas. *Geoscience- J. Graduate Sch. Beijing: China University of Geosciences*, 107–120. doi:10.3969/j.issn.1000-8527.2002.02.001
- Wang, D. Z., and Shen, W. Z. (2003). Genesis of Granitoids and Crustal Evolution in Southeast China. *Earth Sci. Front.* 3, 209. doi:10.3321/j.issn:1005-2321.2003.03.020
- Wang, F. N., Zhou, Y. H., and Yu, C. F. (1986). Kaolin Deposits and Their Geological Characteristics in Jiangxi. *Geology China* 1, 18–20. CNKI:SUN:DZL0.1986-01-007.
- Wang, G. L., Hu, J. S., Hu, F. L., Zhao, L. M., and Hu, G. H. (2018). Characteristics and Prospecting Direction of Pulse Type Kaolin in Jingdezhen-A Case of Study in Ehu Kaolin deposit. *J. East China Univ. Technol. (Natural Sciences)* 4, 379–388. doi:10.3969/j.issn.1674-3504.2018.04.010
- Wang, X. L., Zhou, J. C., Chen, X., Zhang, F. F., and Sun, Z. M. (2017). Formation and Evolution of the Jiangnan Orogen Belt. *Bull. Mineralogy, Petrol. Geochem* 5, 714–735. doi:10.3969/j.issn.1007-2802.2017.05.003
- Wang, Y. J., and Fang, Y. S. (1994). Discussion on the Formation Mechanism of High Quality Kaolin Ore in Yichun, Jiangxi Province. *Nonmetallic Geology*. 6, 2–7.
- Wu, F. J., Yu, J., Liu, C. G., and Deng, J. H. (2016). Basic Features and Significance of Yifeng-Dexing Superimposition Orogenic belt, Jiangxi Province. *Geol. Bull. China* 1, 181–187. doi:10.3969/j.issn.1671-2552.2016.01.017
- Wu, X. Y., Zhang, Z. Y., Zheng, Y. C., Dai, J. L., Fan, X. K., and Sheng, Y. C. (2019). Magmatism, Genesis and Significance of Multi-Stage Porphyry-like Granite in the Giant Dahutang Tungsten deposit, Northern Jiangxi Province. *Acta Petrologica et Mineralogica* 3, 318–338. doi:10.3969/j.issn.1000-6524.2019.03.003
- Xie, G. Q., Mao, J. W., Hu, R. Z., Li, R. L., and Cao, J. J. (2005). Discussion on Some Problems of Mesozoic and Cenozoic Geodynamics of Southeast China. *Geol. Rev.* 6, 613–620. doi:10.3321/j.issn:0371-5736.2005.06.002
- Xu, D. M., Lin, Z. Y., Luo, X. Q., Zhang, K., Zhang, X. H., and Huang, H. (2015). Metallogenic Series of Major Metallic Deposits in the Qinzhou-Hangzhou Metallogenic belt. *Earth Sci. Front.* 2, 7–24. CNKI:SUN:DXQY.0.2015-02-003.
- Xu, X. S., and Xie, X. (2005). Late Mesozoic-Cenozoic Basaltic Rocks and Crust-Mantle Interaction, SE China. *Geol. J. China Universities* 3, 318–334. 006-749303-318-17.
- Yang, M. G., Liu, Y. G., Huang, Z. Z., Wu, F. J., and Song, Z. R. (2012). Subdivision of Meso-Neoproterozoic Strata in Jiangxi and a Correlation with the Neighboring Areas. *Geology China* 1, 43–54. CNKI:SUN:DZL0.2012-01-006.

- Yuan, Y., Liao, Z. T., and Wang, C. (2012). Multi-stage Tectonic Evolution in Jiangnan Uplift (Jiuling Terran) from Granitoids Records. *J. Tongji Univ. (Natural Sciences)* 9, 1414–1421. doi:10.3969/j.issn.0253-374x.2012.09.023
- Zhang, F. R., Shu, L. S., Wang, D. Z., Yu, J. H., and Shen, W. Z. (2009a). Discussions on the Tectonic Setting of Caledonian Granitoids in the Eastern Segment of South China. *Earth Sci. Front.* 1, 248–260. CNKI:SUN:DXQY.0.2009-01-034
- Zhang, J. L., Xu, D. R., Yu, L. L., and Hou, M. Z. (2018). Zircon U-Pb Dating of Granite and Host Rock in Xinyu Iron Ore Area, Jiangxi Province, China. *Chin. J. Nonferrous Met.* 5, 971–984. doi:10.19476/j.ysxb.1004.0609.2018.05.14
- Zhang, W. L., Hua, R. M., Wang, R. C., Li, H. M., Qu, W. J., and Ji, J. Q. (2009b). New Dating of the Piaotang Granite and Related Tungsten Mineralization in Southern Jiangxi. *Acta Geologica Sinica* 5, 659–670. doi:10.3321/j.issn:0001-5717.2009.05.007
- Zhao, P., Jiang, Y. H., Liao, S. Y., Zhou, Q., and Jin, G. D. (2010). SHRIMP Zircon U-Pb Age, Sr-Nd-Hf Isotopic Geochemistry and Petrogenesis of the Ehu Pluton in Northeastern Jiangxi Province. *Geol. J. China Universities* 2, 218–225. doi:10.3969/j.issn.1006-7493.2010.02.009
- Zhong, Y. F., Ma, C. Q., She, Z. B., Lin, G. C., Xu, H. J., Wang, R. J., et al. (2005). SHRIMP U-Pb Zircon Geochronology of the Jiuling Granitic Complex Batholith in Jiangxi Province. *Earth Sci.* 6, 685–691. doi:10.3321/j.issn:1000-2383.2005.06.005
- Zhou, J. C., Wang, X. L., and Qiu, J. S. (2008). Is the Jiangnan Orogenic Belt a Grenvillian Orogenic Belt, Some Problems about the Precambrian Geology of South China. *Geol. J. China Universities* 1, 64–73. CNKI:SUN:GXDX.0.2008-01-009.
- Zhou, X. H., Zhang, Y. J., Liao, S. B., Yu, M. G., Chen, Z. H., Zhao, X. L., et al. (2012). LA-ICP-MS Zircon U-Pb Geochronology of Volcanic Rocks in the Shuangqiaoshan Group at Anhui-Jiangxi Boundary Region and its Geological Implication. *Geol. J. China Universities* 4, 609–622. CNKI:SUN:GXDX.0.2012-04-005.

Conflict of Interest: The authors declare that the research was conducted in the absence of any commercial or financial relationships that could be construed as a potential conflict of interest.

Publisher's Note: All claims expressed in this article are solely those of the authors and do not necessarily represent those of their affiliated organizations, or those of the publisher, the editors, and the reviewers. Any product that may be evaluated in this article, or claim that may be made by its manufacturer, is not guaranteed or endorsed by the publisher.

Copyright © 2022 Li, Sun, Sun, Zhou, Zhang, Chen and Gao. This is an open-access article distributed under the terms of the Creative Commons Attribution License (CC BY). The use, distribution or reproduction in other forums is permitted, provided the original author(s) and the copyright owner(s) are credited and that the original publication in this journal is cited, in accordance with accepted academic practice. No use, distribution or reproduction is permitted which does not comply with these terms.



Experimental Research on Electrical Conductivity of the Olivine-Ilmenite System at High Temperatures and High Pressures

Wenqing Sun¹, Lidong Dai^{1*}, Haiying Hu^{1*}, Mengqi Wang^{1,2}, Ziming Hu^{1,2} and Chenxin Jing^{1,2}

¹Key Laboratory of High-Temperature and High-Pressure Study of the Earth's Interior, Institute of Geochemistry, Chinese Academy of Sciences, Guiyang, China, ²University of Chinese Academy of Sciences, Beijing, China

OPEN ACCESS

Edited by:

Zhicheng Jing,
Southern University of Science and
Technology, China

Reviewed by:

George Amulele,
Case Western Reserve University,
United States
Xiaozhi Yang,
Nanjing University, China

*Correspondence:

Lidong Dai
dailidong@vip.gyg.ac.cn
Haiying Hu
huhaiying@vip.gyg.ac.cn

Specialty section:

This article was submitted to
Earth and Planetary Materials,
a section of the journal
Frontiers in Earth Science

Received: 24 January 2022

Accepted: 10 March 2022

Published: 05 April 2022

Citation:

Sun W, Dai L, Hu H, Wang M, Hu Z and
Jing C (2022) Experimental Research
on Electrical Conductivity of the
Olivine-Ilmenite System at High
Temperatures and High Pressures.
Front. Earth Sci. 10:861003.
doi: 10.3389/feart.2022.861003

Ilmenite is a common metallic oxide distributed in the mafic rocks from the Earth's upper mantle, and thus the effect of ilmenite contents on the electrical structures of the Earth's upper mantle should be investigated in detail. Electrical conductivities of the olivine-ilmenite systems with various contents of ilmenite ($V_{\text{ilm}} = 4, 7, 10, 11$ and 15 vol%) and pure ilmenite aggregates were measured using a complex impedance spectroscopic technique at $1.0\text{--}3.0$ GPa and $773\text{--}1273$ K. Electrical conductivities of the olivine-ilmenite systems increased with increasing temperatures in different degrees, conforming to the Arrhenius law. With the rise of pressure, the conductivities of the olivine-ilmenite systems slightly increased. According to the significant change of the conductivities, the percolation threshold of ilmenite grains in the olivine-ilmenite systems was proposed to be ~ 11 vol%. Isolated ilmenites moderately influence the conductivities of olivine aggregates, but the interconnected ilmenites dramatically enhanced the conductivities of the olivine-ilmenite systems. The conductivities of the olivine aggregates with 11 vol% ilmenites were about $1.5\text{--}3$ orders magnitude higher than those of 10 vol% ilmenites-bearing olivine aggregates. Small polarons were proposed to be the dominant charge carriers for olivine aggregates with isolated ilmenites (activation enthalpies: $0.62\text{--}0.89$ eV) and interconnected ilmenites (activation enthalpies: $0.15\text{--}0.20$ eV). Furthermore, the conductivity-depth profiles of olivine-ilmenite systems in the Earth's upper mantle were constructed, providing an important constraint on the electrical structures of the Earth's interior.

Keywords: electrical conductivity, olivine-ilmenite system, high pressure, conduction mechanism, mantle

INTRODUCTION

Electrical conductivity research for geological materials at high temperatures and pressures is a significant window to watch into the material compositions and thermodynamic state in the interior of the planets. Previous studies on the electrical conductivity were focused on the dominant silicate minerals and rocks, aqueous fluids, and silicate and carbonate melts in the Earth's interior (Huang et al., 2005; Ni et al., 2011; Yang et al., 2012; Dai et al., 2018; Guo et al., 2018; Guo and Keppler, 2019; Huang et al., 2021). It was proposed that the high conductivity anomalies in the Earth's interior can be caused by the various high-conductivity phases (e.g., melts, fluids, hydrogen in the nominally anhydrous minerals) (Wannamaker et al., 2009; Ni et al., 2011; Dai and Karato, 2014; Manthilake

et al., 2016; Laumonier et al., 2017; Sun et al., 2017; Guo et al., 2018; Li et al., 2018), and high-conductivity mineral phases (e.g., graphite, magnetite, iron sulfide) were determined to be one significant influence factor for the high conductivity anomalies (Watson et al., 2010; Wang et al., 2013; Zhang and Pommier, 2017). It is note that the graphite is stable in the cratonic lithospheric mantle (Pearson et al., 1994), and aqueous fluids and melts are widely distributed in the subduction zones (Iwamori, 1998; Scambelluri and Philippot, 2001; Gaillard, 2005; Gaillard et al., 2008). A small quantity of high-conductivity minerals can dramatically enhance the conductivities of polycrystalline olivine (Wang et al., 2013; Zhang and Pommier, 2017; Dai et al., 2019). And thus, the high-conductivity minerals might play a significant role on the electrical structures of the Earth's upper mantle, where the most dominant mineral is olivine.

Ilmenites as mineral inclusions and accessory minerals are widely distributed in the peridotites and kimberlites in various geological regions (Ponomarenko, 1977; Risold et al., 2003; Wirth and Matsyuk, 2005; Pang et al., 2008; Cao et al., 2019), and exsolution of ilmenite from olivine is a common phenomenon (Liu et al., 2005; Massonne and Neuser, 2005). Due to the magmatic fractionation and crystallization, Ilmenite ore deposit can be formed in some special regions, such as Emeishan Large Igneous Province (She et al., 2015). It was implied that ilmenite exist in the interior of the Earth, and ilmenite contents of mafic rocks in various regions might be different. Ilmenites might be enriched in some peridotites of the special regions due to magmatic fractionations and crystallizations in the period of crust-mantle differentiation. In order to in-depth study electrical structures in the Earth's upper mantle, the influence of ilmenite contents on the olivine aggregates should be considered. Previous studies have researched the conductivities of monocrystalline olivine, olivine aggregates and olivine aggregates mixed with graphite, magnetite or metal sulfide (Dai et al., 2010; Wang et al., 2013; Dai and Karato, 2014; Zhang and Pommier, 2017; Dai et al., 2019). Single crystal of hydrous olivine shows the apparent anisotropy of electrical property, and the conductivity of olivine along the crystal orientation of [100], [010] and [001] decreases in order (Dai and Karato, 2014). In addition, water and iron contents significantly enhance the conductivity of olivine, providing a basis for the interpretation of electrical conductivity model of other planets with different iron and hydrogen contents (Dai and Karato, 2014). In the real geological environments, the material compositions of the Earth's interior are complicated, and change with spatial location. It was confirmed that olivine usually coexists with various contents of high-conductivity mineral phases (e.g., graphite, magnetite, et al.) in some special regions of the Earth's interior (Duba and Shankland, 1982; Yamanaka et al., 2001). When the concentration of graphite exceeds percolation threshold (~ 1 wt%), the conductivities of olivine aggregates with graphite was markedly enhanced (Wang et al., 2013). A small quantity of magnetite can also moderately enhance the conductivities of olivine aggregates (Dai et al., 2019). For the olivine-metal systems, the conductivities increased with the increase of metal: olivine

ratios and the contents of metal melt infiltrated into polycrystalline olivine matrix (Zhang and Pommier, 2017). However, electrical conductivities of olivine aggregates mixed with various contents of ilmenites at high temperatures and high pressures have not been investigated.

In the present study, we *in-situ* measured the conductivities of the dry olivine-ilmenite systems under the conditions of 1.0–3.0 GPa and 773–1273 K. Effects of temperature, pressure and ilmenite content on the conductivities of the olivine-ilmenite systems were systematically researched, and the conduction mechanism for the olivine-ilmenite systems was discussed in detail. According to the thermal models of the Earth's interior and electrical conductivity-temperature data of olivine aggregates with various contents of ilmenites, we constructed the electrical conductivity-depth profiles for the olivine-ilmenite systems in the Earth's upper mantles.

EXPERIMENTAL PROCEDURES

Sample Preparation

The main chemical compositions of the natural olivine and ilmenite grains were tested using the electron probe microanalysis, and the weight percentages of the oxides for the main elements were shown in **Table 1**. It is note that the whole iron ions in the olivine and ilmenite were assumed to be ferrous iron, and the slight decrease of the total quantity of the oxides for ilmenite might be due to the presence of ferric irons and hematite (Andreozzi et al., 1996). Due to the very low decrease of the total quantity of oxides for ilmenite, it is revealed that the purity of ilmenite is very high. The fresh olivine and ilmenite grains were ultrasonically cleaned in a mixture of distilled water, acetone and ethanol, and ground to powder (<200 mesh) in an agate mortar. The olivine and ilmenite powders were homogeneously mixed by weight percent, and ilmenite contents of five powder samples were 5, 10, 13, 15, and 20 wt%, respectively. According to the weight fractions and densities of olivine (3.4 g/cm³) and ilmenite (4.7 g/cm³), the volume percent of ilmenite in the five olivine-ilmenite systems was 4, 7, 10, 11, and 15 vol%, respectively. The sample powder was loaded into a copper capsule with a 0.025-mm thick Ni-foil liner, and then sintered for 6 h in a multi-anvil high pressure apparatus at 2.0 GPa and 873 K. The hydrothermally annealed samples were cut and polished into cylinders with diameter and height of 6 mm, and ultrasonically cleaned in a mixture of deionized water, acetone and ethanol. In order to avoid the effect of absorbed water on the electrical conductivity measurements, all synthetic samples were dried at 423 K for 12 h in an oven. The mineral distribution and interior structure of the samples were observed by scanning electron microscopy at the State Key Laboratory of Ore Deposit Geochemistry, Institute of Geochemistry, Chinese Academy of Sciences (CAS), Guiyang, China. As shown in **Figure 1** the olivine and ilmenite grains were relatively uniformly distributed to the samples, and the particle-size ranges in various samples were close to each other. In order to determine the water content in the olivines, we applied the Fourier transform infrared (FTIR) spectrometer (Vertex-70 V

TABLE 1 | Chemical compositions of the initial olivine and ilmenite samples obtained using the electron probe microanalysis. The numbers represent the weight percent (wt.%) of the oxides for main elements of the olivine and ilmenite, and the whole iron elements are assumed to be ferrous irons.

Sample	FeO	MnO	NiO	Cr ₂ O ₃	Al ₂ O ₃	TiO ₂	SiO ₂	MgO	K ₂ O	CaO	Na ₂ O	V ₂ O ₃	CuO	Total
olivine	5.965	0.120	0.117	0.437	0.000	0.000	58.327	34.055	0.009	0.750	0.171	0.000	0.000	99.951
ilmenite	44.787	0.540	0.005	0.113	1.578	49.801	0.000	1.562	0.000	0.000	0.000	0.262	0.008	98.656

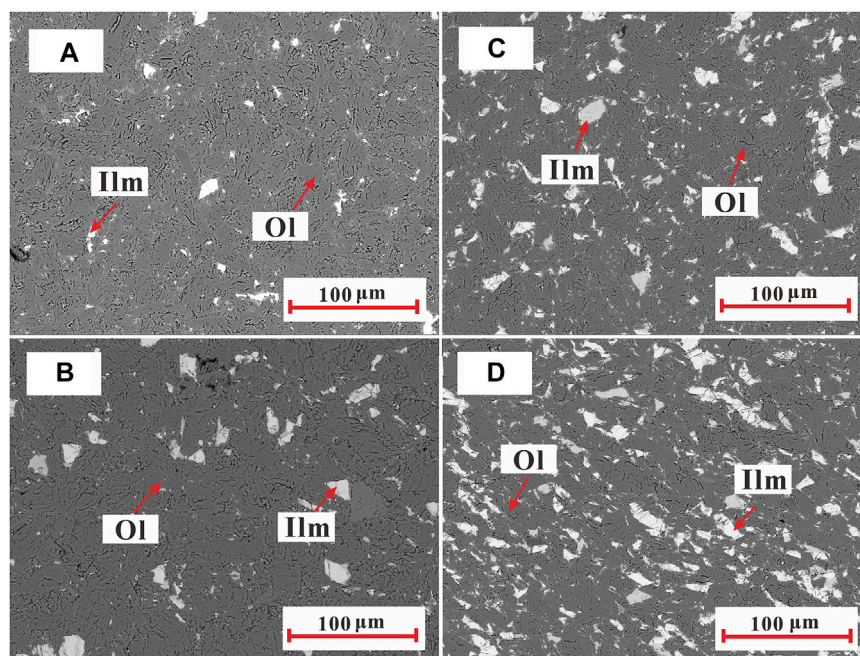


FIGURE 1 | Representative electron backscattered images (BSIs) of the recovered samples of polycrystalline olivine-ilmenite systems with 4 vol% (A), 7 vol% (B), 10 vol% (C), and 15 vol% (D). The dark gray regions represent the olivine (Ol) grains, and the white gray regions are corresponding to the ilmenite (Ilm) grains. The olivine and ilmenite grains (particle size: <50 μm) were relatively homogeneously distributed in the samples.

and Hyperion-1000 infrared microscope) in the Key Laboratory of High-temperature and High-pressure Study of the Earth's Interior, Institute of Geochemistry, Chinese Academy of Sciences, China. The infrared spectra were measured with unpolarized radiation from a mid-IR light source, a mercury-cadmium-telluride detector (aperture size: 100 × 100 μm) and a CaF₂ beam splitter. The FTIR spectra in wavenumber range of 3,000–4,000 cm⁻¹ with 512 scans of the original and annealed olivine grains were obtained. After simple base and smooth treatments, the infrared spectra of the original and annealed olivines were almost flat (Figure 2), indicating no water was absorbed in the original and annealed olivines.

Impedance Measurements

Electrical conductivity measurements were performed in the YJ-3000t multi-anvil apparatus and Solartron-1260 impedance/gain-phase analyzer at the Key Laboratory of High-Temperature and High-Pressure Study of the Earth's Interior, Institute of Geochemistry, CAS, Guiyang, China. The large-volume high-pressure press and complex impedance analyzer have been widely

applied to study the electrical conductivities of a series of minerals and rocks (Wang et al., 2010; Dai et al., 2015a; Dai et al., 2015b, Dai et al., 2016, Dai et al., 2018; Hu et al., 2014, Hu et al., 2017, Hu et al., 2018; Sun et al., 2017). During operation of the high-pressure press, six cubic WC anvils (side length: 25 mm) were driven by oil pressure to compress the cubic sample assembly, providing the pressures of up to 3.0 GPa. Using the lanthanum chromate and stainless steel as heater, temperatures of up to 2,273 and 1573 K can be achieved, respectively. The schematic diagram of the sample assembly for electrical conductivity measurements was shown in Figure 3. In order to remove the water in the sample assembly, all relevant components were baked in a 1073 K muffle furnace for 6 h. A pyrophyllite cube (32.5 × 32.5 × 32.5 mm³) and stainless-steel sheets (thickness: 0.5 mm) were used as the pressure medium and heater, respectively. Alumina and magnesia sleeves were located adjacent to the heater as insulators and pressure medium. To shield against external electromagnetism and spurious signal interference, a layer of nickel foil was placed between the Al₂O₃ and MgO sleeves. The MgO tube (inner diameter: 6 mm, height: 20 mm) was applied as

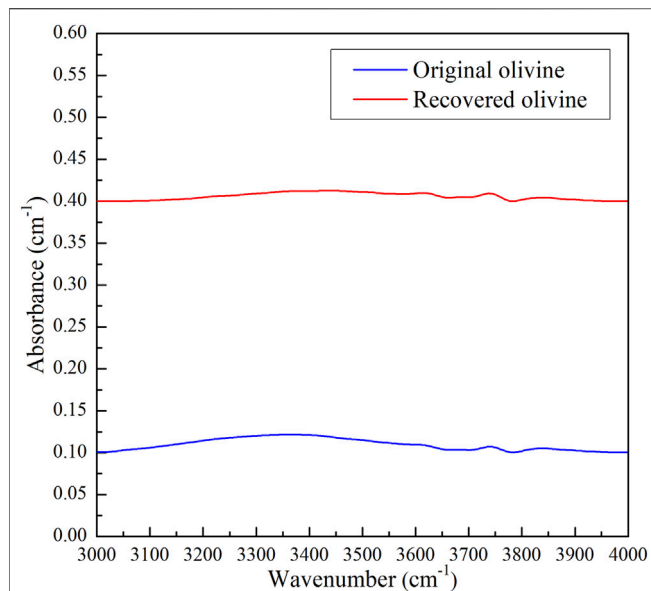


FIGURE 2 | Fourier transform infrared (FTIR) spectra of the original and recovered olivines in the wavenumbers range of 3,000–4,000 cm^{-1} .

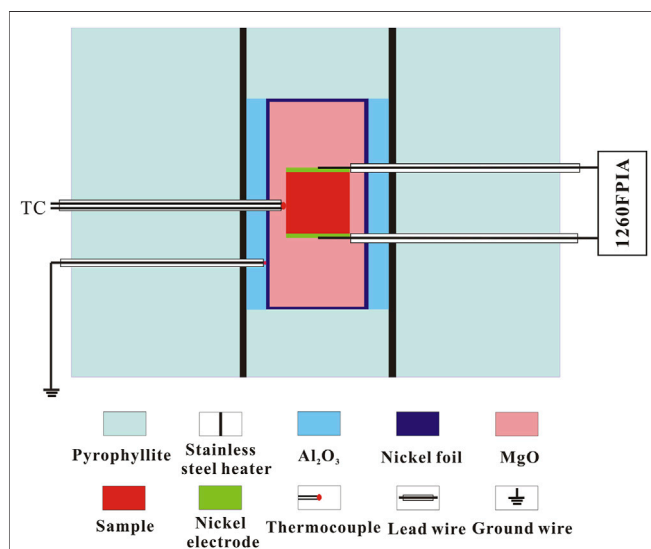


FIGURE 3 | Schematic diagram of experimental setup for the electrical conductivity measurements of olivine-ilmenite systems at high temperatures and high pressures.

sample capsule. The parallel-plate electrode was composed of two nickel disks with the diameter of 6.0 mm and thickness of 0.5 mm. In addition, the nickel electrode and nickel foil can be used to control the oxygen fugacity in the sample capsule at high temperatures and high pressures. It has been demonstrated that the oxygen fugacity controlled by Ni-NiO buffer (NNO) at high temperature and high pressure is close to the oxygen fugacity of the Earth's upper mantle (Xu et al., 2000; Dai et al., 2012). And then, the K-type thermocouple wires (NiCr/NiSi) and ground

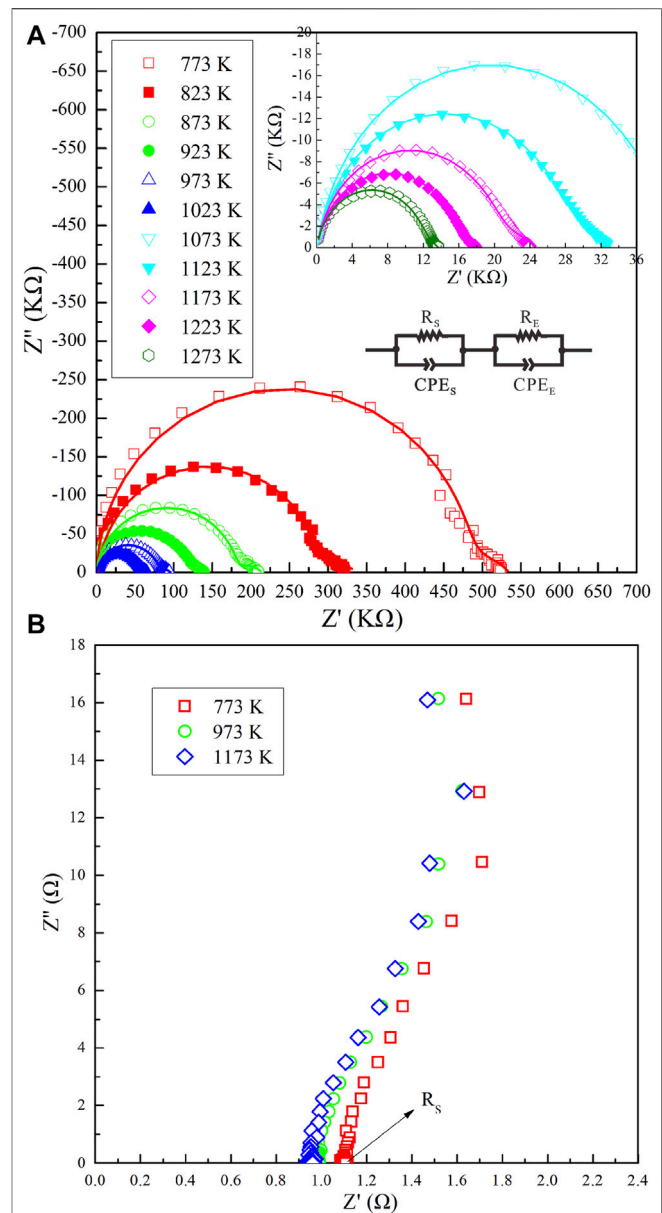


FIGURE 4 | Typical complex impedance spectra for (A) polycrystalline olivine-ilmenite system with 10 vol% ilmenites and (B) pure ilmenite aggregates under the conditions of 2 GPa and various temperatures.

wire (NiSi) were inserted into the holes in the lateral edge of the pyrophyllite cube, and contacted with the sample and nickel foil, respectively. To keep dry, the sample assembly was placed in a 323 K oven for at least 12 h before electrical conductivity measurements.

During the experiments, the pressure was slowly raised at a rate of 0.5 GPa/h until it reached the desired value, and then the temperature was increased with a speed of 10 K/min to the designated value. Under the stable pressure and temperature, impedance spectra of the samples were collected in the frequency range of 10^{-1} – 10^6 Hz at the constant exciting voltage of 1,000 mV. The measurement temperatures change with a 50-K

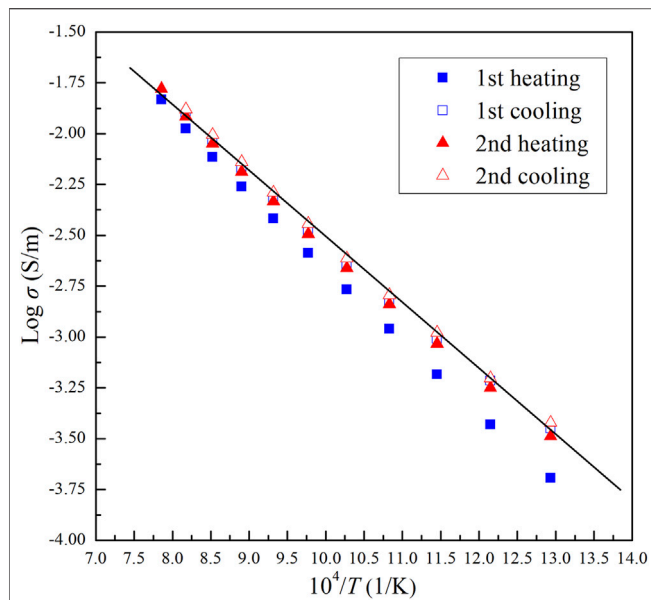


FIGURE 5 | Logarithmic electrical conductivity versus reciprocal temperature for dry olivine aggregates with 10 vol% chromite during multiple heating/cooling cycles at 2.0 GPa and 773–1273 K.

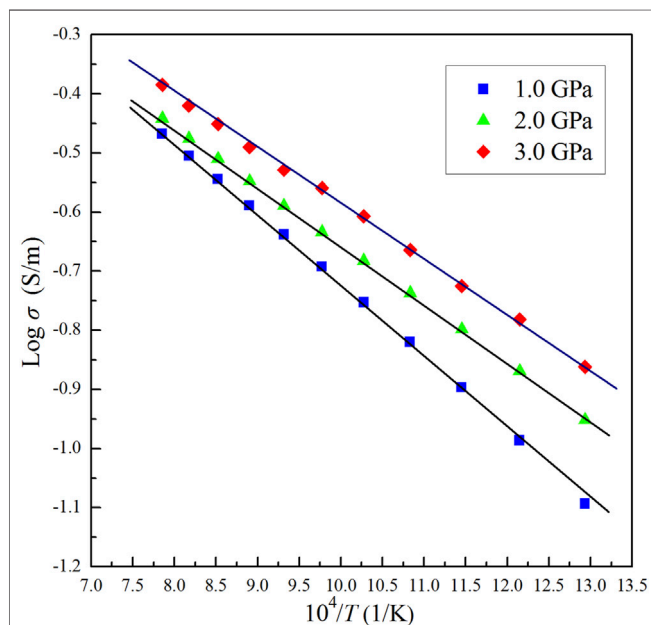


FIGURE 6 | The linear relationship between Logarithmic electrical conductivities and reciprocal temperatures for olivine-ilmenite system with 11 vol% ilmenites under the conditions of 1.0–3.0 GPa and 773–1273 K.

interval. To obtain reproducible data, impedance spectra of samples were collected in multiple heating/cooling cycles under conditions of 1.0–3.0 GPa and 773–1273 K. The errors of temperature and pressure were ± 5 K and ± 0.1 GPa, respectively.

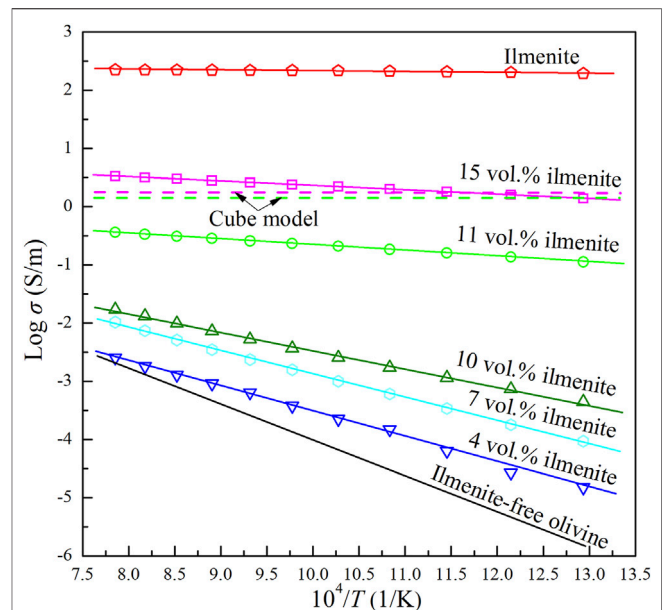


FIGURE 7 | Logarithm of electrical conductivities versus reciprocal temperatures for pure olivine aggregates, polycrystalline olivine with various ilmenite contents (4–15 vol%), and pure ilmenite aggregates at 2.0 GPa and 873–1273 K. The solid lines represent the measurement conductivities of pure olivine aggregates (Dai et al., 2019), olivine-ilmenite systems and pure ilmenite aggregates, and green and pink dash lines stand for the calculated conductivities of olivine-ilmenite systems with 11 vol% and 15 vol% using cube model, respectively.

RESULTS

Representative complex impedance spectra of the dry olivine-ilmenite systems and pure ilmenite aggregates were shown in **Figure 4**. For the pure ilmenite aggregates, the impedance spectra were approximate perpendicular lines, and the intercepts of the lines in the horizontal axis represented the electrical resistances. For the olivine-ilmenite systems, the impedance spectra were composed of an almost ideal semicircle in the high-frequency region and an additional tail in the low-frequency region. Previous studies have proposed that the ideal semicircle in the high-frequency region represents the bulk electrical properties of the sample, and the additional tail is related to the diffusion processes at the sample-electrode interface (Roberts and Tyburczy, 1991; Dai and Karato, 2009; Yang et al., 2012). Therefore, the bulk sample resistance can be obtained by fitting the ideal semicircle in the high-frequency region. A series connection of R_S - CPE_S (R_S and CPE_S represent the resistance and constant-phase element of the sample, respectively) and R_E - CPE_E (R_E and CPE_E represent the resistance and constant-phase element for electrode effect, respectively) were used as the equivalent circuit, and the fitting errors of the electrical resistance were less than 5%. The electrical conductivities of the olivine-ilmenite systems were calculated using the following formula:

$$\sigma = L/SR \quad (1)$$

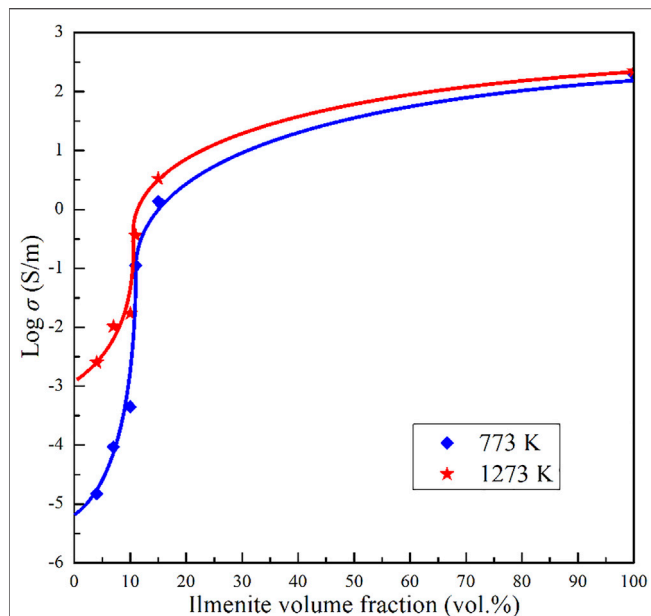


FIGURE 8 | The relationships between logarithmic conductivities of the olivine-ilmenite systems and ilmenite volume fractions at 773 and 1273 K. The diamond symbols and five-star symbols stand for the measured values of electrical conductivities, and solid lines represented the fitted curves.

where L is the height of the sample (m), S is the cross-sectional area of the electrodes (m^2), R is the fitting resistance (Ω), and σ is the electrical conductivity of the sample (S/m).

The impedance spectra of the olivine-ilmenite systems were collected in multiple heating/cooling cycles, and the final stable data were applied to discuss the relevant laws. As shown in **Figure 5**, the electrical conductivities of olivine-ilmenite system with 10 vol% ilmenite were almost repeated in the 2nd heating/cooling cycles. In order to investigate the relationship between the conductivities and temperatures and pressures, we plotted the logarithmic conductivities versus temperatures at the constant pressures. The reproducible data were applied to analyze the electrical properties of the samples at high temperatures and pressures. **Figure 6** revealed pressure influence on the conductivities of the olivine aggregates mixed with 11 vol% ilmenites under the conditions of 1.0–3.0 GPa and 773–1273 K. Pressure was positively related to the conductivities of olivine-ilmenite systems, being the opposite influence for pure olivine aggregates (Dai et al., 2010; Dai et al., 2019). Influence of pressure on the conductivities of the olivine-ilmenite systems was much weaker than that of temperature (**Figure 6**), further supporting the previous conclusion for the slight influence of pressure on the conductivities of silicate minerals with or without some other high-conductivity minerals (Wang et al., 2010; Yang et al., 2011; Hu et al., 2014; Dai et al., 2019; Guo et al., 2020). **Figure 7** showed the influence of ilmenite contents on the conductivities of olivine-ilmenite systems at 2.0 GPa and 773–1273 K. Electrical conductivities of olivine-ilmenite systems with the ilmenite volume fractions of 0–10 vol% moderately increased with increasing ilmenite content. The conductivities of

olivine-ilmenite system with 10 vol% ilmenites were about 0.5 orders of magnitude higher than those of the system with 7 vol% ilmenites. However, the conductivities of olivine aggregates with 11 vol% ilmenites were ~ 1.5 –3 orders of magnitude higher than those for olivine-ilmenite system with 10 vol% ilmenites. And then, the conductivities of olivine-ilmenite system with 15 vol% ilmenites were about 1 order of magnitude higher than those of the system with 11 vol% ilmenites (**Figure 7**). It was clear that the conductivities of olivine-ilmenite systems dramatically increased at the ilmenite content of 11 vol% (**Figure 8**). And thus, the ilmenite grains in the olivine-ilmenite system with 11 vol% ilmenites might be interconnected. In order to further verify the above inference, we applied Cube model which was suitable for the systems with interconnected high-conductivity phase to calculate the conductivities of olivine-ilmenite systems with 11 vol% and 15 vol% ilmenites. The mathematical formula for the cube model is expressed as:

$$\sigma_b = (1 - (1 - \Phi)^{\frac{2}{3}})\sigma_i \quad (2)$$

where σ_b and σ_i are the conductivities of the olivine-ilmenite system and ilmenite aggregates, respectively, Φ is the ilmenite content. Unexpectedly, for the conductivities of olivine-ilmenite systems with 11 vol% ilmenites, the measurement values was 0.5–1.0 orders lower than the calculated values using Cube model; for the conductivities of olivine-ilmenite systems with 15 vol% ilmenites, the measurement values was very close to the calculated values from Cube model (**Figure 7**). It was proposed that ilmenite grains in the olivine-15 vol% ilmenite system were well interconnected, but locally interconnected in olivine-11 vol% ilmenite system. According to the linear relations between the logarithmic conductivities of the olivine-ilmenite systems and reciprocal temperatures (**Figure 7**), the conductivities and temperatures at a certain pressure conformed to the Arrhenius formula,

$$\sigma = \sigma_0 \exp(-\Delta H/kT) \quad (3)$$

where σ_0 is the pre-exponential factor (KS/m), k is the Boltzmann constant (eV/K), T is the absolute temperature (K), and ΔH is the activation enthalpy (eV). The relevant fitting thermodynamic parameters for electrical conductivities of the samples were listed in **Table 2**. Activation enthalpies of the charge carriers for the pure ilmenite aggregates, olivine-ilmenite systems with interconnected and isolated ilmenites were 0.01, 0.15–0.24, 0.62–0.89 eV, respectively, being much lower than the enthalpy for olivine aggregates (1.27 eV) from Dai et al. (2019). The activation enthalpies for the olivine-ilmenite systems dramatically decreased at the ilmenite content of 11 vol% (**Figure 9**), corresponding to the significant increase of the electrical conductivities (**Figure 8**).

DISCUSSIONS

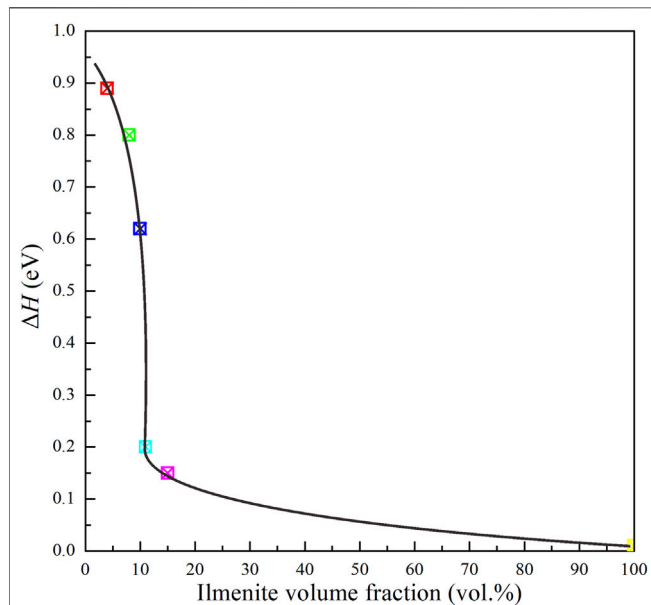
Comparisons With Previous Studies

Under the conditions of 2.0 GPa and 773–1273 K, electrical conductivities of the pure olivine aggregates (Dai et al., 2019),

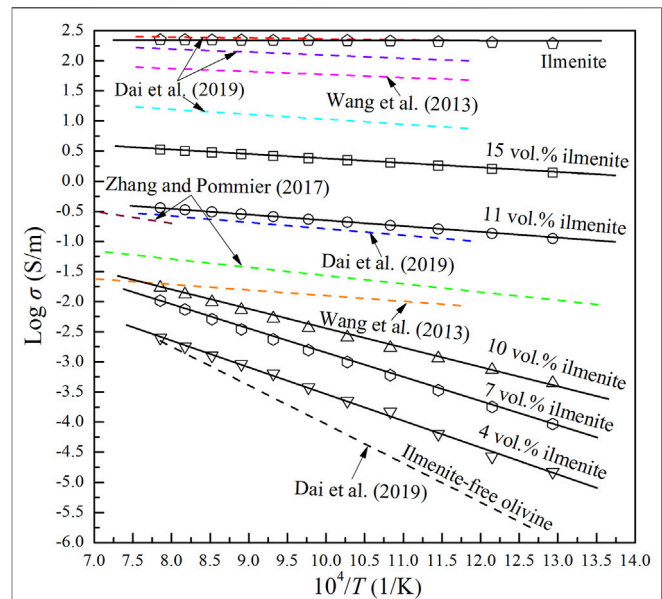
TABLE 2 | Fitted parameters for the Arrhenius relations for the electrical conductivities of the dry olivine aggregates with various volume percents of ilmenite (V_{ilm}).

Sample	V_{ilm} (Vol%)	P (GPa)	T (K)	$\text{Log } \sigma_0$ (S/m)	ΔH (eV)	R^2
Olivine (Ol) ^a	0	2.0	773–1,273	1.27 ± 0.03	1.27 ± 0.01	99.76
Ol-Ilm system ^b	4	2.0	773–1,273	0.93 ± 0.08	0.89 ± 0.02	99.68
Ol-Ilm system ^b	7	2.0	773–1,273	1.14 ± 0.04	0.80 ± 0.01	99.92
Ol-Ilm system ^b	10	2.0	773–1,273	0.65 ± 0.05	0.62 ± 0.01	99.71
Ol-Ilm system ^b	11	1.0	773–1,273	0.50 ± 0.01	0.24 ± 0.01	99.93
Ol-Ilm system ^b	11	2.0	773–1,273	0.34 ± 0.01	0.20 ± 0.01	99.98
Ol-Ilm system ^b	11	3.0	773–1,273	0.34 ± 0.01	0.18 ± 0.01	99.96
Ol-Ilm system ^b	15	2.0	773–1,273	1.12 ± 0.01	0.15 ± 0.01	99.97
Ilmenite (Ilm) ^b	100	2.0	773–1,273	2.44 ± 0.01	0.01 ± 0.00	90.83

Note: *a* and *b* stand for the experimental samples from Dai et al. (2019) and the present study, respectively.

**FIGURE 9** | Activation enthalpies of charge carriers for olivine-ilmenite systems versus the volume fractions of ilmenites at 2.0 GPa and 773–1273 K.

olivine-ilmenite systems with isolated ilmenites, olivine-ilmenite systems with interconnected ilmenites and pure ilmenite aggregates were about 10^{-5} – 10^{-3} , 10^{-5} – 10^{-2} , 10^{-1} – $10^{-0.5}$ and $10^{2.5}$ S/m, respectively. It was indicated that the conductivities of the olivine-ilmenite systems increased with increasing content of ilmenite. According to the abrupt changes of the conductivities and activation enthalpies for the olivine-ilmenite systems, the percolation threshold of the ilmenite grains in the olivine aggregates was proposed to be about 11 vol%. Effect of temperature on the conductivities of the olivine aggregates and olivine-ilmenite systems with isolated ilmenite were much greater than those of the olivine-interconnected ilmenite systems. It might be due to the activation enthalpies for olivine-ilmenite systems decreased with increasing ilmenite contents. Some previous studies have researched the electrical conductivities of olivine aggregates with other high-conductivity mineral phases at high temperatures and high pressures

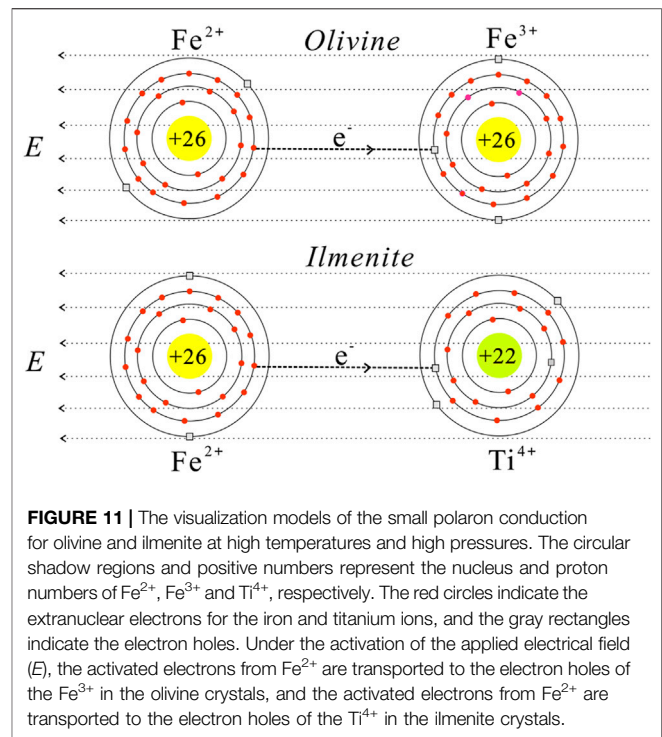
**FIGURE 10** | Electrical conductivities of olivine-ilmenite systems with various ilmenite contents compared with other relevant olivine systems at high temperatures and high pressures. The solid black lines with various symbols denoted the conductivities of olivine-ilmenite systems with various ilmenite contents in this study, the dashed orange and pink lines stood for the conductivities of olivine-magnetite-diamond and olivine-graphite systems (7 vol.% graphite) at 4.0 GPa, respectively (Wang et al., 2013); the dashed green and brown lines indicated the results of the olivine-FeS systems with 10 vol.% and 12 vol.% FeS at 4.7–6.1 GPa, respectively (Zhang and Pommier, 2017); the dashed black, sky blue, pink, purple and red lines represented the conductivities of pure olivine aggregates, olivine-3 vol.% magnetite system, olivine-10 vol.% magnetite system, olivine-20 vol.% magnetite system and pure ilmenite aggregates at 2.0 GPa, respectively (Dai et al., 2019).

(Figure 10). Graphite is widely distributed in cratonic lithospheric mantle (Pearson et al., 1994), and thus plays a significant role on the electrical structure of the stable regions of upper mantle. Wang et al. (2013) researched the conductivities of olivine aggregates with various contents of graphite at 4 GPa and 1,173–1,673 K. When the concentration of graphite exceeds percolation threshold (~ 1 wt%), the conductivities of olivine aggregates with graphite was markedly enhanced. Zhang and Pommier (2017) investigated the conductivities of metal-olivine

systems at ~ 5–6 GPa and up to 1948 K. Both the metal: olivine ratio and the metal phase geometry influenced the electrical conductivities of the two-layer samples. Dai et al. (2019) studied the electrical conductivities of olivine with various contents of magnetite under the conditions of 2.0 GPa and 873–1273 K. The conductivities of olivine–magnetite systems dramatically increased with increasing magnetite contents, and the percolation threshold of magnetite in the olivine aggregates was about 3 vol%. As shown in **Figure 10**, the conductivities of olivine–11 vol% ilmenite system were very close to those of olivine–3 vol% magnetite and olivine–12 vol% FeS systems, but 3–6 orders of magnitude higher than those of the olivine aggregates; the conductivities of olivine–10 vol% ilmenite system were much lower than those of olivine–4 vol% graphite system at lower-temperature range, but close to each other at higher temperature range. The conductivities of olivine–10 vol% FeS system were slightly higher than those of olivine–4 vol% graphite system. In addition, the conductivities of olivine–15 vol% ilmenite system were about 0.75 orders of magnitude lower than those of the olivine–10 vol% magnetite system, whose conductivities were about 1 order of magnitude lower than those of olivine–7 vol% graphite system. Furthermore, the conductivities of ilmenite aggregates were very close to those of magnetite aggregates, slightly higher than those of olivine–20 vol% magnetite system, and 2 orders of magnitude higher than those of olivine–15 vol% ilmenite system. According to the above analysis, we proposed that the graphite and magnetite grains were more easily interconnected than ilmenite grains in the olivine aggregates. The percolation thresholds of various high-conductivity minerals in the olivine aggregates are possibly dominated to the particle sizes, plasticity and interface energy of the high-conductivity minerals.

Conduction Mechanism

The logarithmic electrical conductivities of the dry olivine–ilmenite systems and reciprocal temperatures conformed to only one linear relationship under the experimental conditions (**Figure 7**). This was revealed that the conductivities of a certain olivine–ilmenite system were chiefly constrained by one major conduction mechanism at 1.0–3.0 GPa and 773–1273 K. According to the previous studies, small polaron, proton, and alkali ions were proposed to be the significant charge carriers for silicate minerals and rocks (Wang et al., 2006; Dai et al., 2010; Dai et al., 2018; Karato, 2013; Hu et al., 2014; Hu et al., 2018; Guo et al., 2020). In addition, the main conduction mechanism for a certain mineral was changed with the variation of chemical compositions. The electrical conductivities and conduction mechanisms for natural and synthetic olivine with various chemical compositions have been widely researched, and small polaron and proton conduction was proposed to be the dominant conduction mechanism for the anhydrous and hydrous olivine, respectively. (e.g., Wang et al., 2006; Poe et al., 2010; Karato, 2013; Dai and Karato, 2014; Dai et al., 2019). There was no obvious absorption peak being observed in the FT-IR spectra of the original and recovered olivine (**Figure 2**). And thus, proton conduction was excluded from the possible conduction



mechanism for the olivine. The small polaron conduction was proposed to be the conduction mechanism for dry olivine, reference to Dai et al. (2019). For the ilmenite (FeTiO_3), the activation enthalpy (0.01 eV) was much lower than those for the ionic conduction (Hu et al., 2014), proton conduction (Dai and Karato, 2014) and small polaron conduction (Zhang et al., 2017). The crystal structure of ilmenite was same with that of geikielite (MgTiO_3), and the activation enthalpy for iron-bearing ilmenite (0.01 eV) was much lower than the values (0.23–0.39 eV) for geikielite (Parthasarathy, 2011). The discrepancy might be due to the presence of iron in the ilmenite. Parthasarathy (2011) proposed that the conduction mechanism of geikielite is closely related to the electron transport. In contrast to geikielite, ferrous ions occupy the lattice positions of the ilmenite. Both iron and titanium ions in the ilmenite crystal are variable valence elements, and thus the conduction mechanism for pure ilmenite is proposed to be the small polaron conduction. The conduction processes of the small polarons in the olivine and ilmenite were displayed in **Figure 11**. Electrical conductivity of a mineral or rock was the result of directed migration of all charge carrier species, and the corresponding expression was displayed as follow:

$$\sigma = \sum_j q_j n_j \mu_j \quad (4)$$

where q_j , n_j and μ_j are the effective charge, quantity and mobility of the j -type charge carrier in the sample. Electrical conductivity of ilmenite was much higher than that of olivine (**Figure 7**), indicating the quantity and mobility of small polarons in the ilmenite crystals were superior to those in the olivine crystals. As a

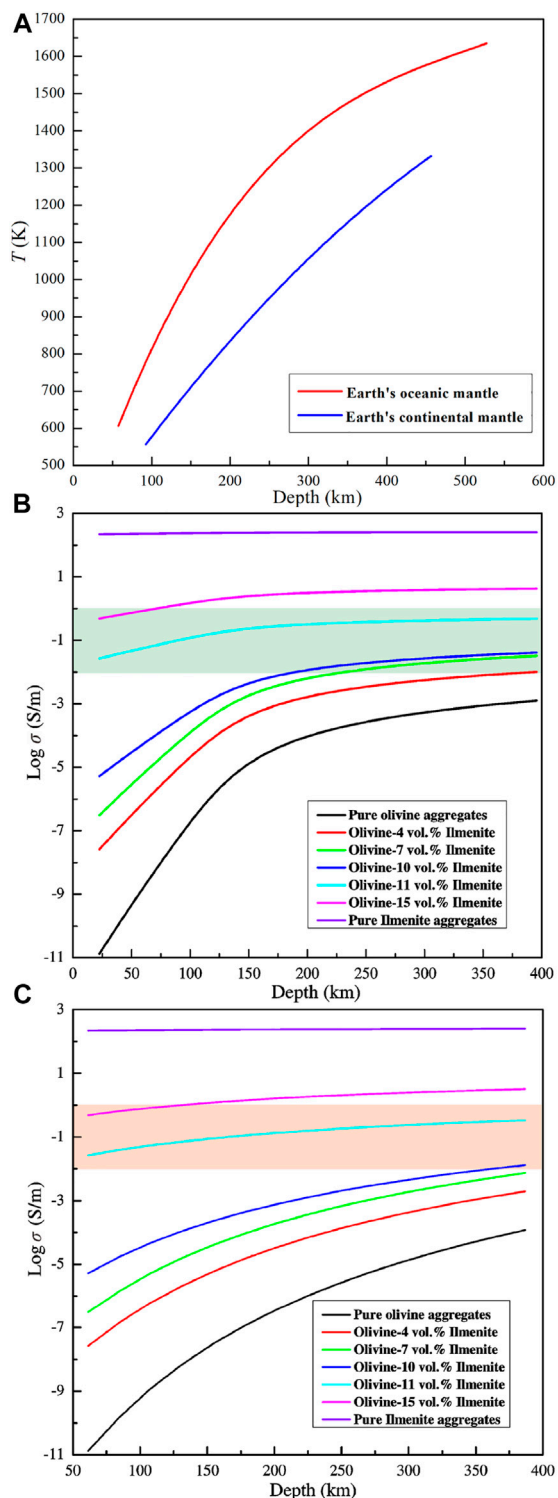


FIGURE 12 | The thermal models for the Earth's continental upper mantle and oceanic upper mantle (A) (Grigné and Combes, 2020), which were used to construct electrical conductivity–depth profiles for olivine aggregates with various ilmenite contents in the Earth's oceanic upper mantle (B) and continental upper mantle (C). Electrical conductivities of olivine aggregates were calculated based on the thermodynamic parameters of the (Continued)

FIGURE 12 | Arrhenius relation (Dai et al., 2019), and the conductivities of the olivine–ilmenite systems and ilmenite aggregates were calculated based on the thermodynamic parameters in this study. The solid lines presented the electrical conductivity–depth profiles of the olivine–ilmenite systems, and shadow regions indicated the high conductivity anomalies in the Earth's oceanic upper mantle and continental upper mantle.

consequence, the conductivities of olivine–ilmenite systems increased with the increase of ilmenite content. The activation enthalpies of the olivine–ilmenite systems with isolated ilmenites (0.62–0.89 eV) were much higher than those for the samples with interconnected ilmenites (0.15–0.20 eV). This revealed that the ilmenite mainly constrained the electrical conductivities of the dry olivine aggregates with interconnected ilmenites, and the dominant charge carriers are the small polarons in the ilmenite crystals. According to the previous studies, the electrical conductivities of the minerals and rocks with the small polaron conduction increase with the increase of oxygen fugacity at high temperatures and high pressures (Dai et al., 2008; Dai et al., 2012). It was implied that the electrical conductivities of the olivine–ilmenite systems probably increase with the increase of oxygen fugacity to some extent. The oxygen fugacity controlled by NNO buffer is close to the oxygen fugacity of the normal region in the Earth's upper mantle (Xu et al., 2000; Dai et al., 2012), and our measured electrical conductivity only represents the conductivity of the peridotite with a certain amount of ilmenite in the regions where the oxygen fugacity is close to that controlled by NNO buffer.

Geophysical Implications

Ilmenite exists as the inclusion in olivine and the accessory mineral of mantle derived mafic rock (Hacker et al., 1997; Risold et al., 2003; Carter Hearn Jr, 2004; Litasov et al., 2003; Bali et al., 2018). The estimated contents of ilmenite in some mafic rocks were lower than 10 vol% based on the scanning electronic microscope images of the natural samples (Risold et al., 2003; Litasov et al., 2003). In some special regions, ilmenite deposits were formed by the magmatism which closely related to the mantle plume (Xu et al., 2001; Charlier et al., 2010). In Emeishan Large Igneous Province (ELIP), ilmenites were enriched in the ultra-basic rocks formed in the process of mantle plume activity in the late Permian (Zhang et al., 2008; Zhang et al., 2009; She et al., 2015). This implied that ilmenite components in the upper mantle might be converged in the magmatism. The conductivities of the olivine aggregates with various ilmenite contents can be applied to invert the magnetotelluric (MT) profiles, and further research electrical structures of the Earth's upper mantle. Combining with the electrical conductivities of olivine–ilmenite systems and the thermal models of the Earth's continental upper mantle and oceanic upper mantle (Grigné and Combes, 2020), the electrical conductivity–depth profiles of the olivine aggregates with various ilmenite contents in the continental and oceanic upper mantles were constructed in detail (Figures 12A–C). As shown in Figure 12, the conductivities of dry olivine aggregates with a certain content of ilmenites at the same depth beneath the

continental plate and oceanic plate were different due to the various thermodynamic conditions. In addition, the electrical conductivity of a certain olivine–ilmenite system increased with depth due to the increase of temperature. According to the MT profiles, the range of the anomaly high electrical conductivity in the upper mantle is about 10^{-2} – 10^0 S/m (Dong et al., 2014; Adetunji et al., 2015). Electrical conductivities of dry olivine aggregates with 11–15 vol% ilmenite (10^{-1} – $10^{0.5}$ S/m) were close to those of the high conductivity layers (10^{-2} – 1 S/m) in the upper mantle (Figure 12). It was implied that the presence of interconnected ilmenite can interpret the high conductivity anomalies in the upper mantle. However, the ilmenite contents in the natural peridotites are much lower than the threshold percolation (11 vol%) for ilmenite, and it is not clear whether ilmenite can reach interconnected state in the present upper mantle. We proposed that the interpretation of high conductivity anomalies using the interconnected ilmenites should be cautious unless the interconnected ilmenites are demonstrated to exist in the upper mantle in the future.

CONCLUSIONS

Electrical conductivities of dry olivine–ilmenite systems with various contents of ilmenite ($V_{\text{ilm}} = 4, 7, 10, 11, 15$ vol%) and pure ilmenite aggregates were $\sim 10^{-5}$ – $10^{0.5}$ and $\sim 10^{2.5}$ S/m, respectively, under the conditions of 1.0–3.0 GPa and 773–1273 K. Temperature moderately enhanced the conductivities of olivine–ilmenite systems, but the positive effect of pressure was slight. Based on the inflection point for the relationship between electrical conductivities of the systems and ilmenite contents, we proposed that the percolation threshold of the ilmenite grains in the dry olivine–ilmenite systems was about 11 vol%. Interconnected ilmenites dramatically enhanced the conductivities of the olivine–ilmenite systems. In addition, activation enthalpies for the charge carriers of olivine–ilmenite systems (0.15–0.89 eV) decreased with increasing ilmenite

contents. The dominant conduction mechanism for the whole olivine–ilmenite systems is small polaron conduction. Electrical conductivity–depth profiles of olivine–ilmenite systems in the Earth's upper mantle have been constructed, being beneficial to research the electrical structures in the Earth's interior. Ilmenite can play an important role on the electrical properties of some special regions in the Earth's interior. Due to the percolation threshold (11 vol%) for the interconnectivity of ilmenites is much higher than the volume percentages of ilmenites in the natural peridotites, it should be very cautious to interpret the high conductivity anomalies in the Earth's upper mantle (Dai and Karato, 2020).

DATA AVAILABILITY STATEMENT

The original contributions presented in the study are included in the article/Supplementary Material, further inquiries can be directed to the corresponding authors.

AUTHOR CONTRIBUTIONS

LD and HH (designing the project). WS and MW (conducting high-P experiments). WS (writing the initial draft of the work). LD, HH, WS, MW, ZH, and CJ (interpreting the results).

FUNDING

This research was financially supported by the NSF of China (42072055, 41774099, 41772042 and 42002043), Youth Innovation Promotion Association of CAS (Grant No. 2019390), Special Fund of the West Light Foundation of CAS, and as well as the Science and Technology Foundation of Guizhou Province (QKHJZ (2013) 2285).

REFERENCES

- Adetunji, A. Q., Ferguson, I. J., and Jones, A. G. (2015). Reexamination of Magnetotelluric Responses and Electrical Anisotropy of the Lithospheric Mantle in the Grenville Province, Canada. *J. Geophys. Res. Solid Earth* 120, 1890–1908. doi:10.1002/2014JB011713
- Andreozzi, G. B., Cellucci, F., and Gozzi, D. (1996). High-temperature Electrical Conductivity of FeTiO₃ and Ilmenite. *J. Mater. Chem.* 6, 987–991. doi:10.1039/jm9960600987
- Bali, E., Hidas, K., Guðfinnsson, G. H., Kovács, Z., Török, K., and Román-Alpiste, M. J. (2018). Zircon and Apatite-Bearing Pyroxene Hornblende Mantle Xenolith from Hungary, Carpathian-Pannonian Region. *Lithos* 316–317, 19–32. doi:10.1016/j.lithos.2018.07.004
- Cao, Y., Wang, C. Y., Huang, F., and Zhang, Z. (2019). Iron Isotope Systematics of the Panzhihua Mafic Layered Intrusion Associated with Giant Fe-Ti Oxide Deposit in the Emeishan Large Igneous Province, SW China. *J. Geophys. Res. Solid Earth* 124, 358–375. doi:10.1029/2018jb016466
- Carter Hearn Jr., B. (2004). The Homestead Kimberlite, central Montana, USA: Mineralogy, Xenocrysts, and Upper-Mantle Xenoliths☆. *Lithos* 77, 473–491. doi:10.1016/j.lithos.2004.04.030
- Charlier, B., Namur, O., Malpas, S., de Marneffe, C., Duchesne, J.-C., Auwera, J. V., et al. (2010). Origin of the Giant Allard Lake Ilmenite Ore deposit (Canada) by Fractional Crystallization, Multiple Magma Pulses and Mixing. *Lithos* 117, 119–134. doi:10.1016/j.lithos.2010.02.009
- Dai, L., Li, H., Li, C., Hu, H., and Shan, S. (2010). The Electrical Conductivity of Dry Polycrystalline Olivine Compacts at High Temperatures and Pressures. *Mineral. Mag.* 74, 849–857. doi:10.1180/minmag.2010.074.5.849
- Dai, L., Li, H., Hu, H., Shan, S., Jiang, J., and Hui, K. (2012). The Effect of Chemical Composition and Oxygen Fugacity on the Electrical Conductivity of Dry and Hydrous Garnet at High Temperatures and Pressures. *Contrib. Mineral. Petrol.* 163, 689–700. doi:10.1007/s00410-011-0693-5
- Dai, L., Jiang, J., Li, H., Hu, H., and Hui, K. (2015a). Electrical Conductivity of Hydrous Natural Basalts at High Temperatures and Pressures. *J. Appl. Geophys.* 112, 290–297. doi:10.1016/j.jappgeo.2014.12.007
- Dai, L., Hu, H., Li, H., Hui, K., Jiang, J., Li, J., et al. (2015b). Electrical Conductivity of Gabbro: the Effects of Temperature, Pressure and Oxygen Fugacity. *Eur. J. Mineralogy* 27, 215–224. doi:10.1127/ejm/2015/0027-2429
- Dai, L. D., Hu, H. Y., Li, H. P., Wu, L., Hui, K. S., Jiang, J. J., et al. (2016). Influence of Temperature, Pressure, and Oxygen Fugacity on the Electrical Conductivity of Dry Eclogite, and Geophysical Implications. *Geochem. Geophys. Geosyst.* 17, 2394–2407. doi:10.1002/2016gc006282

- Dai, L. D., Li, H. P., Hu, H. Y., and Shan, S. M. (2008). Experimental Study of Grain Boundary Electrical Conductivities of Dry Synthetic Peridotite under High-temperature, High-pressure, and Different Oxygen Fugacity Conditions. *J. Geophys. Res. Solid Earth* 113, B12211. doi:10.1029/2008JB005820
- Dai, L. D., Sun, W. Q., Li, H. P., Hu, H. Y., Wu, L., and Jiang, J. J. (2018). Effect of Chemical Composition on the Electrical Conductivity of Gneiss at High Temperatures and Pressures. *Solid Earth* 9, 233–245. doi:10.5194/se-9-233-2018
- Dai, L., Hu, H., Sun, W., Li, H., Liu, C., and Wang, M. (2019). Influence of High Conductive Magnetite Impurity on the Electrical Conductivity of Dry Olivine Aggregates at High Temperature and High Pressure. *Minerals* 9, 44. doi:10.3390/min9010044
- Dai, L., and Karato, S.-i. (2009). Electrical Conductivity of Pyrope-Rich Garnet at High Temperature and High Pressure. *Phys. Earth Planet. Interiors* 176, 83–88. doi:10.1016/j.pepi.2009.04.002
- Dai, L., and Karato, S.-i. (2014). Influence of FeO and H on the Electrical Conductivity of Olivine. *Phys. Earth Planet. Interiors* 237, 73–79. doi:10.1016/j.pepi.2014.10.006
- Dai, L., and Karato, S.-i. (2020). Electrical Conductivity of Ti-bearing Hydrous Olivine Aggregates at High Temperature and High Pressure. *J. Geophys. Res. Solid Earth* 125, e2020JB020309. doi:10.1029/2020JB020309
- Dong, H., Wei, W., Ye, G., Jin, S., Jones, A. G., Jing, J., et al. (2014). Three-dimensional Electrical Structure of the Crust and Upper Mantle in Ordos Block and Adjacent Area: Evidence of Regional Lithospheric Modification. *Geochem. Geophys. Geosyst.* 15, 2414–2425. doi:10.1002/2014GC005270
- Duba, A. G., and Shankland, T. J. (1982). Free Carbon & Electrical Conductivity in the Earth's Mantle. *Geophys. Res. Lett.* 9, 1271–1274. doi:10.1029/g1009i011p01271
- Gaillard, F. (2005). Electrical Conductivity of Magma in the Course of Crystallization Controlled by Their Residual Liquid Composition. *J. Geophys. Res.* 110, B06204. doi:10.1029/2004JB003282
- Gaillard, F., Malki, M., Iacono-Marziano, G., Pichavant, M., and Scaillet, B. (2008). Carbonatite Melts and Electrical Conductivity in the Asthenosphere. *Science* 322, 1363–1365. doi:10.1126/science.1164446
- Grigné, C., and Combes, M. (2020). Thermal History of the Earth: On the Importance of Surface Processes and the Size of Tectonic Plates. *Geochem. Geophys. Geosyst.* 21, e2020GC009123. doi:10.1029/2020GC009123
- Guo, H., and Keppler, H. (2019). Electrical Conductivity of NaCl-Bearing Aqueous Fluids to 900 °C and 5 GPa. *J. Geophys. Res. Solid Earth* 124, 1397–1411. doi:10.1029/2018JB016658
- Guo, X., Zhang, L., Su, X., Mao, Z., Gao, X.-Y., Yang, X., et al. (2018). Melting inside the Tibetan Crust? Constraint from Electrical Conductivity of Peraluminous Granitic Melt. *Geophys. Res. Lett.* 45, 3906–3913. doi:10.1029/2018GL077804
- Guo, X., Chen, S., Li, P., Zhang, Y., Wu, X., and Zhang, J. (2020). Phase Transition of Sanidine (KAlSi₃O₈) and its Effect on Electrical Conductivity at Pressures up to 11 GPa. *Phys. Chem. Minerals* 47, 21. doi:10.1007/s00269-020-01089-4
- Hacker, B. R., Sharp, T., Zhang, R. Y., Liou, J. G., and Hervig, R. L. (1997). Determining the Origin of Ultrahigh-Pressure Lherzolites. *Science* 278, 702–704. doi:10.1126/science.278.5338.702
- Hu, H., Dai, L., Li, H., Jiang, J., and Hui, K. (2014). Electrical Conductivity of K-Feldspar at High Temperature and High Pressure. *Miner. Petrol.* 108, 609–618. doi:10.1007/s00710-014-0325-7
- Hu, H. Y., Dai, L. D., Li, H. P., Hui, K. S., and Sun, W. Q. (2017). Influence of Dehydration on the Electrical Conductivity of Epidote and Implications for High Conductivity Anomalies in Subduction Zones. *J. Geophys. Res. Solid Earth* 122, 2751–2762. doi:10.1002/2016jb013767
- Hu, H., Dai, L., Li, H., Sun, W., and Li, B. (2018). Effect of Dehydrogenation on the Electrical Conductivity of Fe-Bearing Amphibole: Implications for High Conductivity Anomalies in Subduction Zones and continental Crust. *Earth Planet. Sci. Lett.* 498, 27–37. doi:10.1016/j.epsl.2018.06.003
- Huang, X., Xu, Y., and Karato, S.-i. (2005). Water Content in the Transition Zone from Electrical Conductivity of Wadsleyite and Ringwoodite. *Nature* 434, 746–749. doi:10.1038/nature03426
- Huang, Y., Guo, H., Nakatani, T., Uesugi, K., Nakamura, M., and Keppler, H. (2021). Electrical Conductivity in Texturally Equilibrated Fluid-Bearing Forsterite Aggregates at 800°C and 1 GPa: Implications for the High Electrical Conductivity Anomalies in Mantle Wedges. *J. Geophys. Res. Solid Earth* 126, e2020JB021343. doi:10.1029/2020JB021343
- Iwamori, H. (1998). Transportation of H₂O and Melting in Subduction Zones. *Earth Planet. Sci. Lett.* 160, 65–80. doi:10.1016/s0012-821x(98)00080-6
- Karato, S. I. (2013). Theory of Isotope Diffusion in a Material with Multiple Species and its Implications for Hydrogen-Enhanced Electrical Conductivity in Olivine. *Phys. Earth Planet. Inter.* 219, 49–54. doi:10.1016/j.pepi.2013.03.001
- Laumonier, M., Farla, R., Frost, D. J., Katsura, T., Marquardt, K., Bouvier, A.-S., et al. (2017). Experimental Determination of Melt Interconnectivity and Electrical Conductivity in the Upper Mantle. *Earth Planet. Sci. Lett.* 463, 286–297. doi:10.1016/j.epsl.2017.01.037
- Li, P., Guo, X., Chen, S., Wang, C., Yang, J., and Zhou, X. (2018). Electrical Conductivity of the Plagioclase-NaCl-Water System and its Implication for the High Conductivity Anomalies in the Mid-lower Crust of Tibet Plateau. *Contrib. Mineral. Petrol.* 173, 16. doi:10.1007/s00410-018-1442-9
- Litasov, K. D., Malkovets, V. G., Kostrovitsky, S. I., and Taylor, L. A. (2003). Petrogenesis of Ilmenite-Bearing Symplectite Xenoliths from Vitim Alkaline Basalts and Yakutian Kimberlites, Russia. *Int. Geol. Rev.* 45, 976–997. doi:10.2747/0020-6814.45.11.976
- Liu, X., Jin, Z., Qu, J., and Wang, L. (2005). Exsolution of Ilmenite and Cr-Ti Magnetite from Olivine of Garnet-Wehrlite. *Sci. China Ser. D-earth Sci.* 48, 1368–1376. doi:10.1360/03yd0590
- Manthilake, G., Bolfan-Casanova, N., Novella, D., Mookherjee, M., and Andrault, D. (2016). Dehydration of Chlorite Explains Anomalous High Electrical Conductivity in the Mantle Wedges. *Sci. Adv.* 2, e1501631. doi:10.1126/sciadv.1501631
- Massonne, H.-J., and Neuser, R. D. (2005). Ilmenite Exsolution in Olivine from the Serpentinite Body at Zöblitz, Saxonian Erzgebirge - Microstructural Evidence Using EBSD. *Mineral. Mag.* 69, 119–124. doi:10.1180/0026461056920239
- Ni, H., Keppler, H., and Behrens, H. (2011). Electrical Conductivity of Hydrous Basaltic Melts: Implications for Partial Melting in the Upper Mantle. *Contrib. Mineral. Petrol.* 162, 637–650. doi:10.1007/s00410-011-0617-4
- Pang, K.-N., Li, C., Zhou, M.-F., and Ripley, E. M. (2008). Abundant Fe-Ti Oxide Inclusions in Olivine from the Panzhihua and Hongge Layered Intrusions, SW China: Evidence for Early Saturation of Fe-Ti Oxides in Ferrobasic Magma. *Contrib. Mineral. Petrol.* 156, 307–321. doi:10.1007/s00410-008-0287-z
- Parthasarathy, G. (2011). Electrical Properties of Natural and Synthetic Nano-Crystalline MgTiO₃ Geikielite at Mantle Pressure and Temperature Conditions. *Am. Mineral.* 96, 860–863. doi:10.2138/am.2011.3660
- Pearson, D. G., Boyd, F. R., Haggerty, S. E., Pasteris, J. D., Field, S. W., Nixon, P. H., et al. (1994). The Characterisation and Origin of Graphite in Cratonic Lithospheric Mantle: a Petrological Carbon Isotope and Raman Spectroscopic Study. *Contrib. Mineral. Petrol.* 115, 449–466. doi:10.1007/bf00320978
- Poe, B. T., Romano, C., Nestola, F., and Smyth, J. R. (2010). Electrical Conductivity Anisotropy of Dry and Hydrous Olivine at 8 GPa. *Phys. Earth Planet. Interiors* 181, 103–111. doi:10.1016/j.pepi.2010.05.003
- Ponomarenko, A. I. (1977). 1st Find of Garnet-Ilmenite Peridotite with Diamonds from Kimberlite Pipe MIR. *Doklady Akademii Nauk SSSR* 235, 914–917. doi:10.5194/sed-5-1259-2013
- Risold, A.-C., Trommsdorff, V., and Grobety, B. (2003). Morphology of Oriented Ilmenite Inclusions in Olivine from Garnet Peridotites (Central Alps, Switzerland). *Eur. J. Mineralogy* 15, 289–294. doi:10.1127/0935-1221/2003/0015-0289
- Roberts, J. J., and Tyburczy, J. A. (1991). Frequency Dependent Electrical Properties of Polycrystalline Olivine Compacts. *J. Geophys. Res.* 96, 16205–16222. doi:10.1029/91jb01574
- Scambelluri, M., and Philippot, P. (2001). Deep Fluids in Subduction Zones. *Lithos* 55, 213–227. doi:10.1016/S0024-4937(00)00046-3
- She, Y.-W., Song, X.-Y., Yu, S.-Y., and He, H.-L. (2015). Variations of Trace Element Concentration of Magnetite and Ilmenite from the Taihe Layered Intrusion, Emeishan Large Igneous Province, SW China: Implications for Magmatic Fractionation and Origin of Fe-Ti-V Oxide Ore Deposits. *J. Asian Earth Sci.* 113, 1117–1131. doi:10.1016/j.jseas.2015.03.029
- Sun, W., Dai, L., Li, H., Hu, H., Wu, L., and Jiang, J. (2017). Electrical Conductivity of Mudstone (Before and after Dehydration at High P-T) and a Test of High Conductivity Layers in the Crust. *Am. Mineral.* 102, 2450–2456. doi:10.2138/am-2017-6146
- Wang, D., Mookherjee, M., Xu, Y., and Karato, S.-i. (2006). The Effect of Water on the Electrical Conductivity of Olivine. *Nature* 443, 977–980. doi:10.1038/nature05256

- Wang, D., Li, H., Yi, L., Matsuzaki, T., and Yoshino, T. (2010). Anisotropy of Synthetic Quartz Electrical Conductivity at High Pressure and Temperature. *J. Geophys. Res.* 115, B09211. doi:10.1029/2009JB006695
- Wang, D. J., Karato, S. I., and Jiang, Z. T. (2013). An Experimental Study of the Influence of Graphite on the Electrical Conductivity of Olivine Aggregates. *Geophys. Res. Lett.* 40, 2028–2032. doi:10.1002/grl.50471
- Wannamaker, P. E., Caldwell, T. G., Jiracek, G. R., Maris, V., Hill, G. J., Ogawa, Y., et al. (2009). Fluid and Deformation Regime of an Advancing Subduction System at Marlborough, New Zealand. *Nature* 460, 733–736. doi:10.1038/nature08204
- Watson, H. C., Roberts, J. J., and Tyburczy, J. A. (2010). Effect of Conductive Impurities on Electrical Conductivity in Polycrystalline Olivine. *Geophys. Res. Lett.* 37, a–n. doi:10.1029/2009GL041566
- Wirth, R., and Matsyuk, S. (2005). Nanocrystalline (Mg, Fe, Cr)TiO₃ Perovskite Inclusions in Olivine from a Mantle Xenolith, Udachnaya-East Kimberlite Pipe, Siberia. *Earth Planet. Sci. Lett.* 233, 325–336. doi:10.1016/j.epsl.2005.01.023
- Xu, Y., Chung, S.-L., Jahn, B.-m., and Wu, G. (2001). Petrologic and Geochemical Constraints on the Petrogenesis of Permian-Triassic Emeishan Flood Basalts in Southwestern China. *Lithos* 58, 145–168. doi:10.1007/s00410-011-0657-910.1016/s0024-4937(01)00055-x
- Xu, Y., Shankland, T. J., and Poe, B. T. (2000). Laboratory-based Electrical Conductivity in the Earth's Mantle. *J. Geophys. Res.* 105, 27865–27875. doi:10.1029/2000jb900299
- Yamanaka, T., Shimazu, H., and Ota, K. (2001). Electric Conductivity of Fe₂SiO₄-Fe₃O₄ Spinel Solid Solutions. *Phys. Chem. Minerals* 28, 110–118. doi:10.1007/s002690000137
- Yang, X., Keppler, H., McCammon, C., Ni, H., Xia, Q., and Fan, Q. (2011). Effect of Water on the Electrical Conductivity of Lower Crustal Clinopyroxene. *J. Geophys. Res.* 116, B04208. doi:10.1029/2010JB008010
- Yang, X., Keppler, H., McCammon, C., and Ni, H. (2012). Electrical Conductivity of Orthopyroxene and Plagioclase in the Lower Crust. *Contrib. Mineral. Petrol.* 163, 33–48. doi:10.1007/s00410-011-0657-9
- Zhang, Z., Zhi, X., Chen, L., Saunders, A. D., and Reichow, M. K. (2008). Re-Os Isotopic Compositions of Picrites from the Emeishan Flood basalt Province, China. *Earth Planet. Sci. Lett.* 276, 30–39. doi:10.1016/j.epsl.2008.09.005
- Zhang, Z., Mao, J., Saunders, A. D., Ai, Y., Li, Y., and Zhao, L. (2009). Petrogenetic Modeling of Three Mafic-Ultramafic Layered Intrusions in the Emeishan Large Igneous Province, SW China, Based on Isotopic and Bulk Chemical Constraints. *Lithos* 113, 369–392. doi:10.1016/j.lithos.2009.04.023
- Zhang, N., Dygert, N., Liang, Y., and Parmentier, E. M. (2017). The Effect of Ilmenite Viscosity on the Dynamics and Evolution of an Overturned Lunar Cumulate Mantle. *Geophys. Res. Lett.* 44, 6543–6552. doi:10.1002/2017GL073702
- Zhang, Z., and Pommier, A. (2017). Electrical Investigation of Metal-Olivine Systems and Application to the Deep interior of Mercury. *J. Geophys. Res. Planets* 122, 2702–2718. doi:10.1002/2017JE005390

Conflict of Interest: The authors declare that the research was conducted in the absence of any commercial or financial relationships that could be construed as a potential conflict of interest.

Publisher's Note: All claims expressed in this article are solely those of the authors and do not necessarily represent those of their affiliated organizations, or those of the publisher, the editors and the reviewers. Any product that may be evaluated in this article, or claim that may be made by its manufacturer, is not guaranteed or endorsed by the publisher.

Copyright © 2022 Sun, Dai, Hu, Wang, Hu and Jing. This is an open-access article distributed under the terms of the Creative Commons Attribution License (CC BY). The use, distribution or reproduction in other forums is permitted, provided the original author(s) and the copyright owner(s) are credited and that the original publication in this journal is cited, in accordance with accepted academic practice. No use, distribution or reproduction is permitted which does not comply with these terms.



Thermodynamic Properties of Fe-Bearing Wadsleyite and Determination of the Olivine-Wadsleyite Phase Transition Boundary in (Mg,Fe)₂SiO₄ System

Chang Su^{1,2,3}, Yonggang Liu^{2*}, Dawei Fan², Wei Song^{2*}, Jiye Jiang^{1,3}, Zhenjun Sun^{1,3} and Guang Yang⁴

OPEN ACCESS

Edited by:

Vassilios Saltas,
Hellenic Mediterranean University,
Greece

Reviewed by:

Chaowen Xu,
China Earthquake Administration,
China
Guangfu Ji,
China Academy of Engineering
Physics, China

*Correspondence:

Yonggang Liu
liuyonggang@vip.gyig.ac.cn
Wei Song
songwei@vip.gyig.ac.cn

Specialty section:

This article was submitted to
Solid Earth Geophysics,
a section of the journal
Frontiers in Earth Science

Received: 20 February 2022

Accepted: 21 March 2022

Published: 13 April 2022

Citation:

Su C, Liu Y, Fan D, Song W, Jiang J,
Sun Z and Yang G (2022)
Thermodynamic Properties of Fe-
Bearing Wadsleyite and Determination
of the Olivine-Wadsleyite Phase
Transition Boundary in
(Mg,Fe)₂SiO₄ System.
Front. Earth Sci. 10:879678.
doi: 10.3389/feart.2022.879678

¹School of Earth Sciences, Institute of Disaster Prevention, Sanhe, China, ²Key Laboratory of High Temperature and High Pressure Study of the Earth's Interior, Institute of Geochemistry, Chinese Academy of Sciences, Guiyang, China, ³Hebei Key Laboratory of Earthquake Dynamics, Sanhe, China, ⁴School of Information Engineering, Institute of Disaster Prevention, Sanhe, China

The self-consistent molar volumes, elastic properties and thermodynamic properties of β -(Mg_{0.87},Fe_{0.13})₂SiO₄ wadsleyite have been determined over a wide temperature and pressure range based on an iterative numerical approach and experimental data from the literature. The obtained molar volumes, adiabatic bulk modulus, and shear modulus generally agree with the available experimental and theoretical results. The thermodynamic properties of α -(Mg_{0.9},Fe_{0.1})₂SiO₄ were also reinvestigated. Comparisons on thermodynamic properties show that the thermal expansions, heat capacities, and entropies of both β -(Mg_{0.87},Fe_{0.13})₂SiO₄ and α -(Mg_{0.9},Fe_{0.1})₂SiO₄ exhibit negative and nonlinear behavior with increasing pressure. Besides, the pressure plays a more important role in thermodynamic properties of the α -(Mg_{0.9},Fe_{0.1})₂SiO₄ than that of the β -(Mg_{0.87},Fe_{0.13})₂SiO₄. Using the Clausius-Clapeyron equation combined with molar volumes and entropies of both compositions, the phase transition boundary of Fe-bearing olivine and wadsleyite is estimated. The calculated transition pressure shows a nonlinear relationship with increasing temperature, and the value is generally lower than the previous studies on Fe-free olivine and wadsleyite at the same temperature. On the basis of our phase relation, the temperature at the 410 km discontinuity is estimated as 1795 ± 70 K under anhydrous conditions. The results not only confirm the feasibility of the Clausius-Clapeyron equation in obtaining the solid-solid phase transition, but also suggest that the existence of Fe might decrease the transition pressure of olivine-wadsleyite, which would consequently cause a higher temperature at the 410 km discontinuity.

Keywords: Fe-bearing wadsleyite, entropy, Clausius-Clapeyron equation, phase transition boundary, 410 km discontinuity

INTRODUCTION

Olivine (α -phase) and its high-pressure polymorphs (i.e., wadsleyite and ringwoodite) dominate the Earth's upper mantle and mantle transition zone (Ringwood, 1962). Since it has been widely accepted that the Earth's mantle is peridotitic, the seismic wave discontinuities in the Earth's mantle are usually considered to be related to the high-pressure transformations of olivine (Ringwood and Major, 1970). Furthermore, the existence of the 410 and 520 km discontinuities are attributed to the olivine-wadsleyite (β -phase) and wadsleyite-ringwoodite (γ -phase) transformations, respectively. Previous studies reported that temperatures at these seismic wave discontinuities can be estimated by comparing the depth of the seismic wave discontinuities with the phase transition pressures of mantle minerals (Ito and Katsura, 1989). In turn, it indicates that an accurate phase transition boundary of olivine-wadsleyite is necessary to constrain the temperature at the 410 km discontinuity.

Although it has been demonstrated that there is non-negligible Fe (~10 mol%) in natural olivine (Bina and Wood, 1987), most studies on the phase transition boundary of olivine-wadsleyite are still limited in Mg_2SiO_4 system (Morishima et al., 1994; Jacobs et al., 2006; Akaogi et al., 2007; Ottonello et al., 2008; Holland and Powell, 2011; Dorogokupets et al., 2015). To date, the transition pressures in $(\text{Mg,Fe})_2\text{SiO}_4$ system have been only determined at several temperatures (Katsura and Ito, 1989; Chen et al., 2002; Katsura et al., 2004), and the effect of Fe on the olivine-wadsleyite phase transition boundary in a continuous P - T range remains unclear.

The determination of the phase transition boundary is usually based on the phase equilibrium, which requires the volumes and thermodynamic properties of coexisting phases at high-temperatures and high-pressures (HT-HP). The molar volume and thermodynamic properties, including thermal expansion and heat capacity, of San Carlos olivine (α - $(\text{Mg}_{0.9}\text{Fe}_{0.1})_2\text{SiO}_4$) at HT-HP were reported via an iterative numerical approach in Su et al. (2018). Pioneering investigations on Fe-bearing wadsleyite (β - $(\text{Mg,Fe})_2\text{SiO}_4$) has shown the effect of Fe on the elastic properties (Li and Liebermann, 2000; Liu et al., 2009) and electrical conductivities (Dai and Karato, 2009; Yoshino et al., 2012). At the same time, few works have been devoted to the thermodynamic properties of Fe-bearing wadsleyite at HT-HP.

This study aims to determine the thermodynamic properties of Fe-bearing wadsleyite at HT-HP, and apply them to investigate the effect of Fe on the olivine-wadsleyite phase transition boundary. We refined our calculation procedure and derived the self-consistent molar volume, elastic moduli, thermal expansion, heat capacity, and entropy of β - $(\text{Mg}_{0.87}\text{Fe}_{0.13})_2\text{SiO}_4$ based on existing experimental measurements. We also reanalyzed our early investigations on α - $(\text{Mg}_{0.9}\text{Fe}_{0.1})_2\text{SiO}_4$, and compared the effect of pressure on the thermodynamic properties of β - $(\text{Mg}_{0.87}\text{Fe}_{0.13})_2\text{SiO}_4$ and α - $(\text{Mg}_{0.9}\text{Fe}_{0.1})_2\text{SiO}_4$. Then, we determined the phase transition boundary of olivine-wadsleyite in $(\text{Mg,Fe})_2\text{SiO}_4$ system using the obtained molar volumes and entropies of two compositions at HT-HP combined with Clausius-Clapeyron equation. Finally, by

comparing the depth of the discontinuity with the transition pressure, we estimated the temperature at the 410 km discontinuity.

METHODS

Calculation Procedure

The approach used in this study is described in our recent studies (Su et al., 2018; Su et al., 2022), and the fundamental procedure is described below. The uncertainties of the derived parameters at different P - T conditions are estimated from the experimental measuring error propagations using Taylor series expansion.

The thermal expansion (α) at constant pressure is related to volume (V) as:

$$\alpha(T) = \frac{1}{V} \left(\frac{\partial V}{\partial T} \right) \quad (1)$$

And the integration of Eq. 1 yields:

$$V(T) = V_0 \exp \left[\int_{T_0}^T \alpha(T) dT \right] \quad (2)$$

where V_0 represents the volume at ambient condition. The isothermal derivative of volume with respect to pressure can be written as:

$$\left(\frac{\partial V}{\partial P} \right)_T = -V^2 \left(\frac{1}{v_\phi^2} + \frac{T\alpha^2}{C_P} \right) \quad (3)$$

where C_P stands for the heat capacity, v_ϕ refers to the bulk sound velocity (Bina and Silver, 1990). The bulk sound velocity is related to the specific volume and adiabatic bulk modulus (K_S) by $v_\phi = (VK_S)^{1/2}$, which can be calculated from the P -wave velocity (v_P) and S -wave velocity (v_S) by Eq. 4.

$$v_\phi = \left(v_P^2 - \frac{4}{3}v_S^2 \right)^{\frac{1}{2}} \quad (4)$$

Meanwhile, the isothermal derivative of the heat capacity with respect to pressure can be evaluated by Eq. 5.

$$\left(\frac{\partial C_P}{\partial P} \right)_T = -VT \left[\alpha^2 + \left(\frac{\partial \alpha}{\partial T} \right)_P \right] \quad (5)$$

To start the calculation, first, we use the experimental determined volume at high-temperature and ambient pressure conditions to obtain the thermal expansion at ambient pressure. With the obtained thermal expansion and heat capacity as a function of temperature at ambient pressure, the approximate volume at an arbitrary reference pressure could be estimated using Eq. 3. Then resulting volume at this reference pressure can be used to update the value of thermal expansion and heat capacity at the same pressure with Eqs 1, 5, respectively. Hence, iteration of this loop leads to converged volume, thermal expansion, and heat capacity as a function of temperature and pressure based on the experimental elastic wave velocity at HT-HP.

TABLE 1 | Fitting coefficients and their uncertainties of Eq. 10 to calculate the *P*- and *S*- wave velocities of β -(Mg_{0.87}Fe_{0.13})₂SiO₄ at HT-HPs.

	v_0	v_1	v_2	v_3	v_4	v_5
v_P	9,350 (8)	80.8 (25)	-0.42 (2)	-1.97 (19)	-5.59 (377)×10 ⁻⁵	0.016 (3)
v_S	5,465 (9)	25.7 (28)	-0.36 (3)	-0.60 (22)	-8.09 (429)×10 ⁻⁵	0.016 (3)

With the determined volume as well as the elastic wave velocity at HT-HP, the adiabatic bulk modulus (K_S) and shear modulus (G) can be obtained using Eqs 6, 7, respectively.

$$K_S = \frac{1}{V} \left(v_P^2 - \frac{4}{3} v_S^2 \right) \quad (6)$$

$$G = \frac{1}{V} v_S^2 \quad (7)$$

Furthermore, since the temperature and pressure dependences of entropy (S) are related to the heat capacity and thermal expansion via Eqs 8, 9, respectively (Johari, 2021), the entropy at HTHP can be also derived with the entropy measured at ambient conditions.

$$S(P_0, T) = S(P_0, T_0) - \int_{T_0}^T \left(\frac{C_P}{T} \right) dT \quad (8)$$

$$S(P, T_0) = S(P_0, T_0) - \int_{P_0}^P \alpha V dP \quad (9)$$

Thermoelastic Data of Fe-Bearing Wadsleyite

Elastic Wave Velocity at High-Temperature and High-Pressure Conditions

Previous studies have measured the elastic wave velocity of Fe-bearing wadsleyite at high-pressure conditions (Li and Liebermann, 2000; Wang et al., 2014). Besides, by using ultrasonic interferometry in conjunction with synchrotron X-ray diffraction measurements, Liu et al. (2009) presented the elastic wave velocity and unit-cell volume of β -(Mg_{0.87}Fe_{0.13})₂SiO₄ to 12 GPa and 1073 K. Here, we fit the *P*- and *S*- wave velocities by Liu et al. (2009) with Eq. 10, and the fitting coefficients and their uncertainties are listed in Table 1.

$$v(P, T) = v_0 + v_1 P + v_2 (T - 273) + v_3 P^2 + v_4 (T - 273)^2 + v_5 P (T - 273) \quad (10)$$

where pressure is expressed in GPa, temperature is expressed in K, *P*- and *S*- wave velocity are expressed in m/s. The differences are less than 0.5% and 1.5% compared with the results reported by Li and Liebermann (2000) and Wang et al. (2014), respectively.

Thermodynamic Properties at High-Temperature and Ambient Pressure Conditions

At present, there is no experimental or theoretical data for the thermal expansion, heat capacity, or entropy of Fe-bearing wadsleyite yet. Since it is suggested that the volume and heat capacity are linearly proportional to the Fe/(Mg + Fe) ratio

(X_{Fe}) (Xu et al., 2004), the thermal expansion and heat capacity of Fe-bearing wadsleyite as a function of temperature can be estimated from the data of Mg end-member wadsleyite (β -Mg₂SiO₄) and Fe end-member (β -Fe₂SiO₄) wadsleyite.

However, β -Fe₂SiO₄ is a virtual mineral since fayalite (α -Fe₂SiO₄) is transformed directly to Fe end-member ringwoodite (γ -Fe₂SiO₄) with increasing pressure (Akimoto et al., 1967). According to the studies on α -Fe₂SiO₄ and γ -Fe₂SiO₄ (Fei and Saxena, 1986), Saxena (1996) published the molar volume and heat capacity of β -Fe₂SiO₄ at ambient conditions. Besides, Saxena (1996) also concluded the results from previous studies on β -Mg₂SiO₄ (Akimoto et al., 1978; Watanabe, 1982), and provided the thermodynamic data. Here, we use the database presented by Saxena (1996). For the Fe-bearing wadsleyite with a X_{Fe} as 0.13, the temperature dependence of heat capacity is represented by a polynomial equation as shown in Eq. 11. The molar volume data is analyzed using the EoSfit software (Gonzalez-Platas et al., 2016), and the equation for the thermal expansion as a function of temperature is defined as Eq. 12. Additionally, the standard entropy is determined as 99.3 J/mol K.

$$C_P(T) = 179.59(21) + 1.10(1) \times 10^{-2} T - 19171(297) T^{-1} + 1.05(149) \times 10^6 T^{-2} - 4.34(24) \times 10^8 T^{-3} \quad (11)$$

$$\alpha(T) = 2.520(112) \times 10^{-5} + 0.902(55) \times 10^{-8} T - 0.755(269) T^{-2} \quad (12)$$

RESULTS

Based on the calculation procedure and experimental data discussed in *Methods*, the molar volume, adiabatic bulk modulus, shear modulus, thermal expansion, heat capacity, and entropy of β -(Mg_{0.87}Fe_{0.13})₂SiO₄ are derived. All the calculated parameters are provided in **Supplementary Tables S1–S3**, together with their uncertainties approximated using the error propagation calculations.

Molar Volume at High-Temperature and High-Pressure Conditions

The calculated molar volume of β -(Mg_{0.87}Fe_{0.13})₂SiO₄ as a function of pressure at various temperatures is shown in **Figure 1**. The unit-cell volumes of β -(Mg_{0.84}Fe_{0.16})₂SiO₄ and β -(Mg_{0.87}Fe_{0.13})₂SiO₄ were measured by Fei et al. (1992) and Liu et al. (2009) using X-ray diffraction,

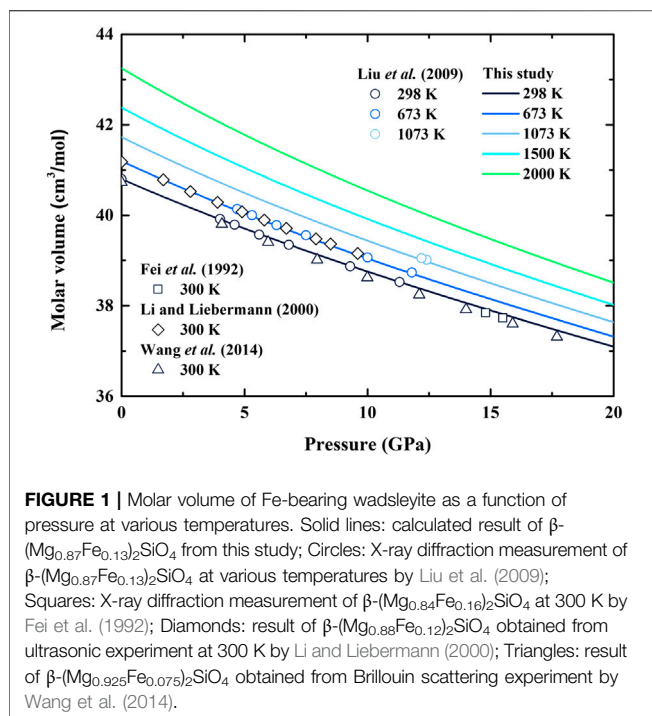


FIGURE 1 | Molar volume of Fe-bearing wadsleyite as a function of pressure at various temperatures. Solid lines: calculated result of β -($\text{Mg}_{0.87}\text{Fe}_{0.13}$) $_2\text{SiO}_4$ from this study; Circles: X-ray diffraction measurement of β -($\text{Mg}_{0.87}\text{Fe}_{0.13}$) $_2\text{SiO}_4$ at various temperatures by Liu et al. (2009); Squares: X-ray diffraction measurement of β -($\text{Mg}_{0.84}\text{Fe}_{0.16}$) $_2\text{SiO}_4$ at 300 K by Fei et al. (1992); Diamonds: result of β -($\text{Mg}_{0.88}\text{Fe}_{0.12}$) $_2\text{SiO}_4$ obtained from ultrasonic experiment at 300 K by Li and Liebermann (2000); Triangles: result of β -($\text{Mg}_{0.925}\text{Fe}_{0.075}$) $_2\text{SiO}_4$ obtained from Brillouin scattering experiment by Wang et al. (2014).

respectively. Also, the densities of β -($\text{Mg}_{0.88}\text{Fe}_{0.12}$) $_2\text{SiO}_4$ and β -($\text{Mg}_{0.925}\text{Fe}_{0.075}$) $_2\text{SiO}_4$ were presented by Li and Liebermann (2000) and Wang et al. (2014) based on ultrasonic and Brillouin scattering measurements, respectively. Based on the molar mass of the Fe-bearing wadsleyite from those previous studies mentioned above, we convert the units of the unit-cell volume (\AA^3) and density (g/cm^3) to molar volume (cm^3/mol), and the results are also illustrated in **Figure 1**.

Our result shows good consistency with the X-ray diffraction measurement by Liu et al. (2009), and the difference is less than 0.1% at room temperature. The excellent agreement also holds at high-temperature conditions, and the largest difference is 0.1% at 1073 K compared with that by Liu et al. (2009). In the meantime, our obtained molar volume is $\sim 0.3\%$ higher than the result by Wang et al. (2014), $\sim 0.12\%$ higher than that by Fei et al. (1992), and $\sim 1.9\%$ lower than that by Li and Liebermann (2000). Overall, except for the result by Li and Liebermann (2000), the molar

volume of Fe-bearing wadsleyite seems to increase with the value of X_{Fe} .

Elastic Properties at High-Temperature and High-Pressure Conditions

Based on the molar volume, the calculated elastic moduli of β -($\text{Mg}_{0.87}\text{Fe}_{0.13}$) $_2\text{SiO}_4$ are shown in **Table 2**; **Figure 2**, along with the previous results of Fe-bearing wadsleyite with different values of X_{Fe} (Sinogeikin et al., 1998; Li and Liebermann, 2000; Katsura et al., 2001; Mayama, 2004; Liu et al., 2009; Isaak et al., 2010; Wang et al., 2014).

In this study, the adiabatic bulk modulus and shear modulus at ambient conditions are determined as $K_{S0} = 173.4$ (12) GPa and $G_0 = 108.6$ (5) GPa, respectively. In **Table 2**, our K_{S0} is consistent within the uncertainties of Liu et al. (2009), in which $X_{\text{Fe}} = 0.13$, and generally larger than those with less Fe contents (Isaak et al., 2010; Katsura et al., 2001; Li and Liebermann, 2000; Mayama, 2004; Sinogeikin et al., 1998; Wang et al., 2014). On the other hand, the values of G_0 listed in **Table 2** do not show apparent X_{Fe} dependence. Our G_0 also agrees well with the result by Liu et al. (2009). Although our G_0 is larger than those with $X_{\text{Fe}} = 0.12$ (Li and Liebermann, 2000) and $X_{\text{Fe}} = 0.09$ (Katsura et al., 2001; Mayama, 2004), it is nearly the same as those with $X_{\text{Fe}} = 0.08$ (Isaak et al., 2010) and $X_{\text{Fe}} = 0.075$ (Sinogeikin et al., 1998; Wang et al., 2014).

In **Figure 2A**, our adiabatic bulk modulus exhibits significant nonlinear variation with the increasing pressure, whereas shear modulus shows the opposite trend. Both of the derived adiabatic bulk modulus and shear modulus are generally comparable with the data obtained from ultrasonic measurements (Li and Liebermann, 2000; Liu et al., 2009), and the largest separation is 1%. Though our adiabatic bulk modulus is $\sim 2.5\%$ larger than that by Wang et al. (2014) in the pressure range of 5–12 GPa, it agrees well with the result by Wang et al. (2014) with the differences less than 1%. Also, the first and second pressure derivatives of adiabatic bulk modulus and shear modulus are obtained as $\partial K_S/\partial P = 5.28$ (1), $\partial^2 K_S/\partial P^2 = -0.0991$ (2) GPa^{-1} , $\partial G/\partial P = 1.48$ (1) and $\partial^2 G/\partial P^2 = -0.0171$ (6) GPa^{-1} , respectively.

The temperature dependences of adiabatic bulk modulus and shear modulus are shown in **Figure 2B**. Our adiabatic bulk modulus is $\sim 2\%$ larger than that of Isaak et al. (2010), while shear modulus is consistent with Isaak's result, and the

TABLE 2 | Elastic moduli of β -($\text{Mg}_{0.87}\text{Fe}_{0.13}$) $_2\text{SiO}_4$ and their pressure and temperature derivatives.

X_{Fe}	K_{S0} GPa	$(\frac{\partial K_S}{\partial P})_T$	$(\frac{\partial^2 K_S}{\partial P^2})_T$ GPa $^{-1}$	$(\frac{\partial K_S}{\partial T})_P$ GPa K $^{-1}$	G_0 GPa	$(\frac{\partial G}{\partial P})_T$ GPa $^{-1}$	$(\frac{\partial^2 G}{\partial P^2})_T$	$(\frac{\partial G}{\partial T})_P$ GPa K $^{-1}$	References
0.075	170 (3)				108 (2)				Sinogeikin et al. (1998)
0.075	170 (3)	4.1 (1)			108 (2)	1.45 (4)			Wang et al. (2014)
0.08	170.8 (1.2)			-0.0175 (7)	108.9 (0.4)			-0.0155 (6)	Isaak et al. (2010)
0.09	165.7 (1)			-0.016 (3)	105.66 (3)			-0.012 (1)	Katsura et al. (2001)
0.09	165.72 (1)			-0.0175 (3)	105.43 (2)			-0.0159 (1)	Mayama (2004)
0.12	172 (2)	4.6 (1)			106 (1)	1.6 (1)			Li and Liebermann (2000)
0.13	175.4 (7)	4.10 (11)		-0.0135 (10)	108.0 (4)	1.56 (5)		-0.0144 (8)	Liu et al. (2009)
0.13	173.4 (12)	5.28 (1)	-0.0991 (2)	-0.0145 (1)	108.6 (5)	1.48 (1)	-0.0171 (6)	-0.0210 (1)	This study

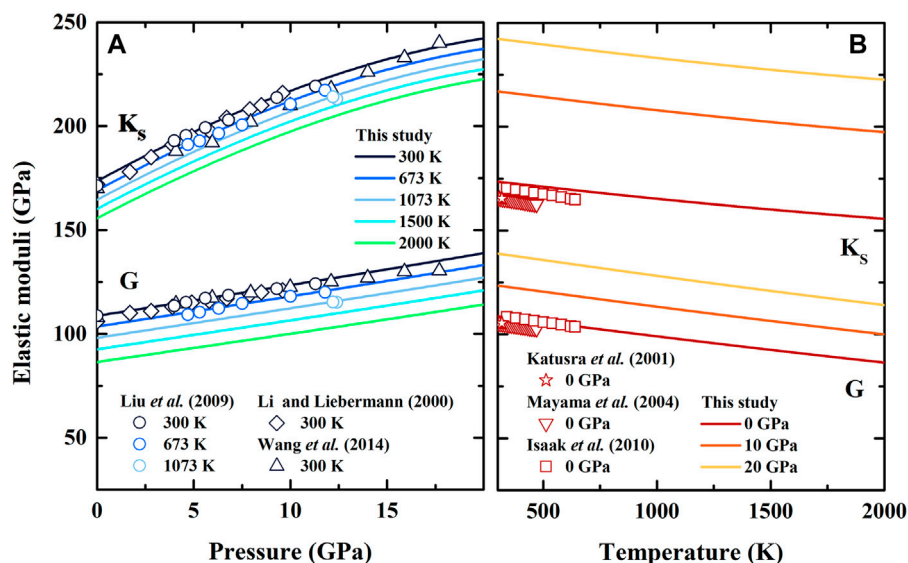


FIGURE 2 | Adiabatic bulk modulus (K_s) and shear modulus (G) of Fe-bearing wadsleyite as a function of (A) pressure and (B) temperature. Solid lines: result of β -($\text{Mg}_{0.87}\text{Fe}_{0.13}$) $_2\text{SiO}_4$ from this study; Diamonds: result of β -($\text{Mg}_{0.88}\text{Fe}_{0.12}$) $_2\text{SiO}_4$ obtained from ultrasonic measurement by Li and Liebermann (2000); Circles: result of β -($\text{Mg}_{0.87}\text{Fe}_{0.13}$) $_2\text{SiO}_4$ obtained from ultrasonic measurement by Liu et al. (2009); Triangles: result of β -($\text{Mg}_{0.925}\text{Fe}_{0.075}$) $_2\text{SiO}_4$ obtained from Brillouin scattering measurement by Wang et al. (2014); Stars, inverted triangles and squares: results of β -($\text{Mg}_{0.91}\text{Fe}_{0.09}$) $_2\text{SiO}_4$ obtained from resonant ultrasound spectroscopy measurements by Katsura et al. (2001), Mayama, (2004) and Isaak et al. (2010), respectively.

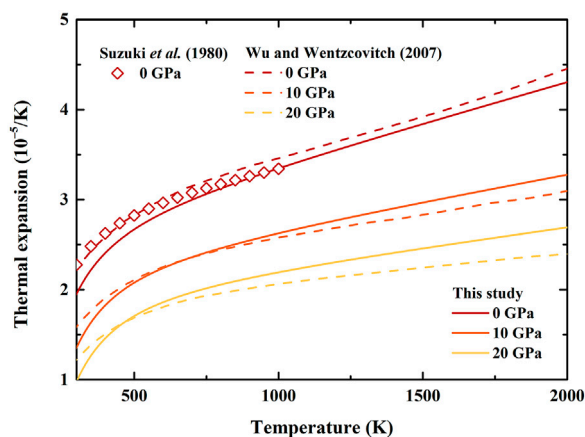


FIGURE 3 | Temperature dependence of thermal expansion of β -($\text{Mg}_{0.87}\text{Fe}_{0.13}$) $_2\text{SiO}_4$ and β - Mg_2SiO_4 at various pressures. Solid lines: result of β -($\text{Mg}_{0.87}\text{Fe}_{0.13}$) $_2\text{SiO}_4$ from this study; Dash lines: first principle calculation result of β - Mg_2SiO_4 by Wu and Wentzcovitch (2007); Diamonds: result modified by Fei et al. (1992) based on X-ray diffraction data of Suzuki et al. (1980).

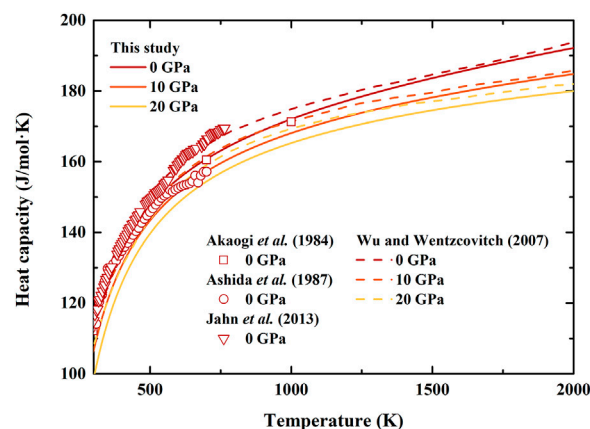
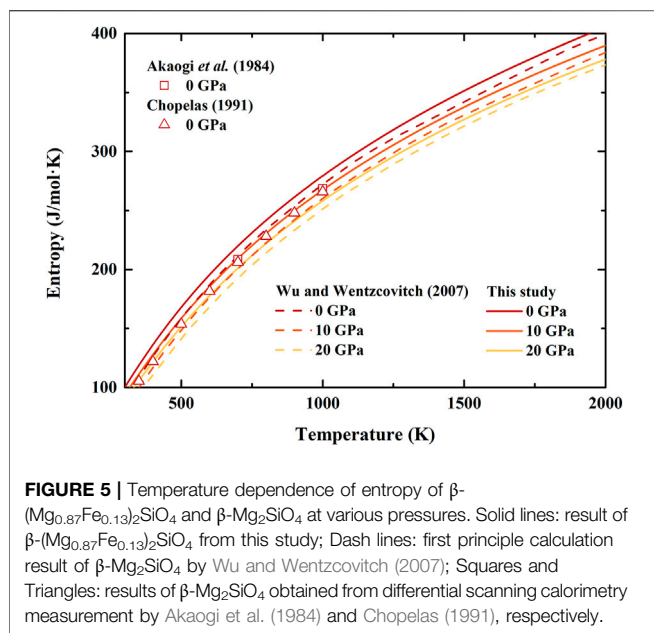


FIGURE 4 | Temperature dependence of heat capacity of β -($\text{Mg}_{0.87}\text{Fe}_{0.13}$) $_2\text{SiO}_4$ and β - Mg_2SiO_4 at various pressures. Solid lines: result of β -($\text{Mg}_{0.87}\text{Fe}_{0.13}$) $_2\text{SiO}_4$ from this study; Dash lines: first principle calculation result of β - Mg_2SiO_4 by Wu and Wentzcovitch (2007); Squares, circles, and inverted triangles: differential scanning calorimetry measurements of β - Mg_2SiO_4 by Akaogi et al. (1984), Ashida et al. (1987), and Jahn et al. (2013), respectively.

differences are within 0.6%. The obtained adiabatic bulk modulus and shear modulus are 5.4% and 3.5% larger than that of Katsura et al. (2001) and Mayama (2004), respectively. The temperature derivatives of adiabatic bulk modulus and shear modulus are determined as $\partial K_s/\partial T = -0.0145(1)$ GPa/K and $\partial G/\partial T = -0.0210(1)$ GPa/K, respectively, which are comparable with those obtained by resonant ultrasound spectroscopy (Katsura et al., 2001; Mayama, 2004; Isaak et al., 2010) (Table 2).

Thermodynamic Properties at High-Temperature and High-Pressure Conditions

The thermal expansion, heat capacity, and entropy of β -($\text{Mg}_{0.87}\text{Fe}_{0.13}$) $_2\text{SiO}_4$ as a function of temperature at various pressures are illustrated in Figures 3–5, respectively. Since there is no thermodynamic data of Fe-bearing wadsleyite at



present, here we only show the available thermal expansion, heat capacity, and entropy of β - Mg_2SiO_4 for comparisons (Suzuki et al., 1980; Akaogi et al., 1984; Ashida et al., 1987; Chopelas, 1991; Wu and Wentzcovitch, 2007; Jahn et al., 2013).

In **Figure 3**, our calculated thermal expansion of β -($\text{Mg}_{0.87}\text{Fe}_{0.13}$) $_2\text{SiO}_4$ at ambient condition is determined as $\alpha_0 = 1.952(428) \times 10^{-5} \text{ K}^{-1}$, which is lower than the results by Suzuki et al. (1980) ($2.27 \times 10^{-5} \text{ K}^{-1}$) and Wu and Wentzcovitch (2007) ($2.21 \times 10^{-5} \text{ K}^{-1}$). With increasing temperature, the difference between our and Suzuki's result becomes smaller, and decreases to 0.12% at 1000 K. Also, our thermal expansion shows a similar trend with that of Wu and Wentzcovitch (2007) at ambient pressure conditions over ~ 700 K, with an average difference of $\sim 3\%$. For high-pressure conditions, our result becomes larger than the result by Wu and Wentzcovitch (2007) over ~ 700 and ~ 450 K at 10 and 20 GPa, respectively, and causes a difference of 5% and 11% at 2000 K at 10 and 20 GPa, respectively.

The calculated heat capacity of β -($\text{Mg}_{0.87}\text{Fe}_{0.13}$) $_2\text{SiO}_4$ as a function of temperature at various pressures is shown in **Figure 4**, together with the ambient pressure results of β - Mg_2SiO_4 measured using differential scanning calorimetry (Akaogi et al., 1984; Ashida et al., 1987; Jahn et al., 2013), as well as high-pressure results determined using first principle calculation (Wu and Wentzcovitch, 2007). At ambient pressure conditions, the separations between these previous results of β - Mg_2SiO_4 are quite large. Our heat capacity is close to that by Akaogi et al. (1984) with a difference of $\sim 0.5\%$, while larger than that by Ashida et al. (1987), and smaller than those by Wu and Wentzcovitch (2007) and Jahn et al. (2013). Moreover, our obtained heat capacity is smaller than the result by Wu and Wentzcovitch (2007) at high-pressure conditions as well.

Furthermore, the determined entropy of β -($\text{Mg}_{0.87}\text{Fe}_{0.13}$) $_2\text{SiO}_4$ is illustrated in **Figure 5**, which is generally larger than previous experimental (Akaogi et al., 1984; Chopelas, 1991) and theoretical (Wu and Wentzcovitch, 2007) results. Though at ambient conditions, the differences between our and previous results are pretty significant, which is $\sim 13\%$, $\sim 15\%$, and $\sim 10\%$ compared to that by Akaogi et al. (1984), Chopelas (1991), and Wu and Wentzcovitch (2007), respectively. Nevertheless, the separations decrease with increasing temperature, and the average differences are $\sim 5\%$, $\sim 8\%$, and $\sim 4\%$ compared to the results by Akaogi et al. (1984), Chopelas (1991), and Wu and Wentzcovitch (2007), respectively. In addition, our calculated entropy of β -($\text{Mg}_{0.87}\text{Fe}_{0.13}$) $_2\text{SiO}_4$ is $\sim 5\%$ larger than that of β - Mg_2SiO_4 by Wu and Wentzcovitch (2007) at 10 and 20 GPa.

Based on the database by Saxena (1996), the values of thermal expansion, heat capacity, and entropy of β - Fe_2SiO_4 are larger than those of β - Mg_2SiO_4 . Theoretically the thermal expansion, heat capacity, and entropy of the Fe-bearing wadsleyite should be slightly larger than those of β - Mg_2SiO_4 . But according to the results, only entropy shows a noticeable increase with the Fe content. Since the differences of the thermal expansions and heat capacities between the available results for β - Mg_2SiO_4 are pretty large (**Figures 3, 4**), it is difficult to identify the effect of Fe on thermal expansion and heat capacity of wadsleyite based on existing results. More experimental and theoretical investigations are needed to clarify the Fe effects on the thermodynamic properties of wadsleyite.

DISCUSSION AND IMPLICATIONS

Comparisons on Thermodynamic Properties of β -($\text{Mg}_{0.87}\text{Fe}_{0.13}$) $_2\text{SiO}_4$ and α -($\text{Mg}_{0.9}\text{Fe}_{0.1}$) $_2\text{SiO}_4$

The thermoelastic properties, including molar volume, thermal expansion, and heat capacity of α -($\text{Mg}_{0.9}\text{Fe}_{0.1}$) $_2\text{SiO}_4$ at HT-HP have been determined in our previous work (Su et al., 2018). The standard entropy of forsterite (α - Mg_2SiO_4) and fayalite at 298 K were defined by Robie et al. (1982a; 1982b), from which the entropy of α -($\text{Mg}_{0.9}\text{Fe}_{0.1}$) $_2\text{SiO}_4$ can be derived as 99.8 (1) J/mol K. Here, we re-analysis the data and present the entropy of α -($\text{Mg}_{0.9}\text{Fe}_{0.1}$) $_2\text{SiO}_4$ at HT-HP, as well as the uncertainties of the determined parameters. The obtained data is shown in **Supplementary Tables S4–S6**.

To investigate the pressure effects on the thermodynamic properties of β -($\text{Mg}_{0.87}\text{Fe}_{0.13}$) $_2\text{SiO}_4$ and α -($\text{Mg}_{0.9}\text{Fe}_{0.1}$) $_2\text{SiO}_4$, we fit the thermodynamic parameters, including thermal expansions, heat capacities, and entropies to an equation of $N = N_0 + \partial N / \partial P \times P + \partial^2 N / \partial P^2 \times P^2$ at different temperatures, where N refers to the thermodynamic properties, N_0 refers to N at ambient pressure, $\partial N / \partial P$ and $\partial^2 N / \partial P^2$ refer to the first and second pressure derivatives of N , respectively. The fitting coefficients are listed in **Table 3**.

In **Table 3**, all the thermodynamic parameters, including thermal expansions, heat capacities, and entropies of β -

TABLE 3 | The thermal expansions, heat capacities, and entropies of β -(Mg_{0.87}Fe_{0.13})₂SiO₄ and α -(Mg_{0.9}Fe_{0.1})₂SiO₄, and their pressure derivatives at various temperatures.

T K	Fe-Bearing wadsleyite (β -(Mg _{0.87} Fe _{0.13}) ₂ SiO ₄)			San Carlos olivine (α -(Mg _{0.9} Fe _{0.1}) ₂ SiO ₄)		
	α_0	$\partial\alpha/\partial P$	$\partial^2\alpha/\partial P^2$	α_0	$\partial\alpha/\partial P$	$\partial^2\alpha/\partial P^2$
	10 ⁻⁵ /K	10 ⁻⁷ /K GPa	10 ⁻⁸ /K GPa ²	10 ⁻⁵ /K	10 ⁻⁷ /K GPa	10 ⁻⁸ /K GPa ²
300	1.952 (428)	-7.01 (2)	1.11 (1)	2.213 (390)	-12.25 (2)	1.39 (1)
700	2.997 (206)	-7.46 (2)	1.21 (1)	3.308 (188)	-13.31 (3)	1.48 (1)
1100	3.449 (196)	-8.84 (3)	1.50 (1)	3.867 (178)	-15.33 (4)	1.81 (2)
1500	3.839 (207)	-10.33 (3)	1.81 (2)	4.369 (189)	-17.45 (5)	2.19 (3)
2000	4.304 (230)	-12.22 (4)	2.19 (2)	4.978 (210)	-20.14 (6)	2.66 (3)
T K	C_{P0}	$\partial C_P/\partial P$	$\partial^2 C_P/\partial P^2$	C_{P0}	$\partial C_P/\partial P$	$\partial^2 C_P/\partial P^2$
	J/mol K	J/mol K GPa	10 ⁻³ J/mol K GPa ²	J/mol K	J/mol K GPa	10 ⁻³ J/mol K GPa ²
300	114.57 (377)	-0.804 (1)	0.09 (1)	120.38 (280)	-0.835 (1)	1.94 (1)
700	160.76 (105)	-0.387 (1)	3.56 (3)	164.64 (78)	-0.487 (1)	6.30 (4)
1100	174.78 (68)	-0.474 (1)	6.18 (5)	179.30 (50)	-0.640 (1)	10.57 (8)
1500	183.61 (56)	-0.625 (2)	8.94 (8)	189.41 (41)	-0.865 (3)	15.27 (12)
2000	192.17 (50)	-0.853 (2)	12.79 (11)	200.13 (37)	-1.196 (3)	21.96 (18)
T K	S_0	$\partial S/\partial P$	$\partial^2 S/\partial P^2$	S_0	$\partial S/\partial P$	$\partial^2 S/\partial P^2$
	J/mol K	J/mol K GPa	J/mol K GPa ²	J/mol K	J/mol K GPa	J/mol K GPa ²
300	99.3	-0.74 (1)	0.010 (1)	99.8 (1)	-0.89 (1)	0.021 (1)
700	219.1 (17)	-1.17 (1)	0.012 (1)	223.1 (14)	-1.37 (1)	0.024 (1)
1100	295.0 (21)	-1.36 (1)	0.014 (1)	300.9 (17)	-1.62 (1)	0.027 (1)
1500	350.6 (23)	-1.53 (1)	0.016 (1)	358.1 (18)	-1.85 (1)	0.032 (1)
2000	404.6 (24)	-1.74 (1)	0.019 (1)	414.1 (19)	-2.14 (1)	0.037 (1)

(Mg_{0.87}Fe_{0.13})₂SiO₄ and α -(Mg_{0.9}Fe_{0.1})₂SiO₄ show negative and nonlinear relationships with the pressure. The thermal expansion of β -(Mg_{0.87}Fe_{0.13})₂SiO₄ is generally smaller than that of α -(Mg_{0.9}Fe_{0.1})₂SiO₄ at the same temperature, which coincides with the principle that wadsleyite has a more densely packed structure than olivine. Also, the pressure effects on the thermal expansions of both β -(Mg_{0.87}Fe_{0.13})₂SiO₄ and α -(Mg_{0.9}Fe_{0.1})₂SiO₄ increase with the temperature. Also, the pressure derivative of β -(Mg_{0.87}Fe_{0.13})₂SiO₄ is larger than that of α -(Mg_{0.9}Fe_{0.1})₂SiO₄ at the same temperature. In the temperature range of 300–2000 K, the $\partial\alpha/\partial P$ of β -(Mg_{0.87}Fe_{0.13})₂SiO₄ decreases from -7.01 (2) 10⁻⁷/K GPa to -12.22 (4) 10⁻⁷/K GPa, and the $\partial\alpha/\partial P$ of α -(Mg_{0.9}Fe_{0.1})₂SiO₄ decreases from -12.25 (2) 10⁻⁷/K GPa to -20.14 (6) 10⁻⁷/K GPa.

For the heat capacity, the $\partial C_P/\partial P$ of β -(Mg_{0.87}Fe_{0.13})₂SiO₄ at 300 K ($\partial C_P/\partial P = -0.804$ (1) J/mol K GPa) is smaller than that at 700 K ($\partial C_P/\partial P = -0.387$ (1) J/mol K GPa). Then, with the temperature increasing to 2000 K, the $\partial C_P/\partial P$ of β -(Mg_{0.87}Fe_{0.13})₂SiO₄ decreases to -0.853 (2) J/mol K GPa. The pressure effect on the heat capacity of α -(Mg_{0.9}Fe_{0.1})₂SiO₄ shows the same pattern with the temperature, but generally, the $\partial C_P/\partial P$ of α -(Mg_{0.9}Fe_{0.1})₂SiO₄ is smaller than that of β -(Mg_{0.87}Fe_{0.13})₂SiO₄.

Similar to thermal expansion, the entropy of β -(Mg_{0.87}Fe_{0.13})₂SiO₄ is generally lower than that of α -(Mg_{0.9}Fe_{0.1})₂SiO₄ at the same condition. The pressure effect on the entropy of β -(Mg_{0.87}Fe_{0.13})₂SiO₄ is also smaller than that of α -(Mg_{0.9}Fe_{0.1})₂SiO₄. The $\partial S/\partial P$ of β -(Mg_{0.87}Fe_{0.13})₂SiO₄

decreases from -0.74 (1) J/mol GPa to -1.74 (1) J/mol GPa with the temperature increases from 300 to 2000 K. Besides, the $\partial S/\partial P$ of α -(Mg_{0.9}Fe_{0.1})₂SiO₄ decreases from -0.89 (1) J/mol GPa to -2.14 (1) J/mol GPa in the temperature range of 300–2000 K.

Phase Transition Boundary of Olivine-Wadsleyite in (Mg,Fe)₂SiO₄ System

The global seismic discontinuity at the depth of 410 km, which separates the upper mantle from the transition zone, is most likely caused by the olivine-wadsleyite transition at ~13–14 GPa (Zhang and Bass, 2016). Therefore, the phase transition boundary of olivine-wadsleyite has been widely studied to infer the composition and temperature at the 410 km discontinuity. By normal and reverse runs using *in-situ* X-ray diffraction in a cubic anvil apparatus, the olivine-wadsleyite transition pressures in Mg₂SiO₄ system from 1073 to 1873 K were proposed by Morishima et al. (1994). Also, the transition pressures of olivine-wadsleyite with different Fe contents were experimentally determined at various temperatures by Katsura and Ito (1989) (1473 and 1873 K), Chen et al. (2002) (1473 K), and Katsura et al. (2004) (1600 and 1900 K). Then, based on the transition pressures determined in Mg₂SiO₄ system, as well as the thermodynamic properties of α -Mg₂SiO₄ and β -Mg₂SiO₄, the phase transition boundary was calculated using Eq. 13 (Jacobs et al., 2006; Akaogi et al., 2007; Ottonello et al., 2008; Holland and Powell, 2011; Dorogokupets et al., 2015).

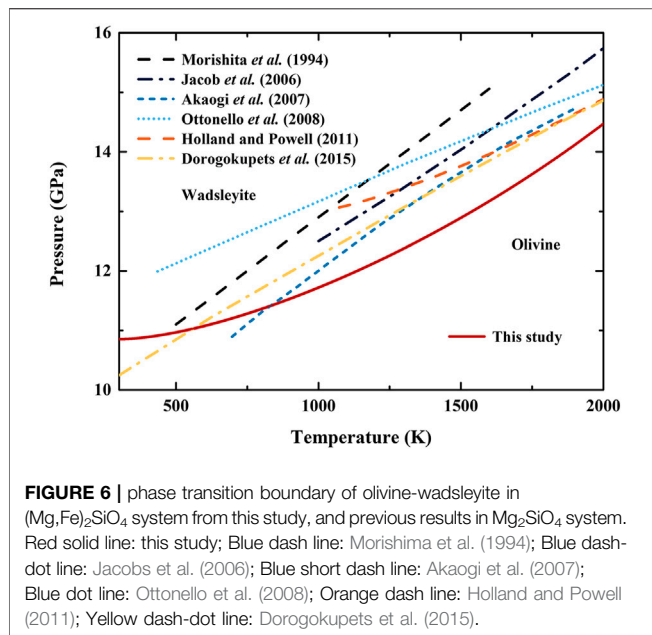


FIGURE 6 | phase transition boundary of olivine-wadsleyite in $(\text{Mg,Fe})_2\text{SiO}_4$ system from this study, and previous results in Mg_2SiO_4 system. Red solid line: this study; Blue dash line: Morishita et al. (1994); Blue dash-dot line: Jacobs et al. (2006); Blue short dash line: Akaogi et al. (2007); Blue dot line: Ottonello et al. (2008); Orange dash line: Holland and Powell (2011); Yellow dash-dot line: Dorogokupets et al. (2015).

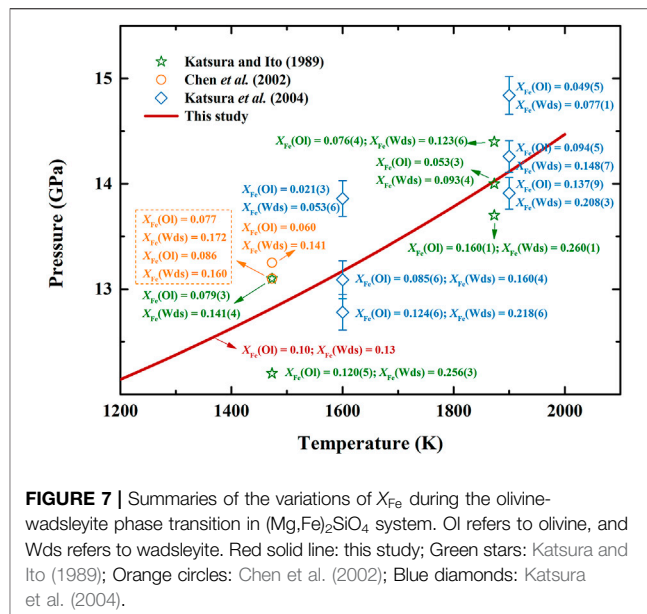


FIGURE 7 | Summaries of the variations of X_{Fe} during the olivine-wadsleyite phase transition in $(\text{Mg,Fe})_2\text{SiO}_4$ system. Ol refers to olivine, and Wds refers to wadsleyite. Red solid line: this study; Green stars: Katsura and Ito (1989); Orange circles: Chen et al. (2002); Blue diamonds: Katsura et al. (2004).

$$\Delta G(P, T) = \Delta H(P_0, T) - T\Delta S(P_0, T) + \int_{1 \text{ atm}}^P \Delta V(P, T) dP = 0 \quad (13)$$

Eq.13 is derived based on the Gibbs free energy equation, in which $\Delta H(P_0, T)$ and $\Delta S(P_0, T)$ are enthalpy and entropy changes between the low and high-pressure phases at high-temperature and ambient pressure conditions, respectively, $\Delta G(P, T)$ and $\Delta V(P, T)$ are the Gibbs free energy and volume changes at HT-HP, respectively. In previous studies, the volumes of olivine and wadsleyite as a function of temperature and pressure were obtained from either theoretical calculations (Jacobs et al., 2006; Ottonello et al., 2008; Dorogokupets et al., 2015), or X-ray diffraction experiments with the combination of the third-order Birch-Murnaghan equation of state (3BM EoS) (Akaogi et al., 2007; Holland and Powell, 2011). The empirical EoS such as 3BM EoS and Mie-Grüneisen-Debye EoS undoubtedly provide convenient ways for determining volumes at specific P - T conditions, but the assumptions in the derivation processes of these empirical EoS might cause uncertainties at high P - T range (Anderson, 1995; Angel et al., 2021).

Meanwhile, the Clausius-Clapeyron equation (Eq. 14) is also one of the classic equations for estimating the phase transition boundaries:

$$\frac{dP}{dT} = \frac{\Delta S(P, T)}{\Delta V(P, T)} \quad (14)$$

where dP/dT is the Clapeyron slope, $\Delta S(P, T)$ and $\Delta V(P, T)$ are, respectively, the entropy and volume changes between the two coexisting phases at HT-HP. Since previous measurements on the transition pressures in $(\text{Mg,Fe})_2\text{SiO}_4$ system were usually conducted at high-temperature conditions (Katsura and Ito, 1989; Chen et al., 2002; Katsura et al., 2004), once the transition pressure at an arbitrary temperature is determined,

the transition boundary can be simply derived with the entropy and volume changes between olivine and wadsleyite at HT-HP. The Clausius-Clapeyron equation was barely applied to the solid-solid phase transitions because the entropy variations with pressure in solids were often ignored in early studies (Ovrutsky et al., 2014). Here, with our obtained molar volumes and entropies of α - $(\text{Mg}_{0.9}\text{Fe}_{0.1})_2\text{SiO}_4$ and β - $(\text{Mg}_{0.87}\text{Fe}_{0.13})_2\text{SiO}_4$ at HT-HP, we try to determine the phase transition boundary of olivine-wadsleyite in $(\text{Mg,Fe})_2\text{SiO}_4$ system using the Clausius-Clapeyron equation. Note that the uncertainties of the transition pressure and Clapeyron slope are estimated using a Taylor series expansion.

In this study, the X_{Fe} are 0.13 and 0.1, respectively, for our wadsleyite and olivine, and the partition coefficients of Fe and Mg between α and β phases ($K_{\text{Fe-Mg}}^{\alpha-\beta} = (X_{\text{Fe}}^{\alpha}/X_{\text{Fe}}^{\beta})/[(1-X_{\text{Fe}}^{\alpha})/(1-X_{\text{Fe}}^{\beta})]$) is calculated as 0.74. The X_{Fe} of our wadsleyite and olivine are close to one of the experimental results proposed by Katsura et al. (2004) that the X_{Fe} increased from 0.094 (5) to 0.148 (7) during the olivine-wadsleyite transition, and the transition temperature and pressure were determined as 1900 K and 14.26 (15) GPa. Since our $K_{\text{Fe-Mg}}^{\alpha-\beta}$ is slightly higher than that by Katsura et al. (2004) [0.60 (5)], the start P - T point for our calculation is placed at 1900 K and 14.11 GPa, which is the lower limit of the transition pressure determined by Katsura et al. (2004).

Figure 6 illustrates our determined phase transition boundary, along with previous results determined in Mg_2SiO_4 system (Morishita et al., 1994; Jacobs et al., 2006; Akaogi et al., 2007; Ottonello et al., 2008; Holland and Powell, 2011; Dorogokupets et al., 2015). Generally, the transition pressures obtained in Mg_2SiO_4 system are higher than ours over ~ 850 K (Ottonello et al., 2008). Also, the transition pressures of most previous studies tend to be linear with increasing temperature (Morishita et al., 1994; Jacobs et al., 2006; Akaogi et al., 2007; Ottonello et al., 2008; Dorogokupets et al., 2015). In contrast, our

obtained transition pressure shows obvious nonlinear temperature dependence, which is caused by the nonlinear relationship between determined dP/dT and temperature. At room temperature, the transition pressure is estimated as 10.85 (1) GPa, with the dP/dT as 0.0005 (2) GPa/K. Then, the dP/dT increases with the temperature and reaches 0.0036 (3) GPa/K at 2000 K, where the transition pressure is estimated as 14.47 (18) GPa. The obtained transition pressure can be approximated modeled by a polynomial function of $p = 10.78 (1) + 6.73 (2) \times 10^{-4} (T-273) + 8.49 (1) \times 10^{-7} (T-273)^2$, where P in GPa and T in K. Detailed data of the calculated transition pressure, dP/dT , and their uncertainties is provided in **Supplementary Table S7**.

Furthermore, to investigate the effect of Fe content on the phase transition boundary of olivine-wadsleyite, we collect the variations of X_{Fe} during the transition from previous work (Katsura and Ito, 1989; Chen et al., 2002; Katsura et al., 2004), and the data is summarized in **Figure 7**. We find that the transition pressures with the $X_{Fe}^a < 0.1$ from previous work are generally higher than our estimation. Also, except for the two data points (1873 K and 14.4 GPa; 1873 K and 14.0 GPa) by Katsura and Ito (1989), the transition pressure decreases with the increasing X_{Fe}^a at the same temperature condition.

Implication for the Temperature at the 410 km Discontinuity

Temperature is one of the essential parameters for modeling the dynamics of the Earth's interior. Nearly 4 decades ago, the mantle temperature profiles were presented with the constructions of Earth models (Stacey, 1977; Brown and Shankland, 1981), in which the temperature at the 410 km discontinuity was estimated in a wide range of ~1700–2000 K. Then, by comparing the depth of the 410 km discontinuity with the pressures of the olivine-wadsleyite transition, Katsura et al. (2004) proposed the temperature as 1760 ± 45 K for a pyrolite model assuming a bulk composition of $X_{Fe} = 0.11$. And later, the value was re-evaluated as 1830 ± 48 K (Katsura et al., 2010).

In this study, we regard the globally averaged depth of the 410 km discontinuity as 411 ± 2 km following the results of seismic investigations (Gu et al., 1998; Chambers et al., 2005), and the pressure can be estimated as 13.76 ± 0.05 GPa according to the depth-pressure conversion (Stacey and Davis, 2008). Therefore, the temperature at the 410 km discontinuity is obtained as 1795 ± 70 K on the basis of our phase relations.

It is worth noting that our temperature at the 410 km discontinuity is determined under anhydrous conditions. It has been confirmed that there is water existing in both olivine and wadsleyite in their crystal structure, which would not only reduce their bulk sound velocity (Jacobsen et al., 2008; Mao et al., 2008), but also enlarge their thermal expansion (Ye et al., 2009) and the heat capacity of wadsleyite (Jahn et al., 2013). Evidence has shown that the presence of water would reduce the pressure interval of olivine-wadsleyite phase transformation by

0.3–0.6 GPa (Chen et al., 2002), which leads to an increase of ~90–176 K in temperature.

Additionally, in this study, we regard $K_{Fe-Mg}^{\alpha-\beta}$ as a constant and only present the olivine-wadsleyite phase transition boundary of a simple model in $(Mg,Fe)_2SiO_4$ system. Previous studies concluded that the values of $K_{Mg-Fe}^{\alpha-\beta}$ are in the ranges of 0.38–0.57, 0.52–0.69, and 0.60–0.62 at 1473, 1873, and 1900 K, respectively, which indicates that $K_{Fe-Mg}^{\alpha-\beta}$ may decrease with the increasing temperature during the phase transition (Katsura and Ito, 1989; Katsura et al., 2004). Therefore, more complicated systems need to be taken into account in future studies.

CONCLUSION

In the present study, the self-consistent molar volume, elastic moduli, thermal expansion, heat capacity, and entropy of β -($Mg_{0.87},Fe_{0.13}$) $_2SiO_4$ have been determined up to 2000 K and 20 GPa based on existing experimental data and thermodynamic relations. The calculated parameters were generally consistent with available results. The thermodynamic properties, including entropy of α -($Mg_{0.9},Fe_{0.1}$) $_2SiO_4$ were also reanalyzed on account of our recent work. The thermal expansions, heat capacities, and entropies of both β -($Mg_{0.87},Fe_{0.13}$) $_2SiO_4$ and α -($Mg_{0.9},Fe_{0.1}$) $_2SiO_4$ show negative and nonlinear relationships with the pressure. Also, the pressure effects on the thermodynamic properties of α -($Mg_{0.9},Fe_{0.1}$) $_2SiO_4$ are larger than that of β -($Mg_{0.87},Fe_{0.13}$) $_2SiO_4$.

Using the Clausius-Clapeyron equation, the olivine-wadsleyite phase transition boundary with the $K_{Fe-Mg}^{\alpha-\beta}$ as 0.74 was estimated with the combination of the obtained molar volumes and entropies of β -($Mg_{0.87},Fe_{0.13}$) $_2SiO_4$ and α -($Mg_{0.9},Fe_{0.1}$) $_2SiO_4$. The transition pressure can be approximately expressed by a polynomial equation of P (GPa) = $10.78 (1) + 6.73 (2) \times 10^{-4} (T(K)-273) + 8.49 (1) \times 10^{-7} (T(K)-273)^2$, which is generally lower than the previous studies on Mg_2SiO_4 system at the same temperature condition. For instance, the temperature at the 410 km discontinuity is obtained as 1795 ± 70 K based on our obtained olivine-wadsleyite phase transition boundary under anhydrous conditions, and it would increase by ~90–176 K if the water effect was considered. The results indicate that both Fe and water contents would influence the transition pressure of olivine-wadsleyite phase transition, which probably leads to a higher temperature at the 410 km discontinuity.

DATA AVAILABILITY STATEMENT

The original contributions presented in the study are included in the article/**Supplementary Material**, further inquiries can be directed to the corresponding authors.

AUTHOR CONTRIBUTIONS

Conceptualization, CS, YL, and WS; methodology, CS, YL, and DF; software, GY; resources, JJ. and ZS; data curation, WS;

writing-original draft preparation, CS; writing-review and editing, YL, WS, and DF; supervision, YL and WS; project administration, YL; funding acquisition, YL. All authors have read and agreed to the published version of the manuscript.

FUNDING

This project was supported by the National Natural Science Foundation of China (Grant Nos. 41873075 and 42174225), and the Key Research Program of Frontier Sciences of CAS (Grant No. ZDBS-LY-DQC015).

REFERENCES

- Akaogi, M., Ross, N., McMillan, P., and Navrotsky, A. (1984). The Mg_2SiO_4 Polymorphs (Olivine, Modified Spinel and Spinel)-Thermodynamic Properties from Oxide Melt Solution Calorimetry, Phase Relations, and Models of Lattice Vibrations. *Am. Mineral.* 69, 499–512.
- Akaogi, M., Takayama, H., Kojitani, H., Kawaji, H., and Atake, T. (2007). Low-temperature Heat Capacities, Entropies and Enthalpies of Mg_2SiO_4 Polymorphs, and α - β - γ and post-spinel Phase Relations at High Pressure. *Phys. Chem. Minerals* 34, 169–183. doi:10.1007/s00269-006-0137-3
- Akimoto, S.-i., Komada, E., and Kushiro, I. (1967). Effect of Pressure on the Melting of Olivine and Spinel Polymorph of Fe_2SiO_4 . *J. Geophys. Res.* 72, 679–686. doi:10.1029/JZ072i002p00679
- Akimoto, S., Matsui, Y., and Syono, Y. (1978). “High-pressure crystal Chemistry of Orthosilicates and the Formation of the Mantle Transition Zone,” in *The Physics and Chemistry of Minerals and Rocks*. Editor R. G. J. Strens (New York: John Wiley & Sons).
- Anderson, D. (1995). *Equations of State of Solids for Geophysics and Ceramic Science*. Oxford University Press.
- Angel, R., Mazzucchelli, M., Gonzalez-Platas, J., and Alvaro, M. (2021). A Self-Consistent Approach to Describe Unit-Cell-Parameter and Volume Variations with Pressure and Temperature. *J. Appl. Cryst.* 54, 1621–1630. doi:10.1107/S1600576721009092
- Ashida, T., Kume, S., and Ito, E. (1987). Thermodynamic Aspects of Phase Boundary Among α -, β -, and γ - Mg_2SiO_4 . *High-Pressure Research in Mineral Physics: A Volume in Honor of Syun-iti Akimoto*, 269–274. doi:10.1029/gm039p0269
- Bina, C. R., and Silver, P. G. (1990). Constraints on Lower Mantle Composition and Temperature from Density and Bulk Sound Velocity Profiles. *Geophys. Res. Lett.* 17, 1153–1156. doi:10.1029/GL017i008p01153
- Bina, C. R., and Wood, B. J. (1987). Olivine-spinel Transitions: Experimental and Thermodynamic Constraints and Implications for the Nature of the 400-km Seismic Discontinuity. *J. Geophys. Res.* 92, 4853–4866. doi:10.1029/JB092iB06p04853
- Brown, J. M., and Shankland, T. J. (1981). Thermodynamic Parameters in the Earth as Determined from Seismic Profiles. *Geophys. J. Int.* 66, 579–596. doi:10.1111/j.1365-246X.1981.tb04891.x
- Chambers, K., Woodhouse, J. H., and Deuss, A. (2005). Topography of the 410-km Discontinuity from PP and SS Precursors. *Earth Planet. Sci. Lett.* 235, 610–622. doi:10.1016/j.epsl.2005.05.014
- Chen, J., Inoue, T., Yurimoto, H., and Weidner, D. J. (2002). Effect of Water on Olivine-Wadsleyite Phase Boundary in the (Mg, Fe) $_2\text{SiO}_4$ system. *Geophys. Res. Lett.* 29, 22–24. doi:10.1029/2001gl014429
- Chopelas, A. (1991). Thermal Properties of β - Mg_2SiO_4 at Mantle Pressures Derived from Vibrational Spectroscopy: Implications for the Mantle at 400 Km Depth. *J. Geophys. Res.* 96, 11817–11829. doi:10.1029/91jb00898
- Dai, L., and Karato, S.-i. (2009). Electrical Conductivity of Wadsleyite at High Temperatures and High Pressures. *Earth Planet. Sci. Lett.* 287, 277–283. doi:10.1016/j.epsl.2009.08.012
- Dorogokupets, P. I., Dymshits, A. M., Sokolova, T. S., Danilov, B. S., and Litasov, K. D. (2015). The Equations of State of Forsterite, Wadsleyite, Ringwoodite, Akimotoite, MgSiO_3 -Perovskite, and Postperovskite and Phase Diagram for the Mg_2SiO_4 System at Pressures of up to 130 GPa. *Russ. Geology. Geophys.* 56, 172–189. doi:10.1016/j.rgg.2015.01.011
- Fei, Y., Mao, H.-k., Shu, J., Parthasarathy, G., Bassett, W. A., and Ko, J. (1992). Simultaneous High-P, High-TX ray Diffraction Study of β -(Mg,Fe) $_2\text{SiO}_4$ to 26 GPa and 900 K. *J. Geophys. Res.* 97, 4489–4495. doi:10.1029/92jb00076
- Fei, Y., and Saxena, S. K. (1986). A Thermochemical Data Base for Phase Equilibria in the System Fe-Mg-Si-O at High Pressure and Temperature. *Phys. Chem. Minerals* 13, 311–324. doi:10.1007/bf00308348
- Gonzalez-Platas, J., Alvaro, M., Nestola, F., and Angel, R. (2016). EosFit7-GUI: a New Graphical User Interface for Equation of State Calculations, Analyses and Teaching. *J. Appl. Cryst.* 49, 1377–1382. doi:10.1107/s1600576716008050
- Gu, Y., Dziewonski, A. M., and Agee, C. B. (1998). Global De-correlation of the Topography of Transition Zone Discontinuities. *Earth Planet. Sci. Lett.* 157, 57–67. doi:10.1016/s0012-821x(98)00027-2
- Holland, T. J. B., and Powell, R. (2011). An Improved and Extended Internally Consistent Thermodynamic Dataset for Phases of Petrological Interest, Involving a New Equation of State for Solids. *J. Metamorphic Geology*. 29, 333–383. doi:10.1111/j.1525-1314.2010.00923.x
- Isaak, D. G., Gwanmesia, G. D., Davis, M. G., Stafford, S. C., Stafford, A. M., and Triplett, R. S. (2010). The Temperature Dependence of the Elasticity of Fe-Bearing Wadsleyite. *Phys. Earth Planet. Interiors* 182, 107–112. doi:10.1016/j.pepi.2010.06.014
- Ito, E., and Katsura, T. (1989). A Temperature Profile of the Mantle Transition Zone. *Geophys. Res. Lett.* 16, 425–428. doi:10.1029/GL016i005p00425
- Jacobs, M. H. G., van den Berg, A. P., and de Jong, B. H. W. S. (2006). The Derivation of Thermo-Physical Properties and Phase Equilibria of Silicate Materials from Lattice Vibrations: Application to Convection in the Earth's Mantle. *Calphad* 30, 131–146. doi:10.1016/j.calphad.2005.10.001
- Jacobsen, S. D., Jiang, F., Mao, Z., Duffy, T. S., Smyth, J. R., Holl, C. M., et al. (2008). Effects of Hydration on the Elastic Properties of Olivine. *Geophys. Res. Lett.* 35, L14303. doi:10.1029/2008gl034398
- Jahn, S., Rahner, R., Dachs, E., Mrosko, M., and Koch-Müller, M. (2013). Thermodynamic Properties of Anhydrous and Hydrated Wadsleyite, β - Mg_2SiO_4 . *High Press. Res.* 33, 584–594. doi:10.1080/08957959.2013.806498
- Johari, G. P. (2021). Entropy, Enthalpy and Volume of Perfect Crystals at Limiting High Pressure and the Third Law of Thermodynamics. *Thermochim. Acta* 698, 178891. doi:10.1016/j.tca.2021.178891
- Katsura, T., and Ito, E. (1989). The System Mg_2SiO_4 - Fe_2SiO_4 at High Pressures and Temperatures: Precise Determination of Stabilities of Olivine, Modified Spinel, and Spinel. *J. Geophys. Res.* 94, 15663–15670. doi:10.1029/JB094iB11p15663
- Katsura, T., Mayama, N., Shouno, K., Sakai, M., Yoneda, A., and Suzuki, I. (2001). Temperature Derivatives of Elastic Moduli of (Mg_{0.91}Fe_{0.09}) $_2\text{SiO}_4$ Modified Spinel. *Phys. Earth Planet. Interiors* 124, 163–166. doi:10.1016/s0031-9201(01)00189-3
- Katsura, T., Yamada, H., Nishikawa, O., Song, M., Kubo, A., Shinmei, T., et al. (2004). Olivine-wadsleyite Transition in the System (Mg,Fe) $_2\text{SiO}_4$. *J. Geophys. Res.* 109, 2438. doi:10.1029/2003jb002438

ACKNOWLEDGMENTS

The authors thank Prof. Wenge Zhou at the Institute of Geochemistry, Chinese Academy of Sciences for helpful discussions and suggestions.

SUPPLEMENTARY MATERIAL

The Supplementary Material for this article can be found online at: <https://www.frontiersin.org/articles/10.3389/feart.2022.879678/full#supplementary-material>

- Katsura, T., Yoneda, A., Yamazaki, D., Yoshino, T., and Ito, E. (2010). Adiabatic Temperature Profile in the Mantle. *Phys. Earth Planet. Interiors* 183, 212–218. doi:10.1016/j.pepi.2010.07.001
- Li, B., and Liebermann, R. C. (2000). Sound Velocities of Wadsleyite β -(Mg_{0.88}Fe_{0.12})₂SiO₄ to 10 GPa. *Am. Mineral.* 85, 292–295. doi:10.2138/am-2000-2-305
- Liu, W., Kung, J., Li, B., Nishiyama, N., and Wang, Y. (2009). Elasticity of (Mg_{0.87}Fe_{0.13})₂SiO₄ Wadsleyite to 12 GPa and 1073 K. *Phys. Earth Planet. Interiors* 174, 98–104. doi:10.1016/j.pepi.2008.10.020
- Mao, Z., Jacobsen, S. D., Jiang, F., Smyth, J. R., Holl, C. M., Frost, D. J., et al. (2008). Single-crystal Elasticity of Wadsleyites, β -Mg₂SiO₄, Containing 0.37–1.66 wt.% H₂O. *Earth Planet. Sci. Lett.* 266, 78–89. doi:10.1016/j.epsl.2007.10.045
- Mayama, N. (2004). Temperature Dependence of Elastic Moduli of β -(Mg, Fe) ₂SiO₄. *Geophys. Res. Lett.* 31. doi:10.1029/2003gl019247
- Morishima, H., Kato, T., Suto, M., Ohtani, E., Urakawa, S., Utsumi, W., et al. (1994). The Phase Boundary between α - and β -Mg ₂ SiO ₄ Determined by *In Situ* X-ray Observation. *Science* 265, 1202–1203. doi:10.1126/science.265.5176.1202
- Ottone, G., Civalleri, B., Ganguly, J., Vetuschi Zuccolini, M., and Noel, Y. (2008). Thermophysical Properties of the α - γ Polymorphs of Mg₂SiO₄: a Computational Study. *Phys. Chem. Minerals* 36, 87–106. doi:10.1007/s00269-008-0260-4
- Ovrtsky, A. M., Prokhoda, A. S., and Rasshchupkyna, M. S. (2014). “Basic Concepts of Theory of Phase Transformations,” in *Computational Materials Science*. Editors A. M. Ovrtsky, A. S. Prokhoda, and M. S. Rasshchupkyna (Oxford: Elsevier), 35–69. doi:10.1016/b978-0-12-420143-9.00002-8
- Ringwood, A. E. (1962). A Model for the Upper Mantle: 2. *J. Geophys. Res.* 67, 4473–4478. doi:10.1029/JZ067i011p04473
- Ringwood, A. E., and Major, A. (1970). The System Mg₂SiO₄-Fe₂SiO₄ at High Pressures and Temperatures. *Phys. Earth Planet. Interiors* 3, 89–108. doi:10.1016/0031-9201(70)90046-4
- Robie, R. A., Finch, C. B., and Hemingway, B. S. (1982a). Heat Capacity and Entropy of Fayalite (Fe₂SiO₄) between 5.1 and 383 K: Comparison of Calorimetric and Equilibrium Values for the QFM Buffer Reaction. *Am. Mineral.* 67, 463–469.
- Robie, R. A., Hemingway, B. S., and Takei, H. (1982b). Heat Capacities and Entropies of Mg₂SiO₄, Mn₂SiO₄, and Co₂SiO₄ between 5 and 380 K. *Am. Mineral.* 67, 470–482.
- Saxena, S. K. (1996). Earth Mineralogical Model: Gibbs Free Energy Minimization Computation in the System MgO-FeO-SiO₂. *Geochimica et Cosmochimica Acta* 60, 2379–2395. doi:10.1016/0016-7037(96)00096-8
- Sinogeikin, S. V., Katsura, T., and Bass, J. D. (1998). Sound Velocities and Elastic Properties of Fe-Bearing Wadsleyite and Ringwoodite. *J. Geophys. Res.* 103, 20819–20825. doi:10.1029/98jb01819
- Stacey, F. D. (1977). A thermal Model of the Earth. *Phys. Earth Planet. Interiors* 15, 341–348. doi:10.1016/0031-9201(77)90096-6
- Stacey, F., and Davis, P. (2008). *Physics of the Earth*. Cambridge: Cambridge Univ. Press.
- Su, C., Liu, Y., Fan, D., Song, W., and Yang, G. (2022). Self-consistent Thermodynamic Parameters of Pyrope and Almandine at High-Temperature and High-Pressure Conditions: Implication on the Adiabatic Temperature Gradient. *Phys. Earth Planet. Interiors* 322, 106789. doi:10.1016/j.pepi.2021.106789
- Su, C., Liu, Y., Song, W., Fan, D., Wang, Z., and Tang, H. (2018). Thermodynamic Properties of San Carlos Olivine at High Temperature and High Pressure. *Acta Geochim.* 37, 171–179. doi:10.1007/s11631-018-0261-z
- Suzuki, I., Ohtani, E., and Kumazawa, M. (1980). Thermal Expansion of Modified Spinel, β -Mg₂SiO₄. *J. Phys. Earth* 28, 273–280. doi:10.4294/jpe.1952.28.273
- Wang, J., Bass, J. D., and Katsura, T. (2014). Elastic Properties of Iron-Bearing Wadsleyite to 17.7 GPa: Implications for Mantle mineral Models. *Phys. Earth Planet. Interiors* 228, 92–96. doi:10.1016/j.pepi.2014.01.015
- Watanabe, H. (1982). “Thermochemical Properties of Synthetic High Pressure Compounds Relevant to the Earth’s Mantle,” in *High Pressure Research in Geophysics*. Editor H. A. a. M. H. Manghnani (Tokyo: Center for Academic Publishing of Japan).
- Wu, Z., and Wentzcovitch, R. M. (2007). Vibrational and Thermodynamic Properties of Wadsleyite: A Density Functional Study. *J. Geophys. Res.* 112. doi:10.1029/2007jb005036
- Xu, Y., Shankland, T. J., Linhardt, S., Rubie, D. C., Langenhorst, F., and Klasinski, K. (2004). Thermal Diffusivity and Conductivity of Olivine, Wadsleyite and Ringwoodite to 20 GPa and 1373 K. *Phys. Earth Planet. Interiors* 143–144, 321–336. doi:10.1016/j.pepi.2004.03.005
- Ye, Y., Schwering, R. A., and Smyth, J. R. (2009). Effects of Hydration on thermal Expansion of Forsterite, Wadsleyite, and Ringwoodite at Ambient Pressure. *Am. Mineral.* 94, 899–904. doi:10.2138/am.2009.3122
- Yoshino, T., Shimojuku, A., Shan, S., Guo, X., Yamazaki, D., Ito, E., et al. (2012). Effect of Temperature, Pressure and Iron Content on the Electrical Conductivity of Olivine and its High-Pressure Polymorphs. *J. Geophys. Res.* 117, a–n. doi:10.1029/2011jb008774

Conflict of Interest: The authors declare that the research was conducted in the absence of any commercial or financial relationships that could be construed as a potential conflict of interest.

Publisher’s Note: All claims expressed in this article are solely those of the authors and do not necessarily represent those of their affiliated organizations, or those of the publisher, the editors and the reviewers. Any product that may be evaluated in this article, or claim that may be made by its manufacturer, is not guaranteed or endorsed by the publisher.

Copyright © 2022 Su, Liu, Fan, Song, Jiang, Sun and Yang. This is an open-access article distributed under the terms of the Creative Commons Attribution License (CC BY). The use, distribution or reproduction in other forums is permitted, provided the original author(s) and the copyright owner(s) are credited and that the original publication in this journal is cited, in accordance with accepted academic practice. No use, distribution or reproduction is permitted which does not comply with these terms.



High-Temperature and High-Pressure Phase Transition of Natural Barite Investigated by Raman Spectroscopy and Electrical Conductivity

Meiling Hong^{1,2}, Lidong Dai^{1*}, Haiying Hu^{1*}, Xinyu Zhang^{1,2} and Chuang Li^{1,2}

¹Key Laboratory of High-Temperature and High-Pressure Study of the Earth's Interior, Institute of Geochemistry, Chinese Academy of Sciences, Guiyang, China, ²University of Chinese Academy of Sciences, Beijing, China

OPEN ACCESS

Edited by:

Nibir Mandal,
Jadavpur University, India

Reviewed by:

Pratik K. Das,
University at Buffalo, United States
Prafulla K. Jha,
Maharaja Sayajirao University of
Baroda, India

*Correspondence:

Lidong Dai
dailidong@vip.gyig.ac.cn
Haiying Hu
huhaiying@vip.gyig.ac.cn

Specialty section:

This article was submitted to
Solid Earth Geophysics,
a section of the journal
Frontiers in Earth Science

Received: 28 January 2022

Accepted: 11 April 2022

Published: 27 April 2022

Citation:

Hong M, Dai L, Hu H, Zhang X and Li C
(2022) High-Temperature and High-
Pressure Phase Transition of Natural
Barite Investigated by Raman
Spectroscopy and
Electrical Conductivity.
Front. Earth Sci. 10:864183.
doi: 10.3389/feart.2022.864183

We investigated the structural, vibrational, and electrical transport properties for natural barite under the conditions of 298–873 K and 1.5–35.0 GPa using a diamond anvil cell by virtue of Raman spectroscopy and electrical conductivity measurements. Upon compression, natural barite transformed into post-barite at 18.9 GPa and atmospheric temperature, which was evidenced by the emergence of ν_5 Raman peak, the discontinuities in the pressure-dependent Raman shifts, FWHM of ν_1 Raman peak and electrical conductivity under non-hydrostatic condition. The phase transition is of good reversibility, whereas a considerable pressure hysteresis was detected during the process of decompression. Under quasi-hydrostatic condition, the structural transition of natural barite occurred at a higher pressure of 21.4 GPa, which is possibly related to the influence of deviatoric stress. Furthermore, our high-temperature and high-pressure Raman spectra and electrical conductivity results for natural barite revealed that the phase transformation pressures decreased as temperatures enhanced and further, the phase boundary between barite and post-barite was described as P (GPa) = $24.00 - 0.0166 T$ (K). Our obtained phase diagram of natural barite can improve the knowledge about the structural and electrical properties for other barite-group minerals MSO_4 ($M = \text{Sr}$ and Pb) under high temperature and high pressure conditions.

Keywords: natural barite, Raman spectroscopy, electrical conductivity, structural phase transition, hydrostaticity, high temperature, high pressure

INTRODUCTION

Barite-group sulfates MSO_4 ($M = \text{Ba}$, Sr , and Pb), the most prominent and common sulfate minerals in the Earth's crust, play a vital role in the recycling of sulfur from crust into mantle through plate subduction (Evans et al., 2014; Canil and Fellows, 2017). Under ambient conditions, barite-group sulfates crystallize into orthorhombic crystal systems, where each M atom coordinates with twelve oxygen atoms derived from six neighboring SO_4 tetrahedrons to constitute MO_{12} polyhedron, leading to the edge sharing between SO_4 and MO_{12} polyhedrons (Antao, 2012; Ye et al., 2019). As a representative barite-group sulfate, barite ($BaSO_4$) primarily outcrops in low temperature hydrothermal deposits and sedimentary deposits (Abidi et al., 2012). In light of its chemical stability, high reservation, and low cost, barite has been extensively applied in the fields of chemical raw materials, drilling mud raw materials, glass raw materials, and chemical fillers (Zhou et al., 2015).

Previous high-pressure phase stability investigations on barite have been performed through synchrotron X-ray diffraction and Raman spectroscopy (Lee et al., 2001; Lee et al., 2003; Crichton et al., 2011; Santamaría-Pérez et al., 2011; Ye et al., 2019). However, there are numerous disputes regarding the phase stability and structural transition pressure for barite. Santamaría-Pérez et al. (2011) conducted the synchrotron X-ray diffraction research on synthetic barite in a diamond anvil cell using three different pressure mediums of the methanol and ethanol mixture (4:1 volume ratio), silicone oil, and helium up to 48.0 GPa. Their experimental results revealed that barite underwent a structural transition from the *Pbnm* to *P2₁2₁2₁* phases within the pressure range of 17.0–27.0 GPa, depending on the employed pressure medium. Subsequently, a similar synchrotron X-ray diffraction study reported the *Pbnm*-to-*P2₁2₁2₁* phase transition at ~20.3 GPa with neon as the pressure medium (Ye et al., 2019). However, Lee et al. (2001); Lee et al. (2003) disclosed the occurrence of a phase transition at a lower pressure of 10.0 GPa under different hydrostatic environments with no pressure medium and the mixture of methanol and ethanol (4:1 volume ratio) as the pressure medium by virtue of synchrotron X-ray diffraction and Raman spectroscopy. By contrast, Crichton et al. (2011) performed the synchrotron X-ray diffraction and Raman spectroscopy measurements on natural barite single crystal from Germany using helium as the pressure medium and results demonstrated that natural barite remained stable up to 21.5 GPa. And thus, the controversies on the high-pressure phase stability and structural transition pressure for barite are worthy of further investigation. Besides the aforementioned two experimental means, electrical conductivity measurement is another sensitive and effective method, since the occurrence of structural transition is often accompanied by the variation in electrical transport characteristic for some rocks and minerals (Pu et al., 2018; Yang et al., 2018; Hong et al., 2022). However, the related investigation on the high-temperature and high-pressure electrical conductivity of natural barite remains blank until now.

On the other hand, temperature is an important factor of influencing the phase transition pressure for some minerals and rocks (Hong et al., 2022). To the best of our knowledge, Lee et al. (2001) have proposed the phase diagram of synthetic barite under the temperature range of 298–1000 K and pressures up to 29.0 GPa through synchrotron X-ray diffraction. Additionally, Raman spectroscopy and electrical conductivity measurements have been proved to be efficient methods of identifying the occurrence of structural transition under high temperature and high pressure conditions and thus have been extensively applied to establish the phase diagram of minerals and rocks (Pu et al., 2018; Yang et al., 2018; Hong et al., 2022). Previously available Raman spectroscopy investigations paid special attention on the structural transition of barite under high pressure and room temperature conditions (Lee et al., 2003; Chen et al., 2009; Crichton et al., 2011), whereas the relevant Raman scattering research on the phase stability of barite under simultaneously high-temperature and high-pressure conditions is still lacking.

In the present study, we reported the structural transition of natural barite up to 35.0 GPa at atmospheric temperature under

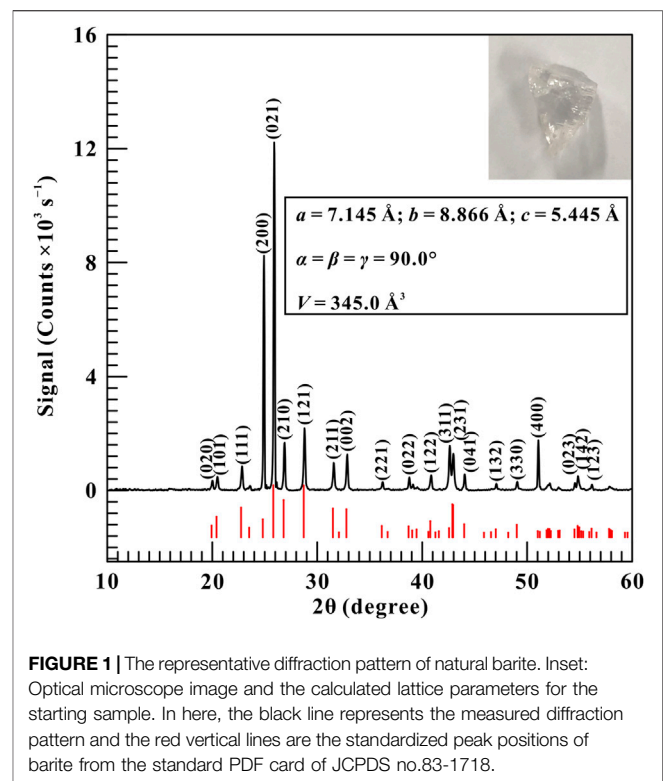


FIGURE 1 | The representative diffraction pattern of natural barite. Inset: Optical microscope image and the calculated lattice parameters for the starting sample. In here, the black line represents the measured diffraction pattern and the red vertical lines are the standardized peak positions of barite from the standard PDF card of JCPDS no.83-1718.

different hydrostatic environments using a diamond anvil cell in conjunction with Raman spectroscopy and alternating current (AC) complex impedance spectroscopy, and the influence of different hydrostatic environments on the phase transition pressures was discussed in detail. Furthermore, we also revealed the influence of temperatures on the phase transformation pressures, and a phase diagram of natural barite was constructed under conditions of 298–873 K and 10.9–18.9 GPa.

MATERIALS AND METHODS

Sample Preparation and Characterization

The natural transparent barite crystal (see the inset of **Figure 1**) was gathered from Huili city, Sichuan province, China. We crushed and ground the bulk sample into powders using an agate mortar. The phase identification of the initial sample was performed by X-ray diffraction (XRD) with a X'Pert Pro X-ray powder diffractometer operating at an acceleration voltage of 45 kV and a beam current of 40 mA, respectively. **Figure 1** shows the typical XRD pattern of the starting sample and the results revealed that the initial sample belongs to orthorhombic structure with the space group of *Pbnm*. The lattice parameters of the starting sample were calculated using MDI Jade 6.5 software and the correspondent results are listed as follows: $a = 7.145 \text{ Å}$, $b = 8.866 \text{ Å}$, $c = 5.445 \text{ Å}$, $\alpha = \beta = \gamma = 90.0^\circ$, and $V = 345.0 \text{ Å}^3$, which coincides well with the standard PDF data of barite (JCPDS no.83-1718). Although our obtained zero-pressure unit cell volume is slightly different from previous investigations (Lee

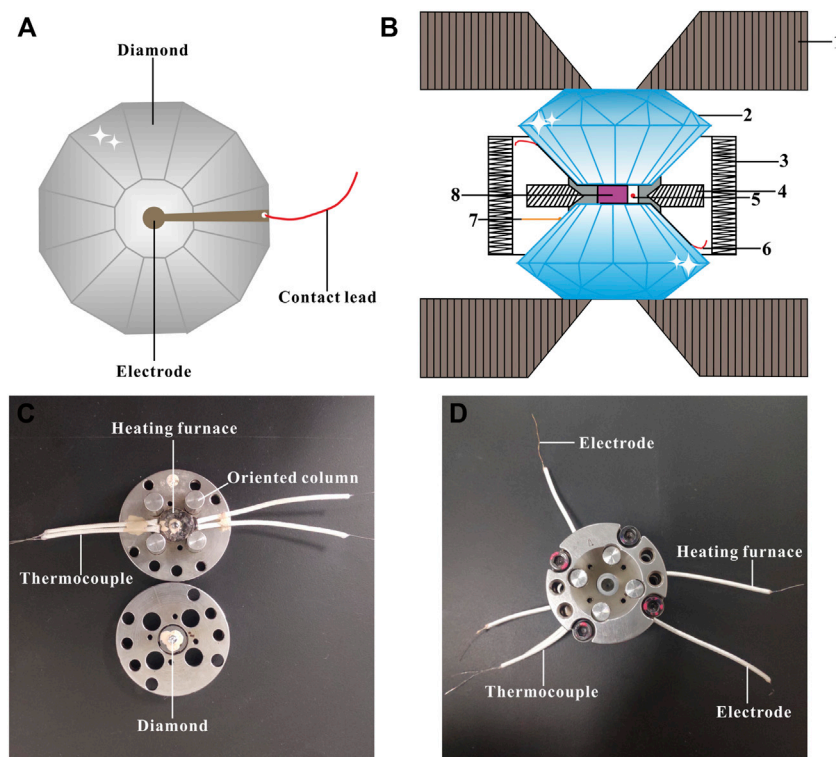


FIGURE 2 | Experimental assemblage of the high-temperature and high-pressure electrical conductivity measurements on natural barite. **(A)** Configuration of plate electrodes installed on two diamond anvils. **(B)** Cross-sectional schematic of the externally heated diamond anvil cell (DAC) applied for the high-temperature and high-pressure electrical conductivity experiments. In here, (1) tungsten carbide seat; (2) diamond; (3) heating furnace; (4) gasket; (5) ruby; (6) electrode; (7) thermocouple; (8) sample. **(C)** and **(D)** The photographs of the external resistance heating DAC assembly employed in high-temperature and high-pressure electrical conductivity measurements.

et al., 2001; Lee et al., 2003; Crichton et al., 2011; Ye et al., 2019), it has a negligible effect on the equation of state (EoS) of barite.

High-Temperature and High-Pressure Raman Spectroscopy Measurements

A four column-type diamond anvil cell (DAC) with a facet diameter of 300 μm and bevel angle of 10° was utilized for high-temperature and high-pressure Raman spectroscopy and electrical conductivity measurements. High temperature was generated by an external resistance heating furnace made up of a 300- μm diametral nickel-chromium wire. We fixed the prepared heating furnace to the tungsten carbide seat by high-temperature cement. Temperature was gradually increased from 298 to 873 K with an interval of 50 K and was monitored through a k-type thermocouple adhered to the diamond with the precise of ± 5 K. Raman spectroscopic experiments were performed using a Renishaw 2000 microconfocal Raman spectrometer equipped with an excitation source of 514.5 nm. In our present work, the mixture of methanol and ethanol (4:1 volume ratio) was selected as the pressure medium to provide quasi-hydrostatic condition and no pressure medium was employed to attain non-hydrostatic condition. A ruby single crystal with a grain size of ~ 5 μm was chosen as the pressure calibration at room temperature based on

the shift of R1 fluorescence peak. Furthermore, we determined the pressure under high temperature based on the high-temperature corrected equation of pressure calibration (Rekhi et al., 1999).

High-Temperature and High-Pressure Electrical Conductivity Measurements

A sheet of 250 μm thick T-301 stainless steel was preindented to ~ 40 μm thickness and later a central hole with the diameter of 180 μm was drilled by a laser drilling machine. Afterwards, a mixture of boron nitride and epoxy powder was compacted into the hole for electrical insulation and another new central hole with a diameter of 100 μm was made as the insulating sample chamber. Subsequently, the remaining part of the gasket was coated by the insulating cement. The sample chamber was surrounded by the resistance heating furnace and thus the sample could be homogeneously heated based on the thermal conduction principle. For the sake of realizing thermal equilibrium, we waited for ~ 10 min at each pre-designed temperature prior to the Raman spectroscopy and electrical conductivity measurements. No pressure medium was utilized to avoid introducing additional impurities and guarantee good contact between sample and electrodes during electrical

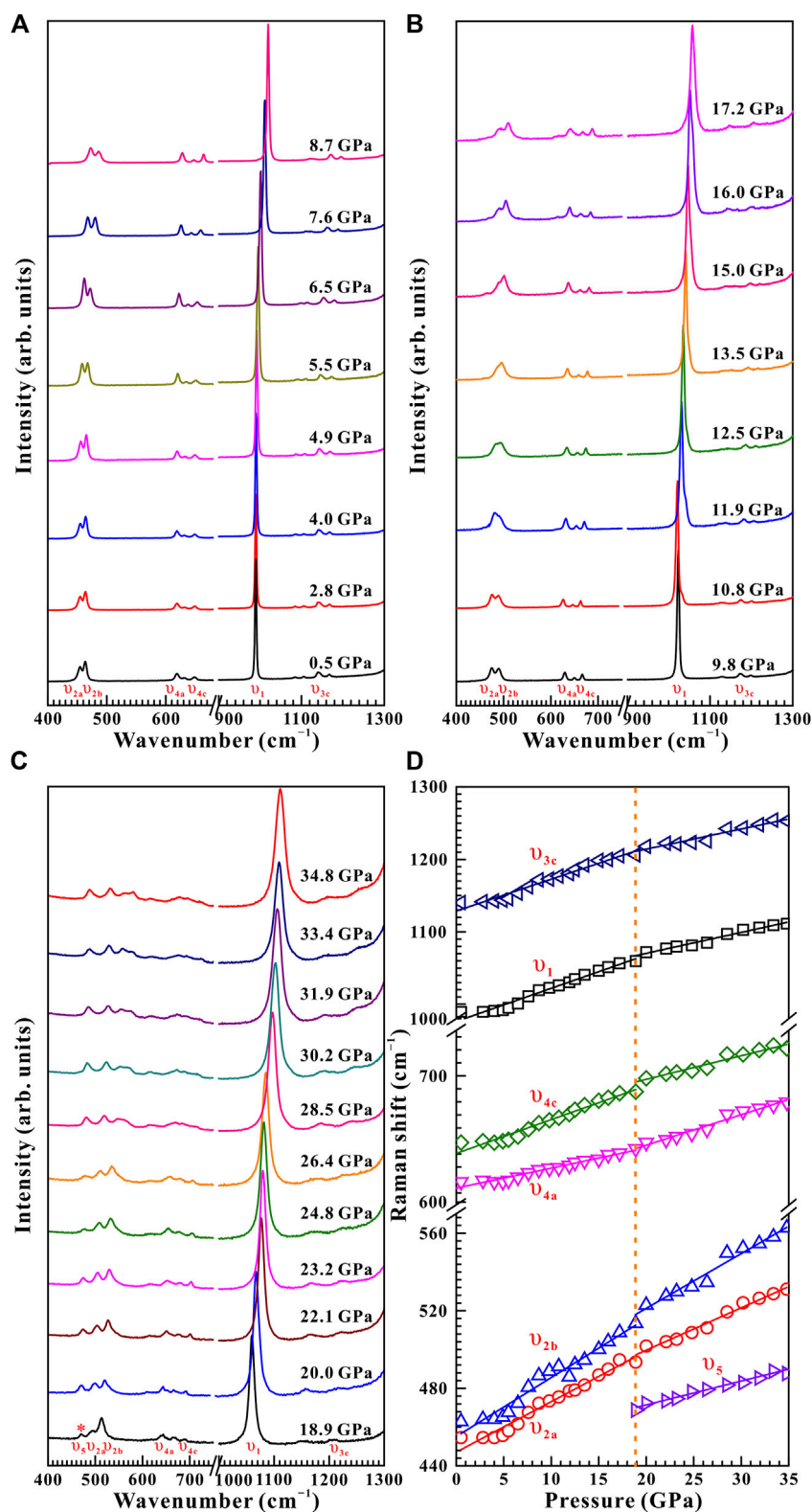


FIGURE 3 | High-pressure Raman spectroscopic results on natural barite within the wavenumber range of 400–1,300 cm^{-1} up to 34.8 GPa and room temperature upon compression. **(A)** 0.5–8.7 GPa; **(B)** 9.8–17.2 GPa; **(C)** 18.9–34.8 GPa. **(D)** The corresponding evolution of Raman shifts with increasing pressure for natural barite under non-hydrostatic condition. The solid and dashed lines are employed to guide to the eyes.

TABLE 1 | Pressure-dependent Raman shift $d\omega/dP$ ($\text{cm}^{-1} \text{ GPa}^{-1}$) for natural barite under non-hydrostatic and quasi-hydrostatic environments at room temperature. Here, ω (cm^{-1}) and P (GPa) represent Raman frequency and pressure, respectively.

Pressure condition	Pressure (GPa)	ω (cm^{-1})	$d\omega/dP$ ($\text{cm}^{-1} \text{ GPa}^{-1}$)	ω (cm^{-1})	$d\omega/dP$ ($\text{cm}^{-1} \text{ GPa}^{-1}$)
Non-hydrostatic	0.5–18.9	454.6 (ν_{2a})	2.60	462.8 (ν_{2b})	3.03
		618.6 (ν_{4a})	1.54	648.7 (ν_{4c})	2.59
	989.6 (ν_1)	4.58	1,140.4 (ν_{3a})	4.39	
	20.0–34.8	501.8 (ν_{2a})	2.18	522.9 (ν_{2b})	2.82
		648.7 (ν_{4a})	2.34	698.2 (ν_{4c})	1.81
		1,071.9 (ν_1)	2.88	1,217.9 (ν_{3a})	2.76
			472.3 (ν_5)	1.25	
Quasi-hydrostatic	1.5–21.4	454.6 (ν_{2a})	2.42	462.8 (ν_{2b})	2.94
		618.6 (ν_{4a})	1.29	648.7 (ν_{4c})	2.50
		989.6 (ν_1)	4.17	1,141.5 (ν_{3a})	3.97
	22.9–35.0	505.3 (ν_{2a})	1.26	527.6 (ν_{2b})	1.85
		649.8 (ν_{4a})	1.25	700.4 (ν_{4c})	1.41
		1,074.2 (ν_1)	1.65	1,222.2 (ν_{3a})	1.32
			475.8 (ν_5)	0.84	

conductivity measurements. **Figure 2** represents the experimental assemblage of the high-temperature and high-pressure electrical conductivity measurement. We measured the complex impedance spectra of natural barite under the conditions of 298–873 K and 2.8–30.0 GPa by a Solartron-1260 impedance/gain phase analyzer within the frequency range of 10^{-1} – 10^7 Hz and at an alternating voltage of 1.0 V. Detailed instructions on the high-temperature and high-pressure measurement principles and experimental procedures have been reported by Hong et al. (2022).

RESULTS AND DISCUSSION

The Phase Transition of Natural Barite at Room Temperature

Raman spectroscopy has been proved to be a sensitive method of exploring the occurrence of pressure-induced structural transition for some minerals and rocks (Pu et al., 2018; Yang et al., 2018; Hong et al., 2022). From **Figure 3A**, ten representative Raman peaks were detected for natural barite within the wavenumber range of 400–1,300 cm^{-1} at a given pressure of 0.5 GPa under non-hydrostatic condition, which can be assigned as ν_1 (989.6 cm^{-1}), ν_{2a} (454.6 cm^{-1}), ν_{2b} (462.8 cm^{-1}), ν_{3a} (1,083.9 cm^{-1}), ν_{3b} (1,105.7 cm^{-1}), ν_{3c} (1,140.4 cm^{-1}), ν_{3d} (1,167.4 cm^{-1}), ν_{4a} (618.6 cm^{-1}), ν_{4b} (631.3 cm^{-1}), and ν_{4c} (648.7 cm^{-1}), respectively. All of these Raman peaks are in good accordance with previous investigations (Lee et al., 2003; Chen et al., 2009; Liu et al., 2015; Zhou et al., 2020). To diminish experimental error, we analyzed six stronger Raman modes of ν_1 , ν_{2a} , ν_{2b} , ν_{3c} , ν_{4a} , and ν_{4c} in the processes of compression and decompression.

Figure 3 displays the high-pressure Raman spectra of natural barite within the pressure range of 0.5–34.8 GPa under non-hydrostatic condition. The corresponding fitting results of the pressure-dependent Raman shifts ($d\omega/dP$, where ω and P are the Raman shift and pressure, respectively) are summarized in **Table 1**. As depicted in **Figure 3A–C**, all of these Raman peaks monotonously shifted towards higher wavenumbers with

increasing pressure. Meanwhile, we found that the ν_{2a} and ν_{2b} Raman peaks overlapped within the pressure range of 11.9–15.0 GPa, while they separated obviously above 16.0 GPa. Notably, as the pressure reached up to 18.9 GPa, an absolutely new Raman peak at 468.7 cm^{-1} (denoted as the ν_5 mode in **Figure 3C**) appeared. Furthermore, we found that the Raman peaks of sample became significant broadening accompanied by the remarkable decrease in their Raman peak intensities, which is possibly related to the intrinsic nature of crystalline structure. To further reveal the occurrence of phase transition, we detailedly analyzed the pressure dependence of Raman shifts for natural barite. Two discrete pressure ranges of 0.5–18.9 GPa and 20.0–34.8 GPa were distinguished. Below 18.9 GPa, the Raman modes of ν_{2a} , ν_{2b} , ν_{4c} , ν_1 , and ν_{3a} displayed blue shifts with larger slopes of 2.60, 3.03, 2.59, 4.58, and 4.39 $\text{cm}^{-1} \text{ GPa}^{-1}$ and the ν_{4a} mode showed a smaller rate of 1.54 $\text{cm}^{-1} \text{ GPa}^{-1}$. However, within the pressure range of 20.0–34.8 GPa, smaller rates of 2.18, 2.82, 1.81, 2.88, and 2.76 $\text{cm}^{-1} \text{ GPa}^{-1}$ were acquired for the ν_{2a} , ν_{2b} , ν_{4c} , ν_1 , and ν_{3a} modes and a larger slope of 2.34 $\text{cm}^{-1} \text{ GPa}^{-1}$ was detected for the ν_{4a} mode, respectively. Additionally, we also analyzed the Raman full width at half-maximum (FWHM) of ν_1 Raman peak with increasing pressure under different hydrostatic environments, as displayed in **Figure 4**. The correspondent fitting results of pressure-dependent FWHM for natural barite under different hydrostatic environments were listed in **Table 2**. Results showed that the Raman FWHM of ν_1 Raman peak exhibited an obvious inflection point at 18.9 GPa under non-hydrostatic condition, which can be attributed to the occurrence of structural phase transition for natural barite. In short, the appearance of ν_5 Raman peak and the inflection points in the pressure-dependent Raman shifts and FWHM of ν_1 Raman peak indicate that natural barite underwent a phase transformation at 18.9 GPa under non-hydrostatic condition.

Upon decompression, within the pressure range of 32.1–2.9 GPa, all these Raman peaks of natural barite continuously shifted towards lower wavenumbers, as illustrated in **Figure 5**. Noteworthily, the ν_5 Raman peak disappeared when the pressure was released to 1.8 GPa. At the same time, all the Raman peaks of sample became sharp and narrow accompanied by the apparent increase in their Raman peak

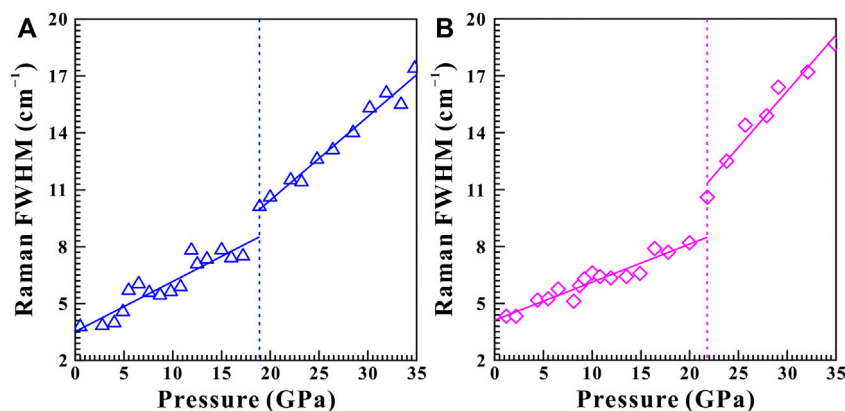


FIGURE 4 | The evolution of Raman FWHM as a function of pressure for ν_1 Raman peak under (A) non-hydrostatic condition and (B) quasi-hydrostatic condition, respectively. The solid and dashed lines serve as visual guidance.

TABLE 2 | Pressure dependence of Raman FWHM dF/dP ($\text{cm}^{-1} \text{ GPa}^{-1}$) for natural barite under non-hydrostatic and quasi-hydrostatic environments. In here, F (cm^{-1}) and P (GPa) stand for Raman FWHM and pressure, respectively.

Mode	Pressure Condition	Pressure (GPa)	dF/dP ($\text{cm}^{-1} \text{ GPa}^{-1}$)
ν_1	Non-hydrostatic	0.5–18.9	0.265
		20.0–34.8	0.439
	Quasi-hydrostatic	1.5–21.4	0.201
		22.9–35.0	0.592

intensities. Furthermore, an available discontinuity in the pressure-dependent Raman shifts was found at 1.8 GPa, indicating the occurrence of phase transformation. After quenched down to ambient conditions, all of these Raman peaks of barite returned to their original Raman peak positions, suggesting the reversibility of the structural transition. However, there exists a huge pressure hysteresis of approximately 17.0 GPa for natural barite, which is probably related to the large kinetic barrier for the structural transition upon decompression. In addition, we compared the pressure-dependent Raman shift relationships obtained in this study and previously available investigations from Lee et al. (2003) and Chen et al. (2009), as shown in **Supplementary Figure S1**. Results indicated that our acquired pressure-dependent Raman shift relationships of barite are in reasonable agreement with previous investigations under both processes of compression and decompression.

Under quasi-hydrostatic condition, the high-pressure Raman spectra of natural barite in the processes of compression and decompression are displayed in **Supplementary Figures S2,S3**, respectively. Accordingly, the fitting results of the pressure-dependent Raman shifts are presented in **Table 1**. Experimental results showed similar phenomena of the emergence of ν_5 Raman peak and the inflection points in the pressure-dependent Raman shifts and FWHM of ν_1 Raman peak at 21.4 GPa under quasi-hydrostatic condition.

As detailedly discussed by Santamaría-Pérez et al. (2011) and Ye et al. (2019), the phase transition pressure of barite is highly sensitive to the hydrostaticity within the sample chamber of the

diamond anvil cell. In other words, the larger deviatoric stress under non-hydrostatic condition can promote the occurrence of phase transition. By contrast, the smaller deviatoric stress within the sample chamber provides a reasonable explanation for the higher phase transition pressure of natural barite under quasi-hydrostatic condition. Additionally, it is indispensable to conduct the high-pressure Raman spectroscopy of natural barite under non-hydrostatic condition based on the following three dominant perspectives including detailed investigation the high-pressure physiochemical behaviors of natural barite by Raman spectroscopy combined with electrical conductivity results, comparisons with previous studies under same hydrostatic environments, as well as a systematic exploration on the influence of hydrostaticity on the structural transition pressure for natural barite.

It is well known that the structural phase transition of minerals and rocks is often accompanied by the variation in electrical transport properties (Pu et al., 2018; Yang et al., 2018; Hong et al., 2022). To further disclose the structural transition of natural barite, high-pressure electrical conductivity measurements were carried out within the pressure range of 2.8–30.0 GPa. As illustrated in **Figure 6A–C**, all of these measured impedance spectra were consisted of a high-frequency semicircle ($\sim 10^2$ – 10^7 Hz) and a small tail in the low-frequency region ($\sim 10^1$ – 10^2 Hz), which can be interpreted as the grain interior and grain boundary contributions of sample, respectively. We determined sample resistances by fitting impedance semicircular arcs using the appropriate equivalent circuit comprised of the parallel combination of R (resistance) and CPE (constant-phase element). In here, the fitting error is not more than 5% of the resistance. The corresponding electrical conductivity (σ) of natural barite was calculated from the resistance (R) and geometric factor (L/S ; where L stands for the distance between the electrodes and S is the cross-sectional area of electrode) based on the equation $\sigma = L/SR$. The logarithmic electrical conductivity of natural barite as a function of pressure during both processes of compression and decompression is plotted in **Figure 6D**. It makes clear that natural barite showed a rapid increase in electrical conductivity at a rate of $0.018 \text{ S cm}^{-1} \text{ GPa}^{-1}$ within

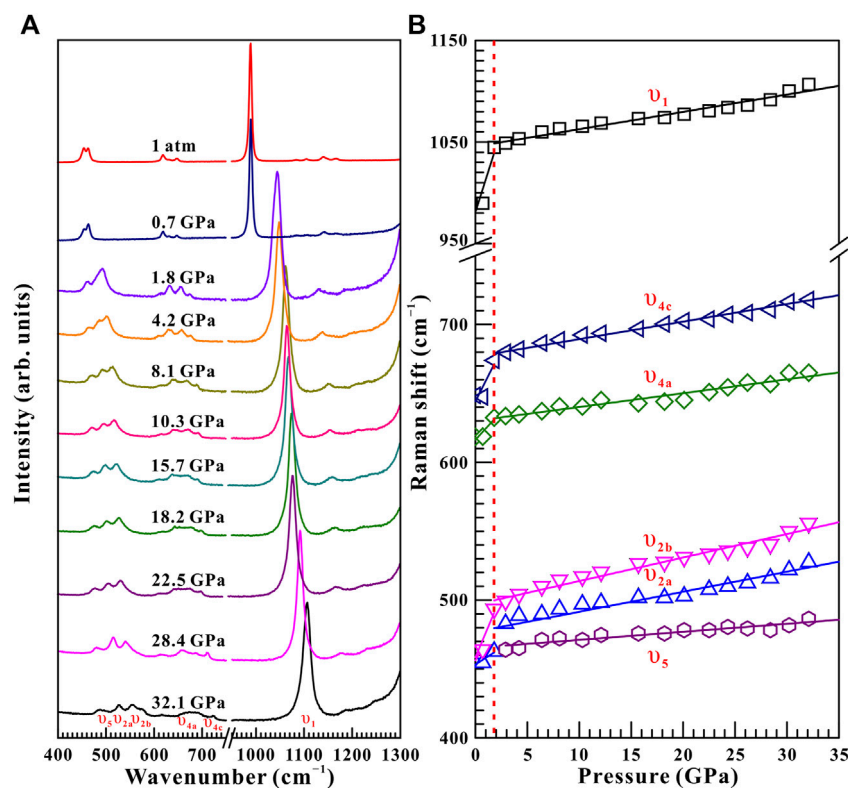


FIGURE 5 | (A) Selected high-pressure Raman spectra of natural barite within the pressure range of 32.1–0.0 GPa and atmospheric temperature during the process of decompression. **(B)** The pressure dependence of Raman shifts for natural barite under non-hydrostatic condition. The solid and dashed lines serve as visual guidance.

the pressure range of 2.8–19.2 GPa. However, beyond 19.2 GPa, the electrical conductivity of sample exhibited a positive pressure-dependent electrical conductivity relation with a smaller speed of $0.0046 \text{ S cm}^{-1} \text{ GPa}^{-1}$. And thus, the apparent discontinuity in electrical conductivity at 19.2 GPa confirms the occurrence of phase transition for natural barite, which is consistent with our Raman spectra results under non-hydrostatic condition. Upon decompression, the electrical conductivity of sample retained almost invariable within the pressure range of 27.2–3.2 GPa. As the pressure decreased from 3.2 to 2.4 GPa, an obvious decrease in electrical conductivity from -5.94 S/cm to -6.05 S/cm was detected. The available inflection point in electrical conductivity at 3.2 GPa can be attributed to the structural transformation of natural barite.

In the present study, we found that natural barite underwent a structural phase transition at $\sim 18.9 \text{ GPa}$ and atmospheric temperature by virtue of two independent experimental methods of Raman spectroscopy and electrical conductivity. A detailed comparison on the high-pressure structural transition of barite between our acquired results and reported investigations was made and summarized in **Table 3**. In terms of the structural stability of barite under high pressure, our results agree well with previous investigations (Lee et al., 2001; Lee et al., 2003; Chen et al., 2009; Crichton et al., 2011; Santamaría-Pérez et al., 2011; Ye

et al., 2019). Crichton et al. (2011) reported that natural barite remained stable up to 21.5 GPa with helium as the pressure medium and they attributed the phase stability of natural barite to the higher hydrostaticity and the limited experimental pressure. Our high-pressure Raman spectra results on natural barite under different hydrostatic environments provided a robust support for their conclusions that natural barite will undergo a structural transition under the conditions of lower hydrostaticity or higher experimental pressure.

On the other hand, another predominate dispute is the phase transition pressure of barite. Under non-hydrostatic condition, our obtained phase transition pressure is substantially higher than that of Chen et al. (2009) with deionized water as the pressure medium and Lee et al. (2001); Lee et al. (2003) without pressure medium. As for quasi-hydrostatic condition, our acquired phase transition pressure is distinctly higher than that of Lee et al. (2001); Lee et al. (2003) and Santamaría-Pérez et al. (2011) with the mixture of methanol and ethanol (4:1 volume ratio) as the pressure medium, whereas is comparable to that of Ye et al. (2019) using neon as the pressure medium. Thus, it seems that the discrepancy in the structural transition pressure of barite cannot be fully explained by the influence of different pressure mediums alone. Although we do not have a definite explanation for the discrepancy in the structural transition pressure among different investigations, it may be

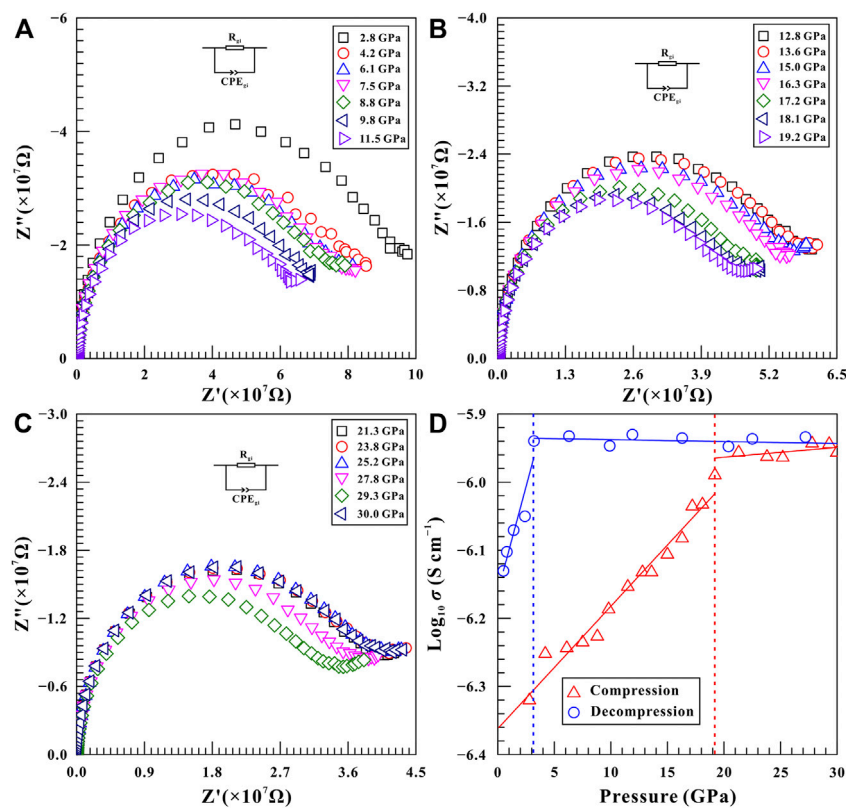


FIGURE 6 | Complex impedance spectra of natural barite under the conditions of 2.8–30.0 GPa and atmospheric temperature during the process of compression. **(A)** 2.8–11.5 GPa; **(B)** 12.8–19.2 GPa; **(C)** 21.3–30.0 GPa. An appropriate equivalent circuit composed of the parallel combination of R (resistance) and CPE (constant-phase element) was selected to fit the impedance semicircular arcs. In here, the signals of Z' and Z'' stand for the real and imaginary parts of complex impedance, respectively. **(D)** The logarithmic electrical conductivity of natural barite as a function of pressure during both processes of compression and decompression at atmospheric temperature. In here, the solid and dashed lines are used to guide to the eyes.

TABLE 3 | Comparison of the experimental details and structural transition pressure (P_{tr}) between present and previous investigations on barite. In here, MeOH-EtOH represents the mixture of methanol and ethanol (4:1 volume ratio).

Samples	Experimental Methods	Pressure Mediums	Pressure Calibrations	P_{tr} (GPa)	References
Natural barite	Raman spectroscopy	No	Ruby	18.9	This study
Natural barite	Electrical conductivity	MeOH-EtOH	Ruby	21.4	
Natural barite	Synchrotron X-ray diffraction	Helium	Ruby	–	Crichton et al. (2011)
Synthetic barite	Raman spectroscopy	Helium	Ruby	17.0	Santamaría-Pérez et al. (2011)
Synthetic barite	Synchrotron X-ray diffraction	MeOH-EtOH	Ruby	19.0	
Synthetic barite	Synchrotron X-ray diffraction	Silicone oil	Ruby	27.0	
Synthetic barite	Synchrotron X-ray diffraction	Neon	Au	20.3	Ye et al. (2019)
Synthetic barite	Raman spectroscopy	Deionized water	Ruby	6.0/15.0	Chen et al. (2009)
Synthetic barite	Synchrotron X-ray diffraction	No	Au	10.0	Lee et al. (2001); Lee et al. (2003)
Synthetic barite	Raman spectroscopy	MeOH-EtOH	Ruby		

related to the comprehensive influences of the difficulty in phase identification since the significant decrease in the Raman peak intensity of barite as the pressure was increased (Lee et al., 2003; Chen et al., 2009), the choice of pressure calibrations, the different starting samples, the various experimental methods, the selection of pressure mediums, and so on.

The Phase Transition of Natural Barite at High Temperature

As usual, temperature plays a crucial role in influencing the phase transition pressure for some minerals and rocks (Hu et al., 2017; Sun et al., 2017; Hu et al., 2018; Hong et al., 2022). To illustrate the effect of temperature on the phase transition pressure of natural barite, five

TABLE 4 | Temperature-dependent Raman shift $d\omega/dT$ ($\text{cm}^{-1} \text{K}^{-1}$) for natural barite at some representative pressures of 10.9, 11.9, 13.2, 15.5, and 19.5 GPa within the temperature range of 298–873 K under non-hydrostatic condition. Here, ω (cm^{-1}) and T (K) represent the Raman frequency and temperature, respectively.

Pressure (GPa)	Temperature (K)	ω (cm^{-1})	$d\omega/dT$ ($\text{cm}^{-1} \text{K}^{-1}$)	ω (cm^{-1})	$d\omega/dT$ ($\text{cm}^{-1} \text{K}^{-1}$)
10.9	298–773	468.7 (ν_{2a})	−0.0021	486.4 (ν_{2b})	−0.0025
		626.6 (ν_{4a})	−0.0012	647.5 (ν_{4b})	−0.0052
		664.8 (ν_{4c})	−0.0054	1,019.3 (ν_1)	−0.0072
		1,170.6 (ν_{3c})	−0.0060		
	773–873	471.1 (ν_{2a})	−0.012	485.2 (ν_{2b})	−0.035
		626.6 (ν_{4a})	−0.023	645.1 (ν_{4b})	−0.023
		661.3 (ν_{4c})	−0.035	1,016.0 (ν_1)	−0.044
		1,168.5 (ν_{3c})	−0.054		
11.9	298–723	475.8 (ν_{2a})	−0.0011	491.1 (ν_{2b})	−0.00030
		630.1 (ν_{4a})	−0.0025	652.1 (ν_{4b})	−0.0050
		669.4 (ν_{4c})	−0.0059	1,027.1 (ν_1)	−0.0097
		1,178.2 (ν_{3c})	−0.0073		
	723–873	475.8 (ν_{2a})	−0.018	491.1 (ν_{2b})	−0.029
		629.0 (ν_{4a})	−0.017	649.8 (ν_{4b})	−0.023
		667.1 (ν_{4c})	−0.039	1,023.7 (ν_1)	−0.043
		1,174.9 (ν_{3c})	−0.047		
13.2	298–673	484.1 (ν_{2a})	0.0000	498.2 (ν_{2b})	−0.0089
		634.7 (ν_{4a})	−0.0033	660.1 (ν_{4b})	−0.010
		678.6 (ν_{4c})	−0.012	1,041.3 (ν_1)	−0.012
		1,192.2 (ν_{3c})	−0.014		
	673–873	484.1 (ν_{2a})	−0.0096	497.1 (ν_{2b})	−0.0074
		633.6 (ν_{4a})	−0.011	657.8 (ν_{4b})	−0.023
		675.1 (ν_{4c})	−0.025	1,038.0 (ν_1)	−0.035
		1,186.7 (ν_{3c})	−0.024		
15.5	298–523	489.9 (ν_{2a})	−0.0049	506.5 (ν_{2b})	−0.0053
		638.2 (ν_{4a})	−0.000050	664.8 (ν_{4b})	−0.0022
		684.4 (ν_{4c})	−0.0036	1,050.1 (ν_1)	−0.0035
		1,197.5 (ν_{3c})	−0.0013		
	523–873	489.9 (ν_{2a})	−0.0080	505.3 (ν_{2b})	−0.019
		637.1 (ν_{4a})	−0.014	664.0 (ν_{4b})	−0.017
		683.2 (ν_{4c})	−0.018	1,049.0 (ν_1)	−0.026
		1,198.6 (ν_{3c})	−0.018		
19.5	298–873	502.4 (ν_{2a})	−0.030	515.3 (ν_{2b})	−0.036
		648.2 (ν_{4a})	−0.019	674.8 (ν_{4b})	−0.033
		694.4 (ν_{4c})	−0.042	1,061.2 (ν_1)	−0.060
		1,212.9 (ν_{3c})	−0.058		

sets of representative high-temperature Raman spectroscopy experiments were performed at pre-determined pressures of 10.9, 11.9, 13.2, 15.5, and 19.5 GPa within the temperature range of 298–873 K. The fitting results of the temperature dependence of Raman shifts ($d\omega/dT$, where ω and T are the Raman shift and temperature, respectively) are displayed in **Table 4**.

Figure 7 represents the high-temperature Raman spectra of natural barite at a pre-designed pressure of 10.9 GPa. In contrast to the influence of pressure-induced crystal lattice contraction, all of these Raman peaks monotonously shifted towards lower wavenumbers, indicating the thermal expansion of the crystal lattice as the sample was subjected to high temperature. According to diverse temperature-dependent Raman shifts ($d\omega/dT$, where ω and T are the Raman shift and temperature, respectively), two temperature regions of 298–773 K and 773–873 K were identified at 10.9 GPa. Below 773 K, the Raman peaks of ν_{2a} , ν_{2b} , ν_{4a} , ν_{4b} , ν_{4c} , ν_1 , and ν_{3c} exhibited smaller rates of −0.0021, −0.0025, −0.0012, −0.0052, −0.0054, −0.0072, and −0.0060 $\text{cm}^{-1} \text{K}^{-1}$ with increasing temperature, respectively.

Nevertheless, larger slopes of −0.012, −0.035, −0.023, −0.023, −0.035, −0.044, and −0.054 $\text{cm}^{-1} \text{K}^{-1}$ were obtained for the ν_{2a} , ν_{2b} , ν_{4a} , ν_{4b} , ν_{4c} , ν_1 , and ν_{3c} modes within the temperature range of 773–873 K. Therefore, at a representative pressure of 10.9 GPa, the available inflection point in the temperature-dependent Raman shifts at 773 K is probably attributed to the occurrence of phase transition. To verify this speculation, we performed an absolutely new high-temperature Raman scattering experiment for post-barite at 19.5 GPa. As shown in **Supplementary Figure S4**, all the Raman peaks of post-barite continuously shifted towards lower wavenumbers up to the maximum temperature of 873 K without anomaly in the temperature dependence of Raman shifts, which implies that post-barite remained stable in our investigated temperature range. Therefore, the discontinuity in the temperature dependence of Raman shifts is most possibly caused by the occurrence of structural transition for natural barite under high temperature. Furthermore, similar inflection points in Raman shifts at 723, 673, and 523 K were also detected at other three pressures of 11.9, 13.2, and 15.5 GPa, as shown in **Figure 8**,

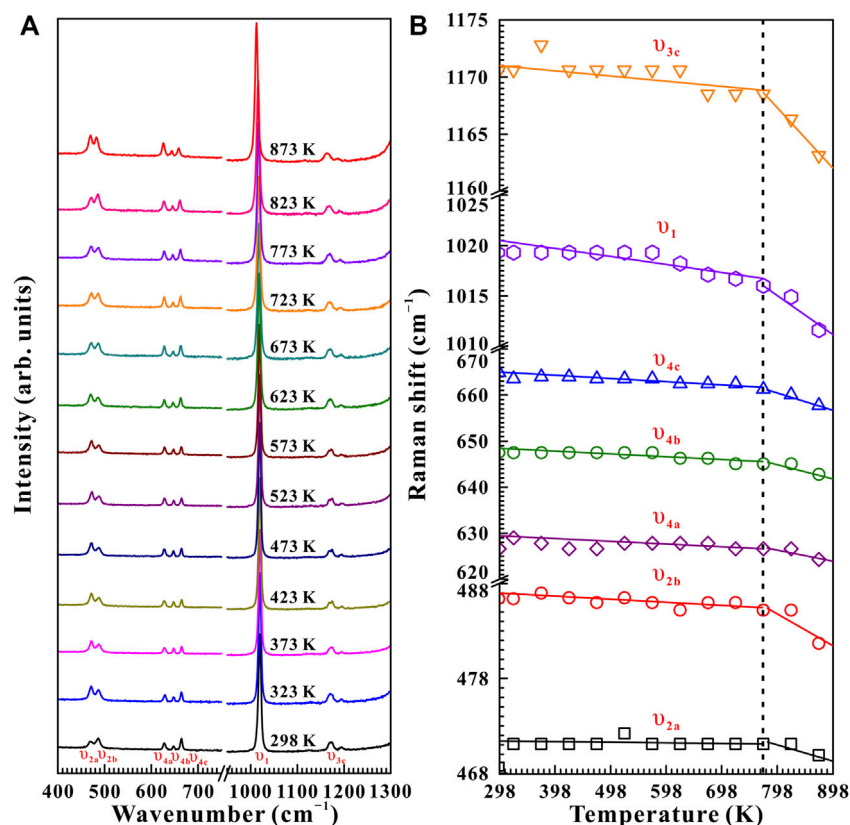


FIGURE 7 | (A) High-temperature Raman spectroscopy results of natural barite at a fixed pressure of 10.9 GPa within the wavenumber range of 400–1,300 cm^{-1} over the temperature range of 298–873 K with the temperature interval of 50 K. **(B)** The evolution of Raman shifts against temperature for natural barite under non-hydrostatic condition. The solid and dashed lines act as visual guides.

Supplementary Figure S5, S6Material. However, we have never observed the appearance of ν_5 Raman peak up to the maximum temperature of 873 K at all of these measured pressures (10.9, 11.9, 13.2, 15.5, and 19.5 GPa). One possible explanation is the influence of high temperature. More specifically, under cold compression, the deviatoric stress within the sample chamber of the diamond anvil cell enhanced significantly as the pressure increased, resulting in the increase of dislocations and defects within the sample, which may be responsible for the emergence of ν_5 Raman peak. Conversely, high temperature plays a vital role in relaxing deviatoric stress and thus minimizing the dislocations and defects inside sample, which may suppress the appearance of ν_5 Raman peak. As a matter of fact, similar phenomenon has been detected in another anhydrous mineral of calcite under high temperature condition (Yuan et al., 2021). In comprehensive comparison the Raman spectroscopy results of natural barite during both processes of decompression and heating, we concluded that the decompression and heating have same effect on expanding the crystalline lattice of natural barite, which is characterized by the red shifts of Raman peaks with increasing temperature or releasing pressure.

A series of high-temperature impedance spectra on natural barite were also collected at some typical pressures of 11.5, 12.6, and 15.7 GPa within the temperature range of 298–873 K to further demonstrate the relationship between phase transition

pressures and temperatures. **Figure 9** shows the high-temperature complex impedance spectra for natural barite at a representative pressure of 11.5 GPa. The electrical conductivity of sample decreased obviously from -4.95 S/cm to -5.91 S/cm as the temperature enhanced from 298 to 323 K, which is probably attributed to the removal of the absorbed water from the sample surfaces (Hong et al., 2022). Within the temperature ranges of 323–523 K and 773–873 K, two positive temperature-dependent electrical conductivity correlations were obtained due to the enhanced mobility of charge carriers with increasing temperature, which satisfies with the representative electrical transport characteristic of semiconductor (Hu et al., 2017; Hu et al., 2018; Hong et al., 2022). More importantly, we found that the electrical conductivity of sample decreased significantly by approximately two orders of magnitude when the temperature was increased from 523 to 773 K. Therefore, at the given pressure of 11.5 GPa, the remarkable drop in electrical conductivity may be related to the structural phase transition of natural barite, which started at 523 K and was completed at 773 K. Furthermore, the high-temperature electrical conductivity variation tendencies observed at 11.5 GPa resemble to that at other two pressures of 12.6 and 15.7 GPa. From **Supplementary Figure S7,S8**, the evident decrease in the electrical conductivity of natural barite was observed within the temperature ranges of 523–673 K and

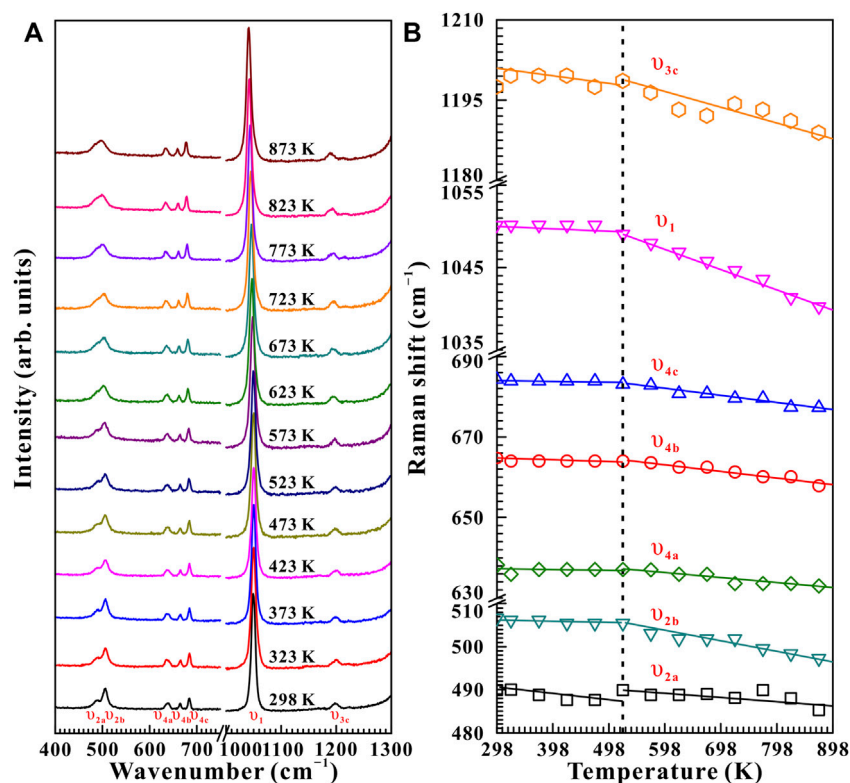


FIGURE 8 | (A) High-temperature Raman spectra of natural barite at a pre-designed pressure of 15.5 GPa within the wavenumber range of 400–1,300 cm^{-1} in the temperature interval of 298–873 K. **(B)** The temperature dependence of Raman shifts for natural barite under non-hydrostatic condition.

473–623 K at the respective pressures of 12.6 and 15.7 GPa. Therefore, it is reasonable to speculate that these decreases in electrical conductivities are possibly associated with the occurrence of phase transitions at high temperature.

By comparing the variation in the electrical conductivity of natural barite under high pressure and high temperature conditions, we found that only a feeble increase by less than 0.5 log unit in the electrical conductivity of natural barite was observed as the pressure increased from 2.8 to 30.0 GPa at room temperature, as illustrated in **Figure 6**. However, at a certain pressure, the electrical conductivity of natural barite varies by several orders of magnitude with increasing temperature. Therefore, temperature has a much more pronounced influence on the electrical conductivity of natural barite compared with pressure, which has been extensively reported among other minerals and rocks (Hu et al., 2017; Sun et al., 2017; Hu et al., 2018; Hong et al., 2022).

Based on our high-pressure Raman spectroscopy and electrical conductivity results at room temperature, the emergence of ν_5 Raman peak and the discontinuities in the pressure-dependent Raman shifts and FWHM of ν_1 Raman peak indicated the occurrence of structural phase transition in natural barite at 18.9 GPa under non-hydrostatic condition, which agrees well with the inflection point in electrical conductivity at 19.2 GPa. Under high temperature and high pressure conditions, we found that the Raman shifts of natural barite exhibited obvious

discontinuities in 773, 723, 673, and 523 K at the corresponding pressure points of 10.9, 11.9, 13.2, and 15.5 GPa. Furthermore, the negative correlation between the phase transition temperatures and pressures was confirmed by our electrical conductivity results. Similar phenomena of the remarkable decrease in electrical conductivities at 773, 673, and 623 K were detected at three representative pressure points of 11.5, 12.6, and 15.7 GPa, respectively.

In combination with the high-temperature and high-pressure Raman spectroscopy and electrical conductivity measurements, we concluded that the phase transition pressures decreased as temperatures increased and thus, a negative Clapeyron slope (dP/dT) was acquired for the barite to post-barite phase transition. On the basis of the phase transition temperatures and pressures derived from high-temperature and high-pressure Raman spectra results, a P – T phase diagram over broad temperature and pressure ranges of 298–873 K and 10.9–18.9 GPa was constructed for natural barite, and the phase transition boundary between barite and post-barite was described as P (GPa) = $24.00 - 0.0166 T$ (K), as shown in **Figure 10**. Moreover, the phase diagram obtained in our present study on natural barite was compared with that in previously available study on synthetic barite. Lee et al. (2001); Lee et al. (2003) claimed that synthetic barite transformed into post-barite at 10.0 GPa and atmospheric temperature, and further, the phase boundary of barite and post-barite under high-temperature and

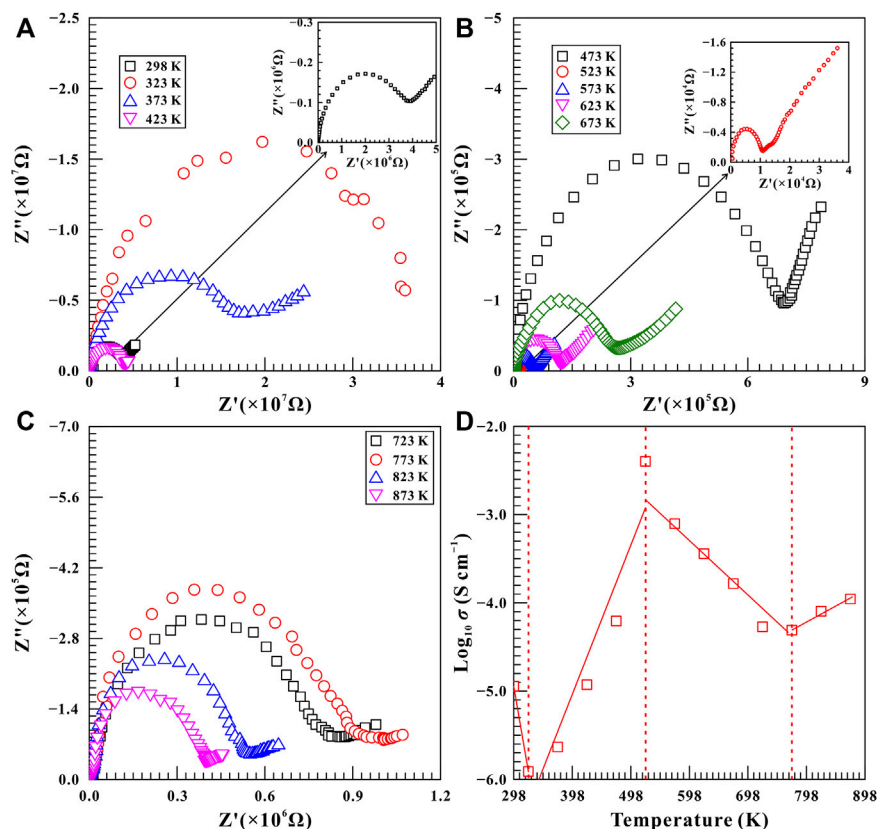


FIGURE 9 | Representative complex spectra of natural barite within the temperature range of 298–873 K at a constant pressure of 11.5 GPa. **(A)** 298–423 K; **(B)** 473–673 K; **(C)** 723–873 K. **(D)** The logarithm of electrical conductivity versus temperature for natural barite. The solid and dashed lines serve as visual guides.

high-pressure conditions was determined as 90 K/GPa by virtue of synchrotron X-ray diffraction. As we know, the Clapeyron slope (dP/dT) is closely related to the variations in volumes and entropy before and after the phase transition, and they satisfy the following Clapeyron equation: $dP/dT = \Delta S/\Delta V$ (Lee et al., 2001). Previous synchrotron X-ray diffraction investigations disclosed that there exists an obvious volume contraction of approximately 2% during the barite-to-post-barite phase transition (Lee et al., 2001; Santamaría-Pérez et al., 2011). Therefore, the ΔV is a negative value. Meanwhile, entropy (S) is an important thermodynamic parameter characterizing the disorder of crystal. As usual, an ordered crystal is of a smaller entropy value and a larger entropy value can be obtained for a disordered crystal. At ambient conditions, barite belongs to orthorhombic structure with the space group of $Pbnm$. Lee et al. (2001) reported that barite transformed into post-barite under high pressure and the post-barite is of triclinic structure. However, subsequent synchrotron X-ray diffraction investigations disclosed that the post-barite belongs to orthorhombic structure with the space group of $P2_12_12_1$ (Santamaría-Pérez et al., 2011; Ye et al., 2019). In the above-mentioned two cases, the initial high-symmetry barite transformed into the low-symmetry post-barite under high pressure, and thus, the ΔS is a positive value. In comprehensive consideration of the negative ΔV value and the

positive ΔS value, the Clapeyron slope (dP/dT) for the barite to post-barite phase boundary yields a negative value, which agrees well with our acquired phase transition results under high temperature and high pressure conditions.

It is well known that barite (BaSO_4) is isostructural with other barite-group minerals, including celestine (SrSO_4) and anglesite (PbSO_4), and they share the same orthorhombic crystal systems with the space group of $Pbnm$ under ambient conditions. To our knowledge, there exists huge controversies on the high-pressure phase stability and structural transition pressure for other barite-group minerals until now (Kuang et al., 2017; Li et al., 2018; Ye et al., 2019). Chen et al. (2010) reported that celestine underwent a structural phase transformation at ~ 12.0 GPa and atmospheric temperature with the mixture of methanol and ethanol as the pressure medium by means of Raman spectroscopy and synchrotron X-ray diffraction. However, some researchers proposed that celestine remained stable up to 22.2 GPa using neon as the pressure medium (Kuang et al., 2017; Ye et al., 2019). Our results provide a new insight into the causes of the discrepancies in the high-pressure phase stability and structural transition pressure for barite among previous investigations, which may be applied to other barite-group minerals. Additionally, the high-temperature and high-pressure phase diagram of barite-group minerals is still limited. And thus, our acquired

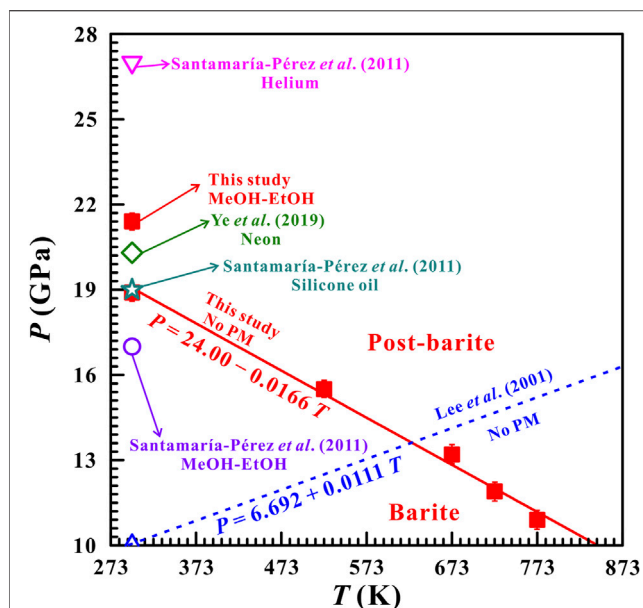


FIGURE 10 | Comparisons of the P – T phase diagram obtained from this study and previous investigations from Lee et al. (2001), Santamaría-Pérez et al. (2011), and Ye et al. (2019) with different pressure mediums. The red solid line and the blue dashed line represent the phase transition boundary of barite-to-post-barite obtained from our present result and the result reported by Lee et al. (2001), respectively. In here, MeOH-EtOH stands for the methanol and ethanol mixture (4:1 volume ratio).

phase diagram of natural barite can improve the knowledge about the high-temperature and high-pressure structural and electrical transport characterizations for other barite-group minerals.

CONCLUSION

Raman spectroscopy and electrical conductivity measurements have been conducted to investigate the structural transition of natural barite under different hydrostatic environments at temperatures of 298–873 K and pressures of 1.5–35.0 GPa using a diamond anvil cell. At room temperature, natural barite underwent a phase transformation at 18.9 GPa under non-hydrostatic condition, which was characterized by the appearance of ν_5 Raman peak, the kinks in the pressure-dependent Raman shifts, FWHM of ν_1 Raman peak and electrical conductivity. Moreover, the smaller deviatoric stress within the sample chamber is responsible for the higher phase transition pressure of 21.4 GPa under quasi-hydrostatic condition. On the other hand, the phase transition

REFERENCES

Abidi, R., Slim-Shimi, N., Marignac, C., Hatira, N., Gasquet, D., Renac, C., et al. (2012). The Origin of Sulfate Mineralization and the Nature of the BaSO₄-SrSO₄

pressures increased from 10.9, 11.9, 13.2, and 15.5 GPa as the temperatures decreased from 773, 723, 673, and 523 K, respectively. Furthermore, the phase boundary between barite and post-barite was established as P (GPa) = $24.00 - 0.0166 T$ (K).

DATA AVAILABILITY STATEMENT

The original contributions presented in the study are included in the article/Supplementary Material, further inquiries can be directed to the corresponding authors.

AUTHOR CONTRIBUTIONS

LD designed the project. MH and LD wrote the initial draft of the work and the final paper. LD, HH, and MH contributed in interpreting the results. MH, XZ, and CL performed and interpreted the high-temperature and high-pressure Raman scattering and electrical conductivity results.

FUNDING

This research was financially supported by the NSF of China (grant number 42072055), the Youth Innovation Promotion Association of CAS (grant number 2019390), the Special Fund of the West Light Foundation of CAS, Guizhou Provincial 2019 and 2020 Science and Technology Subsidies (grant numbers GZ2019SIG and GZ2020SIG), and as well as the Science and Technology Foundation of Guizhou Province (grant number QKHJZ (2013) 2285).

ACKNOWLEDGMENTS

Some kind guidance and helps from Professor Heping Li in the Key Laboratory of High-temperature and High-pressure Study of the Earth's Interior, Institute of Geochemistry, Chinese Academy of Sciences are obtained for the *in-situ* high-pressure Raman scattering measurements.

SUPPLEMENTARY MATERIAL

The Supplementary Material for this article can be found online at: <https://www.frontiersin.org/articles/10.3389/feart.2022.864183/full#supplementary-material>

Solid-Solution Series in the Ain Allega and El Aguiba Ore Deposits, Northern Tunisia. *Ore Geology. Rev.* 48, 165–179. doi:10.1016/j.oregeorev.2012.03.003
Antao, S. M. (2012). The crystal Structure of Tin Sulphate, SnSO₄, and Comparison with Isostructural SrSO₄, PbSO₄, and BaSO₄. *Powder Diffr.* 27, 179–183. doi:10.1017/s0885715612000450

- Canil, D., and Fellows, S. A. (2017). Sulphide-sulphate Stability and Melting in Subducted Sediment and its Role in Arc Mantle Redox and Chalcophile Cycling in Space and Time. *Earth Planet. Sci. Letters Planet. Sci. Lett.* 470, 73–86. doi:10.1016/j.epsl.2017.04.028
- Chen, Y.-H., Huang, E., and Yu, S.-C. (2009). High-pressure Raman Study on the Series. *Solid State. Commun.* 149, 2050–2052. doi:10.1016/j.ssc.2009.08.023
- Chen, Y.-H., Yu, S.-C., Huang, E., and Lee, P.-L. (2010). Raman Spectroscopy and X-ray Diffraction Studies on Celestite. *Physica B: Condensed Matter* 405, 4386–4388. doi:10.1016/j.physb.2010.08.001
- Crichton, W. A., Merlini, M., Hanfland, M., and Muller, H. (2011). The crystal Structure of Barite, BaSO₄, at High Pressure. *Am. Mineral.* 96, 364–367. doi:10.2138/am.2011.3656
- Evans, K. A., Tomkins, A. G., Cliff, J., and Fiorentini, M. L. (2014). Insights into Subduction Zone Sulfur Recycling from Isotopic Analysis of Eclogite-Hosted Sulfides. *Chem. Geology.* 365, 1–19. doi:10.1016/j.chemgeo.2013.11.026
- Hong, M., Dai, L., Hu, H., and Zhang, X. (2022). Pressure-induced Structural Phase Transitions in Natural Kaolinite Investigated by Raman Spectroscopy and Electrical Conductivity. *Am. Mineral.* 107, 385–394. doi:10.2138/am-2021-7863
- Hu, H., Dai, L., Li, H., Hui, K., and Sun, W. (2017). Influence of Dehydration on the Electrical Conductivity of Epidote and Implications for High-Conductivity Anomalies in Subduction Zones. *J. Geophys. Res. Solid Earth* 122, 2751–2762. doi:10.1002/2016JB013767
- Hu, H., Dai, L., Li, H., Sun, W., and Li, B. (2018). Effect of Dehydrogenation on the Electrical Conductivity of Fe-Bearing Amphibole: Implications for High Conductivity Anomalies in Subduction Zones and continental Crust. *Earth Planet. Sci. Lett.* 498, 27–37. doi:10.1016/j.epsl.2018.06.003
- Kuang, Y. Q., Xu, J. G., Zhao, D. Y., Fan, D. W., Li, X. D., Zhou, W. G., et al. (2017). The High-Pressure Elastic Properties of celestine and the High-Pressure Behavior of Barite-type Sulphates. *High Temp.-High Press.* 46, 481–495.
- Lee, P.-L., Huang, E., and Yu, S.-C. (2003). High-pressure Raman and X-ray Studies of Barite, BaSO₄. *High Press. Res.* 23, 439–450. doi:10.1080/0895795031000115439
- Lee, P.-L., Huang, E., and Yu, S.-C. (2001). Phase Diagram and Equations of State of BaSO₄. *High Press. Res.* 21, 67–77. doi:10.1080/08957950108201005
- Li, B., Xu, J., Chen, W., Ye, Z., Huang, S., Fan, D., et al. (2018). Compressibility and Expansivity of Anglesite (PbSO₄) Using *In Situ* Synchrotron X-ray Diffraction at High-Pressure and High-Temperature Conditions. *Phys. Chem. Minerals* 45, 883–893. doi:10.1007/s00269-018-0970-1
- Liu, C., Wang, D., and Zheng, H. (2015). *In Situ* Raman Spectroscopic Study of Barite as a Pressure Gauge Using a Hydrothermal diamond Anvil Cell. *Appl. Spectrosc.* 70, 347–354. doi:10.1177/0003702815620556
- Pu, C., Dai, L., Li, H., Hu, H., Zhuang, Y., Liu, K., et al. (2018). High-pressure Electrical Conductivity and Raman Spectroscopy of Chalcanthite. *Spectrosc. Lett.* 51, 531–539. doi:10.1080/00387010.2018.1522646
- Rekhi, S., Dubrovinsky, L., and Saxena, S. (1999). Temperature-induced Ruby Fluorescence Shifts up to a Pressure of 15 GPa in an Externally Heated diamond Anvil Cell. *High Temp.-High Press.* 31, 299–305. doi:10.1068/htrt161
- Santamaría-Pérez, D., Gracia, L., Garbarino, G., Beltrán, A., Chulía-Jordán, R., Gomis, O., et al. (2011). High-pressure Study of the Behavior of mineral Barite by X-ray Diffraction. *Phys. Rev. B* 84, 054102. doi:10.1103/PhysRevB.84.054102
- Sun, W., Dai, L., Li, H., Hu, H., Wu, L., and Jiang, J. (2017). Electrical Conductivity of Mudstone (Before and after Dehydration at High *P-T*) and a Test of High Conductivity Layers in the Crust. *Am. Mineral.* 102, 2450–2456. doi:10.2138/am-2017-6146
- Yang, L., Dai, L., Li, H., Hu, H., Zhuang, Y., Liu, K., et al. (2018). Pressure-induced Structural Phase Transition and Dehydration for gypsum Investigated by Raman Spectroscopy and Electrical Conductivity. *Chem. Phys. Lett.* 706, 151–157. doi:10.1016/j.cplett.2018.06.007
- Ye, Z., Li, B., Chen, W., Tang, R., Huang, S., Xu, J., et al. (2019). Phase Transition and Thermoelastic Behavior of Barite-Group Minerals at High-Pressure and High-Temperature Conditions. *Phys. Chem. Minerals* 46, 607–621. doi:10.1007/s00269-019-01026-0
- Yuan, X., Mayanovic, R. A., and Zhang, G. (2021). Phase Transitions in CaCO₃ under Hydrous and Anhydrous Conditions: Implications for the Structural Transformations of CaCO₃ during Subduction Processes. *Am. Mineral.* 106, 1780–1788. doi:10.2138/am-2021-7575
- Zhou, H., Wang, M., Ding, H., and Du, G. (2015). Preparation and Characterization of Barite/TiO₂ Composite Particles. *Adv. Mater. Sci. Eng.* 2015, 1–8. doi:10.1155/2015/878594
- Zhou, L., Mernagh, T. P., Mo, B., Wang, L., Zhang, S., and Wang, C. (2020). Raman Study of Barite and celestine at Various Temperatures. *Minerals* 10, 260. doi:10.3390/min10030260

Conflict of Interest: The authors declare that the research was conducted in the absence of any commercial or financial relationships that could be construed as a potential conflict of interest.

Publisher's Note: All claims expressed in this article are solely those of the authors and do not necessarily represent those of their affiliated organizations, or those of the publisher, the editors and the reviewers. Any product that may be evaluated in this article, or claim that may be made by its manufacturer, is not guaranteed or endorsed by the publisher.

Copyright © 2022 Hong, Dai, Hu, Zhang and Li. This is an open-access article distributed under the terms of the Creative Commons Attribution License (CC BY). The use, distribution or reproduction in other forums is permitted, provided the original author(s) and the copyright owner(s) are credited and that the original publication in this journal is cited, in accordance with accepted academic practice. No use, distribution or reproduction is permitted which does not comply with these terms.



Acoustoelastic FD Simulation of Elastic Wave Propagation in Prestressed Media

Haidi Yang^{1,2}, Li-Yun Fu^{1,2*}, Bo-Ye Fu^{3,4} and Tobias M. Müller⁵

¹Shandong Provincial Key Laboratory of Deep Oil and Gas, China University of Petroleum (East China), Qingdao, China,

²Laboratory for Marine Mineral Resources, Qingdao National Laboratory for Marine Science and Technology, Qingdao, China,

³Key Laboratory of Earth and Planetary Physics, Institute of Geology and Geophysics, Chinese Academy of Sciences, Beijing, China,

⁴Institutions of Earth Science, Chinese Academy of Sciences, Beijing, China, ⁵Centro de Investigación Científica y de Educación Superior de Ensenada (CICESE), Department of Seismology, Ensenada, Mexico

Insights into wave propagation in prestressed media are important in geophysical applications such as monitoring changes in geo-pressure and tectonic stress. This can be addressed by acoustoelasticity theory, which accounts for nonlinear strain responses due to stresses of finite magnitude. In this study, a rotated staggered grid finite-difference (RSG-FD) method with an unsplit convolutional perfectly matched layer absorbing boundary is used to solve the relevant acoustoelastic equations with third-order elastic constants for elastic wave propagation in prestressed media. We partially verify our numerical simulations by the plane-wave theoretical solution. Comparisons of theoretical and calculated wave velocities are conducted for both P-wave and S-wave as a function of hydrostatic prestresses. We discuss several aspects of the numerical implementation. Numerical acoustoelasticity simulations for wave propagation in single- and double-layer models are carried out under four states of prestresses, confining, uniaxial, pure-shear, and simple-shear. The results display the effective anisotropy of elastic wave propagation in acoustoelastic media, illustrating that the prestress-induced velocity anisotropy is of orthotropic features strongly related to the orientation of prestresses. These examples demonstrate the significant impact of prestressed conditions on seismic responses in both phase and amplitude.

Keywords: acoustoelasticity, elastic wave propagation, modelling, CPML absorbing boundary condition, rotated staggered grid (RSG) method

OPEN ACCESS

Edited by:

Lidong Dai,
Institute of geochemistry (CAS), China

Reviewed by:

Hao Chen,
Institute of Acoustics (CAS), China
Tianyue Hu,
Peking University, China

*Correspondence:

Li-Yun Fu
lfu@upc.edu.cn

Specialty section:

This article was submitted to
Solid Earth Geophysics,
a section of the journal
Frontiers in Earth Science

Received: 01 March 2022

Accepted: 14 March 2022

Published: 28 April 2022

Citation:

Yang H, Fu L-Y, Fu B-Y and Müller TM
(2022) Acoustoelastic FD Simulation of
Elastic Wave Propagation in
Prestressed Media.
Front. Earth Sci. 10:886920.
doi: 10.3389/feart.2022.886920

INTRODUCTION

The impact of prestressed zones on seismic waves is an important issue that affects the interpretation of the results by seismic imaging and inversion. It is well known that acoustic velocities in rocks are sensitive to prestresses. The theory of acoustoelasticity, as an extension of the classical theory of elasticity, is set up under the framework of hyperelasticity (e.g., Toupin and Bernstein, 1961; Thurston and Brugger, 1964; Norris, 1983; Shams et al., 2011). The theory relates elastic moduli to prestresses (or residual stresses) in solids (e.g., Pao et al., 1984), resulting in an effective anisotropy for wave propagation in acoustoelastic media. It has been used to account for stress-induced velocity variations in rocks (e.g., Johnson and Shankland, 1989; Meegan et al., 1993), therefore perhaps providing the potential to understand the acoustic response to *in-situ* stresses (Sinha and Kostek, 1996; Huang et al., 2001) and, in turn, to monitor changes in geopressure and tectonic stress. Theoretical and

experimental investigations of acoustoelasticity for wave propagation in prestressed rocks have made great signs of progress, but with limited literature on numerical simulations for acoustoelastic wave propagation. As a useful complement to the theoretical solutions of acoustoelastic equations, numerical acoustoelasticity simulations are thought to provide further insights into the stress-induced variations in velocity and anisotropy.

Finite-difference (FD) numerical simulations of elastic wave propagation have been extensively studied over the past decades. A comprehensive review and mathematical details are discussed by Carcione (2007). The standard staggered grid (SSG) FD operator (Virieux, 1986) has been widely applied to various types of velocity-stress equations for wave propagation. It calculates spatial derivatives halfway between two gridpoints, where some modeling parameters defined on intergrid locations must be averaged, yielding inaccurate results or instability problems for wave propagation in media with strong fluctuations in elastic parameters (Crase, 1990; Seron et al., 1996). The SSG-FD algorithm has been improved significantly, for example, with the staggered mesh for anisotropic and viscoelastic wave equations (Carcione, 1999), the volume harmonic and arithmetic averaging of parameters (Moczo et al., 2002), the Lebedev FD scheme for anisotropic media (Lisitsa and Vishnevskiy, 2010), and the high-order operator for anisotropy simulations (e.g., Hu and McMechan, 2010; Pei et al., 2012). It is worth noting that a rotated staggered grid (RSG) FD method (Saenger et al., 2000; Saenger and Shapiro, 2002) is presented with no averaging of elastic moduli required in an elementary cell. The method has been applied to viscoelastic and anisotropic wave propagation (Saenger and Bohlen, 2004) and to poroelastic equations for ultrasonic propagation (coda waves) in digital porous cores (Zhang et al., 2014). Gao and Huang (2017) develop an improved RSG scheme for elastic-wave modeling in anisotropic media, with fourth-order temporal accuracy to reduce the numerical dispersion associated with prolonged wave propagation or a large temporal step size. Recent and valuable contributions to the FD numerical simulation of wave propagation include a high-performance FD architecture for wave propagation in anisotropic poroelastic media (Alkhimenkov et al., 2021) and a discrete FD grid representation for strongly heterogeneous media (Moczo et al., 2019; Gregor et al., 2021).

Great progress has been made in both the theoretical and experimental aspects of acoustoelasticity, but dedicated computational literature is rare. Mavko et al. (1995) present a simple transformation to calculate the stress-induced anisotropy in homogeneous rocks. Liu and Sinha (2000) solve acoustoelastic equations using a second-order FD time-domain (FDTD) method to simulate borehole acoustic wave propagation in prestressed formations. Chen et al. (2006) parallelize the FDTD simulation in the super computer for ultrasonic wave propagation in prestressed media with a perfectly matched layer (PML) as an absorbing boundary condition. Fang et al. (2013) propose an iterative finite-element numerical approach to calculate stress-induced anisotropy around a borehole by incorporating the rock-physics transformation (Mavko et al.,

1995). Yang et al. (2019) present a finite-element prediction of acoustoelastic effects associated with Lamb wave propagation in prestressed plates. Li et al. (2020) simulate acoustoelastic effects associated with ultrasound wave propagation by time-space finite element formulation based on quadratic interpolation of the acceleration. It is worth mentioning that Lys et al. (2015) use the general theory of finite deformations to formulate a governing equation in terms of velocities, stresses, and small rotations in the form of the first-order hyperbolic system. They apply the RSG-FD method to the governing equation for wave propagation in a homogeneous medium under a simple prestress mode, but with the results unvalidated.

In this study, we introduce the theory of acoustoelasticity as a base to support numerical simulations for wave propagation in prestressed media. We follow the works of Pao et al. (1984), Pao and Gamer (1985), and Winkler and Liu (1996) for the theory of acoustoelasticity with a detailed description of the third-order elastic constants that are important for building physically meaningful prestressed models. The presented numerical scheme is based on the RSG-FD method which is implemented by an eighth-order (for the space derivatives) and second-order (for the time derivatives) FD operator. The classical split PML and conventional unsplit PML absorbing boundaries suffer from large spurious reflections at grazing incidences, especially for low-frequency numerical simulations. An unsplit convolutional PML (CPML) absorbing boundary (Komatitsch and Martin, 2007; Martin and Komatitsch, 2009) is used in this study to overcome this difficulty with less memory and more computational efficiency. For insights into the effect of third-order elastic constants on the velocity, we conduct a plane-wave analysis, combined with the closed-pore jacketed sandstone experiment (Winkler and Liu, 1996), which describes P-wave and S-wave velocities against prestresses. The presented numerical scheme is partially validated using the plane-wave theoretical solution through the comparison of theoretical and calculated wave velocities. Four states of prestress, not only the conventional confining and uniaxial modes but also the pure-shear and simple-shear patterns, are investigated with different simplified stiffness matrices to model the prestress-induced anisotropy of velocities and its effect on the characteristics of wavefronts. The acoustoelastic modeling scheme can be applied to double-layered cases.

We first briefly introduce the theory of acoustoelasticity based on the third-order elastic constants, followed by a stress-velocity plane-wave analysis. Then, we apply the RSG-FD method to the acoustoelastic equations with the velocity-stress CPML absorbing boundaries. Numerical examples are presented for elastic wave propagation in an isotropic and homogeneous medium and a double-layer model under different kinds of prestress modes.

Theoretical Background Acoustoelastic Equations

For wave propagation in prestressed media, there exist three configurations involved: the stress-free natural configuration as a reference state, the initial configuration of finite static deformations as a prestressed state, and the final configuration associated with wave-induced dynamic deformations. The

theory of acoustoelasticity superposes small-amplitude dynamic deformations of a wave onto a prestressed finite deformation. The relevant acoustoelastic equation of motion can be derived either in the natural or in the initial states.

As defined by Pao et al. (1984) for a predeformed medium, the dynamic displacement $u(\xi, t)$ from the initial to the final state satisfies the following acoustoelastic equation of motion in the natural frame of reference,

$$A_{\alpha\beta\gamma\delta} \frac{\partial^2 u_\gamma}{\partial \xi_\beta \partial \xi_\delta} = \rho \frac{\partial^2 u_\alpha}{\partial t^2} \quad (1)$$

with

$$A_{\alpha\beta\gamma\delta} = T_{\beta\delta}^i \delta_{\alpha\gamma} + \Gamma_{\alpha\beta\gamma\delta} \quad (2)$$

where $\delta_{\alpha\gamma}$ represent the Kronecker symbol, $\Gamma_{\alpha\beta\gamma\delta}$ and $T_{\beta\delta}^i$ denote the fourth-order stiffness tensor and the second Piola-Kirchhoff stress tensor caused by a finite static deformation, respectively. The mass density ρ refers to the natural state. The fourth-order stiffness tensor $A_{\alpha\beta\gamma\delta}$ can be expanded about the material's elastic constants in the initial state,

$$A_{\alpha\beta\gamma\delta} = c_{\alpha\beta\gamma\delta} (1 - e_{\eta\eta}) + c_{\alpha\beta\gamma\delta\epsilon\eta} e_{\epsilon\eta} + c_{\epsilon\beta\gamma\delta} \frac{\partial u_\alpha^i}{\partial \xi_\epsilon} + c_{\alpha\epsilon\gamma\delta} \frac{\partial u_\beta^i}{\partial \xi_\epsilon} + c_{\alpha\beta\epsilon\delta} \frac{\partial u_\gamma^i}{\partial \xi_\epsilon} + c_{\alpha\beta\gamma\epsilon} \frac{\partial u_\delta^i}{\partial \xi_\epsilon} \quad (3)$$

where $e_{\eta\eta} = \frac{1}{2} (\frac{\partial u_\eta^i}{\partial \xi_\eta} + \frac{\partial u_\eta^i}{\partial \xi_\eta})$ is the infinitesimal strain, $u^i(\xi)$ denotes the static displacement caused by the applied static loading of material points for the natural state, and $c_{\alpha\beta\gamma\delta}$ and $c_{\alpha\beta\gamma\delta\epsilon\eta}$ are the second-order and third-order elastic constants of the medium in the prestressed configuration, respectively. The coefficients $A_{\alpha\beta\gamma\delta}$ depend on both the material constants and the prestress strains. These coefficients possess the same symmetry (Pao et al., 1984) as the Hookean stiffness tensor $c_{\alpha\beta\gamma\delta}$, namely,

$$A_{\alpha\beta\gamma\delta} = A_{\beta\alpha\gamma\delta} = A_{\alpha\beta\delta\gamma} = A_{\gamma\delta\alpha\beta} \quad (4)$$

For convenience, we use the following Voigt's compressed notation for the tensorial indices to contract the indices of $c_{\alpha\beta\gamma\delta}$ ($\alpha, \beta, \gamma, \delta = 1, 2, 3$) to c_{pq} ($p, q = 1, 2, \dots, 6$) whereby.

$$11 \rightarrow 1, 22 \rightarrow 2, 33 \rightarrow 3, 23 \rightarrow 4, 13 \rightarrow 5, \text{ and } 12 \rightarrow 6. \quad (5)$$

The second-order tensor $c_{\alpha\beta\gamma\delta}$ is replaced hereafter with a 6 by 6 matrix c_{pq} as follows (Pao et al., 1984),

$$\begin{bmatrix} c_{11} & c_{12} & c_{13} & 0 & 0 & 0 \\ c_{21} & c_{22} & c_{23} & 0 & 0 & 0 \\ c_{31} & c_{32} & c_{33} & 0 & 0 & 0 \\ 0 & 0 & 0 & c_{44} & 0 & 0 \\ 0 & 0 & 0 & 0 & c_{55} & 0 \\ 0 & 0 & 0 & 0 & 0 & c_{66} \end{bmatrix} \quad (6)$$

The medium has 9 independent second-order elastic constants because of the symmetry of c_{pq} and 20 third-order elastic constants with the following symmetry,

$$\begin{cases} c_{111} = c_{222} = c_{333}, \\ c_{144} = c_{255} = c_{366}, \\ c_{112} = c_{223} = c_{133} = c_{113} = c_{122} = c_{233} \\ c_{155} = c_{244} = c_{344} = c_{166} = c_{266} = c_{355} \\ c_{123}, \text{ and } c_{456} \end{cases} \quad (7)$$

Acoustoelastic Constants

Compared to the linear elasticity with two elastic constants for an isotropic medium, the third-order nonlinear elasticity invokes three additional elastic constants (sometimes called A , B , and C) (Green, 1973). Following Winkler and Liu (1996), the static strain tensor caused by static loading with respect to the natural state can be expressed as a function of $u^i(\xi)$,

$$\epsilon_{\alpha\beta} = \frac{1}{2} (u_{\alpha,\beta}^i + u_{\beta,\alpha}^i + u_{\delta,\alpha}^i u_{\delta,\beta}^i) \quad (8)$$

The elastic strain energy density is expressed as

$$W = \mu \epsilon_{\alpha\beta}^2 + \left(\frac{K}{2} - \frac{\mu}{3} \right) \epsilon_{\delta\delta}^2 + \frac{A}{3} \epsilon_{\alpha\beta} \epsilon_{\alpha\delta} \epsilon_{\beta\delta} + B \epsilon_{\alpha\beta}^2 \epsilon_{\delta\delta} + \frac{C}{3} \epsilon_{\delta\delta}^3 \quad (9)$$

where μ is the shear modulus, K is the bulk modulus, and (A , B , C) are the third-order elastic constants. We see that there are two sources of nonlinearity in Eqs. 8, 9, as described by Pau and Vestroni (2019), one from the geometrical nonlinearity term in the strain tensor and the other from the cubic terms referred to physical nonlinearity through the potential energy.

For infinitesimally small strains, the geometrical nonlinearity term in Eq. 8 and the cubic terms in Eq. 9 are negligible, leading to the standard equation of linear elasticity. The (A , B , C) nomenclature used above is common, but it is not universal. Green (1973) presents a table that correlates five definitions of the third-order elastic constants used by different authors. With the Goldberg, 1961, the third-order elastic constants c_{pqr} can be represented by

$$\begin{cases} c_{111} = c_{333} = 2C + 6B + 2A, \\ c_{133} = c_{113} = 2C + 2B, \\ c_{155} = c_{355} = \frac{c_{111} - c_{113}}{4} = B + A/2 \end{cases} \quad (10)$$

Based on the above third-order elastic constants and the Voigt abbreviated symbol in Eq. 5, the second-order effective elastic constants $A_{\alpha\beta\gamma\delta}$ for a 2D homogeneous medium can be reduced to

$$\begin{cases} A_{11} = (\lambda + 2\mu)(1 + 3e_{11} - e_{33}) + (6B + 2C + 2A)e_{11} + (2B + 2C)e_{33}, \\ A_{13} = \lambda(1 + e_{11} + e_{33}) + (2B + 2C)(e_{11} + e_{33}), \\ A_{33} = (\lambda + 2\mu)(1 - e_{11} + 3e_{33}) + (6B + 2C + 2A)e_{33} + (2B + 2C)e_{11}, \\ A_{31} = 2\left(B + \frac{A}{2}\right)e_{13} + 2(\lambda + 2\mu)e_{13}, \\ A_{53} = 2\left(B + \frac{A}{2}\right)e_{13} + 2(\lambda + 2\mu)e_{13}, \\ A_{55} = \mu(1 + e_{11} + e_{33}) + \left(B + \frac{A}{2}\right)(e_{11} + e_{33}) \end{cases} \quad (11)$$

where $e_{\alpha\beta}$ are the components of the total prestrain tensor, and λ and μ are the Lamé constants in the initial configuration.

Plane-Wave Analysis

The plane-wave analysis of acoustoelastic equations provides a simple way to understand the physics of wave propagation in acoustoelastic media. In this section, we follow the plane-wave analysis in Section 3.2 of Pao et al. (1984), with attempts to compare with experimental measurements (Winkler and Liu, 1996). The resulting analytical solution will be used to validate our numerical results.

Let us assume that the displacement components in **Eq. 1** can be described by a time-harmonic plane wave,

$$u_\alpha = U_\alpha \exp[i(kl_\beta \xi_\beta - \omega t)] \quad (12)$$

where ω is the angular frequency, l_β denotes the component of the wave normal (a unit vector), k is the wave number with the wave velocity $v = \omega/k$, U_α is the amplitude constant, and $i = \sqrt{-1}$. Substituting **Eq. 12** into (1), we obtain a system of equations for the amplitude vector \mathbf{U} ,

$$[A_{\alpha\beta\gamma} \delta l_\beta l_\gamma - \rho v^2 \delta_{\alpha\gamma}] U_\gamma = 0 \quad (13)$$

Considering the case of orthotropic predeformations, the orthotropic body possesses three axes of symmetry, called the principal axes of orthotropy. For a plane wave propagating in the direction of the ξ_3 axis, **Eq. 13** can be simplified to

$$[A_{\alpha 3 \gamma} - \rho v^2 \delta_{\alpha \gamma}] U_\gamma = 0 \quad (14)$$

Equation 14 has a solution under the condition that the determinant of coefficients is zero, namely,

$$\det[A_{\alpha 3 \gamma} - \rho v^2 \delta_{\alpha \gamma}] = 0 \quad (15)$$

The corresponding characteristic equation in the contracted notation is,

$$\det \begin{bmatrix} A_{55} - \rho v^2 & A_{54} & A_{53} \\ A_{45} & A_{44} - \rho v^2 & A_{43} \\ A_{35} & A_{34} & A_{33} - \rho v^2 \end{bmatrix} = 0 \quad (16)$$

where the second-order effective elastic constants are defined by Pao et al. (1984) as

$$\begin{cases} A_{33} = T_{33}^i + c_{33}(1 + 2e_{33}) + c_{331}e_{11} + c_{332}e_{22} + c_{333}e_{33}, \\ A_{44} = T_{33}^i + c_{44}(1 + 2e_{22}) + c_{441}e_{11} + c_{442}e_{22} + c_{443}e_{33}, \\ A_{55} = T_{33}^i + c_{55}(1 + 2e_{11}) + c_{551}e_{11} + c_{552}e_{22} + c_{553}e_{33}, \\ A_{34} = A_{43} = c_{33}(\partial u_2^i / \partial \xi_3) + c_{44}(\partial u_3^i / \partial \xi_2) + 2c_{344}e_{23}, \\ A_{35} = A_{53} = c_{33}(\partial u_1^i / \partial \xi_3) + c_{55}(\partial u_3^i / \partial \xi_1) + 2c_{355}e_{31}, \\ A_{45} = A_{54} = c_{44}(\partial u_1^i / \partial \xi_2) + c_{55}(\partial u_2^i / \partial \xi_1) + 2c_{456}e_{12} \end{cases} \quad (17)$$

Because ξ_3 is in the direction of one of the strains, we have $A_{43} = A_{53} = 0$ (due to $e_{31} = e_{32} = 0$), **Eq. 16** reduces to

$$(A_{33} - \rho v^2)[(\rho v^2)^2 - (A_{55} + A_{44})\rho v^2 + A_{55}A_{44} - A_{45}^2] = 0 \quad (18)$$

The solution to this equation for three eigenvalues can be obtained in terms of the following two cases. For the cubic-symmetric medium under the confining prestress, the resulting three eigenvalues lead to one longitudinal mode and two transverse modes as follows,

$$\begin{cases} v_P^2 = A_{11}/\rho, \\ v_{SV}^2 = A_{44}/\rho, \\ v_{SH}^2 = A_{44}/\rho \end{cases} \quad (19)$$

For the symmetric plane, for example when $\theta_2 = 0^\circ$, the velocities can be expressed as (Zong, 2014)

$$\begin{cases} v_P^2 = (A_{11} + A_{44} + \sqrt{K})/\rho, \\ v_{SV}^2 = (A_{11} + A_{44} - \sqrt{K})/\rho, \\ v_{SH}^2 = A_{44}/\rho \end{cases} \quad (20)$$

where

$$\begin{aligned} K = & 4A_{11}^2 \sin^4 \theta_1 - 8A_{11}A_{44} \sin^4 \theta_1 - 4A_{12}^2 \sin^4 \theta_1 - 8A_{12}A_{44} \sin^4 \theta_1 \\ & - 4A_{11}^2 \sin^2 \theta_1 + 8A_{11}A_{44} \sin^2 \theta_1 + 4A_{12}^2 \sin^2 \theta_1 \\ & + 8A_{12}A_{44} \sin^2 \theta_1 + (A_{11} - A_{44})^2 \end{aligned} \quad (21)$$

Figure 1 shows the definition of angles θ_1 , θ_2 , and θ_3 , where θ_1 is the angle between the z -axis and the line linking a point in the space and the origin of coordinates, θ_2 is the angle between the x -axis and the projection line on the xoy plane, and θ_3 is the angle between the y -axis and the projection line on the xoy plane. These angles define the relationship between the reference-coordinate and orthotropy axes which should be coincident for the cases of confining stress, uniaxial stress, and pure shear stress, but with a difference of 45° for the case of simple shear stress. We see that these modes are strongly related to stress changes. The stress-induced velocity anisotropies depend on the orientation of external stresses.

Based on the experimental measurements (Winkler and Liu, 1996) under the hydrostatic pressures for Portland sandstone, we calculate velocities for the longitudinal mode against pressure. The physical constants for the simulation are picked from Tables III-IV of (Winkler and Liu, 1996). The prestress condition in the simulation is regarded as the confining stress with its implementation described in detail in Section 4.1. The result is shown in **Figure 2**, where the circles (experimental measurements) are obtained by picking the pixel coordinates in **Figure 4** of (Winkler and Liu, 1996). We see a weak nonlinearity for velocity variations with increasing pressures, resulting from the third-order elasticity with a cubic term for the strain energy function. Some departures from experimental measurements can be observed during the pressure of 20–60 MPa possibly because of the deformation of pores in the sandstone which the third-order elasticity for solids cannot account for. In general, for most consolidated rocks, the third-order elasticity could be enough to describe the nonlinear stress dependence of velocity variations.

Numerical Methodology

Velocity–Stress Version of Acoustoelastic Equations for Space- and Time-Derivative Approximations

Equation 1 can be written as the first-order velocity-stress equation,

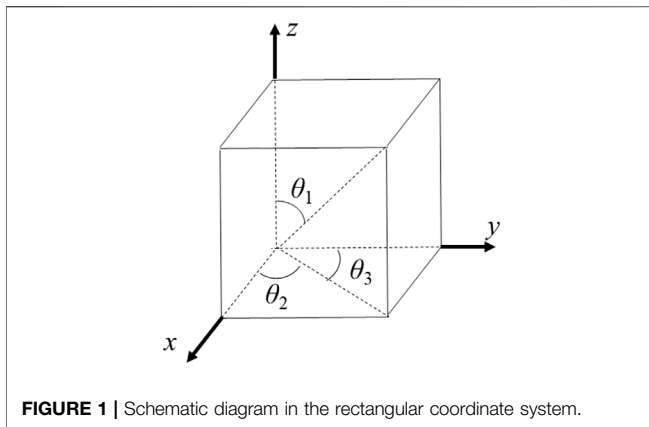


FIGURE 1 | Schematic diagram in the rectangular coordinate system.

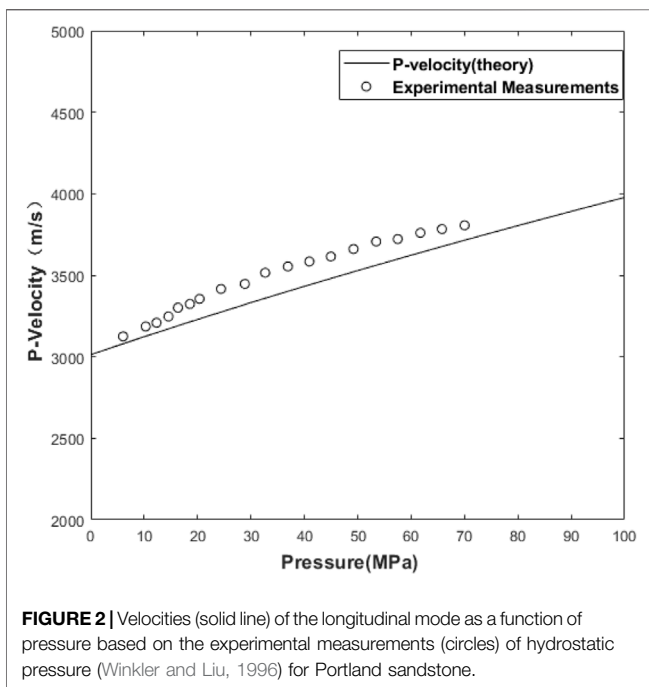


FIGURE 2 | Velocities (solid line) of the longitudinal mode as a function of pressure based on the experimental measurements (circles) of hydrostatic pressure (Winkler and Liu, 1996) for Portland sandstone.

$$\begin{cases} \rho v_{\beta,t} = \tau_{\alpha\beta,\alpha} \\ \tau_{\alpha\beta,t} = A_{\alpha\beta\gamma\delta} v_{\gamma,\delta} \end{cases} \quad (22)$$

where v and τ are velocity and stress, respectively. With Eq. 11 and the Cartesian tensor notation with the x - and z -coordinates for convenience, we rewrite Eq. 22 as its velocity-stress FD formulation,

$$\begin{cases} \rho v_{x,t} = \tau_{xx,z} + \tau_{xz,x} \\ \rho v_{z,t} = \tau_{xz,x} + \tau_{zz,z} \\ \tau_{xx,t} = A_{11} v_{x,x} + A_{13} v_{z,z} + A_{15} (v_{x,z} + v_{z,x}) \\ \tau_{zz,t} = A_{13} v_{x,x} + A_{33} v_{z,z} + A_{35} (v_{x,z} + v_{z,x}) \\ \tau_{xz,t} = A_{15} v_{x,x} + A_{35} v_{z,z} + A_{55} (v_{x,z} + v_{z,x}) \end{cases} \quad (23)$$

The nonlinear effect of predeformation is introduced by the effective elastic constants. Equation 23 can be reduced to

the classical elastic wave equation when no static stress is applied.

The SSG-FD method is widely used in seismology to simulate elastic wave propagation. The method defines velocity components, stress components, and physical properties in four grids crosswise shown in Figure 3A, whereas the RSG-FD method defines velocity components in one grid and stress components and elastic parameters in another grid shown in Figure 3B. The RSG-FD method is employed in this study to solve the first-order velocity-stress acoustoelastic equations.

As shown in Figure 3B, the RSG technique calculates the spatial derivative along the diagonal direction of grids, and then interpolates the result along the normal coordinate axis to obtain the spatial derivative along the horizontal and vertical directions. We rotate the direction of spatial derivatives from the horizontal (x) and vertical (z) directions to the diagonal directions (\bar{x} and \bar{z}) as

$$\begin{cases} \bar{x} = \frac{\Delta x}{\Delta r} x - \frac{\Delta z}{\Delta r} z, \\ \bar{z} = \frac{\Delta x}{\Delta r} x + \frac{\Delta z}{\Delta r} z, \end{cases} \quad (24)$$

where $\Delta r = \sqrt{\Delta x^2 + \Delta z^2}$. The first-order spatial derivatives along the horizontal and vertical directions become,

$$\begin{cases} \frac{\partial}{\partial x} = \frac{\Delta r}{2\Delta x} \left(\frac{\partial}{\partial \bar{z}} + \frac{\partial}{\partial \bar{x}} \right), \\ \frac{\partial}{\partial z} = \frac{\Delta r}{2\Delta z} \left(\frac{\partial}{\partial \bar{z}} - \frac{\partial}{\partial \bar{x}} \right). \end{cases} \quad (25)$$

With Eq. 25, it is easy to define the differentiation operators $D_{\bar{x}}$ and $D_{\bar{z}}$, which implement the spatial derivatives along diagonal directions (\bar{x} and \bar{z}) in the time domain (Saenger et al., 2000),

$$\begin{cases} D_{\bar{x}} u(x, z, t) = \frac{1}{\Delta r} \left[u\left(x - \frac{\Delta x}{2}, z + \frac{\Delta z}{2}, t\right) - u\left(x + \frac{\Delta x}{2}, z - \frac{\Delta z}{2}, t\right) \right], \\ D_{\bar{z}} u(x, z, t) = \frac{1}{\Delta r} \left[u\left(x + \frac{\Delta x}{2}, z + \frac{\Delta z}{2}, t\right) - u\left(x - \frac{\Delta x}{2}, z - \frac{\Delta z}{2}, t\right) \right]. \end{cases} \quad (26)$$

With Eqs. 25, 26, the numerical differentiation operators are obtained that perform the spatial derivatives along the x and z directions in the rotated staggered grid by a linear combination of the derivatives along the \bar{x} and \bar{z} directions,

$$\begin{cases} \frac{\partial}{\partial x} u(x, z, t) \approx \frac{\Delta r}{2\Delta x} (D_{\bar{x}} u(x, z, t) + D_{\bar{z}} u(x, z, t)), \\ \frac{\partial}{\partial z} u(x, z, t) \approx \frac{\Delta r}{2\Delta z} (D_{\bar{x}} u(x, z, t) - D_{\bar{z}} u(x, z, t)). \end{cases} \quad (27)$$

A detailed process of the implementation of the RGS-FD scheme is addressed as follows.

By that analogy, we express the L -order RSG of each physical quantity in the discrete form as

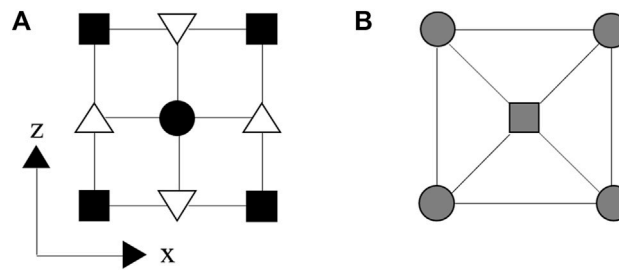


FIGURE 3 | Schematic diagram of finite difference operators for SSG (A) and RSG (B). The SSG defines normal stress and all physical parameters in the solid squares, and shear stress in the solid circle, but with horizontal and vertical velocities in the downward and upward triangles, respectively. The RSG defines horizontal and vertical velocities in the square, but with normal and shear stresses and all physical parameters in the circles, where the line represents the direction of differentiation.

$$\begin{aligned}
 v_{x,x}(x, z) &\approx \sum_{l=1}^{L/2} \frac{c_n}{2\Delta x} \{v_x(x + (l-1/2)\Delta x, z + (l-1/2)\Delta z) + v_x(x + (l-1/2)\Delta x, z \\
 &\quad - (l-1/2)\Delta z) - v_x(x - (l-1/2)\Delta x, z - (l-1/2)\Delta z) - v_x(x - (l-1/2)\Delta x, z \\
 &\quad + (l-1/2)\Delta z)\} \\
 v_{z,z}(x, z) &\approx \sum_{l=1}^{L/2} \frac{c_n}{2\Delta z} \{v_z(x + (n-1/2)\Delta x, z + (n-1/2)\Delta z) + v_z(x + (n-1/2)\Delta x, z \\
 &\quad - (n-1/2)\Delta z) - v_z(x - (n-1/2)\Delta x, z - (n-1/2)\Delta z) - v_z(x - (n-1/2)\Delta x, z \\
 &\quad + (n-1/2)\Delta z)\} \\
 v_{x,z}(x, z) &\approx \sum_{l=1}^{L/2} \frac{c_n}{2\Delta z} \{v_x(x + (l-1/2)\Delta x, z + (l-1/2)\Delta z) - v_x(x + (l-1/2)\Delta x, z \\
 &\quad - (l-1/2)\Delta z) - v_x(x - (l-1/2)\Delta x, z - (l-1/2)\Delta z) + v_x(x - (l-1/2)\Delta x, z \\
 &\quad + (l-1/2)\Delta z)\} \\
 v_{z,x}(x, z) &\approx \sum_{l=1}^{L/2} \frac{c_n}{2\Delta z} \{v_z(x + (l-1/2)\Delta x, z + (l-1/2)\Delta z) - v_z(x + (l-1/2)\Delta x, z \\
 &\quad - (l-1/2)\Delta z) - v_z(x - (l-1/2)\Delta x, z - (l-1/2)\Delta z) + v_z(x - (l-1/2)\Delta x, z \\
 &\quad + (l-1/2)\Delta z)\} \\
 \tau_{xx,x}(x + \Delta x/2, z + \Delta z/2) &\approx \sum_{l=1}^{L/2} \frac{c_n}{2\Delta x} \{\tau_{xx}(x + l\Delta x, z + l\Delta z) + \tau_{xx}(x + l\Delta x, z \\
 &\quad - (l-1)\Delta z) - \tau_{xx}(x - l\Delta x, z - (l-1)\Delta z) - \tau_{xx}(x - l\Delta x, z + l\Delta z)\} \\
 \tau_{xz,x}(x + \Delta x/2, z + \Delta z/2) &\approx \sum_{l=1}^{L/2} \frac{c_n}{2\Delta x} \{\tau_{xz}(x + l\Delta x, z + l\Delta z) + \tau_{xz}(x + l\Delta x, z \\
 &\quad - (l-1)\Delta z) - \tau_{xz}(x - l\Delta x, z - (l-1)\Delta z) - \tau_{xz}(x - l\Delta x, z + l\Delta z)\} \\
 \tau_{zz,x}(x + \Delta x/2, z + \Delta z/2) &\approx \sum_{n=1}^{L/2} \frac{c_n}{2\Delta x} \{\tau_{zz}(x + n\Delta x, z + n\Delta z) + \tau_{zz}(x + n\Delta x, z \\
 &\quad - (n-1)\Delta z) - \tau_{zz}(x - n\Delta x, z - (n-1)\Delta z) - \tau_{zz}(x - n\Delta x, z + n\Delta z)\} \\
 \tau_{xx,z}(x + \Delta x/2, z + \Delta z/2) &\approx \sum_{n=1}^{L/2} \frac{c_n}{2\Delta z} \{\tau_{xx}(x + n\Delta x, z + n\Delta z) - \tau_{xx}(x + n\Delta x, z \\
 &\quad - (n-1)\Delta z) - \tau_{xx}(x - n\Delta x, z - (n-1)\Delta z) + \tau_{xx}(x - n\Delta x, z + n\Delta z)\} \\
 \tau_{xz,z}(x + \Delta x/2, z + \Delta z/2) &\approx \sum_{l=1}^{L/2} \frac{c_n}{2\Delta z} \{\tau_{xz}(x + l\Delta x, z + l\Delta z) - \tau_{xz}(x + l\Delta x, z \\
 &\quad - (l-1)\Delta z) - \tau_{xz}(x - l\Delta x, z - (l-1)\Delta z) + \tau_{xz}(x - l\Delta x, z + l\Delta z)\} \\
 \tau_{zz,z}(x + \Delta x/2, z + \Delta z/2) &\approx \sum_{l=1}^{L/2} \frac{c_n}{2\Delta z} \{\tau_{zz}(x + l\Delta x, z + l\Delta z) - \tau_{zz}(x + l\Delta x, z \\
 &\quad - (l-1)\Delta z) - \tau_{zz}(x - l\Delta x, z - (l-1)\Delta z) + \tau_{zz}(x - l\Delta x, z + l\Delta z)\} \quad (28)
 \end{aligned}$$

where the differential coefficients c_l will be specified subsequently. For the time derivatives, we use the second-order FD approximation with $v_i((l+1/2)\Delta t) = v_i^{l+1/2}$ for velocity, where Δt is the time step.

Simultaneous Matrix Equations

Substituting Eq. 28 into (23) and adding a source field in the simulation, we obtain the discrete form of the first-order velocity-stress acoustoelastic equations,

$$\begin{cases} \dot{v}_x = (\partial_x \tau_{xx} + \partial_z \tau_{xz} - f_x)/\rho, \\ \dot{v}_z = (\partial_x \tau_{xz} + \partial_z \tau_{zz} - f_z)/\rho, \\ \dot{\tau}_{xx} = A_{11} \partial_x v_x + A_{13} \partial_z v_z + A_{15} (\partial_z v_x + \partial_x v_z) + \dot{f}_{xx}, \\ \dot{\tau}_{zz} = A_{13} \partial_x v_x + A_{33} \partial_z v_z + A_{35} (\partial_z v_x + \partial_x v_z) + \dot{f}_{zz}, \\ \dot{\tau}_{xz} = A_{15} \partial_x v_x + A_{35} \partial_z v_z + A_{55} (\partial_z v_x + \partial_x v_z) + \dot{f}_{xz}, \end{cases} \quad (29)$$

where the cap dot represents the first-order partial derivative of time, and f denotes the components of the external body force. The set of equations can be combined into a matrix system as

$$\dot{\mathbf{v}} + \mathbf{s} = \mathbf{M}\mathbf{v} \quad (30)$$

where the product $\mathbf{M}\mathbf{v}$ is given by

$$\begin{aligned}
 \mathbf{M}\mathbf{v} &= \begin{bmatrix} 0 & 0 & \partial_x/\rho & 0 & \partial_z/\rho \\ 0 & 0 & 0 & \partial_z/\rho & \partial_x/\rho \\ A_{11}\partial_x + A_{15}\partial_z & A_{13}\partial_z + A_{15}\partial_x & 0 & 0 & 0 \\ A_{13}\partial_x + A_{35}\partial_z & A_{33}\partial_z + A_{35}\partial_x & 0 & 0 & 0 \\ A_{15}\partial_x + A_{55}\partial_z & A_{35}\partial_z + A_{55}\partial_x & 0 & 0 & 0 \end{bmatrix} \\
 &\times \begin{bmatrix} v_x \\ v_z \\ \tau_{xx} \\ \tau_{zz} \\ \tau_{xz} \end{bmatrix}, \quad (31)
 \end{aligned}$$

and the source vector is

$$\mathbf{s} = \begin{bmatrix} f_x/\rho & f_z/\rho & \dot{f}_{xx} & \dot{f}_{zz} & \dot{f}_{xz} \end{bmatrix}^T \quad (32)$$

For the time integration from t to $t + \Delta t$, with the discretizing time as $t = n\Delta t$, we have,

$$\begin{cases} v_x^{n+1} = v_x^n + \Delta t (\partial_x \tau_{xx}^n + \partial_z \tau_{xz}^n - f_x^n)/\rho, \\ v_z^{n+1} = v_z^n + \Delta t (\partial_x \tau_{xz}^n + \partial_z \tau_{zz}^n - f_z^n)/\rho, \\ \tau_{xx}^{n+1} = \tau_{xx}^n + \Delta t (A_{11} \partial_x v_x^n + A_{13} \partial_z v_z^n + A_{15} (\partial_z v_x^n + \partial_x v_z^n) + f_{xx}^n), \\ \tau_{zz}^{n+1} = \tau_{zz}^n + \Delta t (A_{13} \partial_x v_x^n + A_{33} \partial_z v_z^n + A_{35} (\partial_z v_x^n + \partial_x v_z^n) + f_{zz}^n), \\ \tau_{xz}^{n+1} = \tau_{xz}^n + \Delta t (A_{15} \partial_x v_x^n + A_{35} \partial_z v_z^n + A_{55} (\partial_z v_x^n + \partial_x v_z^n) + f_{xz}^n). \end{cases} \quad (33)$$

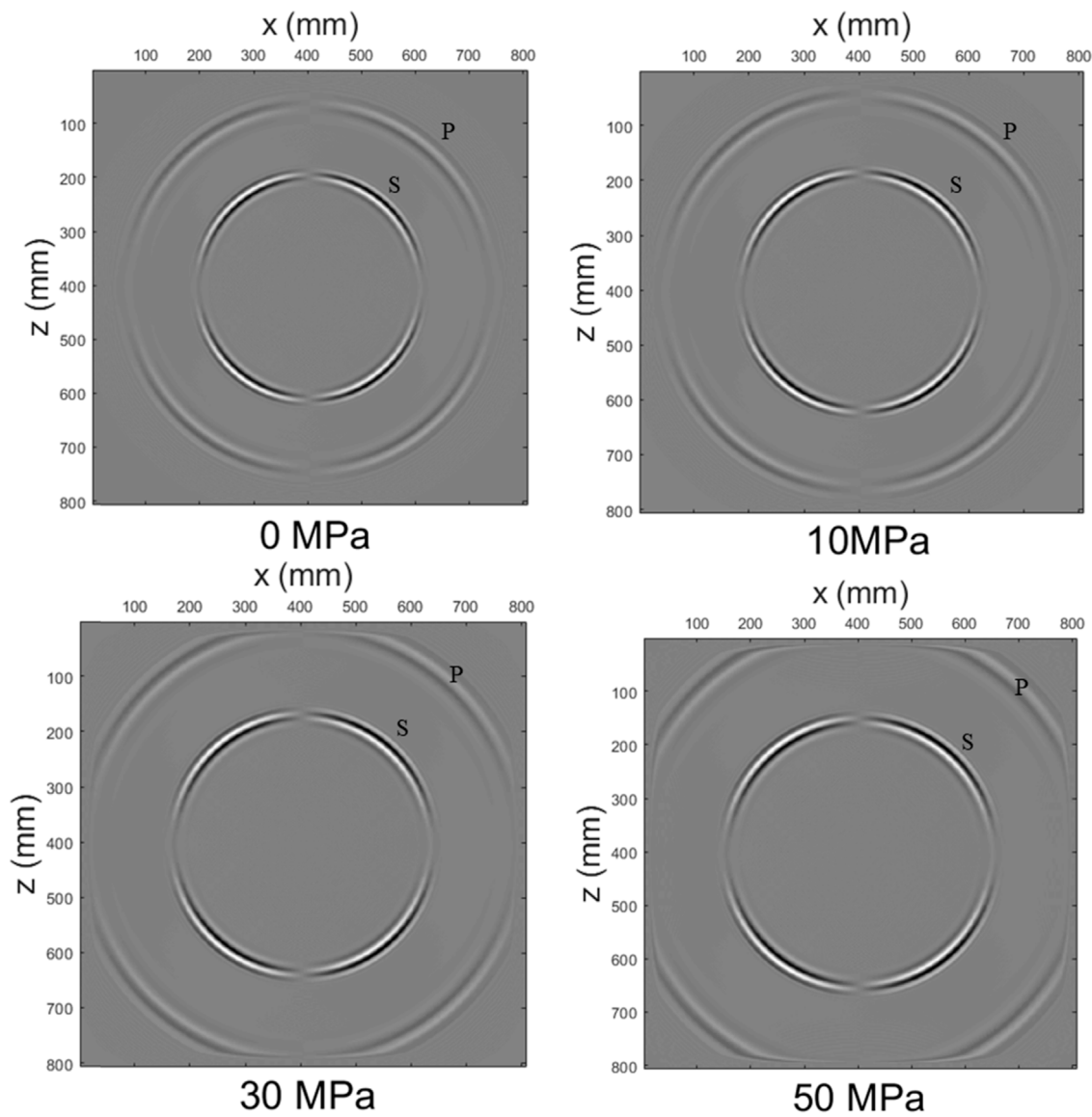


FIGURE 4 | Wavefield snapshots of the x-component of the particle velocity at $t = 0.12$ ms for various hydrostatic stresses.

The set of **Eq. 33** can be combined into a matrix system as. $\mathbf{v}^{n+1} = \mathbf{M}^n \mathbf{v}^n + \mathbf{s}^n$.

CPML Absorbing Boundary

The conventional PML absorption boundary is unable to handle the reflections (evanescent waves) at grazing incidences, especially for low-frequency components. The CPML absorption boundary improves the absorption effect of evanescent waves, with efficient computations by introducing auxiliary variables to avoid convolutional calculations that need to store past-time wavefields. The implementation of the CPML boundary does not need to split velocity and stress fields, and is easily incorporated into the RSG-FD program.

The CPML absorption boundary with the selection of parameters is detailed in **Appendix**. The algorithm is developed by modifying the complex coefficient S_k and introducing the auxiliary variables d_k , α_k , and χ_k , where d_k denotes the damping profile, and two real variables $\chi_k \geq 1$ and $\alpha_k \geq 0$. Substituting **Eq. A4** into **Eq. A2** yields,

$$\partial \tilde{x}_k = \frac{1}{S_k} \partial x_k = \left[\frac{1}{\chi_k} - \frac{d_k}{\chi_k^2 (i\omega + a_k + d_k/\chi_k)} \right] \partial x_k = \frac{1}{\chi_k} \partial x_k + \tilde{\psi}_k \quad (34)$$

where $\tilde{\psi}_k$ is a memory variable that can be rewritten as

$$i\omega \tilde{\psi}_k + \left(a_k + \frac{d_k}{\chi_k} \right) \tilde{\psi}_k = -\frac{d_k}{\chi_k^2} \partial x_k \quad (35)$$

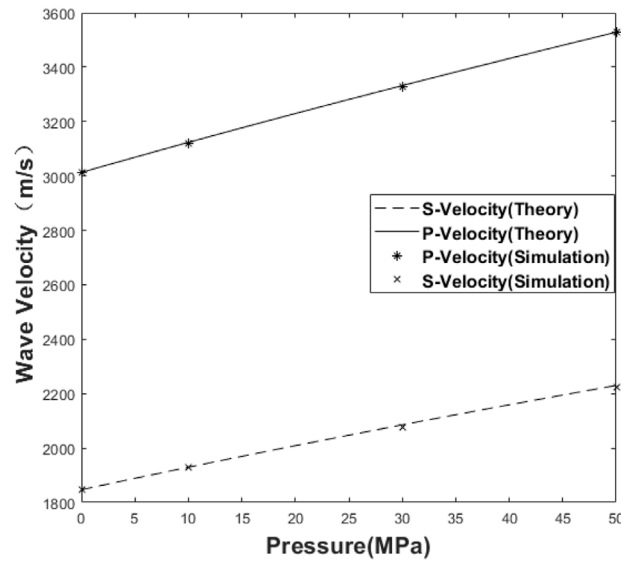


FIGURE 5 | Comparison of the theoretical and calculated wave velocities for both the P-wave and S-wave as a function of hydrostatic prestresses ($\theta_1 = 0^\circ$).

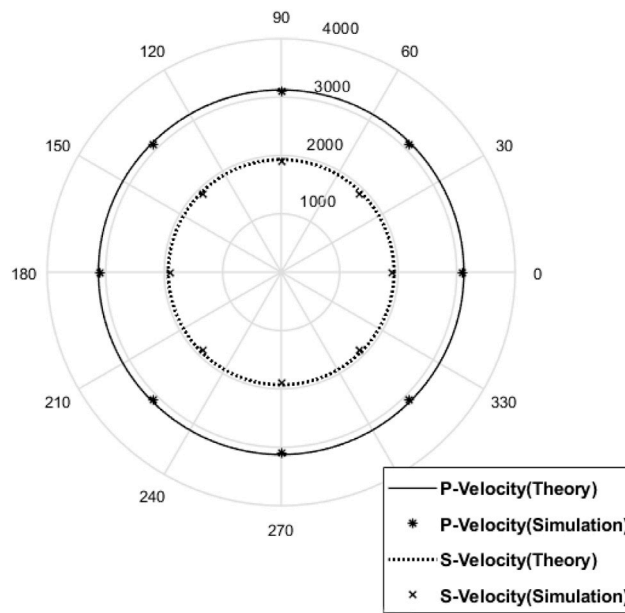


FIGURE 6 | Comparison of the theoretical and calculated wave velocities for both the P-wave and S-wave under the same pressure (10 MPa) but with different directions.

Using an inverse Fourier transform to Eq. 35, we have,

$$\frac{\partial \psi_k}{\partial t} + \left(a_k + \frac{d_k}{\chi_k} \right) \psi_k = -\frac{d_k}{\chi_k^2} \partial x_k \quad (36)$$

where ψ_k is the inverse of $\tilde{\psi}_k$. This equation has an iterative solution of the form,

$$\psi_k^n = \psi_k^{n-1} e^{-(a_k + d_k/\chi_k)\Delta t} + \frac{d_k \partial x_k}{\chi_k (a_k \chi_k + d_k)} (e^{-(a_k + d_k/\chi_k)\Delta t} - 1) \quad (37)$$

Equation 37 is derived simply by solving a first-order differential equation, leading to the same result in

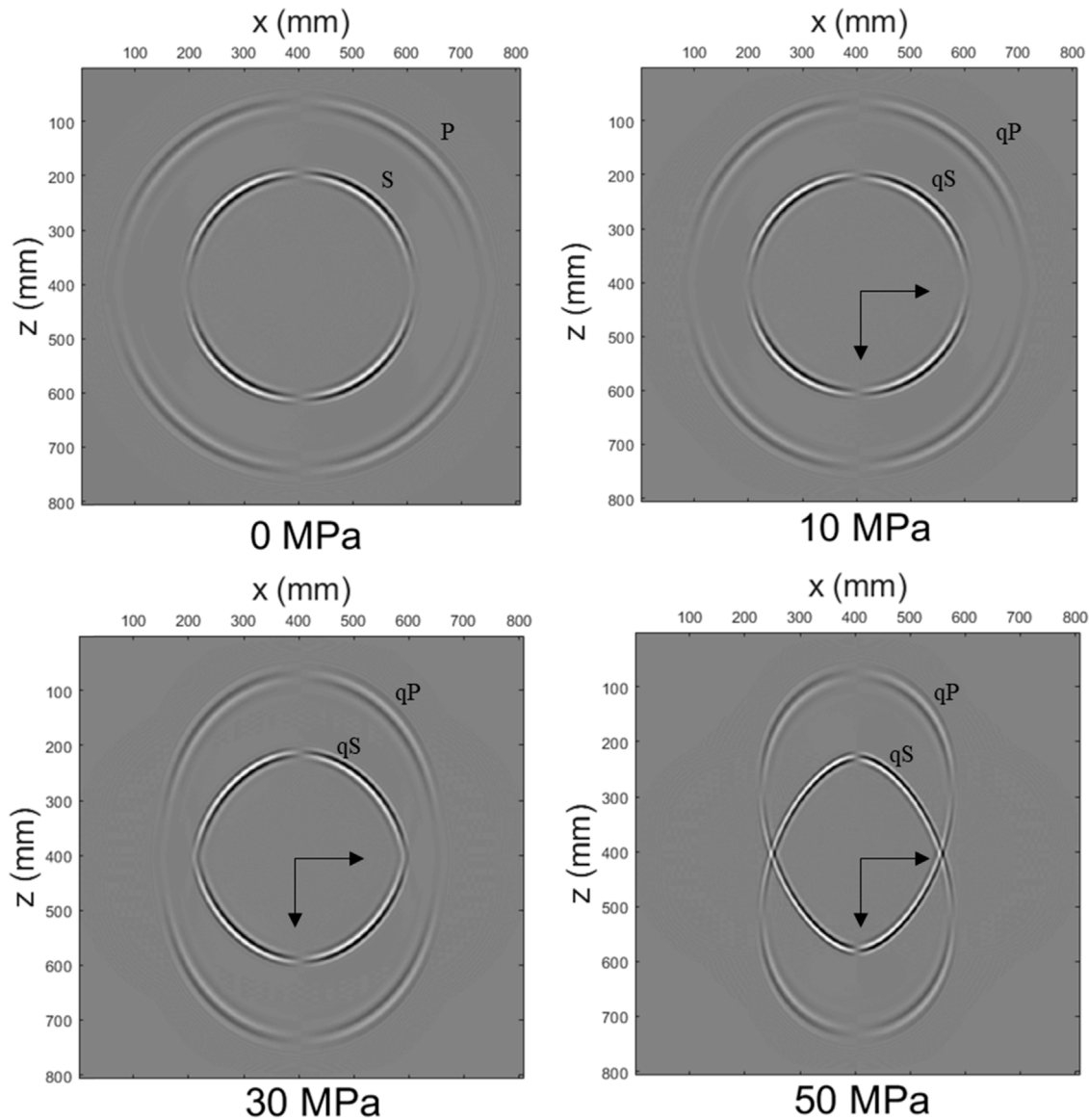


FIGURE 7 | Wavefield snapshots of the x-component of the particle velocity at $t = 0.12$ ms for various uniaxial stresses. The arrow indicates the principal strain direction calculated by **Eq. 45**.

Komatitsch and Martin (2007) obtained by a recursive convolution method.

The CPML absorbing boundary for the first-order velocity-stress formulation of acoustoelastic equations can be implemented by 1) applying **Eqs. 27–38** for the estimation of various memory variables in the rotated operators, 2) substituting these memory variables into **Eq. 34** to obtain the spatial derivatives of all the field components in the stretched coordinates, and 3) substituting the resulting spatial derivatives into the velocity-stress formulas (**Eq. 22**) to yield the following C-PML formulation of acoustoelastic equations,

$$\begin{cases} \rho \dot{v}_x = \frac{1}{\chi_x} \partial_x \tau_{xx} + \psi_{x,\tau_{xx}} + \frac{1}{\chi_z} \partial_z \tau_{xz} + \psi_{z,\tau_{xz}}, \\ \rho \dot{v}_z = \frac{1}{\chi_x} \partial_x \tau_{xz} + \psi_{x,\tau_{xz}} + \frac{1}{\chi_z} \partial_z \tau_{zz} + \psi_{z,\tau_{zz}}, \\ \dot{\tau}_{xx} = A_{11} \left(\frac{1}{\chi_x} \partial_x v_x + \psi_{x,v_x} \right) + A_{13} \left(\frac{1}{\chi_x} \partial_x v_z + \psi_{z,v_x} \right) + A_{15} \left(\frac{1}{\chi_z} \partial_z v_x + \psi_{x,v_z} + \frac{1}{\chi_x} \partial_x v_z + \psi_{x,v_z} \right), \\ \dot{\tau}_{zz} = A_{13} \left(\frac{1}{\chi_x} \partial_x v_x + \psi_{x,v_x} \right) + A_{33} \left(\frac{1}{\chi_z} \partial_z v_z + \psi_{z,v_z} \right) + A_{35} \left(\frac{1}{\chi_x} \partial_x v_x + \psi_{x,v_x} + \frac{1}{\chi_z} \partial_z v_z + \psi_{z,v_z} \right), \\ \dot{\tau}_{xz} = A_{15} \left(\frac{1}{\chi_x} \partial_x v_x + \psi_{x,v_x} \right) + A_{35} \left(\frac{1}{\chi_z} \partial_z v_z + \psi_{z,v_z} \right) + A_{55} \left(\frac{1}{\chi_x} \partial_x v_x + \psi_{x,v_x} + \frac{1}{\chi_z} \partial_z v_z + \psi_{z,v_z} \right). \end{cases} \quad (38)$$

Stability Analysis

The stability criterion for the velocity-stress RSG-FD operator with equal grid spacings can be generally expressed as the following inequality (Masson et al., 2006),

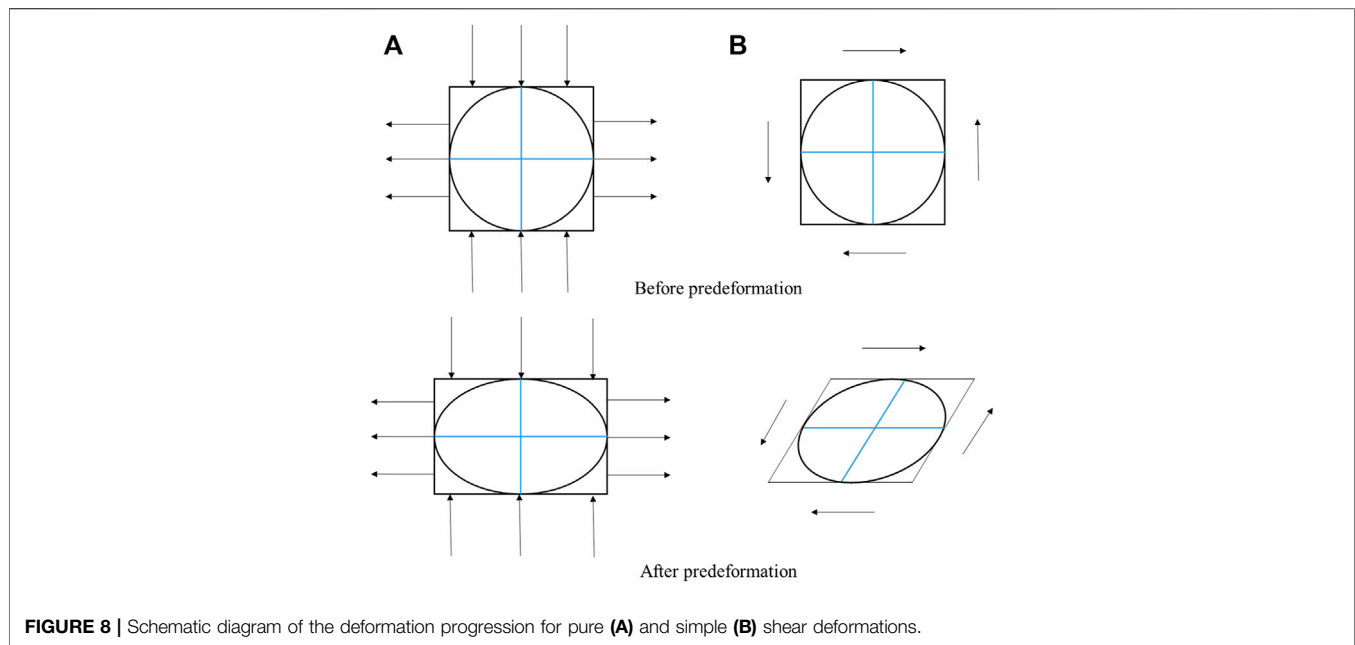


FIGURE 8 | Schematic diagram of the deformation progression for pure (A) and simple (B) shear deformations.

$$\frac{\Delta t V_{\max}}{\Delta r} \leq C, \quad (39)$$

with

$$C = \frac{1}{\sqrt{D} \sum_{k=1}^n |c_k|}, \quad (40)$$

where V_{\max} represents the maximum phase velocity in the medium, D represents the spatial dimension, and c_n are the differential coefficients depending on the order of the spatial operator. For an eighth-order spatial and second-order temporal 2D FD operators with coefficients $c_1 = \frac{1225}{1024}$, $c_2 = -\frac{245}{3072}$, $c_3 = \frac{49}{5120}$, and $c_4 = -\frac{5}{7168}$, we can calculate $C = 0.5497$.

Numerical dispersion is one of the main factors affecting the accuracy of the finite-difference method. To reduce the level of numerical dispersions in the RSG-FD method, a discretization interval should be selected to ensure a good number of grid points n_λ per minimum wavelength, which is generally calculated by

$$n_\lambda = \frac{V_{\min}}{\Delta r f_{\max}}, \quad (41)$$

where V_{\min} is the minimum phase velocity and f_{\max} is the maximum frequency, usually taken as four times the center frequency of the source. Dispersion errors accumulate with increasing propagation distances, which can be reduced by refining grids. Numerical experiments by Chen et al. (2006) show that no less than 3 grid points per wavelength are required for the RSG eighth-order operator.

Numerical Examples

In this section, we calculate wavefield snapshots under various prestress conditions. The RSG-FD numerical method is applied to the first-order velocity-stress acoustoelastic equations. The

effective second-order elastic constants, generally as shown in Eq. 11, can be further simplified in terms of prestressed conditions addressed as follows.

To simplify calculations, we set the y -direction of the model to infinity, so that the 3D case is simplified into a plane strain problem. Numerical examples are calculated using the properties from the Portland sandstone (807×807) mm with the bulk and shear moduli and density set to 9.7 GPa, 7.3 GPa, and 2,140 kg/m³ (Winkler and Liu, 1996), respectively. The third-order elastic constants (A, B, C) = (−1,122, −419, −340) GPa. The RSG-FD numerical simulation is conducted by the eighth-order spatial and second-order temporal FD operators. The source is a vertical force located at the center of the model domain with the time history,

$$s(t) = (t - t_0)e^{-[\pi f_0(t-t_0)]^2}, \quad (42)$$

where the central frequency $f_0 = 1.42$ MHz, and t_0 is a delay time. According to Eq. 35 where the maximum frequency $f_{\max} = 4f_0$ and $n_\lambda = 3$ (Chen et al., 2006), we obtain $V_{\min} = 1704$ m/s as the condition of stability. Generally, for a given frequency, we determine the maximum velocity of the medium v_{\max} at a maximum prestress 50 MPa, but with v_{\min} at 0 MPa. From the parameters listed above, we can obtain $v_{\max} = v_P = 3,528$ m/s at 50 MPa and $v_{\min} = v_S = 1,848$ m/s at 0 MPa, which enables a time step of $2 \cdot 10^{-7}$ s and a grid size of 10^{-4} m to satisfy the condition of stability.

Acoustoelastic Simulation Under the Confining Prestress

For this case, the stress field is isotropic under the hydrostatic stress P , leading to the same stress and strain in all the directions. The principal strain components can be expressed as,

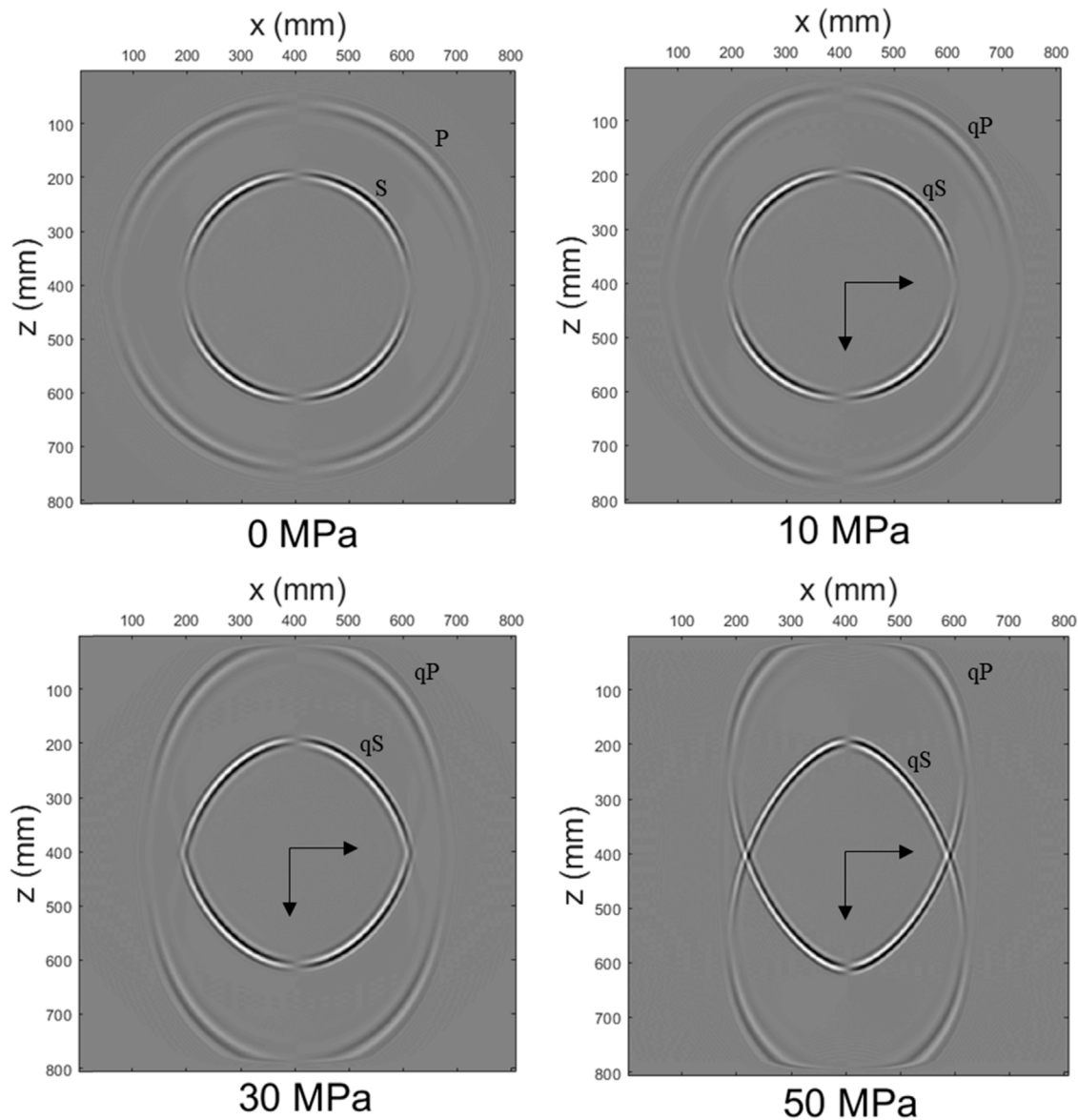


FIGURE 9 | Wavefield snapshots of the x -component of the particle velocity at $t = 0.12$ ms for various pure-shear stresses. The arrow indicates the principal strain direction calculated by **Eq. 47**.

$$\begin{cases} e_{11} = e_{33} = -\frac{P}{3K}, \\ e_{13} = 0. \end{cases} \quad (43)$$

Substituting into **Eq. 11** leads to a stiffness matrix

$$\begin{cases} A_{11} = \lambda + 2\mu + (2\lambda + 4\mu + 4C + 8B + 2A)(-P/3K), \\ A_{33} = \lambda + 2\mu + (2\lambda + 4\mu + 4C + 8B + 2A)(-P/3K), \\ A_{55} = \mu + (2\mu + 2B + A)(-P/3K), \\ A_{13} = \lambda + (2\lambda + 4C + 4B)(-P/3K), \\ A_{51} = 0, \\ A_{53} = 0. \end{cases}, \quad (44)$$

Wavefield snapshots are calculated with increasing hydrostatic stresses, as shown in **Figure 4** for the x -component of the particle velocity at $t = 0.12$ ms. We see that the stress-induced velocity variations are isotropic, with the amplitude along the wavefront changing in accordance with the characteristics of a vertical force source. We calculate the theoretical wave velocity by **Eqs. 20, 21**. **Figure 5** compares the theoretical and simulated wave velocities at the same angle but with different prestresses. **Figure 6** compares the theoretical and calculated wave velocities under the same pressure (10 MPa) but with different directions. Both the theoretical and simulated wave velocities agree well under the different prestress conditions. These comparisons validate numerical simulations at least in travel time.

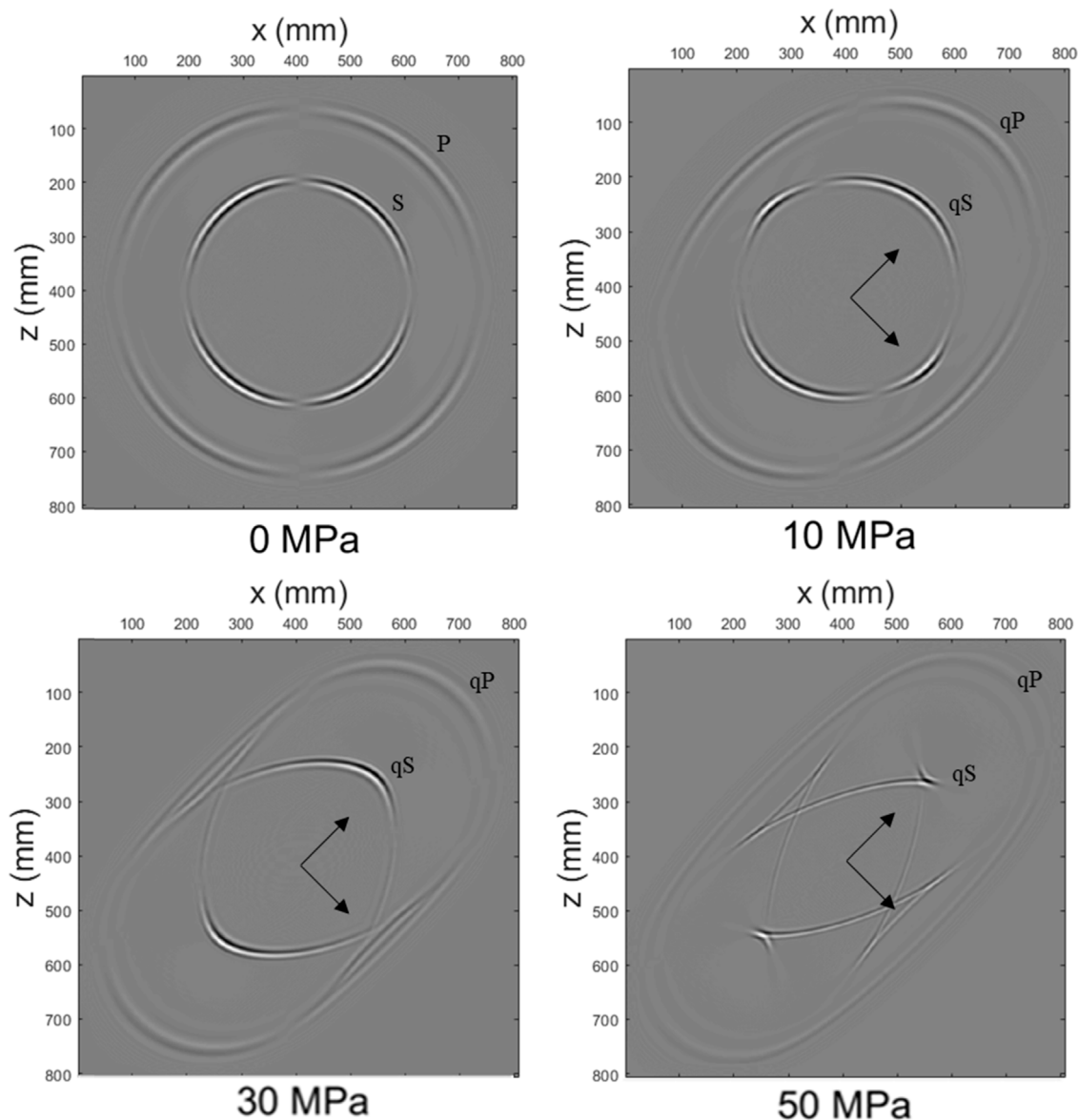


FIGURE 10 | Wavefield snapshots of the x -component of the particle velocity at $t = 0.12$ ms for various simple shear stresses. The arrow indicates the principal strain direction calculated by **Eq. 49**.

Acoustoelastic Simulation Under the Uniaxial Prestress

For this case, the stress field is anisotropic under the uniaxial stress P . The principal strain components can be expressed as

$$\begin{cases} e_{11} = \frac{P(\lambda + \mu)}{\mu(3\lambda + 2\mu)}, \\ e_{33} = -\frac{P\lambda}{2\mu(3\lambda + 2\mu)}, \\ e_{13} = 0. \end{cases} \quad (45)$$

The corresponding stiffness matrix becomes,

$$\begin{cases} A_{11} = \lambda + 2\mu + (3\lambda + 6\mu + 2C + 6B + 2A)e_{11} + (2B + 2C - \lambda - 2\mu)e_{33}, \\ A_{33} = \lambda + 2\mu + (2B + 2C - \lambda - 2\mu)e_{11} + (6B + 2C + 2A + 3\lambda + 6\mu)e_{33}, \\ A_{55} = \mu + \left(\mu + B + \frac{A}{2}\right)e_{11} + \left(\mu + B + \frac{A}{2}\right)e_{33}, \\ A_{13} = \lambda + (\lambda + 2C + 2B)e_{11} + (2B + 2C + \lambda)e_{33}, \\ A_{51} = 0, \\ A_{53} = 0, \end{cases} \quad (46)$$

Figure 7 shows the wavefield snapshots with increasing uniaxial stresses for the x -component of the particle velocity at $t = 0.12$ ms. With increasing uniaxial stresses, the P-wave and S-wave are gradually coupled together, with the

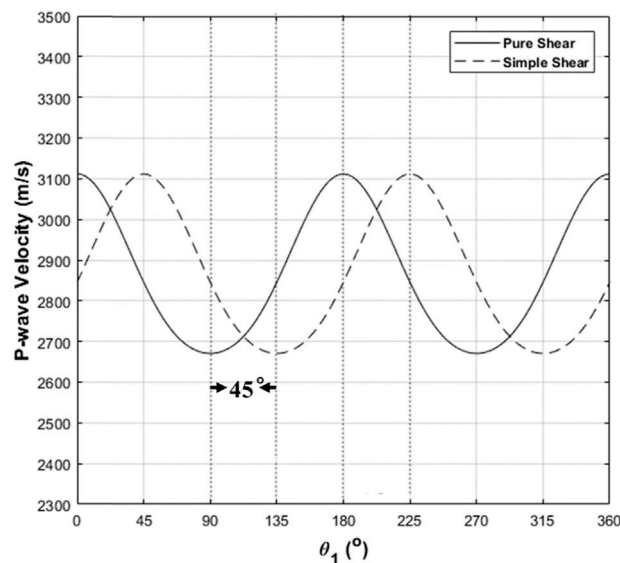


FIGURE 11 | Variations of P-wave velocity against θ_1 under the pure-shear (solid line) and simple-shear (dashed line) conditions.

wavefronts of qP-wave and qS-wave becoming more elliptical due to the stress-induced anisotropy of velocities. For $p = 10$ MPa, the qP-wave becomes elliptical slightly, but the qS-wave is almost a circle. For $p = 30$ MPa, we see a trigeminal region occurring symmetrically to connect the qS-wave and the qP-wave. The oval aspect ratio of the qP-wave becomes larger, implying an increasing velocity anisotropy on the longitudinal and transverse symmetry axes. For $p = 50$ MPa, we see more pronounced trigeminal region, approximately rhombic qS-wave, and elliptical qP-wave. Under the anisotropic predeformed condition, the polarization direction changes with the propagation direction, but neither parallel nor perpendicular to the propagation direction. These polarized waves are usually denoted by qP and qS, with their wavefronts deforming along the x -axis as the uniaxial stress increases. The azimuthal anisotropy of qP-wave is more and more obvious than that of the qS-wave, consistent with the mechanical mechanism of uniaxial stress. We calculate the principal strain direction according to **Eq. 45** and mark it in the figure. It coincides with the directions of maximum/minimum velocities, which validates our numerical simulations. Thus, the directions of the velocity principal axis can indicate the directions of the principal strain for this case.

Acoustoelastic Simulation Under the Shear Prestress

As shown in **Figure 8**, the shear prestress can be classified into two cases: pure-shear and simple-shear deformations (Means and Williams, 1976). Different pre-deformations correspond to the different geological features. In order to identify these geological features in the seismic wave field, the simulations of pure shear and simple shear wavefield are carried out. For the former (see **Figure 8A**), the principal strain direction does not rotate with the progression of deformations, which is also called the non-rotational deformation or the coaxial

deformation. In this case, the horizontal elongation and vertical contraction of deformations occur simultaneously under the uniaxial loading. The geological tensile and compressive effects produce a pure shear deformation.

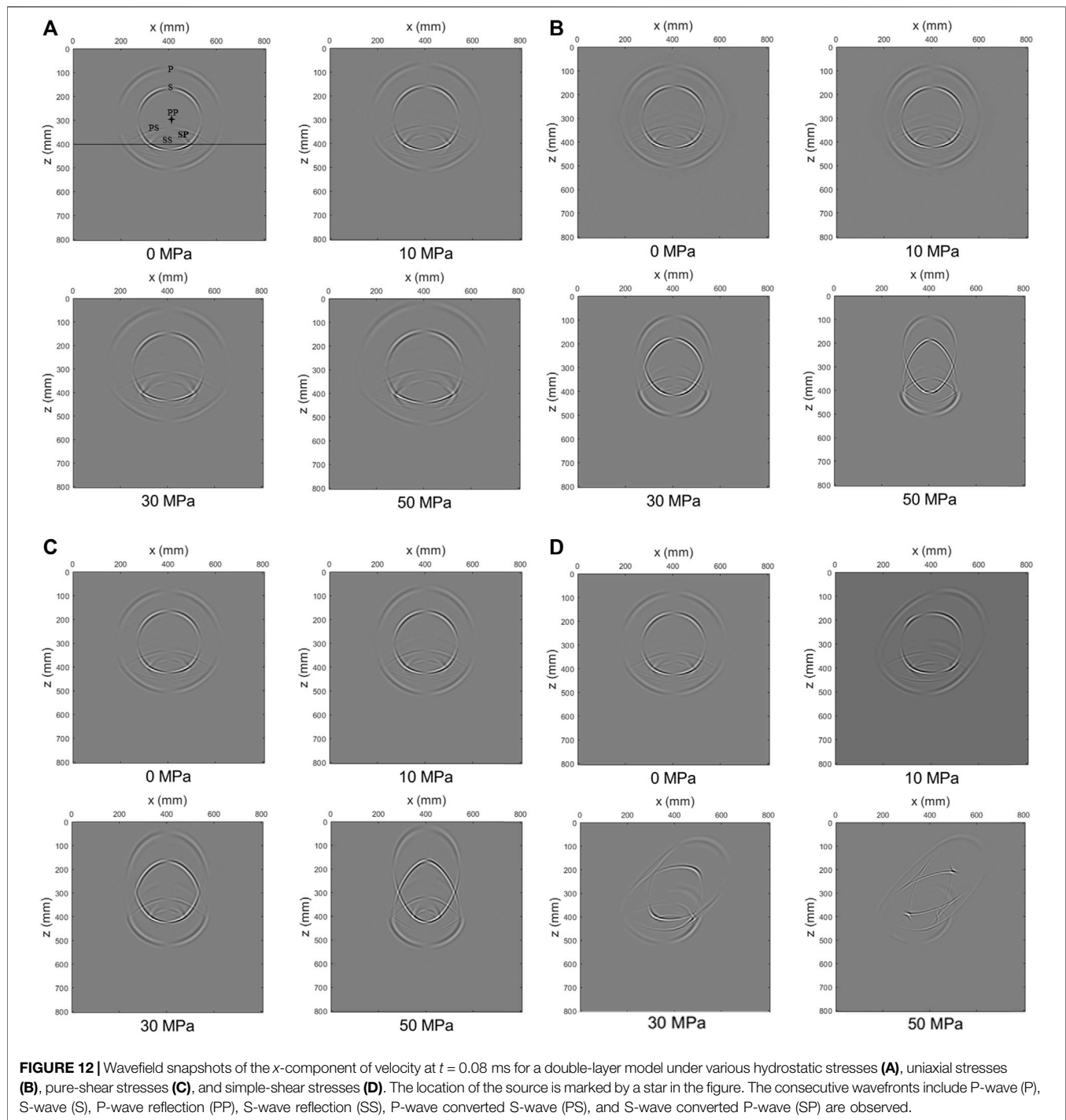
The principal strain components for the pure-shear prestress become,

$$\begin{cases} e_{11} = -e_{33} = \frac{P}{\lambda + 2\mu}, \\ e_{13} = 0, \end{cases} \quad (47)$$

yielding the following stiffness matrix,

$$\begin{cases} A_{11} = \lambda + 2\mu + (4\lambda + 8\mu + 4B - 2A)e_{11}, \\ A_{33} = \lambda + 2\mu - (4\lambda + 8\mu + 4B - 2A)e_{11}, \\ A_{55} = \mu, \\ A_{13} = \lambda, \\ A_{53} = 0, \\ A_{51} = 0. \end{cases} \quad (48)$$

Wavefield snapshots are calculated with increasing pure-shear stresses and shown in **Figure 9** for the x -component of the particle velocity at $t = 0.12$ ms. Similar to the case of uniaxial stresses, the circular wavefront at 0 MPa becomes more and more elliptical with increasing pure-shear stresses. The same changes in azimuthal anisotropy and amplitude can be seen as the uniaxial case. Unlike the uniaxial pressure condition, the absolute values of strains along the two axes of a pure-shear stress field are the same, implying that the stress-induced velocity anisotropy is more sensitive under the pure-shear prestress. Therefore, the velocities of qP-wave and qS-wave increase much more in the z -axis direction compared to the uniaxial case, as shown in **Figure 7**. We also calculate the principal strain direction according to **Eq. 47** and mark it in the figure. It coincides with the directions of



maximum/minimum velocities. Similarly, the directions of the velocity principal axis indicate the directions of the principal strain.

The deformation under the simple-shear prestress, as shown in **Figure 8B**, is rotational deformation or non-coaxial deformation. The direction and magnitude of two principal strains vary with increasing shear stresses, except

for the strain parallel to the shear plane. Simple shear deformation is caused by shear sliding of a series of parallel sliding layers. For the simple-shear prestress, we have,

$$\begin{cases} e_{13} = \frac{P}{\mu}, \\ e_{11} = e_{33} = 0, \end{cases} \quad (49)$$

with the stiffness matrix as

$$\begin{cases} A_{11} = \lambda + 2\mu, \\ A_{33} = \lambda + 2\mu, \\ A_{55} = \mu, \\ A_{13} = \lambda, \\ A_{53} = (2\lambda + 4\mu + 2B - A)e_{13}, \\ A_{51} = (2\lambda + 4\mu + 2B - A)e_{13}. \end{cases} \quad (50)$$

Wavefield snapshots are calculated with increasing shear stresses and shown in **Figure 10** for the x -component of the particle velocity at $t = 0.12$ ms, respectively. We see that the wavefront characterizes the orientation of stresses. The stress-induced anisotropy becomes stronger with increasing stresses. Unlike the pure-shear stress loading, the axis of symmetry rotates in terms of stress orientations, which is consistent with the characteristics of shear stresses. The wavefronts of qP-wave and qS-wave become more elliptical and rotational with increasing shear stresses.

To improve the understanding of the phenomenon observed in **Figures 9, 10**, we compare the changes in the P-wave velocity with θ_1 under both the pure-shear and simple-shear conditions, as shown in **Figure 11**. We see that the principal axis in the simple-shear case is shifted by about 45° relative to that in the pure-shear case, which is consistent with the direction by a shift of the principal strain axis. Therefore, the shift of the velocity principal axis direction can be used to judge the geological characteristics of the region.

Acoustoelastic Simulation for a Double-Layer Model

The double-layer model, separated by a plane interface, is presented to investigate the reflection/transmission at the interface under the four different cases of loading prestress. The upper medium has the same properties as previous simulations. The lower medium has $K = 5.6$ GPa, $\mu = 2.3$ GPa (A, B, C) = (-23, -10, -13) GPa, and $\rho = 1,200$ kg/m³. Consider an interface between two elastic media indicated by the + and - superscripts. The boundary condition at the interface requires the continuity of tractions and displacements. These conditions could be written as

$$\begin{cases} \tau_{ij}^+ n_j = \tau_{ij}^- n_j, \\ u_i^+ = u_i^-, \end{cases} \quad (51)$$

where n_i represents the unit normal to the interface. Einstein's summation convention for repeating indices is assumed.

Figure 12 shows the x -component of the particle velocity snapshots at $t = 0.08$ ms under four different prestress conditions: hydrostatic, uniaxial stress, pure-shear, and simple-shear stresses. The location of the source is marked by a star in **Figure 12A**. All the wave types of reflection/transmission can be observed from these snapshots which illustrate that the stress-induced velocity anisotropy is strongly related to the orientation of prestresses.

CONCLUSION

Acoustoelastic theory describes wave propagation in prestressed media and relates elastic wave velocities to prestresses, resulting from the third-order elasticity with a cubic term for the strain energy function. We propose an acoustoelastic modeling scheme for elastic wave propagation in prestressed media based on the RSG-FD method with the CPML absorbing boundary. The RSG-FD numerical method is applied to the first-order velocity-stress acoustoelastic equations. We address several aspects in the numerical implementation. Four states of prestress, confining-hydrostatic, uniaxial-stress, pure-shear, and simple-shear patterns, are investigated with different simplified stiffness matrices to model the prestress-induced anisotropy of velocities and its effect on the characteristics of wavefronts. The main conclusions can be summarized as follows.

- 1) A plane-wave analysis combined with closed-pore jacketed sandstone experiments illustrates the effect of third-order elastic constants on the P- and S-wave velocities under various prestresses. For most consolidated rocks, the third-order elasticity could be enough to describe the nonlinear stress dependence of velocity variations.
- 2) We partially validate the presented numerical scheme by the plane-wave theoretical solution. Comparisons between theoretical and calculated wave velocities are performed at the same angle but with different prestresses and under the same pressure (10 MPa) but with different directions, respectively.
- 3) Acoustoelastic simulations demonstrate that the confining prestress leads to the same stress and strain in all the directions, yielding isotropic velocity variations, whereas the uniaxial stress generates an anisotropic stress field, making the P-wave and S-wave be gradually coupled together, with the wavefronts of qP-wave and qS-wave becoming more elliptical due to the stress-induced anisotropy of velocities.
- 4) The pure-shear prestress with a coaxial deformation (horizontal elongation and vertical contraction) induces obvious elliptical wavefronts because of the stress-induced anisotropy of velocities that, unlike the uniaxial prestress, becomes more sensitive to the z -axis direction along which the velocities of qP-wave and qS-wave increase much more compared with the uniaxial case.
- 5) Unlike the pure-shear stress loading, the simple-shear prestress with a non-coaxial rotational deformation rotates the axis of symmetry in terms of stress orientations. The direction and magnitude of strains vary with increasing shear stresses, except for the strain parallel to the shear plane. The stress-induced anisotropy of velocities is sensitive to the orientation of stresses. the wavefronts of qP-wave and qS-wave become more elliptical and rotational with increasing shear stresses.
- 6) Numerical acoustoelastic simulations provide us with the possibility to explore wave propagation in deep high-

pressure formations. However, the third-order elastic constants used are limited to isotropic solid media without microstructures. Considering that fractures are sensitive to prestress conditions, we will develop numerical schemes for anisotropic acoustoelastic equations of fractured media in the near future.

DATA AVAILABILITY STATEMENT

The original contributions presented in the study are included in the article/Supplementary Material, further inquiries can be directed to the corresponding author.

REFERENCES

- Alkhimenkov, Y., Räss, L., Khakimova, L., Quintal, B., and Podladchikov, Y. (2021). Resolving Wave Propagation in Anisotropic Poroelastic media Using Graphical Processing Units (GPUs). *J. Geophys. Res. Solid Earth* e2020JB021175. doi:10.1029/2020jb021175
- Carcione, J. M. (1999). Staggered Mesh for the Anisotropic and Viscoelastic Wave Equation. *Geophysics* 64, 1863–1866. doi:10.1190/1.1444692
- Carcione, J. M. (2007). *Wavefields in Real Media: Wave Propagation in Anisotropic, Anelastic, Porous and Electromagnetic Media*. 2nd Edn. Elsevier Science.
- Chen, H., Wang, X., and Lin, W. (2006). Parallel Numerical Simulation of the Ultrasonic Waves in a Prestressed Formation. *Ultrasonics* 44, e1013–e1017. doi:10.1016/j.ultras.2006.05.049
- Cruse, E. (1990). High-order (Space and Time) Finite-Difference Modeling of the Elastic Wave Equation. *60th Annu. Internat. Mtg., Soc. Expl. Geophys., Expanded Abstr.* 90, 987
- Fang, X., Fehler, M., Zhu, Z., Chen, T., Brown, S., Cheng, A., et al. (2013). An Approach for Predicting Stress-Induced Anisotropy Around a Borehole. *Geophysics* 78, D143–D150. doi:10.1190/geo2012-0145.1
- Gao, K., and Huang, L. (2017). An Improved Rotated Staggered-Grid Finite-Difference Method with Fourth-Order Temporal Accuracy for Elastic-Wave Modeling in Anisotropic media. *J. Comput. Phys.* 350, 361–386. doi:10.1016/j.jcp.2017.08.053
- Goldberg, Z. A. (1961). Interaction of Plane Longitudinal and Transverse Elastic Waves. *Sov. Phys. Acoust.* 63, 306–310.
- Green, R. E. (1973). Ultrasonic Investigation of Mechanical Properties.” in *Treatise on Materials Science and Technology*, Vol. 3. New York: Academic Press.
- Gregor, D., Moczo, P., Kristek, J., Mesgouez, A., Lefeuvre-Mesgouez, G., and Kristekova, M. (2021). Subcell-resolution Finite-Difference Modelling of Seismic Waves in Biot and JKD Poroelastic media. *Geophys. J. Int.* 224, 760. doi:10.1093/gji/ggaa454
- Hu, Y., and McMechan, G. (2010). Sensitivity of Three-Component 3D Finite-difference Elastic Seismic Modeling to Inclusion Parameters in HTI and TTI media with High Inclusion Density. *Geophysics* 75, 48–61. doi:10.1190/1.3358159
- Huang, X., Burns, D. R., and Toksöz, M. N. (2001). *The Effect of Stresses on the Sound Velocity in Rocks: Theory of Acoustoelasticity and Experimental Measurements*. Tech. Report. Boston: Earth Resources Laboratory, Massachusetts Institute of Technology.
- Johnson, P. A., and Shankland, T. J. (1989). Nonlinear Generation of Elastic Waves in Granite and sandstone: Continuous Wave and Travel Time Observations. *J. Geophys. Res.* 94, 17729–17733. doi:10.1029/jb094ib12p17729
- Komatitsch, D., and Martin, R. (2007). An Unsplit Convolutional Perfectly Matched Layer Improved at Grazing Incidence for the Seismic Wave Equation. *Geophysics* 72, SM155–SM167. doi:10.1190/1.2757586
- Li, Y., Liu, H., Wang, Y., Liu, Y., Liu, T., and Luo, Q. (2020). Acoustoelastic Effect Simulation by Time-Space Finite Element Formulation Based on Quadratic Interpolation of the Acceleration. *Wave Motion* 93, 102465. doi:10.1016/j.wavemoti.2019.102465

AUTHOR CONTRIBUTIONS

L-YF and HY conceive this research. HY writes the manuscript and prepares the figures. L-YF and B-YF reviews and supervises the manuscript. The coauthors TM are involved in the discussion of the manuscript. All authors finally approve the manuscript and thus agree to be accountable for this work.

FUNDING

The research was supported by the National Natural Science Foundation of China (Grant Nos. 41,821,002, 41,720,104,006).

- Lisitsa, V., and Vishnevskiy, D. (2010). Lebedev Scheme for the Numerical Simulation of Wave Propagation in 3D Anisotropic Elasticity. *Geophys. Prospecting* 58, 619–635. doi:10.1111/j.1365-2478.2009.00862.x
- Liu, Q. H., and Sinha, B. K. (2000). Multipole Acoustic Waveforms in Fluid-filled Boreholes in Biaxially Stressed Formations: A Finite-difference Method. *Geophysics* 65, 190–201. doi:10.1190/1.1444710
- Lys, E., Romenski, E., Tcheverda, V., Epov, M., and Epov, M. I. (2015). “Finite-difference Simulation of Wave Propagation through Prestressed Elastic media,” in *International Conference on Finite Difference Methods* (Springer), 282–289. doi:10.1007/978-3-319-20239-6_30
- Martin, R., and Komatitsch, D. (2009). An Unsplit Convolutional Perfectly Matched Layer Technique Improved at Grazing Incidence for the Viscoelastic Wave Equation. *Geophys. J. Int.* 179, 333–344. doi:10.1111/j.1365-246x.2009.04278.x
- Masson, Y. J., Pride, S. R., and Nihei, K. T. (2006). Finite Difference Modeling of Biot’s Poroelastic Equations at Seismic Frequencies. *Modeling of Biot’s Poroelastic Equations at Seismic Frequencies. J. Geophys. Res.* 111, B10305. doi:10.1029/2006jb004366
- Mavko, G., Mukerji, T., and Godfrey, N. (1995). Predicting Stress-induced Velocity Anisotropy in Rocks. *Geophysics* 60, 1081–1087. doi:10.1190/1.1443836
- Means, W. D., and Williams, P. F. (1976). *An Outline of Structural Geology*. John Wiley.
- Meegan, G. D., Jr, Johnson, P. A., Guyer, R. A., and McCall, K. R. (1993). Observations of Nonlinear Elastic Wave Behavior in sandstone. *The J. Acoust. Soc. America* 94, 3387–3391. doi:10.1121/1.407191
- Moczo, P., Gregor, D., Kristek, J., and de la Puente, J. (2019). A Discrete Representation of Material Heterogeneity for the Finite-Difference Modelling of Seismic Wave Propagation in a Poroelastic Medium. *Geophys. J. Int.* 216, 1072–1099. doi:10.1093/gji/ggy412
- Moczo, P., Kristek, J., Vavryčuk, V., Archuleta, R. J., and Halada, L. (2002). 3D Heterogeneous Staggered-Grid Finite-Difference Modeling of Seismic Motion with Volume Harmonic and Arithmetic Averaging of Elastic Moduli and Densities. *Bull. Seismological Soc. America* 92, 3042–3066. doi:10.1785/0120010167
- Norris, A. N. (1983). Propagation of Plane Waves in a Pre-stressed Elastic Medium. *J. Acoust. Soc. America* 74, 1642–1643. doi:10.1121/1.390131
- Pao, Y.-H., Sachse, W., and Fukuoka, H. (1984). “Acoustoelasticity and Ultrasonic Measurements of Residual Stresses,” in *Physical Acoustics, Principles and Methods*. Editors W. P. Mason and R. N. Thurston (Orlando: Academic Press), 17, 61–143.
- Pao, Y. H., and Gamer, U. (1985). Acoustoelastic Waves in Orthotropic media. *J. Acoust. Soc. America* 77, 806–812. doi:10.1121/1.392384
- Pau, A., and Vestroni, F. (2019). The Role of Material and Geometric Nonlinearities in Acoustoelasticity. *Wave Motion* 86, 79–90. doi:10.1016/j.wavemoti.2018.12.005
- Pei, Z., Fu, L.-Y., Sun, W., Jiang, T., and Zhou, B. (2012). Anisotropic Finite-Difference Algorithm for Modeling Elastic Wave Propagation in Fractured Coalbeds. *Geophysics* 77, C13–C26. doi:10.1190/geo2010-0240.1
- Saenger, E. H., and Bohlen, T. (2004). Finite-difference Modeling of Viscoelastic and Anisotropic Wave Propagation Using the Rotated Staggered Grid. *Geophysics* 69, 583–591. doi:10.1190/1.1707078
- Saenger, E. H., Gold, N., and Shapiro, S. A. (2000). Modeling the Propagation of Elastic Waves Using a Modified Finite-Difference Grid. *Wave Motion* 31, 77–92. doi:10.1016/s0165-2125(99)00023-2

- Saenger, E. H., and Shapiro, S. A. (2002). Effective Velocities in Fractured media: a Numerical Study Using the Rotated Staggered Finite-Difference Grid. *Geophys. Prospect.* 50, 183–194. doi:10.1046/j.1365-2478.2002.00309.x
- Seron, F. J., Badal, J., and Sabadell, F. J. (1996). A Numerical Laboratory for Simulation and Visualization of Seismic Wavefields1. *Geophys. Prospect.* 44, 603–642. doi:10.1111/j.1365-2478.1996.tb00168.x
- Shams, M., Destradé, M., and Ogden, R. W. (2011). Initial Stresses in Elastic Solids: Constitutive Laws and Acoustoelasticity. *Wave Motion* 48, 552–567. doi:10.1016/j.wavemoti.2011.04.004
- Sinha, B. K., and Kostek, S. (1996). Stress-induced Azimuthal Anisotropy in Borehole Flexural Waves. *Geophysics* 61, 1899–1907. doi:10.1190/1.1444105
- Thurston, R. N., and Brugger, K. (1964). Third-order Elastic Constants and the Velocity of Small Amplitude Elastic Waves in Homogeneously Stressed media. *Phys. Rev.* 133, 1604–1610. doi:10.1103/physrev.133.a1604
- Toupin, R. A., and Bernstein, B. (1961). Sound Waves in Deformed Perfectly Elastic Materials. Acoustoelastic Effect. *J. Acoust. Soc. America* 33, 216–225. doi:10.1121/1.1908623
- Virieux, J. (1986). P-SV Wave Propagation in Heterogeneous media: Velocity-stress Finite-difference Method. *Geophysics* 51, 889–901. doi:10.1190/1.1442147
- Winkler, K. W., and Liu, X. (1996). Measurements of Third-order Elastic Constants in Rocks. *J. Acoust. Soc. America* 100, 1392–1398. doi:10.1121/1.415986
- Yang, Y., Ng, C. T., Mohabuth, M., and Kotousov, A. (2019). Finite Element Prediction of Acoustoelastic Effect Associated with Lamb Wave Propagation in Pre-stressed Plates. *Smart Mater. Struct.* 28, 095007. doi:10.1088/1361-665x/ab2dd3
- Zhang, Y., Fu, L.-Y., Zhang, L., Wei, W., and Guan, X. (2014). Finite Difference Modeling of Ultrasonic Propagation (Coda Waves) in Digital Porous Cores with Un-split Convolutional PML and Rotated Staggered Grid. *J. Appl. Geophys.* 104, 75–89. doi:10.1016/j.jappgeo.2014.02.012
- Zong, J. (2014). *Elastic Properties of Salt: Laboratory Measurements, Well-Log Analysis, and a Seismic Survey over the Hockley Salt Mine, Texas. Master Thesis.* Texas: University of Houston.

Conflict of Interest: The authors declare that the research was conducted in the absence of any commercial or financial relationships that could be construed as a potential conflict of interest.

Publisher's Note: All claims expressed in this article are solely those of the authors and do not necessarily represent those of their affiliated organizations, or those of the publisher, the editors and the reviewers. Any product that may be evaluated in this article, or claim that may be made by its manufacturer, is not guaranteed or endorsed by the publisher.

Copyright © 2022 Yang, Fu, Fu and Müller. This is an open-access article distributed under the terms of the Creative Commons Attribution License (CC BY). The use, distribution or reproduction in other forums is permitted, provided the original author(s) and the copyright owner(s) are credited and that the original publication in this journal is cited, in accordance with accepted academic practice. No use, distribution or reproduction is permitted which does not comply with these terms.

CPML ABSORBING BOUNDARY

This appendix summarizes the CPML absorption boundary (Komatitsch and Martin, 2007; Martin and Komatitsch, 2009). The conventional PML absorption boundary formulates various memory variables in the FD operator from the Cartesian coordinate to the complex coordinate by introducing a complex factor

$$\tilde{x} = x - \frac{i}{\omega} \int_0^x d_x(s) ds, \quad (\text{A1})$$

where $i = \sqrt{-1}$ and ω is the angular frequency. The damping factor $d_x(s) = 0$ inside the computational domain and $d_x(s) > 0$ in the PML region. The regular coordinate variable x is replaced by the complex coordinate variable \tilde{x} , with the corresponding differential operator as

$$\partial_{\tilde{x}} = \frac{1}{S_x} \partial_x, \quad (\text{A2})$$

where

$$S_x = \frac{i\omega + d_x}{i\omega} = 1 + \frac{d_x}{i\omega}. \quad (\text{A3})$$

The PML formulation is implemented directly by changing original wave equations written in terms of the variable x into new equations in terms of the variable \tilde{x} .

The conventional PML absorption boundary suffers from poor accuracy at grazing incidences. It also requires much memory and computation. The problem is related to the complex coefficient S_x in Eq. A3. The CPML approach improves the performance of the PML by introducing two

auxiliary variables, α_x and χ_x . The modified complex coefficient becomes

$$S_x = \chi_x + \frac{d_x}{\alpha_x + i\omega}, \quad (\text{A4})$$

where $\chi_x \geq 1$ and $\alpha_x \geq 0$.

The CPML absorption boundary involves a number of absorption parameters. The maximum damping factor is usually set as

$$d_{\max} = -\frac{(m+1)V_{\max}}{2L} \ln(R), \quad (\text{A5})$$

where V_{\max} is the maximum phase velocity in the medium, L is the thickness of the absorption boundary layer, R is the theoretical reflection coefficient, and m is the order of the polynomial (typically 2 or 3). The damping factor can be determined by

$$d_x(l) = d_{\max} \left(\frac{l}{L} \right)^m, \quad (\text{A6})$$

where l ($0 \leq l \leq L$) is the distance from the calculated point to the boundary. The other parameters are accordingly set as

$$\chi_x = 1 + (\chi_{\max} - 1) \left(\frac{l}{L} \right)^m, \quad (\text{A7})$$

and

$$\alpha_x = \pi \left(1 - \frac{l}{L} \right) \alpha_{\max} \quad (\text{A8})$$

The auxiliary variable α_x varies linearly between 0 and α_{\max} in the absorption region. We usually take $\alpha_{\max} = f_0$ with f_0 the main frequency of the source. For $\alpha_{\max} = 0$ and $\chi_x = 1$, S_x is reduced to that of the conventional PML boundary.



Geodynamics Based on Solidification of Liquid/Molten Substances in the Earth's Interior

Xin Li¹, Mingjiang Tao² and Duanwei He^{1,3*}

¹Institute of Atomic and Molecular Physics, Sichuan University, Chengdu, China, ²School of Electrical Engineering, Southwest Jiaotong University, Chengdu, China, ³Key Laboratory of High Energy Density Physics and Technology of Ministry of Education, Sichuan University, Chengdu, China

OPEN ACCESS

Edited by:

Lidong Dai,

Institute of Geochemistry (CAS), China

Reviewed by:

Feiwu Zhang,

Institute of Geochemistry (CAS), China

Yu He,

Institute of Chemistry (CAS), China

Lei Liu,

China Earthquake Administration,

China

*Correspondence:

Duanwei He

duanweihe@scu.edu.cn

Specialty section:

This article was submitted to

Solid Earth Geophysics,

a section of the journal

Frontiers in Earth Science

Received: 17 March 2022

Accepted: 04 April 2022

Published: 03 May 2022

Citation:

Li X, Tao M and He D (2022)

Geodynamics Based on Solidification

of Liquid/Molten Substances in the

Earth's Interior.

Front. Earth Sci. 10:898190.

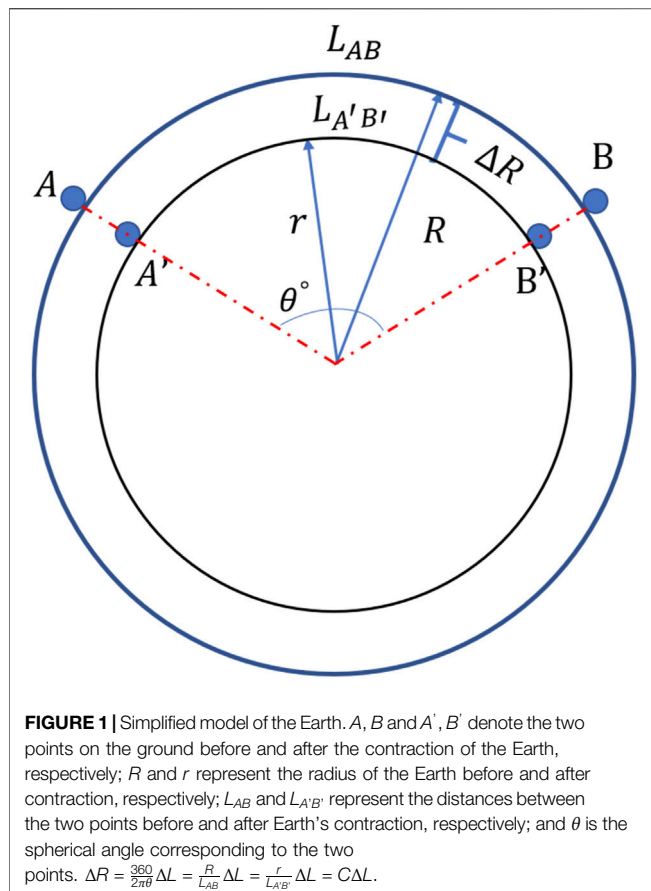
doi: 10.3389/feart.2022.898190

Since its formation, the Earth has cooled from molten magma to the present layered structure. The liquid and molten substance in the interior of the Earth continuously solidifies, radiating heat to the outer space and causing changes in the pressure and density inside the Earth. Constrained by the rigid lithosphere, the change in density decreases the pressure at the bottom of the crust, and thereby supports the rigid lithosphere. Under the effect of gravity, there is an increased interaction between tectonic plates, which leads to local stress accumulation. Eventually, this stress exceeds the strength of the rock and makes the mechanical structure of the crustal lithosphere unstable. This process is iterative, and the Earth continuously adjusts to new mechanical equilibria by releasing the accumulated stress through geological events such as earthquakes. In this study, using three sets of observations (Global Positioning System data, length of day data, and the latent heat of Earth solidification), we show that these observations are consistent with the aforementioned assumption that the solidification of liquid cause changes in density and volume in the Earth's interior. Mechanical analyses indicate that liquid solidification in the interior of the Earth leads to decrease in the Earth's volume. This increases the intensity of plate interactions, which leads to the movement of large plates, triggering geological events such as earthquakes. Thus, it is determined that liquid solidification in the Earth's interior is the main source for the movement of plates.

Keywords: liquid-solid transition, variation of Earth's volume and radius, seismic mechanism, crustal ultimate load, geodynamics

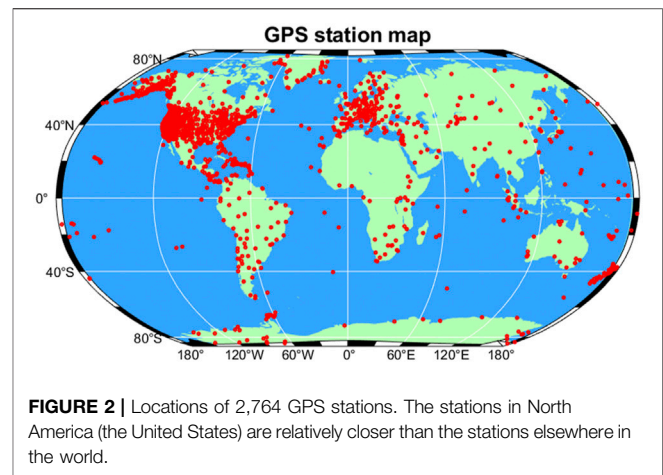
INTRODUCTION

The Earth has evolved from a molten state (magma ocean) to today's layered structure *via* large-scale cooling and solidification (Elkins-Tanton, 2012). The cooling and solidification continue as the Earth keeps evolving and emitting energy (46 ± 3 TW, as estimated from the current global heat flow) (Lay et al., 2008). The difference between then and now is that the early magma ocean might have solidified faster. These contents of the Earth's core go through molten-solid transitions at physical conditions (pressure and temperature) that change according to the thermodynamics and evolution of the Earth. Solidification is a universal and crucial phenomenon, and it leads to noticeable changes in density accompanied by heat release and volume contraction (Dziewonski and Anderson, 1981; Massonne et al., 2007; Sakamaki et al., 2010; Hirose et al., 2013). Global magmatism, reaching a rate of $25.8\text{--}33.6 \text{ km}^3 \text{ yr}^{-1}$, is caused due to magma solidification at the shallow Earth (Wilson, 2007). At



deep Earth, the inner core grows at a rate of $0.5\text{--}2.4 \text{ mm yr}^{-1}$ due to crystallization of molten iron (Labrosse et al., 2001; Ohta et al., 2016; Bono et al., 2019). Released latent heat is a key heat source that influences the processes such as inner core growth and the geodynamo. Thus, solidification governs the thermodynamics of the Earth (Buffett et al., 1992; Buffett, 2000). The lithosphere, the topmost layer of the Earth, is a poor conductor of heat, and it is mechanically rigid and brittle (Shimada and Cho, 1990; Rychert and Shearer, 2009; Whittington et al., 2009). It operates like a ceramic outer shell, constraining the ductile mantle beneath it. The energy released by the solidification of melts in the Earth powers the dynamics of the Earth's lithosphere and plate tectonics. The liquid–solid conversion in the Earth's interior is a continuous process, and it leads to continuous heat dissipation to the outer space. Under the law of conservation of mass, the change in density due to solidification reflects a volume change, which eventually leads to the geometric variation of the Earth.

Modern space geodesy techniques have revealed that the Earth's geometry is continuously changing and is not constant. Geodetic studies employing the data obtained from various techniques, such as Global Positioning System (GPS), Satellite Laser Ranging (SLR), Very Long Baseline Interferometry (VLBI), and Doppler Orbitography and Radiopositioning Integrated by Satellite (DORIS), suggest that the current rate of change of the Earth's radius spans from -4.0 to 1.3 mm yr^{-1} . Because of this, it is unclear whether the Earth is expanding or contracting and also



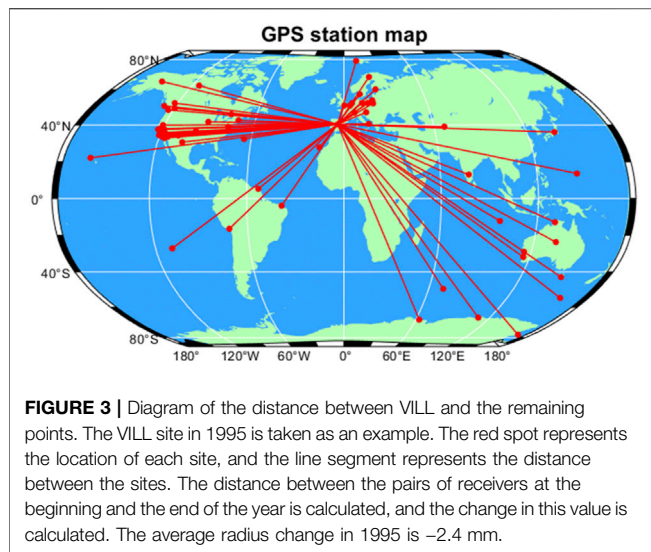
difficult to determine the extent of the change (Huang et al., 2002; Sun et al., 2006; Wu et al., 2011; Zhu et al., 2013). The paleomagnetic data indicate that the radius of the ancient Earth was 0.99–1.12 times of that of the present radius in the late Paleozoic and early Mesozoic Era (Cox and Doell, 1961; Ward, 1963). Another evidence of the varying nature of the Earth's geometry is the Earth's rotation rate, which has been observed to fluctuate in the interdecadal and longer periods as recorded based on the values of length of day (LOD). The changes in LOD are associated with the change of the Earth's moment of inertia and impacts of large earthquakes (Stephenson and Morrison, 1984; Chao and Gross, 1987; Holme and De Viron, 2013).

The liquid and molten substance inside the Earth continues to solidify with the latent heat release and volume and density changes. Heat radiates to the surface *via* conduction, convective, radiation, and so on, and the volume change macroscopically manifests as volume contraction of the Earth. The volume contraction causes the tectonic plates to squeeze together, making them move under the influence of gravity, which in turn leads to various geological events. The traditional plate motion driving force model (mantle convection, slab pull, and ridge push) (Forsyth and Uyeda, 1975; Bott, 1991; Bokelmann, 2002a; Bokelmann, 2002b; van Summeren et al., 2012) has some limitations, as it cannot reasonably explain the plate motion cycle (Sun, 2019). Herein, we propose that the solidification of the Earth drives the dynamics of the Earth's crust and gives rise to the volume variation of the Earth, and this theory is verified *via* the analyses of GPS data, LOD observations, and global heat flow estimates.

THEORY VALIDATION

Global Positioning System Data Analysis

The solidification of molten substance leads to changes in the internal volume, and it macroscopically manifests as the collapse of the Earth's volume. If this happened, akin to a deflating balloon, the Earth's radius would decrease, thereby decreasing



the distance between the corresponding points on the Earth's surface. When the Earth is considered a standard sphere, there is a definite relationship between the reduction of the Earth's radius and any changes in distance between the two points on the surface, as shown in **Figure 1**.

Herein, variations in the radius and volume of the Earth are derived from the GPS data of 2,674 ground-based receivers during 1995–2019. A detailed site information is presented in **Figure 2**. These GPS data, recorded by NASA and processed by the Jet Propulsion Laboratory, provide the time series of longitude, latitude, and altitude of the individual sites over time (Heflin, 1994). The relationship between the change in distance (ΔL) of two receivers and the change in the Earth's radius (ΔR) is given using **Eq. 1**:

$$\Delta R = C \Delta L, \quad (1)$$

where $\Delta R = r - R$ and $\Delta L = L_{AB} - L_{A'B'} = R/L$ (**Figure 1**). R is the current radius of the Earth ($= 6,371$ km), and d is the distance between the two receivers. The Haversine formula (**Eq. 2**) is used to calculate the distance (L) between the two receivers (Josiah, 2010):

$$\text{haversin}\left(\frac{L}{R}\right) = \text{haversin}(\varphi_2 - \varphi_1) + \cos \varphi_2 \cos \varphi_1 \text{haversin}(\Delta \lambda), \quad (2)$$

where $\text{haversin}\left(\frac{L}{R}\right) = \sin\left(\frac{L}{2R}\right)^2$, φ_2 and φ_1 denote the latitudes of two points, and $\Delta \lambda$ denotes the difference in their longitudes.

The data are processed by a self-written Python code. The arc length between any two stations on the Earth is calculated. Then, the relation between the annual radius change of the Earth and the change in the arc length between the two sites is given using **Eq. 3**:

$$\Delta \bar{R} = \frac{1}{n} \sum_i^n \left\{ \frac{1}{m} \sum_j^m \left[\frac{R}{L_j} (L_j - L'_j) \right] \right\}, \quad (3)$$

where i is the i -th year of calculation, n is the total number of years, j denotes the j -th pair of sites, m is the total number of j in

year i , and L_j , L'_j are the arc distance of the j -th pair at the beginning of the i -th year and the end of i -th year, respectively. By using the error propagation law and GPS positioning error estimation, the accuracy estimate of the annual radius variation of the Earth can be obtained, and the average relative error is 15%.

During data processing, the data from sites whose observation time was less than 12 months for any year are omitted. To reduce errors caused by certain geological factors at close range, only those points are considered for which the distance is ≥ 100 km. For example, taking the calculation of 1995, we draw a diagram of one of the points (VILL) as shown in **Figure 3**. According to the longitude and latitude information of each station, the change of distance between the two sites with time is obtained, and the corresponding change in radius is determined. The average of the change in the Earth's radius for 1995 is obtained by traversing the distances among all the points, and the value is -2.4 ± 0.27 mm.

A total number of 14 million calculations are carried out for ΔR , and 25 annual average radius changes from 1995 to 2019 are derived, among which, 20 results are negative, as shown in **Figure 4**. The annual average $\Delta \bar{R}$ is -1.65 ± 0.25 mm yr $^{-1}$, which corresponds to a volume decrease of -841.60 ± 127.5 km 3 yr $^{-1}$.

Latent Heat of Earth Solidification

The global heat flow is estimated to be 46 TW, and it mainly comprises radiogenic heat and heat from the core and mantle (Lay et al., 2008). The most accessible integrative energy for the planet is the total amount released at the surface. However, there may be uncertainties in the present-day energy budget. Specifically, there is considerable uncertainty in the radiogenic concentrations (Gessmann and Wood, 2002; Murthy et al., 2003) and the present-day mantle and core secular cooling rates (Lay

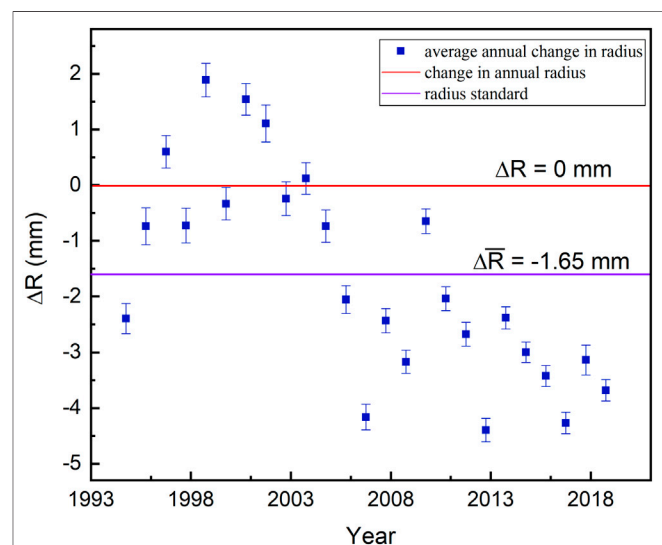


FIGURE 4 | Annual average radius changes of the Earth from 1995 to 2019. Black circles: average change of Earth's radius in that year; red and purple lines represent the annual average radius change (0 and -1.65 mm yr $^{-1}$, respectively). 20 out of 25 results are negative.

TABLE 1 | Values of the specific latent heat and densities of the melt and solid used for latent heat analysis (Ohtani and Maeda, 2001; Suzuki and Ohtani, 2003; Massonne et al., 2007; Sakamaki et al., 2009; Zhang et al., 2014; Zhang et al., 2020).

	Specific latent heat (L , J/g)	Density of melt (ρ_{melt} , g/cm ³)	Density of solid (ρ_{solid} , g/cm ³)
Earth's core	600	9.9	10.1
Earth's crust	418	2.9	3.3

et al., 2008; Herzberg et al., 2010). Although geoneutrino detectors promise new constraints in the near future (Araki et al., 2005; Dye, 2012), macroscopically, the Earth's internal temperature distribution is constant, and secular cooling can be neglected over a short period of time. The results of Chang 'e-5 samples research showed that the characteristics of creep-potassium enrichment in the basalt were formed in the late magmatic period, thus ruling out the main hypothesis that this moon mantle source region is rich in radioactive thermogenic elements (Hu et al., 2021; Li et al., 2021; Tian et al., 2021). The world's uranium deposits do not overlap with the geothermal anomalies. This suggests that there is not a lot of radioactive material in the Earth's crust. Thus, radioactive heat may not be a major source of heat loss on the Earth.

According to the thermal evolution of the Earth, the latent heat released from solidification of molten substance is considered an important heat source on the Earth. Herein, to simplify the calculation, the total energy budget of the Earth is assumed to comprise only latent and crustal radiogenic heat. The latent heat released from solidification of the Earth is calculated using Eq. 4:

$$Q_t = Q_m + Q_c + Q_r, \quad (4)$$

where Q_t is the total heat flow, Q_m is the latent heat of the mantle and crust, Q_c is the latent heat of the core, and Q_r is the radioactive heat from the Earth's crust (from direct sample sources). The volume change caused by solidification is calculated using Eq. 5:

$$\Delta V = \frac{m}{\rho_{\text{molten}}} - \frac{m}{\rho_{\text{solid}}}, \quad (5)$$

where $m = Q/L$ is the mass of solidified substance, Q stands for Q_c and Q_m , respectively, L is the specific latent heat, and ρ_{molten} ρ_{solid} are the densities of melts and solids, respectively. The specific values are shown in Table 1.

When $Q_c = 3$ TW (Stacey and Loper, 2007), the mass of the solidified iron alloy is 1.6×10^{14} kg yr⁻¹, and it corresponds to $\Delta V = -0.24$ km³ yr⁻¹. $\Delta R = -1.6 \times 10^{-3}$ mm yr⁻¹ corresponds to the amount of solidification in the core. Because of the uncertainty of the radioactive heat in the mantle and core and the nonoverlap between uranium deposits and geothermal anomalies around the world, we consider the crustal radioactive heat from the direct rock samples as the entire radioactive heat, omitting other radioactive heat for the time being. Thus, Q_r is assumed to be 7 TW (Lay et al., 2008), and we get $Q_m = Q_t - Q_r - Q_c = 36$ TW. The mass of the magma

solidified at the shallow Earth is 2.7×10^{15} kg yr⁻¹, which corresponds to a volume change of -120 km³ yr⁻¹ and a radius change of -0.24 mm yr⁻¹. Overall, the heat flow of the Earth is in agreement with a shrinkage of -120.24 km³ yr⁻¹ in the Earth's volume. This process considers the total solidification rather than the net solidification. However, if melting is also considered when computing the contributions of the crystallization process, it will make the calculation more complex and the volume changes involved may be smaller.

Analysis of Diurnal Length Variation

The variation of the Earth's moment of inertia is calculated using the LOD data and angular momentum conservation. Based on occultation and solar and lunar eclipses, the long-term average change rate of LOD in the last 1,000 years is determined to be approximately -0.01 ms yr⁻¹ (Stephenson and Morrison, 1984). The LOD variation associated with large earthquakes is estimated to be approximately 0.0102 ms yr⁻¹, and the direct LOD observation suggests a rate of -0.0371 ms yr⁻¹ (O'Connell and Dziewonski, 1976).

When the conservation of angular momentum is achieved, the variation in LOD manifests as the variation of the radius (Eq. 6):

$$L = m\omega r^2 = I_1\omega_1 = I_2\omega_2, \quad (6)$$

where m is the mass of the Earth, r is its radius, I and ω are its moment of inertia and angular velocity, 1 and 2 denote the first state of the Earth with a radius of 6,371 km and the second state where the Earth's radius is decreased by an annual average radius change, respectively. The moment of inertia of the Earth is calculated by dividing it into several shells and approximating the integral with respect to r by summation, as shown in Eq. 7:

$$I_{\text{total}} = \sum_{i=1}^n I_i, \quad (7)$$

where I_i is the moment of inertia of each layer and ω_1 ω_2 are calculated using Eqs 8, 9:

$$\omega_1 = \frac{2\pi}{86400} = 7.27 \times 10^{-5} \text{ (rad s}^{-1}\text{)}, \quad (8)$$

$$\omega_2 = \frac{2\pi}{86400 - \Delta\text{LOD}}, \quad (9)$$

where ΔLOD is the average variation of LOD. Herein, the Earth is divided into 638 shells, each with a thickness of 10 km and a homogeneous density distribution. The moment of inertia of the i th shell is calculated using Eq. 10:

$$I_i = \frac{2}{5} m_i \left(\frac{r_{i2}^5 - r_{i1}^5}{r_{i2}^3 - r_{i1}^3} \right), \quad (10)$$

where r_{i1} and r_{i2} are the inner and outer radii of i th shell, respectively, and m_i is its mass, which is calculated as $m_i = \frac{4}{3} \pi (r_{i2}^3 - r_{i1}^3) \rho_i$. The density (ρ_i) of each shell is obtained using the PREM model (Dziewonski and Anderson, 1981). The total moment of inertia of the Earth in the first state (I_1) is 7.98×10^{37} kg m². For the second state, the annual average radius change for the Earth's core is set to -1.6×10^{-6} m yr⁻¹ at the topmost outer core in accordance with the latent heat analysis

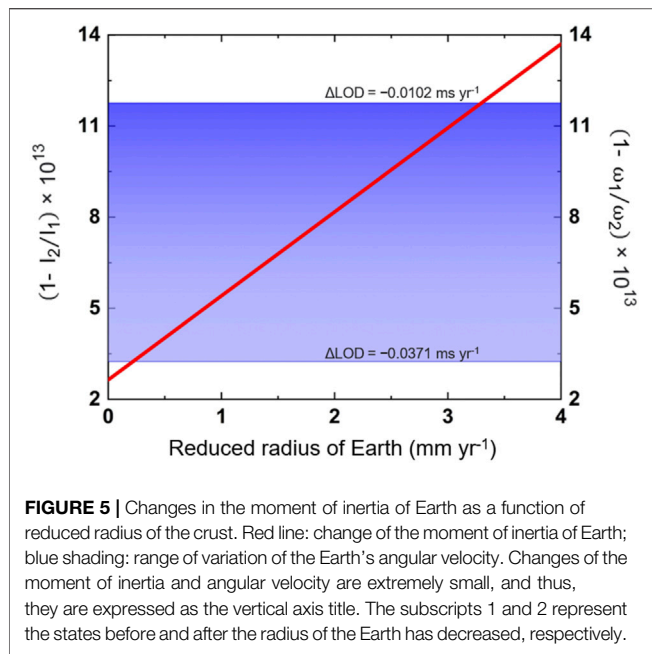


FIGURE 5 | Changes in the moment of inertia of Earth as a function of reduced radius of the crust. Red line: change of the moment of inertia of Earth; blue shading: range of variation of the Earth's angular velocity. Changes of the moment of inertia and angular velocity are extremely small, and thus, they are expressed as the vertical axis title. The subscripts 1 and 2 represent the states before and after the radius of the Earth has decreased, respectively.

and that for the Earth's crust is a variable (Δr). The inner and outer radii of shells in the second state (r'_{i1} and r'_{i2}) are less than that in the first state owing to change in the Earth's radius. The moment of inertia of the 348th shell (the first shell is the center of Earth) at the topmost outer core where the radius is 3,471 km (r_2) is calculated using Eq. 11:

$$I_i = \frac{2}{5} m_{348} \left(\frac{r_{i2}^5 - r_{i1}^5}{r_{i2}^3 - r_{i1}^3} \right), \quad (11)$$

where $r'_{i2} = r_2 - 1.6 \times 10^{-3} \text{ mm}$. The moments of inertia of shells from 349th to 637th are calculated using Eq. 12:

$$I_i = \frac{2}{5} m_i \left(\frac{r_{i2}^5 - r_{i1}^5}{r_{i2}^3 - r_{i1}^3} \right), \quad (12)$$

where $r'_{i1} = r_{i1} - 1.6 \times 10^{-6} \left(\frac{3471}{r_{i1}} \right)^2$ and $r'_{i2} = r_{i2} - 1.6 \times 10^{-6} \left(\frac{3471}{r_{i2}} \right)^2$. The moment of inertia of the last shell (638th) is calculated using Eq. 13:

$$I_{638} = \frac{2}{5} m_{638} \left(\frac{(r'_{6382} - \Delta r)^5 - r_{6381}^5}{(r'_{6382} - \Delta r)^3 - r_{6381}^3} \right). \quad (13)$$

The total moments of inertia of the Earth in the first and second states are quite similar due to minute changes in the radius, and thus, $(1 - I_{2nd}/I_{1st})10^{13}$ and $(1 - \omega_1/\omega_2)10^{13}$ are introduced for comparison in Figure 5. When the angular momentum conservation is realized, the radius change is -0.2 to -3.3 mm yr^{-1} , which corresponds to a volume change of -111 to $-1,676 \text{ km}^3 \text{ yr}^{-1}$.

Summary

The annual average volume variation of the Earth obtained from the analysis of GPS data, LOD observations, and global heat flux

estimates are $-841.60 \text{ km}^3 \text{ yr}^{-1}$, $-120.24 \text{ km}^3 \text{ yr}^{-1}$, and -111 to $-1,676 \text{ km}^3 \text{ yr}^{-1}$, respectively, and these are in good agreement with each other. The values are on the same order of magnitude but with some differences, which can be attributed to the uncertainty of global heat flux estimates and the specific latent heat reported in previous studies. The density profile of the Earth and density of iron under high pressure and high temperature are also likely sources of uncertainty. Moreover, the GPS tracking stations are sparsely distributed in some regions, which could have led to the gaps in data. Nevertheless, these results are sufficient for validating the theory of solidification-driven dynamics of the Earth.

MECHANICAL ANALYSIS

The molten substance in the Earth's interior continues to solidify. When the volume change at the shallow Earth due to solidification accumulates, after a specific peak value is reached, the pressure changes because of which the rigid lithosphere become mechanically unstable and eventually fails, decreasing the Earth's radius and volume. The volume shrinkage increases the influence of gravity on the crust, triggering a pressure drop at the bottom of the lithosphere and a large-scale fracture and dislocation of the overlying strata, which induces geological events such as earthquakes. This is similar to the elastic buckling load that an ordinary spherical shell model can bear under external pressure. The Earth's crust is thus simplified by a spherical shell model, and the ultimate load of the spherical shell is calculated. For a spherical shell, the ultimate load is only 70% of the ideal case because of the accuracy, and the ultimate load P_c that can sustain under external pressure is calculated using Eq. 14 (Pan and Cui, 2010),

$$P_c = 0.7 \times \frac{2E}{\sqrt{3(1-\mu^2)}} \left(\frac{t}{R} \right)^2, \quad (14)$$

where E and μ are Young's modulus and Poisson's ratio of crustal rocks, t is the mean thickness of the crust (30 km), and R is the mean radius of the sphere (6,371 km). For most crustal rocks, values of Poisson's ratio are between 0.2 and 0.3 (Hyndman, 1979; Zandt and Ammon, 1995; Wang, 2009). Herein, an average value of 0.25 is selected to simplify the calculation. For most crustal rocks, values of Young's moduli vary in the range 20–100 GPa (Wang, 2009); we selected the maximum and minimum values to get a range. Therefore, according to the crustal temperature and pressure conditions at different depths ($\leq 30 \text{ km}$), we obtained $P_c = 0.37\text{--}1.85 \text{ MPa}$.

The results show that the limit load of the overlying crust is small and much less than the stress caused by self-weight ($\sim 1000 \text{ MPa}$). However, it can exist stably because of the support of the lower shell. When the magma solidifies, more magma diffuses up to occupy the newly available volume, which decreases the density and pressure and increases the influence of gravity on the crust, as shown in Figure 6. Eventually, for the new shell to reach mechanical equilibrium, the buildup strain is released in the form of earthquakes and other geologic

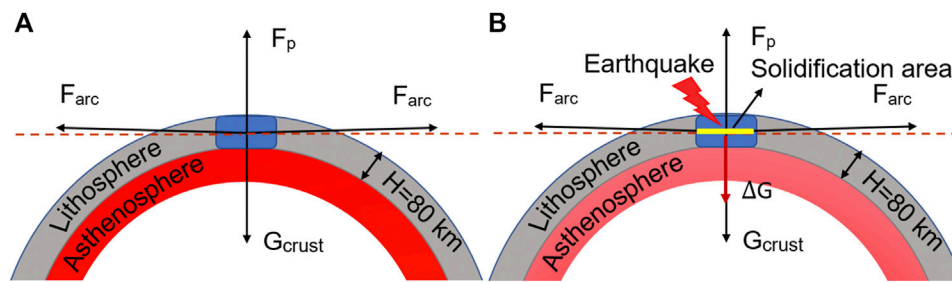


FIGURE 6 | The mechanical models of the Earth before and after solidification. Red shading: density of magma, a darker color implies greater density; F_p denotes supporting the force of asthenosphere, and F_{arc} denotes the circumferential force. **(A)** The mechanical structure of the overlying crust is balanced before solidification. **(B)** When the magma continues solidifying, it accumulates the weight of the overlying crust, and the mechanical structure of the overlying crust becomes unstable when its limit load is reached, causing collapse and rupture and triggering an earthquake.

activities. The pressure change (ΔP) caused by the increase of gravity of the solidified magma (ΔG) is calculated using Eq. 15:

$$\Delta P = \frac{\Delta G}{S} = \frac{mg}{S}, \quad (15)$$

where g is the gravitational constant, m is the mass of the solidified magma, and S is the solidified area. Since the stress accumulated by magma solidification is released by earthquakes, herein, we assume that the area of solidified magma is equal to the area of the earthquake's hardest-hit area. The relationship between the radius and intensity in the worst-hit area is given using Eq. 16 (Bath, 2013):

$$I_0 - I = 3 \log \frac{d^2 + h^2}{h^2}, \quad (16)$$

where I_0 is the maximum intensity, I is the intensity of the site located at distance d from the epicenter, and h is the mean focal depth. The maximum intensity can be obtained from the magnitude (M) (Båth, 1975) using Eq. 17:

$$M = 0.62I_0 + 1.68 \log_{10} h - 0.95. \quad (17)$$

Taking the hardest-hit area of Mw 8 earthquake as an example, the results show that the pressure change (ΔP) is 1.84–5.51 MPa, and it decreases with increasing depth. As shown in Figure 7, the pressure variation within a depth of 30 km exceeds the ultimate load of the crust. Small changes in the interior can cause the mechanical structure of the Earth's crust to break down, and when the strain is beyond the strength limit of the crust, geological movements such as earthquakes are triggered. This finding is consistent with the depth and frequency of the shallow earthquakes.

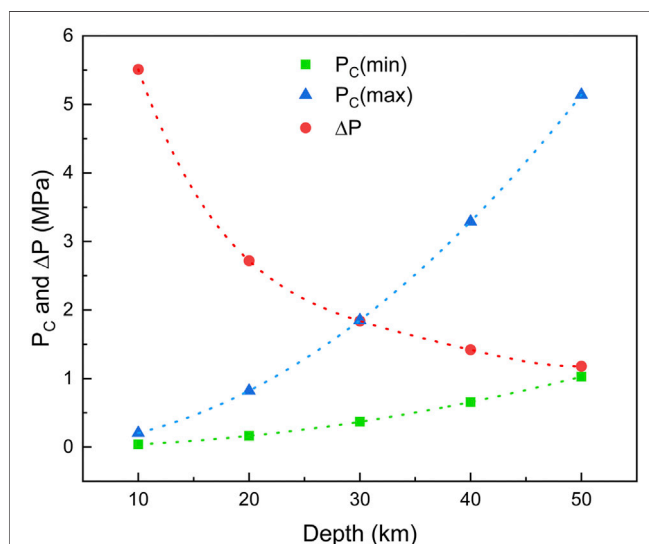


FIGURE 7 | Relationship between the pressure change caused by the magma solidification and the ultimate load of the overlying crust. $P_c(\max)$ and $P_c(\min)$ are obtained from the average maximum and minimum Young's moduli of the main components of the crust (basalt and granite), respectively (Schultz, 1993; Yang et al., 2019).

DISCUSSION AND CONCLUSION

Based on the analysis of the GPS data, changes in the total volume and radius of the Earth are determined, and these changes demonstrate that the Earth is undergoing contraction at an average rate of 1.65 mm yr^{-1} . The change in the radius causes changes in the moment of inertia of the Earth, which increases the Earth's rotation speed. This can explain the physical phenomenon of the change in the Earth's speed and the change in LOD. The change of the Earth's radius is mainly attributed to the solidification of molten substance in the Earth's interior, and this liquid–solid transformation is the main power source for geodynamics. The abovementioned phenomena and principles can be extended to other planets whose structures are similar to that of the Earth, that is, planets on which the liquid–solid transformation of the inner material is not yet complete.

The pressure-volume work ($W = P \times \Delta V$), as a result of solidification, is a critical energy source for geodynamics and earthquakes. At the shallow Earth (10 km), $W = \sim 2.3 \text{ TW}$. For major earthquakes ($M_w > 7$), $W = \sim 2 \text{ TW}$ (Kanamori, 1978). Therefore, the estimated energy from the pressure–volume work is sufficient to generate earthquakes, and the remaining energy

contributes to power plate tectonics and other geologic movements. At the Earth's core, $W = \sim 1$ TW, which contributes to the geodynamic processes.

Based on the previous discussion, earthquakes can be predicted based on the energy provided by solidification and the energy required for earthquakes. The expectation of energy of earthquakes from Mw M_1 to M_2 can be calculated using Eq. 18:

$$E[X] = \int_{M_1}^{M_2} e(x)f(x)dx, \quad (18)$$

where $E[X]$ is the expected value of the energy released by earthquakes from Mw M_1 to M_2 , $e(x)$ is the energy released by an Mw x earthquake, and $f(x)$ is the probability density function of earthquakes (derived from the Gutenberg–Richter relationship). The frequency of earthquakes (N) of a certain magnitude range within a period is thus calculated using Eq. 19:

$$N = f(x)W/E[X], \quad (19)$$

where W is the pressure–volume work at the shallow Earth. If more sufficient LOD and GPS data are available, the volume change of the Earth can be calculated more accurately, which will enable precise earthquake prediction.

In conclusion, the Earth has been going through a nonlinear solidification process since the magma ocean stage, which has been accompanied by the release of latent heat and volume contraction. Our analyses based on the GPS data, LOD observations, and heat flux estimates demonstrate that the current rate of change of the Earth's volume is $-841 \text{ km}^3 \text{ yr}^{-1}$. The decrease in the Earth's internal volume reduces the pressure at the bottom of the crust and rock layers. Under the action of gravity, the interactions between the crustal plates intensify, which makes the mechanical structure unstable. Our

mechanical model shows that the decrease of pressure (1.84–5.51 MPa) is greater than the ultimate load (0.37–1.85 MPa) that most of the Earth's crust can bear. Therefore, volume shrinkage leads to stress buildup followed by mechanical failure, which manifests as earthquakes and powers the geodynamics of the crust. The findings of this study reveal the connection between the liquid–solid transformation inside the Earth and geodynamics and provides a new perspective for predicting earthquakes.

DATA AVAILABILITY STATEMENT

The original contributions presented in the study are included in the article/Supplementary Material, further inquiries can be directed to the corresponding author.

AUTHOR CONTRIBUTIONS

DH contributed to conception of the study; DH and XL designed the study; XL and MT collected the data and performed the analysis; XL wrote the first draft of the article; DH and XL revised the article. All authors contributed to manuscript revision, read, and approved the submitted version.

ACKNOWLEDGMENTS

The authors would like to thank all the reviewers who participated in the review, as well as MJEditor (www.mjeditor.com) for providing English editing services during the preparation of this manuscript.

REFERENCES

- Araki, T., Enomoto, S., Furuno, K., Gando, Y., Ichimura, K., Ikeda, H., et al. (2005). Experimental Investigation of Geologically Produced Antineutrinos with KamLAND. *Nature* 436 (7050), 499–503. doi:10.1038/nature03980
- Bath, M. (2013). *Introduction to Seismology*. Basel: Birkhäuser.
- Báth, M. (1975). Seismicity of the Tanzania Region. *Tectonophysics* 27 (4), 353–379. doi:10.1016/0040-1951(75)90004-9
- Bokelmann, G. H. R. (2002b). Convection-driven Motion of the North American Craton: Evidence from P-Wave Anisotropy. *Geophys. J. Int.* 148 (2), 278–287. doi:10.1046/j.1365-246X.2002.01614.x
- Bokelmann, G. H. R. (2002a). Which Forces Drive North America? *Geol* 30 (11), 1027–1030. doi:10.1130/0091-7613(2002)030<1027:wfdna>2.0.co;2
- Bono, R. K., Tarduno, J. A., Nimmo, F., and Cottrell, R. D. (2019). Young Inner Core Inferred from Ediacaran Ultra-low Geomagnetic Field Intensity. *Nat. Geosci* 12 (2), 143–147. doi:10.1038/s41561-018-0288-0
- Bott, M. (1991). Ridge Push and Associated Plate interior Stress in normal and Hot Spot Regions. *Tectonophysics* 200 (1-3), 17–32. doi:10.1016/0040-1951(91)90003-B
- Buffett, B. A. (2000). Earth's Core and the Geodynamo. *Science* 288 (5473), 2007–2012. doi:10.1126/science.288.5473.2007
- Buffett, B. A., Huppert, H. E., Lister, J. R., and Woods, A. W. (1992). Analytical Model for Solidification of the Earth's Core. *Nature* 356 (6367), 329–331. doi:10.1038/356329a0
- Chao, B. F., and Gross, R. S. (1987). Changes in the Earth's Rotation and Low-Degree Gravitational Field Induced by Earthquakes. *Geophys. J. Int.* 91 (3), 569–596. doi:10.1111/j.1365-246X.1987.tb01659.x
- Cox, A., and Doell, R. R. (1961). Palaeomagnetic Evidence Relevant to a Change in the Earth's Radius. *Nature* 189 (4758), 45–47. doi:10.1038/189045a0
- Dye, S. (2012). Geoneutrinos and the Radioactive Power of the Earth. *Rev. Geophys.* 50 (3), 1–19. doi:10.1029/2012RG000400
- Dziewonski, A. M., and Anderson, D. L. (1981). Preliminary Reference Earth Model. *Phys. Earth Planet. Interiors* 25 (4), 297–356. doi:10.1016/0031-9201(81)90046-7
- Elkins-Tanton, L. T. (2012). Magma Oceans in the Inner Solar System. *Annu. Rev. Earth Planet. Sci.* 40, 113–139. doi:10.1146/annurev-earth-042711-105503
- Forsyth, D., and Uyeda, S. (1975). On the Relative Importance of the Driving Forces of Plate Motion. *Geophys. J. Int.* 43 (1), 163–200. doi:10.1111/j.1365-246X.1975.tb00631.x
- Gessmann, C., and Wood, B. (2002). Potassium in the Earth's Core? *Earth Planet. Sci. Lett.* 200 (1-2), 63–78. doi:10.1016/S0012-821X(02)00593-9
- Heflin, M. (1994). GNSS Time Series. Available: <https://www.frontiersin.org/about/author-guidelines> (Accessed May 20, 2021).
- Herzberg, C., Condie, K., and Korenaga, J. (2010). Thermal History of the Earth and its Petrological Expression. *Earth Planet. Sci. Lett.* 292 (1-2), 79–88. doi:10.1016/j.epsl.2010.01.022
- Hirose, K., Labrosse, S., and Hernlund, J. (2013). Composition and State of the Core. *Annu. Rev. Earth Planet. Sci.* 41, 657–691. doi:10.1146/annurev-earth-050212-124007

- Holme, R., and De Viron, O. (2013). Characterization and Implications of Intradeccadal Variations in Length of Day. *Nature* 499 (7457), 202–204. doi:10.1038/nature12282
- Hu, S., He, H., Ji, J., Lin, Y., Hui, H., Anand, M., et al. (2021). A Dry Lunar Mantle Reservoir for Young Mare Basalts of Chang'e-5. *Nature* 600, 49–53. doi:10.1038/s41586-021-04107-9
- Huang, L.-r., Ma, Z.-j., and Zhu, J.-x. (2002). The Newest Observational Evidence on Asymmetrical Deformation of the Earth. *Acta Seimol. Sin.* 15 (2), 210–213. doi:10.1007/s11589-002-0010-5
- Hyndman, R. (1979). Poisson's Ratio in the Oceanic Crusta Review. *Developments in Geotectonics* 15, 321–333. doi:10.1016/B978-0-444-41851-7.50022-4
- Josiah, R. (2010). *Distance Calculation Using Haversine Formula*. Available: <https://www.mathworks.com/matlabcentral/fileexchange/27785-distance-calculation-using-haversine-formula> (Accessed August 18, 2021).
- Kanamori, H. (1978). Quantification of Earthquakes. *Nature* 271 (5644), 411–414. doi:10.1038/271411a0
- Labrosse, S., Poirier, J.-P., and Le Mouél, J.-L. (2001). The Age of the Inner Core. *Earth Planet. Sci. Lett.* 190 (3–4), 111–123. doi:10.1016/S0012-821X(01)00387-9
- Lay, T., Hernlund, J., and Buffett, B. A. (2008). Core-mantle Boundary Heat Flow. *Nat. Geosci* 1 (1), 25–32. doi:10.1038/ngeo.2007.44
- Li, Q.-L., Zhou, Q., Liu, Y., Xiao, Z., Lin, Y., Li, J.-H., et al. (2021). Two-billion-year-old Volcanism on the Moon from Chang'e-5 Basalts. *Nature* 600, 54–58. doi:10.1038/s41586-021-04100-2
- Massonne, H., Willner, A., and Gerya, T. (2007). Densities of Metapelitic Rocks at High to Ultrahigh Pressure Conditions: What Are the Geodynamic Consequences? *Earth Planet. Sci. Lett.* 256 (1–2), 12–27. doi:10.1016/j.epsl.2007.01.013
- Murthy, V. R., Van Westrenen, W., and Fei, Y. (2003). Experimental Evidence that Potassium Is a Substantial Radioactive Heat Source in Planetary Cores. *Nature* 423 (6936), 163–165. doi:10.1038/nature01560
- O'Connell, R. J., and Dziewonski, A. M. (1976). Excitation of the Chandler Wobble by Large Earthquakes. *Nature* 262 (5566), 259–262. doi:10.1038/262259a0
- Ohta, K., Kuwayama, Y., Hirose, K., Shimizu, K., and Ohishi, Y. (2016). Experimental Determination of the Electrical Resistivity of Iron at Earth's Core Conditions. *Nature* 534 (7605), 95–98. doi:10.1038/nature17957
- Ohtani, E., and Maeda, M. (2001). Density of Basaltic Melt at High Pressure and Stability of the Melt at the Base of the Lower Mantle. *Earth Planet. Sci. Lett.* 193 (1–2), 69–75. doi:10.1016/S0012-821X(01)00505-2
- Pan, B., and Cui, W. (2010). An Overview of Buckling and Ultimate Strength of Spherical Pressure hull under External Pressure. *Mar. Structures* 23 (3), 227–240. doi:10.1016/j.marstruc.2010.07.005
- Rychert, C. A., and Shearer, P. M. (2009). A Global View of the Lithosphere-Asthenosphere Boundary. *Science* 324 (5926), 495–498. doi:10.1126/science.1169754
- Sakamaki, T., Ohtani, E., Urakawa, S., Suzuki, A., and Katayama, Y. (2010). Density of Dry Peridotite Magma at High Pressure Using an X-ray Absorption Method. *Am. Mineral.* 95 (1), 144–147. doi:10.2138/am.2010.3143
- Sakamaki, T., Ohtani, E., Urakawa, S., Suzuki, A., and Katayama, Y. (2009). Measurement of Hydrous Peridotite Magma Density at High Pressure Using the X-ray Absorption Method. *Earth Planet. Sci. Lett.* 287 (3–4), 293–297. doi:10.1016/j.epsl.2009.07.030
- Schultz, R. A. (1993). Brittle Strength of Basaltic Rock Masses with Applications to Venus. *J. Geophys. Res.* 98 (E6), 10883–10895. doi:10.1029/93JE00691
- Shimada, M., and Cho, A. (1990). Two Types of Brittle Fracture of Silicate Rocks under Confining Pressure and Their Implications in the Earth's Crust. *Tectonophysics* 175 (1–3), 221–235. doi:10.1016/0040-1951(90)90139-Y
- Stacey, F. D., and Loper, D. E. (2007). A Revised Estimate of the Conductivity of Iron alloy at High Pressure and Implications for the Core Energy Balance. *Phys. Earth Planet. Interiors* 161 (1–2), 13–18. doi:10.1016/j.pepi.2006.12.001
- Stephenson, F. R., and Morrison, L. V. (1984). Long-term Changes in the Rotation of the Earth : 700 B.C. To A.D. 1980. *Phil. Trans. R. Soc. Lond. A.* 313 (1524), 47–70. doi:10.1098/rsta.1984.0082
- Sun, F.-P., Zhu, X.-H., Wang, R., and Li, J.-T. (2006). Detection of Changes of the Earth's Volume and Geometry by Using GPS and VLBI Data. *Chin. J. Geophys.* 49 (4), 900–906. doi:10.1002/cjg2.910
- Sun, W. (2019). The Magma Engine and the Driving Force of Plate Tectonics. *Chin. Sci. Bull.* 64 (28–29), 2988–3006. doi:10.1360/n972019-00274
- Suzuki, A., and Ohtani, E. (2003). Density of Peridotite Melts at High Pressure. *Phys. Chem. Minerals* 30 (8), 449–456. doi:10.1007/s00269-003-0322-6
- Tian, H.-C., Wang, H., Chen, Y., Yang, W., Zhou, Q., Zhang, C., et al. (2021). Non-KREEP Origin for Chang'e-5 Basalts in the Procellarum KREEP Terrane. *Nature* 600, 59–63. doi:10.1038/s41586-021-04119-5
- van Summeren, J., Conrad, C. P., and Lithgow-Bertelloni, C. (2012). The Importance of Slab Pull and a Global Asthenosphere to Plate Motions. *Geochem. Geophys. Geosyst.* 13 (2), a–n. doi:10.1029/2011GC003873
- Wang, Q. (2009). *Seismic Velocities, Anisotropy, Hysteresis and Poisson's Ratio of Ultrahigh Pressure (UHP) Metamorphic Rocks*. Quebec: École Polytechnique de Montréal.
- Ward, M. A. (1963). On Detecting Changes in the Earth's Radius. *Geophys. J. Int.* 8 (2), 217–225. doi:10.1111/j.1365-246X.1963.tb06285.x
- Whittington, A. G., Hofmeister, A. M., and Nabelek, P. I. (2009). Temperature-dependent thermal Diffusivity of the Earth's Crust and Implications for Magmatism. *Nature* 458 (7236), 319–321. doi:10.1038/nature07818
- Wilson, B. M. (2007). *Igneous Petrogenesis a Global Tectonic Approach*. Berlin: Springer Science & Business Media.
- Wu, X., Collilieux, X., Altamimi, Z., Vermeersen, B. L. A., Gross, R. S., and Fukumori, I. (2011). Accuracy of the International Terrestrial Reference Frame Origin and Earth Expansion. *Geophys. Res. Lett.* 38 (13), a–n. doi:10.1029/2011GL047450
- Yang, L., Feng, X., and Sun, Y. (2019). Predicting the Young's Modulus of Granites Using the Bayesian Model Selection Approach. *Bull. Eng. Geol. Environ.* 78 (5), 3413–3423. doi:10.1007/s10064-018-1326-2
- Zandt, G., and Ammon, C. J. (1995). Continental Crust Composition Constrained by Measurements of Crustal Poisson's Ratio. *Nature* 374 (6518), 152–154. doi:10.1038/374152a0
- Zhang, Y., Hou, M., Liu, G., Zhang, C., Prakapenka, V. B., Greenberg, E., et al. (2020). Reconciliation of Experiments and Theory on Transport Properties of Iron and the Geodynamo. *Phys. Rev. Lett.* 125 (7), 078501. doi:10.1103/PhysRevLett.125.078501
- Zhang, Y., Sekine, T., He, H., Yu, Y., Liu, F., and Zhang, M. (2014). Shock Compression of Fe-Ni-Si System to 280 GPa: Implications for the Composition of the Earth's Outer Core. *Geophys. Res. Lett.* 41 (13), 4554–4559. doi:10.1002/2014GL060670
- Zhu, X., Sun, F., and Wang, R. (2013). Study on the Earth's Volume Change by Using Space Observed Technology." in China Satellite Navigation Conference (CSNC) 2013 Proceedings, Wuhan, May 15–17 (Berlin, Heidelberg: Springer), 15–24.

Conflict of Interest: The authors declare that the research was conducted in the absence of any commercial or financial relationships that could be construed as a potential conflict of interest.

Publisher's Note: All claims expressed in this article are solely those of the authors and do not necessarily represent those of their affiliated organizations or those of the publisher, the editors, and the reviewers. Any product that may be evaluated in this article, or claim that may be made by its manufacturer, is not guaranteed or endorsed by the publisher.

Copyright © 2022 Li, Tao and He. This is an open-access article distributed under the terms of the Creative Commons Attribution License (CC BY). The use, distribution or reproduction in other forums is permitted, provided the original author(s) and the copyright owner(s) are credited and that the original publication in this journal is cited, in accordance with accepted academic practice. No use, distribution or reproduction is permitted which does not comply with these terms.



Stress-Strain-Sorption Behaviour of Smectites Upon Exposure to Dry and Wet CO₂

Miao Zhang^{1,2*}, Christopher James Spiers², Jinfeng Liu^{3,4} and Hongwei Zhou⁵

¹State Key Laboratory of Earthquake Dynamics, Institute of Geology, China Earthquake Administration, Beijing, China, ²HPT Laboratory, Faculty of Geosciences, Utrecht University, Utrecht, Netherlands, ³School of Earth Sciences and Engineering, Sun Yat-Sen University, Guangzhou, China, ⁴Guangdong Provincial Key Lab of Geodynamics and Geohazards, Sun Yat-Sen University, Zhuhai, China, ⁵School of Energy and Mining Engineering, China University of Mining and Technology, Beijing, China

OPEN ACCESS

Edited by:

Lidong Dai,
Chinese Academy of Sciences, China

Reviewed by:

Jiadun Liu,
Hebei University of Engineering, China
Chao Wang,
Peking University, China

*Correspondence:

Miao Zhang
zmcumtb@qq.com

Specialty section:

This article was submitted to
Solid Earth Geophysics,
a section of the journal
Frontiers in Earth Science

Received: 02 April 2022

Accepted: 25 April 2022

Published: 20 May 2022

Citation:

Zhang M, Spiers CJ, Liu J and Zhou H
(2022) Stress-Strain-Sorption
Behaviour of Smectites Upon
Exposure to Dry and Wet CO₂.
Front. Earth Sci. 10:911247.
doi: 10.3389/feart.2022.911247

The swelling-shrinkage behavior of smectites induced by interlayer uptake or sorption of CO₂ and H₂O has been investigated with increasing interest recent years, primarily because of its potential impact on the sealing efficiency of clay-bearing caprocks overlying CO₂ storage reservoirs. To get a better understanding of the stress-strain-sorption coupling in smectite exposed to supercritical CO₂, we performed multiple stepwise axial loading and unloading, oedometer-type experiments on ~1 mm thick discs of pre-pressed Na-SWy-1 and of Ca-SAz-1 montmorillonite. Initially air-dry (AD) samples were first tested in the presence of wet CO₂ (20% RH) at 10 MPa pressure, and in the vacuum-dry (VD) state in the presence of pure (dry) CO₂ at 10 MPa. The samples were incrementally loaded and unloaded at 40°C, employing effective axial stresses ranging from 0.5 to 44 MPa. Control tests using wet and dry He or Ar instead of CO₂, were performed to distinguish strains due to loading-related CO₂ sorption/desorption from purely poroelastic effects. All samples saturated with CO₂ exhibited 30–65% lower apparent stiffness moduli than when saturated with He or Ar, showing that CO₂ adsorption/desorption altered the mechanical response of pre-pressed smectites. Relative to the He and Ar tests, swelling strains of a few % (corrected for poroelastic effects) were measured for AD Na-SWy-1 smectite exposed to wet CO₂, decreasing from 4.9 to 3.8% with increasing effective axial stresses in the range 1.6–36.2 MPa. AD SAz-1 material exhibited similar trends. VD samples tested with dry CO₂ showed much smaller relative swelling strains (0.5–1.5%), which also decreased with increasing applied effective stresses. The experimental data on relative swelling strain versus effective stress are well fitted by a recent thermodynamic model for stress-strain-sorption behavior in coal. Results derived from model fits indicate that smectite-rich rocks have significant storage capacity for CO₂ at shallow depths (up to 1.5–2 km) through CO₂ sorption by the clay minerals. However, this component of storage capacity is reduced by more than 80% with increasing burial depth beyond 3 km. The model provides a first step towards modelling stress-strain-sorption effects in smectite rich caprocks penetrated by CO₂, though further refinements are needed for broader application to the smectite-CO₂-H₂O system.

Keywords: CO₂ geological storage, CO₂ sorption, swelling clay, CO₂-smectite interactions, stress-strain-sorption

INTRODUCTION

Geological storage of CO₂ by injection into depleted hydrocarbon reservoirs and saline aquifers, as well as enhanced oil and gas recovery operations combined with CO₂ storage, are all under consideration for reducing anthropogenic greenhouse gas emissions into the atmosphere (Holloway, 1997; Alvarado and Manrique, 2010; Bachu, 2008). Safe, long-term storage of CO₂ *via* these routes depends on the sealing capacity of the storage system, i.e. on good caprock integrity (Gaus, 2010; Kaldi et al., 2013). Since smectite clays are a significant component (3–20 wt%) of many clay-rich caprocks and faults (Chadwick et al., 2004; Espinoza and Santamarina, 2017; Nooraiepour et al., 2017), the swelling-shrinkage behavior exhibited by smectites, due to intercalation of supercritical (Sc) CO₂ and H₂O in their interlayer structure, has been investigated vigorously in the past few years (Cygan et al., 2012; Giesting et al., 2012a; Giesting et al., 2012b; Loring et al., 2012; Rother et al., 2013; Schaef et al., 2015). The aim of such studies has been to determine whether CO₂-induced swelling-shrinkage effects are large enough to significantly impact the geo-mechanical and transport properties of smectite-bearing caprocks and crosscutting faults and fractures.

Montmorillonite is the most common group of smectite clays in caprocks. Montmorillonites consist of stacked aluminosilicate layers, each consisting of one octahedrally-coordinated Al-O sheet (O-sheet) sandwiched by two tetrahedrally-coordinated Si-O sheets (T-sheets). Isomorphous substitutions of lower valency cations for Al and Si mean that the T-O-T layers carry a charge deficiency. This is balanced by intercalation of cations (e.g. Na⁺, Ca²⁺) between the T-O-T layers. Hydration of these cations by uptake of 0, 1, 2 or 3 layers of water molecules into the T-O-T interlayer region, causes the (001) interlayer spacing (d_{001}) to increase by an amount equal to the thickness of water layers intercalated (i.e. by 2.5–3 Å per layer). The corresponding hydration states are referred to as the 0, 1, 2 and 3 W states. The magnitude of the associated swelling effect depends on the properties of the interlayer cation, the T-O-T layer charge density, temperature, relative humidity and other factors.

Swelling due to water (vapor) uptake into the interlayer structure of montmorillonite and other smectites is a well-known problem in soil mechanics and has been studied extensively through experiments (Moore and Hower, 1986; Ferrage et al., 2005; Ferrage et al., 2007a; Ferrage et al., 2007b; Ferrage et al., 2007c; Michot et al., 2016) and molecular dynamic simulations (Suter et al., 2012; Cygan et al., 2015; Greathouse et al., 2015). Intercalation of CO₂ plus associated interlayer swelling is a more recent finding, first proved by Loring et al. (2012) using spectroscopic methods. Subsequently, much work has been done on the topic, revealing the following key points.

First, dry (pure) (Sc)CO₂ can cause either expansion or contraction of the interlayer spacing of the smectite crystallites, depending primarily on the initial hydration state of the smectite, the types of interlayer cations present, and the TOT layer charge (Loring et al., 2011; Giesting et al., 2012a; Giesting et al., 2012b; Ilton et al., 2012; Loring et al., 2012; Rother et al., 2013). Expansion is due to CO₂ uptake in the interlayer,

whereas contraction is due to interlayer water loss driven by dissolution in the external CO₂ environment. As an example, when exposed to ScCO₂ at 9 MPa pressure and 40–50°C, Na-montmorillonite, with an initial d_{001} spacing of 11.0 Å and corresponding to sub 1 W hydration state, exhibits CO₂ uptake alongside an increase in interlayer spacing toward that of the completely monohydrated state (1 W, 12.3 Å). This causes swelling strains up to 12% (Rother et al., 2013). By contrast, Ca-montmorillonite with an initial hydration state of 1W < H < 2 W (d_{001} = 14.4 Å) shows contraction of the interlayer to 12.4 Å (–14% strain) when exposed to pure ScCO₂, due to interlayer water loss (Schaef et al., 2012).

Second, smectite swelling/shrinkage caused by exposure to mixed (Sc)CO₂ and water vapor are determined by repartitioning of CO₂ and water in the interlayer. This in turn depends on the composition of the mixture (partial pressures of CO₂ and H₂O) and the initial hydration state of the clay. Available data on this repartitioning of CO₂/H₂O in the interlayer gallery suggest that intercalation of H₂O and CO₂ is competitive in montmorillonite, with H₂O uptake being preferable (Loring et al., 2014; Schaef et al., 2015).

Third, besides interlayer intercalation, H₂O and CO₂ uptake also occur *via* sorption at sites located on the external surfaces of the clay platelets, including inter-particle pore surfaces and crystallites edges, causing a swelling effect as well (Prost et al., 1998; Loring et al., 2014; Zhang et al., 2018). In the present paper, CO₂ uptake both into the smectite interlayer and onto the external smectite grain surfaces, will be referred to as sorption or adsorption.

Against this background, CO₂/H₂O-related swelling and/or shrinkage of smectite clays can be expected to lead to substantial changes in stress-strain state and hence transport properties of smectite-bearing caprock and faults under subsurface CO₂ storage conditions (Rother et al., 2013; Song and Zhang, 2013). Zhang et al. (2018) experimentally measured the swelling stresses exerted by volumetrically confined Na-SWy-1 and Ca-SAz-1 montmorillonite aggregates upon exposure to ScCO₂ under P-T conditions relevant to CO₂ storage, finding values of 5–11 MPa, when swelling strains were limited to 1–3%. The measured swelling stresses also showed an inverse dependence on the initial effective stress applied to the clay samples, demonstrating coupled stress-strain-sorption characteristics, similar to those reported for coal exposed to CH₄ and CO₂ (e.g. Hol et al., 2012; Liu et al., 2016b). Zhang (2019) went on to measure the permeability of laterally confined Opalinus Claystone cores (~5% smectite) and simulated smectite fault gouge (all initially air-equilibrated), to dry and wet CO₂ and He, at a mean pressure of 10 MPa. Self-sealing (i.e. permeability reduction) was observed in all samples tested with CO₂ versus He. Moreover, alternating flow of wet then dry CO₂ through the simulated fault gouge correspondingly decreased and increased sample permeability. The observed effects were attributed to clay swelling and shrinkage and clearly depended on initial smectite hydration state and the water content of the injected CO₂. However, the magnitude and impact of these coupled stress-strain-sorption phenomena on clay-rich caprock integrity and storage capacity, under the subsurface hydration states, CO₂

pressures and effective stress conditions associated with CO₂ storage, remain unclear.

In the present paper, we aim to achieve a better understanding of the effect of applied (Terzaghi) effective stress on the strain response of smectites subject to interactions with CO₂ and H₂O. To this end, we performed oedometer-type, cyclic loading and unloading experiments on pre-compressed, ~1 mm-thick discs, prepared from Na-SWy-1 and Ca-SAz-1 montmorillonite, injecting CO₂, Ar and/or He as pore fluid. We focus on how the strain response of the smectite to loading is changed due to sorptive interactions of smectite with CO₂ and H₂O versus the inert gases. In addition, we compare the experimental data with a thermodynamic model developed for stress-strain-sorption phenomena in coal (Hol et al., 2012; Liu et al., 2016a; Liu et al., 2016b), showing that such models can at least qualitatively explain the behaviour seen. We go on to consider the implications for both the CO₂ storage capacity and sealing integrity of clay-rich formations.

EXPERIMENTAL METHODS

The experiments consisted of 1-D oedometer tests aimed at measuring the volumetric response (i.e. change in thickness) of pre-pressed smectite discs, exposed to CO₂ at a pressure of 10 MPa at 40°C, to incremental cycling of the applied axial effective stress (Terzaghi) under varying hydration conditions. Multiple experiments were performed on one Na-montmorillonite and one Ca-montmorillonite sample, employing repeated loading cycles. The samples were tested first in an air-dry (AD) hydration state (pre-equilibrated with heated lab air having relative humidity RH ≈ 20% at 40°C) and then vacuum dry (VD). Control experiments were performed on both samples in the AD and VD conditions, employing inert gas (He and/or Ar) at 10 MPa in place of CO₂. This was done to discriminate purely mechanical effects of effective stress (e.g. poroelastic volume change) from effects related to sorption and desorption of CO₂ and/or H₂O. In all tests performed on AD samples, water-bearing (“wet”) pore fluids (with RH ≈ 20%) were employed to buffer the initial AD hydration state, while tests on VD samples employed pure (dry) pore fluids.

Materials

Raw Clays and Pore Fluids

The raw clays used were naturally occurring Na-SWy-1 and Ca-SAz-1 montmorillonite obtained from the Source Clay Repository of the Clay Mineral Society. The Na-SWy-1 is a Na-rich Wyoming type (SWy-1) low charge montmorillonite (CEC = 80 cmolc kg⁻¹) with solid substitutions occurring in both the tetra- and octahedral sheets (Jaynes and Bigham, 1986). The Ca-SAz-1 material is a high charge (CEC = 120 cmolc kg⁻¹) (Borden and Giese, 2001) Arizona type with solid substitutions occurring solely in the tetrahedral sheet. The interlayer cations present in this montmorillonite are mainly calcium, with smaller amounts of potassium and sodium. Both types of clay were used as-received, without any chemical pre-treatment or grain size fractionation. Baseline studies of both montmorillonite can be

found in previous literature (Chipera and Bish, 2001; Madejova and Komadel, 2001; Mermut and Lagaly, 2001). The pore fluids used here were respectively CO₂, He and Ar, with a purity >99.99% supplied in cylinder form by Air Products NL. “Wet” pore fluids with a water content equivalent to the lab air humidity of ~20% (at 40°C) were prepared by introducing a controlled amount of water vapor into the pore fluid system using a multistep Mg(NO₃) salt buffer method described in **Appendix 1**.

Sample Preparation

The experiments were performed on one disc-shaped sample derived from the SWy-1 montmorillonite and one derived from the SAz-1 montmorillonite. The samples were pre-formed in a stainless steel die with the same inner diameter (19.15 mm) as the 1-D compaction vessel subsequently used in the experiments. For the sample pre-forming, ~0.6 g of sample powder (0.55 and 0.608 g respectively for SAz-1 and SWy-1), which had been pre-dried in lab air at 40°C, was distributed evenly in the die and lightly compressed between an upper and a lower stainless steel piston by hand. The sample was subsequently compressed at an axial stress of 10 MPa for ~3 min using a hydraulic press, to obtain a flat, disc-shaped sample of ~1.1 mm thickness, which was then transferred to the main experimental apparatus.

Experimental Set-Up

The experimental setup (**Figure 1**) consists of a uniaxial, oedometer-type (i.e. one dimensional) compaction vessel, constructed of Remanit 4,122 stainless steel, mounted in an Instron 8562 servo-controlled loading frame to apply axial load (**Figure 1A**, *c.f.* Zhang et al., submitted). The pre-formed sample was axially loaded, within the Remanit vessel, *via* two Remanit pistons (diameter 19 mm) sealed against the Remanit compaction vessel using Viton O-rings. Applied axial load was measured external to the compaction vessel using a 100 kN capacity Instron load cell, which allows load measurement and control to within ±2.3 N. Instron ram displacement was measured with an internally mounted linear variable differential transformer (LVDT). Axial displacement of the upper piston relative to the Remanit vessel top (i.e. axial sample deformation) was measured using a high precision external LVDT (measurement range ± 1 mm, accuracy better than ± 0.1 μm). This allowed changes in sample thickness to be measured accurately at any instant, by correcting for piston distortion.

The pore fluid system (**Figure 1C**) consisted of an ISCO 65D, servo-controlled syringe pump employed to introduce pressurized fluid (e.g. CO₂) into the sample through an inlet in the upper Remanit piston. The fluid pressure was measured and controlled using a Honeywell TJE pressure transducer (range 0–137.90 MPa, absolute accuracy ± 0.6895 MPa), located at the top of the ISCO pump cylinder. For better measurement accuracy, a more sensitive MSI 0–35 MPa (±0.035 MPa) pressure transducer was installed at the fluid inlet in the upper piston. Fluid pressure at the bottom of the sample was limited using an Equibar back pressure regulator connected to a pore fluid port in the lower piston. Note that the pore fluid entered and exited the sample *via* bar-shaped, porous stainless steel plates

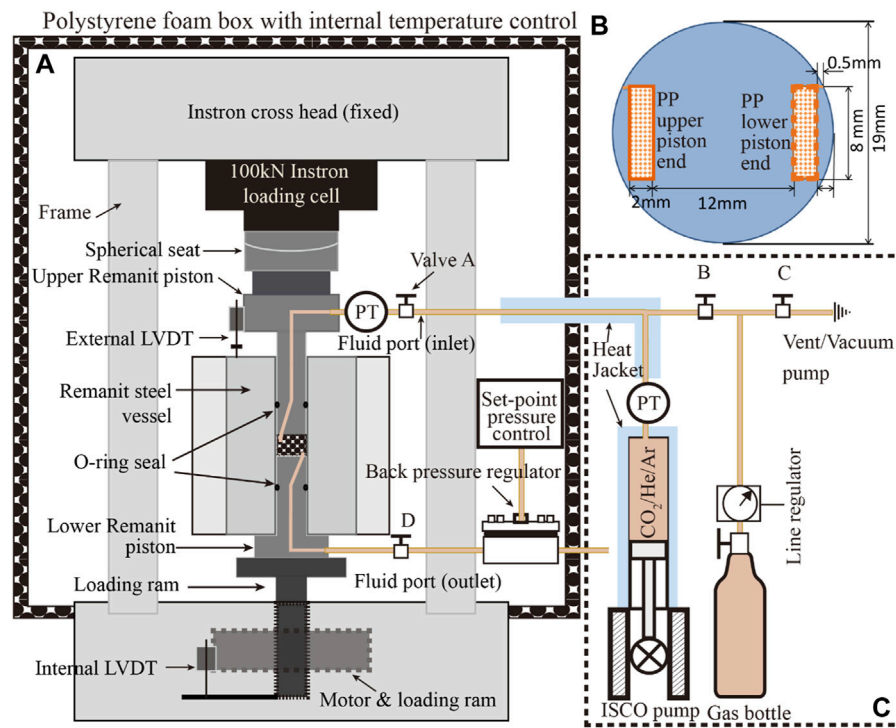


FIGURE 1 | Schematic illustration of the experimental set-up. **(A)** The uniaxial compaction vessel located in the Instron loading frame. **(B)** Schematic illustration of the piston ends, in contact with the upper and lower sample surfaces. Note that the porous stainless steel plates (PP) were located on opposite sides of the sample, and penetrated ~0.3 mm into the sample (refer to a). **(C)** Pore fluids system consisting of an ISCO 65D syringe pump and gas supply cylinder.

located at diametrically opposite sides of the sample, above and below it (see **Figures 1A,B**). The porous plates penetrated 0.3 mm into the sample surface and were employed in this configuration to achieve horizontal fluid flow through the sample, when fluid pressure applied by the ISCO pump was set higher than the set-point of the back pressure regulator.

The temperature of the compaction vessel and sample were controlled at 40°C ($\pm 0.1^\circ\text{C}$) by means of an external heater mounted around the Remanit compaction vessel. This was regulated using a Eurotherm temperature controller, connected to a type K thermocouple located in the external furnace windings. Sample temperature was measured using a second type K thermocouple placed in a small recess in the compaction pressure vessel at a distance of a few mm from the sample. The experimental set-up, excluding the ISCO syringe pump, was enclosed in a 1.5 m³ foam-polystyrene box (wall thickness ~50 mm). The air temperature inside the box was controlled within $\pm 0.2^\circ\text{C}$ at 40°C, using a lamp (500 W) regulated by a Pt-100 element plus a CAL 9900 PID-controller, with a fan circulating the air to guarantee homogeneity of temperature (c.f. Hol and Spiers, 2012). The ISCO pump and the pipelines of the pore fluid system were heated at 40°C using purpose-built heating jackets.

The output signals of all transducers and sensors were recorded using a National Instruments, 16-channel DAOPad-6015 A/D convertor and VI-logger data acquisition system, using a sampling rate of 0.2 Hz. Signals recorded included those

obtained from the external LVDT (mm), the Instron load (kN) and internal LVDT position (mm), the pressure (MPa) measured by the MSI pressure transducer at the upper pore fluid inlet, and ISCO output pressure and volume signals, as well as the thermocouple signals representing the temperature ($^\circ\text{C}$) of the sample and the air in the polystyrene box.

Experimental Procedure

The following multistage testing procedure was applied to each of the two samples investigated (Na-SWy-1 and Ca-SAz-1, see **Table 1**).

Stage 1: Pre-compaction and Cyclic Loading With Pore Fluid Inlets Open to Lab Air (AD Condition)

After pre-forming, the sample disc was carefully removed from the die and located in the compaction vessel. The apparatus was subsequently heated to the target experimental temperature (40°C) and the sample was pre-compacted under an axial (effective) stress of 70 MPa, with the sample exposed to lab air humidity by keeping the fluid inlet port in the top piston open to the heated lab air (RH \approx 23%, T = 40°C). Pre-compaction was continued for 50 h, i.e. until ~5 h after the external LVDT position had reached a stable asymptotic value. Pre-compaction aimed to minimize irreversible sample deformation in the subsequent load-cycling tests at lower (effective) stress, and to allow the sample to approach equilibrium with lab air humidity in the loaded state.

TABLE 1 | Summary of experiments, experimental conditions and key data obtained.

σ_e	P_f	Equilibrium sample thickness change	Cumulative compaction	Cumulative strain	Relative swelling	Relative swelling strain
MPa	MPa	mm	mm	%	mm	%
Sample 1: Na-SWy-1 material						
Stage 1	Initial condition: Air-dry (AD) Estimated sample thickness = 1.0 mm Rapid loading and unloading steps, following stress path 36-27-18-10-2.5-10-18-27-36 MPa					
Stage 2	Sample condition: AD Estimated sample thickness = 1.0 mm					
Series 1 CO ₂						
40.63	9.97	0.00000	0.03322	3.32	-0.03317	-3.32
1.68 ^a	9.96	-0.03322	0 ^a	0.00	-0.05121	-5.12
10.40	9.95	-0.02768	0.00554	0.55	-0.04927	-4.93
18.95	9.98	-0.02051	0.01271	1.27	-0.04631	-4.63
27.56	9.98	-0.01319	0.02003	2.00	-0.04378	-4.38
36.17	9.98	-0.00637	0.02685	2.69	-0.03967	-3.97
Series 2 CO ₂						
36.17	9.98	-0.00637	0.02685	2.69	-0.03967	-3.97
1.63	9.99	-0.02947	0.00375	0.38	-0.04739	-4.74
36.18	9.97	-0.00570	0.02752	2.75	-0.03890	-3.89
Series 3 CO ₂						
36.18	9.97	-0.00570	0.02752	2.75	-0.03890	-3.89
1.68	9.96	-0.02939	0.00383	0.38	-0.04730	-4.73
10.40	9.95	-0.02285	0.01037	1.04	-0.04433	-4.43
18.95	9.98	-0.01553	0.01769	1.77	-0.04123	-4.12
27.56	9.98	-0.00859	0.02463	2.46	-0.03908	-3.91
36.17	9.98	-0.00278	0.03044	3.04	-0.03601	-3.60
Series 4 CO ₂						
36.18	9.97	-0.00494	0.02828	2.83	-0.03821	-3.82
1.64	9.98	-0.02804	0.00518	0.52	-0.04593	-4.59
Rapid unloading and loading at the end of Series 4 - 1cycle						
Series 5 Ar						
36.18	9.97	0.03341	0.01644	1.64	RF	-0.00
1.66 ^a	9.97	0.01697	0 ^a	0.00	RF	-0.00
10.35	9.97	0.02060	0.00363	0.36	RF	-0.00
18.96	9.97	0.02487	0.00790	0.79	RF	-0.00
27.58	9.97	0.02971	0.01274	1.27	RF	-0.00
36.18	9.97	0.03251	0.01554	1.55	RF	-0.00
Rapid unloading and loading at the end of Series 5-1 cycle						
Stage 3	Sample condition: Vacuum-dry (VD), Estimated sample thickness = 0.95 mm					
Series 1 He						
42.05	10.04	0.00000	0.01027	1.08	RF	—
1.11 ^a	10.03	-0.01027	0 ^a	0	RF	—
7.20	10.04	-0.00851	0.00176	0.19	RF	—
14.30	10.06	-0.00585	0.00442	0.47	RF	—
28.19	10.03	-0.00285	0.00742	0.78	RF	—
42.08	10.05	-0.00076	0.00951	1.00	RF	—
Series 2 CO ₂						
41.98	10.08	-0.00456	0.02091	2.20	-0.00456	-0.48
1.11 ^a	10.06	-0.02547	0 ^a	0	-0.01520	-1.60
7.20	10.03	-0.02181	0.00366	0.39	-0.01330	-1.40
14.30	10.05	-0.01805	0.00742	0.78	-0.01220	-1.28
28.13	10.04	-0.01169	0.01378	1.45	-0.00884	-0.93
42.00	10.06	-0.00584	0.01963	2.07	-0.00508	-0.53
Sample 2: SAz-1 material						
Stage 1	Initial condition: AD Estimated sample thickness = 1.1 mm Rapid loading and unloading, 3 cycles in the range of 1.2–41 MPa					
Stage 2	Initial condition: AD Estimated sample thickness = 1.1 mm					
Series 1 Ar						
0.51 ^a	9.96	-0.01762	0 ^a	0	—	—
5.74	9.97	-0.01339	0.00423	0.38	—	—
10.93	9.97	-0.00702	0.01060	0.96	—	—
17.90	9.97	0.00087	0.01849	1.68	—	—

(Continued on following page)

TABLE 1 | (Continued) Summary of experiments, experimental conditions and key data obtained.

σ_e	P_f	Equilibrium sample thickness change	Cumulative compaction	Cumulative strain	Relative swelling	Relative swelling strain
26.48	9.97	0.00907	0.02669	2.43	—	—
35.16	9.97	0.01642	0.03404	3.09	—	—
43.84	9.97	0.02392	0.04154	3.78	—	—
Series 2 CO₂						
43.90	9.98	0.01883	0.07251	7.25	−0.01468	−1.47
0.50 ^a	9.97	−0.05368	0 ^a	0	−0.05368	−5.37
5.71	9.98	−0.04524	0.00844	0.84	−0.04956	−4.96
10.92	9.98	−0.03366	0.02003	2.00	−0.04224	−4.22
17.90	9.98	−0.02011	0.03357	3.36	−0.03465	−3.46
26.48	9.98	−0.00674	0.04694	4.69	−0.02804	−2.80
35.21	9.98	0.00487	0.05855	5.85	−0.02217	−2.22
43.90	9.98	0.01608	0.06976	6.98	−0.01620	−1.62
Series 3 He-1						
43.90	9.98	0.03228	0.03228	3.23	RF	—
0.50 ^a	9.97	0.00000	0 ^a	0	RF	—
5.71	9.98	0.00432	0.00432	0.43	RF	—
10.92	9.98	0.00858	0.00858	0.86	RF	—
17.90	9.98	0.01454	0.01454	1.45	RF	—
26.48	9.98	0.02129	0.02129	2.13	RF	—
35.21	9.98	0.02704	0.02704	2.70	RF	—
43.90	9.98	0.03351	0.03351	3.35	RF	—
Series 4 Ar-2						
43.92	9.98	0.03212	0.03659	3.66	—	—
0.51	9.98	−0.00447	0.00000	0.00	—	—
43.92	9.98	0.03228	0.03675	3.67	—	—
Series 5 He-2						
43.90	9.98	0.03156	0.03168	3.17	—	—
0.51	9.98	−0.00006	0.00006	0.01	—	—
43.90	9.98	0.03131	0.03143	3.14	—	—
Series 6 He-3						
43.90	9.98	0.03131	0.03143	3.14	—	—
0.50	9.97	−0.00420	−0.00408	−0.41	—	—
43.90	9.98	0.03006	0.03018	3.02	—	—
Stage 3 Initial condition: VD Estimated sample thickness = 0.95 mm						
Series 1 He						
1.11 ^a	9.97	0	0 ^a	0	RF	—
7.36	9.98	0.00362	0.00362	0.36	RF	—
24.72	9.98	0.00841	0.00841	0.84	RF	—
42.18	9.98	0.01139	0.01139	1.14	RF	—
59.44	9.98	0.01457	0.01457	1.46	RF	—
Series 2 CO₂						
1.11 ^a	9.98	−0.01030	0 ^a	0.00	−0.01030	−1.08
7.36	9.98	−0.00576	0.00454	0.48	−0.00938	−0.99
24.72	9.98	0.00047	0.01077	1.13	−0.00794	−0.84
42.18	9.97	0.00534	0.01564	1.65	−0.00605	−0.64
59.44	9.98	0.01053	0.02083	2.19	−0.00404	−0.43
59.44	9.98	0.01053	0.02083	2.19	−0.00404	−0.43
42.18	9.98	0.00654	0.01684	1.77	−0.00485	−0.51
24.72	9.98	0.00237	0.01267	1.33	−0.00604	−0.64
7.36	9.98	−0.00446	0.00584	0.61	−0.00808	−0.85
1.11	9.98	−0.00850	0.00180	0.19	−0.00850	−0.89

RF denotes the data (obtained with He or Ar) selected as reference points for calculating relative sample deformation with CO₂ versus with inert pore fluid. Equilibrium LVDT data have been corrected for elastic machine deformation, hence representing only deformation of the sample, i.e. change in sample thickness. N.B. Compressive stress, compressive LVDT displacement sample compaction (strain) take positive sign. Relative swelling (strain) of the sample saturated with CO₂ relative to He/Ar, (i.e. increase in sample thickness with CO₂ versus He/Ar), is accordingly defined as negative. Each series shown represents a load cycling sequence performed with a given fluid.

^aIndicates the reference state, relative to which the cumulative sample compaction and compaction strain were calculated.

Following pre-compaction, the axial stress was adjusted to a lower value, equal to the starting effective stress for subsequent Stage 1 cycling experiments, i.e. 2.5 MPa for the Na-SWy-1 sample and to 0.5 MPa for the Ca-SAz-1 sample. Minor time-

dependent expansion of the samples was observed after lowering the axial stress, presumably due to relaxation of residual elastic stress by reverse creep processes and/or stress-dependent changes in hydration state. To further minimize permanent deformation

effects during subsequent testing, a series of two to three continuous loading and unloading cycles were conducted in the range of 0.5 or 2.5–70 MPa. A similar number of rapid loading and unloading cycles was then applied between the minimum and maximum effective stresses employed in the subsequent Stage 2 and Stage 3 tests. This was done to determine the time-independent elastic response of the samples under Stage 2 and 3 conditions and was conducted in either continuous or stepwise (step interval = 4–6 MPa) loading mode at an active loading rate of ~0.1–0.3 MPa/s. Each loading and unloading cycle was finished within 30 min, and indeed exhibited more or less fully recoverable elastic behaviour.

Stage 2: Load Cycling Applied to AD Samples Exposed to Wet CO₂, He and Ar

After completion of Stage 1 load cycling on samples pre-equilibrated with lab air humidity, the axial load was adjusted to ~60 MPa, and the Instron switched from load to displacement control mode, such that the piston position was fixed. The set-point value of the back pressure regulator was subsequently adjusted to ~10.05 MPa. The compaction vessel plus the sample and pore fluid system was then briefly evacuated and pore fluid (CO₂, He, or Ar, all with controlled moisture content equivalent to RH ≈ 20% at 40°C) was introduced into the sample from the ISCO pump *via* the inlet in the upper piston (Figure 1, see also Appendix 1). The ISCO pump was operated in constant pressure mode, with a set-point of 10 MPa. When the pore fluid pressure stabilized at 10 MPa, with little/no further volume change recorded by the ISCO pump, the Instron load was adjusted to the chosen starting axial effective stress (σ_e^0) for initiating stress cycling. Thereafter, the Instron was operated in load control mode.

After the sample reached apparent equilibrium, i.e. when no further change in external LVDT signal was seen for a period of ~3 h, the axial effective stress was cycled in steps of ~5–9 MPa, allowing apparent equilibrium to be re-established after each step and continuously monitoring the (time-dependent) sample deformation response. Cycling was performed in both up/down and down/up modes, depending on the value of σ_e^0 (low versus high, see Table 1). Return cycles were sometimes performed in a single step at fixed rate (~0.3 MPa/s) (see Table 1 for stress path employed).

Following load cycling with a given pore fluid, the pore fluid system was briefly evacuated and refilled by flushing the system and sample with the next pore fluid. The above initialization and stepwise loading/unloading procedure was then repeated using the new pore fluid, again cycling several times. In a few cases, early pore fluids were reintroduced to examine the effects of varying the fluid sequence. Such tests were usually conducted using a simplified stress path, i.e. directly cycling between the maximum and minimum effective stresses, without intermediate steps (Table 1). In addition, when cycling with a specific pore fluid was completed using the AD Na-SWy-1 sample, rapid continuous loading and unloading (loading rate = 0.3 MPa/s) was performed to assess any changes in the poroelastic behaviour of the sample after being saturated with CO₂ and He or Ar.

Stage 3: Load Cycling Applied to VD Samples Exposed to dry CO₂ and He

After completion of the Stage 1 and 2 experiments on each of the initially AD samples, the sample was evacuated in the compaction vessel at 40°C (Na-SWy-1) or 108°C (Ca-SAz-1), for 60–70 h, under an axial stress of ~40 MPa. This treatment was aimed at dehydrating the samples to the collapsed interlayer or 0 W hydration state (following the findings of Ferrage et al., 2007b). When the sample had reached apparent equilibrium under vacuum (i.e. stopped compacting), the pore fluid system was isolated from the vacuum pump. Sample temperature was then readjusted to 40°C and continuous rapid load cycling was applied, as in Stage 1. Pure (dry) CO₂ or pure (dry) He was then introduced at 10 MPa from the ISCO pump and the stepwise loading and unloading procedure applied in Stage 2 was repeated for the VD samples. For the specific sequence of fluids and stress paths used, see Table 1.

Data Processing

The thermocouple and pressure transducer signals obtained from the apparatus directly yielded temperature and pore fluid pressure data versus time. Axial force given by the Instron load cell was not corrected for seal friction acting on the upper piston, since calibration runs showed this to be less than 0.4 MPa. Displacement measured using the external LVDT was corrected for machine stiffness to obtain sample length change using a pre-determined, fifth order machine stiffness calibration characterized at true test P-T conditions using a 1 mm thick stainless steel dummy sample. Hysteresis in the machine stiffness calibration, induced by the effect of O-ring friction acting between the upper piston and vessel wall, caused a maximum discrepancy of ~2 μm between displacements measured in loading versus unloading runs, with a standard deviation of 1.4 μm implying an error limit of ±1.4 μm in obtaining sample length changes from corrected LVDT data.

In the present paper, compressive stress, compressive displacement and compaction (strain) of the sample take a positive sign. Axial strain measured during continuous loading and/or unloading was calculated using the relation $\varepsilon(t) = \frac{\Delta L(t)}{L_0}$, where t represents time since initiation of loading/unloading and ΔL is the length change at that time. Axial strain occurring in response to a stepwise increment i in applied effective stress σ_e (i.e. from σ_e^{i-1} to σ_e^i , MPa), was calculated as $\Delta \varepsilon^i(t) = \frac{\Delta L^i(t)}{L_0} \cdot 100\%$, where $\Delta L^i(t)$ represents sample length change measured (relative to the equilibrium displacement attained at σ_e^{i-1}) at time t following application of the i th effective stress step. L_0 is the referential sample thickness. As sample strains were small, L_0 for the VD runs was taken as the thickness measured upon VD sample retrieval after termination of all loading cycles. L_0 for AD runs was estimated by adding the total sample shortening measured during vacuum-dry testing to the final thickness of the VD sample measured after retrieval. The average external LVDT signal measured over the last 1–2 h of the i th effective stress step (i.e. the apparent equilibrium LVDT value) was used to calculate the corresponding sample strain at apparent equilibrium, using $\Delta \varepsilon^i(\text{eq}) = \frac{\Delta L^i(\text{eq})}{L_0}$. Since the samples tested in the present study were laterally confined, axial strain also represents volumetric strain of the samples. To examine the

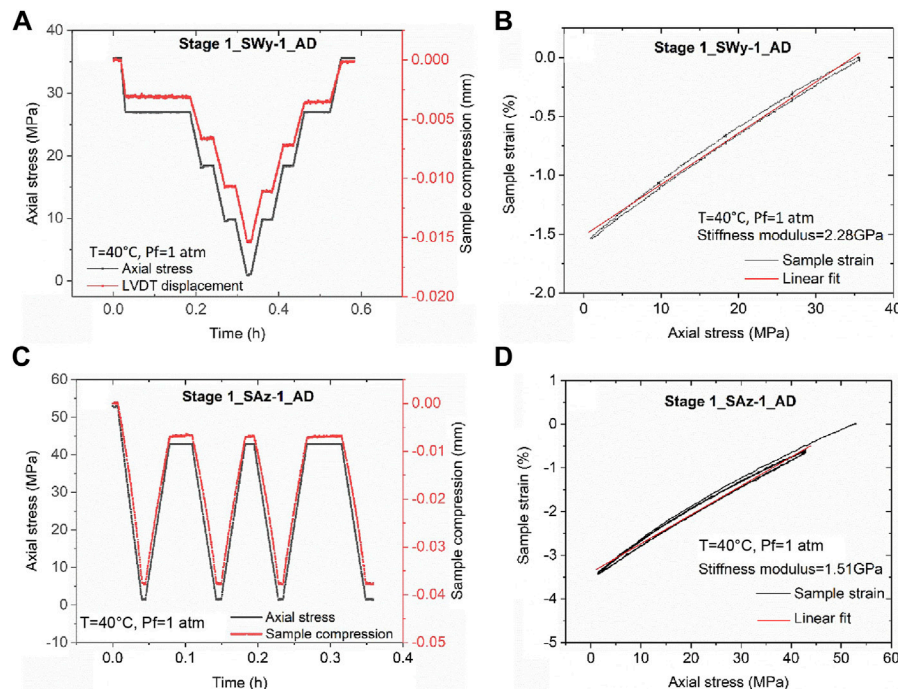


FIGURE 2 | Data obtained in rapid Stage 1 stress cycling runs performed to assess the elastic properties of the AD samples before pore fluid addition. **(A)** Stress path employed in a rapid unloading/loading cycle applied to the AD Na-SWy-1 sample, plus concurrent change in sample thickness. **(B)** Corresponding sample strain versus applied axial stress data for the AD Na-SWy-1 sample. Note the largely reversible elastic behaviour and constrained stiffness modulus of 2.28 GPa. **(C)** Stress path and concurrent change in sample thickness for the AD SAz-1 sample during a rapid Stage 1 unloading/loading cycle. **(D)** Corresponding sample strain versus applied axial stress data for the AD Ca-SAz-1, giving a constrained stiffness modulus of 1.51 GPa.

‘equilibrium’ deformation response of the samples throughout the full sequence of stress steps applied in the Stage 2 and 3 runs, cumulative (equilibrium) strains relative to the state pertaining to the lowest effective stress (σ_e^l) were calculated using $\epsilon^i = \sum \Delta \epsilon^i(eq)$. Where multiple values of equilibrium sample strain (ϵ^i) were obtained at a given effective stress due to cyclic loading and unloading, we take the average of these values to represent ϵ^i for that effective stress. In addition, to quantify the mechanical response per stress step in terms of a net sample stiffness measured over the time to reach equilibrium, we also computed the apparent tangent stiffness modulus C_{app}^i per step using the equation $C_{app}^i = (\sigma_e^i - \sigma_e^{i-1}) / \Delta \epsilon^i(eq) = \Delta \sigma_e^i / \Delta \epsilon^i(eq)$.

RESULTS

A complete list of the experimental runs performed on the two samples investigated is shown in **Table 1**, along with the experimental conditions and key data obtained.

Stage 1 Data: Rapid Cyclic Loading and Unloading of AD Samples Exposed to Lab Air

Data illustrating the stress cycling procedure and stress-strain data obtained in the rapid loading cycles applied to AD samples in

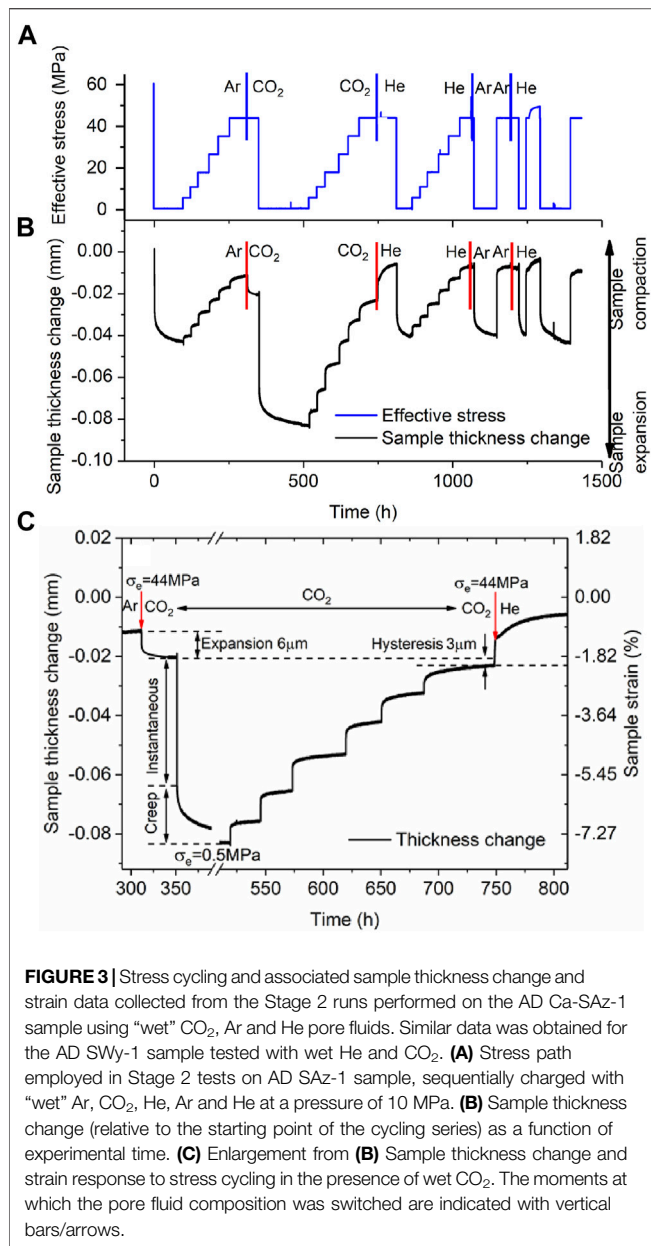
Stage 1, i.e. to assess their time-independent elastic behaviour prior to pore fluid addition, are shown in **Figure 2**.

Figure 2A illustrates the stress path and sample thickness change data measured as a function of time, during the loading and unloading runs on AD Na-SWy-1 sample. Note that, on the time scale of the Stage 1 runs, sample thickness changes (mm) and strains, were largely instantaneous, recoverable and linear with stress, confirming essentially elastic behaviour of the AD SWy-1 sample in Stage 1—see **Figure 2B**. Best fitting to the stress versus strain data gave an apparent constrained stiffness of 2.28 GPa.

Similar stress path and sample deformation data were obtained in a typical rapid cyclic loading run on the AD SAz-1 sample and shown in **Figure 2C**. The corresponding sample strain versus axial stress data is plotted in **Figure 2D**. Reversible, linear stress versus strain behaviour was again seen for the AD Ca-SAz-1 sample, as for the AD Na-SWy-1 sample, but the best-fit stiffness modulus was lower, amounting to 1.23 GPa (**Figure 2D**).

Stage 2 Data: Stepwise Cyclic Loading of AD Samples Saturated With “Wet” Fluids

The results obtained in Stage 2 of the experiments performed on the AD Na-SWy-1 and the AD Ca-SAz-1 samples were qualitatively closely similar. We therefore present “raw” cycling data for the AD Ca-SAz-1 sample in **Figure 3**, as representative for both AD samples. **Figure 3A** plots the effective stress applied to the sample versus time elapsed throughout the stepwise loading runs performed on the AD



Ca-SAz-1 sample using wet Ar, wet CO₂ and wet He pore fluid at 10 MPa. Sample thickness change relative to the starting point of the Stage 2 experimental series is presented in **Figure 3B**. This plot shows that the sample expanded when wet Ar is displaced by wet CO₂. Compaction then occurs upon displacement of wet CO₂ by wet He, but no axial dimensional change occurs when the wet He is replaced by wet Ar. These data clearly show that swelling/shrinkage of the AD Ca-SAz-1 sample is induced by interaction with CO₂. In addition, **Figure 3B** shows that all up/down steps in applied effective stress are accompanied by an instantaneous compaction/expansion response of sample AD SAz-1, followed by time-dependent compaction/expansion until a steady asymptotic (equilibrium) strain is achieved. This behaviour is seen regardless of fluid type, through the magnitude of the instantaneous and time-dependent

response is greater for cycling performed with wet CO₂, than using wet Ar and He (which showed similar responses per step). **Figures 3B,C** also show that the equilibration time for time-dependent compaction increases with increasing applied effective stress, again for all fluids used. Note that both trends, i.e. an increased strain response in the presence of wet CO₂, and an increase in equilibration time with increasing effective stress for all pore fluids, were seen not only for the AD Ca-SAz-1 sample but also for the AD Na-SWy-1 sample.

A final observation for the Stage 2 runs on both the AD Ca-SAz-1 and AD Na-SWy-1 samples is that the total strain response of the samples to load cycling (i.e. the combined time-dependent and time-independent response) was close to reversible (**Figures 3B,C**). Hysteresis that was observed was minor and of similar magnitude to the hysteresis (~2 μm) induced by seal friction and seen in Stage 1 cycling.

We turn now to the data obtained in the rapid load cycling runs performed on the Na-SWy-1 samples only in the final stages of the Stage 2 tests on this material. Typical data obtained for the Na-SWy-1 sample charged with wet Ar and wet CO₂ are presented in **Figures 4A,B**. Both stress-strain curves indicate largely reversible mechanical behaviour, with best linear fits giving similar values of apparent stiffness modulus for the Ar and CO₂ runs of 2.65 and 2.44 GPa respectively.

Stage 3 Data: Stepwise Cyclic Loading of VD Samples Saturated With Pure (dry) He and Pure (dry) CO₂

Representative data obtained from the Stage 3 cyclic loading and unloading steps applied to both samples in the VD state shown in **Figure 5** (see also **Table 1**). **Figure 5A** shows the history of pore fluid charging and stress stepping applied to the VD Ca-SAz-1 sample, while **Figure 5B** shows the corresponding changes in sample thickness as a function of elapsed experimental time. The Na-SWy-1 sample showed qualitatively very similar behaviour. Both exhibited a largely reversible and reproducible strain response to stress cycling when saturated with either dry He or dry CO₂ (see **Figure 5B**). In addition, the samples expanded by a small amount (~10 μm for the Ca-SAz-1 sample) when the pore fluid was switched from dry He to dry CO₂ at a reference effective stress of ~1.1 MPa and standard pore pressure of 10 MPa. These trends are typical for both samples tested in Stage 3 (VD) and are similar to those observed for AD samples (Stage 2). However, in contrast to the AD samples tested in Stage 2 employing wet pore fluids, the VD samples saturated with dry CO₂ or dry He (Stage 3) show only very minor time-dependent compaction in response to changes in effective stress (c.f. **Figures 5B** versus **3B**).

Equilibrium Thickness Changes Versus Applied Effective Stress in Stage 2 and 3 Runs

Both smectite samples showed time-dependent strain development towards equilibration, following the stress steps applied in the Stage 2 stress cycling runs (AD samples plus wet fluid) and in the Stage 3 runs (VD samples, dry fluid).

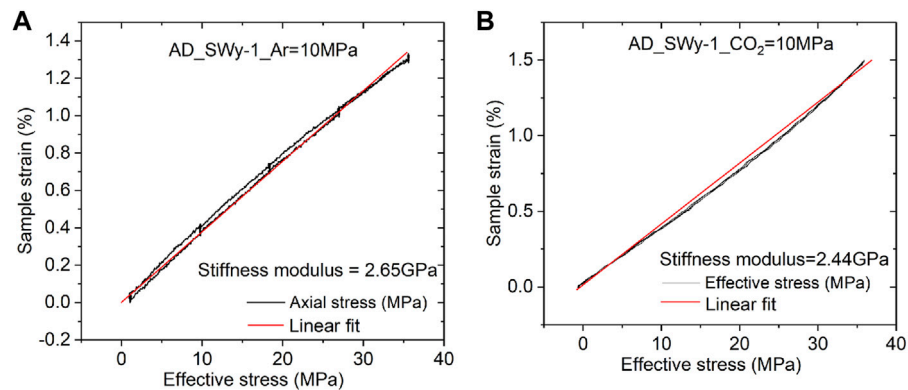


FIGURE 4 | Effective stress versus sample strain measured in the rapid stress cycling runs performed on the AD SWy-1 sample at the end of Stage 2 experimentation. **(A)** Stress-strain data obtained in cycle performed using wet Ar. Best linear fit shows a constrained axial stiffness modulus of 2.65 GPa **(B)** Stress-strain data obtained in cycle performed using wet CO₂. Best linear fit shows a constrained axial stiffness modulus of 2.44 GPa.

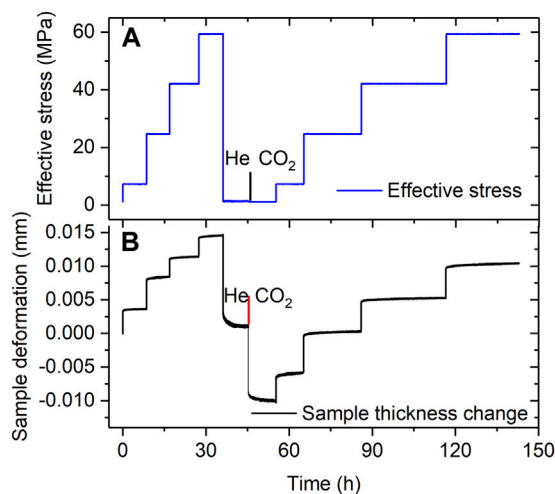


FIGURE 5 | Representative data obtained in Stage 3 experiments performed on VD samples using pure (dry) He and CO₂ (illustrated here for the VD Ca-SAz-1 sample). **(A)** Stress path employed in runs on VD sample SAZ-1, sequentially charged with dry He and dry CO₂ at a pressure of 10 MPa. **(B)** Corresponding sample thickness change versus experimental time. All data measured relative to the starting state in the Stage 3 experimental series.

The stable equilibrium value in sample thickness change attained after each stress step, are listed in **Table 1** and plotted as a function of effective stress in **Figure 6** - for both samples and for the Stage 2 and 3 runs. These data show that equilibrium deformation of both samples was largely recoverable with only minor permanent strain accumulating during load cycling. This is evidenced by 1) the closely similar stress-displacement curves obtained in repeated loading runs performed on the same sample using the same pore fluid, regardless of pore fluid sequence (see **Figure 6A**, wet Ar₁ versus wet Ar₄), and 2) the minor hysteresis in sample thickness change observed in loading and unloading cycles performed with a given sample and fluid (e.g. **Figures 6A–D**). In addition, all experiments performed with

CO₂, dry or wet, yield lower values of equilibrium sample compaction than He and Ar under otherwise identical conditions (**Figures 6A–D**). This is observed at all stresses applied, and can alternatively be expressed as a relative expansion or swelling with respect to equivalent runs saturated with He or Ar. Notably, all data (**Figure 6**) show a decrease in magnitude of this relative swelling with increasing effective stress.

Cumulative Equilibrium Strain Versus Applied Effective Stress Data (Stage 2 and 3 Runs)

The cumulative equilibrium strains (ϵ_i) calculated from the equilibrium sample thickness changes represented per stress step in **Figure 6** are plotted against the applied effective stress in **Figures 7A–D**, for both the SWy-1 and SAZ-1 samples tested in Stage 2 (AD using wet pore fluid) and Stage 3 (VD using dry pore fluid). Recall from Section 4.2.4 that cumulative strain is defined as the total strain accrued by the samples during loading, relative to the thickness attained at the lowest effective stress applied in the first loading series conducted with a given fluid (**Table 1**). From **Figure 7**, it is evident that all samples saturated with CO₂ exhibited significantly different cumulative equilibrium strain versus stress behaviour compared with samples saturated with Ar and He, in Stages 2(wet fluids) and 3 (dry fluids). By contrast, the cumulative equilibrium strain-stress curves obtained for samples charged with He and Ar do not differ much (**Figure 7A**). Clearly, samples exposed to CO₂ generally showed more compressive deformation than those exposed to He or Ar (**Figure 7**) at a given stress. Note also that, the initially air-dry samples (AD SWy-1 and AD SAZ-1) tested with wet pore fluids (Stage 2) exhibited more or less linear stress-strain behaviour (**Figures 7A,C**). This linear behaviour at equilibrium is characterized by low “stiffness” values obtained using wet CO₂ versus high “stiffness” values obtained using He or Ar (see **Figures 7A,C** plus **Table 2**). By contrast, the VD samples showed nonlinear behaviour (**Figures 7B,D**), characterized by equilibrium “stiffness” values that increase with increasing axial

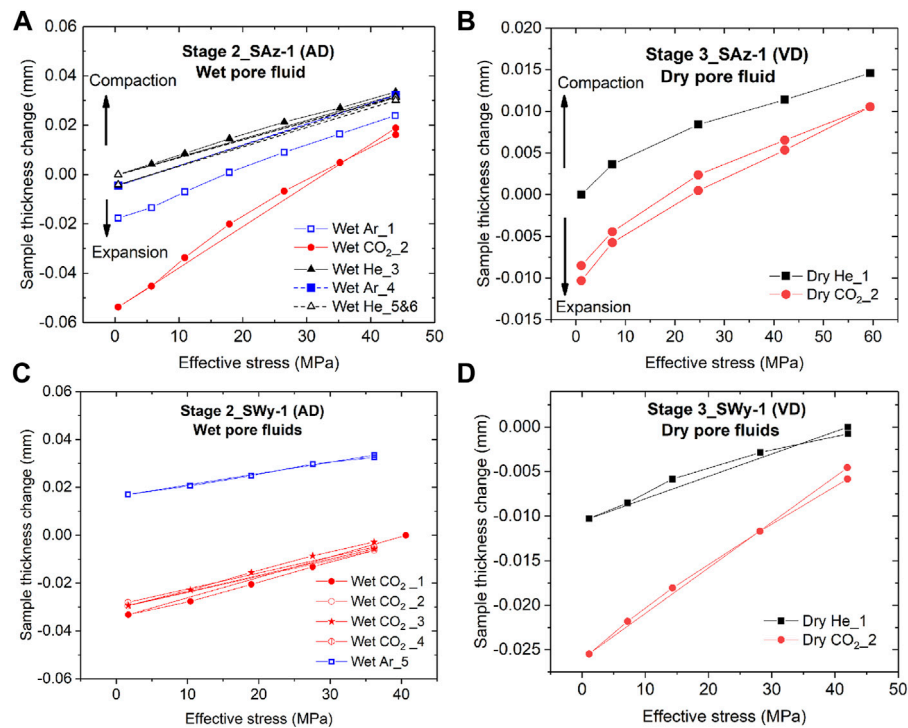


FIGURE 6 | Equilibrium sample thickness change (hence strain) versus effective stress data obtained in the Stage 2 and Stage 3 stress cycling experiments. Note that Stage 2 experiments were conducted on AD samples saturated with wet pore fluids, while Stage 3 runs were conducted on VD samples saturated with dry pore fluids. **(A)** Stage 2 data for the initially AD Ca-SAz-1 sample. **(B)** Stage 3 data for the VD SAz-1 sample. **(C)** Stage 2 data for the initially AD Na-SWy-1 sample. **(D)** Stage 3 data for the VD Na-SWy-1 sample.

effective stress. These dry Stage 3 stiffness values at two to five times higher than obtained in the wet Stage 2 tests for each gas used, and again show substantially lower values in CO₂ runs than in runs with inert gas (He) – see **Figures 7B,D** and **Table 2**.

DISCUSSION

The rapid load cycling data obtained here for the AD SWy-1 and SAz-1 samples before pore fluid addition (Stage 1), and in the presence of wet Ar and CO₂ at 10 MPa (AD sample SWy-1, end Stage 2), demonstrated reversible near-linear stress-strain behaviour, implying a constrained elastic stiffness of the samples of $\sim 2.1 \pm 0.5$ GPa. This range narrowed to 2.44–2.65 GPa for the AD SWy-1 sample exposed to wet CO₂ and wet Ar respectively, pointing to little effect of CO₂ versus inert gas on elastic behaviour obtained in rapid loading. By contrast, our stepwise loading and unloading experiments performed on the AD Ca-SAz-1 and Na-SWy-1 montmorillonite discs using wet gases (Stage 2), and on the vacuum-dried samples using dry gases (Stage 3), showed that CO₂ enhanced compressive strains and reduced sample stiffness in comparison with He and/or Ar, in the wet and dry equilibrium states. In this section, we analyze and discuss the effect of CO₂ versus He and Ar on the mechanical response and stepwise equilibration behaviour of our pressed smectites discs. We go

on to compare our equilibrium stress-strain data with the thermodynamic model for stress-strain-sorption processes developed by Hol et al. (2012) and Liu et al. (2016b). Finally, the implications of our findings for geological storage of CO₂ are considered.

Effect of CO₂ Versus He and Ar on Mechanical Behaviour of the SWy-1 and SAz-1 Samples

The present stepwise stress cycling data obtained using wet pore fluids (AD SWy-1 and SAz-1, Stage 2) and dry pore fluids (VD SWy-1 and SAz-1 samples, Stage 3) show that all samples exposed to CO₂ attained larger equilibrium strains than those exposed to Ar and He, following any increment in effective stress (**Figure 7**). The apparent equilibrium stiffness for samples saturated with CO₂ versus He and Ar was accordingly 20–65% lower (see **Table 2** and **Figure 7**).

These effects of CO₂ in the wet and dry states, mean that CO₂ somehow caused excess compression (lower stiffness) relative to tests employing He or Ar. A possible role of changing hydration state on basal spacing (Schaefer et al., 2012; Loring et al., 2013; Romanov, 2013) due to pore fluid switching, can be excluded by the fact that all pore fluids employed in the Stage 2 tests on initially AD samples contained similar water content (i.e. RH or activity), while the Stage 3 runs on VD samples used fully dry

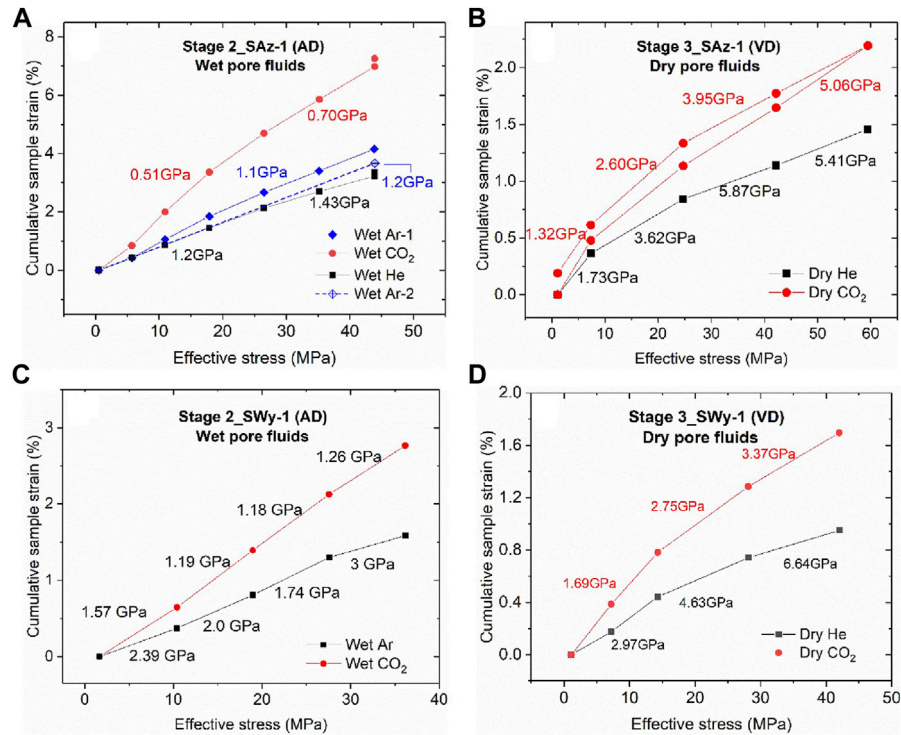


FIGURE 7 | Cumulative compressive sample strains, measured at equilibrium per stress step, plotted against applied effective stresses, for the Stage 2 and 3 stress cycling experiments performed on both the SAZ-1 and SWy-1 samples. Cumulative sample strains are calculated relative to sample thickness at the lowest effective stress applied, i.e. lowest effective stress in each plot. Values of cumulative strain measured at the same effective stress but in different loading cycles were averaged and only the mean value was plotted for a given stress. The apparent stiffness values (GPa) shown per stress interval are tangent moduli ($C_{app} = \Delta\sigma_e / \Delta\epsilon$) derived from equilibrium strain-stress data obtained over the corresponding interval. **(A)** Stage 2 data for the initially AD Ca-SAZ-1 sample. **(B)** Stage 3 data for the VD SAZ-1 sample. **(C)** Stage 2 data for the initially AD Na-SWy-1 sample. **(D)** Stage 3 data for the VD Na-SWy-1 sample.

TABLE 2 | Apparent stiffness data for samples tested in Stages 2 and 3.

Sample	Range of σ_e	C_{app} (He)	C_{app} (CO ₂)	$C(\text{CO}_2): C(\text{He})$	Sample	Range of σ_e	C_{app} (He)	C_{app} (CO ₂)	$C(\text{CO}_2): C(\text{He})$
	MPa	GPa	GPa			MPa	GPa	GPa	
Stage 2 AD samples saturated with wet pore fluids (RH \approx 20%)									
AD SAZ-1	0.5–43 ^a	1.33	0.61	0.45	AD SWy-1	1.7–36.2 ^a	2.1 ^b	1.23	0.59
	0.5–5.7	1.21	0.62	0.51	—	1.7–10.4	2.4 ^a	1.57	0.66
	5.7–10.9	1.22	0.45	0.37	—	10.4–19	2.02 ^a	1.19	0.59
	10.9–17.9	1.17	0.51	0.44	—	19–27.6	1.78 ^a	1.18	0.66
	17.9–26.5	1.27	0.64	0.51	—	27.6–36.2	3.07 ^a	1.26	0.41
	26.5–35.2	1.52	0.75	0.50	—	—	—	—	—
	35.2–43.9	1.34	0.77	0.58	—	—	—	—	—
Stage 3 VD samples saturated with dry pore fluids									
VD SAZ-1	1.1–59.4 ^a	2.88	4.21	0.68	VD SWy-1	1.1–42.0 ^a	2.97	1.69	0.49
	1.1–7.4	1.73	1.39	0.80	—	1.1–7.2	3.23	2.37	0.48
	7.4–24.7	3.62	2.53	0.70	—	7.2–14.3	2.54	3.37	0.71
	24.7–42.2	5.87	3.70	0.63	—	14.3–28.1	4.40	2.37	0.47
	42.2–59.4	5.41	3.63	0.67	—	28.1–42	6.31	3.37	0.36

The “stiffness” values (C_{app}) given here represent apparent stiffness ($\Delta\sigma_e / \Delta\epsilon$) derived from equilibrium strain-stress data obtained over the corresponding effective stress interval.

^aRepresents the full range of effective stress explored for each sample, so that the stiffness values in the corresponding row represent linear best fit values for this full range.

^bDenotes the apparent stiffness values calculated from stress versus strain data obtained in an Ar test, due to a lack of data using He.

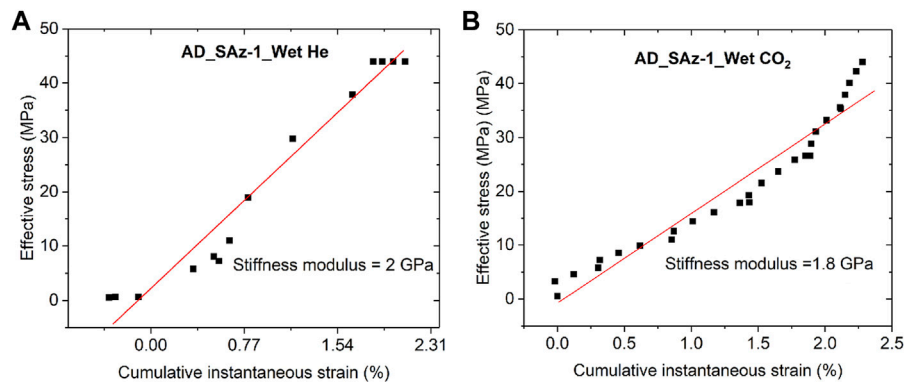


FIGURE 8 | Cumulative instantaneous strain developed in the AD SAz-1 sample during Stage 2 stress stepping using (A) wet He and (B) wet CO₂ as pore fluid. Best linear fits yield similar values of axial stiffness for both fluids used.

fluids. Other mechanisms potentially contributing to the axial strain response to effective stress steps include: 1) Permanent deformation associated with clay plate plasticity or kinking, crystallite cleavage or platelet rearrangement and alignment; 2) poroelastic strain (ϵ^{el}); and 3) time-dependent reversible deformation (ϵ^{td}) due to reversible CO₂ (and possibly H₂O) expulsion from sorption sites in the interlayer structure, from surface sorption sites or intergranular pores as the aggregate deforms poroelastically. Each of these is considered below.

First, permanent deformation effects caused by CO₂ can be ruled out because all stepwise loading and unloading experiments demonstrated almost completely recoverable behaviour, with little hysteresis in sample thickness change using CO₂, He or Ar as pore fluid, wet or dry (see **Figure 6**). The small permanent strains and minor hysteresis effects that are seen are too small to explain the much larger sample thickness changes and cumulative compressive strains visible in experiments employing CO₂ as opposed to He or Ar (**Figures 6, 7**). Taking into account that ~2 μ m of this is related to seal friction, permanent strains can only account for sample strains <0.3%. These values are well below the total strains measured for samples tested with CO₂ and the amount of hysteresis in sample thickness changes appears no change with different pore fluid phases.

Second, we examine the possibility of CO₂-induced reduction in elastic stiffness. This has been considered previously as a possible interpretation for lowering of the apparent uniaxial stiffness modulus of coal seen upon CO₂ or CH₄ sorption (Viète and Ranjith, 2006; Hol et al., 2014). However, this mechanism is not supported by the results of the fast load cycling runs performed on the SWy-1 sample at the end of Stage 2 testing (see **Figure 4**), which yielded almost the same values of axial stiffness for Ar and CO₂ tests, specifically 2.65 and 2.44 GPa. To further examine if CO₂ caused any change in time-independent sample response, we extracted the instantaneous strains (see **Figure 2**) developed, per stress increment applied, in the Stage 2 tests performed on the AD Ca-SAz-1 sample using wet He and wet CO₂ as pore fluid. These stress-strain data are plotted in **Figure 8**. Though more bi-linear than linear (perhaps due to difficulty

in identifying truly instantaneous strain), linear best fitting showed no significant difference between He runs and CO₂ runs (~2 versus 1.8 GPa – see **Figure 8**). On this basis, we infer that the CO₂-induced decrease in apparent stiffness modulus seen in our (slow) incremental loading tests is not achieved through lowering of the samples' elastic modulus.

Rather, our results from the slow stepwise (equilibrated) load cycling runs, versus the fast loading experiments, imply that the reduction of apparent sample stiffness in the slow stepwise runs with CO₂ likely involves a mechanism featuring reversible, time-dependent strain – at least in the wet Stage 2 experiments. This assertion is supported by the fact that the time-dependent and equilibrium strains occurring in the wet CO₂ stepping tests on both sample types (Stage 2) are much larger than in the wet He and Ar tests, over the same increments in effective stresses.

Against this background, and given the reversibility (and variable degree of time-dependence) of deformation seen in our stress increment/decrement tests employing wet and dry gases (Stages 2 and 3), it seems likely that the relevant mechanism for the increased equilibrium strain response of samples tested with CO₂, as opposed to He or Ar (**Figures 6, 7**), is one of stress-driven desorption of CO₂ molecules (or H₂O molecules or both). Alternatively stated, we infer that increasing compressive effective stress leads to desorption of CO₂ (and/or H₂O) molecules that were previously adsorbed and at equilibrium in the montmorillonite interlayer or surface sorption sites. Such behaviour is closely similar to the stress-driven desorption of CH₄ and CO₂ observed in coal exposed to these fluids/gases at fixed fluid pressure, and to the predictions of thermodynamic models for the effects of stress on sorption (Hol et al., 2011; Brochard et al., 2012; Hol et al., 2013; Espinoza et al., 2016; Liu et al., 2016a).

The strongly time-dependent deformation seen following stress steps imposed in all (wet) Stage 2 runs on both Na-SWy-1 and Ca-SAz-1 samples (**Figure 3**), in particular the wet CO₂ runs, is similarly inferred to represent the approach to a new equilibrium state between clay, H₂O and CO₂ (or He/Ar). The much smaller degree of time-dependent deformation seen in the dry Stage 3 tests (**Figure 5**) may reflect a correspondingly smaller equilibration effect. Possible reasons for the observed time

dependence, assuming zero interaction between our smectite samples and inert He and Ar (following Busch and Gensterblum, 2011), include a time-dependent release of CO₂ and/or H₂O from the sample due to reversible stress-induced desorption. However, since rates of CO₂ and H₂O sorption/desorption by montmorillonite are known to be rapid (Ferrage et al., 2007a; Giesting et al., 2012a; Giesting et al., 2012b; de Jong et al., 2014) and generally limited by transport of CO₂ and H₂O into or out of the sample (depending on sample size), we suggest that the time-dependent effects seen in our samples were likely controlled by their permeability to CO₂, H₂O, He, Ar or notably to mixed CO₂ and H₂O.

Relative Swelling Induced by CO₂ Versus He/Ar

Our Stage 2 (wet) and Stage 3 (dry) stepping experiments performed on the SWy-1 and SAz-1 samples, in the initially AD (Stage 2) and VD (Stage 3) states, consistently showed sample expansion when the pore fluid was switched from Ar or He to CO₂ under constant effective stress condition, thus indicating a swelling effect induced by exposure to CO₂ (refer to Figures 3, 4). Relative swelling of samples tested with CO₂ versus He or Ar is also evident in the equilibrium thickness change versus stress data derived from our Stage 2 (wet) and Stage 3 (dry) stepping tests on both samples, as reported in Figure 6. Being inert pore fluids, He and Ar do not intercalate into clay interlayer structures (Eltantawy and Arnold, 1972), and volumetric strain effects due to sorption of He and Ar onto clay platelet surfaces has been shown to be negligible (e.g. Giesting et al., 2012a; Heller and Zoback, 2014; Zhang et al., 2018). Therefore, we assume that sample thickness changes observed in the present He/Ar tests reflect the poroelastic behaviour of the sample in response to changes in effective stress. We further use the differences in equilibrium sample thickness changes measured between the CO₂ and He/Ar tests to quantify the relative swelling deformation (in excess of poroelastic effects) due to CO₂ exposure (Figure 6). These differences are listed as a function of corresponding applied effective stress in Table 1, for both the Ca-SAz-1 and Na-SWy-1 samples and for the Stages 2 (wet) and 3 (dry) experiments. All differential values of equilibrium sample thickness changes are negative (see Table 1), confirming a relative swelling or expansion effect caused by exposure to CO₂ at 10 MPa pressure. The corresponding CO₂-induced swelling strains were calculated as the ratio of the relative swelling deformation to the referential (initial) sample thickness (L_0). The results are listed against applied effective stress in Table 1 and plotted versus applied effective stress in Figure 9.

With reference to Figure 9, it is clear that the relative swelling strains calculated for AD samples saturated with wet CO₂ versus wet Ar/He are substantial, i.e. 4%–5% for the AD Na-SWy-1 sample at effective axial stresses of 1.6–36.2 MPa, and ~1.5–5.5% at 0.5–44.0 MPa effective stress for the AD SAz-1 sample. Lower swelling strains of 0.5–1.5% and 0.4–0.9% were recorded for vacuum-dried (VD) SWy-1 and SAz-1 samples tested with pure dry CO₂ versus dry He/Ar. For all samples, relative swelling strain attained decreased consistently with increasingly applied effective

stresses (Figure 9). This trend is again qualitatively consistent with that predicted by the thermodynamic model for single species gas/fluid adsorption by stressed solids put forward by Hol et al. (2011, 2012) and Liu et al. (2016b) (Brochard et al., 2012; cf. models by; Espinoza et al., 2014; Nikoosokhan et al., 2014; and Espinoza et al., 2016).

Experimental Results for CO₂ Charged Samples Versus the Hol-Liu-Spiers Model

The Hol-Liu-Spiers model predicts that applied effective stress reduces the sorption capacity of solid sorbents, desorbing the sorbate and causing associated solid shrinkage/strain. To assess the applicability of this model to our results for the AD and VD SWy-1 and SAz-1 samples tested with wet and dry CO₂ versus wet and dry He or Ar, we now fit the Hol-Liu-Spiers model to our experimental data on relative swelling strain versus effective stress (Figure 9), evaluating the quality of the fit and the physical viability of the parameter values obtained.

Summary of Hol-Liu-Spiers Model and Application to Present Experiments

The Hol-Liu-Spiers model presents an expression for the adsorbed concentration of a gas or fluid species in a stressed solid by obtaining the condition of equilibrium between the free gas or fluid at pressure P and its adsorbed equivalent. In doing so, the free energy of adsorption is modified to include a stress-strain work term associated with the Terzaghi effective stress supported by the solid, in addition to the pressure-volume work term found in conventional sorption models that assume identical hydrostatic pressure in both the solid and fluid phases (see Hol et al., 2012; Espinoza et al., 2014; Espinoza et al., 2016; Liu et al., 2016b). The model predicts that the equilibrium concentration (C_σ) of adsorbed molecules of a single sorbing species (mol/kg) in a solid adsorbent phase decreases with total hydrostatic stress (σ_n) applied to the solid according to the relation

$$C_\sigma = C_s \theta = \frac{C_s a_g \exp\left(\frac{\mu_{g0} - \mu_s^{p0}}{RT}\right) \exp\left(\frac{-(\sigma_n - P_0)V_0}{RT}\right)}{1 + a_g \exp\left(\frac{\mu_{g0} - \mu_s^{p0}}{RT}\right) \exp\left(\frac{-(\sigma_n - P_0)V_0}{RT}\right)} \quad (1)$$

Here C_s (mol/kg) is the adsorption site density in the adsorbent, θ is the adsorption site occupancy, a_g is the activity of the sorbing gas/fluid at given pressure and temperature conditions, μ_{g0} is the chemical potential of free gas/fluid phase at a standard reference pressure (e.g. $P_0 = 0.1$ MPa), μ_s^{p0} is the chemical potential of the adsorbed species at the reference pressure P_0 , R ($J \cdot K^{-1} \cdot mol^{-1}$) is the gas constant, T (K) is the absolute temperature and V_0 (m^3/mol) is the partial molar volume of the adsorbed molecules (i.e. the volume increase experienced by the solid sorbent due to absorption of 1 mol of sorbate).

To apply the above equation to describe our experimental results, and to assess its suitability, we must now assume 1) that the relative strains derived from our CO₂ tests and the equivalent He/Ar tests are solely due to CO₂ sorption/desorption, 2) that CO₂ sorption takes place in both clay interlayer and platelet

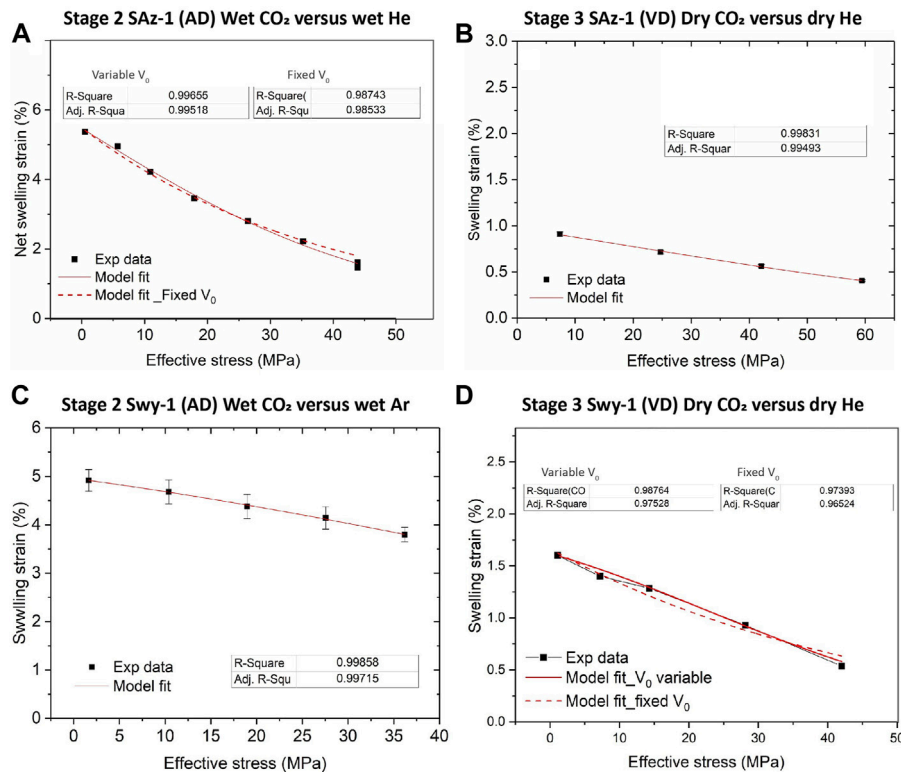


FIGURE 9 | Experimentally derived data on relative swelling strain as a function of applied stress, as obtained for CO₂ versus He and/or Ar in the Stage 2 (wet) and Stage 3 (dry) tests. Model fits using Eq. 2 are added (red curves) for comparison. **(A)** Stage 2 data for the initially AD Ca-SAZ-1 sample. **(B)** Stage 3 data for the VD SAz-1 sample. **(C)** Stage 2 data for the initially AD Na-SWy-1 sample. **(D)** Stage 3 data for the VD Na-SWy-1 sample.

surface sites, 3) that the parameters in equation 1 are constant and apply to both sites with equal values, 4) that ad/de-sorption of CO₂ and H₂O are fully independent, and 5) that swelling/shrinkage due to CO₂ sorption/desorption occurs in the axial loading direction only (i.e. normal to the expected alignment of [001] basal planes in the compacted samples). It then follows that the sorption-induced volumetric and axial swelling strain ϵ_V^{ads} is linearly proportional to the adsorbed concentration C_σ (mol/kg_{absorbent}) (c.f. Hol et al., 2012), such that $\epsilon_V^{ads} = C_\sigma \rho V_0$, where ρ is the density of the clay sample. Combining this with Eq. 1 and substituting the total axial stress $\sigma_e + P$ in our experiments for σ_n , an axial stress-strain-sorption model is obtained for smectites upon uptake of CO₂ (independently of adsorption of water), written

$$\epsilon_V^{ads} = \frac{a_1 a_2 \exp\left(\frac{-(\sigma_e + P - P_0)V_0}{RT}\right)}{1 + a_2 \exp\left(\frac{-(\sigma_e + P - P_0)V_0}{RT}\right)} \quad (2)$$

Where $a_1 = C_s \rho V_0$ and $a_2 = a_g \exp\left(\frac{(\mu_{g0} - \mu_s^0)}{RT}\right)$.

Fitting to Present Data

To assess its applicability, the above model was fitted to the experimental data on relative, CO₂-induced swelling strain versus effective stress presented in Figure 9 (and Table 1), using a nonlinear fitting routine. Regression iterations were continued until the fit converged with a Chi-Sqr tolerance value of 10^{-9} . The

model fits to the experimental data are superimposed on Figure 9, and the key parameters derived from the fits are given in Table 3. The primary fitting parameters obtained from the regression were a_1 , a_2 and V_0 . The adsorption site density (C_s) present per kilogram of sample material was derived from values of a_1 and V_0 . The density of the adsorbed CO₂ phase (ρ_{ads}) was calculated from the partial molar volume V_0 determined from our model fit, using $\rho_{ads} = M(\text{CO}_2)/V_0$ where $M(\text{CO}_2)$ is the molar mass of CO₂. The adsorbed concentration of CO₂ (C_σ) was simultaneously obtained as a function of effective stress using Eqs 1, 2.

Comparison of Fit-Derived Parameters and Model Predictions With Previous Data

Fit-Derived Parameters and Sorbed Concentration Versus Previous Data

We now compare the parameter values obtained above with previous data on sorption site density (C_s), partial molar volume (V_0) and density (ρ_{ads}) of sorbed CO₂ (Table 3). We also compare the present fitting results for the adsorbed concentration of CO₂ (C_σ) under stressed conditions with previous information.

Several studies have reported the sorption capacity of smectite clays for CO₂ at P-T conditions relevant to CO₂ storage but at fully hydrostatic conditions, i.e. at zero effective stress. Schaefer et al. (2014) reported that the CO₂ sorption capacity of dry Ca-rich SWy-2 montmorillonite at 9 MPa CO₂ pressure and 50°C was 0.92 mol/kg. Busch et al. (2008) reported ~0.3 and ~1.0 mol/kg

TABLE 3 | Parameter values obtained from best fit of Hol-Liu-Spiers Model (Eq. 2) to our data for samples exposed to CO₂ relative to He and/or Ar.

Sample/Condition	Stage	a1	a2	V ₀	C _s	ρ _{ads}	C(σ ₀)
				m ³ /mol	mol/kg	kg/m ³	mol/kg
SWy-1.AD	Stage 2	6.22	5.07	66.08 × 10 ⁻⁶	0.42	665.86	0.1
SWy-1.VD	Stage 3	2.1	5.54	134 × 10 ⁻⁶	0.74	328.36	0.06
SWy-1.VD ^a	Stage 3	11.23	0.22	66.08 × 10 ⁻⁶	0.07	665.86	0.03
SAZ-1 AD	Stage 2	11.33	1.39	103.87 × 10 ⁻⁶	0.50	423.61	0.47
SAZ-1 AD ^a	Stage 2	47312	1.49 × 10 ⁻⁰⁴	66.08 × 10 ⁻⁶	3254.46	665.86	NR
SAZ-1 VD	Stage 3	1.56	2.15	67.97 × 10 ⁻⁶	0.10	647.34	0.03

ρ_{ads} represents the adsorbed phase density of CO₂. C(σ) reported in the table is the predicted sorbed concentration of CO₂ (C_d) obtained at the lowest effective stress applied to each sample during the stress cycling runs. NR denotes that data is not reported due to no convergence achieved in the model fitting.

^aRepresents model fits performed using a V₀ value derived from the model fit to the AD SWy-1 run.

CO₂ excess sorption capacities for Na and Ca montmorillonites, respectively, at a CO₂ pressure of 10 MPa and a temperature of 45°C. The sorbed CO₂ concentrations (C_o) at low effective stress (0.5–1.5 MPa), as derived from fitting our experimental data for Stages 2 (wet) and 3 (dry) to the Hol-Liu-Spiers model (Eq. 2), are 0.1 mol/kg for Na-SWy-1 montmorillonite and 0.47 mol/kg for Ca-SAZ-1 montmorillonite (Table 3). These values are of the same order as reported in the above studies. However, the C_s value of 0.5 mol/kg for AD Ca-SAZ-1 montmorillonite tested with wet CO₂ versus wet He, as derived from the present model fit, is ~50% lower than that reported for Ca-montmorillonite at similar P-T conditions by Busch et al. (2008) and Schaefer et al. (2015). For AD Na-SWy-1 tested with wet gases, our C_s of 0.42 mol/kg is ~35% of that reported by Busch et al. (2008). These discrepancies might be caused by the different compositions of the samples tested and/or different hydration states attained by the samples when charged with CO₂. On the other hand, the discrepancies might result from the assumptions made in applying the Hol-Liu-Spiers model or from other factors not accounted for.

The values of ρ_{ads} listed in Table 3 show similar densities for CO₂ adsorbed by our AD SWy-1 and VD SAZ-1 montmorillonite samples, respectively 665 kg/m³ and 647 kg/m³. These are slightly higher than the bulk density (ρ_{bulk} = 628 kg/m³) of free supercritical CO₂ at the present experimental conditions (i.e. 10 MPa and 40°C), implying positive excess sorption. By contrast, our ρ_{ads} values for VD SWy-1 and AD SAZ-1 are much lower than ρ_{bulk}, being 326 kg/m³ and 424 kg/m³ and indicating negative excess sorption. Our ρ_{ads} value for the VD SWy-1 and AD SAZ-1 samples are, however, consistent with the densities (0.3–0.4 g/cm³) reported by Rother et al. (2013) for CO₂ adsorbed in the interlayer space of Na montmorillonite with <1W hydration state. On the other hand, the ρ_{bulk} values obtained for the adsorbed CO₂ phase in the AD SWy-1 and VD SAZ-1 samples (Table 3) are closer to the density of H₂O adsorbed in the interlayer of smectite clays (Fu et al., 1990). This suggests that H₂O adsorption/desorption might occur alongside CO₂ adsorption/desorption, contributing to the overall stress-strain-sorption behaviour observed for the AD SWy-1 and VD SAZ-1 samples in the Stages 2 (wet) and 3 (dry) experiments respectively.

Model Predictions Versus Previous Experimental Data on Swelling Stress

We now apply the Hol-Liu-Spiers model, with the (He-relative) parameter values for VD SWy-1 material given in Row 2 of

Table 3, to predict swelling stresses (σ_{sw}) developed in VD SWy-1 montmorillonite charged with dry CO₂ at 10 MPa at 50°C under restricted swelling strain (ε_{sw}) conditions, i.e. under the same conditions and same restricted swelling strain condition as the swelling stress experiments reported in Zhang (2019) (see Table 4). First, we combine the Hol-Liu-Spiers model with Hook's Law to establish a relationship between (total) restricted sample strain (ε_r) and the effective stress applied, thus accounting for elastic and adsorptive strain. This yields

$$\varepsilon_r = \varepsilon^{el} + \varepsilon_V^{ads} = \frac{\sigma_e - \sigma_e^{in}}{E} + \frac{a_1 a_2 \exp\left(\frac{-(\sigma_e + P - P_0)V_0}{RT}\right)}{1 + a_2 \exp\left(\frac{-(\sigma_e + P - P_0)V_0}{RT}\right)} \quad (3)$$

Here, ε^{el} is the axial elastic strain of the sample induced by change in effective stress relative to the initial effective stress (σ_eⁱⁿ) applied to the sample, and E is the constrained uniaxial stiffness (C_{app}, mean value = 3 GPa, see Table 2) for the VD SWy-1 sample measured in the present study. Second, we inserted the restricted swelling strains measured in the experiments (i.e. the sorption-induced swelling strain) into Eq. 3, as the boundary strain condition and solved for the final effective stress (σ_e) associated with this strain. Subtracting the initial effective stress σ_eⁱⁿ then yielded the predicted swelling stress (see Table 4). The results show that the swelling stress values predicted per experiment are of the same order as the experimental data, but differ significantly in individual values. This is presumably caused by inconsistencies between the mean stiffness modulus (C_{app} = 3 GPa) used in the model fit versus the specific elastic modulus of the individual samples tested in each experiment.

Model Evaluation

On the basis of the above, we can conclude that the Hol-Liu-Spiers model, applied with the additional assumption made here, can be fitted to accurately describe the relative CO₂-induced swelling data, and its inverse dependence on applied effective stress, obtained in our Stage 2 (wet) and Stage 3 (dry) experiments on SWy-1 and SAZ-1 montmorillonites (Figure 9). The parameter values obtained in the fitting procedure are in reasonable, broad agreement with values independently reported in the literature. Moreover, the model fits obtained for Na-SWy-1 material under VD conditions (see Table A1) adequately predict the CO₂ exposure-induced swelling stresses measured for similar material at slightly higher temperatures (50°C) conditions in Zhang (2019) and Zhang (2019). In detail,

TABLE 4 | Comparison of model prediction with experimental data on swelling stresses measured for VD SWy-1 samples exposed to CO₂ pressure at 10 MPa at 50°C (Zhang, 2019).

Exp number	$\sigma_e^{in} (exp)$	$\varepsilon_{sw} (exp)$	$\sigma_{sw} (exp)$	Sorption-induced $\varepsilon_{sw} (exp)$	Predicted σ_{sw}
	MPa	%	MPa	%	MPa
T50VD-CS1	11.13	1.89	6.81	1.24	3
T50VD-CS2	11.6	1.7	6.12	1.05	5.5
T50VD-CS3	17.96	1.39	5.89	0.74	8
T50VD-CS4	18.46	1.57	6.66	0.92	4.7
T50VD-CS5	25.52	1.16	4.88	0.51	8.6

$\sigma_e^{in} (exp)$ is the initial effective stress applied to each sample tested in the swelling stress measurement performed on the VD SWy-1 montmorillonite disks exposed to 10 MPa CO₂ pressure at 50°C. $\sigma_{sw} (exp)$ and $\varepsilon_{sw} (exp)$ are the experimentally measured swelling stress and accompanying swelling strain reported by Zhang et al. (2018). Sorption-induced $\varepsilon_{sw} (exp)$ is the measured swelling strain after correction for pore-elastic effect, i.e. swelling strain contributed by CO₂ adsorption.

however, there are a variety of inconsistencies between model and measurements, presumably reflecting inadequacies of the model assumptions, such as non-equivalence of interlayer and clay surface sorption sites, or interdependence and competition between CO₂ and H₂O uptake (Busch et al., 2008; see also; Giesting et al., 2012a; Loring et al., 2013; Loring et al., 2014; as reported by; Schaefer et al., 2015). Future application of the Hol-Liu-Spiers model to describe stress-strain-sorption behaviour of smectite clays under CO₂ storage conditions, in a more reliable and exact way, therefore requires extension of the model to take into account factors such as these.

Implications for CCS

CO₂ Storage Capacity of Smectite-Rich Rocks Under Subsurface Stress and Temperature Conditions

Conventional CO₂ sorption experiments conducted on montmorillonite clays at zero effective stress conditions (clay sample “immersed” in (Sc) CO₂), show that sorbed concentrations at P-T conditions relevant for CO₂ storage conditions are equivalent to bulk sorption capacities in the range of 380–900 mol/m³, assuming that the density of the clay rock is 2250 kg/m³ (Rother et al., 2013; Busch et al., 2016). This suggests that adsorption could provide storage capacity for CO₂ in clays present in reservoir rocks and caprocks (Song and Zhang, 2013; Busch et al., 2016). Our fits of the Hol-Liu-Spiers model to our experimental data (see Figure 9 and Table 3) imply adsorbed concentrations of CO₂ at low effective stress conditions that are consistent with this speculation. For example, the fit of Eq. 2 shown in Figure 9A implies $C_g = 0.47$ mol/kg, equivalent to 1058 mol/m³, at a CO₂ pressure of 10 MPa at 40°C under an effective axial stress of ~0.5 MPa. On the other hand, the results of model fitting show that the CO₂ sorption capacity of both Na- and Ca-montmorillonites, decreases dramatically with increasing effective stress acting on the clay, especially under “wet” (RH ≈ 20%) conditions (Figures 9A,B). Indeed, from the fit of Eq. 2 in Figure 9A, the CO₂ concentration sorbed by AD Ca-SA-1 montmorillonite decreases from the above mentioned 0.47 mol/kg at an effective stress of 0.5 MPa to 0.08 mol/kg at 40 MPa (see also Table 3). In addition, predictions using the Hol-Spiers-Liu model (Eq. 2) show a negative effect of increasing temperature on sorption capacity. Applying our model fits for typical upper crustal geothermal and lithostatic stress gradients implies that positive contributions to CO₂ storage capacity by sorption onto smectites are likely to be prominent only at shallow depths, where the temperature and lithostatic

stress are relatively low. For example, at depths up to 1.5–2 km (i.e. $T \leq 60^\circ\text{C}$ and $\sigma_e \leq 25$ MPa), bulk sorption capacities in the range of 500–1100 mol/m³ are predicted for smectite clays. However, at greater depth (e.g. >3 km), storage capacity contributed by uptake of CO₂ by smectites will quickly become negligible, decreasing to <210 mol/m³, i.e. <20% of that at zero effective stress conditions. Investigations into these aspects of ScCO₂-smectite interactions, at pressures, temperatures and water activities characteristic of geologic sequestration of CO₂, in particular under the effect of overburden stresses, have only recently begun (Schaefer et al., 2015; Zhang et al., 2018), and still need further study to achieve a better understanding.

Numerical Modelling of Caprock Integrity

Comparing the Hol-Liu-Spiers model with the swelling stress experiments presented in Zhang (2019), it gives a reasonable match to the experimental results. The model can therefore be used as a first quantification of the stress-strain-sorption relationships needed for numerical modelling to assess stress-strain-permeability changes when CO₂ penetrates into a fractured clay-rich caprock or fault, i.e. at slow rates which do not change the clay hydration state. The coupling to fracture permeability changes can be achieved using an appropriate elastic (Hertzian-contact) relationship between stress and fracture apertures, of the type put forward by Walsh (1981) - see also Cook, 1992; Connell et al., 2010). Numerical modelling work of this type has already been performed in the context of enhanced coalbed methane extraction and CO₂ storage in coal (Pan and Connell, 2007; Espinoza et al., 2013; Espinoza et al., 2014; Espinoza et al., 2016; Liu et al., 2017). In line with the conclusions drawn by Zhang et al. (2018) on CO₂-induced swelling stress, the expectation is that penetration of CO₂ into smectite-bearing clay caprocks and faults will in general cause swelling strains and swelling stresses that will tend to close migration pathways, unless desiccation of interlayer water occurs as described in Zhang (2019). To account for this in a numerical model, the present (Hol-Liu-Spiers) modelling approach would need to be extended to account for H₂O sorption and desorption, alongside CO₂.

CONCLUSION

We performed oedometric, stress-cycling experiments (i.e. laterally confined, uniaxial strain tests) on two pre-compressed

discs (~1 mm thick), respectively made of Na-SWy-1 and Ca-SAz-1 montmorillonite and initially equilibrated with He, Ar and CO₂ at 10 MPa at a temperature of 40°C. The effective stress exerted on the samples was cycled at this temperature, both continuously and incrementally (stepwise), in the range from 0.5 to 1.7 to ~43 MPa. The samples were pre-treated to obtain reference hydration states equilibrated with lab air humidity at 40°C (RH ≈ 20%) or else pre-dried under vacuum at temperatures designed to remove all interlayer water. The air-dried (AD) samples were tested using wet (RH = 20%) pore fluids while the vacuum-dried (VD) samples were tested with dry (pure) pore fluids. Our findings can be summarized as follows:

1. When subjected to rapid load cycling under atmospheric pressure or under Ar and CO₂ pressure at 10MPa, the AD Na-SWy-1 and Ca-SAz-1 samples showed reversible and recoverable stress-strain behaviour indicating elastic behaviour with a constrained uniaxial stiffness modulus in the range of 1.3–3.1 GPa when in AD state and 1.7–6.3 GPa when in VD state. This behaviour observed is more or less independent of exposure to gas type, wet or dry.
2. When subjected to stepwise stress -cycling runs, the Na-SWy-1 and Ca-SAz-1 samples, tested in initially AD state in presence of wet pore fluids (Stage 2 tests) or in initially VD state using pure (dry) pore fluids (Stage 3 tests), showed a time-dependent approach to equilibrium after each stress step. The stress-strain behaviour measured for each stepwise equilibrium state was reproducible and reversible. Both samples, tested in either the AD/wet or VD/dry state, exhibited 20–65% lower apparent stiffness, i.e. more strain, when equilibrated with CO₂ as opposed to He or Ar, showing that CO₂-smectite interactions altered the equilibrium mechanical response of pre-pressed smectites.
3. The above effect of (wet and dry) CO₂ on enhancing deformation or reducing the apparent stiffness of the present smectite discs is related to the increased equilibrium strain response of samples tested with CO₂, as opposed to He or Ar. This is inferred to be induced by stress-driven desorption of CO₂ molecules (or H₂O molecules or both) from the smectite interlayer region and possibly from clay surface sites. Desorption occurs in a time-dependent manner, especially in the case of AD samples exposed to wet pore fluid (Stage 2), probably because of permeability limited expulsion of gas/water mixtures. Only minor time-dependence was observed for VD samples exposed to dry CO₂ (Stage 3).
4. Equilibrium sample thickness changes measured in our Stage 2 (wet) and Stage 3 (dry) stress stepping experiments performed on both samples, show a relative swelling/expansion of the sample charged with CO₂ as opposed to He/Ar, per stress step applied. The magnitude of the relative swelling strain consistently decreased with increasing applied stress, being in the range of 1.5–5.5% for AD samples charged with wet CO₂, and only 0.5–1.8% relative swelling strain in the case of the VD samples exposed to dry CO₂.
5. We fitted thermodynamics-based Hol-Liu-Spiers model (Hol et al., 2012; Liu et al., 2016a; Liu et al., 2016b) for

stress-strain-sorption behaviour of a binary sorbent-sorbate system to the data on the relative swelling strain versus stress obtained in our experiments. The model fits described the experimental data accurately and yielded parameter values for CO₂ sorption capacity, sorption site concentration and density of the adsorbed CO₂ phase that are similar to independently determined values from other studies. Moreover, the fitted model predicts swelling stresses that favourably match those measured under restricted strain conditions. This suggests potential for applying such thermodynamically based models to describe and predict the stress-strain-sorption behaviour of smectite in the presence of varying CO₂ and water activities, though the model has yet to be developed to consider the mutual interaction between CO₂, H₂O and smectites.

6. The present experimental results and model fits indicate that smectite-rich rocks have significant storage capacity for CO₂ at shallow depths (up to 1.5–2 km) by means of CO₂ sorption by the clay minerals. However, the sorption capacity of CO₂ by smectite clays decreases with increasing Terzaghi effective stress and temperature, implying that the contribution of sorption by clay minerals to storage capacity is weakened by more than 80% with increasing burial depth beyond 3 km.
7. The model fitted to our data provides a first way of modelling stress-strain-sorption effects in smectite rich caprocks, and of modelling permeability changes due to penetration by CO₂. However, the assumptions behind it are strong and improvements are needed to account for interdependence and competition between H₂O and CO₂ sorption/desorption.

DATA AVAILABILITY STATEMENT

The raw data supporting the conclusions of this article will be made available by the authors, without undue reservation.

AUTHOR CONTRIBUTIONS

The authors confirm contribution to the paper as follows: MZ carried out the experimental studies and data analysis and drafted the manuscript. CS supervised the project, participated in results interpretation and helped to draft the manuscript. JL contributed to the Modelling work. HZ participated in the result discussion and helped in manuscript preparation. All authors contributed to the final manuscript.

ACKNOWLEDGMENTS

The China Scholar Council and Shell International are acknowledged for funding the first author MZ and the research presented in this paper. Suzanne Hangx, Andreas Busch and Hendrik M. Wentinck are thanked for their valuable discussion during the course of this study. Eimert de Graaff, Gert Kastelein, Peter van Krieken and Floris van Oort are thanked for their technical support.

REFERENCES

- Alvarado, V., and Manrique, E. (2010). Enhanced Oil Recovery: An Update Review. *Energies* 3, 1529–1575. doi:10.3390/en3091529
- Bachu, S. (2008). CO₂ Storage in Geological Media: Role, Means, Status and Barriers to Deployment. *Prog. Energy Combust. Sci.* 34, 254–273.
- Borden, D., and Giese, R. (2001). Baseline Studies of the Clay Minerals Society Source Clays: Cation Exchange Capacity Measurements by the Ammonia-Electrode Method. *Clays Clay Minerals* 49, 444–445. doi:10.1346/ccmn.2001.0490510
- Brochard, L., Vandamme, M., Pellenq, R. J.-M., and Fen-Chong, T. (2012). Adsorption-Induced Deformation of Microporous Materials: Coal Swelling Induced by CO₂-CH₄ Competitive Adsorption. *Langmuir* 28, 2659–2670. doi:10.1021/la204072d
- Busch, A., and Gensterblum, Y. (2011). CBM and CO₂-ECBM Related Sorption Processes in Coal: A Review. *Int. J. Coal Geol.* 87, 49–71. doi:10.1016/j.coal.2011.04.011
- Busch, A., Alles, S., Gensterblum, Y., Prinz, D., Dewhurst, D., Raven, M., et al. (2008). Carbon Dioxide Storage Potential of Shales. *Int. J. Greenh. Gas Control* 2, 297–308. doi:10.1016/j.ijggc.2008.03.003
- Busch, A., Bertier, P., Gensterblum, Y., Rother, G., Spiers, C. J., Zhang, M., et al. (2016). On Sorption and Swelling of CO₂ in Clays. *Geomech. Geophys. Geoenerg. Geo-resour.* 2, 111–130. doi:10.1007/s40948-016-0024-4
- Chadwick, R. A., Zweigel, P., Gregersen, U., Kirby, G. A., Holloway, S., and Johannessen, P. N. (2004). Geological Reservoir Characterization of a CO₂ Storage Site: The Utsira Sand, Sleipner, Northern North Sea. *Energy* 29, 1371–1381. doi:10.1016/j.energy.2004.03.071
- Chipera, S. J., and Bish, D. L. (2001). Baseline Studies of the Clay Minerals Society Source Clays: Powder X-Ray Diffraction Analyses. *Clays Clay Minerals* 49, 398–409. doi:10.1346/ccmn.2001.0490507
- Connell, L. D., Lu, M., and Pan, Z. (2010). An Analytical Coal Permeability Model for Tri-axial Strain and Stress Conditions. *Int. J. Coal Geol.* 84, 103–114. doi:10.1016/j.coal.2010.08.011
- Cook, N. G. W. (1992). Natural Joints in Rock: Mechanical, Hydraulic and Seismic Behaviour and Properties Under Normal Stress. *Int. J. Rock Mech. Min. Sci. Geomechan. Abstr.* 29, 198–223. doi:10.1016/0148-9062(92)93656-5
- Cygan, R. T., Romanov, V. N., and Myshakin, E. M. (2012). Molecular Simulation of Carbon Dioxide Capture by Montmorillonite Using an Accurate and Flexible Force Field. *J. Phys. Chem. C* 116, 13079–13091. doi:10.1021/jp3007574
- Cygan, R. T., Daemen, L. L., Ilgen, A. G., Krumhansl, J. L., and Nenoff, T. M. (2015). Inelastic Neutron Scattering and Molecular Simulation of the Dynamics of Interlayer Water in Smectite Clay Minerals. *J. Phys. Chem. C* 119, 28005–28019. doi:10.1021/acs.jpcc.5b08838
- de Jong, S. M., Spiers, C. J., and Busch, A. (2014). Development of Swelling Strain in Smectite Clays through Exposure to Carbon Dioxide. *Int. J. Greenh. Gas Control* 24, 149–161. doi:10.1016/j.ijggc.2014.03.010
- Eltantawy, I. M., and Arnold, P. W. (1972). Adsorption of N-Alkanes by Wyoming Montmorillonite. *Nat. Phys. Sci.* 237, 123–125. doi:10.1038/physci237123a0
- Espinoza, D. N., and Santamarina, J. C. (2017). CO₂ Breakthrough-Caprock Sealing Efficiency and Integrity for Carbon Geological Storage. *Int. J. Greenh. Gas Control* 66, 218–229. doi:10.1016/j.ijggc.2017.09.019
- Espinoza, D. N., Vandamme, M., Dangla, P., Pereira, J.-M., and Vidal-Gilbert, S. (2013). A Transverse Isotropic Model for Microporous Solids: Application to Coal Matrix Adsorption and Swelling. *J. Geophys. Res. Solid Earth* 118, 6113–6123. doi:10.1002/2013jb010337
- Espinoza, D. N., Vandamme, M., Pereira, J.-M., Dangla, P., and Vidal-Gilbert, S. (2014). Measurement and Modeling of Adsorptive–Poromechanical Properties of Bituminous Coal Cores Exposed to CO₂: Adsorption, Swelling Strains, Swelling Stresses and Impact on Fracture Permeability. *Int. J. Coal Geol.* 134–135, 80–95. doi:10.1016/j.coal.2014.09.010
- Espinoza, D. N., Vandamme, M., Dangla, P., Pereira, J.-M., and Vidal-Gilbert, S. (2016). Adsorptive-mechanical Properties of Reconstituted Granular Coal: Experimental Characterization and Poromechanical Modeling. *Int. J. Coal Geol.* 162, 158–168. doi:10.1016/j.coal.2016.06.003
- Ferrage, E., Lanson, B., Malikova, N., Plançon, A., Sakharov, B. A., and Drits, V. A. (2005). New Insights on the Distribution of Interlayer Water in Bi-hydrated Smectite from X-Ray Diffraction Profile Modeling of 00l Reflections. *Chem. Mater.* 17, 3499–3512. doi:10.1021/cm047995v
- Ferrage, E., Kirk, C. A., Cressey, G., and Cuadros, J. (2007a). Dehydration of Ca-Montmorillonite at the Crystal Scale. Part 2. Mechanisms and Kinetics. *Am. Mineral.* 92, 1007–1017. doi:10.2138/am.2007.2397
- Ferrage, E., Kirk, C. A., Cressey, G., and Cuadros, J. (2007b). Dehydration of Ca-Montmorillonite at the Crystal Scale. Part I: Structure Evolution. *Am. Mineral.* 92, 994–1006. doi:10.2138/am.2007.2396
- Ferrage, E., Lanson, B., Sakharov, B. A., Geoffroy, N., Jacquot, E., and Drits, V. A. (2007c). Investigation of Dioctahedral Smectite Hydration Properties by Modeling of X-Ray Diffraction Profiles: Influence of Layer Charge and Charge Location. *Am. Mineral.* 92, 1731–1743. doi:10.2138/am.2007.2273
- Fu, M. H., Zhang, Z., and Low, P. (1990). Changes in the Properties of a Montmorillonite-Water System during the Adsorption and Desorption of Water: Hysteresis. *Clays Clay Minerals* 38, 485–492. doi:10.1346/ccmn.1990.0380504
- Gaus, I. (2010). Role and Impact of CO₂-rock Interactions during CO₂ Storage in Sedimentary Rocks. *Int. J. Greenh. Gas Control* 4, 73–89. doi:10.1016/j.ijggc.2009.09.015
- Giesting, P., Guggenheim, S., Koster van Groos, A. F., and Busch, A. (2012a). Interaction of Carbon Dioxide with Na-Exchanged Montmorillonite at Pressures to 640bars: Implications for CO₂ Sequestration. *Int. J. Greenh. Gas Control* 8, 73–81. doi:10.1016/j.ijggc.2012.01.011
- Giesting, P., Guggenheim, S., Koster van Groos, A. F., and Busch, A. (2012b). X-Ray Diffraction Study of K- and Ca-Exchanged Montmorillonites in CO₂ Atmospheres. *Environ. Sci. Technol.* 46, 5623–5630. doi:10.1021/es3005865
- Greathouse, J. A., Hart, D. B., Bowers, G. M., Kirkpatrick, R. J., and Cygan, R. T. (2015). Molecular Simulation of Structure and Diffusion at Smectite–Water Interfaces: Using Expanded Clay Interlayers as Model Nanopores. *J. Phys. Chem. C* 119, 17126–17136. doi:10.1021/acs.jpcc.5b03314
- Heller, R., and Zoback, M. (2014). Adsorption of Methane and Carbon Dioxide on Gas Shale and Pure Mineral Samples. *J. Unconv. Oil Gas Resour.* 8, 14–24. doi:10.1016/j.juogr.2014.06.001
- Hol, S., Gensterblum, Y., and Massarotto, P. (2014). Sorption and Changes in Bulk Modulus of Coal - Experimental Evidence and Governing Mechanisms for CBM and ECBM Applications. *Int. J. Coal Geol.* 128, 119–133.
- Hol, S., and Spiers, C. J. (2012). Competition between Adsorption-Induced Swelling and Elastic Compression of Coal at CO₂ Pressures up to 100MPa. *J. Mech. Phys. Solids* 60, 1862–1882. doi:10.1016/j.jmps.2012.06.012
- Hol, S., Peach, C. J., and Spiers, C. J. (2011). Applied Stress Reduces the CO₂ Sorption Capacity of Coal. *Int. J. Coal Geol.* 85, 128–142. doi:10.1016/j.coal.2010.10.010
- Hol, S., Peach, C. J., and Spiers, C. J. (2012). Effect of 3-D Stress State on Adsorption of CO₂ by Coal. *Int. J. Coal Geol.* 93, 1–15. doi:10.1016/j.coal.2012.01.001
- Hol, S., Zoback, M. D., and Spiers, C. J. (2013). “Role of Adsorption in the Creep Behavior of Coal and Shale,” in *Poromechanics V: Proceedings of the Fifth Biot Conference on Poromechanics (ASCE)*, 668–677.
- Holloway, S. (1997). An Overview of the Underground Disposal of Carbon Dioxide. *Energy Convers. Manag.* 38, S193–S198. doi:10.1016/s0196-8904(96)00268-3
- Ilton, E. S., Schaefer, H. T., Qafoku, O., Rosso, K. M., and Felmy, A. R. (2012). *In Situ* X-ray Diffraction Study of Na+ Saturated Montmorillonite Exposed to Variably Wet Super Critical CO₂. *Environ. Sci. Technol.* 46, 4241–4248. doi:10.1021/es300234v
- Jaynes, W. F., and Bigham, J. (1986). Multiple Cation-Exchange Capacity Measurements on Standard Clays Using a Commercial Mechanical Extractor. *Clays Clay Minerals* 34, 93–98. doi:10.1346/ccmn.1986.0340112
- Kaldi, J., Daniel, R., Tenthorey, E., Michael, K., Schacht, U., Nicol, A., et al. (2013). Containment of CO₂ in CCS: Role of Caprocks and Faults. *Energy Proc.* 37, 5403–5410. doi:10.1016/j.egypro.2013.06.458
- Liu, J., Peach, C. J., and Spiers, C. J. (2016a). Anisotropic Swelling Behaviour of Coal Matrix Cubes Exposed to Water Vapour: Effects of Relative Humidity and Sample Size. *Int. J. Coal Geol.* 167, 119–135. doi:10.1016/j.coal.2016.09.011
- Liu, J., Spiers, C. J., Peach, C. J., and Vidal-Gilbert, S. (2016b). Effect of Lithostatic Stress on Methane Sorption by Coal: Theory vs. Experiment and Implications for Predicting In-Situ Coalbed Methane Content. *Int. J. Coal Geol.* 167, 48–64. doi:10.1016/j.coal.2016.07.012
- Liu, J., Fokker, P. A., and Spiers, C. J. (2017). Coupling of Swelling, Internal Stress Evolution, and Diffusion in Coal Matrix Material during Exposure to Methane. *J. Geophys. Res. Solid Earth* 122, 844–865. doi:10.1002/2016jb013322

- Loring, J. S., Thompson, C. J., Wang, Z., Joly, A. G., Sklarew, D. S., Schaef, H. T., et al. (2011). In Situ Infrared Spectroscopic Study of Forsterite Carbonation in Wet Supercritical CO₂. *Environ. Sci. Technol.* 45, 6204–6210. doi:10.1021/es201284e
- Loring, J. S., Schaef, H. T., Turcu, R. V. F., Thompson, C. J., Miller, Q. R. S., Martin, P. F., et al. (2012). In Situ Molecular Spectroscopic Evidence for CO₂ Intercalation into Montmorillonite in Supercritical Carbon Dioxide. *Langmuir* 28, 7125–7128. doi:10.1021/la301136w
- Loring, J. S., Schaef, H. T., Thompson, C. J., Turcu, R. V., Miller, Q. R., Chen, J., et al. (2013). Clay Hydration/dehydration in Dry to Water-Saturated Supercritical CO₂: Implications for Caprock Integrity. *Energy Procedia* 37, 5443–5448. doi:10.1016/j.egypro.2013.06.463
- Loring, J. S., Ilton, E. S., Chen, J., Thompson, C. J., Martin, P. F., Bénéth, P., et al. (2014). In Situ Study of CO(2) and H(2)O Partitioning between Na-Montmorillonite and Variably Wet Supercritical Carbon Dioxide. *Langmuir* 30, 6120–6128. doi:10.1021/la500682t
- Madejová, J., and Komadel, P. (2001). Baseline Studies of the Clay Minerals Society Source Clays: Infrared Methods. *Clays Clay Minerals* 49, 410–432. doi:10.1346/ccmn.2001.0490508
- Mermut, A. R., and Lagaly, G. (2001). Baseline Studies of the Clay Minerals Society Source Clays: Layer-Charge Determination and Characteristics of Those Minerals Containing 2: 1 Layers. *Clays Clay Minerals* 49, 393–397. doi:10.1346/ccmn.2001.0490506
- Michot, L. J., Ferrage, E., DelvilleJimenez-Ruiz, M., and Jiménez-Ruiz, M. (2016). Influence of Layer Charge, Hydration State and Cation Nature on the Collective Dynamics of Interlayer Water in Synthetic Swelling Clay Minerals. *Appl. Clay Sci.* 119, 375–384. doi:10.1016/j.clay.2015.11.005
- Moore, D. M., and Hower, J. (1986). Ordered Interstratification of Dehydrated and Hydrated Na-Smectite. *Clays Clay Minerals* 34, 379–384. doi:10.1346/ccmn.1986.0340404
- Nikoosokhan, S., Vandamme, M., and Dangla, P. (2014). A Poromechanical Model for Coal Seams Saturated with Binary Mixtures of CH₄ and CO₂. *J. Mech. Phys. Solids* 71, 97–111. doi:10.1016/j.jmps.2014.07.002
- Nooraiepour, M., Haile, B. G., and Hellevang, H. (2017). Compaction and Mechanical Strength of Middle Miocene Mudstones in the Norwegian North Sea – the Major Seal for the Skade CO₂ Storage Reservoir. *Int. J. Greenh. Gas Control* 67, 49–59. doi:10.1016/j.ijggc.2017.10.016
- Pan, Z., and Connell, L. D. (2007). A Theoretical Model for Gas Adsorption-Induced Coal Swelling. *Int. J. Coal Geol.* 69, 243–252. doi:10.1016/j.coal.2006.04.006
- Prost, R., Koutit, T., Benchara, A., and Huard, E. (1998). State and Location of Water Adsorbed on Clay Minerals: Consequences of the Hydration and Swelling-Shrinkage Phenomena. *Clays Clay Minerals* 46, 117–131. doi:10.1346/ccmn.1998.0460201
- Romanov, V. N. (2013). Evidence of Irreversible CO₂ Intercalation in Montmorillonite. *Int. J. Greenh. Gas Control* 14, 220–226. doi:10.1016/j.ijggc.2013.01.022
- Rother, G., Ilton, E. S., Wallacher, D., Hauß, T., Schaef, H. T., Qafoku, O., et al. (2013). CO₂ Sorption to Subsingle Hydration Layer Montmorillonite Clay Studied by Excess Sorption and Neutron Diffraction Measurements. *Environ. Sci. Technol.* 47, 205–211. doi:10.1021/es301382y
- Schaef, H. T., Ilton, E. S., Qafoku, O., Martin, P. F., Felmy, A. R., and Rosso, K. M. (2012). In Situ XRD Study of Ca²⁺ Saturated Montmorillonite (STX-1) Exposed to Anhydrous and Wet Supercritical Carbon Dioxide. *Int. J. Greenh. Gas Control* 6, 220–229. doi:10.1016/j.ijggc.2011.11.001
- Schaef, H. T., Davidson, C. L., Owen, A. T., Miller, Q. R. S., Loring, J. S., Thompson, C. J., et al. (2014). CO₂ Utilization and Storage in Shale Gas Reservoirs: Experimental Results and Economic Impacts. *Energy Procedia* 63, 7844–7851. doi:10.1016/j.egypro.2014.11.819
- Schaef, H. T., Loring, J. S., Glezakou, V.-A., Miller, Q. R. S., Chen, J., Owen, A. T., et al. (2015). Competitive Sorption of CO₂ and H₂O in 2:1 Layer Phyllosilicates. *Geochim. Cosmochim. Acta* 161, 248–257. doi:10.1016/j.gca.2015.03.027
- Song, J., and Zhang, D. (2013). Comprehensive Review of Caprock-Sealing Mechanisms for Geologic Carbon Sequestration. *Environ. Sci. Technol.* 47, 9–22. doi:10.1021/es301610p
- Suter, J. L., Sprik, M., and Boek, E. S. (2012). Free Energies of Absorption of Alkali Ions onto Beidellite and Montmorillonite Surfaces from Constrained Molecular Dynamics Simulations. *Geochim. Cosmochim. Acta* 91, 109–119. doi:10.1016/j.gca.2012.04.060
- Viete, D. R., and Ranjith, P. G. (2006). The Effect of CO₂ on the Geomechanical and Permeability Behaviour of Brown Coal: Implications for Coal Seam CO₂ Sequestration. *Int. J. Coal Geol.* 66, 204–216. doi:10.1016/j.coal.2005.09.002
- Walsh, J. B. (1981). Effect of Pore Pressure and Confining Pressure on Fracture Permeability. *Int. J. Rock Mech. Min. Sci. Geomech. Abstr.* 18, 429–435. Elsevier. doi:10.1016/0148-9062(81)90006-1
- Zhang, M., de Jong, S. M., Spiers, C. J., Busch, A., and Wentinck, H. M. (2018). Swelling Stress Development in Confined Smectite Clays through Exposure to CO₂. *Int. J. Greenh. Gas Control* 74, 49–61. doi:10.1016/j.ijggc.2018.04.014
- Zhang, M. (2019). *Stress-strain-sorption Behaviour and Permeability Evolution in Clay-Rich Rocks under CO₂ Storage Conditions*. *Utrecht Studies in Earth Sciences* 188, 217.

Conflict of Interest: The authors declare that the research was conducted in the absence of any commercial or financial relationships that could be construed as a potential conflict of interest.

Publisher's Note: All claims expressed in this article are solely those of the authors and do not necessarily represent those of their affiliated organizations, or those of the publisher, the editors and the reviewers. Any product that may be evaluated in this article, or claim that may be made by its manufacturer, is not guaranteed or endorsed by the publisher.

Copyright © 2022 Zhang, Spiers, Liu and Zhou. This is an open-access article distributed under the terms of the Creative Commons Attribution License (CC BY). The use, distribution or reproduction in other forums is permitted, provided the original author(s) and the copyright owner(s) are credited and that the original publication in this journal is cited, in accordance with accepted academic practice. No use, distribution or reproduction is permitted which does not comply with these terms.

APPENDIX 1 PREPARATION OF WATER-BEARING/WET PORE FLUID

Pore fluids employed in all tests on AD samples were prepared having a partial water vapor pressure (RH~20%) equivalent to that characterizing the AD samples in the pre-equilibration stage. This was necessary to minimize any desiccation effects induced by flow of pore fluids through the samples. The wet pore fluid was produced following the steps below:

1. Connect the ISCO pump to a flask containing saturated Mg(NO₃)₂ solution with excess salt and the solid, solution and vapor phases present.

2. Adjust the ISCO to operate in constant volume mode. Briefly evacuate the ISCO pump plus flask system, and then isolate the system from the external atmosphere for ~5 h. In this

procedure, the pump and pipes of the pore fluid system are primed with water vapor pressure equivalent to RH~20%.

3. Close the connection between the pore fluid system and the flask, then introduce the target pore fluid from the gas cylinder into the ISCO pump at 10MPa using a regulator mounted at the outlet of the gas cylinder. Note that pore fluid introduction was done in multiple steps *via* a “trial and error” method. In each step, a small amount of fluid at room temperature (~22°C) and ~10 MPa was injected into the pump (heated at 40°C). The fluid pressure in the pump changed with time due to thermal expansion, and was monitored using a pressure transducer attached to the ISCO pump. When the measured (total) pressure reached a stable value it was further incremented until the target pressure of 10 MPa) was attained.

Table A1 | Comparison of model prediction with experimental data on swelling stresses measured by Zhang (2019) for VD SWy-1 samples exposed to CO₂ pressure at 10 MP at 50°C

σ_e^{in}	ε_{sw} (exp)	σ_{sw} (exp)	Poroelectric corrected ε_{sw} (exp)	Predicted ε_{sw} at σ_e^{in}	Restricted ε_{sw}	Predicted σ_{sw}
MPa	%	MPa	%	mm	%	MPa
11.13	1.89	6.81	1.24	1.38309	0.99662	6.65
11.6	1.7	6.12	1.05	1.37197	0.98861	6.6
17.96	1.39	5.89	0.74	1.21461	0.87522	5.73
18.46	1.57	6.66	0.92	1.2018	0.86599	5.66
25.52	1.16	4.88	0.51	1.01784	0.73343	4.8
Average	1.54	6.07	0.892	1.24	0.892	5.89



High P-T Calcite-Aragonite Phase Transitions Under Hydrous and Anhydrous Conditions

Xia Zhao^{1,2}, Zhi Zheng¹, Jiangzhi Chen¹, Yue Gao^{1,2}, Jianhui Sun¹, Xue Hou¹, Mengjun Xiong^{1,2} and Shenghua Mei^{1*}

¹CAS Key Laboratory for Experimental Study Under Deep-Sea Extreme Conditions, Institute of Deep-Sea Science and Engineering, Chinese Academy of Sciences, Sanya, China, ²University of Chinese Academy of Sciences, Beijing, China

OPEN ACCESS

Edited by:

Xi Liu,
Peking University, China

Reviewed by:

Zheng Haifei,
Peking University, China
Mingda Lv,
Argonne National Laboratory (DOE),
United States
Sean Shieh,
University of Western Ontario, Canada

*Correspondence:

Shenghua Mei
mei@idsse.ac.cn

Specialty section:

This article was submitted to
Solid Earth Geophysics,
a section of the journal
Frontiers in Earth Science

Received: 30 March 2022

Accepted: 12 May 2022

Published: 17 June 2022

Citation:

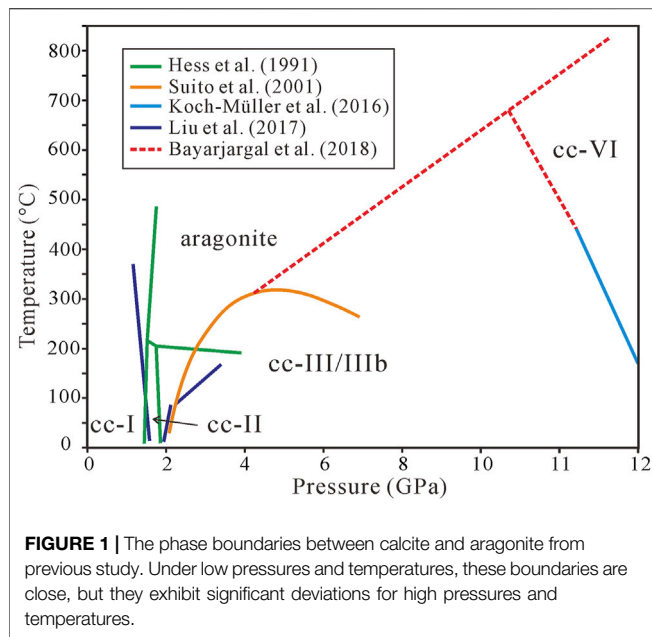
Zhao X, Zheng Z, Chen J, Gao Y,
Sun J, Hou X, Xiong M and Mei S
(2022) High P-T Calcite-Aragonite
Phase Transitions Under Hydrous and
Anhydrous Conditions.
Front. Earth Sci. 10:907967.
doi: 10.3389/feart.2022.907967

The subduction of calcite into deep Earth and subsequent phase change are important for global carbon cycle. However, the study of the phase boundary between calcite and aragonite under high P-T conditions is insufficient due to sparse existing phase points and narrow pressure range. In addition, the impact of aqueous fluid on the phase transition requires further investigation. In this work, the calcite-aragonite phase transitions in both anhydrous and hydrous conditions were studied using diamond anvil cell (DAC) with *in-situ* Raman spectroscopy. In the anhydrous condition, investigations were conducted up to 12 GPa and 400°C and only the solid recrystallization-reconstructive (SRR) phase transition was observed. The calcite-aragonite boundary shows a convex upward curve with the minimum transformation temperature at around 150°C and a wide transformation pressure range from 1 to 12 GPa, consistent with the molar volume change between aragonite and calcite-I/II/III/IIIb. In the hydrous condition, both the SRR phase transition and dissolution-precipitation-dehydration (DPD) phase transition were observed under different heating conditions, and in the DPD phase transition ikaite serves as an intermediate phase precipitated from dissolved calcite and then dehydrates into aragonite. Our results suggest the phase transition of calcite-aragonite in the subduction zone, where the SRR phase transition can exist in slabs under wide P-T conditions (1–2 GPa and 160–400°C), and the DPD process can only occur under lower P-T conditions (less than 1.5 GPa and 110°C).

Keywords: calcite, aragonite, ikaite, phase transition, high P-T, Raman spectroscopy

1 INTRODUCTION

Carbonate minerals, as the main carbon carriers, control carbon migration in different geochemical reservoirs (Dasgupta and Hirschmann, 2010; Merlini et al., 2012; Liu et al., 2017; Zhang Z. et al., 2018). Among them, calcite (CaCO₃) is the most common carbonate mineral. It is reported that calcite can exist at the top of the lower mantle (Wirth et al., 2009; Ague and Nicolescu, 2014; Kaminsky et al., 2016; Zhang Z.-W. et al., 2018; Lv et al., 2021), and under the mantle P-T conditions, it must adapt changes of pressure and temperature with depth and undergo significant phase changes (Suito et al., 2001; Hagiya et al., 2005; Merlini et al., 2012; Gavryushkin et al., 2017; Nestola et al., 2018; Hou et al., 2019). Understanding the CaCO₃ phase transitions and the structural properties of high P-T CaCO₃ phases is critical for predicting carbon states in deep Earth and their contributions to anomalies in the physicochemical parameters of subducting slab (Litasov and Ohtani, 2009;



Dasgupta and Hirschmann, 2010; Litasov et al., 2017; Yuan et al., 2021). Until now, more than 12 structural polymorphs, such as cc-I–VII (referred to as cc-I to cc-VII hereafter), aragonite, and pyroxene CaCO_3 , have been verified (Maslen et al., 1993; Suito et al., 2001; Catalli and Williams, 2005; Hagiya et al., 2005; Ono et al., 2005; Oganov et al., 2006; Ono et al., 2007; Oganov et al., 2008; Merlini et al., 2012; Merlini et al., 2014; Gavryushkin et al., 2017; Li et al., 2018). Among various polymorphs of CaCO_3 , the phase relationships among cc-I, cc-II, cc-III, and cc-VI have been well studied. However, the understanding of the phase boundary between calcite and aragonite at high P – T conditions is insufficient, and noteworthy discrepancy exists in previous works. Hess et al. (1991) obtained the phase boundaries among cc-I, cc-II, cc-III, and aragonite by Raman spectroscopy, and found that aragonite exists above 1.5 GPa and 150°C. Suito et al. (2001) performed XRD and Raman spectroscopy of the CaCO_3 phase transition and concluded that the boundary of cc-III and aragonite has a positive P – T slope in the pressure range 2–4.5 GPa followed by a negative P – T slope in the range of 4.5–6.2 GPa. Recently, Liu et al. (2017) obtained the transition temperature from calcite to aragonite increasing with pressure varying from 2.57 to 3.42 GPa according to Raman scattering measurements, consistent with Suito et al. (2001). These experiments (Figure 1) were based on very sparse phase points and narrow pressure ranges, leading to large uncertainty on the phase boundary. For a better understanding of the phase transitions of calcite under mantle conditions, we need to further investigate and clarify the phase relationship between calcite and aragonite.

Furthermore, due to dehydration of aqueous minerals (e.g., talcum, amphibole, brucite), the subduction zone is a place with plenty of water. Plummer and Busenberg (1982) and Morse and Mackenzie (1990) studied the solubility of CaCO_3 minerals and the aqueous speciation of carbon in great detail at ambient conditions

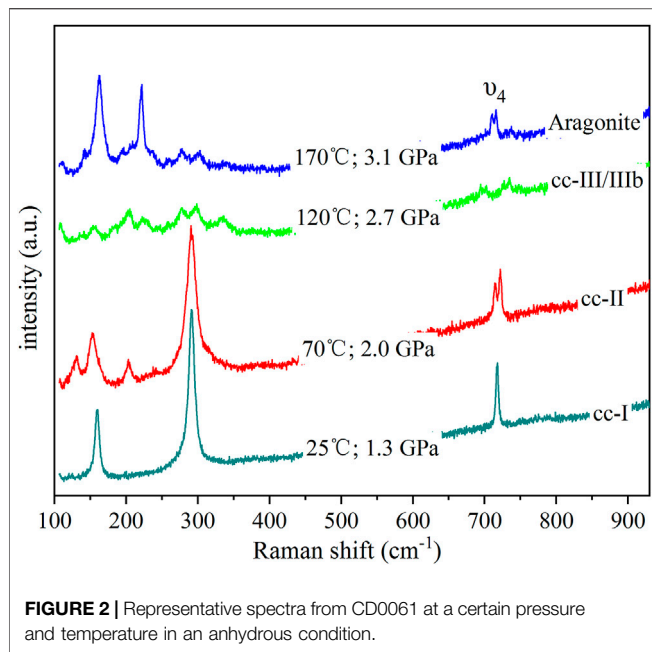
and temperatures up to 90°C. Perdikouri et al. (2008) investigated the transformation of natural aragonite crystal to calcite by reaction with aqueous solutions of calcium carbonate at hydrothermal conditions for different periods of time, which indicated the replacement of aragonite by calcite followed an interface-coupled dissolution-precipitation mechanism. Yuan et al. (2021) found a dissolution-precipitation process between CaCO_3 -I/II and aragonite phase transitions in hydrous fluids at P – T conditions lower than 1.5 GPa and 375°C and a solid recrystallization phase transition process at 1.7–1.8 GPa and 500–520°C. However, these studies neglect the role of aqueous fluid on phase transition between calcite and aragonite at higher pressure and more experimental conditions. Therefore, besides the study of phase boundaries, we also need to elucidate the impact of aqueous fluid.

In this study, the high P – T stability and behavior of CaCO_3 were investigated under both hydrous and anhydrous conditions using an externally heated Bassett-type DAC combined with the laser Raman and Fourier transform infrared (FTIR) spectroscopy technique. In the anhydrous condition, various Raman spectra of calcite polymorphs at high P – T conditions were collected, and the phase boundaries between cc-I, cc-II, cc-III, cc-VI, and aragonite were determined up to 12 GPa and 400°C. We used the Clausius–Clapeyron equation to analyze the thermodynamic significance of our experimentally determined phase boundaries. In the hydrous condition, two transition processes from calcite/aragonite to aragonite, i.e., solid recrystallization-reconstructive (SRR) phase transition and dissolution-precipitation-dehydration (DPD) process, were studied and the implications on plate subduction zone were discussed.

2 MATERIALS AND METHODS

Highly pure natural CaCO_3 crystals were used in all experiments. Ikaite was synthesized in water at 0.6–1 GPa, room temperature, with the original material of calcite or aragonite. High-pressure experiments for single-crystal calcite were performed at the CAS Key Laboratory for Experimental Studies under Deep-Sea Extreme Conditions, Institute of Deep-Sea Science and Engineering, Chinese Academy of Sciences (Sanya, Hainan, China). High pressure and high temperature are produced by an externally heated Bassett-type DAC (Bassett et al., 1993), in which nichrome wire heaters are wrapped around the seats and the two diamonds are externally heated to create a homogeneous temperature field in the pressure chamber by applying an electrical current. The temperature inside the sample chamber was the mean value measured by two K-type thermocouples (NiCr–NiSi) attached to the two diamond anvils. The temperature error is within 1°C. The DAC is equipped with two types of IIA low-fluorescence diamonds with a culet diameter of 300 μm . The DAC sample chamber has an ~ 100 μm diameter hole in the center of a rhenium gasket that was produced by a Drilex-2000 laser hole puncher. Water and a mixture of methanol and ethanol in a ratio of 4:1 were used as the pressure-transmitting medium. Pressure was determined by the fluorescence line of Y1 (617.8 nm) of Sm:YAG (Trots et al., 2013) or the ruby method (Mao and Bell, 1978).

Raman spectra of calcite and fluorescence spectra of ruby or Sm:YAG were collected by two spectrometers simultaneously to



ensure getting the real time pressure values. The Raman spectrum was collected from 100 to 930 cm^{-1} or 100 to 1200 cm^{-1} . The fluorescence spectrum was collected at approximately 617.8 or 694 nm. An Andor Shamrock SR500i spectrometer equipped with a Leica DM2700 microscope, a Plan Apo SL Infinity Corrected 20 \times objective with a numerical aperture value of 0.28, and a 532 nm frequency-doubled Nd: YAG laser. A 1800 or 1200 gr. mm^{-1} holographic grating coupled with a CCD detector (2000 \times 256 ppi) with a spectral resolution of 1.5 or 3 cm^{-1} was used for the measurement of Raman spectra. The 1200 gr. mm^{-1} holographic grating was used to measure fluorescence spectrum, which lead to ± 0.23 and ± 0.28 GPa of pressure error for ruby and Sm:YAG method. For all the Raman experiments, an externally heated Bassett-type DAC was first pressurized to the desired pressure, and then the sample chamber was heated (20°C/min) to the desired temperature. Raman and fluorescence spectra were simultaneously obtained after approximately 30 s at the desired condition to reach the equilibrium condition. Spectra were collected at a certain temperature and pressure interval to better understand the thermal stability of CaCO_3 at high pressure and high temperature.

To determine the influence of molecular water on phase transition in hydrous condition, FTIR spectra were collected using a Nicolet IS50 FTIR spectrophotometer (Thermo Fisher Scientific, China), equipped with a mercury cadmium telluride detector (MCT-A), a Continuum microscope with 15 \times Reffachromat objective lens and a Ge-plated KBr beam splitter. Each sample was air-dried before measuring. Typically, 128 scans were recorded at a resolution of 4 cm^{-1} in the range of 700–4000 cm^{-1} . The frequency scale was internally calibrated by a helium-neon reference laser with an accuracy of 0.005 cm^{-1} . OMNIC software was used for spectra collection and manipulation. The three experiments used ultrapure water as pressure mediums were slowly heated to 460, 480, and 500°C. We

kept the samples at their highest temperature for 20 min, and then quenched the samples to obtain FTIR spectra.

3 RESULTS AND DISCUSSION

3.1 Phase Transition in the Anhydrous Condition

For the anhydrous condition, mixed methanol and ethanol was used as the transmission medium. Representative Raman spectra are shown in **Figure 2**. Raman spectra of CaCO_3 can reveal different phases with distinctive structures (Koch-Mueller et al., 2016): cc-I is rhombohedral ($R\bar{3}c$), cc-II is monoclinic ($P2_1/c$) (Merrill and Bassett, 1975; Yuan et al., 2019), cc-III is less symmetrical than cc-II with triclinic ($P\bar{1}$) symmetry (Merlini et al., 2012), cc-VI crystallizes in the triclinic space group P1 (Bayarjargal et al., 2018), and aragonite has an orthorhombic structure of 2/m 2/m 2/m (Palaich et al., 2016). As shown in **Figure 2**, among 100–930 cm^{-1} , cc-I has three main peaks, including two external modes at about 160 and 280 cm^{-1} , and one ν_4 mode at about 720 cm^{-1} , whereas cc-II has four main peaks, including two external modes at about 150 and 280 cm^{-1} , and two ν_4 modes at about 720 cm^{-1} . Phases cc-III/IIIb can be distinguished from others based on the ν_4 modes, which have more than three peaks, and aragonite has four main peaks: two external modes at approximately 160 and 220 cm^{-1} , two ν_4 modes at about 720 cm^{-1} . All identified phases of the alcohol system are shown in **Figure 3**, showing five regimes: cc-I, cc-II, cc-III, cc-IIIb, and aragonite. The difference between cc-III and cc-IIIb has not been determined.

The dense phase points allow for much more accurate phase boundaries. In **Figure 3**, we observed that cc-I, cc-II, and cc-III/

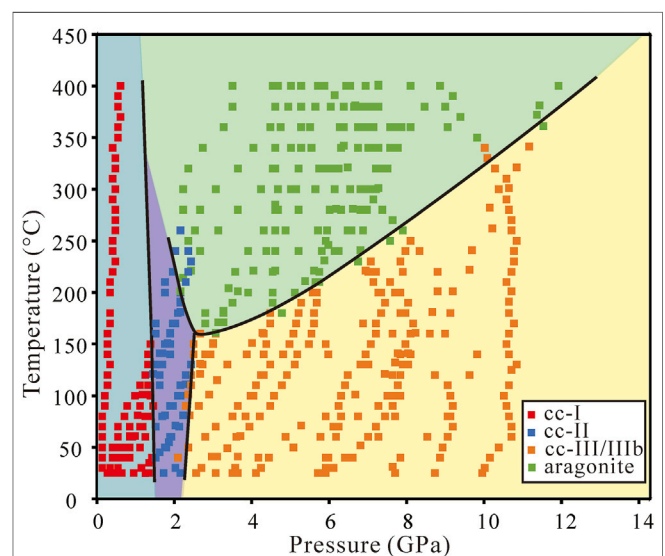


FIGURE 3 | Phase diagram of CaCO_3 in the anhydrous condition. The phase boundary between calcite and aragonite shows a minimum transition temperature at around 150°C and 2.4 GPa. Near each segment of the phase boundaries, there are some ambiguous points in which two phases can exist in a small vicinity, especially between cc-II and aragonite.

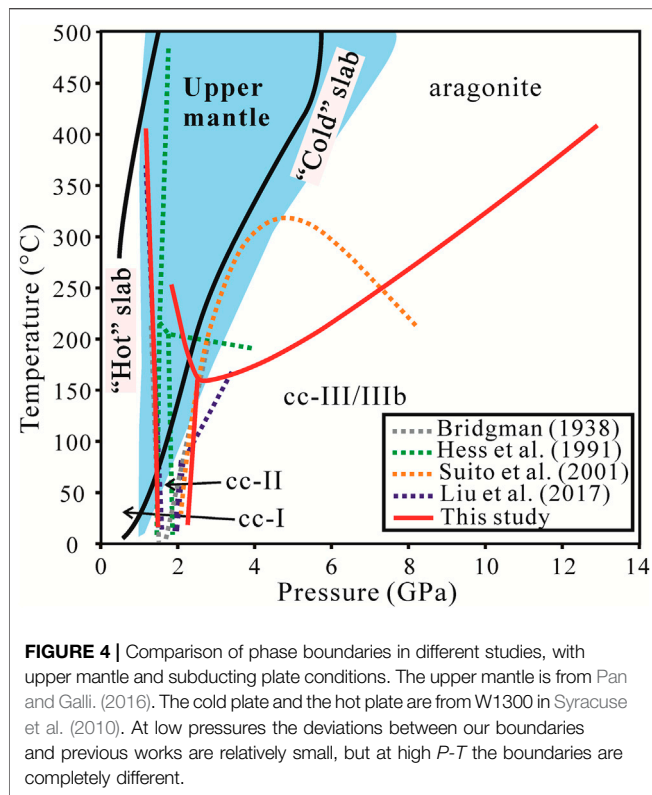


FIGURE 4 | Comparison of phase boundaries in different studies, with upper mantle and subducting plate conditions. The upper mantle is from Pan and Galli, (2016). The cold plate and the hot plate are from W1300 in Syracuse et al. (2010). At low pressures the deviations between our boundaries and previous works are relatively small, but at high P - T the boundaries are completely different.

IIIb can all transform directly to aragonite. The transformation from cc-I to cc-II and cc-II to cc-III occurs at about 1.7 and 2.2 GPa, with no significant temperature dependence. The calcite-aragonite boundary is a convex upward curve with the minimum transformation temperature at around 150°C and a wide transformation pressure range from 1 to 12 GPa. The transition temperature decreases with the pressure from 1.5 to 2.4 GPa, and above 2.4 GPa the transition temperature increases with the pressure.

The transformation from cc-I to cc-II is approximately 1.5 GPa (Figure 4), showing as an almost vertical line, consistent with Bridgman (1939), Hess et al. (1991), Suito et al. (2001), and Liu et al. (2017). According to the Clausius–Clapeyron equation,

$$dP/dT = L/(T\Delta V)$$

where P is the pressure, T is the temperature, L is the enthalpy change, and ΔV is the change of molar volume. The vertical phase boundary means $dP/dT \approx 0$, suggesting that the enthalpy from cc-I to cc-II is almost unchanged, and that the entropy change is very small.

The transformation pressure of cc-II to cc-III/IIIb is from 2.2 to 2.4 GPa (Figure 4) slightly different from Bridgman (1939), Hess et al. (1991), and Liu et al. (2017). This could result from the experimental condition and pressure error of different researches. The slopes for the phase boundaries of cc-II to cc-III/IIIb are positive with a high angle. Again, the Clausius–Clapeyron equation suggests a small enthalpy change when cc-II transforms to cc-III/IIIb.

TABLE 1 | Crystallographic data for calcite I–VI and aragonite. V_c is the value of the cell, and Z is the number of formula units in the unit cell.

Phase	Space Group	Z	V_c (Å ³)	Reference
CaCO ₃	R $\bar{3}c$	6	368.07	Maslen et al. (1993)
CaCO ₃ - II	P2 ₁ /c	4	239.57	Merrill and Bassett (1975)
CaCO ₃ - III	P $\bar{1}$	10	555.26	Merlini et al. (2012)
CaCO ₃ - III b	P $\bar{1}$	4	224.33	Merlini et al. (2012)
CaCO ₃ - VI	P $\bar{1}$	2	87.86	Merlini et al. (2012)
CaCO ₃ aragonite	Pmcn	4	226.97	Negro and Ungaretti (1971)

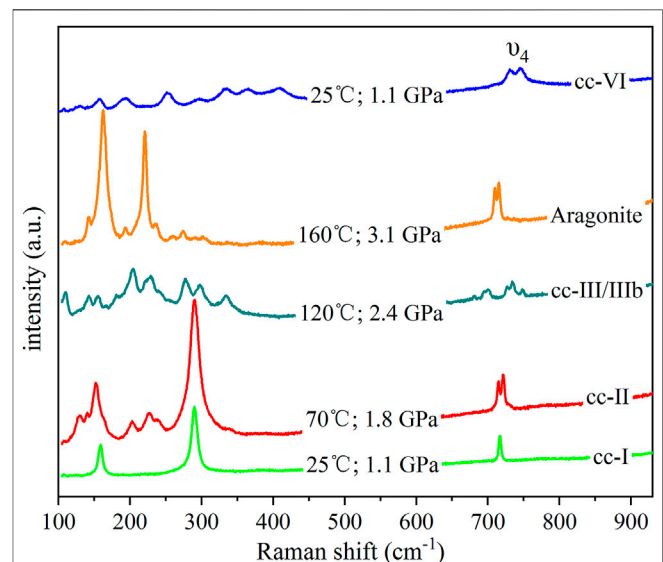
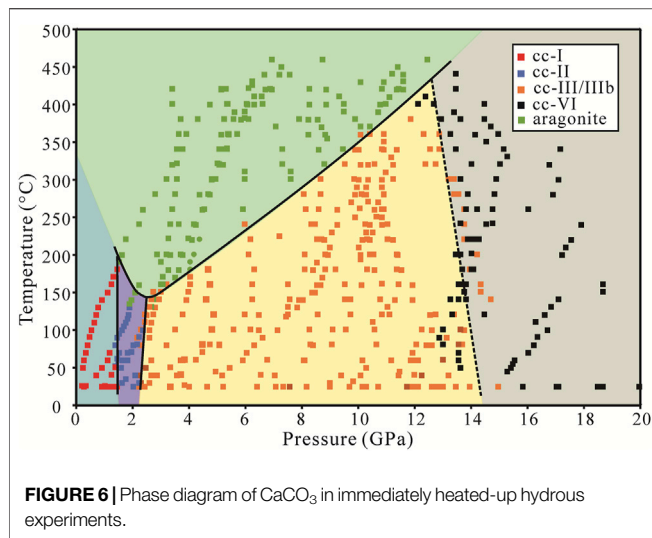


FIGURE 5 | Representative spectra from CD0036 (except cc-VI) at different pressures and temperatures in immediately heated up hydrous experiments. Cc-VI is from CD0054.

The transition temperature of calcite-aragonite decreases with pressure at low pressure from 1.5 to 2.4 GPa but increases with pressure at high pressure from 2.4 to 12 GPa (Figure 4). This is inconsistent with Bridgman (1939), Hess et al. (1991), and especially Suito et al. (2001). The phase boundaries are similar regardless of the water or alcohol system. From the thermodynamic perspective, the nearly-vertical phase boundaries between cc-I and cc-II, cc-II and cc-III/IIIb ensure that the enthalpy change between calcite and aragonite remains relatively unchanged, and the change in dP/dT slope can be easily explained by the change in molar volumes: the molar volume of cc-I, cc-II, cc-III, cc-IIIb, and aragonite was calculated as 36.93, 36.06, 33.43, 33.76, and 34.16 cm³/mol from the crystallographic parameters V_c and Z in Table 1 using

$$V_m = \frac{N_A V_c}{Z}$$

where N_A is the Avogadro constant. Given that the transition from calcite to aragonite is generally exothermic, i.e., $L > 0$, the sign of the slope dP/dT of the phase boundary will be negative for cc-I and cc-II to aragonite transition and positive for the cc-III/

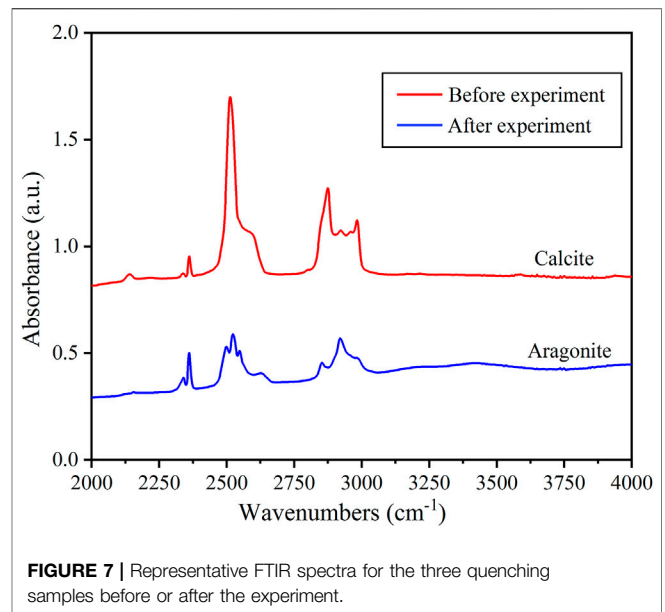


IIIb to aragonite transition. Suito et al. (2001), however, had a concave phase boundary between calcite and aragonite, possibly due to their sparse data points, that clearly contradicts the thermodynamics, and they had to resort to nonequilibrium kinetics as an explanation.

3.2 Phase Transition in the Hydrous Condition

In these experiments, calcite was heated up immediately after being loaded into the sample chamber. Ultrapure water was used as the transmission medium. The representative spectra at certain pressures and temperatures are shown in Figure 5. In addition to the Raman peak identification of each phase mentioned above, the cc-VI has many weak peaks in external modes and two main peaks in the ν_4 modes. All identified phases for the experiments in hydrous conditions are plotted in Figure 6, and we observed six regimes: cc-I, cc-II, cc-III, cc-IIIb, cc-VI, and aragonite. The phase boundaries among cc-I, cc-II, cc-III, cc-IIIb, and aragonite are similar to those in the anhydrous condition. Phase cc-VI was observed in this system, during the transformation from a low-pressure phase cc-III/IIIb to a high-temperature phase aragonite. The transition pressure from cc-VI to aragonite ranges from 13 to 15 GPa between 25 and 380°C. Because the phase boundary between cc-III/IIIb and cc-VI is less distinctive, it is not the focus of this study.

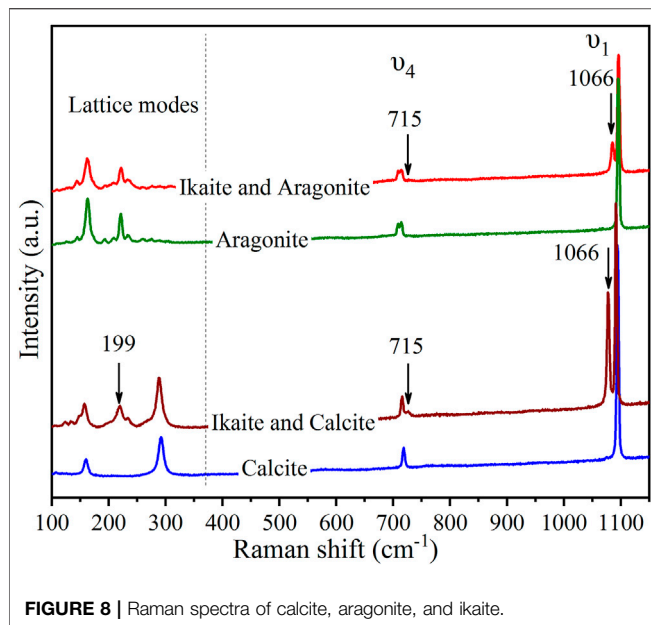
As mentioned in Zheng and Hermann (2014), when subducting to mantle depths, more molecular water can dissolve into nominally anhydrous minerals (NAMs) with increasing pressure. Because our experiments used ultrapure water as a pressure medium, it was possible that molecular water dissolved into calcite. To determine whether molecular water dissolved, we measured the water content of three quenched samples after the high-pressure and temperature experiments. FTIR spectra are the most widely used method to detect and analyze hydrous components (OH or H_2O) in minerals and glasses because of their high sensitivity and fast



performance. It can identify a few to tens of ppm wt of H_2O in a mineral (Rossman, 2006). The FTIR spectra of free (gaseous) hydroxide and OH of mineral stretching frequency are adjacent but can be separated. Stretching vibrations of H_2O have broad bands at about 3248 and 3444 cm^{-1} . The FTIR spectra for the three quenched samples are almost the same as shown in Figure 7. The stretching vibration of OH for different minerals ranges from 3600 to 3700 cm^{-1} (Zhang and Moxon, 2012). We used FTIR spectroscopy to measure the water content, and no signal of structured water, with a band at 3600–3700 cm^{-1} , was shown in Figure 7. Therefore, there was no dissolution of water in calcite for the three quenched samples. The phase boundaries of heated up immediately experiments in the hydrous environment (Figure 6) are similar to that in the anhydrous condition (Figure 3), indicating that the transformation from calcite to aragonite is an SRR process. Water plays the role of pressure-transmitting medium, which did not participate in the transformation process of calcite and aragonite.

3.3 Ikaite as an Intermediate Phase During Calcite Transition in the Hydrous Condition

Ikaite ($\text{CaCO}_3 \cdot 6\text{H}_2\text{O}$) is the hydrous form of calcium carbonate (Shahar et al., 2005), with a C2/c space group and $Z = 4$. Its structure contains discrete CaCO_3 ion pairs, each surrounded by 18 water molecules (Dickens and Brown, 1970). Pelouze (1831) was the first to synthesize $\text{CaCO}_3 \cdot 6\text{H}_2\text{O}$ in the laboratory, and Pauly (1963) discovered natural $\text{CaCO}_3 \cdot 6\text{H}_2\text{O}$ developing at the bottom of the Ika Fjord in Greenland, from which the name ikaite comes. In our experiments, we found that calcite transformed to ikaite after staying in the hydrous condition at 0.6–1 GPa and room temperature for hours. The formation conditions of ikaite in our experiments are consistent with Dickens and Brown (1970) and Van Valkenburg et al. (1971), where they found calcite and

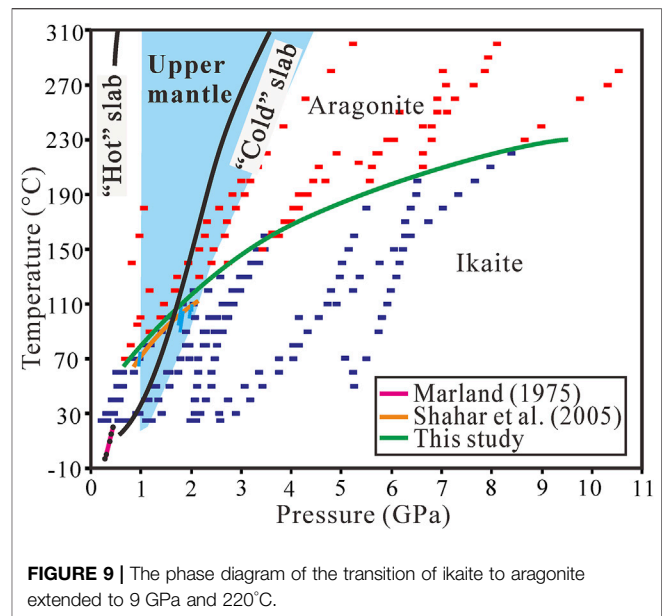


aragonite become increasingly soluble in water as the pressure exceeds 0.6 GPa, and ikaite grows at the expense of both calcite and aragonite at pressures above 0.6–0.7 GPa.

Thus, we also investigate precipitated ikaite produced from dissolved calcite and aragonite in hydrous condition. The experiment process was similar with **Section 3.2**, expect that calcite stayed in an aqueous environment at room temperature and 0.6–1 GPa for hours to dissolve and precipitate as ikaite, and then started to be heated up. Ikaite has a spectrum similar to other calcium carbonate polymorphs (Rutt and Nicola, 1974; Long, 1977; Shahar et al., 2005), but they can be identified by the lattice modes ν_1 and ν_4 . **Figure 8** compares the Raman spectra of calcite, aragonite, and ikaite. The main difference between aragonite and ikaite is the ν_1 mode, in which the peak of ikaite at 1066 cm^{-1} clearly distinguishes from aragonite, while cc-I and ikaite differ with the lattice modes ν_1 and ν_4 , where the peaks of ikaite are at 199, 715, and 1066 cm^{-1} , consistent with Sánchez-Pastor et al. (2016).

In early work, Marland (1975) observed the transitions from ikaite to calcite/aragonite under very low P - T conditions (0.296–0.414 GPa and -2 – 14.3°C), and the phase diagram was extended to 2.5 GPa and 150°C by Shahar et al. (2005). In our work, we further extended the water saturated calcium carbonate phase diagram to 9 GPa and 220°C , shown in **Figure 9**. The phase boundary is consistent with Shahar et al. (2005) at a pressure below 2.5 GPa.

Calcite/aragonite first dissolved and then precipitated as ikaite, and subsequently dehydrated into aragonite when heated after staying at 0.6–1 GPa for hours, which is the DPD process. Compared to SRR, water molecules in DPD participate in the reaction process of transformation. Therefore, it can be concluded that different hydrous conditions in SRR and DPD processes lead to the distinction of the phase transition diagrams. Specifically, the phase boundary between calcite and aragonite in the SRR process is a convex upward curve with a minimum



transformation temperature of around 150°C . It has a negative slope at 1.5–2.4 GPa and a positive slope at 2.4–12 GPa. While the ikaite-calcite boundary in DPD is a curve with a consistently positive slope, as the transition temperature increases with the increased pressure from 0.5 to 9 GPa. Additionally, at a certain pressure, the transition from ikaite to aragonite always occurs at a lower temperature compared to the calcite-aragonite phase transition.

3.4 Calcite to Aragonite Transition in Deep Earth

The Subduction zone is an area with plenty of aqueous fluid with some closed systems that don't contain water. When subducted into deep Earth, crystals in the oceanic slab will undergo hydrous or anhydrous phase transitions. Yuan et al. (2021) found two processes for calcite to aragonite transition in the hydrous system. One is the SRR phase transition, in which calcite transforms directly to aragonite, and the other is a dissolution-precipitation (DP) process, in which calcite dissolves and precipitates into aragonite.

In this paper, SRR is the only phase transition in the anhydrous system. As shown in **Figure 4**, the SRR phase transition can exist in both "hot" (i.e., high temperature low pressure) and "cold" (i.e., low temperature high pressure) slabs. During the subduction process, only cc-I and cc-II can transform to aragonite, and the transition occurs at P - T conditions at 1–2 GPa and 160 – 400°C . In the hydrous system, the phase diagram from the immediately heated experiments is an SRR phase transition, it can exist in both "hot" and "cold" slabs. On the contrary, the experiments heated after calcite/aragonite stayed at 0.6–1 GPa for hours is the DPD process. Thus, the DP process was not found in a hydrous system but SRR and DPD were observed instead. The DPD process needs ikaite as an intermediate phase, which can be formed in water at

0.6–1 GPa and room temperature or lower temperature and pressure conditions (Van Valkenburg et al., 1971; Marland, 1975; Shahar et al., 2005), but difficult to synthesize at higher pressure and temperature. As shown in **Figure 9**, the dehydration of ikaite into aragonite occurred under low P - T conditions (less than 1.5 GPa and 110°C). Therefore, in the subduction process, ikaite can only be dissolved and precipitated in a “cold” slab.

Aragonite is the main calcium carbonate in the deep upper mantle, which exists at more than 1 GPa and 100 °C according to the phase diagram (**Figures 4, 9**). In both the hydrous and the anhydrous upper mantle, with pressure below 1.5 GPa, cc-I can exist in a temperature range of 25–400°C, and cc-II can exist at 1.5–2 GPa in a temperature range of 70–220°C. Ikaite can only be produced in the hydrous upper mantle under low P - T conditions (0.6–1 GPa and room temperature). But it can exist in 1–1.5 GPa at a temperature range of 40–100°C in the upper mantle.

4 CONCLUSION

We used DAC combined with Raman and FTIR spectra to study the phase diagram of the calcite to aragonite transition and the impact of aqueous fluid on this transition in this study. Two types of transmission media (water and alcohol) were used. In anhydrous system, the calcite to aragonite diagram was extended to 12 GPa and 400°C, with the calcite-aragonite boundary shown as a convex curve, which is consistent with the molar volume changes between the transition from aragonite to cc-III/IIIb and from aragonite to cc-I and cc-II. In the hydrous system, we observed two kinds of phase transformation mechanisms, the SRR phase transition, and the DPD process. The SRR occurred in an immediately heated process. It can exist in both “hot” and “cold” slabs, under high P - T conditions

(1–2 GPa and 160–400°C) in the subduction zone. The DPD occurred in the system where calcite stayed at 0.6–1 GPa and room temperature for hours, then heated up. It can only occur on a “cold” slab under lower P - T conditions (less than 1.5 GPa and 110°C).

DATA AVAILABILITY STATEMENT

The original contributions presented in the study are included in the article/supplementary Materials, further inquiries can be directed to the corresponding author.

AUTHOR CONTRIBUTIONS

XZ, ZZ, JC, YG, and SM contributed to the conception and design of the study. XZ wrote the first draft of the manuscript and led the data analysis and interpreted the results with SM, XH, JS, and MX. All authors contributed to manuscript revision, read and approved it for publication.

FUNDING

This research was financially supported by Chinese Academy of Sciences (Grants Nos QYZDY-SSW-DQC029 and XDA22040501).

ACKNOWLEDGMENTS

We thank Junwei Li for his technical help on experiments.

REFERENCES

- Ague, J. J., and Nicolescu, S. (2014). Carbon Dioxide Released from Subduction Zones by Fluid-Mediated Reactions. *Nat. Geosci.* 7, 355–360. doi:10.1038/ngeo2143
- Bassett, W. A., Shen, A. H., Bucknum, M., and Chou, I. M. (1993). A New Diamond Anvil Cell for Hydrothermal Studies to 2.5 GPa and from –190 to 1200 °C. *Rev. Sci. Instrum.* 64, 2340–2345. doi:10.1063/1.1143931
- Bayarjargal, L., Fruhner, C.-J., Schrodt, N., and Winkler, B. (2018). CaCO₃ Phase Diagram Studied with Raman Spectroscopy at Pressures up to 50 GPa and High Temperatures and DFT Modeling. *Phys. Earth Planet. Interiors* 281, 31–45. doi:10.1016/j.pepi.2018.05.002
- Bridgman, P. W. (1939). The High Pressure Behavior of Miscellaneous Minerals. *Am. J. Sci.* 237, 7–18.
- Catalli, K., and Williams, Q. (2005). A High-Pressure Phase Transition of Calcite-III. *Am. Mineralogist* 90, 1679–1682. doi:10.2138/am.2005.1954
- Dasgupta, R., and Hirschmann, M. M. (2010). The Deep Carbon Cycle and Melting in Earth's Interior. *Earth Planet. Sci. Lett.* 298, 1–13. doi:10.1016/j.epsl.2010.06.039
- Dickens, B., and Brown, W. E. (1970). Crystal Structure of Calcium Carbonate Hexahydrate at about –120.Deg. *Inorg. Chem.* 9, 480–486. doi:10.1021/ic50085a010
- Gavryushkin, P. N., Martirosyan, N. S., Inerbaev, T. M., Popov, Z. I., Rashchenko, S. V., Likhacheva, A. Y., et al. (2017). Aragonite-II and CaCO₃-VII: New High-Pressure, High-Temperature Polymorphs of CaCO₃. *Cryst. Growth & Des.* 17, 6291–6296. doi:10.1021/acs.cgd.7b00977
- Hagiya, K., Matsui, M., Kimura, Y., and Akahama, Y. (2005). The Crystal Data and Stability of Calcite III at High Pressures Based on Single-Crystal X-Ray Experiments. *J. Mineralogical Petrological Sci.* 100, 31–36. doi:10.2465/jmps.100.31
- Hess, N. J., Ghose, S., and Exarhos, G. J. (1991). “Raman Spectroscopy at Simultaneous High Pressure and Temperature: Phase Relations of CaCO₃ and the Lattice Dynamics of the Calcite CaCO₃(II) Phase Transition,” in Proceedings XIII th AIRAPT international conference on high pressure science and technology, Oxford, New Delhi, 236–241.
- Hou, M., Zhang, Q., Tao, R., Liu, H., Kono, Y., Mao, H.-K., et al. (2019). Temperature-induced Amorphization in CaCO₃ at High Pressure and Implications for Recycled CaCO₃ in Subduction Zones. *Nat. Commun.* 10, 1963. doi:10.1038/s41467-019-09742-5
- Kaminsky, F., Matzel, J., Jacobsen, B., Hutcheon, I., and Wirth, R. (2016). Isotopic Fractionation of Oxygen and Carbon in Decomposed Lower-Mantle Inclusions in Diamond. *Min. Pet.* 110, 379–385. doi:10.1007/s00710-015-0401-7
- Koch-Mueller, M., Jahn, S., Birkholz, N., Ritter, E., and Schade, U. (2016). Phase Transitions in the System CaCO₃ at High P and T Determined by *In Situ* Vibrational Spectroscopy in Diamond Anvil Cells and First-Principles Simulations. *Phys. Chem. Minerals* 43, 545–561.
- Li, X., Zhang, Z., Lin, J. F., Ni, H., Prakapenka, V. B., and Mao, Z. (2018). New High-Pressure Phase of CaCO₃ at the Topmost Lower Mantle: Implication for the Deep-Mantle Carbon Transportation. *Geophys. Res. Lett.* 45, 1355–1360. doi:10.1002/2017gl076536
- Litasov, K. D., and Ohtani, E. (2009). Solidus and Phase Relations of Carbonated Peridotite in the System CaO-Al₂O₃-MgO-SiO₂-Na₂O-CO₂ to the Lower

- Mantle Depths. *Phys. Earth Planet. Interiors* 177, 46–58. doi:10.1016/j.pepi.2009.07.008
- Litasov, K. D., Shatskiy, A., Gavryushkin, P. N., Bekhtenova, A. E., Dorogokupets, P. I., Danilov, B. S., et al. (2017). P-V-T Equation of State of CaCO₃ Aragonite to 29 GPa and 1673 K: *In Situ* X-Ray Diffraction Study. *Phys. Earth Planet. Interiors* 265, 82–91. doi:10.1016/j.pepi.2017.02.006
- Liu, C., Zheng, H., and Wang, D. (2017). Raman Spectroscopic Study of Calcite III to Aragonite Transformation under High Pressure and High Temperature. *High Press. Res.* 37, 545–557. doi:10.1080/08957959.2017.1384824
- Long, D. A. (1977). *Raman Spectroscopy*. New York City: McGraw-Hill, 276.
- Lv, M., Dorfman, S. M., Badro, J., Borensztajn, S., Greenberg, E., and Prakapenka, V. B. (2021). Reversal of Carbonate-Silicate Cation Exchange in Cold Slabs in Earth's Lower Mantle. *Nat. Commun.* 12, 1712. doi:10.1038/s41467-021-21761-9
- Mao, H. K., and Bell, P. M. (1978). High-Pressure Physics: Sustained Static Generation of 1.36 to 1.72 Megabars. *Science* 200, 1145–1147. doi:10.1126/science.200.4346.1145
- Marland, G. (1975). The Stability of CaCO₃-6H₂O (Ikaite). *Geochimica Cosmochimica Acta* 39, 83–91. doi:10.1016/0016-7037(75)90186-6
- Maslen, E. N., Streltsov, V. A., and Streltsova, N. R. (1993). X-ray Study of the Electron Density in Calcite, CaCO₃. *Acta Crystallogr. Sect. B* 49, 636–641. doi:10.1107/s0108768193002575
- Merlini, M., Crichton, W. A., Chantel, J., Guignard, J., and Poli, S. (2014). Evidence of Interspersed Co-existing CaCO₃-III and CaCO₃-IIIb Structures in Polycrystalline CaCO₃ at High Pressure. *Mineral. Mag.* 78, 225–233. doi:10.1180/minmag.2014.078.2.01
- Merlini, M., Hanfland, M., and Crichton, W. A. (2012). CaCO₃-III and CaCO₃-VI, High-Pressure Polymorphs of Calcite: Possible Host Structures for Carbon in the Earth's Mantle. *Earth Planet. Sci. Lett.* 333–334, 265–271. doi:10.1016/j.epsl.2012.04.036
- Merrill, L., and Bassett, W. A. (1975). The Crystal Structure of CaCO₃(II), a High-Pressure Metastable Phase of Calcium Carbonate. *Acta Crystallogr. Sect. B* 31, 343–349. doi:10.1107/s0567740875002774
- Morse, J. W., and Mackenzie, F. T. (1990). *Geochemistry of Sedimentary Carbonates*. Amsterdam: Elsevier.
- Negro, A. D., and Ungaretti, L. (1971). Refinement of the Crystal Structure of Aragonite. *Am. Mineralogist* 56, 768–772.
- Nestola, F., Korolev, N., Kopylova, M., Rotiroti, N., Pearson, D. G., Pamato, M. G., et al. (2018). CaSiO₃ Perovskite in Diamond Indicates the Recycling of Oceanic Crust into the Lower Mantle. *Nature* 555, 237–241. doi:10.1038/nature25972
- Oganov, A. R., Glass, C. W., and Ono, S. (2006). High-pressure Phases of CaCO₃: Crystal Structure Prediction and Experiment. *Earth Planet. Sci. Lett.* 241, 95–103. doi:10.1016/j.epsl.2005.10.014
- Oganov, A. R., Ono, S., Ma, Y., Glass, C. W., and Garcia, A. (2008). Novel High-Pressure Structures of MgCO₃, CaCO₃ and CO₂ and Their Role in Earth's Lower Mantle. *Earth Planet. Sci. Lett.* 273, 38–47. doi:10.1016/j.epsl.2008.06.005
- Ono, S., Kikegawa, T., and Ohishi, Y. (2007). High-pressure Transition of CaCO₃. *Am. Mineralogist* 92, 1246–1249. doi:10.2138/am.2007.2649
- Ono, S., Kikegawa, T., Ohishi, Y., and Tsuchiya, J. (2005). Post-aragonite Phase Transformation in CaCO₃ at 40 GPa. *Am. Mineralogist* 90, 667–671. doi:10.2138/am.2005.1610
- Palaich, S. E. M., Heffern, R. A., Hanfland, M., Lausi, A., Kavner, A., Manning, C. E., et al. (2016). High-pressure Compressibility and Thermal Expansion of Aragonite. *Am. Mineralogist* 101, 1651–1658. doi:10.2138/am-2016-5528
- Pan, D., and Galli, G. (2016). The Fate of Carbon Dioxide in Water-Rich Fluids under Extreme Conditions. *Sci. Adv.* 2, e1601278. doi:10.1126/sciadv.1601278
- Pauly, H. (1963). *Ikaite, nyt mineral der danner skaer*. Copenhagen: Naturens Verden, 168–192.
- Pelouze, J. (1831). Sur la production artificielle du carbonate de chaux cristallise, et sur deux combinaisons de ce sel avec l'eau. *Ann. de Chimie de Physique* 2, 301–307.
- Perdikouri, C., Kasiopas, A., Putnis, C. V., and Putnis, A. (2008). The Effect of Fluid Composition on the Mechanism of the Aragonite to Calcite Transition. *Mineral. Mag.* 72, 111–114. doi:10.1180/minmag.2008.072.1.111
- Plummer, L. N., and Busenberg, E. (1982). The Solubilities of Calcite, Aragonite and Vaterite in CO₂-H₂O Solutions between 0 and 90°C, and an Evaluation of the Aqueous Model for the System CaCO₃-CO₂-H₂O. *Geochimica Cosmochimica Acta* 46, 1011–1040. doi:10.1016/0016-7037(82)90056-4
- Rossmann, G. R. (2006). "1. Analytical Methods for Measuring Water in Nominally Anhydrous Minerals," in *Water in Nominally Anhydrous Minerals*. Editors H. Keppler and J. R. Smyth, 1–28. doi:10.1515/9781501509476-005
- Rutt, H. N., and Nicola, J. H. (1974). Raman Spectra of Carbonates of Calcite Structure. *J. Phys. C. Solid State Phys.* 7, 4522–4528. doi:10.1088/0022-3719/7/24/015
- Sánchez-Pastor, N., Oehlerich, M., Manuel, J., Melanie, A., and Christoph, K. (2016). Crystallization of Ikaite and its Pseudomorphic Transformation into Calcite: Raman Spectroscopy Evidence. *Geochimica Cosmochimica Acta* 175, 271–281. doi:10.1016/j.gca.2015.12.006
- Shahar, A., Bassett, W. A., Mao, H. K., Chou, I., and Mao, W. (2005). The Stability and Raman Spectra of Ikaite, CaCO₃[middle dot]6H₂O, at High Pressure and Temperature. *Am. Mineralogist* 90, 1835–1839. doi:10.2138/am.2005.1783
- Suito, K., Namba, J., Horikawa, T., Taniguchi, Y., Sakurai, N., Kobayashi, M., et al. (2001). Phase Relations of CaCO₃ at High Pressure and High Temperature. *Am. Mineralogist* 86, 997–1002. doi:10.2138/am-2001-8-906
- Syracuse, E. M., Van Keken, P. E., Abers, G. A., Suetsugu, D., Bina, C., Inoue, T., et al. (2010). The Global Range of Subduction Zone Thermal Models. *Phys. Earth Planet. Interiors* 183, 73–90. doi:10.1016/j.pepi.2010.02.004
- Trots, D. M., Kurnosov, A., Ballaran, T. B., Tkachev, S., Zhuravlev, K., Prakapenka, V., et al. (2013). The Sm:YAG Primary Fluorescence Pressure Scale. *J. Geophys. Res. Solid Earth* 118, 5805–5813. doi:10.1002/2013jb010519
- Van Valkenburg, A., Mao, H. K., and Bell, P. M. (1971). Ikaite (CaCO₃-6H₂O), a Phase More Stable Than Calcite and Aragonite (CaCO₃) at High Water Pressure. *Carnegie Inst. Geophys. Lab., Annu. Rep. Dir.* 1971, 233–237.
- Wirth, R., Kaminsky, F., Matsyuk, S., and Schreiber, A. (2009). Unusual Micro- and Nano-Inclusions in Diamonds from the Juina Area, Brazil. *Earth Planet. Sci. Lett.* 286, 292–303. doi:10.1016/j.epsl.2009.06.043
- Yuan, X., Gao, C., and Gao, J. (2019). An *In Situ* Study of the Phase Transitions Among CaCO₃ High-Pressure Polymorphs. *MinMag* 83, 191–197. doi:10.1180/mgm.2018.140
- Yuan, X., Mayanovic, R. A., and Zhang, G. (2021). Phase Transitions in CaCO₃ under Hydrous and Anhydrous Conditions: Implications for the Structural Transformations of CaCO₃ during Subduction Processes. *Am. Mineralogist* 106, 1780–1788. doi:10.2138/am-2021-7575
- Zhang, M., and Moxon, T. (2012). *In Situ* infrared Spectroscopic Studies of OH, H₂O and CO₂ in Moganite at High Temperatures. *ejm* 24, 123–131. doi:10.1127/0935-1221/2011/0023-2165
- Zhang, Z.-W., Wang, Y.-L., Qian, B., Liu, Y.-G., Zhang, D.-Y., Lü, P.-R., et al. (2018b). Metallogeny and Tectonomagmatic Setting of Ni-Cu Magmatic Sulfide Mineralization, Number 1 Shitoukengde Mafic-Ultramafic Complex, East Kunlun Orogenic Belt, NW China. *Ore Geol. Rev.* 96, 236–246. doi:10.1016/j.oregeorev.2018.04.027
- Zhang, Z., Mao, Z., Liu, X., Zhang, Y., and Brodholt, J. (2018a). Stability and Reactions of CaCO₃ Polymorphs in the Earth's Deep Mantle. *J. Geophys. Res. Solid Earth* 123, 10. doi:10.1002/2017jb015019
- Zheng, Y.-F., and Hermann, J. (2014). Geochemistry of Continental Subduction-Zone Fluids. *Earth, Planets Space* 66, 93. doi:10.1186/1880-5981-66-93

Conflict of Interest: The authors declare that the research was conducted in the absence of any commercial or financial relationships that could be construed as a potential conflict of interest.

Publisher's Note: All claims expressed in this article are solely those of the authors and do not necessarily represent those of their affiliated organizations, or those of the publisher, the editors, and the reviewers. Any product that may be evaluated in this article, or claim that may be made by its manufacturer, is not guaranteed or endorsed by the publisher.

Copyright © 2022 Zhao, Zheng, Chen, Gao, Sun, Hou, Xiong and Mei. This is an open-access article distributed under the terms of the Creative Commons Attribution License (CC BY). The use, distribution or reproduction in other forums is permitted, provided the original author(s) and the copyright owner(s) are credited and that the original publication in this journal is cited, in accordance with accepted academic practice. No use, distribution or reproduction is permitted which does not comply with these terms.



The Effect of Quartz Particle Size on the Frictional and Electrically Conductive Properties of Mixed Graphite–Quartz Gouges

Jinyu Chen*

State Key Laboratory of Earthquake Dynamics, Institute of Geology, China Earthquake Administration, Beijing, China

OPEN ACCESS

Edited by:

Lidong Dai,
Institute of geochemistry (CAS), China

Reviewed by:

Caiyun Lan,
Northwest University, China
Tao Yang,
China University of Geosciences,
China

Shuyun Cao,
China University of Geosciences
Wuhan, China

Fabrice Gaillard,
Université d'Orléans, France

*Correspondence:

Jinyu Chen
jinyu@ies.ac.cn

Specialty section:

This article was submitted to
Solid Earth Geophysics,
a section of the journal
Frontiers in Earth Science

Received: 05 April 2022

Accepted: 11 May 2022

Published: 17 June 2022

Citation:

Chen J (2022) The Effect of Quartz Particle Size on the Frictional and Electrically Conductive Properties of Mixed Graphite–Quartz Gouges. *Front. Earth Sci.* 10:913315. doi: 10.3389/feart.2022.913315

Mature faults usually contain fault rocks with a wide range of mineral grain sizes. Despite the importance of mineral grain sizes in affecting fault slip behaviors, little is known about the potential mechanism(s). To better understand this problem, electrical conductivity measurements on synthetic carbon-bearing gouges were conducted along a fault-parallel direction under progressive fault slip. All experiments were carried out under a slip rate of 1 mm/s, a normal stress of 2 MPa, ambient temperature, and a pure N₂ atmosphere. The specimens that were used were mixtures of identical 6 wt% graphite (Gr) powders and 94 wt% quartz (Qz) particles with five different particle sizes (#100–12500 mesh). As Gr has a low friction coefficient and high electrical conductivity, the approach in this study may provide a favorable opportunity to examine the relation between the evolutions of friction and shear textures. The experimental results indicated that the reduction in Qz particle sizes causes gradual segregation of the Gr powders in the skeletal frame formed by granular Qz particles, resulting in the decreased interconnectivity of the anastomosing Gr-film networks and the destruction of Gr-lubricated slip surface(s). Then, it eventually manifests as an increase in the steady-state frictional coefficient (μ_{ss}) and a logarithmic decrease in the steady-state electrical conductivity (σ_{ss}) for Gr-bearing specimens. Furthermore, the Gr-bearing gouges containing >3 μ m Qz particles first develop foliated layers, and subsequent Gr films penetrate around the boundary of the Qz particles to form conductive interconnected networks during a progressive fault slip. These experimental results implied that carbonaceous materials (CMs) represented by Gr may complicate the frictional properties of fine-grained fault gouges in mature faults.

Keywords: electrical conductivity, grain-boundary graphite film, quartz particle size, graphite-bearing microstructure, friction coefficient

INTRODUCTION

In the upper crust, the principle slip zones of mature faults accommodate the bulk of fault displacements and develop narrow, highly localized-deformed zones, i.e., strain localization zones, which are embedded in the wide damage zones of relatively low deformation and inactivity (e.g., Sibson, 2003; Wibberley and Shimamoto, 2005; Keulen et al., 2007). Thus, mature faults usually contain fault rocks with a wide range of mineral grain sizes at the microscopic scale (Marone and Scholz, 1989; Blenkinsop, 1991; Billi and Storti, 2004; Wilson

et al., 2005). The mineral particle sizes of granitoid or carbonate fault rocks can be reduced under the cataclastic process in a brittle regime, and the dominant comminution mechanism changes from grain cracking due to initial rupturing to grain comminution, grinding, and attrition (Blenkinsop, 1991; Storti et al., 2003; Keulen et al., 2007). These fine gouges control the fault strength and earthquake stability, and studying the properties of fault rocks from mature faults can help us understand the earthquake process (Wilson et al., 2005; Ikari et al., 2011; Smith et al., 2015; Scholz, 2019).

As a specific weak mineral, the carbonaceous materials (CMs), especially graphite (Gr), exhibit a low frictional coefficient and lubricated property ($\mu \leq 0.2$) over a wide range of slip rates (0.05–1.3 m/s) under water-free conditions (Oohashi et al., 2011, 2013; Kaneki and Hirono, 2019). They cause a much weaker shear strength for a mature fault than that expected from Byerlee's law (0.6–0.7, Byerlee, 1978). The strengths of steady-state mixed quartz (Qz)–Gr gouges exhibit nonlinear weakening with an increasing weak Gr fraction, characterized by an abrupt decay above ~10% and slip transfer from the contacts between the particles of Qz–Qz to powders of Gr–Gr (Oohashi et al., 2013). CM or crystalline Gr is exposed in several fault zones (Cao and Neubauer, 2019), e.g., the Longmenshan fault zone, China (Wang et al., 2014; Chen et al., 2016; Kouketsu et al., 2017), the Atotsugawa fault system, Japan (Oohashi et al., 2012), the Tanakura Tectonic Line, Japan (Oohashi et al., 2011), the German Continental Deep Drilling Program (KTB) borehole on the western edge of the Bohemian Massif, Germany (Zulauf et al., 1999), and the Err nappe detachment fault, Switzerland (Manatschal, 1999). In general, CM or crystalline Gr occupies approximately 5–36% of the fault rocks (Manatschal, 1999; Oohashi et al., 2012; Wang et al., 2014; Chen et al., 2016).

In addition, the highly interconnected networks composed of grain-boundary Gr films can enhance the electrical conductivity of rocks by several orders of magnitude and cause a layer of high-conductivity anomalies (e.g., Duba and Shankland, 1982; Frost et al., 1989; Mareschal et al., 1992). Chen et al. (2017) proposed that the electrical conductivity of carbon-bearing (including Gr and amorphous carbon) gouges can logarithmically increase when the volumetric fraction of CM reaches the percolation threshold (Gueguen and Dienes, 1989; Wang et al., 2013). Yamashita et al. (2014) first attempted to develop a new experimental assembly to monitor the electrical properties of fault zones during frictional slipping. Han et al. (2019) revised Yamashita's assembly and tried to measure the electrical resistance of simulated Gr-bearing gouges after a frictional slip. They found that the conductive properties could significantly change due to Gr enrichment on the slipping surfaces. In brief, the conductive properties can provide information on the textural evolution of Gr-bearing gouges.

Therefore, the fine gouge of a mature fault plays a crucial role in fault stability and electrical conductivity measurements can more sophisticatedly depict the continuous processes of textural developments in Gr-bearing gouges relative to traditional rotary shear experiments. In addition, most blackish fault gouges contain less than 12 wt% Gr in the bulk fault gouge (Manatschal, 1999; Oohashi et al., 2012), and mixed Gr–Qz

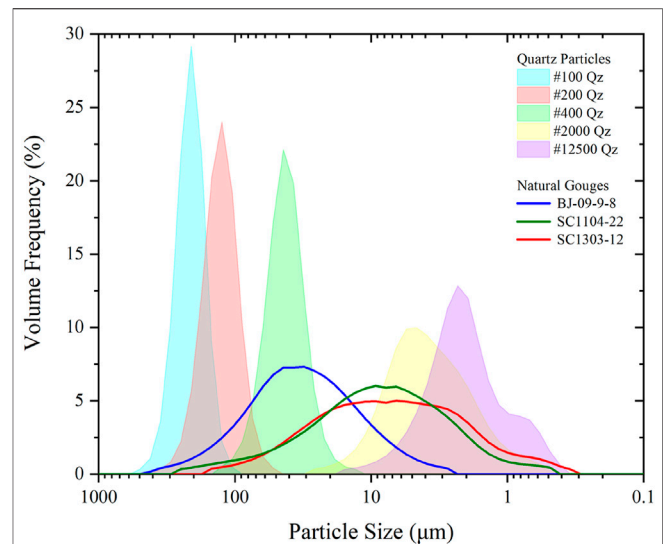


FIGURE 1 | Comparison with the initial particle size distribution (PSD) of the #100–12500 mesh Qz particles indicated by colored areas. The solid lines are natural gouges collected from the co-seismic slip zone of the Longmenshan fault zone in Sichuan Province, China P.R. (Chen et al., 2017).

gouges with more than 5 wt% Gr that experienced fault slip can form conductive interconnected networks (Han et al., 2019). Then, the overall trends of the mixed Gr–Qz gouge in the relationship of friction to slip rates of <0.1 m/s seem to be similar (Oohashi et al., 2013). Given this trend, the transient electrical response of synthetic 6 wt% Gr-bearing gouges with different Qz particle sizes at ~1.0 mm/s was monitored to explain the effect of Qz particle sizes on the textural developments of interconnected conductive networks and the frictional properties of Gr-bearing fault zones at a low slip rate. These experiments were conducted along a fault-parallel direction during progressive fault slip. As a typical rock-forming mineral, Qz can be represented as the strong mineral in the gouge mixture (Oohashi et al., 2013). It should be noted that our synthetic specimens are biminerale mixtures whose particle size distributions, mineralogical compositions, and slipping behaviors are oversimplified than those of natural materials. However, this topic facilitates systematic study and understanding of bulk physical properties for carbon-bearing gouges.

EXPERIMENTAL METHODS

Specimen Preparation and Experimental Assembly

The experimental specimens were five synthetic Gr-bearing gouges prepared through 6 wt% identical Gr powders mixed with 94 wt% Qz particles of five different particle sizes, including #100, #200, #400, #2000, and #12500 mesh. Each specimen was fully stirred in the container for at least 10 min to ensure that the graphite powders were homogeneously

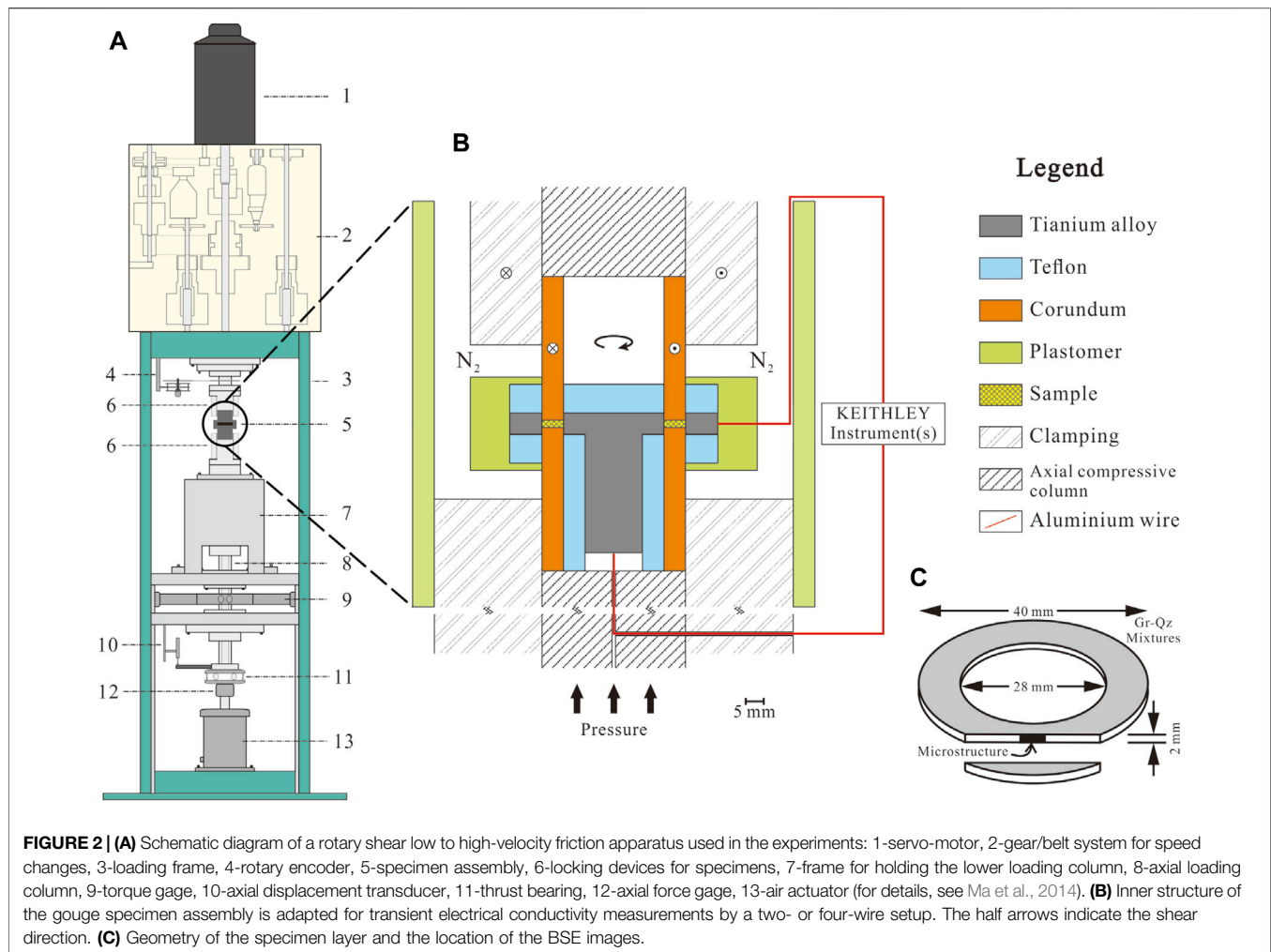


FIGURE 2 | (A) Schematic diagram of a rotary shear low to high-velocity friction apparatus used in the experiments: 1-servo-motor, 2-gear/belt system for speed changes, 3-loading frame, 4-rotary encoder, 5-specimen assembly, 6-locking devices for specimens, 7-frame for holding the lower loading column, 8-axial loading column, 9-torque gage, 10-axial displacement transducer, 11-thrust bearing, 12-axial force gage, 13-air actuator (for details, see Ma et al., 2014). **(B)** Inner structure of the gouge specimen assembly is adapted for transient electrical conductivity measurements by a two- or four-wire setup. The half arrows indicate the shear direction. **(C)** Geometry of the specimen layer and the location of the BSE images.

distributed among the Qz particles. The purity of Qz was 99.34%, as monitored by Anhui Province Quality Supervision and Inspection Center, while Gr was an analytical grade chemical reagent (CAS number: 7,782-42-5) with a purity greater than 98.5% and was supplied by Xilong Scientific Co., Ltd. The initial particle size distribution (PSD) of all Qz particles was determined by a Microtrac S3500 laser diffraction analyzer (see different colored areas in **Figure 1**). The analytical results indicated that all synthetic Qz particle sizes are concentrated within ~1.5 orders of magnitude, and their median diameters (ϕ_{ave}) are 199, 121, 40.8, 4.08, and 2.13 μm , respectively.

Chen et al. (2017) analyzed the PSD of natural carbonaceous gouges collected from the co-seismic slip zone of the Longmenshan fault zone in Sichuan Province, China P.R. They found that the natural gouges have platykurtic distributions, and their mineral grain sizes span up to ~3 orders of magnitude (see solid lines in **Figure 1**). Thus, every distribution range of synthetic Qz particles (#100–12500 mesh) is relatively narrow, while their overall span almost covers the PSD of the entire natural gouge. That is, these five specimens can reflect the properties of portions with five different mineral grain sizes of the same natural carbonaceous gouge. For convenience,

the Qz particle size of each specimen is represented by a single particle size value (i.e., ϕ_{ave}) in the following discussion section. According to the density of Gr (2.31 g/cm³) and Qz (2.66 g/cm³) determined by a true density analyzer, the Gr volume fractions of all specimens are 6.85 vol%.

An experimental setup was designed to monitor the transient electrical response of specimens along a fault-parallel direction (the schematic diagram is shown in **Figure 2B**). In this setup, a 2.0 g Gr-bearing gouge (~2.0 mm thick) was pressed into a circular ring with an internal diameter of ~16 mm and an external diameter of ~28 mm between a pair of corundum cylinders. These cylinders were treated as the surrounding rocks of a fault zone. Then, a T-shaped titanium alloy cylinder as an inner electrode and a titanium alloy ring as an outer electrode bracketed the ring-shaped gouge. Furthermore, a series of softer Teflon components, including a disc shape, a hollow cylinder, and two ring shapes were placed around the electrodes to prevent gouge leakage. Finally, a high-purity flowing N₂ gas, which was limited by a plastomer vessel, provided a relatively dry and anoxic environment around the specimen holder, and all resistance values of specimens (R) were measured by Keithley (precise resistance-measuring)

TABLE 1 | Summary of the friction conductivity parameters on synthetic Gr-bearing gouges in this study.

No.	Sample	φ_{ave} μm	$D_{\mu ss}$ m	μ_{ss}	$\mu_{ss}^{(+)}$	$\mu_{ss}^{(-)}$	D_{ech} m	D_{ess} m	σ_0 S/m	σ_{ss} S/m	$\sigma(+)$ ss S/m	$\sigma(-)$ ss S/m
LHV2823	6 wt% Gr+94 wt% #100 Qz	199	0.400	0.365	0.090	0.102	nd	nd	nd	nd	nd	nd
LHV2434	6 wt% Gr+94 wt% #100 Qz	199	nd	nd	nd	nd	4.69×10^{-4}	0.408	0.005	3.090	0.407	0.634
LHV1379	6 wt% Gr+94 wt% #200 Qz	121	0.190	0.494	0.073	0.039	0	0.652	0.001	3.972	3.979	1.840
LHV2424	6 wt% Gr+94 wt% #400 Qz	40.8	0.115	0.652	0.012	0.011	0.428	0.705	1.42×10^{-11}	0.001	4.55×10^{-4}	0.001
LHV2430	6 wt% Gr+94 wt% #2000 Qz	4.08	0.288	0.742	0.093	0.067	1.616	3.357	2.37×10^{-11}	7.58×10^{-5}	2.82×10^{-5}	3.81×10^{-5}
LHV1376	6 wt% Gr+94 wt% #12500 Qz	2.13	0.625	0.768	0.079	0.027	0	1.561	1.34×10^{-7}	1.07×10^{-9}	3.89×10^{-9}	5.53×10^{-10}

instrument(s) (Model 6,221, Model 2182A, and Model 6,514), which were connected to electrodes by aluminum wires.

Experimental Procedures

Using a low-to high-velocity rotary shear apparatus (LHVR; Marui Co., Ltd., Osaka, Japan, MIS-233-1-76) at the Institute of Geology, China Earthquake Administration (IGCEA) (Hou et al., 2012; Yao et al., 2013a; Ma et al., 2014; **Figure 2A**), five friction-conduction experiments were carried out at the room temperature (**Table 1**). All the specimens equipped with the experimental assembly were dried in an oven at least at 75°C for >24 h before the experiment. The specimens were first pressed at 2.0 MPa for >2 h (pre-slip stage) and then sheared through clockwise rotation of the upper corundum cylinder with large displacements of 1.5–4.4 m under constant normal stress. In addition, each specimen was subjected to a slide-hold-slide test to examine fault strength recovery and Gr-bearing microstructural alteration, *i.e.*, slippage was stopped and the specimen was held for less than 10 min (hold period) during the experimental process (Marone, 1998; Yao et al., 2013b). It should be noted that all the experiments were conducted at a constant “equivalent slip velocity (V_e)” (simply referred to as “slip rate” hereafter) of ~1.0 mm/s. V_e is based on the definition that $\tau V_e S$ is the rate of frictional work on the sliding surface area (S) and the assumption that the shear stress (τ) is constant over the entire fault surface (for details, see Hirose and Shimamoto, 2005; Togo et al., 2011; Yao et al., 2013a). Thus, the relationship between torque (I) and shear stress (τ) can be obtained by integration:

$$I = \int_{r_i}^{r_e} dF = \int_{r_i}^{r_e} \tau \cdot 2\pi r dr = \frac{2\pi\tau}{3} (r_e^3 - r_i^3), \quad (1)$$

where r_e and r_i are external (20 mm) and internal (14 mm) radii, respectively. The experimental data, including torque, axial force, axial displacement, rate of revolution, and the analog signal of the Keithley data, were recorded with a digital data recorder (KYOWA EDX-100A) at a sampling rate of 20 Hz. Then, according to the geometric factor of the specimen dimensions, the normal stress (P , MPa), frictional coefficient (μ , calculated by τ/P , $\pm 5\%$ uncertainty), thickness (δ , m), slip rate (V_e , mm/s), and slip displacement (D , m) were acquired. In particular, to correctly

eliminate the effect of shear traction between the Teflon components and the rotatory corundum cylinder in the experiments, the traction was subtracted from the raw data following the method of Togo *et al.* (2011) and Hou *et al.* (2012), which are 0.084 MPa for the peak friction and 0.077 MPa for the steady-state friction.

Based on the approximate range of the measuring resistance value, a two- or four-wired setup to measure the electrical resistance values were applied during the experiments: (a) for $R < 200 \Omega$, Model 6,221 supplied the stable DC current- I , and Model 2182A acquired the electrical potential- E . (b) For $200 \Omega < R < 200 \text{ G}\Omega$, the Model 6,514 Ω mode directly obtained the electrical resistance. (c) For $R > 200 \text{ G}\Omega$, the measurement mode was the same as that in (a) but the potential- E was measured by the Model 6,514 volt mode. LabVIEW 7 Express or KickStart software recorded the electrical resistance data. For the specimen geometry of a coaxial circular ring, the electrical conductivity along the fault-parallel direction (σ , S/m) was calculated by taking the inverse of the resistance (R or E/I , Ω) and normalizing it with the scale as follows:

$$\sigma = \frac{1}{\rho} = \frac{\ln(r_e/r_i)}{2\pi\delta R}, \quad (2)$$

where ρ is the resistivity ($\Omega\cdot\text{m}$). Then, the recording time of mechanical data was adapted to the conductive data by uniformizing analog and digital Keithley instrumental signals. Note that the measured electrical currents during the experiments inevitably interfere with the assembled components surrounding the specimen. However, such measured errors are negligible in this study since these components were relatively insulated (*e.g.*, Teflon $>10^{18} \Omega\cdot\text{m}$, Al_2O_3 $10^{14}\sim 10^{15} \Omega\cdot\text{m}$, Keithley, 2013). The background electrical resistance of the experimental assembly (R') was assessed through the direct connection between the inner and outer electrodes (0.0041 Ω), and then all the measured resistance values that were applied to calculate σ with **Eq 1** were corrected by subtracting R' from the raw data.

Furthermore, several critical parameters of these experimental curves were determined as follows: (a) the initial electrical conductivity (σ_0) is the σ of the specimen at the end of the pre-slip stage and before the frictional slip. (b) The steady-state

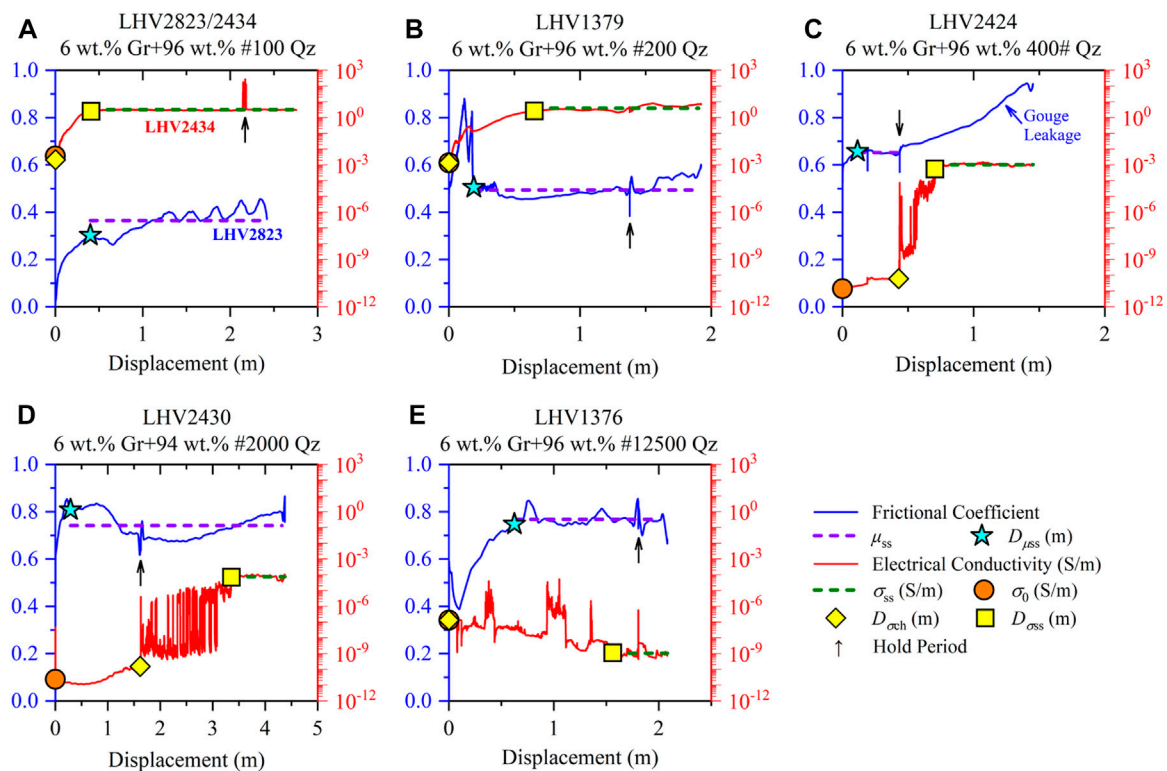


FIGURE 3 | Frictional coefficient (solid blue line) and electrical conductivity (solid red line) plotted against slip displacement for all specimens. The particle sizes of Qz particles include (A) #100 mesh, (B) #200 mesh, (C) #400 mesh, (D) #2000 mesh, and (E) #12500 mesh.

frictional coefficient (μ_{ss}) and steady-state electrical conductivity (σ_{ss}) were obtained from the arithmetic and logarithmic average values of all experimental data from frictional and conductive steady states (not including the hold period), respectively. (c) The slip displacements achieved some critical moments, including μ reaching μ_{ss} ($D_{\mu ss}$), σ starting the logarithmical change ($D_{\sigma ch}$), and σ reaching σ_{ss} ($D_{\sigma ss}$). All the critical parameters for each experiment (i.e., μ_{ss} , $D_{\mu ss}$, σ_0 , $D_{\sigma ch}$, $D_{\sigma ss}$, and σ_{ss}) are listed in Table 1.

The symbols listed in the table are as follows: φ_{ave} is the median diameter of Qz particles, $D_{\mu ss}$ is the slip displacement as μ achieves μ_{ss} , μ_{ss} is the steady-state frictional coefficient, $\mu_{ss}^{+}/\mu_{ss}^{-}$ is the positive/negative error of μ_{ss} , $D_{\sigma ch}$ is the slip displacement as σ starts to logarithmically change, $D_{\sigma ss}$ is the slip displacement as σ achieves σ_{ss} , σ_0 is the initial electrical conductivity, σ_{ss} is the steady-state electrical conductivity, $\sigma_{ss}^{+}/\sigma_{ss}^{-}$ is the positive/negative error of σ_{ss} , and nd indicates that the parameter could not be determined due to erratic frictional behavior.

After the experiments, a Zeiss Sigma scanning electron microscopy (SEM) analysis was conducted at IGCEA to investigate the Gr-bearing microstructure on the synthetic specimens. The backscattered electron (BSE) images were from the gold-coated thin sections of epoxy-impregnated recovery specimens parallel to the specimen axis (Figure 2C). They were obtained under a 15 kV accelerating voltage and 8.6–8.7 mm working distance.

RESULTS

Experimental Data

All friction-conductivity experimental data plotted against slip displacement are shown in Figures 3A–E. Due to the slight misalignment of the assembly resulting in the fluctuation of friction at each revolution of the rotatory corundum cylinder, all friction curves and most conductivity curves were smoothed out under linear and log scales, respectively. They used the moving average method, which takes an average of data points corresponding to one revolution (for more details, see Yao et al., 2013a). The slide-hold-slide test of each experiment (black arrows in Figure 3) showed that a non-noticeable change was detected in the mechanical behaviors of the specimens. Every dashed violet and dark green line in Figure 3 corresponds to μ_{ss} and σ_{ss} , respectively, and their lengths represent the data range used to calculate μ_{ss} or σ_{ss} . The blue stars, orange circles, yellow diamonds, and yellow squares located on each curve in Figure 3 indicated $D_{\mu ss}$, σ_0 , $D_{\sigma ch}$, and $D_{\sigma ss}$, respectively.

With the increase in slip displacement, the frictional coefficient (μ) reached a friction steady state after 0.1–0.7 m and remained stable within 0.1 fluctuations to the end. In contrast, the electrical conductivity (σ) increased logarithmically by 3–8 orders of magnitude after a displacement slippage of 0–1.6 m. Then, the parameter maintained a conductivity steady-state that varied within one order of magnitude to the end. As an exception, the σ of the

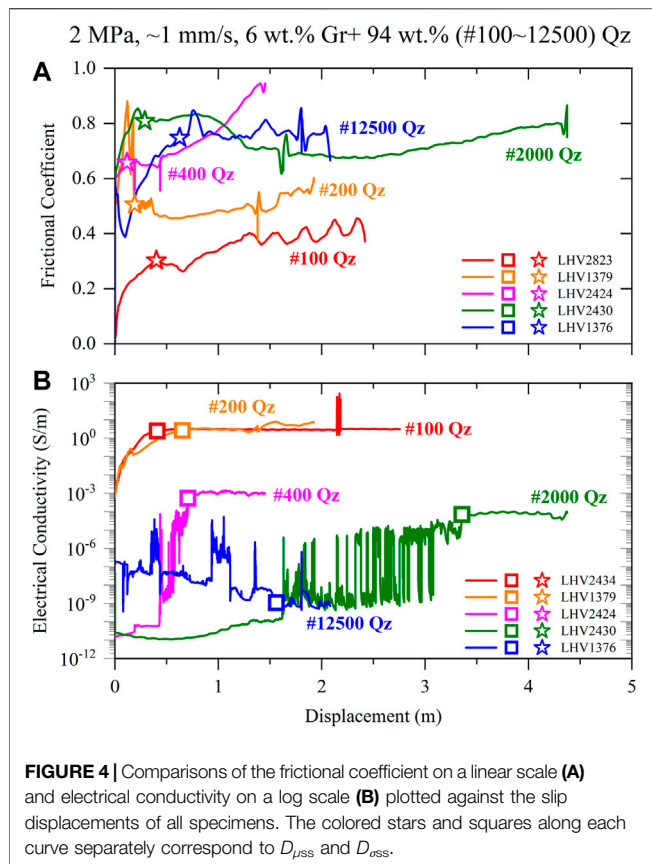


FIGURE 4 | Comparisons of the frictional coefficient on a linear scale (A) and electrical conductivity on a log scale (B) plotted against the slip displacements of all specimens. The colored stars and squares along each curve separately correspond to $D_{\mu ss}$ and $D_{\sigma ss}$.

ultrafine Qz-bearing gouge (LHV 1376, #12500 mesh) declined to 10^{-9} S/m. Moreover, the electrical conductivity of specimens with relatively small quartz particle sizes, including #400, #2000, and #12500 meshes, exhibited a period of oscillation before achieving a conductive steady state. Due to some Qz particles leaking into the gap between the ring-shaped Teflon and the rotary corundum cylinder, anomalously high μ values were observed during the whole LHV2434 experiment (#100 Qz, not present in this study) and part of the LHV2424 experiment (#400 Qz, after the slide-hold-slide test, **Figure 3C**). To solve these problems, a single frictional experiment for the #100 Qz-bearing gouge (LHV2823) was conducted in an LHVR equipped with a high-pressure vessel under identical conditions, and its μ replaced the mechanical data of LHV2434 (**Figure 3A**), while the μ_{ss} of LHV2424 was calculated using the mechanical data prior to the hold period (see the length of the dashed violet line in **Figure 3C**).

The comparisons of frictional behaviors on linear scales and conductive behaviors on log scales against slip displacement for all specimens are shown in **Figure 4**. In summary, with the reduction in Qz grain sizes, the μ_{ss} of Gr-bearing gouges increased from 0.37 to 0.77, which indicates that the slip behaviors changed from slip-weakening to slip-strengthening. σ_{ss} logarithmically decreased from 3 to 10^{-9} S/m, which suggested that the specimens were gradually insulated. Meanwhile, its electrical conductivity needs to experience more frictional displacements to remain stabilized.

Microstructure

According to these BSE images, the initial #100 mesh Qz-bearing gouge under frictional steady-state conditions consists of three different strain level layers (LHV2434, bounded by yellow dotted lines in **Figure 5A**) as follows: (a) ~ 20 μm thick intensive-foliated layer on the side of gouge-cylinder boundaries (100-I). This layer is composed of submicron-sized Qz particles surrounded by anastomosing networks of nanoscale particle-boundary Gr films (**Figure 5D**). (b) A ~ 200 μm thick weakly foliated layer in the middle of the gouge zone contains Qz particles of several microns in size, coexisting with relatively weakly attrited Qz particles (100-II). (c) The non-foliated layer in the bottom involves relatively undeformed angular Qz particles and is enriched in Gr flakes, which are present in the pores of the Qz skeletal frames (100-III). From the particle size analysis results, the distribution range of synthetic original Qz particles is relatively narrow (**Figure 1**), and the ϕ_{ave} of #100 Qz particles is of the order of hundreds of microns (199 μm , **Table 1**). Therefore, the fabric of layer 100-III is comparable to the original nonslipped gouge, and submicron- and micron-sized Qz particles were produced by the intense comminution of the original synthetic particles.

As the initial Qz particle sizes decrease to #400 mesh (LHV2424), the synthetic gouge produces only an intensive-foliated layer (400-I) on the slip surface (**Figure 5B**). Similar to layer 100-I (**Figure 5D**), the layer 400-I also comprises comminuted fine Qz particles and interconnected Gr-film networks (**Figure 5E**). Then, the rest of the gouge exhibits isolated angular Qz particles mixed with isolated Gr flakes (400-II), which is comparable to the original undeformed microstructure. In contrast, the Gr-bearing gouge that is composed of the finest Qz particles (#12,500 mesh, LHV1376) does not show apparent microstructural delamination. The Gr flakes are segregated by ultrafine Qz particles (**Figure 5C**). Gr flakes cannot form interconnected Gr-film networks, even on the slip layer of gouge-cylinder boundaries (**Figure 5F**).

DISCUSSION

The relationships between ϕ_{ave} and μ_{ss} , σ_0 and σ_{ss} of the 6 wt% Gr-bearing gouges are summarized in **Figure 6A**. Thus, according to the trends of μ_{ss} , σ_0 , and σ_{ss} against the ϕ_{ave} of all specimens, the whole ϕ_{ave} for the initial Qz particles in this study can be divided into three regimes bounded by 100 and 3 μm (black dotted lines in **Figure 6A**) as follows: (a) in the large particle size regime ($\phi_{ave} > 100$ μm), the gouge with low μ_{ss} exhibits slip weakening behavior, and σ_0 is already high (10^{-3} S/m) at the pre-slip stage. Then, σ slightly increases by ~ 3 orders of magnitude after fault slip (the thin red arrow in **Figure 6A**). (b) In the medium particle size regime (3 $\mu\text{m} < \phi_{ave} < 100$ μm), the gouge with high μ_{ss} values (> 0.65) exhibits slip strengthening behavior, and σ sharply increases by 6.5–8 orders of magnitude during progressive fault slip (the bold red arrow in **Figure 6A**). (c) In the small particle size regime ($\phi_{ave} < 3$ μm), the gouge with high μ_{ss} (0.77) also exhibits slip strengthening behavior, and σ_{ss} is ~ 2 orders of magnitude lower than σ_0 (the orange arrow in

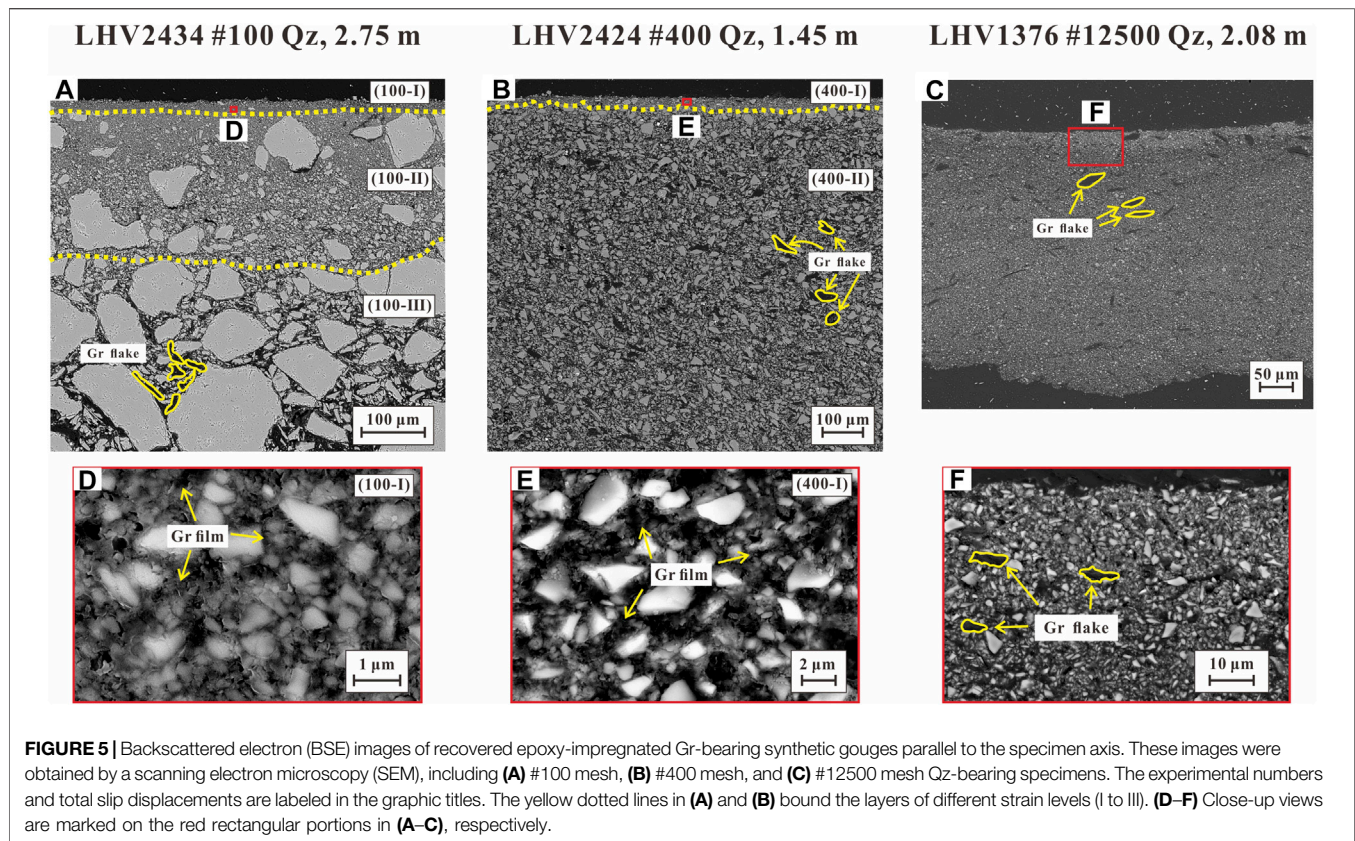


FIGURE 5 | Backscattered electron (BSE) images of recovered epoxy-impregnated Gr-bearing synthetic gouges parallel to the specimen axis. These images were obtained by a scanning electron microscopy (SEM), including (A) #100 mesh, (B) #400 mesh, and (C) #12500 mesh Qz-bearing specimens. The experimental numbers and total slip displacements are labeled in the graphic titles. The yellow dotted lines in (A) and (B) bound the layers of different strain levels (I to III). (D–F) Close-up views are marked on the red rectangular portions in (A–C), respectively.

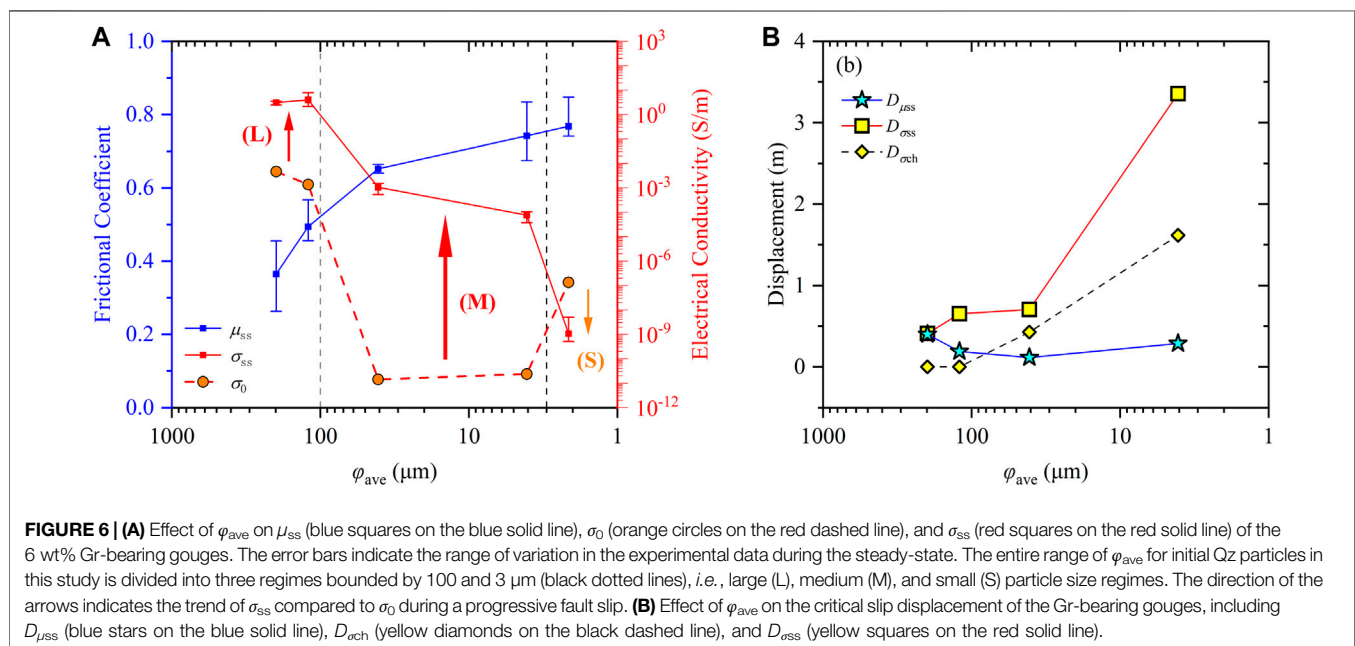
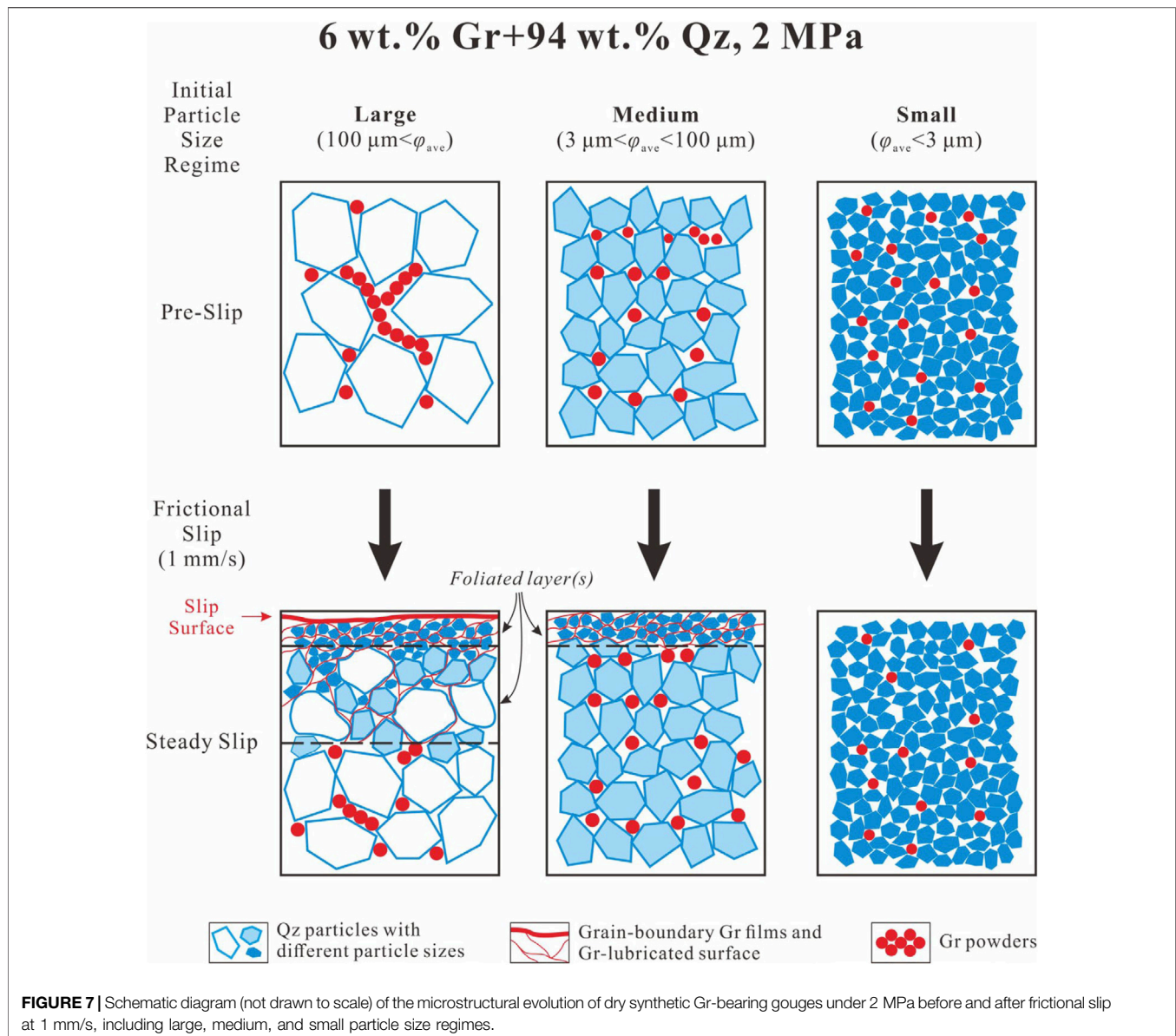


FIGURE 6 | (A) Effect of ϕ_{ave} on μ_{ss} (blue squares on the blue solid line), σ_0 (orange circles on the red dashed line), and σ_{ss} (red squares on the red solid line) of the 6 wt% Gr-bearing gouges. The error bars indicate the range of variation in the experimental data during the steady-state. The entire range of ϕ_{ave} for initial Qz particles in this study is divided into three regimes bounded by 100 and 3 μm (black dotted lines), i.e., large (L), medium (M), and small (S) particle size regimes. The direction of the arrows indicates the trend of σ_{ss} compared to σ_0 during a progressive fault slip. (B) Effect of ϕ_{ave} on the critical slip displacement of the Gr-bearing gouges, including $D_{\mu ss}$ (blue stars on the blue solid line), $D_{\sigma ch}$ (yellow diamonds on the black dashed line), and $D_{\sigma ss}$ (yellow squares on the red solid line).

Figure 6A). Due to the large difference in electrically conductive properties between Qz particles and Gr powders, the logarithmic enhancement of σ_{ss} in a medium or large grain size regime implies that the insulated Qz particle boundary was surrounded by the

interconnected conductive Gr films. In contrast, the logarithmic decrease in a small grain size regime indicates that an interconnected conductive network cannot form in the gouge (Chen et al., 2017). Then, the period of oscillation indicates



constantly adjusting conductive paths within carbon-bearing microstructures during a fault slip before a conductive steady state.

Furthermore, combined with the BSE images of the experimental specimens (**Figures 5A–D**), the characteristics of Gr-bearing microstructures in these three regimes before and after frictional slip can be summarized (**Figure 7**): (a) for the large particle size regime, the Gr flakes concentrating on the pores of Qz particles have already formed interconnected conductive networks at the pre-slip stage. Then, after a frictional slip, the foliated layer(s) composed of comminuted Qz particles are produced near the ends of the slip layers. Anastomosing Gr-film networks are formed by enriching Gr powders in the foliated layer(s), resulting in the enhancement of σ in the Gr-bearing gouge. Moreover, Gr powders are further enriched on the slip surface and form Gr-lubricated layers, leading to slip weakening

behavior of the Gr-bearing gouge. (b) For the medium particle size regime, isolated Gr flakes are present in the pores of the Qz framework at the pre-slip stage and cannot interconnect with each other to form a conductive pathway. After fault slip, a $\sim 20 \mu\text{m}$ thick intensive-foliated layer is produced and develops anastomosing interconnected Gr-film networks, which causes the logarithmic enhancement of σ . However, the high μ_{ss} values (>0.65) and slip-strengthening behavior indicate that Gr powders cannot enrich this regime to form a Gr-lubricated layer. (c) For the small particle size regime, isolated Gr flakes are gradually submerged in ultrafine Qz particles during progressive fault slip, especially in the layer close to the slip surface, resulting in high μ_{ss} values (0.77) and progressive σ values.

Thus, the microstructural evolution model of Gr-bearing gouges with different initial Qz particle sizes can be proposed.

For dry 6 wt% Gr-bearing gouges under 2 MPa and at room temperature, hard and angular Qz particles constitute the skeletal frames of Gr-bearing fault gouges. As the initial Qz particle sizes gradually decrease, the Qz particle boundary area per unit volume (*i.e.*, specific surface area) occupied by the particle-boundary Gr film increases resulting in the progressive segregation of Gr flakes. Then, the Gr fragments gradually submerge among the quartz particles, resulting in decreased interconnectivity and reduced electrical conductivity of the anastomosing Gr-film networks in Gr-bearing gouges. Moreover, the lubricated slip surface formed by the interconnected Gr powders is gradually destroyed, and the friction transitions from slipping mainly at the contacts between Gr powders to slipping at the contacts between Qz particles, resulting in enhanced frictional strength. Finally, the frictional behavior of the Gr-bearing gouges change from slip weakening to slip strengthening. It should be noted that the change in particle sizes and the division of φ_{ave} correspond to the initial synthetic Qz particles of graphite-bearing specimens before frictional experiments, *i.e.*, the proposed model of this study indicates that the microstructural developments of original undeformed Gr-bearing gouges with different particle sizes undergo a progressive frictional slip. Although a few Qz particles from an ~2 mm gouge in a large or middle particle size regime can be comminuted to several microns or even submicron particle sizes and constitute 20–200 μm foliated layer(s) (Figures 5D,E), these fine particles account for only a small fraction of an experimental specimen. Moreover, Gr powders exhibit optical absorption properties and their accurate powder size distribution cannot be obtained by laser analyzers. Gr powders are also much weaker than Qz particles, and the shape of their powders varies with the geometry of the Qz pores. It is speculated that the Gr powder size does not affect the frictional properties of synthetic graphite-bearing specimens. Therefore, this study does not constrain the sizes of the comminuted Qz particles and Gr powders.

In addition, the comparisons of the slip displacement to achieve the critical moments, *i.e.*, $D_{\mu ss}$, $D_{\sigma ch}$, and $D_{\sigma ss}$, for the Gr–Qz mixtures with Qz particle sizes of 4–199 μm are shown in Figure 6B. Based on the unified slip rates (~1 mm/s) for all experiments, $D_{\mu ss}$, $D_{\sigma ch}$, and $D_{\sigma ss}$ represent the required times for stable slip surface(s) to develop, Gr-film networks to be generated, and fully interconnected Gr-film networks to develop, respectively. The foliated layer(s) and Gr-film networks are not simultaneously formed. $D_{\mu ss}$ varies within 0.1–0.6 m, while $D_{\sigma ch}$ (from 3.4 to 0.4 m) and $D_{\sigma ss}$ (from 1.6 to ~0 m) abruptly decrease with increasing φ_{ave} . Based on these results, with a progressive fault slip, it is speculated that homogeneous Gr-bearing gouges develop foliated layer(s) at first, and then anastomosing Gr films progressively penetrate around the boundary of the Qz particles to form the interconnected networks; the speed of its formation depends on the value of φ_{ave} . In other words, the increase in φ_{ave} can distinctly accelerate the formation of Gr films but the increase has no discernible influence on the form of foliated layer(s). In addition, considering that the Gr powders in ultrafine Qz particles (#12500 mesh) cannot develop foliated layers and interconnected conductive networks, the parameters of experiment LHV1376 are not involved in Figure 6B.

The PSD is commonly used to quantify fault-related deformation intensity in fault core rocks (Cortinovis et al., 2019). During the cataclastic process in a brittle regime, the development of the PSD along the granitoid or carbonate fault zone in mature faults is a two-stage process, *i.e.*, initial fragmentation by rupturing causes cracked grains, and subsequent grain comminution, grinding, attrition, or shear during slip develops gouges (Blenkinsop, 1991; Storti et al., 2003; Keulen et al., 2007). The grinding limit in Qz is $1.2 \pm 0.3 \mu\text{m}$ (Keulen et al., 2007), which coincides with our small grain size regime. Several viewpoints suggested that fine gouges control earthquake instability (Billi and Storti, 2004; Wilson et al., 2005; Scholz, 2019). However, the traditional studies on the PSDs of fault zones ignore the effects of weak minerals, especially CM (including Gr, amorphous carbon, and organic carbon), as represented by Gr, on the strength of fine gouges. For Gr-bearing gouges, our experimental results implied that reducing the particle size of rock-forming minerals destroys the lubricated Gr surface and leads to the slip-strengthening behavior of the fault zone. Thus, the CM of fault gouges may make the mechanical properties of the principal slip zone in mature faults more complicated, and we should pay more attention to this phenomenon in the future.

CONCLUSION

This study monitored the transient electrical response of dry synthetic 6 wt% Gr-bearing gouges along the fault-parallel direction during a progressive frictional slip of 1 mm/s and 2 MPa. As Qz particle sizes decrease from 199 to 2 μm , the steady-state frictional coefficient (μ_{ss}) of Gr-bearing gouges increases from 0.37 to 0.77, while their steady-state electrical conductivity (σ_{ss}) values logarithmically decrease from 3 to 10^{-9} S/m. According to the frictional and conductive properties of the specimens, the whole particle size distribution (PSD) in the initial Qz particles of Gr-bearing gouges can be divided into three regimes bounded by 100 and 3 μm , *i.e.*, large, medium, and small particle size regimes. Then, it can be concluded that with the decrease in the diameters of the Qz particles (φ_{ave}), weak and conductive Gr flakes are gradually segregated into the skeletal frame of granular Qz particles near the gouge-cylinder boundaries, resulting in a decrease in the interconnectivity and electrical conductivity of the anastomosing Gr-film networks and the destruction of the Gr-lubricated slip surface(s). Thus, the frictional behaviors of Gr-bearing gouges change from slip strengthening to slip weakening. Furthermore, with a progressive fault slip, Gr-bearing gouges first develop foliated layers and subsequently anastomosing Gr films progressively penetrate around the boundary of the comminuted Qz particles to form interconnected networks. Our experimental results indicate that the conductivity data can successfully capture the microstructural evolution of Gr-bearing gouges during frictional slip. As they are inconsistent with earthquake instability controlled by fine gouges, the carbonaceous materials (CM) represented by Gr within fault gouges may make the mechanical properties of the principal slip zone in mature faults more complicated.

DATA AVAILABILITY STATEMENT

The original contributions presented in the study are included in the article further inquiries can be directed to the corresponding author.

AUTHOR CONTRIBUTIONS

JC made a full contribution, including designing the experimental setup, carrying out the experiments and textural observations, and writing the final manuscript.

FUNDING

This work was supported by the National Natural Science Foundation of China with Grant No. 41904087, the

REFERENCES

- Billi, A., and Storti, F. (2004). Fractal Distribution of Particle Size in Carbonate Cataclastic Rocks from the Core of a Regional Strike-Slip Fault Zone. *Tectonophysics* 384, 115–128. doi:10.1016/j.tecto.2004.03.015
- Blenkinsop, T. G. (1991). Cataclasis and Processes of Particle Size Reduction. *Pure Geophys.* 136, 59–86. doi:10.1007/bf00878888
- Cao, S., and Neubauer, F. (2019). Graphitic Material in Fault Zones: Implications for Fault Strength and Carbon Cycle. *Earth-Science Rev.* 194, 109–124. doi:10.1016/j.earscirev.2019.05.008
- Chen, J.-Y., Yang, X.-S., and Chen, J.-Y. (2017). Experimental Studies on the Relationship Between Carbonaceous Structure and Electrical Conductivity of the Longmenshan Fault Zone. *Chin. J. Geophys. (in Chinese)* 60, 3475–3492. doi:10.6038/cjg20170917
- Chen, J., Yang, X., Ma, S., Yang, T., and Niemeijer, A. (2016). Hydraulic Properties of Samples Retrieved from the Wenchuan Earthquake Fault Scientific Drilling Project Hole-1 (WFSD-1) and the Surface Rupture Zone: Implications for Coseismic Slip Weakening and Fault Healing. *Geochem. Geophys. Geosyst.* 17, 2717–2744. doi:10.1002/2016gc006376
- Cortinovis, S., Balsamo, F., and Storti, F. (2019). Influence of Analytical Operating Procedures on Particle Size Distributions in Carbonate Cataclastic Rocks. *J. Struct. Geol.* 128, 103884. doi:10.1016/j.jsg.2019.103884
- Duba, A. G., and Shankland, T. J. (1982). Free Carbon and Electrical Conductivity in the Earth's Mantle. *Geophys. Res. Lett.* 9, 1271–1274. doi:10.1029/g1009i011p01271
- Frost, B. R., Fyfe, W. S., Tazaki, K., and Chan, T. (1989). Grain-boundary Graphite in Rocks and Implications for High Electrical Conductivity in the Lower Crust. *Nature* 340, 134–136. doi:10.1038/340134a0
- Gueguen, Y., and Dienes, J. (1989). Transport Properties of Rocks from Statistics and Percolation. *Math Geol* 21, 1–13. doi:10.1007/bf00897237
- Han, M., Yang, X., Yao, L., Chen, J., and Ma, S. (2019). A Research on the Conductivity Characteristics of Carbon-Rich Fault Zones Based on the Middle-To High-Velocity Frictional Experiments. *Chin. J. Geophys. (in Chinese)* 62, 967–981. doi:10.6038/cjg2019M0143
- Hirose, T., and Shimamoto, T. (2005). Growth of Molten Zone as a Mechanism of Slip Weakening of Simulated Faults in Gabbro during Frictional Melting. *J. Geophys. Res.* 110, B05202. doi:10.1029/2004jb003207
- Hou, L., Ma, S., Shimamoto, T., Chen, J., Yao, L., Yang, X., et al. (2012). Internal Structures and High-Velocity Frictional Properties of a Bedding-Parallel Carbonate Fault at Xiaojiaqiao Outcrop Activated by the 2008 Wenchuan Earthquake. *Earthq Sci* 25, 197–217. doi:10.1007/s11589-012-0846-2
- Ikari, M. J., Marone, C., and Saffer, D. M. (2011). On the Relation between Fault Strength and Frictional Stability. *Geology* 39, 83–86. doi:10.1130/g31416.1
- Independent Research Project of the State Key Laboratory of Earthquake Dynamics with Grant No. LED2021A09, and the Basic Scientific Funding of the Chinese National Nonprofit Institutes of the Institute of Geology, China Earthquake Administration, with Grant No. IGCEA1821.
- Kaneki, S., and Hirono, T. (2019). Diagenetic and Shear-Induced Transitions of Frictional Strength of Carbon-Bearing Faults and Their Implications for Earthquake Rupture Dynamics in Subduction Zones. *Sci Rep* 9, 7884. doi:10.1038/s41598-019-44307-y
- Keithley (2013). *Low Level Measurements Handbook. Precision DC Current, Voltage, and Resistance Measurements.* 7th ed. Cleveland, OH, USA: Keithley Instruments Inc.
- Keulen, N., Heilbronner, R., Stünitz, H., Boullier, A.-M., and Ito, H. (2007). Grain Size Distributions of Fault Rocks: A Comparison between Experimentally and Naturally Deformed Granitoids. *J. Struct. Geol.* 29, 1282–1300. doi:10.1016/j.jsg.2007.04.003
- Kouketsu, Y., Shimizu, I., Wang, Y., Yao, L., Ma, S., and Shimamoto, T. (2017). Raman Spectra of Carbonaceous Materials in a Fault Zone in the Longmenshan Thrust Belt, China; Comparisons with Those of Sedimentary and Metamorphic Rocks. *Tectonophysics* 699, 129–145. doi:10.1016/j.tecto.2017.01.015
- Ma, S., Shimamoto, T., Yao, L., Togo, T., and Kitajima, H. (2014). A Rotary-Shear Low to High-Velocity Friction Apparatus in Beijing to Study Rock Friction at Plate to Seismic Slip Rates. *Earthq Sci* 27, 469–497. doi:10.1007/s11589-014-0097-5
- Manatschal, G. (1999). Fluid- and Reaction-Assisted Low-Angle Normal Faulting: Evidence from Rift-Related Brittle Fault Rocks in the Alps (Err Nappe, Eastern Switzerland). *J. Struct. Geol.* 21, 777–793. doi:10.1016/s0191-8141(99)00069-3
- Mareschal, M., Fyfe, W. S., Percival, J., and Chan, T. (1992). Grain-boundary Graphite in Kapuskasing Gneisses and Implications for Lower-Crustal Conductivity. *Nature* 357, 674–676. doi:10.1038/357674a0
- Marone, C., and Scholz, C. H. (1989). Particle-size Distribution and Microstructures within Simulated Fault Gouge. *Journal of Structural Geology* 11, 799–814. doi:10.1016/0191-8141(89)90099-0
- Marone, C. (1998). The Effect of Loading Rate on Static Friction and the Rate of Fault Healing During the Earthquake Cycle. *Nature* 391, 69–72. doi:10.1038/34157
- Oohashi, K., Hirose, T., Kobayashi, K., and Shimamoto, T. (2012). The Occurrence of Graphite-Bearing Fault Rocks in the Atotsugawa Fault System, Japan: Origins and Implications for Fault Creep. *J. Struct. Geol.* 38, 39–50. doi:10.1016/j.jsg.2011.10.011
- Oohashi, K., Hirose, T., and Shimamoto, T. (2013). Graphite as a Lubricating Agent in Fault Zones: An Insight from Low- to High-Velocity Friction Experiments on a Mixed Graphite-Quartz Gouge. *J. Geophys. Res. Solid Earth* 118, 2067–2084. doi:10.1002/jgrb.50175
- Oohashi, K., Hirose, T., and Shimamoto, T. (2011). Shear-induced Graphitization of Carbonaceous Materials during Seismic Fault Motion: Experiments and Possible Implications for Fault Mechanics. *J. Struct. Geol.* 33, 1122–1134. doi:10.1016/j.jsg.2011.01.007
- Scholz, C. H. (2019). *The Mechanics of Earthquakes and Faulting.* Cambridge, United Kingdom: Cambridge University Press.

- Sibson, R. H. (2003). Thickness of the Seismic Slip Zone. *Bulletin. Seismol. Soc. Am.* 93, 1169–1178. doi:10.1785/0120020061
- Smith, S. A. F., Nielsen, S., and Di Toro, G. (2015). Strain Localization and the Onset of Dynamic Weakening in Calcite Fault Gouge. *Earth and Planetary Science Letters* 413, 25–36. doi:10.1016/j.epsl.2014.12.043
- Storti, F., Billi, A., and Salvini, F. (2003). Particle Size Distributions in Natural Carbonate Fault Rocks: Insights for Non-self-similar Cataclasis. *Earth and Planetary Science Letters* 206, 173–186. doi:10.1016/s0012-821x(02)01077-4
- Togo, T., Shimamoto, T., Ma, S., and Hirose, T. (2011). High-velocity Frictional Behavior of Longmenshan Fault Gouge from Hongkou Outcrop and its Implications for Dynamic Weakening of Fault during the 2008 Wenchuan Earthquake. *Earthq Sci* 24, 267–281. doi:10.1007/s11589-011-0790-6
- Wang, D., Karato, S.-i., and Jiang, Z. (2013). An Experimental Study of the Influence of Graphite on the Electrical Conductivity of Olivine Aggregates. *Geophys. Res. Lett.* 40, 2028–2032. doi:10.1002/grl.50471
- Wang, Y., Ma, S., Shimamoto, T., Yao, L., Chen, J., Yang, X., et al. (2014). Internal Structures and High-Velocity Frictional Properties of Longmenshan Fault Zone at Shexigou Activated during the 2008 Wenchuan Earthquake. *Earthq Sci* 27, 499–528. doi:10.1007/s11589-014-0096-6
- Wibberley, C. A. J., and Shimamoto, T. (2005). Earthquake Slip Weakening and Asperities Explained by Thermal Pressurization. *Nature* 436, 689–692. doi:10.1038/nature03901
- Wilson, B., Dewers, T., Reches, Z. e., and Brune, J. (2005). Particle Size and Energetics of Gouge from Earthquake Rupture Zones. *Nature* 434, 749–752. doi:10.1038/nature03433
- Yamashita, F., Fukuyama, E., and Mizoguchi, K. (2014). Probing the Slip-Weakening Mechanism of Earthquakes with Electrical Conductivity: Rapid Transition from Asperity Contact to Gouge Communion. *Geophys. Res. Lett.* 41, 341–347. doi:10.1002/2013gl058671
- Yao, L., Ma, S., Shimamoto, T., and Togo, T. (2013a). Structures and High-Velocity Frictional Properties of the Pingxi Fault Zone in the Longmenshan Fault System, Sichuan, China, Activated during the 2008 Wenchuan Earthquake. *Tectonophysics* 599, 135–156. doi:10.1016/j.tecto.2013.04.011
- Yao, L., Shimamoto, T., Ma, S., Han, R., and Mizoguchi, K. (2013b). Rapid Post-seismic Strength Recovery of Pingxi Fault Gouge from the Longmenshan Fault System: Experiments and Implications for the Mechanisms of High-Velocity Weakening of Faults. *J. Geophys. Res.-Sol. Ea.* 118, 1–17. doi:10.1002/jgrb.50308
- Zulauf, G., Palm, S., Petschick, R., and Spies, O. (1999). Element Mobility and Volumetric Strain in Brittle and Brittle-Viscous Shear Zones of the Superdeep Well KTB (Germany). *Chemical Geology* 156, 135–149. doi:10.1016/s0009-2541(98)00189-2

Conflict of Interest: The author declares that the research was conducted in the absence of any commercial or financial relationships that could be construed as a potential conflict of interest.

Publisher's Note: All claims expressed in this article are solely those of the authors and do not necessarily represent those of their affiliated organizations, or those of the publisher, the editors, and the reviewers. Any product that may be evaluated in this article, or claim that may be made by its manufacturer, is not guaranteed or endorsed by the publisher.

Copyright © 2022 Chen. This is an open-access article distributed under the terms of the Creative Commons Attribution License (CC BY). The use, distribution or reproduction in other forums is permitted, provided the original author(s) and the copyright owner(s) are credited and that the original publication in this journal is cited, in accordance with accepted academic practice. No use, distribution or reproduction is permitted which does not comply with these terms.

NOMENCLATURE

PSD: Particle size distribution

CM: Carbonaceous material

φ_{ave} : Median diameter of the quartz particle

μ : Frictional coefficient

μ_{ss} : Steady-state frictional coefficient

$D_{\mu\text{ss}}$: Slip displacement as μ achieves μ_{ss}

σ : Electrical conductivity

σ_0 : Initial electrical conductivity

σ_{ss} : Steady-state electrical conductivity

$D_{\sigma\text{ch}}$: Slip displacement as σ starts to logarithmically change

$D_{\sigma\text{ss}}$: Slip displacement as σ achieves σ_{ss}



Processing Method of Soil Temperature Time Series and Its Application in Geothermal Heat Flow

Liming Yang¹, Rongcai Song^{2,3*}, Ben Dong^{2,3}, Likun Yin¹, Yifan Fan¹, Bo Zhang¹, Ziwei Wang¹, Yingchun Wang^{2,3} and Shuyi Dong⁴

¹China Three Gorges Corporation, Beijing, China, ²College of Energy Resources, Chengdu University of Technology, Chengdu, China, ³State Key Laboratory of Oil and Gas Reservoir Geology and Exploitation, Chengdu University of Technology, Chengdu, China, ⁴Chengdu University of Technology, Chengdu, China

OPEN ACCESS

Edited by:

Lidong Dai,
Institute of Geochemistry (CAS), China

Reviewed by:

Chang Su,
Institute of Disaster Prevention, China
Dongsheng Ren,
China Earthquake Administration,
China

*Correspondence:

Rongcai Song
417102145@qq.com

Specialty section:

This article was submitted to
Solid Earth Geophysics,
a section of the journal
Frontiers in Earth Science

Received: 11 April 2022

Accepted: 29 April 2022

Published: 17 June 2022

Citation:

Yang L, Song R, Dong B, Yin L, Fan Y,
Zhang B, Wang Z, Wang Y and Dong S
(2022) Processing Method of Soil
Temperature Time Series and Its
Application in Geothermal Heat Flow.
Front. Earth Sci. 10:910328.
doi: 10.3389/feart.2022.910328

Nowadays, geothermal resources have become one of the important means for mankind to solve global energy problems and environmental problems, and the exploration and development of geothermal resources are of great significance for sustainable development. However, in view of the complex geological background of the plateau region, the number of heat flow measurement points in this area is small or even blank, thus becoming an important factor limiting the exploration of geothermal resources in this region. In this article, a new model based on Fourier analysis and heat conduction principle is established to process and analyze the long-term monitoring data of soil temperature and eliminate the influence of temperature change on soil temperature as far as possible, so as to improve the calculation accuracy of soil conduction heat dissipation. The experimental results show that the fluctuation range of soil temperature at 20 cm before the correction was large, and the fluctuation range was 2.58°C–14.284°C, which was because the soil here was closer to the land surface and was affected too much by the temperature fluctuation, and as the soil depth deepened, the temperature fluctuation slowly became smaller, and the fluctuation range was 6.67°C–11.15°C at 50 cm, but the effect of temperature fluctuation was still obvious. Also, the fluctuation range was basically reduced within 0.3°C after temperature correction. In this method, the thermal diffusion coefficients of the soil at different depths can be obtained, and the calculated temperatures at the corresponding depths can also be obtained, which can be used to infer the approximate ground temperature gradient of the measured area. This study aims to develop a convenient and fast model for processing soil temperature time series and to provide technical support for developing geothermal resources in highland areas or assessing the geothermal potential of the region.

Keywords: Ganzi county, geothermal resources, Fourier analysis, temperature time series, soil thermal diffusion coefficient

INTRODUCTION

Geothermal energy, a zero-carbon and clean energy source, has an important value for carbon neutrality in its development and utilization. As one of the important resources of non-fossil energy, it has the characteristics of large reserves, wide distribution, and good stability and is not disturbed by external factors such as seasonal, climatic, and diurnal changes and has a broad prospect of development and utilization and shows strong development potential as one

of the rising stars of non-fossil energy (Zhu, 1997; Liang et al., 2018; Ma et al., 2021; Wang et al., 2022).

Obtaining soil temperature data combined with statistical relationships between heat dissipation (Benseman, 1959) can be used to evaluate thermal relationships in geothermal fields, and currently, methods using soil temperature time series data are also widely used in heat dissipation studies in geothermal zones (Sorey et al., 1994; Fridriksson et al., 2006; Rissmann et al., 2012; Wang et al., 2019). Soil temperature-based heat flux measurements are an economical and applicable method for assessing geothermal potential (Dawson and Author, 1970; Sorey et al., 1994), and soil temperature not only acts as an important factor in surface processes but also plays a key role in energy balance applications, including land surface modeling, numerical weather forecasting, and climate prediction (Holmes et al., 2008).

Thermal conductivity, thermal diffusion coefficient, and volumetric heat capacity are three important soil thermal properties (Domenico et al., 1998). These thermodynamic properties are the basic parameters for modeling soil temperature, considering the thermal conductivity of the soil, and considering that the soil thermal conductivity and thermal diffusion coefficient are related to the soil volumetric heat capacity, it is only necessary to determine the soil thermal conductivity or thermal diffusion coefficient. Also, the thermal diffusion coefficient is usually estimated because it describes the transient process of heat transfer (Hu et al., 2016). Temperature, heat flow, and thermal properties of the soil determine the heat flow transferred from the ground to the soil and the heat stored in the soil. The soil thermal diffusion coefficient is a state parameter by which not only the soil thermal properties can be understood, but also the soil temperature and heat flux can be simulated (Liu et al., 1991). As early as the 20th century, Horton et al. (1983) proposed that soil thermal diffusion coefficient could be determined by simulating soil heat flux from near-surface soil temperature observations under the same soil conditions. Liu et al. (1991) calculated their soil thermal diffusion coefficients by different methods under four different soil conditions and the simulated soil temperature and surface heat flux values at different soil depths. The daily contours of the simulated soil temperature and surface heat flux values at different soil depths were compared with the measured values to find a highly accurate method for calculating the soil heat diffusion coefficient. However, the biggest problem with the application of the soil temperature method in geothermal exploration is the effect of temperature variation on the ground temperature gradient and soil properties, which limits the development of this method (LeSchack et al., 1983). Hurwitz et al. (2012) used a 6-week monitoring of soil temperature at different depths to correct the ground temperature gradient. Coolbaugh et al. (2014) fitted temperature–time curves to correct geothermal gradients by measuring temperatures at different depths for multiple times; Wang et al. (2019) and Wang and Pang (2022) gave the method a great advance by eliminating the effect of seasonal changes on geothermal gradients through long-term temperature monitoring (more than 1 year).

When sufficient temperature time series data are obtained, one is faced with the choice of methods to process these data for

solving scientific problems. Ramos et al. (2012) calculated the thickness of the active soil layer and the thermal diffusivity of the unfrozen active soil layer by a sine wave heat transfer conduction model using data monitored by Ground Temperature Sensor (GTS). Zou et al. (2008) used a BP (back propagation) neural network model to analyze and predict the time series data of surface soil temperature at long-term location monitoring sites with good results. Wang et al. (2021) used LSTM (long short-term memory) neural network with a 2-60-80-1 network structure for time-averaged soil temperature time series prediction and found the advantage of the LSTM neural network model for soil temperature time series prediction, which reduced the mean square error by 0.053 compared with BP neural network model, which can meet the needs of daily soil temperature forecasting. However, the high accuracy prediction of LSTM neural networks is accompanied by a complex model structure and a time-consuming computational process. Also, using Fourier analysis to deal with temperature time series data is probably the earliest method of time series analysis (18th century), for time domain and frequency domain, which is very suitable for time series data with periodic characteristics. Hu et al. (2016) proposed a new Fourier level-based analysis of the conduction convection equation, using single sinusoidal conduction and conduction convection model, and Fourier level conduction convection model to calculate the soil temperature; and soil thermal properties were calculated using single sinusoidal conduction, conduction convection models, and Fourier series conduction convection models. In fact, the daily variation of soil surface temperature does not follow a single sinusoidal curve in the strict sense. The use of the Fourier series to accurately describe the daily variation of surface soil temperature can reduce the error caused by the assumption that the soil surface temperature follows a single sinusoidal wave (Wang et al., 2010). In this study, we developed a model combining Fourier series analysis and heat conduction principle, which can realize the fast processing of soil temperature time series, so as to obtain soil thermal diffusion coefficient with high accuracy to correct the effect of temperature change on soil temperature.

STUDY AREA

Geographical Location

Ganzi County belongs to Ganzi Tibetan Autonomous Prefecture of Sichuan Province, located in the northwestern part of Ganzi Tibetan Autonomous Prefecture, upstream of the Yalong River, a tributary of the Yangtze River, bordering Furho County in the east, adjacent to Dege County in the west, bordering Xinlong County and Baiyu County in the south, and relying on Shiqu County, Seda County, and Qinghai Province in the north, located at 99°08' -100°25' E longitude and 31°24' -32°54' N latitude -100°25' East and 31°24' -32°54' North. The highest mountain in the county is 5,688 m above the sea level, the lowest elevation is 3,325 m, and the county town is 3,410 m above the sea level. Ganzi County has an alpine cold-temperate climate, with long winters and short summers; the area around the county has a plateau valley climate, cold and dry, clear and sunny, with open

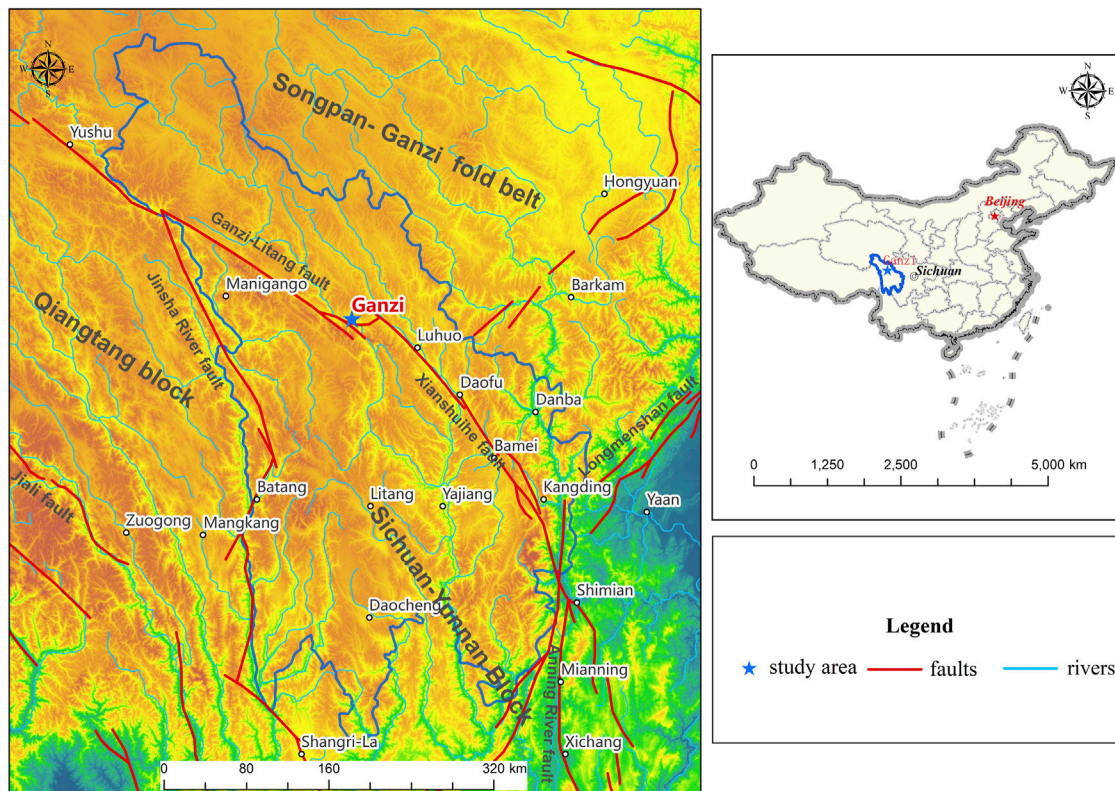


FIGURE 1 | Geographical location of the study area.

terrain, more sunshine, strong radiation, an annual average temperature of 5.6°C, maximum temperature of 31.7°C, minimum temperature of extreme -28.9°C, annual average precipitation of 636.5 mm, and oxygen content equivalent to 67% of the plain. **Figure 1** shows the geographical location of Ganzi County in the study area.

Geological Background

Ganzi Tibetan Autonomous Prefecture is located in the extrusion and intersection zone of three tectonic units with different geotectonic characteristics, namely, the Eurasian plate, the Indian plate, and the Yangzi plate. The eastern Kangding-Luding area is located at the westernmost edge of the Yangtse plate and belongs to the northern section of the north-south tectonic zone of Kang-Dian. The western region is the easternmost edge of the Qinghai-Tibet plate that has the three major plates, especially the north and south of the two plates of multiple subductions—collision extrusion zone. Since the Paleozoic period, this region is still the most active area of neotectonic movements on the Qinghai-Tibet Plateau. There has been strong tectonic movement since the Paleozoic period, and because of the control of the boundary and subduction force of the three plates, the area is rapidly uplifted to become the highest terrain in the eastern part of the Tibetan Plateau; at the same time, because of the control of the direction of the plate suture zone and tectonic lines along the north-south direction,

the mountains and water systems in the area are spread in a north-south direction, along the huge suture zone and tectonic lines which formed the famous Jinsha River, Yalong River, Xianshui River, Dadu River rift zone and its corresponding water system as well as the high mountain valley landscape. Influenced by the convergence-collision-mountain building of the Indian and Eurasian plates, many lithospheric scale strike-slip and retrograde fracture zones and volcanic island arcs have formed a plateau area with an average elevation of over 4000 m. Three deep and large fracture zones are developed in the region, namely, the Xianshui River Fracture Zone, the Ganzi-Litang Fracture Zone, and the Jinsha River Fracture Zone.

EXPERIMENTAL METHODS

Fourier Transform

In different research fields, the Fourier transform has many different variant forms, such as the continuous Fourier transform and the discrete Fourier transform. It is based on the following principle: $f(t)$ is a periodic function of t . If t satisfies the Dirichlet condition, in a period of $2T$ for $f(x)$ continuous or only finite intermittent points of the first type, attached $f(x)$ monotonic or divisible into finite monotonic intervals, then $F(x)$ converges with a Fourier series of $2T$ for the period, and the function $S(x)$ is also a periodic function of $2T$ for the period, and

at these intermittent points, the function is finite-valued, has a finite number of extremal points in a period, and is absolutely productable, then **Equation 1** holds (Liang et al., 2020). **Eq. 1** is called the Fourier transform of the integral operation $f(t)$, and the integral operation of **Equation 2** is called the Fourier inverse transform of $F(\omega)$.

$$F(\omega) = F[f(t)] = \int_{-\infty}^{\infty} f(t)e^{-i\omega t} dt, \quad (1)$$

where $F(\omega)$ is called the image function of $f(t)$ and $f(t)$ is called the image original function of $F(\omega)$. $f(\omega)$ is the image of $f(t)$. $f(t)$ is the original image of $F(\omega)$.

$$f(t) = F^{-1}[F(\omega)] = \frac{1}{2\pi} \int_{-\infty}^{\infty} F(\omega)e^{i\omega t} dt. \quad (2)$$

The Fourier analysis used in this model is the fast Fourier transform (FFT), a method for quickly computing the discrete Fourier transform (DFT) or its inverse transform of a sequence. It is based on the principle of transforming a signal from the original domain (usually time or space) to a representation in the frequency domain or vice versa. The FFT will quickly compute such a transform by decomposing the DFT matrix into a product of sparse (mostly zero) factors. Thus, it is able to reduce the complexity of computing the DFT from $O(N^2)$, which is needed to compute it using only the DFT definition, to $O(N \log N)$, where N is the data size. All known FFT algorithms require $O(N \log N)$ operations (technically O only marks the upper bound), although there is no known evidence that a lower complexity is not possible. Let x_0, \dots, x_{N-1} be complex and the DFT be defined by the following equation:

$$X_k = \sum_{n=0}^{N-1} x_n e^{-i2\pi k n / N} \quad K = 0, 1, \dots, N-1. \quad (3)$$

Soil Temperature Time Series Solving

Soil temperature gradients are affected by seasonal and daily variations of solar illumination. Soil temperature gradients measured during fieldwork can only represent the temperature gradient at that time, but not the temperature gradient of the whole year, which is not important for the indication of annual heat dissipation, and a correction of the temperature gradient is needed to obtain an average surface temperature gradient on an interannual scale. In order to obtain stable values of the ground temperature gradient and conduct heat dissipation, the seasonal and diurnal effects of solar insolation on the ground temperature gradient can be corrected by our long-term temperature monitoring. We assume that the seasonal and daily variations of the atmospheric temperature can be synthesized in Fourier series form:

$$T(0, t) = T_0 + \sum_{i=1}^n A_i \cos\left(\frac{2\pi t}{P_i} - \varphi_i\right), \quad (4)$$

where $T(0, t)$ is the temperature time series of the atmosphere, T_0 is the average temperature of the atmosphere, A_i is the i th order amplitude, P_i is the i th order period, and φ_i is the i th order

phase. We assume that the soil is homogeneous and that the heat transfer at depth is dominated by conduction. Through the one-dimensional heat conduction equation:

$$\frac{\partial T}{\partial t} = \kappa \frac{\partial^2 T}{\partial z^2}, \quad (5)$$

where κ is the soil thermal diffusion coefficient in m^2/s and z is the depth in m. The time series of soil temperature affected by temperature change at any depth can be deduced as:

$$T(z, t) = T_0 + \sum_{i=1}^n A_i \exp\left(-\sqrt{\frac{\pi}{\kappa P_i}} z\right) \cos\left(\sqrt{\frac{2\pi t}{P_i}} - \varphi_i - \sqrt{\frac{\pi}{\kappa P_i}} z\right). \quad (6)$$

The above equation shows that soil temperature fluctuations decrease exponentially with increasing depth and show a phase lag, while they are both a function of period. The amplitude appears to decay with increasing depth, and the phase increases with depth. By comparing the equations, we can see that the temperature at any depth can be decomposed to represent the average temperature and the relative amplitude change at that depth, which is quite important for us to make temperature corrections later.

Calculation of Geothermal Heat Flux

In contrast to direct measurements, indirect measurements of heat flow are usually used, and the two parameters mainly used for indirect measurements are the ground temperature gradient and the thermal conductivity of rocks. Based on the field monitoring results, this article uses the interannual average temperature gradient data to estimate the thermal conductivity by calculating the obtained soil thermal diffusivity. In the calculation of the measured heat flow, it is assumed that the heat transfer in the earth's crust conforms to a bunch of Fourier's laws of steady-state heat conduction, and the heat flow q is:

$$q = -K \frac{dT}{dz}. \quad (7)$$

Soil thermal conductivity (K) indicates the characteristics of the soil when transferring heat, and the physical meaning is: the heat flux passed per unit time along the direction of heat transfer at a temperature difference of 1°C on both sides of a unit thickness of rock, numerically equal to the product of the thermal diffusion coefficient α , density ρ , and specific heat capacity c :

$$K = \alpha \cdot \rho \cdot c. \quad (8)$$

DATA AND MODELING

Data

The data source of this experiment was selected from the measured temperature data collected in the field using self-developed probes from 1 November 2020 to 5 November 2021. Probe measurement is the measurement of temperature in the sediment using probes equipped with equally spaced temperature sensors to obtain

temperature gradients. This equipment combined with the model proposed in this article can establish a geothermal flow measurement system based on low-temperature measurement and control in a borehole-free area to achieve convenient and efficient geothermal flow detection under low-temperature and low-power conditions. A total of four different depths of soil temperature data (20–50 cm) were collected and divided into four sets of temperature time series data for the purpose of experimental comparison and analysis. Details of the data are shown in **Supplementary Table S1**.

Data Preprocessing

First, the temperature time series data need to be Fourier-transformed, the T - t data into complex $(a+bi)$ form of spectral data, and then according to the Fourier transform requirements, combined with the linear interpolation approach to complete the data preprocessing. Since the prerequisite for the Fourier transform requires a sampled data size of 2^n , we need to eliminate some of the sampled data, which may lead to temperature fluctuations with periods, amplitudes, and phases that may be more off the mark. However, due to the long monitoring time of this experiment and the fact that the actual number of deleted data represents less than 1% (1,082 samples were actually collected at each depth, with 1,024 remaining after deletion), this does not affect the results of this experiment too much. Using the Fourier-transformed data in complex form $(a+bi)$, we calculate the period, amplitude, and phase of the temperature fluctuations that we really care about. The conversion relationship is as follows:

The imaginary part of the first complex point, $b = 0$, indicates a DC component (expanding the non-sinusoidal periodic signal by the Fourier series, the component with zero frequency), which in our case is actually the equilibrium temperature $T_0(z)$ at a depth unaffected by atmospheric temperature fluctuations, and the relationship between the remaining complexes is:

$$T_0(z) = \frac{a}{M}. \quad (9)$$

The relationship between the period P_i , amplitude A_i , and phase φ_i of the temperature fluctuation components and the complex number $(a+bi)$ starting from the second complex point is as follows, where P_s is the actual sampling interval:

$$P_i = \left(\frac{M}{i-1} \right) \cdot P_s, \quad (10)$$

$$\varphi_i = \operatorname{atan}\left(\frac{b_i}{a_i}\right), \quad (11)$$

$$A_i = \frac{\sqrt{a_i^2 + b_i^2}}{\frac{n}{2}}. \quad (12)$$

The temperature fluctuation period is the phase corresponding to the P_i component. $a_i > 0$, $\varphi_i = \operatorname{atan}\left(\frac{b_i}{a_i}\right) + 2\pi$; $a_i < 0$, $\varphi_i = \operatorname{atan}\left(\frac{b_i}{a_i}\right) + \pi$.

Modeling

The model built in this study has five panels (done using Python): data preprocessing, fast Fourier transform, solving the thermal diffusion coefficient, calculating the temperature time series, and plotting the temperature fluctuations (the detailed process of the

whole model run is shown in the attached FFTcode.py). Regarding the solution of the soil thermal diffusion coefficient, after we get the period P_i , amplitude A_i , and phase φ_i of the desired temperature fluctuation components, in order to calculate the most suitable soil thermal diffusion coefficient, we use different values (here, we use 10^{-9} – 10^{-5} for a total of 12 values) to substitute into $T(z, t)$, and then the solved time series $T(z, t)$ of soil temperature affected by temperature change and the measured values were fitted with the variance (assume that 20 cm is the observed value and 30 cm is the measured value). We considered that the value of the thermal diffusion coefficient that obtained the minimum fitted variance was the most reasonable thermal diffusion coefficient for the soil between the two depths of 20 and 30 cm, and the variance fitting equation is as follows:

$$MSE = \sqrt{\frac{\sum_{i=1}^n (y_{ic} - y_{im})^2}{n}}, \quad (13)$$

where y_{ic} and y_{im} denote the calculated and measured temperatures at a depth of 30 cm, respectively. After obtaining what we consider to be the optimal thermal diffusion coefficient of the soil at 20 cm, the κ is substituted into $T(z, t)$ to calculate the soil temperature time series T at a depth of 30 cm and then compared with the measured data temperature and analyzed the change of the two sets of data by comparing them by drawing a line graph to see whether the calculated soil temperature time series data eliminate the temperature fluctuations. Following the aforementioned method, we can calculate the soil temperature time series data at 30, 40, and 50 cm, so that we get three sets of theoretical optimal soil thermal diffusion coefficients at different depths and soil temperature data after correction for air temperature.

EXPERIMENTAL RESULTS AND ANALYSIS

Selection of κ

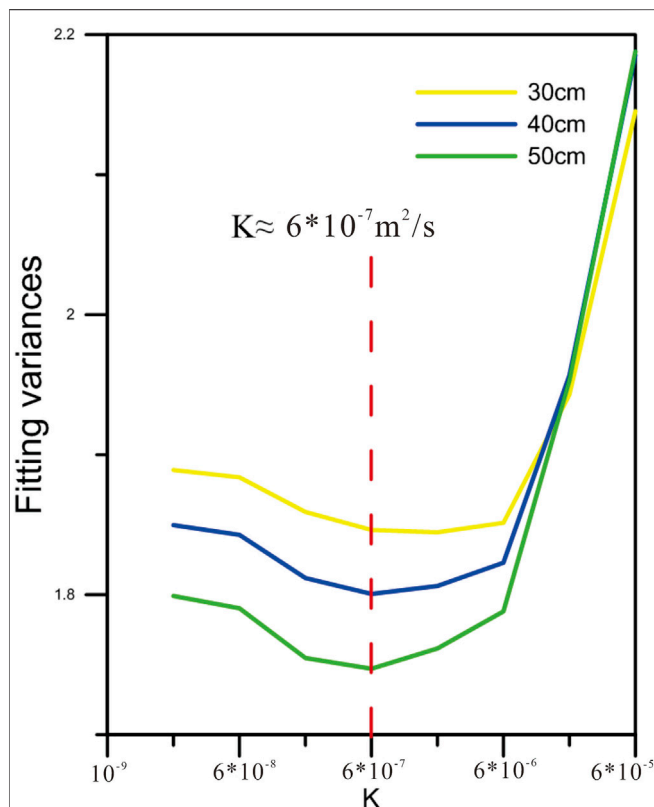
Through the variance fitting formula, we obtained the variance corresponding to different values of the three sets of data, and the details are shown in **Table 1**; then, the horizontal coordinate is κ , and the vertical coordinate is the variance plotted as a line graph, as in **Figure 2**. Through the graph of the thermal diffusion coefficient and fitted variance in **Figure 2**, we can choose the most suitable κ from the fitted κ graph for the next calculation, in which the two curves at the lowest point of the trend is the best value for the fit. We found that the two measured curves fluctuate in a similar trend, which also indicates that the results obtained from the two sides are correct and the optimal points of the values are similar, and the most suitable soil thermal diffusion coefficient (κ) is obtained to be approximately $6 \times 10^{-7} \text{ m}^2/\text{s}$.

Time Temperature Series Correction

We made a temperature correction for the measured time temperature series of the original data, and the values of soil thermal diffusion coefficient (κ) were chosen to be $6 \times 10^{-7} \text{ m}^2/\text{s}$. Details of the time temperature series data before and after

TABLE 1 | Heat diffusion coefficient corresponding to the solution variance.

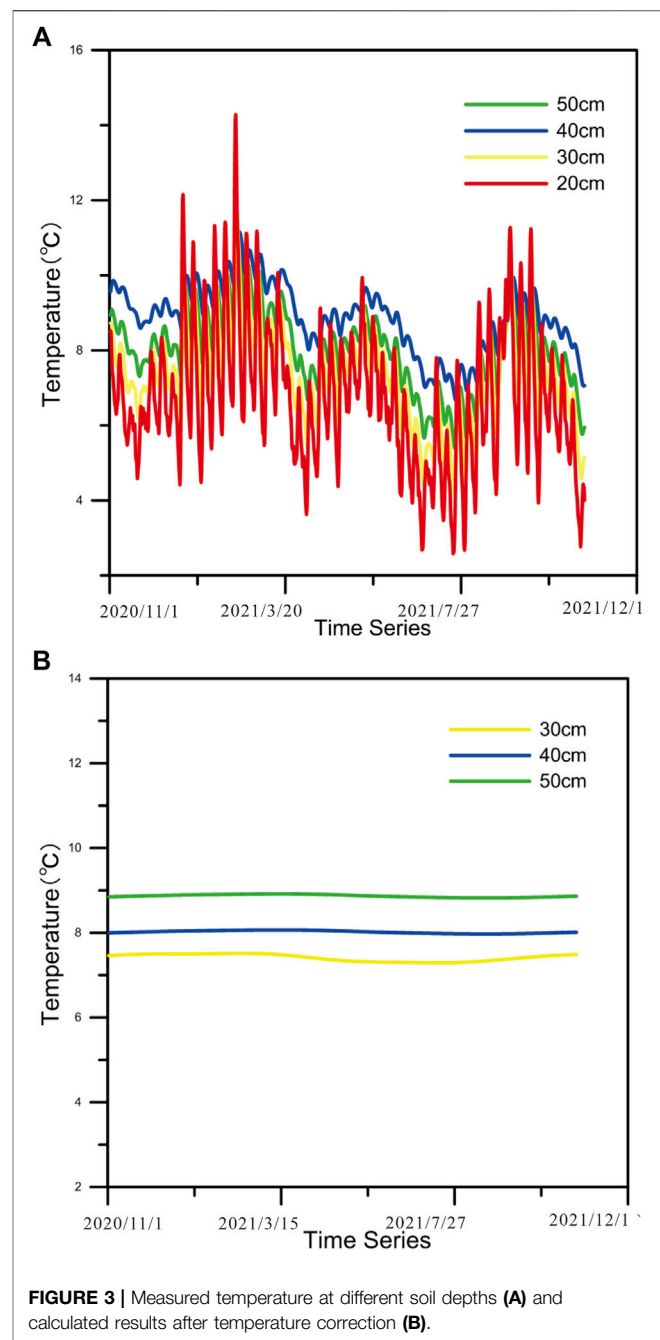
Value of k	30 cm	40 cm	50 cm
1×10^{-8}	1.889082723	1.849742996	1.799102275
4×10^{-8}	1.883900368	1.842755071	1.790303297
8×10^{-8}	1.859110982	1.811872447	1.754774657
2×10^{-7}	1.846279396	1.800517054	1.747105508
6×10^{-7}	1.844588413	1.800203938	1.74155709
1×10^{-6}	1.851323747	1.822828318	1.788082929
4×10^{-6}	1.942836581	1.956641878	1.953235425
8×10^{-6}	2.145391405	2.185522123	2.188078432
2×10^{-5}	2.29618493	2.335610802	2.328112534
6×10^{-5}	2.409874244	2.441019804	2.42232851
1×10^{-5}	2.498994781	2.51982876	2.491273384
4×10^{-5}	2.759906233	2.738072318	2.679902736

**FIGURE 2** | Fitted κ -value (for better visualization, only the first eight data are selected for the horizontal coordinates of the plot, which do not affect the results).

correction are shown in **Supplementary Table S1**, and then the line graphs were drawn as shown in **Figure 3**. **Figure 3** shows the measured soil time temperature series data at different time periods and depths of 20–50 cm. It can be seen that the corrected temperature fluctuations are significantly reduced.

Analysis of Experimental Results

From the results in **Figure 3**, the fluctuation range of soil temperature at 20 cm before the correction was large, and the

**FIGURE 3** | Measured temperature at different soil depths (A) and calculated results after temperature correction (B).

fluctuation range was 2.58°C – 14.284°C , which was because the soil here was closer to the land surface and was affected too much by the temperature fluctuation, and as the soil depth deepened, the temperature fluctuation slowly became smaller, and the fluctuation range was 6.67°C – 11.15°C at 50 cm, but the effect of temperature fluctuation was still obvious. Also, the fluctuation range was basically reduced to within 0.3°C after temperature correction.

From the analysis of the aforementioned experimental results, it can be seen that after correction for atmospheric temperature, the effect of temperature fluctuations is basically eliminated, so

that the thermal diffusion coefficient of the soil at different depths can be obtained, and also the calculated temperatures at the corresponding depths can be obtained, as a way to presume the approximate geothermal gradient of the measured area. However, it needs to be recognized that this treatment of ours considers that the measured temperature is only influenced by diffusion and ignores the effect of convection. From the final results of the treatment, the deviation of the calculated results ignoring the effect of convection is not significant, and therefore, we believe that the effect of convection can be ignored in this experiment.

DISCUSSION

Geothermal heat flow is the basic physical parameter that characterizes the heat dissipation in the Earth by conduction. It is an indispensable parameter for studying the thermal state of the Earth's interior, obtaining the temperature of the deep crust, and analyzing the thermal structure of the lithosphere, and it is a key parameter for assessing regional geothermal resources, and it can also provide basic parameters for the optimal selection of other new energy sources. It is also a direct display of the Earth's internal thermal processes at the surface (or seafloor), which is not only a key data for understanding the rate of heat dissipation in the Earth but also a basic data for conducting kinetic studies and reconstructing the evolution of sedimentary basins and evaluating the potential of oil and gas and hydrate resources. Geothermal heat flow is important for the study of crustal activity, the thermal structure of the crust and upper mantle, and the evaluation of regional thermal state and geothermal resource potential (Qiu, 1998).

Methods

Usually, geothermal heat flow parameters depend on drilling conditions and can be obtained indirectly through geothermal temperature measurements and rock thermal conductivity tests, but in areas where drilling is lacking, geothermal heat flow is extremely difficult to obtain. The drilling temperature continuous acquisition system manufactured by R.G, United Kingdom, and the thermal conductivity scanner (TCS) made in Germany are the more commonly used temperature measurement and rock thermal conductivity testing equipment in China at present. Compared with rock thermal conductivity testing, temperature measurement requires more demanding conditions and requires the use of existing drilled wells, so it is limited in terms of quantity, spatial coverage, and depth. Influenced by the distribution of drilling wells, geothermal heat flow measurement points in China's mainland are currently mainly distributed in the Sichuan Basin, Ordos Basin, Tarim Basin, and other hydrocarbon-bearing basins.

Geothermal Fluxes in the Study Area

According to previous studies, the density of soils in the middle of the Ganzi County area is in the range of $0.94\text{--}1.56\text{ g/cm}^3$, and the specific heat capacity of soils is greatly influenced by the dryness and humidity of soils, and the geotechnical soils in the study area are mainly seasonal permafrost soils with local area soil

representatives, and the specific heat capacity is taken as the average value of $1,741\text{ kJ/m}^3\cdot\text{K}$ (Guo et al., 2014; Wang et al., 2014; Zhu et al., 2019; Yi et al., 2020). For the seasonal average temperature gradient data obtained in the field, it is necessary to take the temperature correction to eliminate the effect on soil temperature and then use it. The average of the corrected temperature data can better represent the temperature at that depth. After obtaining the corrected temperature at each depth, the variance of the temperature at the corresponding depth can be obtained at the same time. By doing the fitting curve of temperature versus depth, a better linear relationship was obtained for the temperature–depth profile. Therefore, the annual average ground temperature gradient can be obtained from the temperature–depth profile, and the seasonal average gradient in the study area obtained by removing the temperature influenced by temperature fluctuations is 7.3°C/m . According to **Equations 7, 8**, we can calculate the range of soil thermal conductivity as $0.986\text{--}1.585$, and the preliminary heat flux Q is $9.3845 \pm 2\text{ W/m}^2$.

The geothermal flux calculated in this way has a large error. We used the random sampling method to take 500 samples as experimental parameters in the derived soil thermal conductivity range to calculate the geothermal flux of the area, and then the results were randomly divided into five groups to calculate the standard error separately, and the group with the smaller error was taken as the final geothermal flux calculation result, and then its mean value was sought as the geothermal flux valuation of the study area. After the calculation, the sample group with the SE of 0.951 was selected as the experimental object, and the geothermal flux of the area was found to be 7.863 W/m^2 , and the details of the calculation are shown in **Supplementary Table S2**. Due to the limited number of field monitoring instruments, the experiment could not be conducted in more areas, and the lack of experimental data made it impossible to fit the total geothermal flux of the area. However, the method and the new model used in this study achieved good results in the experiments, which can also provide technical support for subsequent scholars to study the geothermal resources in the plateau region or to evaluate the geothermal potential of the region.

CONCLUSION

In this study, a new model is established based on Fourier analysis and heat conduction principle, and the long-term monitoring data of soil temperature in the field are processed, and two sets of temperature time series data measured at different soil depths are selected for experimental analysis, as a way to improve the calculation accuracy of soil conduction heat dissipation by eliminating the influence of temperature changes on soil temperature. The following preliminary conclusions were obtained:

- 1) From the results of tests on four groups of soils at different depths, the fluctuation range of soil temperature at 20 cm before the correction was large, and the fluctuation range was $2.58^\circ\text{C--}14.284^\circ\text{C}$, and as the soil depth deepened, the temperature fluctuation slowly became smaller, and the fluctuation range was $6.67^\circ\text{C--}11.15^\circ\text{C}$ at 50 cm. Also, the

fluctuation range was basically reduced to within 0.3°C after temperature correction. The results show that the influence of temperature variation on soil temperature has been eliminated as much as possible, which can provide help to improve the calculation accuracy of heat dissipation in the following calculations.

- 2) Through the seasonal average temperature data obtained in the field and previous research results, and then after eliminating the influence of temperature changes on soil temperature, the geothermal temperature gradient in the region can be calculated as 7.3°C/m and the geothermal flux valued as 7.863 W/m². Although the number of monitoring points is not enough to fit the geothermal flux situation in the whole study area, the soil temperature time series processing method proposed in this study is feasible and can provide technical support for subsequent researchers to evaluate the geothermal situation in the region or to develop geothermal resources.
- 3) A model combining Fourier series analysis and heat conduction principle is established, which can realize the rapid processing of soil temperature time series, so as to obtain the soil thermal diffusion coefficient with high accuracy to correct the effect of temperature change on soil temperature, and the experimental results show that the accuracy of the correction is high, and the model is widely applicable, and the parameters can be adjusted according to the needs of researchers to improve the accuracy of the model in different areas of testing.

REFERENCES

- Benseman, R. F. (1959). The Calorimetry of Steaming Ground in Thermal Areas. *J. Geophys. Res.* 64 (1), 123–126. doi:10.1029/jz064i001p00123
- Coolbaugh, M., Sladek, C., Zehner, R., and Kratt, C. (2014). Shallow Temperature Surveys for Geothermal Exploration in the Great Basin, USA and Estimation of Shallow Convective Heat Loss. *Geotherm. Resour. Counc. Trans.* 38, 115–122. doi:10.1016/j.rse.2006.09.001
- Dawson, G. B., and Author, A., (1970). Heat Flow Studies in Thermal Areas of the North Island of New Zealand. *Geothermics*, 2: 466–473. doi:10.1016/j.coldregions.2011
- Domenico, P. A., and Schwartz, F. W. (1998). *Physical and Chemical Hydrogeology*. New York, NY: Wiley. doi:10.2767/1/d.cnki.gcjtc.2019.000407
- Fridriksson, T., Kristjánsson, B. R., and Ármannsson, H. (2006). CO₂ Emissions and Heat Flow through Soil, Fumaroles, and Steam Heated Mud Pools at the Reykjanes Geothermal Area, SW Iceland. *Appl. Geochem.* 21 (9), 1551–1569. doi:10.1016/j.apgeochem.2006.04.006
- Guo, Y. (2014). *Research on Vegetation Protection of Slope of Shima Highway in High Altitude and Cold Area*. Chengdu, China: Chengdu University of Technology.
- Holmes, T. R. H., Owe, M., De Jeu, R. A. M., and Kooi, H. (2008). Estimating the Soil Temperature Profile from a Single Depth Observation: a Simple Empirical Heatflow Solution. *Water Resour. Res.* 44 (2), 2412. doi:10.1029/2007wr005994
- Horton, R., Wierenga, P. J., and Nielsen, D. R. (1983). Evaluation of Methods for Determining the Apparent Thermal-Diffusivity of Soil Near the Surface. *Soil Sci.* 47 (1), 25–32. doi:10.2136/sssaj1983.03615995004700010005x
- Hu, G. J., Zhao, L., Wu, X. D., Li, R., Wu, T. H., Xie, C. W., et al. (2016). New Fourier-Series-Based Analytical Solution to the Conduction Convection Equation to Calculate Soil Temperature, Determine Soil Thermal Properties, or Estimate Water Flux. *Int. J. Heat Mass Transf.* 95, 815–823. doi:10.1016/j.jheatmasstransfer.2015.11.078

DATA AVAILABILITY STATEMENT

The original contributions presented in the study are included in the article/**Supplementary Material**; further inquiries can be directed to the corresponding author.

AUTHOR CONTRIBUTIONS

LYa: algorithm analysis, methodology, and writing—original draft. RS: writing—review and editing and methodology. BD: mapping and analysis of results. LYi: algorithm analysis and mapping. YF: writing—original draft and analysis of results. BZ: writing—review and editing and methodology. ZW: methodology and modeling. YW: writing—review and modeling. SD: review and editing.

FUNDING

This study was supported by the Joint Scientific Research Project of the Corporation (No. WWKY-2020-0103).

SUPPLEMENTARY MATERIAL

The Supplementary Material for this article can be found online at: <https://www.frontiersin.org/articles/10.3389/feart.2022.910328/full#supplementary-material>

- Hurwitz, S., Harris, R. N., Werner, C. A., and Murphy, F. (2012). Heat Flow in Vapor Dominated Areas of the Yellowstone Plateau Volcanic Field: Implications for the Thermal Budget of the Yellowstone Caldera. *J. Geophys. Res. Solid Earth* 117 (B10). doi:10.1029/2012jb009463
- LeSchack, L. A., and Lewis, J. E. (1983). Geothermal Prospecting with Shallow-Temp Surveys. *Geophysics* 48 (7), 975–996. doi:10.1190/1.1441523
- Liang, K. M., Liu, F., Miao, G. Q., and Shao, L. B. (2020). *Methods in Mathematical Physics*. Beijing, China: Higher Education Press, 62–74.
- Liang, S. J., Feng, B., and Yan, T. Z. (2018). Geothermal Resources and Their Development and Utilization. *Environ. Dev.* 30 (08), 247–249. doi:10.16647/j.cnki.cn15-1369/X.2018.08.150
- Liu, S. H., Cui, Y., and Liu, H. P. (1991). Determination of Soil Thermal Diffusion Coefficient and its Application. *J. Appl. Meteorology* 04 (2), 337–345.
- Ma, B., Jia, L. X., Yu, Y., Wang, H., Chen, J., Zhong, Si., et al. (2021). Earth Science and Carbon Neutrality: Current Status and Development Direction. *Geol. China* 48 (02), 347–358.
- Qiu, N. S. (1998). Thermal Condition Profiles of Sedimentary Basins in Continental China. *Adv. Earth Sci.* (05), 34–38.
- Ramos, M., de Pablo, M. A., Sebastian, E., Armien, C., and Gómez-Elvira, J. (2012). Temperature Gradient Distribution in Permafrost Active Layer, Using a Prototype of the Ground Temperature Sensor (REMS-MSL) on Deception Island (Antarctica). *Cold Regions Sci. Technol.* 72, 23–32. doi:10.1016/j.coldregions.2011.10.012
- Rissmann, C., Christenson, B., and Werner, C. (2012). Surface Heat Flow and CO₂ emissions within the Ohaaki Hydrothermal Field, Taupo Volcanic Zone, New Zealand. *Appl. Geochem.* 27 (1), 223–239. doi:10.1016/j.apgeochem.2011.10.006
- Sorey, M. L., and Colvard, E. M. (1994). *Measurements of Heat and Mass Flow from Thermal Areas in Lassen Volcanic National Park, California*. Menlo Park, California: US Geological Survey.
- Wang, L., Gao, Z., and Horton, R. (2010). Comparison of Six Algorithms to Determine the Soil Apparent Thermal Diffusivity at a Site in the Loess Plateau of China. *Soil Sci.* 175 (2), 51–60. doi:10.1097/ss.0b013e3181cdda3f

- Wang, X., Xiang, C. H., Li, X. W., and Wen, D. J. (2014). Effects of Winter Fire on the Physicochemical Properties of Subalpine Meadow Soils in Western Sichuan. *Grassl. Sci.* 31 (05), 811–817.
- Wang, Y. C., Li, L., Wen, H. G., and Hao, Y. L. (2022). Geochemical Evidence for the Nonexistence of Supercritical Geothermal Fluids at the Yangbajing Geothermal Field, Southern Tibet. *J. Hydrology* 604, 127243. doi:10.1016/j.jhydrol.2021.127243
- Wang, J. Y., Qie, Z. H., Wu, T. Q., Liu, J. S., Wang, C., Wang, X. L., et al. (2021). Research on LSTM Neural Network for Soil Temperature Time Series Prediction. *J. Anhui Agric. Univ.* (05), 119–125. doi:10.13320/j.cnki.jauh.2021.0093
- Wang, Y. C., Pang, Z. H., Hao, Y. L., Fan, Y. F., Tian, J., and Li, J. (2019). A Revised Method for Heat Flux Measurement with Applications to the Fracture Controlled Kangding Geothermal System in the Eastern Himalayan Syntaxis. *Geothermics* 77, 188–203. doi:10.1016/j.geothermics.2018.09.005
- Wang, Y. C., and Pang, Z. H. (2021). Heat Flux Measurements and Thermal Potential of the Garze Geothermal Area in the Eastern Himalayan Syntaxis. *J. Volcanol. Geotherm. Res.* 420, 107407. doi:10.1016/j.jvolgeores.2021.107407
- Yi, P. F. (2020). *Hydrodynamic Mechanism of Subalpine Meadow Soil Slip Erosion and its Spatial Prediction and Evaluation*. Chengdu, China: Chengdu University of Technology.
- Zhu, J. L. (1997). Geothermal Resources and Their Utilization. *Sol. Energy* 1997 (04), 27–28.
- Zhu, R. (2019). *Research on the Application of Foam Concrete for Roads in Monsoon Freeze Zone*. Chongqing, China: Chongqing Jiaotong University.
- Zou, P., Yang, J. S., and Yao, R. J. (2008). Soil Temperature Time Series Prediction by BP Nerve Network Modeling Study. *Chin. J. Ecosyst. Agric.* 2008 (4), 835–838. doi:10.3724/sp.j.1011.2008.00835

Conflict of Interest: Authors LMY, LKY, YF, BZ, and ZW were employed by the company China Three Gorges Corporation.

The remaining authors declare that the research was conducted in the absence of any commercial or financial relationships that could be construed as a potential conflict of interest.

Publisher's Note: All claims expressed in this article are solely those of the authors and do not necessarily represent those of their affiliated organizations, or those of the publisher, the editors, and the reviewers. Any product that may be evaluated in this article, or claim that may be made by its manufacturer, is not guaranteed or endorsed by the publisher.

Copyright © 2022 Yang, Song, Dong, Yin, Fan, Zhang, Wang, Wang and Dong. This is an open-access article distributed under the terms of the Creative Commons Attribution License (CC BY). The use, distribution or reproduction in other forums is permitted, provided the original author(s) and the copyright owner(s) are credited and that the original publication in this journal is cited, in accordance with accepted academic practice. No use, distribution or reproduction is permitted which does not comply with these terms.



Pseudotachylyte-Mylonites Record of Transient Creep From Inter-Seismic Ductile to Co-Seismic Rupture

Wenhao Dai, Yongsheng Zhou* and Xi Ma

State Key Laboratory of Earthquake Dynamics, Institute of Geology, China Earthquake Administration, Beijing, China

OPEN ACCESS

Edited by:

Lidong Dai,
Institute of Geochemistry (CAS), China

Reviewed by:

Qiaomu Qi,
Chengdu University of Technology,
China
Maining Ma,
University of Chinese Academy of
Sciences, China
Xiaoge Huang,
Institute of Geology and Geophysics
(CAS), China

*Correspondence:

Yongsheng Zhou
zhouysh@ies.ac.cn

Specialty section:

This article was submitted to
Solid Earth Geophysics,
a section of the journal
Frontiers in Earth Science

Received: 28 April 2022

Accepted: 10 May 2022

Published: 22 June 2022

Citation:

Dai W, Zhou Y and Ma X (2022)
Pseudotachylyte-Mylonites Record of
Transient Creep From Inter-Seismic
Ductile to Co-Seismic Rupture.
Front. Earth Sci. 10:931005.
doi: 10.3389/feart.2022.931005

Transient creep during an earthquake cycle is very important to understand the rheology of fault and deformation mechanisms in the brittle-plastic transition zone. In this paper, we analyzed the microstructures of samples for mylonites, *pseudotachylyte*, and *cataclasite* under optical microscope, SEM, and EBSD, which were collected from the Red River fault in southwest of China, where we uncovered a series of ductile to brittle deformed rocks which recorded transient creep related to earthquakes. The results show that mylonites formed at the inter-seismic creep were overprinted by *pseudotachylyte* and *cataclasite* which were produced during co-seismic rupture, and cracks in *cataclasite* were healed during the post-seismic relaxation. Based on the analysis of the microstructures and deformation mechanism of fault rocks, we propose the oscillation deformation model to explain transient creep of the brittle-plastic transition zone during the seismic cycle in the Red River fault.

Keywords: *pseudotachylyte*, mylonites, *cataclasite*, transient creep, earthquake, brittle-plastic transition, Red River fault

1 INTRODUCTION

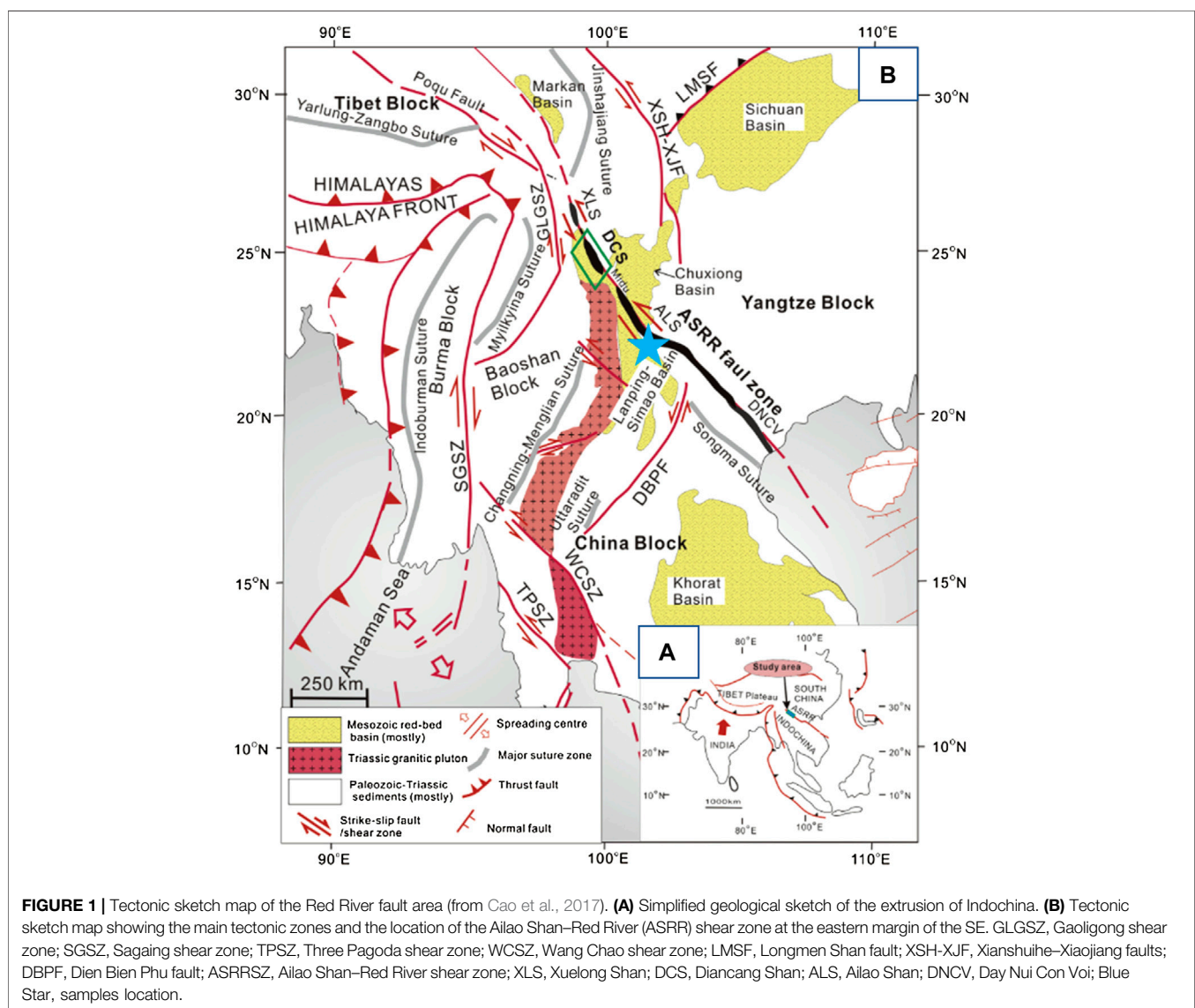
The continental crust has strong rheological layering. The deformation of the upper crust is dominated by brittle deformations of frictional sliding and fractures. In the middle and lower crusts, thermally related dislocation creep is considered to be the main deformation (Brace and Kohlstedt, 1980). The transition from brittle deformation to plastic flow is called as brittle-plastic transition, which is considered as a key layer for determining the depth limit of seismicity in the continental crust (Tse and Rice, 1986; Scholz, 1988).

There are several factors which affect the brittle-plastic transition of crustal rocks, mainly including geothermal gradient, strain rate, mineralogy, structure, fault orientation, and fluid (Sibson, 1983; Tullis and Yund, 1992; Kohlstedt et al., 1995; Montési and Zuber, 2002; Gueydan et al., 2004; Chernak et al., 2009; Ikari et al., 2011). Recent studies show that temperature, strain rate, and pore fluid pressure are the most important factors affecting the deformation of the brittle-plastic transition zone related to the seismic fault during inter-seismic creep, co-seismic loading, and post-seismic relaxation creep (Trepmann and Stöckhert, 2003; Trepmann et al., 2007; Trepmann and Stöckhert, 2013; Trepmann et al., 2017; Dai and Zhou, 2019).

To understand the transient creep of the brittle-plastic transition zone under oscillation conditions of stress and transient strain rate during the earthquake cycle, it is necessary to study in detail the microstructures and deformation mechanism of fault rocks in the deep crust (Campbell and Menegon, 2019). *Pseudotachylytes* and mylonites in the exhumed mid-to-lower crustal rocks record transient seismic slip, representative of brittle-plastic transition and ductile flow layer

of the seismogenic crust can propagate downward into the underlying ductile crust (Tse and Rice, 1986), producing pseudotachylytes that are overprinted by mylonitisation during post- and inter-seismic creep (Sibson, 1980; Hobbs et al., 1986; Camacho et al., 1995; White, 1996; Pennacchioni and Cesare, 1997; Lin et al., 2005; Moecher and Steltenpohl, 2009). Some cases revealed that mylonite is produced under a long-term low strain rate and low stress conditions during inter-seismic creep, whereas pseudotachylyte is the result of a short-term high strain rate and high stress deformation by accelerating viscous creep during co-seismic rupture (Trepmann and Stöckhert, 2003; Trepmann et al., 2007; Trepmann and Stöckhert, 2013; Trepmann et al., 2017; Wintsch and Yeh, 2013; Papa et al., 2020).

- 1) Pseudotachylyte formed within ductile deformed rocks. The ductile shear zone is overprinted by pseudotachylyte (White, 2012). Earthquake ruptures nucleating at the base
- 2) Co-seismic crystal-plastic deformation. Mylonites located adjacent to fault melt and associated cataclasis are interpreted to be a result of enhanced ductility arising from



the frictionally generated thermal pulse that causes melting (Kim et al., 2010; Bestmann et al., 2011; Bestmann et al., 2012; White, 2012).

- 3) Pseudotachylyte transforms into ultramylonite. Hydration and grain growth within pseudotachylyte layers form ultra-fine-grained rock which can be deformed by grain-size sensitive diffusion creep (Passchier, 1982; White, 1996; Takagi et al., 1999; Pennacchioni et al., 2006; White, 2012).

The mylonite and associated pseudotachylyte from the Red River fault provide an example to study transient creep of the brittle–plastic transition zone during the earthquake cycle. In this study, the microstructures of mylonite, *cataclasite*, and pseudotachylyte collected in the Red River fault zone were analyzed. Based on the deformation characteristics and mechanisms, the oscillation deformation model of inter-seismic creep and co-seismic rupture was determined following the former conception (Trepmann and Stöckhert, 2003; Trepmann et al., 2007; Trepmann and Stöckhert, 2013; Trepmann et al., 2017).

2 GEOLOGICAL SETTING

2.1 Background

The Red River fault (RRF) is a large-scale strike-slip fault in the southeast Asian continent (Molnar and Tapponnier, 1975; Molnar and Tapponnier, 1977; Tapponnier et al., 1982; Tapponnier et al., 1986; Cao et al., 2011a; Cao et al., 2011b; Cao et al., 2012; Cao et al., 2017), which is the consequence of Cenozoic continental collision between the Indian and Eurasian plates since the Eocene (Molnar and Tapponnier, 1977) (**Figure 1A**). Along the RRF zone, the Dianchang Shan and Ailao Shan metamorphic complexes are exposed. The high-grade metamorphic complexes comprise metamorphosed pelitic, mafic, carbonate rocks, and granitic intrusions (Leloup et al., 1995; Liu et al., 2008; Cao et al., 2011a; Cao et al., 2011b; Cao et al., 2012; Cao et al., 2017). These rocks experienced both high-grade metamorphism from upper greenschist to upper amphibolite or granulite facies and high-temperature deformation developing medium to strong foliation (Leloup and Kienast, 1993; Cao et al., 2011a; Cao et al., 2011b; Cao et al., 2012; Cao et al., 2017), which were subsequently sheared at relatively low temperature conditions during late tectonic processes (Cao et al., 2011a; Cao et al., 2011b; Cao et al., 2012; Cao et al., 2017). The ductile shear zone developed in the localized strong deformed zone, and mylonite was formed by high-temperature shear deformation. Pseudotachylyte was found within the local area of the ductile shear zone at Ailao Shan metamorphic complexes (Dai and Zhou, 2019) and Dianchang Shan metamorphic complexes (Li et al., 2022). The deformed metamorphic complexes preserve information on the thermal and tectonic evolution of the RRF fault zone (Leloup et al., 1995; Liu et al., 2006; Cao et al., 2011a; Cao et al., 2011b; Cao et al., 2012). Based on a large number of age data, the ductile deformed granite underwent three stages of cooling history (Wintsch and Yeh, 2013; Cao et al., 2017): quick cooling from 700 to 400°C before

24 Ma, the temperature remaining about 250–350°C with nearly no cooling during the geological period of about 24–5 Ma, and quick upliftment to the ground after 5 Ma. Wintsch and Yeh (2013) suggest that the protolith of granitic rock was deformed to foliated schist and mylonite by dislocation creep at the first cooling stage at a temperature of 400–700°C. However, the deformed granitic rock was overprinted by multiple brittle–plastic deformations during the second cooling period, which includes cataclasis–reaction creep–fracture and K-feldspar vein filling—dissolution creep occurred at 250–350°C (Wintsch and Yeh, 2013). The multiple brittle–plastic–brittle deformations under the similar temperature condition indicates the change of strain rate and pore fluid pressure at the constant depth of crust, which is believed to be related to fault activity during the seismic cycle (Trepmann and Stöckhert, 2003; Trepmann et al., 2007; Trepmann and Stöckhert, 2013; Zhou et al., 2014; Nevitt et al., 2017; Trepmann et al., 2017). Pseudotachylyte found in the ductile shear zone provides direct evidence of co-seismic rupture in geological times.

2.2 Samples

The samples of mylonite (Y11-1A, Y11-1C, Y11-3, and 110827-2), pseudotachylyte (Y11-1B and 110827-3), and cataclasite (Y11-2A, Y11-2B, and Y11-1D) were collected at location of the small valley besides the Qingshuihe Power Station from the Yuanjiang-Mojiang section in the middle segment of the Red River fault zone, and the samples of mylonite (110829-1 and 110829-2) were collected from the section west of Honghe town in the southern segment of the Red River fault zone in Yunnan, China (**Figure 1B**). The sampling locations are in the ductile shear zone developed at the Ailaoshan metamorphic complex.

The mylonite specimens mainly developed the foliation accompanied augen-shaped structure (**Figure 2A**). The elongated σ -type eyeball-like phenocrysts are dominated by feldspar, and the matrix consists of banded quartz, biotite, muscovite, and hornblende, which consists of foliation by plastic flow. Under the microscope, it can be observed that the directional arrangement of minerals constitutes stretching lineation, quartz, and feldspar undulose extinction. The elongated feldspar porphyroclasts and quartz with undulose extinction develop typical core-and-mantle structures.

Pseudotachylyte displays a kind of black vein with a width of about 2–5 cm which appeared within cataclasite and mylonite (**Figures 2B,C**), and the boundary between the pseudotachylyte and the host rock is sharp. The mylonite foliation is obliquely cut by the black veins of pseudotachylyte. The mylonite around the pseudotachylyte underwent brittle fracture to form cataclasite. Cataclasite developed fragmented structures (**Figures 2C,D**). The grinded structure is obvious under the microscope (**Figures 2E,F**), and the cracks are filled with the quartz vein and calcite vein.

3 ANALYTICAL METHODS

All analyses were carried out on oriented samples. Polished XZ-oriented thin sections were prepared by cutting parallel to the

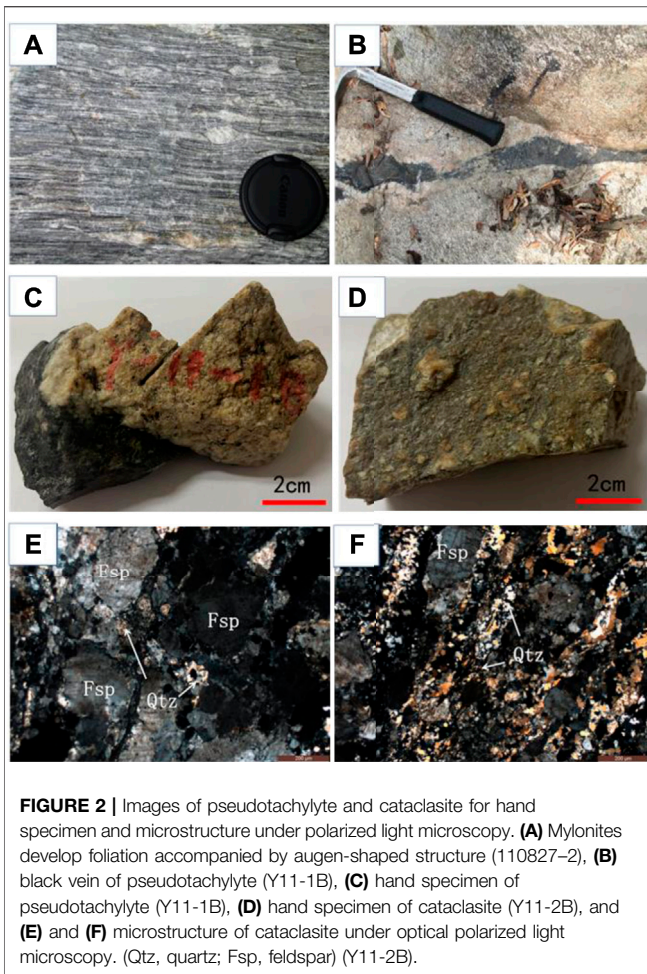


FIGURE 2 | Images of pseudotachylite and cataclasite for hand specimen and microstructure under polarized light microscopy. (A) Mylonites develop foliation accompanied by augen-shaped structure (110827-2), (B) black vein of pseudotachylite (Y11-1B), (C) hand specimen of pseudotachylite (Y11-1B), (D) hand specimen of cataclasite (Y11-2B), and (E) and (F) microstructure of cataclasite under optical polarized light microscopy. (Qtz, quartz; Fsp, feldspar) (Y11-2B).

mineral lineation (*X*-axis) and perpendicular to the foliation (*XY* plane) of the mylonites. The microstructures and quartz fabrics were analyzed using an optical microscope (OM), scanning electron microscopy (SEM), and electron backscatter diffraction (EBSD). The chemical composition was analyzed using scanning electron microscopy with energy-dispersive X-ray (EDS).

SEM is an effective instrument to observe the microstructure of rocks. It focuses on observing the spatial relationship between mineral materials by giving a different greyscale contrast, but it cannot measure the crystal orientations of mineral materials. EBSD is a kind of SEM-based technique to measure crystal orientations. It is applicable to any crystalline material (in theory) to provide the absolute crystal orientation with sub-micron resolution. EBSD is a useful tool for discriminating between phases.

The microstructures of mylonite, pseudotachylite, and cataclasite were observed under SEM, and the quartz fabrics were measured by SEM-EBSD analysis using a Zeiss Sigma scanning electron microscope (SEM) coupled with an Oxford Nordlys nano electron backscattered diffraction (EBSD) detector at the State Key Laboratory of Earthquake Dynamics, Institute of Geology, China Earthquake Administration, Beijing, China.

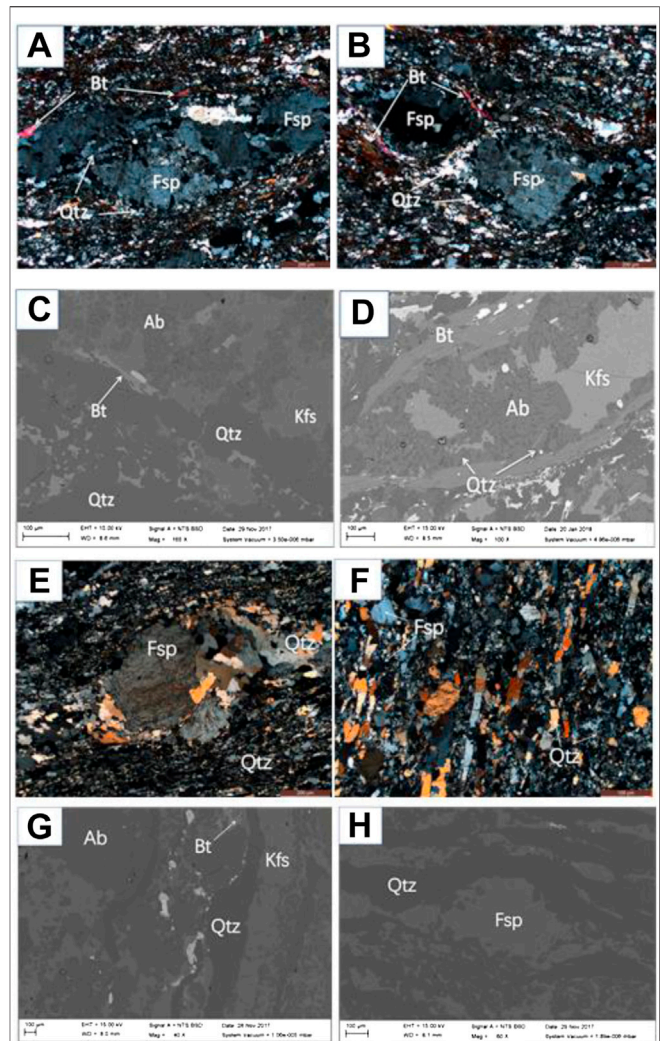


FIGURE 3 | Microstructure of mylonite under optical microscopy (OM) and scanning electron microscope (SEM). (A) and (B) images of 110827-2 under OM (crossed polarized light), (C) and (D) images of 110827-2 under SEM, (E) image of Y11-3 under OM (crossed polarized light), (F) image of 110829-1 under OM (crossed polarized light), (G) image of 110829-1 under SEM, and (H) image of Y11-3 under SEM. (Qtz, quartz; Fsp, feldspar; Bt, biotite; Ab, albite; Kfs, K-feldspar).

Polished thin sections were carbon-coated prior to EBSD analysis. EBSD allows the determination of the full crystallographic orientation of crystals in a thin section using a backscattered electron (BSE) signal. Automatic EBSD measurements were used to obtain orientation maps and crystallographic preferred orientation (CPO) patterns. Working conditions during acquisition of the EBSD patterns were 20 kV accelerating voltage, 12-nA probe current, 70° sample tilt, ~20 mm working distance, and high vacuum. EBSD patterns of quartz were acquired and indexed with AZtec software (Oxford Instruments) which selected the direction of the stretching lineation as the *X*-axis direction, that is, the quartz-mica strip direction is the *X*-axis direction and the plane-oriented direction is the *XY*-plane direction. CHANNEL 5 software (Oxford

Instruments) was used for noise reduction and for filling the missing data with at least eight identical neighbors with similar orientation. All stereographic diagrams of EBSD are lower hemisphere projections.

4 RESULTS

4.1 Mylonite

4.1.1 Microstructures of Plastic Deformation of Mylonite

Sample 110827-2 is a typical fine-grained mylonite. The samples of mylonite (110829-1, 110829-2, Y11-3, Y11-1A, and Y11-1C) contain augen-shaped feldspar porphyroclasts. The microstructures on all six samples were observed, and the deformation characters are similar for all thin sections. Results from three examples (110827-2, Y11-3, and 110829-1) were presented here to show representative deformation behaviors.

The fine-grained mylonite sample 110827-2 was collected from the same section as the pseudotachylyte (Y11-1B and 110827-3). Optical polarized light microscope images show that quartz developed sub-grain textures, feldspar is larger in size than quartz grains, and the grain boundaries are irregular and most edges of the grains became sinuous (**Figures 3A,B**). All of these phenomena show that feldspar and quartz underwent middle temperature deformation of dynamic recrystallization (**Figures 3A,B**). Fine-grained quartz and mica bands constitute the foliation. Mechanical twinned crystals developed in feldspar porphyroclasts which have a crushed structure inside, and the cracks are filled with recrystallized quartz and feldspar (**Figure 3B**). Mica is distributed in the interstices of quartz aggregates which surround the feldspar phenocrysts, showing water–rock reaction at the rims of feldspar (**Figures 3A,B**).

Under the scanning electron microscope, the grains of quartz are elongated and form foliation with mica bands, indicating that the rock has undergone strong plastic deformation (**Figures 3C,D**). The backscattered electron (BSE) images and the EDS analysis show that composition variations of the feldspar due to the dissolution, feldspar porphyroclasts underwent dissolution and decomposition to albite and potassium feldspar (**Figure 3D**).

Sample Y11-3 has a plaque-like structure under an optical polarizing microscope. The boundaries of feldspar phenocrysts are mostly sinuous, with crushed structures, and the matrix is composed of an aggregate of fine-grained feldspar, quartz, and elongated biotite bands, which display the characteristics of plastic flow (**Figure 3E**). Fine-grained quartz and mica aggregates are accumulated on both sides of the trailing tail of the ocular feldspar phenocryst and biotite distributed between the quartz grains or around the edge of the feldspar (**Figure 3E**), indicating that the feldspar has undergone pressure solution. Quartz has a semi-automorphic shape with developed sub-grains and bulging texture at the grain boundaries (**Figure 3E**). The boundaries of feldspar grains in the matrix are bulged, and all of these characteristics indicate that the fine-grained feldspar, quartz, and biotite have undergone low-temperature dislocation creep. It can be seen under the scanning electron

micrograph that quartz bands are thin and feldspar bands are thick, and feldspar bands are cut and intersected by the quartz bands (**Figure 3G**).

Sample 110829-1 has an augen-shaped structure under an optical polarizing microscope. The phenocryst of feldspar is automorphic or semi-automorphic. The boundaries are irregular and sinuous, and some feldspars develop cracks (**Figure 3F**). The matrix is composed of feldspar, quartz, and a small amount of mica. Feldspar is elongated and arranged in a short rod shape with smooth boundaries. The quartz grains are elongated and oriented, the boundary is relatively flat, and the undulose extinction is visible under crossed polarized light (**Figure 3F**). All of the microstructures indicate that feldspar and quartz are flattened and elongated and that they have undergone low-temperature dislocation creep. Scanning electron microscopy shows that quartz grains and small K-feldspar grains are distributed in a strip shape (**Figure 3H**), indicating strong ductile shear deformation.

4.1.2 Electron Backscatter Diffraction Fabric of Quartz for Samples of Mylonite

Quartz fabrics were mapped by EBSD in a total of 10 mylonite thin sections from six samples, and the fabrics of quartz in most thin sections are similar. We present the results of six thin sections from three samples in **Figure 4**. Section 1 (such as Y11-3-1) was cut parallel to the mineral lineation (*X*-axis) and perpendicular to the foliation (*XY* plane) of the mylonites, and section 2 (such as Y11-3-2) was cut perpendicular to *X*-axis and *XY* plane. Grains of quartz, feldspar, and biotite are strongly elongated to form the foliation of mylonite samples, except some phenocrysts of feldspar which display significant plastic deformation for all minerals.

Figure 4 shows the EBSD pole figure of quartz in mylonite samples. The dense concentration of the *c*-axes of quartz grains in samples of Y11-3 (**Figures 4A,B**) and 110829-1 (**Figures 4C,D**) are distributed in the north and south poles, indicating that the slip system is the basal *a* slip, which is a typical fabric of low-temperature (below 400°C) deformation, corresponding to bulge creep of quartz. However, the *c*-axes of quartz grains in samples of 110827-2 (**Figures 4E,F**) are distributed in the center point, indicating that the slip system is the prism *a* slip, which is a typical fabric of medium-to-high temperature (between 450 and 600°C) deformation. The EBSD results are consistent with the results of microstructural analysis with sub-grain recrystallization creep of quartz. The medium-to-high temperature deformation corresponds to the plastic flow behavior in ductile shear of deep fault zone during the inter-seismic period, while the low-temperature deformation stands for the transient creep of the brittle–plastic transition zone of fault during the inter-seismic period.

4.2 Pseudotachylyte and Cataclasite

4.2.1 Microstructure of Pseudotachylyte and Cataclasite

Samples 110827-3 and Y11-1B are protomylonites overprinted by the cataclasite and pseudotachylyte vein (**Figures 2B,C**). The major minerals of the samples are quartz, feldspar, and biotite

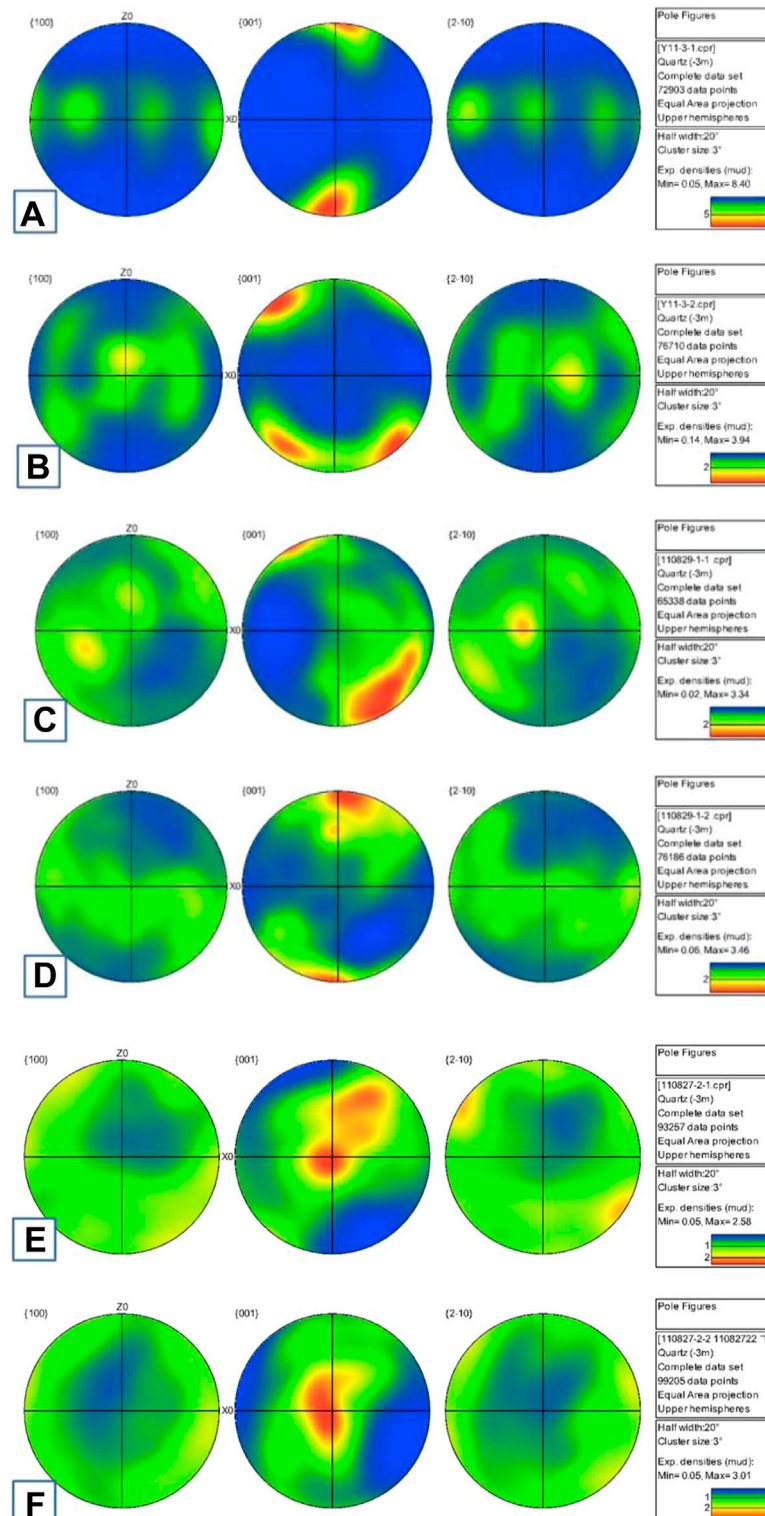


FIGURE 4 | Quartz fabric from EBSD in samples of mylonites. **(A)** Thin section of Y11-3-1, **(B)** thin section of Y11-3-2, **(C)** thin section of 110829-1-1, **(D)** thin section of 110829-1-2, **(E)** thin section of 110827-2-1, and **(F)** thin section of 110827-2-2 (All sections were cut perpendicular to the XY plane of the mylonites, and different numbers -1 or -2 in the same sample were parallel or perpendicular to X-axis).

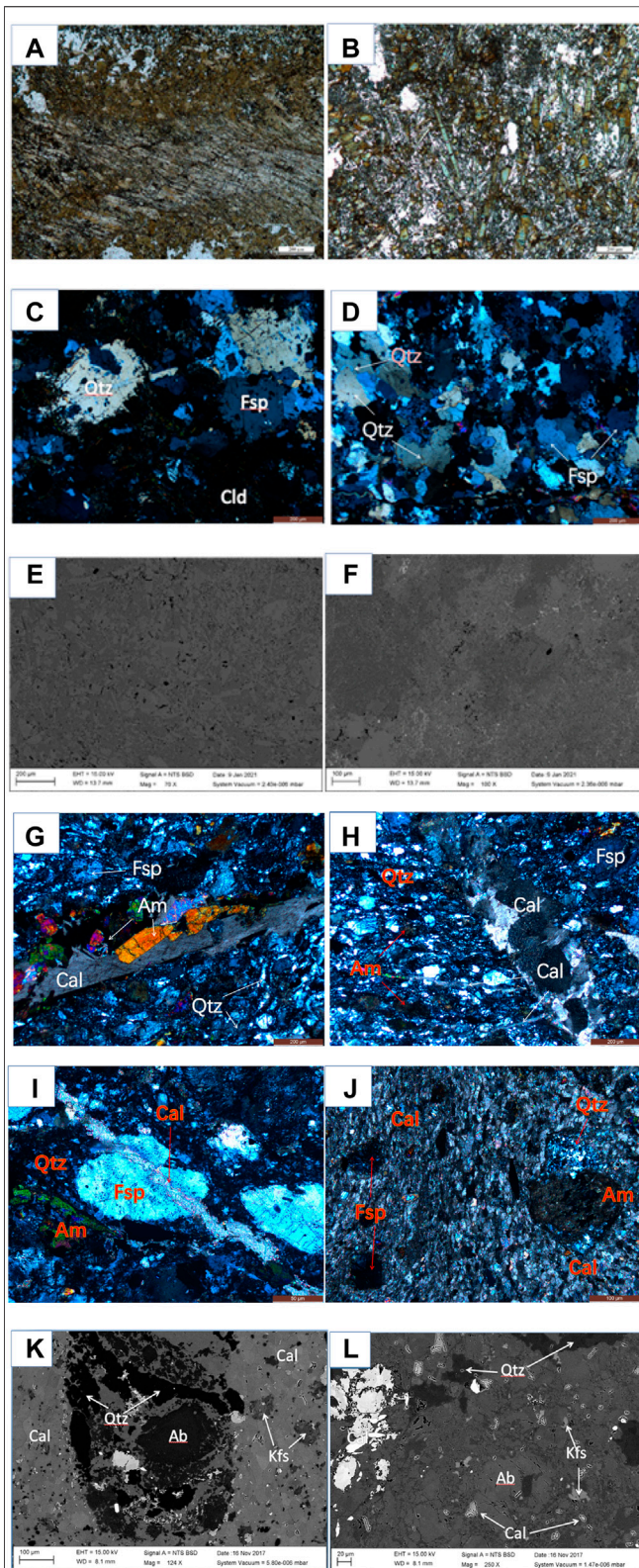


FIGURE 5 | Microstructure of pseudotachylyte and cataclasite under optical microscopy (OM) and scanning electron microscope (SEM). (A) and (B) images of Y11-1B under OM (crossed polarized light); (C) and (D) images (Continued)

FIGURE 5 | of 110827-3 under OM (crossed polarized light); (E) and (F) images of Y11-1B under SEM; (G), (H), (I), and (J) images of Y11-2A under OM (crossed polarized light); and (K) and (L) images of Y11-2A under SEM. (Qtz, quartz; Fsp, feldspar; Cld, chloritoid; Am, amphibole; Ab, albite; Kfs, K-feldspar; Ca, calcite).

with obvious stretching lineation shown by quartz and biotite. In the hand specimens, the protomylonite was fractured to form cataclasite, and a black vein of pseudotachylyte developed within cataclasite (Figures 2B,C). The boundary between the black vein of pseudotachylyte and wall rock of cataclasite is clear, and the cracks in pseudotachylyte were healed by calcite and sparse pyrite. Sample Y11-2A is a typical cataclasite which is a kind of localized strong cataclastic rock from Y11-1B (Figure 2D), the grains of quartz and feldspar developed mesh-like veins, which were healed by quartz and calcite.

There is a cataclastic zone between the protomylonite and pseudotachylyte vein (Figure 5A). Feldspar grains in cataclasite were fractured, and coarse-grained feldspar developed with mechanical twinning and undulose extinction (Figure 5C) under an optical polarizing microscope. The cracks in feldspar were healed using statically recrystallized quartz and calcite veins, and calcite underwent plastic deformation which represents a post-seismic relaxation deformation. A large number of randomly distributed needle-shaped chloritoid, feldspar, and quartz crystallized in the pseudotachylyte vein (Figures 5B,E,F) which are the products of rapid cooling after co-seismic frictional melting. Two kinds of quartz were found: the first one is semi-automorphic, the boundaries are bulged and recrystallized (Figure 5D), and some grains can be observed as undulose extinction, which is the pre-existing low-temperature deformed quartz in the parent rock; the other one has the characteristics of static recrystallization (Figure 5D in red), which is quartz recrystallized statically from the pseudotachylyte after the rock is broken.

Sample Y11-2A is a typical cataclasite which develops a porphyritic structure, and fractures were healed by calcite veins under a polarized light microscope (Figures 5G-J). The phenocrysts were mostly feldspar grains and altered amphibole. The feldspar grains in the phenocrysts are mostly euhedral to subhedral with irregular grain boundaries generally developing cracks that are filled by calcite veins (Figures 5H,I). The amphibole grains in the phenocrysts are mostly euhedral or subhedral, and there are obvious transcrystalline cracks across the grains. The main components of the matrix are fine-grained feldspar, quartz, and a small amount of mica and amphibole. Fine-grained feldspar and quartz have undulose extinction, and directional elongation shows the characteristics of plastic flow (Figure 5J). The fractures were healed by two types of calcite veins. Among them, the first type of calcite veins is mainly fine-grained aggregates (Figure 5J), which form a band and cuts through the entire cataclasite sample, indicating significant plastic flow. It is speculated that the cracks were produced in the co-seismic slip, were healed by calcite during the post-seismic relaxation period, and then the calcite was plastically deformed under low-temperature condition. The second type of calcite veins is mainly subhedral aggregates, without any deformation

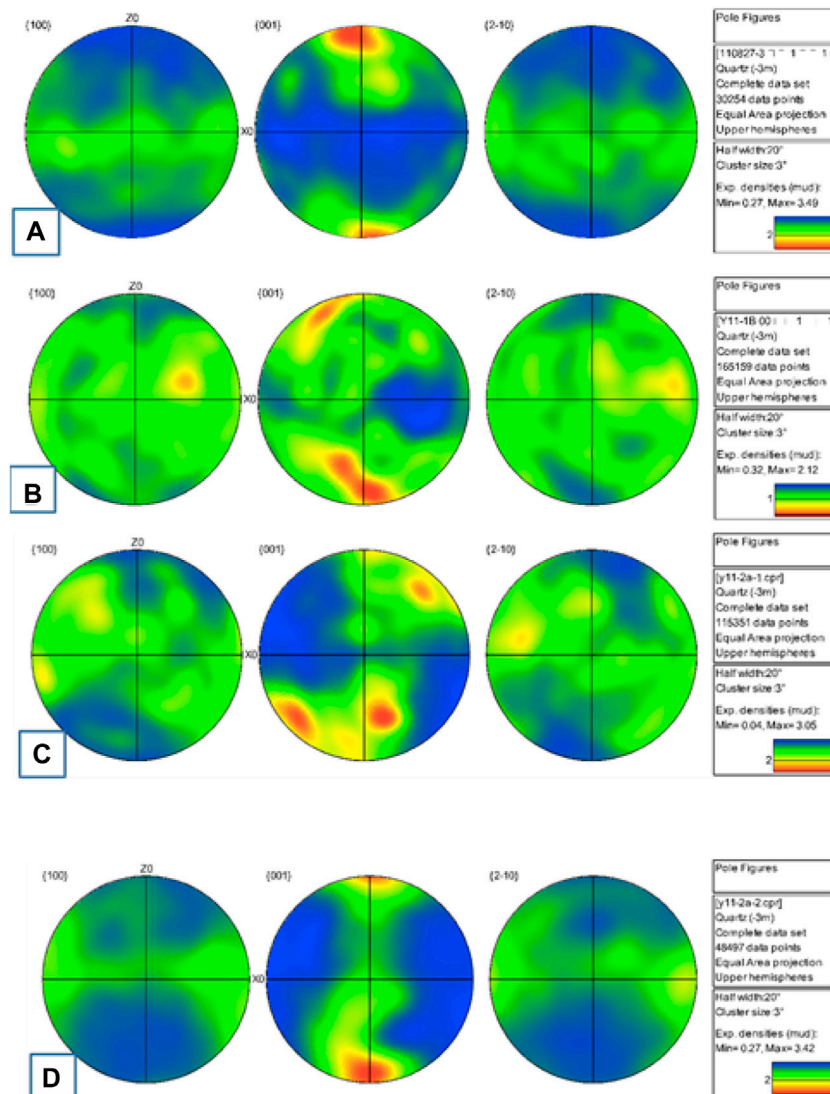


FIGURE 6 | Quartz fabric from EBSD in samples of pseudotachylite and cataclasite. **(A)** Thin section of 110827-3, **(B)** thin section of Y11-1B, **(C)** thin section of Y11-2A-1, **(D)** thin section of Y11-2A-2 (All sections were cut perpendicular to the XY plane of the mylonites, and different numbers –1 or –2 in a same sample was parallel or perpendicular to the X-axis).

features (Figure 5G), which is the product of carbonate-containing fluid precipitation in the cracks and the slow growth of calcite in the cracks during the later crack-healing stage. Under the scanning electron microscope, it can be observed that the feldspar phenocrysts have crushed cracks (Figures 5K, 5L). The mineral composition and composition variations of the phenocrysts are very complicated. The whole grain is feldspar-shaped (Figure 5K), and the veins are filled with quartz and calcite veins. The matrix of fine-grained feldspar and quartz were cemented with anhedral calcite, plagioclase dissolves into albite, and is partially replaced by amphibole due to reaction with mafic-rich fluid amphibole. These characteristics indicate that the solution and precipitation occurred in the fragmentation of rocks accompanied by the action of fluid after the cataclastic process.

4.2.2 Electron Backscatter Diffraction Fabric of Quartz for Samples of Pseudotachylite and Cataclasite

All of the pseudotachylite and cataclasite samples were mapped by EBSD. Images of micro-structures for four sections were given. For pseudotachylite samples, EBSD analysis focuses on locations of cataclasite beside the pseudotachylite vein.

In 110827-3 (Figure 6A), the c-axes of quartz minerals are distributed in the north and south poles, showing basal $\langle a \rangle$ slip, which is the result of low temperature deformation. In sample Y11-1B (Figure 6B), the c-axes of quartz show a dense concentration of intensive areas and no obvious dense concentration. In Y11-2A-1 (Figure 6C), the c-axes of quartz are distributed in the north and south poles, showing that the slip system is basal $\langle a \rangle$ slip with low temperature deformation too.

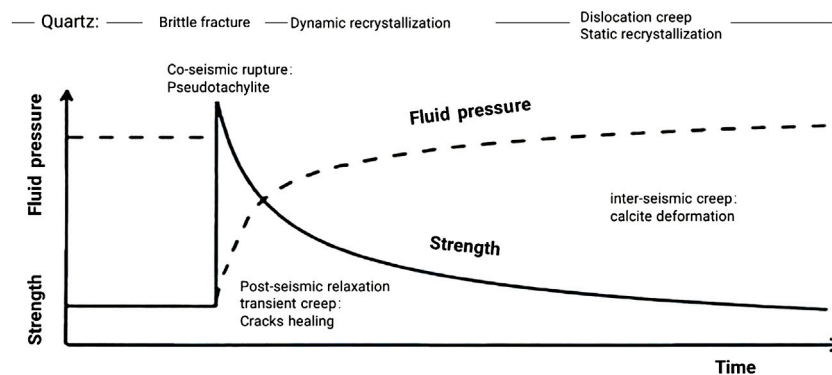


FIGURE 7 | Transient creep model of quartz from co-seismic rupture and post-seismic relaxation to inter-seismic ductile in the brittle-plastic transition of Red River fault (modified from Treppmann and Stöckhert, 2003).

5 DISCUSSION

The dominant sliding system of quartz is the basal sliding, the rhomb sliding, and the prism sliding in turn when the temperature is from low to high or the strain rate is from high to low (Schmid and Casey, 1986; Toy et al., 2008). Under a high-temperature environment, with the increase of the differential stress, the sliding system is the basal $\langle a \rangle$, rhomb $\langle a \rangle$, prism $\langle a \rangle$, and prism $\langle c \rangle$ (Schmid and Casey, 1986; Ji, 1988; Toy et al., 2008; Xia and Liu, 2011). During the ductile deformation of quartz, under the conditions of low temperature (250–400°C), it mainly creeps through the basal $\langle a \rangle$ dislocation slip system; under the conditions of medium temperature (450–600°C), it mainly creeps through the prism $\langle a \rangle$ dislocation slip system; and under high temperature (600–700°C), it mainly creeps through the prism $\langle c \rangle$ dislocation slip system (Schmid and Casey, 1986; Ji, 1988; Heidelbach et al., 2000; Toy et al., 2008; Ábalos et al., 2011). The quartz c -axes pole figure can be used to analyze the slip system inside the crystal to determine its deformation temperature.

The EBSD data show that the slip system of quartz in mylonite samples are basal $\langle a \rangle$ slip and prism $\langle a \rangle$ slip, which display quartz deformed under low-to-medium temperature conditions (250–600°C). EBSD data of quartz in cataclasite samples show basal $\langle a \rangle$ slip only, indicating that the samples deformed under low-temperature deformation environment (250–400°C) which is consistent with Wintsch and Yeh (2013) and Cao et al. (2017). However, EBSD data of quartz in pseudotachylyte does not show an obvious orientation. The EBSD data are consistent with microstructures under optical microscope and SEM.

The medium-to-high temperature deformation of mylonite corresponds to the rheology of ductile layers of the fault zone during the inter-seismic period, while the low-temperature deformation of quartz corresponds to transient creep of the brittle-plastic transition zone of fault. The cataclasite and pseudotachylyte are the results during co-seismic rupture which were superimposed on mylonite. The cracks' healing by quartz and calcite veins in the cataclasite and pseudotachylyte

represents deformation behavior during the post-seismic relaxation period.

Based on microstructures and quartz fabrics of EBSD in this study, we recommend the deformation model of Red River fault for the earthquake period (Figure 7). (1) During the inter-seismic period, the plastic layer in the fault underwent ductile shear deformation to form fine-grained mylonite and ocular-shaped mylonite; (2) as the stress continued to accumulate, when the stress reached the fault strength, the rocks underwent co-seismic rupture, pseudotachylyte was produced at co-seismic friction slip, and the cataclastic process occurred; (3) and in the subsequent stress relaxation stage, high stress and high strain rate caused feldspar in the rocks to continue to undergo brittle fracture, but fluid filled the cracks which caused healing by quartz and calcite, accompanied by pressure solution. (4) With the gradual stress relaxation, minerals such as quartz and calcite in the cracks transform into static recrystallization, which induced cracks to heal and stress to accumulate; the strength of the fault gradually increases, accumulating energy for the next earthquake.

6 CONCLUSION

Deformation recorded by pseudotachylyte-mylonites in the Red River fault indicates transient creep from inter-seismic ductile to co-seismic rupture. Based on the microstructures and quartz fabrics, we distinguished between different deformations of the brittle-plastic transition zone during the earthquake cycle. 1) Bulge recrystallization with basal $\langle a \rangle$ slip and sub-grain recrystallization with prism $\langle a \rangle$ slip of quartz in samples of mylonite, which are typical fabrics at the low-to-medium temperature dislocation creep, representing inter-seismic ductile shear of fault under the conditions of low stress and low strain rate. 2) Cataclasite and pseudotachylyte which were produced by brittle fracture and frictional melting during co-seismic rupture. 3) Crack healing and pressure solution, as well as plastic deformation of calcite, static recrystallization of quartz, and calcite in the veins, which are results of transient creep at the

post-seismic relaxation period. The oscillation deformation model adapted from Trepmann and Stöckhert (2003) could be used to explain transient creep of the brittle–plastic transition zone during the seismic cycle in the Red River fault.

DATA AVAILABILITY STATEMENT

The original contributions presented in the study are included in the article/Supplementary Material, further inquiries can be directed to the corresponding author.

AUTHOR CONTRIBUTIONS

ZY contributed to conception, collection of samples, and design of this study. DW conducted the experiments, DW and ZY wrote the

manuscript. MX guided the use of instruments and discussed the results of SEM and EBSD. All authors contributed to manuscript revision, and read and approved the submitted version.

FUNDING

This research was funded by the National Natural Science Foundation of China (41772223) and National Key Research and Development Project (2018YFC1503404).

ACKNOWLEDGMENTS

We thank prof. Lidong Dai of the Editor and three reviewers for a thoughtful review. We also thank Prof. Changrong He, Prof. Shimamoto, and Prof. Xiaosong Yang for the field works.

REFERENCES

- Ábalos, B., Puelles, P., Fernández-Armas, S., and Sarrionandia, F. (2011). EBSD Microfabric Study of Pre-Cambrian Deformations Recorded in Quartz Pebbles from the Sierra de la Demanda (N Spain). *J. Struct. Geol.* 33, 500–518. doi:10.1016/j.jsg.2011.01.005
- Bestmann, M., Pennacchioni, G., Frank, G., Göken, M., and de Wall, H. (2011). Pseudotachylyte in Muscovite-Bearing Quartzite: Coseismic Friction-Induced Melting and Plastic Deformation of Quartz. *J. Struct. Geol.* 33, 169–186. doi:10.1016/j.jsg.2010.10.009
- Bestmann, M., Pennacchioni, G., Nielsen, S., Göken, M., and de Wall, H. (2012). Deformation and Ultrafine Dynamic Recrystallization of Quartz in Pseudotachylyte-Bearing Brittle Faults: A Matter of a Few Seconds. *J. Struct. Geol.* 38, 21–38. doi:10.1016/j.jsg.2011.10.001
- Brace, W. F., and Kohlstedt, D. L. (1980). Limits on Lithospheric Stress Imposed by Laboratory Experiments. *J. Geophys. Res.* 85, 6248–6252. doi:10.1029/jb085ib11p06248
- Camacho, A., Vernon, R. H., and Fitz Gerald, J. D. (1995). Large Volumes of Anhydrous Pseudotachylyte in the Woodroffe Thrust, Eastern Musgrave Ranges, Australia. *J. Struct. Geol.* 17, 371–383. doi:10.1016/0191-8141(94)00069-c
- Campbell, L. R., and Menegon, L. (2019). Transient High Strain Rate during Localized Viscous Creep in the Dry Lower Continental Crust (Lofoten, Norway). *J. Geophys. Res. Solid Earth* 124, 10240–10260. doi:10.1029/2019jb018052
- Cao, S., Liu, J., Leiss, B., Neubauer, F., Genser, J., and Zhao, C. (2011b). Oligo-Miocene Shearing along the Ailao Shan-Red River Shear Zone: Constraints from Structural Analysis and Zircon U/Pb Geochronology of Magmatic Rocks in the Diancang Shan Massif, SE Tibet, China. *Gondwana Res.* 19, 975–993. doi:10.1016/j.gr.2010.10.006
- Cao, S., Liu, J., Leiss, B., Vollbrecht, A., Genser, J., Neubauer, F., et al. (2012). Initiation of Left-Lateral Deformation along the Ailao Shan-Red River Shear Zone: New Microstructural, Textural, and Geochronological Constraints from the Diancang Shan Metamorphic Massif, SW Yunnan, China. *Int. Geol. Rev.* 54, 348–367. doi:10.1080/00206814.2010.543789
- Cao, S., Neubauer, F., Liu, J., Bernroider, M., Cheng, X., Li, J., et al. (2017). Rheological Weakening of High-Grade Mylonites during Low-Temperature Retrogression: The Exhumed Continental Ailao Shan-Red River Fault Zone, SE Asia. *J. Asian Earth Sci.* 139, 40–60. doi:10.1016/j.jseas.2016.10.002
- Cao, S., Neubauer, F., Liu, J., Genser, J., and Leiss, B. (2011a). Exhumation of the Diancang Shan Metamorphic Complex along the Ailao Shan-Red River Belt, Southwestern Yunnan, China: Evidence from 40 Ar/39 Ar Thermochronology. *J. Asian Earth Sci.* 42, 525–550. doi:10.1016/j.jseas.2011.04.017
- Chernak, L. J., Hirth, G., Selverstone, J., and Tullis, J. (2009). Effect of Aqueous and Carbonic Fluids on the Dislocation Creep Strength of Quartz. *J. Geophys. Res.* 114, B04201. doi:10.1029/2008jb005884
- Cowan, D. S. (1999). Do faults Preserve a Record of Seismic Slip? A Field Geologist's Opinion. *J. Struct. Geol.* 21, 995–1001. doi:10.1016/s0191-8141(99)00046-2
- Dai, W. H., and Zhou, Y. S. (2019). Deformation of the Brittle-Plastic Transition Zone at the Post-Seismic Relaxation Period: A Case Study of the Red River Fault. *Seismol. Geol.* 41 (4), 996–1011. doi:10.3969/j.issn.0253-4967.2019.04.012 (in Chinese with English Abstract)
- Gueydan, F., Leroy, Y. M., and Jolivet, L. (2004). Mechanics of Low-Angle Extensional Shear Zones at the Brittle-Ductile Transition. *J. Geophys. Res.* 109, B12407. doi:10.1029/2003jb002806
- Heidelbach, F., Kunze, K., and Wenk, H.-R. (2000). Texture Analysis of a Recrystallized Quartzite Using Electron Diffraction in the Scanning Electron Microscope. *J. Struct. Geol.* 22 (1), 91–104. doi:10.1016/s0191-8141(99)00125-x
- Hobbs, B. E., Ord, A., and Teyssier, C. (1986). Earthquakes in the Ductile Regime? *Pure Appl. Geophys.* 124, 309–336. doi:10.1007/bf00875730
- Ikari, M. J., Niemeijer, A. R., and Marone, C. (2011). The Role of Fault Zone Fabric and Lithification State on Frictional Strength, Constitutive Behavior, and Deformation Microstructure. *J. Geophys. Res.* 116, B08404. doi:10.1029/2011JB008264
- Ji, S. C. (1988). Dislocation Splitting in Main Rock-Forming Minerals and its Rheological Implications. *Geoscience* 1988 (4), 118–125. (in Chinese with English Abstract).
- Kim, J.-W., Ree, J.-H., Han, R., and Shimamoto, T. (2010). Experimental Evidence for the Simultaneous Formation of Pseudotachylyte and Mylonite in the Brittle Regime. *Geology* 38, 1143–1146. doi:10.1130/G31593.1
- Kohlstedt, D. L., Evans, B., and Mackwell, S. J. (1995). Strength of the Lithosphere: Constraints Imposed by Laboratory Experiments. *J. Geophys. Res.* 100 (B9), 17587–17602. doi:10.1029/95jb01460
- Leloup, P. H., and Kienast, J.-R. (1993). High-Temperature Metamorphism in a Major Strike-Slip Shear Zone: The Ailao Shan-Red River, People's Republic of China. *Earth Planet. Sci. Lett.* 118, 213–234. doi:10.1016/0012-821x(93)90169-a
- Leloup, P. H., Lacassin, R., Tapponnier, P., Schärer, U., Zhong, D., Liu, X., et al. (1995). The Ailao Shan-Red River Shear Zone (Yunnan, China), Tertiary Transform Boundary of Indochina. *Tectonophysics* 251, 3–84. doi:10.1016/0040-1951(95)00070-4
- Li, W., Cao, S., Zhan, L., Cheng, X., Li, W., and Lyu, M. (2022). Crush-Origin Pseudotachylyte in Granitic Mylonites of Continental Exhumed Ailaoshan-Red River Shear Zone Southeastern Asia. *J. Struct. Geol.* 159, 104606. doi:10.1016/j.jsg.2022.104606
- Lin, A., Maruyama, T., Aaron, S., Michibayashi, K., Camacho, A., and Kano, K.-I. (2005). Propagation of Seismic Slip from Brittle to Ductile Crust: Evidence from Pseudotachylyte of the Woodroffe Thrust, Central Australia. *Tectonophysics* 402, 21–35. doi:10.1016/j.tecto.2004.10.016
- Liu, J. L., Wang, A. J., Cao, S. Y., Zou, Y. X., Tang, Y., and Chen, Y. (2008). Geochronology and Tectonic Implication of Migmatites from Diancangshan, Western Yunnan, China. *Acta Petrol. Sin.* 24, 413–420. doi:10.1016/j.sedgeo.2008.02.002

- Liu, Y. P., Ye, L., Li, C. Y., Song, B., Li, T. S., Guo, L. G., et al. (2006). Discovery of the Neoproterozoic Magmatism in Southeastern Yunnan: Evidence from SHRIMP Zircon U–Pb Dating and Lithogeochemistry. *Acta Petrol. Sin.* 22, 916–926. doi:10.1016/j.sedgeo.2005.11.021
- McKenzie, D., and Brune, J. N. (1972). Melting on Fault Planes during Large Earthquakes. *Geophys. J. Int.* 29, 65–78. doi:10.1111/j.1365-246x.1972.tb06152.x
- Moecher, D. P., and Steltenpohl, M. G. (2009). Direct Calculation of Rupture Depth for an Exhumed Paleoseismogenic Fault from Mylonitic Pseudotachylyte. *Geology* 37, 999–1002. doi:10.1130/G30166A.1
- Molnar, P., and Tapponnier, P. (1975). Cenozoic Tectonics of Asia: Effects of a Continental Collision: Features of Recent Continental Tectonics in Asia Can Be Interpreted as Results of the India-Eurasia Collision. *Science* 189 (4201), 419–426. doi:10.1126/science.189.4201.419
- Molnar, P., and Tapponnier, P. (1977). Relation of the Tectonics of Eastern China to the India-Eurasia Collision: Application of Slip-Line Field Theory to Large-Scale Continental Tectonics. *Geology* 5 (4), 212–216. doi:10.1130/0091-7613(1977)5<212:rottoe>2.0.co;2
- Montési, L. G. J., and Zuber, M. T. (2002). A Unified Description of Localization for Application to Large-Scale Tectonics. *J. Geophys. Res.* 107, ECV1.1–ECV1.21. doi:10.1029/2001JB000465
- Nevitt, J. M., Warren, J. M., and Pollard, D. D. (2017). Testing Constitutive Equations for Brittle-Ductile Deformation Associated with Faulting in Granitic Rock. *J. Geophys. Res. Solid Earth* 122, 6269–6293. doi:10.1002/2017JB014000
- Papa, S., Pennacchioni, G., Menegon, L., and Thielmann, M. (2020). High-Stress Creep Preceding Coseismic Rupturing in Amphibolite-Facies Ultramylonites. *Earth Planet. Sci. Lett.* 541, 116260. doi:10.1016/j.epsl.2020.116260
- Passchier, C. W. (1982). Pseudotachylyte and the Development of Ultramylonite Bands in the Saint-Barthélemy Massif, French Pyrenees. *J. Struct. Geol.* 4, 69–79. doi:10.1016/0191-8141(82)90008-6
- Pennacchioni, G., and Cesare, B. (1997). Ductile-Brittle Transition in Pre-Alpine Amphibolite Facies Mylonites during Evolution from Water-Present to Water-Deficient Conditions (Mont Mary Nappe, Italian Western Alps). *J. Metamorph. Geol.* 15, 777–791. doi:10.1111/j.1525-1314.1997.00055.x
- Pennacchioni, G., Di Toro, G., Brack, P., Menegon, L., and Villa, I. M. (2006). Brittle-Ductile-Brittle Deformation during Cooling of Tonalite (Adamello, Southern Italian Alps). *Tectonophysics* 427, 171–197. doi:10.1016/j.tecto.2006.05.019
- Schmid, S. M., and Casey, M. (1986). Complete Fabric Analysis of Some Commonly Observed Quartz C-Axis Patterns. *Geophys. Monogr.* 36, 263–286. doi:10.1029/gm036p0263
- Scholz, C. H. (1988). The Brittle-Plastic Transition and the Depth of Seismic Faulting. *Geol. Rundsch.* 77, 319–328. doi:10.1007/bf01848693
- Sibson, R. H. (1983). Continental Fault Structure and the Shallow Earthquake Source. *J. Geol. Soc.* 140, 741–767. doi:10.1144/gsjgs.140.5.0741
- Sibson, R. H. (1975). Generation of Pseudotachylyte by Ancient Seismic Faulting. *Geophys. J. Int.* 43, 775–794. doi:10.1111/j.1365-246x.1975.tb06195.x
- Sibson, R. H. (1980). Transient Discontinuities in Ductile Shear Zones. *J. Struct. Geol.* 2, 165–171. doi:10.1016/0191-8141(80)90047-4
- Song, B. R., Johnson, S. E., Song, W. J., Gerbi, C. C., and Yates, M. G. (2020). Coseismic Damage Runs Deep in Continental Strike-Slip Faults. *Earth Planet. Sci. Lett.* 539, 116226. doi:10.1016/j.epsl.2020.116226
- Takagi, H., Goto, K., and Shigematsu, N. (1999). Ultramylonite Bands Derived from Cataclasite and Pseudotachylyte in Granites, Northeast Japan. *J. Struct. Geol.* 22, 1325–1339.
- Tapponnier, P., Peltzer, G., and Armijo, R. (1986). On the Mechanics of the Collision between India and Asia. *Geol. Soc. Spec. Publ.* 19, 115–157. doi:10.1144/gsl.sp.1986.019.01.07
- Tapponnier, P., Peltzer, G., Le Dain, A. Y., Armijo, R., and Cobbold, P. (1982). Propagating Extrusion Tectonics in Asia: New Insights from Simple Experiments with Plasticine. *Geology* 10, 611–616.
- Toy, V. G., David, J. P., and Richard, J. N. (2008). Quartz Fabrics in the Alpine Fault Mylonites: Influence of Pre-Existing Preferred Orientations on Fabric Development during Progressive Uplift. *J. Struct. Geol.* 30, 602–621. doi:10.1016/j.jsg.2008.01.001
- Trepmann, C. A., Hsu, C., Hentschel, F., Döhler, K., Schneider, C., and Wichmann, V. (2017). Recrystallization of Quartz after Low-Temperature Plasticity - The Record of Stress Relaxation below the Seismogenic Zone. *J. Struct. Geol.* 95, 77–92. doi:10.1016/j.jsg.2016.12.004
- Trepmann, C. A., Stöckhert, B., Dorner, D., Moghadam, R. H., Küster, M., and Röller, K. (2007). Simulating Coseismic Deformation of Quartz in the Middle Crust and Fabric Evolution during Postseismic Stress Relaxation - An Experimental Study. *Tectonophysics* 442, 83–104. doi:10.1016/j.tecto.2007.05.005
- Trepmann, C. A., and Stöckhert, B. (2003). Quartz Microstructures Developed during Non-Steady State Plastic Flow at Rapidly Decaying Stress and Strain Rate. *J. Struct. Geol.* 25, 2035–2051. doi:10.1016/s0191-8141(03)00073-7
- Trepmann, C. A., and Stöckhert, B. (2013). Short-Wavelength Undulatory Extinction in Quartz Recording Coseismic Deformation in the Middle Crust - an Experimental Study. *J. Geophys. Res. Solid Earth* 4, 263–276. doi:10.5194/se-4-263-2013
- Tse, S. T., and Rice, J. R. (1986). Crustal Earthquake Instability in Relation to the Depth Variation of Frictional Slip Properties. *J. Geophys. Res.* 91, 9452–9472. doi:10.1029/jb091ib09p09452
- Tullis, J., and Yund, R. (1992). “Chapter 4 the Brittle-Ductile Transition in Feldspar Aggregates: An Experimental Study,” in *Fault Mechanisms and Transport Properties of Rocks*. Editors B. Evans and T.-F. Wong (New York: Academic Press), 89–117. doi:10.1016/s0074-6142(08)62816-8
- White, J. C. (2012). Paradoxical Pseudotachylyte - Fault Melt outside the Seismogenic Zone. *J. Struct. Geol.* 38, 11–20. doi:10.1016/j.jsg.2011.11.016
- White, J. C. (1996). Transient Discontinuities Revisited: Pseudotachylyte, Plastic Instability and the Influence of Low Pore Fluid Pressure on Deformation Processes in the Mid-Crust. *J. Struct. Geol.* 18, 1471–1486. doi:10.1016/s0191-8141(96)00059-4
- Wintsch, R. P., and Yeh, M.-W. (2013). Oscillating Brittle and Viscous Behavior through the Earthquake Cycle in the Red River Shear Zone: Monitoring Flips between Reaction and Textural Softening and Hardening. *Tectonophysics* 587, 46–62. doi:10.1016/j.tecto.2012.09.019
- Xia, H. R., and Liu, J. L. (2011). The Crystallographic Preferred Orientation of Quartz and its Applications. *Geol. Bull. China* 30 (1), 58–70. doi:10.3969/j.issn.1671-2552.2011.01.006 (in Chinese with English Abstract)
- Zhou, Y. S., Han, L., Jing, C., He, C.-R., and Dang, J. (2014). The Rheological Structures of Brittle-Plastic Transition in Longmenshan Fault Zone and Seismogenic Mechanism of Wenchuan Earthquake. *Seismol. Geol.* 36 (3), 882–895. (in Chinese with English Abstract). doi:10.3969/j.issn.0253-4967.2014.03.025

Conflict of Interest: The authors declare that the research was conducted in the absence of any commercial or financial relationships that could be construed as a potential conflict of interest.

Publisher's Note: All claims expressed in this article are solely those of the authors and do not necessarily represent those of their affiliated organizations, or those of the publisher, the editors, and the reviewers. Any product that may be evaluated in this article, or claim that may be made by its manufacturer, is not guaranteed or endorsed by the publisher.

Copyright © 2022 Dai, Zhou and Ma. This is an open-access article distributed under the terms of the Creative Commons Attribution License (CC BY). The use, distribution or reproduction in other forums is permitted, provided the original author(s) and the copyright owner(s) are credited and that the original publication in this journal is cited, in accordance with accepted academic practice. No use, distribution or reproduction is permitted which does not comply with these terms.



OPEN ACCESS

EDITED BY
Nibir Mandal,
Jadavpur University, India

REVIEWED BY
Qin Wang,
Nanjing University, China
Qiaomu Qi,
Chengdu University of Technology,
China

*CORRESPONDENCE
Lidong Dai,
dailidong@vip.gyig.ac.cn

SPECIALTY SECTION
This article was submitted to Solid Earth
Geophysics,
a section of the journal
Frontiers in Earth Science

RECEIVED 04 July 2022
ACCEPTED 12 August 2022
PUBLISHED 30 August 2022

CITATION
Hu H, Jing C, Dai L, Yin C and Chen D
(2022), Electrical conductivity of siderite
and its implication for high conductivity
anomaly in the slab-mantle
wedge interface.
Front. Earth Sci. 10:985740.
doi: 10.3389/feart.2022.985740

COPYRIGHT
© 2022 Hu, Jing, Dai, Yin and Chen. This
is an open-access article distributed
under the terms of the [Creative
Commons Attribution License \(CC BY\)](#).
The use, distribution or reproduction in
other forums is permitted, provided the
original author(s) and the copyright
owner(s) are credited and that the
original publication in this journal is
cited, in accordance with accepted
academic practice. No use, distribution
or reproduction is permitted which does
not comply with these terms.

Electrical conductivity of siderite and its implication for high conductivity anomaly in the slab-mantle wedge interface

Haiying Hu¹, Chenxin Jing^{1,2}, Lidong Dai^{1*}, Chuanyu Yin^{1,2} and Dongmei Chen³

¹Key Laboratory for High-Temperature and High-Pressure Study of the Earth's Interior, Institute of Geochemistry, Chinese Academy of Sciences, Guiyang, Guizhou, China, ²University of Chinese Academy of Sciences, Beijing, China, ³Key Laboratory of Macrocyclic and Supramolecular Chemistry of Guizhou Province, Guizhou University, Guiyang, China

Carbonate minerals as a dominant carbon host can be transported to the Earth's deep interior *via* subduction of the oceanic lithosphere, and their physicochemical behavior potentially has a significant influence on the compositional heterogeneity and physical properties in the deep mantle. In this study, we measured the electrical conductivity of natural siderite at 1–3 GPa and 100–700°C using a complex impedance analyzer in a large volume multi-anvil high-pressure apparatus. A sharp increase in conductivity was observed at ~400°C under various pressures, and subsequently, the electrical conductivity keeps anomalously high values in the whole temperature range owing to a small quantity of interconnected highly conductive phases (graphite and magnetite) produced from the low degree decarbonation of siderite. The change in electrical conductivity and activation enthalpy suggest that the conduction mechanisms before and after low degree decarbonation of siderite are the small polaron (electron hopping in Fe²⁺–Fe³⁺) and highly conductive phases, respectively. Our results indicate the incipient decarbonation temperatures at 1–3 GPa are considerably lower than the decomposition boundary of siderite determined by phase equilibrium experiments, implying the initial decarbonation reaction of Fe-bearing carbonates in the subducting oceanic crust occurs at a shallower depth. The 30 vol.% of siderite is required to enhance the electrical conductivity of (Mg, Fe)CO₃ solid solutions. Magnetite and graphite generated from the decarbonation reaction of the siderite component of Fe-bearing carbonate make a significant contribution to the high conductivity anomaly observed in the slab-mantle wedge interface.

KEYWORDS

electrical conductivity, siderite, decarbonation, highly conductive anomaly, slab-mantle wedge interface

Introduction

Carbonates are the main phases of carbon-bearing materials that can be transported into the deep Earth mantle *via* subduction of the oceanic crust. Since carbon has very low solubility in the mantle silicate minerals (Keppler et al., 2003), carbonate minerals are regarded as one of the dominant hosts for carbon in the deep mantle that even can be stable in the transition zone or lower mantle as new high-pressure carbon-bearing phases (Boulard et al., 2011; Liu et al., 2015; Cerantola et al., 2017). Simultaneously, the decomposition, melting, and dissolution of carbonates in the slab-released aqueous fluid can lead to the carbon released to Earth's surface *via* volcanism. Therefore, carbonate minerals play an important role in the global deep carbon cycle (Alt and Teagle, 1999; Sverjensky et al., 2014; Thomson et al., 2016; Farsang et al., 2021). The change of state for carbonates during the subduction process dramatically affects the physical and chemical properties of the subducting oceanic crust and the mantle, including lower the melting point (solidus) (Dasgupta et al., 2004; Dasgupta and Hirschmann, 2006, 2007; Ghosh et al., 2009), redox state (Luth, 1993), and electrical structure (Gaillard et al., 2008; Sifré et al., 2015). In particular, the electrical conductivity of carbonates is of principal importance for exploring the carbon storage and spatial distribution in the Earth's interior in conjunction with geophysical surveys (electromagnetic data, seismic velocity) and petrologic studies.

Most of the previous conductivity measurements for carbonate minerals have been mainly performed on (Mg, Ca) CO₃ samples (e.g., calcite, magnesite, dolomite, aragonite, etc.) at high temperature and high pressure, and primarily focused on the discussion on the effect of temperature and pressure on conductivity in order to quantify their nature of transport mechanism (Papathanassiou and Grammatikakis, 1996; Papathanassiou, 1998; Ter Heege and Renner, 2007; Mibe and Ono, 2011; Ono and Mibe, 2013; Ono and Mibe, 2015). These experimental results have indicated that Mg-Ca carbonate minerals have a relatively low conductivity value within their stability and hardly make a pronounced contribution to the electrical structure of the surrounding mantle. However, the presence of iron has a crucial effect on the thermodynamic stability of carbonate phases, and the high-pressure experimental results have demonstrated that the stability of Fe-bearing carbonate (i.e., dolomite-ankerite and magnesite-siderite solid solutions) dramatically decreases with increasing Fe content (Dubrawaski, 1991; Tao et al., 2013; Tao et al., 2014; Bataleva et al., 2020). Accordingly, the incorporation of iron into carbonates potentially has an essential effect on the electrical conductivity of carbonate minerals owing to its multiple valence states, unlike Fe-free counterparts in which their cations do not oxidize. However, until now, the electrical conductivity of Fe-bearing carbonate has not yet been reported in high temperature and pressure experiments.

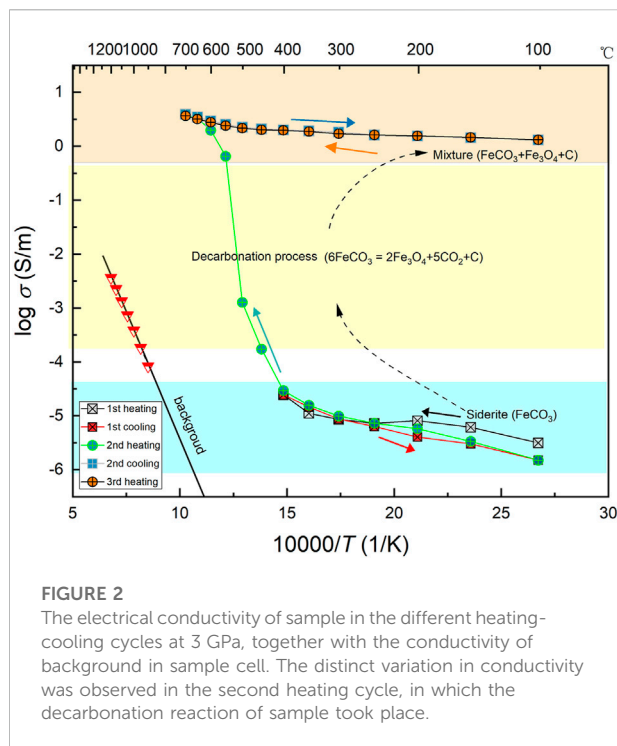
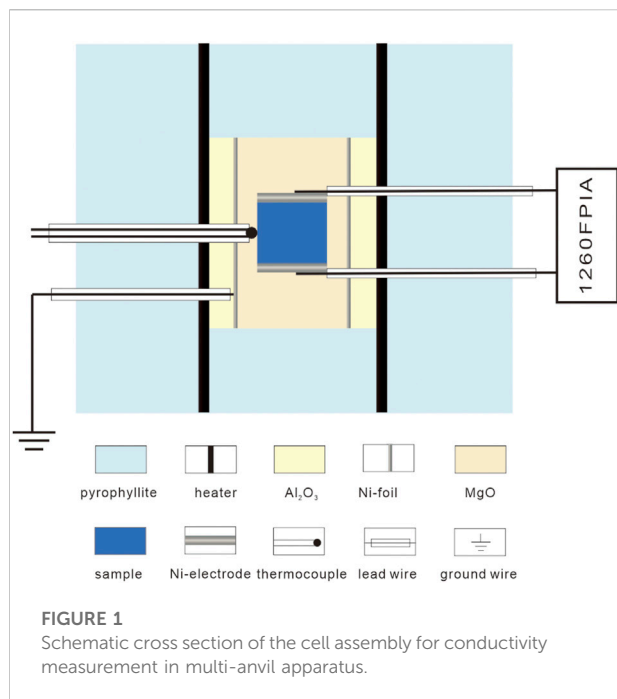
Siderite (FeCO₃), as the end-member of (Mg, Ca, Fe)CO₃ carbonate, can form a continuous solid solution with magnesite (MgCO₃) in rocks, which can be extensively outcropped in the regions of subducted carbonated oceanic and continental crust (Zhu and Ogasawara, 2002; Tao et al., 2013). The study on the siderite stability has revealed that the decomposition temperature is much lower than that of magnesite by several hundred degrees Celsius, simultaneously, the reaction products, i.e., iron oxides (wüstite, magnetite, and hematite) and carbon species (graphite, CO, and CO₂) strongly depend on oxygen fugacity (Kozioł, 2004; Tao et al., 2013). These highly conductive phases from the thermal dissociation of Fe-bearing carbonate can be a good indicator of the storage and distribution of carbon in the Earth's interior if they could make a significant contribution to the high conductivity anomalies of the surrounding context observed by the geophysical probing. Consequently, the electrical conductivity of siderite plays a principal and fundamental role in evaluating the effect of Fe content on the conductivity of Fe-bearing carbonate minerals, and the corresponding measurement of siderite is urgently requires at present for systematically understanding the electrical property of carbonate minerals as well as for potentially detecting the carbon storage and distribution in the mantle.

In this study, we carried out the *in-situ* electrical conductivity measurements of siderite at pressures of 1–3 GPa and temperatures up to 700°C in a multi-anvil high-pressure apparatus using the complex impedance spectroscopy under controlling oxygen fugacity condition. The low degree decarbonation of siderite was observed through the marked variation of electrical conductivity during the heating process, and the reaction products were determined and quantified by the integrated analysis in a combination of confocal Raman spectroscopy and TESCAN Integrated Mineral Analyzer (TIMA). Additionally, the microscopic conduction behavior before and after partial decomposition of siderite was clarified. The potential contribution of siderite decarbonation to the origin of the high conductivity anomaly observed at the slab-mantle wedge interface was discussed in detail.

Experimental procedure

Sample preparation

The starting materials for the electrical conductivity experiments are natural polycrystalline siderite aggregates, which were commercially purchased from the geological specimen incorporation. The massive block sample with a grayish-yellow color is fresh and unaltered with trace amounts of pyrite. The starting sample was confirmed to be siderite by the laser Raman spectroscopy measurement. The chemical composition of siderite was accurately determined by the electron probe microanalysis (EPMA) using a JEOL-JXA-



8230 electron microprobe operating at a 25 kV accelerating voltage and a beam current of 10 nA at the State Key Laboratory of Ore-Deposit Geochemistry in the Institute of Geochemistry, CAS, Guiyang, China. The result is given in [Supplementary Table S1](#). The sample contains small amounts of Mg^{2+} and Mn^{2+} , and its corresponding molecular formula is determined as $\text{Fe}_{0.88}\text{Mn}_{0.03}\text{Mg}_{0.09}\text{CO}_3$ that is close to the end-member of Fe-carbonate. During the conductivity preparation process, the sample was to first cut into cubic pieces using a diamond low-speed slicer, then polished into cylinders (diameter: 6 mm, height: 6.0–6.5 mm) in a diamond disc grinder. During these processes, water was adopted as the lubricant and cooling liquid in order to avoid the possible oxidation of siderite owing to the friction heat produced in the course of cutting and polishing. The cylindrical samples are successively ultrasonically cleaned in acetone and ethanol for 10 min, and finally dried at the temperature of 60°C in the dry vacuum furnace to remove the absorbed water that possibly affects the electrical conductivity measurement.

Electrical conductivity measurements and data analysis

Electrical conductivity experiments were carried out in a conventional large volume multi-anvil high-pressure apparatus installed in the Key Laboratory of High-Pressure Study of the Earth's interior, Institute of Geochemistry, CAS, China. The design of sample cell assembly for conductivity measurement

is shown in [Figure 1](#), which is analogous to our previous work ([Hu et al., 2018](#)). The cubic pyrophyllite with each edge length of 32.5 mm was adopted as the pressure-transmitting medium. Since the stability of siderite is closely associated with oxygen fugacity due to the presence of ferrous iron, the oxygen fugacity is indispensable to be sufficiently controlled during conductivity measurements at high temperatures and pressure. In this study, a nickel foil placed between MgO and Al_2O_3 insulative sleeves as well as two symmetric Ni electrodes directly contacted with the sample were adopted to control oxygen fugacity close to the nickel-nickel oxide (NNO) buffer, which is generally corresponding to redox environments in the subduction zone and upper mantle. In addition, the Ni foil grounding is also used as a shield preventing the external electromagnetic disturbance from the heating current. The sample was surrounded by the MgO sleeve. The Al_2O_3 cylindrical sleeve is placed between the MgO sleeve and the heater that is consisted of three-layer stainless steel, so as to maintain a good insulation environment around the sample. The temperature was controlled using a K-type ($\text{Ni}_{90}\text{Cr}_{10}$ – $\text{Ni}_{97}\text{Al}_3$) thermocouple, in which of one end was welded to a small ball in direct contact with the middle of the sample. The temperature gradient was not more than 5°C between the middle and end of the sample.

Complex impedance spectra measurements were performed over 100–700°C and 1–3 GPa by virtue of a Solartron-1260 Impedance/Gain-Phase analyzer in a YJ-3000t multi-anvil apparatus. The applied signal voltage is 1 V and the frequency for the electrical conductivity measurement is scanning within

TABLE 1 Experimental conditions and the Arrhenius fitting parameters for the electrical conductivity of siderite ($\text{Fe}_{0.88}\text{Mn}_{0.03}\text{Mg}_{0.09}\text{CO}_3$) before decomposition and after partly decomposition as well as previous results of other carbonate minerals.

Run No.	<i>P</i> (GPa)	<i>T</i> (°C) Before DCP	$\log \sigma_0$ (S/m)	ΔH (eV)	ΔU (eV)	ΔV (cm ³ /mole)	<i>T</i> (°C) After DCP	$\log \sigma_0$ (S/m)	ΔH (eV)	Comments
YJ206	1	100–350	0.64 (20)	0.49 (2)			100–500	1.96	0.08	Sd(94) + Mag(4.37) + Gr(1.63)
YJ207	2	100–400	−1.79 (20)	0.32 (2)	0.64	−14.47	100–600	2.05	0.01	Sd(88.5) + Mag(10.16) + Gr(1.34)
YJ208	3	100–400	−3.19 (16)	0.20 (1)			100–700	0.74	0.05	Sd(98.7) + Mag(0.83) + Gr(0.47)
Dol, $\text{Mg}_{0.48}\text{Ca}_{0.52}\text{CO}_3$	4.5–6.0	377–727			1.64	−1.00				OM15
Mgs, MgCO_3	3–6	377–727			1.76	−3.95				MO11
Arg, CaCO_3	3–6	527–727			0.40	9.28				OM13

References: OM15: Ono and Mibe (2015); OM13: Ono and Mibe (2013); MO11: Mibe and Ono (2011). Abbreviations: DCP, decarbonation process; Dol, dolomite; Mgs, magnesite; Arg, aragonite, Sd, siderite; Gr, graphite. The numbers in parentheses after the minerals in the last column represent the volume percentage of each mineral phases in samples after conductivity measurements determined from the TIMA, analysis.

the range of $10\text{--}10^6$ Hz. To ensure a high insulation environment around the sample, the background resistance was first assessed by replacing the sample with a cylindrical MgO that has the same dimension as the sample. Since the background resistance is too high to acquire good impedance data at low temperatures, impedance spectra of MgO were measured at relatively high temperatures (850–1,200°C). If extrapolated the background conductivity to low temperature, it is several orders of magnitude lower than the sample conductivity as shown in Figure 2, therefore, the good insulative background avoids the possible leakage current through the Al_2O_3 and MgO sleeves placed out of the sample.

For each run, when pressure reached the designated value, the temperature started to increase with a step of 50°C, and the impedance spectra were collected at 100–700°C with the same temperature interval. At various pressures, the maximum temperature for impedance measurement is different, as illustrated in Table 1. After the first heating-cooling cycle measurements, we found a large variation of impedance spectra with temperature, implying the possible occurrence of decarbonation in siderite. In order to obtain the conductivity within the stability of siderite and during the decomposition process, two different heating-cooling modes for conductivity measurements were employed: one is performed at the low-temperature ranges before the occurrence of decarbonation reaction, and another is temperature increases up to ~700°C after the completion of the first low-temperature cycle. Firstly, when the target pressure was reached, the impedance spectra were collected at temperatures of 100–400°C (or 350°C) in 50°C intervals, and the heating-cooling cycles in this temperature range were performed until the reproducibility of resistance values was acquired. Subsequently, the complex impedance spectra were collected in the successive heating-cooling cycles at 100–700°C with a temperature interval of 50°C. An abrupt variation of impedance arc was observed in the heating process at a temperature of ~400°C at different pressures, reflecting the

occurrence of siderite decomposition. In the subsequent heating-cooling cycles, the reproducible impedances were attained. After completion of the conductivity measurements, the sample was quenched by switching the heating current and slowly decompressed to room pressure. The experimental conditions are listed in Table 1 in detail.

The sample conductivity (σ , S/m) was calculated from the resistance and the geometric factor (l/S) using the equation, $\sigma = l/SR$, where l is the sample length (m), S is the electrode area (m²) that is equal to the cross-sectional area of the sample in our experiments, and R (Ω) is the measured resistance of sample obtained by the equivalent circuit fitting. The change in sample dimensions caused by thermal expansion and compression is very small by measuring the geometrical shape of the recovered sample, which almost can be neglected. The uncertainties from temperature and pressure on the sample conductivity owing to the thermal gradient along the length of the sample and the accuracy of pressure calibration, are not more than 5%. Consequently, the overall uncertainty of the sample conductivity values is estimated to be less than 8% including the fitting error (<3%) of impedance spectra for all measurements.

Sample characterization after experiments

The recovered samples were mounted in the epoxy resin, sectioned, and then polished for the sample characterization after electrical conductivity measurements. The chemical composition of the recovered sample at different pressures was determined by EPMA using JEOL-JXA-8230 electron microprobe, and the backscattered electron images (BSE) were simultaneously acquired, the results are given in Supplementary Table S1 and Supplementary Figure S1. Since the iron oxide appeared and the potential presence of carbon in voids was not efficiently identified by the EMPA analysis owing to the samples coated with carbon,

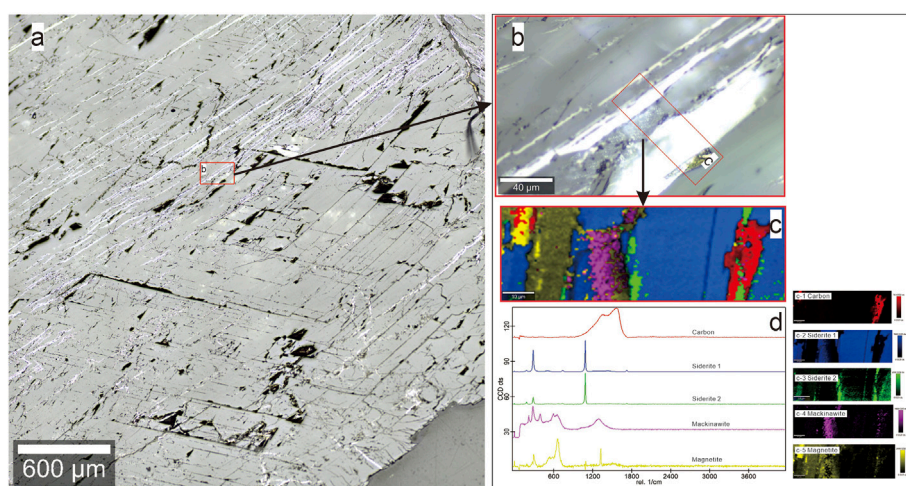


FIGURE 3

A representative Raman analysis results of the recovered siderite sample. **(A)** The optical microscope image showing the presence of microfracture and some new phases in siderite sample after high pressure. **(B)** The enlarged microscope image of the selected area in **(A)** and the red enframed region of **(C)** further analyzed. Combined false-color Raman image in **(C)**, and the colors correspond to the spectra shown in **(D)**. Scale bars are shown in each of images. After conductivity measurement, siderite is still the dominant phase with high abundances $\geq 88.5\%$, whereas it underwent low degree decarbonation reaction, generating a very small amount of highly conductive phases (graphite and magnetite). Additionally, mackinawite is probably present in the starting sample.

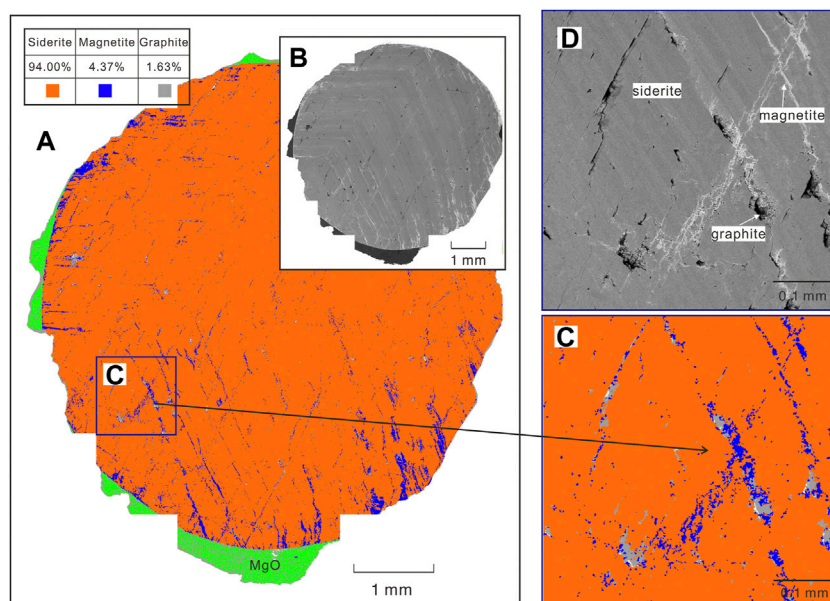
the confocal Raman imaging by the use of WITec alpha300R confocal Raman microscopy installed in the Key Laboratory of Macrocyclic and Supramolecular Chemistry of Guizhou Province, Guizhou University, China, was employed to confirm the iron oxide and carbon species as well as to investigate the spatial distribution of different mineral phases in sample. In Raman imaging, a confocal microscope was combined with a spectrometer, and Raman spectra were collected at every image pixel. The excitation wavelength and laser powers are 532 nm and 2.4 mW, respectively. The confocal signals are collected using a charge-coupled device thermoelectrically cooled to minus 60°C. The Raman data are analyzed by virtue of the WITec Project software package. A representative microscopic image and color-coded Raman image and corresponding spectra are shown in Figure 3, in which new phases coexisting with the siderite sample are observed and microfractures are present owing to compression crushing at high pressure. The released volatiles are evident from the voids.

In order to accurately quantify the mineral proportions after low degree decarbonization of siderite, the recently developed technique of TESCAN Integrated Mineral Analyzer (TIMA) was adopted, that is equipped with an automated quantitative analysis system for the mineral mass analysis and phase/mineral distribution mapping by the use of a fully integrated quantitative energy-dispersive X-ray spectrometry (EDS) and an advanced statistical approach to scanning electron microscopy (SEM) system. The TIMA analyses were completed at the Xi'an Kuangpu Geological Exploration Technology Co., Ltd. For the

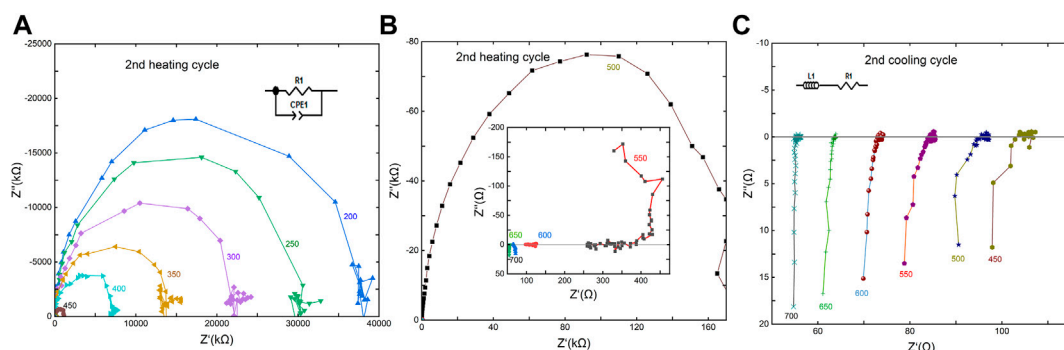
TIMA analyses, the recovered samples were cut and polished along the cross-section of the sample and coated with a thin gold layer. The high-resolution SEM images for the whole plane of the polished cross-section of the sample were used to determine the phase proportions. A representative TIMA analysis result from the sample at 1 GPa is shown in Figure 4, and some similar results at different pressures are indicated in Supplementary Figure S2. Since the sample at 3 GPa was partly lost during the sample preparation process, the error in the calculated phase proportion would be relatively larger compared to other samples. The results of mineral proportion in the recovered samples are summarized in Table 1.

Results

Figure 5 indicates the typical impedance spectra of the sample measured in the second heating-cooling modes at 3 GPa. At temperatures below 500°C (Figure 5A), the impedance spectra exhibit an approximate semicircular arc with a center on or slightly below the real axis (Z'). Hence, an equivalent circuit consisting of a parallel resistor (R) and a constant phase element (CPE) is employed to fit these impedance spectra in order to obtain sample resistance. In the first heating-cooling cycles at temperatures $\leq 400^\circ\text{C}$, the impedance spectra have similar features as shown in Figure 5A and are reproducible at each temperature point. As temperature increases (Figure 5B), the impedance spectra change

**FIGURE 4**

A representative mineral mapping of the plane of the cross-section of the recovered sample after conductivity measurement at 1 GPa by TIMA analysis. **(A)** TIMA mineral phases map and simultaneously acquired BSE image **(B)** of the whole cross-section of the sample. The mineral map **(C)** and corresponding BSE image **(D)** of the zoomed area selected from **(A)**. The dark voids shown in BSE images **(D)** are the evidence of the release of volatiles and indicate precipitation of graphite. The volume fraction of each mineral was summarized [Table 1](#) acquired from TIMA analysis. The green region shown in **(A)** represents the MgO sample chamber, as detailed in the experimental assembly diagram.

**FIGURE 5**

Representative complex impedance spectra measured at the second heating and cooling cycles at 2 GPa. The numbers alongside the impedance arcs are the temperature ($^{\circ}\text{C}$). Impedance spectra gradually change from nearly semi arcs **(A)** to lines **(B)** with increasing temperature, reflecting the occurrence of sample decarbonation. In the second cooling cycle **(C)**, the vertical lines are across the real impedance line at all temperature points that are characteristic of a conductor, thus the equivalent circuit composed of an inductor and resistor is used to model the resistance of sample.

from a complete semicircular arc to a partial distorted semicircular arc until a line vertical to the real part of impedance Z'' appears, accompanying the impedance value sharply decreases from a hundred of kilo-ohm ($k\Omega$) at 500°C to less than one hundred ohms (Ω) at temperature $<600^{\circ}\text{C}$. It

may reflect the decomposition reaction of the sample that occurred in high-temperature regions and produced highly conductive materials, resulting in the abrupt increase of conductivity. The analogous spectra were also observed in some highly conductive materials such as silicate/carbonatite

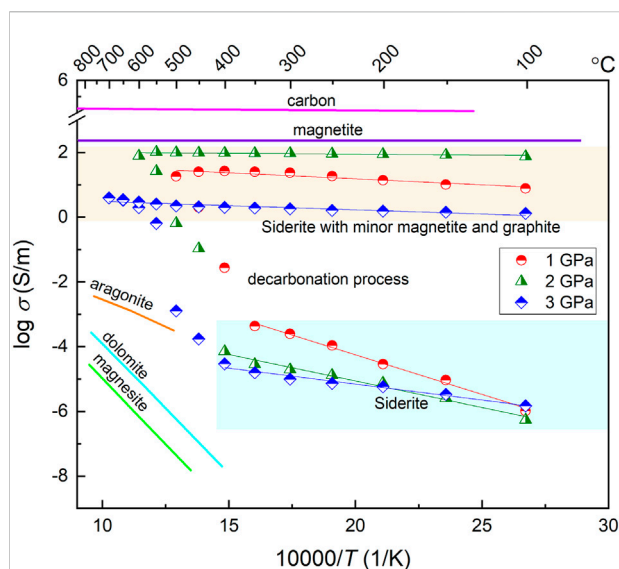


FIGURE 6

Temperature-dependent electrical conductivity of siderite at 1–3 GPa. The straight lines before and after the occurrence of sample decarbonation are the fitting results from Arrhenius equation. For comparison, the electrical conductivity of other carbonate minerals, e.g., aragonite Ono and Mibe (2013), dolomite Ono and Mibe (2015), and magnesite Mibe and Ono (2011), as well as the high conductive phases, e.g., magnetite Dai et al. (2019) and graphite Yoshino and Noritake (2011) are shown as solid lines with different color.

melts (Sifré et al., 2015; Guo et al., 2017; Guo et al., 2018; Yoshino et al., 2018; Guo et al., 2021), NaCl-bearing (Guo and Keppler, 2019; Klumbach and Keppler, 2020) or water-bearing fluids from the dehydration of hydrous minerals (Manthilake et al., 2016; Pommier et al., 2019), and metallic minerals (Dai et al., 2019). In the second cooling cycle shown in Figure 5C, all of the impedance spectra exhibit similar vertical lines, implying the highly conductive phases in the sample dominate the conductivity. On a basis of the vertical lines caused by the relatively large contribution of the induction component from an electrode or lead wire, the equivalent circuit composed of an inductor and resistor as shown in Figure 5C is adopted to model the electrical response of the sample over the whole frequency range. The feature of impedance spectra in different heating-cooling cycles at 1 and 2 GPa resembles that obtained at 3 GPa.

The conductivity results in different heating-cooling cycles at 3 GPa is shown in Figure 2, along with the background conductivity of the sample cell. In the low-temperature regions (100–400°C), the electrical conductivities of the sample gradually increase with increasing temperature and are almost reproducible after the first heating-cooling cycles. The slightly higher conductivity in the first heating cycle was probably attributed to the remaining moisture in the system, and these data were usually excluded from the analysis. The sample in the

low-temperature regimes have relatively low conductivity values, falling in the range of $10^{-4.5}$ – 10^{-6} S/m. Once the sample heated beyond 400°C in the second heating cycle, a large jump in conductivity was observed and the conductivity at 700°C is higher than that at 400°C by nearly five orders of magnitude. In the subsequent cooling/heating cycles, the conductivities cannot be reversible and still keep the high value with around 0.5 log unit (S/m) over the whole temperature range. In addition, the dependence of electrical conductivity on temperature can be almost negligible compared to that observed at low temperatures in the first heating-cooling cycle. The abrupt increase in conductivity is a consequence of the partial decomposition of the siderite sample, producing the highly conductive minerals that were confirmed by Raman spectroscopic analysis and TIMA results as shown in Figures 3, 4. Therefore, the reversible high conductivity yielded after the second heating cycle is attributed to the presence of highly conductive minerals in the sample. The variation in electrical conductivity with the temperature at 1 and 2 GPa is analogous to that at 3 GPa.

Figure 6 displays the electrical conductivity of the siderite sample as a function of reciprocal temperature at 1–3 GPa, together with previous conductivity results of carbonate minerals as well as some highly conductive minerals for comparison. At low temperatures (<450°C), the conductivity linearly increases with increasing temperature under different pressures, and almost decreases with increasing pressure at the same temperature, whereas the effect of pressure on the conductivity is smaller relative to that of temperature. The initial decarbonation temperature determined based on the sudden change of conductivity seems to gradually increase with increasing pressure, e.g., 350°C at 1 GPa, 400°C at 2 GPa, and 450°C at 3 GPa, that is because the stability field of siderite expands as pressure increases. After the decarbonation occurrence, the conductivity shows an extremely weak temperature dependence and even can be considered to be independent of temperature. Nevertheless, the marked variation of conductivity at different pressure is directly associated with the different amounts of highly conductive phases (i.e., magnetite and graphite), and the electrical conductivity increases with an increasing amount of those conductive phases, for instance, a sample with 11.5 vol.% of highly conductive phases at 2 GPa has higher conductivity than those at 1 GPa and at 3 GPa, with values of 6 vol.% and 1.3 vol.%, respectively.

The linear relationship between conductivity and reciprocal temperature for the samples before and after the decarbonation occurrence can be expressed by the Arrhenius equation:

$$\sigma = \sigma_0 \exp \left(\frac{-\Delta H}{kT} \right), \quad (1)$$

where σ_0 is a pre-exponential factor (S/m), k is the Boltzmann constant (eV/K), and ΔH is the activation enthalpy for

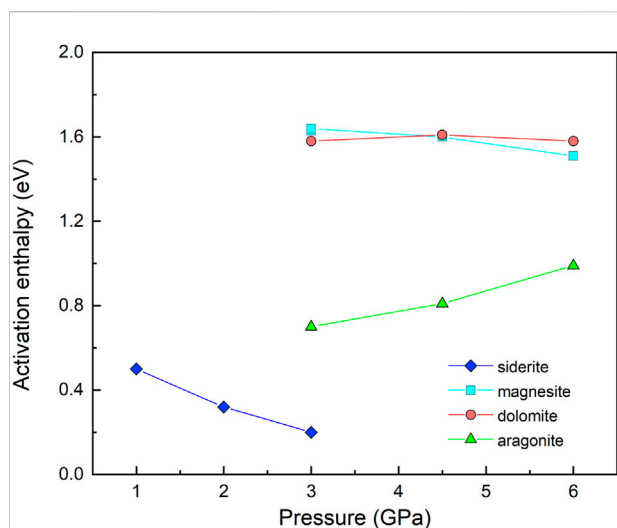


FIGURE 7

Activation enthalpies of carbonate minerals as a function of pressure before decarbonation reaction. The data of magnesite, dolomite and aragonite are from Mibe and Ono (2011), Ono and Mibe (2015), Ono and Mibe (2013), respectively.

conduction (eV). The reproducible conductivity data obtained before and after the decarbonation occurrence were fitted separately by Eq. 1, and the fitting parameters are summarized in Table 1. ΔH determined from conductivity data before the sample decarbonation occurred at various pressures is no more than 0.50 eV and gradually decreases with increasing pressure, whereas ΔH obtained after the decarbonation occurrence is considerably low, with the values of 0.01–0.08 eV. The large change in activation enthalpy before and after the occurrence of sample decarbonation is associated with the change in conduction mechanism, which will be discussed in detail below.

Discussion

Conduction behavior

Under our experimental conditions, the siderite samples exhibit a large variation in conductivity with the temperature that is associated with the occurrence of sample decomposition. The notably diverse activation enthalpies obtained before and after the decomposition reaction imply the possible different conduction mechanisms respectively dominating the conductivity of the sample in the two processes. In the low temperature regime before sample decomposition, the electrical conductivities are reproducible and relatively high with the values of $\sim 10^{-3}$ – $10^{-6.5}$ S/m and can be nearly comparable to those of aragonite (Ono and Mibe, 2013) at similar temperatures, but higher than those of dolomite and

magnesite (Mibe and Ono, 2011; Ono and Mibe, 2015) as indicated in Figure 6. All of the previous conductivity measurements on carbonate minerals are within their stability field at a temperatures no more than 727°C. In this study, the conductivity measurements on siderite in the low-temperature region less than 500°C are also performed within its stability field based on the phase diagram of siderite (Tao et al., 2013). Consequently, the conduction mechanism at low temperature region should be the intrinsic conduction of the sample rather than the external conduction from other materials. The activation enthalpies obtained at low temperature decrease as pressure increases as shown in Figure 6; accordingly, the activation volume is -14.47 cm³/mole as indicated in Table 1. The negative pressure effect on the conductivity in siderite resembles that in dolomite and magnesite as shown in Figure 7, however, the much lower activation volume of siderite (-14.47 cm³/mole) compared to those of dolomite (-1.00 cm³/mole) and magnesite (-3.95 cm³/mole), is probably related to the iron of bivalence-variable metallic cation in the lattice position, unlike the unable oxidized cations in Ca-Mg carbonates, i.e., Ca, Mg. Due to the high activation energy of Ca-Mg carbonates (1.64 eV for dolomite and 1.76 eV for magnesite), the hopping conduction due to the large polarons process involving magnesium or/and calcium vacancies and a trapped hole is suggested to be the dominant mechanism in previous studies (Mibe and Ono, 2011; Ono and Mibe, 2015). For iron-rich carbonate, resembling to other Fe-bearing silicate minerals, e.g., Fe-bearing olivine, garnet, pyroxene, and erovskites (Xu et al., 2000; Romano et al., 2006; Yang and Heidelberg, 2012; Dai and Karato, 2014; Sinmyo et al., 2014), the small polaron that electron-hole hopping between ferrous (Fe²⁺) and ferric (Fe³⁺) ions are likely to be the predominant conduction mechanism. Hence, it is proposed that the small polaron dominates the conductivity of siderite before the occurrence of the decarbonation reaction, with the characteristic of a relatively lower activation energy (0.64 eV).

Once the decarbonation reaction of the sample occurred when heated to a high temperature, the electrical conductivity abruptly increases by several orders of magnitude, and it is irreversible when the sample was annealed to low temperature. The BSE image and confocal Raman imaging of the recovered sample (Figures 3, 4) have confirmed that a low degree of decarbonation took place at a high temperature. Simultaneously, except for mackinawite derived from the original sample, a very small amount of carbon and magnetite are produced during the partial decomposition process. Previous experimental studies have revealed that the percolation threshold of the highly-conductive phase concentrations in olivine aggregates are ~ 1.7 vol.% graphite and ~ 5 vol.% magnetite, respectively (Wang et al., 2013; Dai et al., 2019), and the critical volume fraction for connectivity of magnetite in serpentinite aggregates is even up to 25 vol.% (Kawano et al., 2012). In contrast, the theoretical calculation and experimental

results on the conductivity of the natural chlorite have demonstrated that even less than 0.1 vol.% magnetite can form interconnectivity in the insulative matrix (Manthilake et al., 2016, see Supplementary Figure S1). In this study, the siderite sample only with the 1.3 vol.% of highly conductive minerals also has dramatically enhanced conductivity, and thus, it can be speculated that the interconnected networks or channels can easily be established in natural samples with a relatively low amount of highly conductive phases, compared to a synthetic sample from powder mixture. On the other hand, the large change in conductivity after the occurrence of siderite decarbonation accompanies the notable change in activation enthalpy, with the extremely low values of 0.01–0.08 eV as shown in Table 1, which are generally in accordance with that (0.02 eV) of graphite (Yoshino and Noritake, 2011) and magnetite (Kawano et al., 2012; Dai et al., 2019), and is also comparable to that of chlorite (i.e., 0.04 eV for low temperature and 0.15 eV for high temperature) after magnetite formation during dehydration reaction (Manthilake et al., 2016). Therefore, the anomalously high conductivity and low activation enthalpy after the onset of siderite decarbonation is a consequence of the presence of these interconnected highly-conductive phases (carbon and magnesite). Accordingly, the decomposition reaction of siderite at high temperature and high pressure is generally expressed as:



As illustrated in Figure 4, the microfractures and voids are developed during the conductivity measurement process, which may be attributed to the released gas phase. Meanwhile, the precipitation of graphite appears in these microfractures and voids. Actually, CO gas as an intermediate product was potentially formed during the decarbonation process of siderite by the reaction $3\text{FeCO}_3 = \text{Fe}_3\text{O}_4 + 2\text{CO}_2 + \text{CO}$, whereas the ratio of CO_2 to CO is metastable with respect to the formation of graphite, that would be precipitated from the gas phase by the reaction $2\text{CO} = \text{CO}_2 + \text{C}$ (Yui, 1966; Tao et al., 2013).

Constraints on the incipient temperature of siderite decarbonation

The electrical conductivity measurement is a very efficient approach to trace the state change (e.g., dehydration, dehydrogenation, decarbonation, melt, phase transition, etc.) of the sample at high temperature and high pressure, since a slight change of sample state usually can cause an observable variation in conductivity with temperature or pressure (Maugus et al., 2005; Manthilake et al., 2016; Hu et al., 2017; Hu et al., 2018; Manthilake et al., 2021; Hong et al., 2022). In this study, the sudden change in the conductivity occurred 350–450°C at

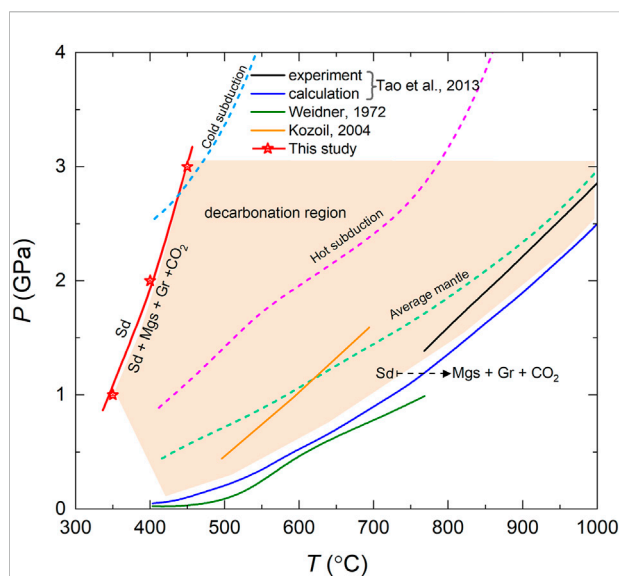


FIGURE 8

The incipient decomposition temperature of siderite = magnetite + graphite + CO_2 determined in this study, along with previous phase boundary results from phase equilibrium experiments and thermodynamically calculation. The thermal structures of deduction slab in typical hot and cool subduction zones and average mantle geotherm indicated as dashed lines from Syracuse et al. (2010) and Akaogi et al. (1989).

different pressure has demonstrated that the siderite sample underwent a low degree decarbonation, producing magnetite and graphite that confirmed and quantified by confocal Raman imaging and TIMA image. Previous experimental study on the stability of siderite indicated that the decarbonation reaction is rather sluggish, even if duration up to 36 h at 900°C and 2.5 GPa, 88.3% siderite is still present in the quenched sample (Tao et al., 2013). Our experiments further verified the sluggishness of decarbonation reaction of siderite, even though the conductivity measurements were performed in three heating-cooling cycles within several hours, no less than 88.5 vol.% of siderite are still present in the recovered samples under experimental conditions as shown in Table 1. On the basis of the criteria of the phase boundary of siderite established by Tao et al. (2013), the run products with abundances >85% of siderite is regarded as siderite stable. It implies that in this study the recovered sample is within the stability field of siderite because ≥ 88.5 vol.% of siderite is still present after conductivity measurement. In light of the dramatical variation in electrical conductivity, our experimental results have clearly indicated that siderite have become to be thermally unstable and launched to breakdown at temperatures of 350–450°C under pressures of 1–3 GPa at oxygen fugacity of NNO buffer. From Figure 8, we found that the initial decarbonation temperature (350–450°C) of siderite determined by this study is far lower than

TABLE 2 The calculated fugacities of oxygen and carbon dioxide at the initial decomposition temperature of siderite at different pressure based on the formula given by Yui (1966).

<i>T</i> and <i>P</i>	350°C, 1 GPa	400°C, 2 GPa	450°C, 3 GPa
log f_{O_2} , atm	−31.02	−28.07	−25.53
log f_{CO_2} , atm	2.07	2.56	2.99

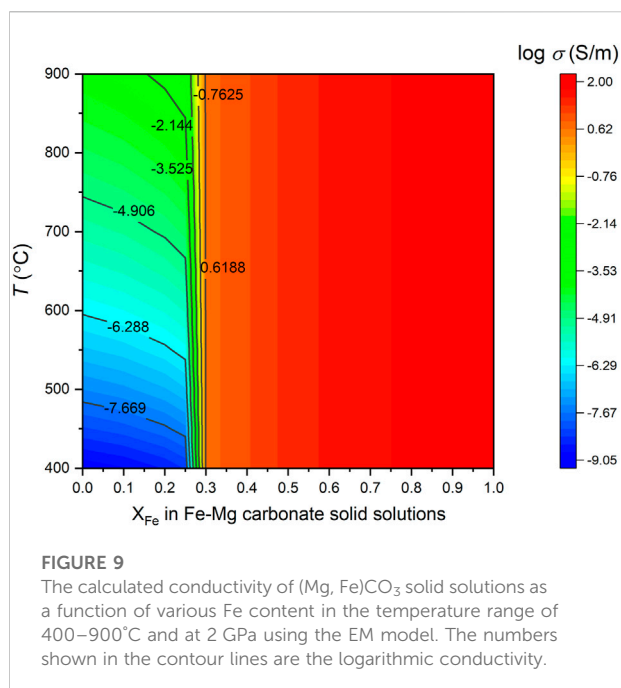
that of previously reported decomposition boundary temperature (>600°C) determined by phase equilibrium experiments at same pressure ranges (Weidner, 1972; Kozioł, 2004; Tao et al., 2013). These previously determined phase boundary of siderite decomposition was acquired under conditions of enough long duration in order to reach fully high-pressure phase equilibrium, correspondingly, the reaction products were quenched and analyzed. Hence, it is incapable to investigate the initial temperature of siderite decomposition, unless the high-temperature and high-pressure *in-situ* synchrotron X-ray diffraction technique is employed. In contrast, our present *in-situ* electrical conductivity of siderite measured in continuous heating process at different pressures constrained the incipient decarbonation temperature. As shown in Figure 8, the boundaries of the onset and completion of siderite decomposition are very wide, spanning several hundred degrees of Celsius due to the sluggishness of decarbonation reaction, implying that the occurrence of initial decarbonation of Fe-bearing carbonate is at a shallower depth in subducting oceanic crust. On the other hand, the initial decomposition temperature of siderite is much lower the geotherms of hot subduction and mantle, but intersect with the geotherm of cool subduction zone at below 450°C, hence, it is inferred that siderite is probably decomposed before subducted into the mantle.

The decarbonation reaction of siderite is not only dependent on *P-T* conditions, but is also strongly dependent on the oxygen fugacity, owing to the Fe element that can exist in multiple valence states. The experimental and theoretical results of Fe-C-O phase diagram in *T-P-f_{O2}* have indicated that the siderite stability field is wedge-shaped, and has its thermal maximum at the intersection with the CCO buffer (Yui, 1966; Kozioł, 2004; Kang et al., 2015). Pressure and carbon dioxide fugacity (f_{CO_2}) can expand the siderite stability field. In this study, f_{CO_2} was not controlled due to the absence of an internal graphite buffer, whereas carbon dioxide buffering was gradually established by gas phase and graphite precipitation from the decarbonation reaction of siderite, and the bulk system moved onto the CCO buffer. As pointed out by Yui (1966), for a given temperature and pressure, the presence of graphite defines the fugacities of CO₂, CO, and O₂, meanwhile, they gave relevant formula for the relations between absolute temperature and the fugacities of oxygen and carbon dioxide in equilibrium with the siderite-magnetite-graphite assemblage. Since our sample after

conductivity measurements became the same four-phase assemblage (i.e., siderite, magnetite, graphite, and gas), the fugacities of oxygen and carbon dioxide at initial breakdown temperature and different pressures are calculated by the formula given by Yui (1966), and the results are shown in Table 2. The oxygen fugacity lower or too higher than these values would result in the decomposition of siderite to magnetite + graphite + gas or magnetite (hematite) + gas, therefore, at given temperature and pressure, the oxygen fugacity falls in a limited range for the siderite stability. In contrast, carbon dioxide fugacity higher than those for the initial decomposition of siderite as shown in Table 2, e.g., 2.56 log units at 400°C and 2 GPa, would facilitate to maintain the stability of siderite and avoid the formation of new phases. In addition, the increase of f_{CO_2} can significantly promote the maximum values of temperature and f_{O_2} for siderite stability. In a consequence, our results give the critical values of f_{CO_2} for the siderite stability at high temperature and pressure, which is of importance for understanding the formation conditions of siderite in nature.

Implications for high conductivity anomalies at slab-mantle wedge interface

Magnetotelluric images of the subduction zones has indicated that highly conductive anomalies are extensively present along or above the slab at variable depths, that are commonly interpreted as the presence of aqueous fluid or melt due to the dehydration of the descending slab (Wannamaker et al., 2009; Worzewski et al., 2011; McGary et al., 2014). Fluid accumulation in the forearc at depths of 20–40 km is regarded as a global phenomenon based on the consistent perception of electromagnetic (high conductivity) and seismic (low velocity) results. However, the compositions of fluid released from slabs are not well constrained, while the electrical conductivity of fluids has a strong compositional dependence, therefore, fluid fraction in the forearc has not been accurately estimated until now. Recent studies have demonstrated that the majority of CO₂ (likely up to ~65%) can be released at forearc depths in the typical subducting oceanic crust by decarbonation reactions, rather than subducted to the deep mantle, meanwhile, the released CO₂ may be stored in the lithospheric mantle of the overriding plate (Barry et al., 2019; Stewart and Ague, 2020). The slab-released aqueous fluids could dissolve carbonate minerals stored in sediments, altered oceanic crust and carbonated mantle peridotite, producing carbon-bearing fluids. The present lack of the electrical conductivity of CHO fluids as a function of temperature, pressure and composition makes it difficult to constrain the carbon content in CHO fluids and its fluid fraction under subduction conditions while combining with magnetotelluric results. In addition, recent experimental results have indicated the substantial replacement of Ca²⁺ by Mg²⁺ in carbonate can decrease the solubility by at least two



orders of magnitude (Farsang et al., 2021). It is speculated that the substitution of Fe²⁺ for Mg²⁺ in magnesite and dolomite probably has an important influence on the solubility of these carbonate minerals during subduction process, because the presence of Fe in carbonate can dramatically affect the physical properties, for instance, reducing the decarbonation temperature and the stability field of carbonates (Tao et al., 2014; Bataleva et al., 2020). Hence, the electrical conductivity of CHO fluids and the solubility of Fe-bearing carbonate at high temperature and pressure are required to better constrain the carbon content in aqueous fluid present in the forearc.

On the other hand, the highly conductive minerals, e.g., magnetite and graphite, are likely an important candidate for the explanation of high conductivity anomalies in the subduction zones, particularly, in the slab-mantle wedge interface where the buoyant fluid and melt phases are gravitationally unstable and can migrate upward *via* channels and fractures that formed by dehydration reactions (Plümper et al., 2017). Hydration and carbonation of mantle peridotite in the subduction zone generate carbonated serpentinites that commonly contain a certain amount of magnetite, some even up to 6.15 wt% magnetite (Klein et al., 2014; Guillot et al., 2015). The presence of magnetite in serpentinite would have a considerable effect on the electrical conductivity of serpentinites owing to its highly conductive feature. Nevertheless, the experimental results have shown that the conductivity of serpentinite was not significantly enhanced by the addition of 5 vol.% magnetite, and more than 25 vol.%

magnetite is needed for the establishment of interconnectivity, but the shear deformation at the plate interface can promote the conductivity of serpentinite by an order of magnitude (Kawano et al., 2012). It implies that the connectivity of magnetite in the natural serpentinite under subduction context is likely established with far less than the percolation threshold (i.e., 25 vol.% magnetite).

Siderite often occurs with magnesite in rock and commonly form a continuous solid solution of (Mg,Fe)CO₃ in natural carbonated oceanic and continental crust. To evaluate the contribution of siderite to the high conductivity at slab-mantle wedge interface, the threshold volume fraction of siderite in Fe-bearing carbonates is firstly qualified. Correspondingly, the electrical conductivity of Mg-Fe carbonate solid solutions, as a representative for Fe-bearing carbonates, are calculated by the effective medium (EM) theory model (Landauer, 1952), in combination with the conductivity data of magnesite from Mibe and Ono, (2011) and siderite from this study. The EM model can be expressed as

$$\sigma_{EM} = \frac{1}{4} \{ (3f_1 - 1)\sigma_1 + (3f_2 - 1)\sigma_2 + [\{ (3f_1 - 1)\sigma_1 + (3f_2 - 1)\sigma_2 \}^2 + 8\sigma_1\sigma_2]^{0.5} \}. \quad (3)$$

Here σ_1 and σ_2 are the conductivities of magnesite and siderite, and f_1 and f_2 are their volume percentages.

Figure 9 shows the calculation results of ferromagnesian carbonate solid solutions as a function of various Fe content (X_{Fe} : the mole fraction of iron in the Mg site) within the temperature range of 400–900°C at 2 GPa. In this temperature range, the decarbonation reaction of siderite will take place, whereas magnesite is still within its stability field and has very low conductivity values, thus, it acts as the insulative matrix in (Fe, Mg)CO₃ solid solutions. The electrical conductivity of magnesite-siderite solid solutions slightly increases with the increase of Fe concentration. When the content of the siderite component is increased up to 25% in the magnesite-siderite solid solutions, the conductivity of Mg-Fe carbonate is apparently enhanced with a value close to 0.1 S/m. Once the siderite component exceeds the percolation threshold of 30%, (Mg, Fe)CO₃ solid solutions have the conductivity almost equal to siderite. Consequently, the component of (Mg_{0.7}Fe_{0.3})CO₃ is needed so as to make a contribution to high conductivity in the temperature ranges of 400–900°C.

Our results have indicated that the low degree decarbonation of siderite with even only 1.3 vol.% of magnetite and graphite produced, cause a dramatical increase in electrical conductivity. It has also been demonstrated that the interconnectivity of graphite in resistive matrix can be easily established with the lower volume fraction (1.7 vol.%) (Wang et al., 2013). Consequently, the addition of highly conductivity materials

(magnetite and graphite) generated from the siderite component of the Fe-bearing carbonate, into serpentinite will improve the interconnectivity of magnetite, that likely become the origin of highly conductivity anomalies observed in the slab-mantle wedge interface at relatively shallow depth of ~20–40 km. As the plate subducts downwards, besides the progressive decarbonation of Fe-bearing carbonate, the dehydration of hydrous minerals, e.g., chlorite (Manthilake et al., 2016) and epidote (Hu et al., 2017), as well as devolatilization of carbonate-bearing serpentinite (Manthilake et al., 2021) can provide substantial iron oxides (e.g., hematite, magnetite). The accumulation of iron oxides at the slab-mantle wedge interface is potentially responsible for the anomalous high conductivity observed at relatively deep depths.

Conclusion

The electrical conductivity of natural siderite was determined at temperatures of 100–700°C and pressures of 1–3 GPa. An abrupt increase in conductivity observed at ~400°C is attributed to the low degree decarbonation of siderite, accompanying the formation of a small amount of highly conductive phases (graphite and magnetite). The obvious variation in electrical conductivity and activation enthalpy before and after the occurrence of siderite decarbonation suggest two different conduction mechanisms, the small polaron (electron hopping between Fe^{2+} and Fe^{3+}) and highly conductive phases dominating electrical conductivity, respectively. The incipient decarbonation temperature determined in this study is much lower than complete decomposition temperature of siderite determined by phase equilibrium experiments; implying the initial decomposition of Fe-bearing carbonates in subducting oceanic crust occurs at a shallower depth. The 30 vol.% of siderite is required to enhance the electrical conductivity of $(\text{Mg,Fe})\text{CO}_3$ solid solutions. Magnetite and graphite derived from the siderite component of Fe-bearing carbonate will promote the interconnectivity of magnetite in natural serpentinite, in addition to a significant contribution of magnetite from devolatilization of hydrous minerals in subduction zone. Therefore, magnetite is likely a new candidate for the origin of anomalously high conductivity observed in slab-mantle wedge interface.

Data availability statement

The original contributions presented in the study are included in the article/Supplementary Material, further inquiries can be directed to the corresponding author.

Author contributions

HH: conceptualization, writing-original draft preparation. CJ: software, analysis, and data curation. LD: supervision, discussion, editing. CY and DC: visualization, investigation. All authors contributed to the final manuscript.

Funding

This study was financially supported by the National Natural Science Foundation of China (Grant No. 42072055), the Youth Innovation Promotion Association of CAS (Grant No. 2019390), Special Fund of the West Light Foundation of CAS (2018) as well as the Science and Technology Foundation of Guizhou Province [grant number QKHJZ (2013) 2285] as well as Guizhou Provincial 2019 and 2020 Science and Technology Subsidies (grant numbers GZ2019SIG and GZ2020SIG).

Acknowledgments

The authors thank the senior technicians of Dr. Qian Cheng for their technical assistance with Raman spectroscopic analysis from the WITec (Beijing) Scientific Technology Co., Ltd. Shengping Li is thanked for his help with the TIMA analyses.

Conflict of interest

The authors declare that the research was conducted in the absence of any commercial or financial relationships that could be construed as a potential conflict of interest.

Publisher's note

All claims expressed in this article are solely those of the authors and do not necessarily represent those of their affiliated organizations, or those of the publisher, the editors, and the reviewers. Any product that may be evaluated in this article, or claim that may be made by its manufacturer, is not guaranteed or endorsed by the publisher.

Supplementary material

The Supplementary Material for this article can be found online at: <https://www.frontiersin.org/articles/10.3389/feart.2022.985740/full#supplementary-material>

References

- Akaogi, M., Ito, E., and Navrotsky, A. (1989). Olivine-modified spinel-spinel transitions in the system $\text{Mg}_2\text{SiO}_4\text{-Fe}_2\text{SiO}_4$: Calorimetric measurements, thermochemical calculation, and geophysical application. *J. Geophys. Res.* 94, 15671–15685. doi:10.1029/JB094iB11p15671
- Alt, J. C., and Teagle, D. A. H. (1999). The uptake of carbon during alteration of ocean crust. *Geochim. Cosmochim. Acta* 63, 1527–1535. doi:10.1016/S0016-7037(99)00123-4
- Barry, P. H., de Moor, J. M., Giovannelli, D., Schrenk, M., Hummer, D. R., Lopez, T., et al. (2019). Forearc carbon sink reduces long-term volatile recycling into the mantle. *Nature* 568, 487–492. doi:10.1038/s41586-019-1131-5
- Bataleva, Y. V., Kruk, A. N., Novoselov, I. D., Furman, O. V., and Palyanov, Y. N. (2020). Decarbonation reactions involving ankerite and dolomite under upper mantle P , T -parameters: Experimental modeling. *Minerals* 10, 715. doi:10.3390/min10080715
- Boulard, E., Gloter, A., Corgne, A., Antonangeli, D., Auzende, A.-L., Perrillat, J.-P., et al. (2011). New host for carbon in the deep Earth. *Proc. Natl. Acad. Sci. U. S. A.* 108, 5184–5187. doi:10.1073/pnas.1016934108
- Cerantola, V., Bykova, E., Kuppenko, I., Merlini, M., Ismailova, L., McCammon, C., et al. (2017). Stability of iron-bearing carbonates in the deep Earth's interior. *Nat. Commun.* 8, 15960. doi:10.1038/ncomms15960
- Dai, L., Hu, H., Sun, W., Li, H., Liu, C., and Wang, M. (2019). Influence of high conductive magnetite impurity on the electrical conductivity of dry olivine aggregates at high temperature and high pressure. *Minerals* 9, 44. doi:10.3390/min910044
- Dai, L., and Karato, S. (2014). Influence of FeO and H on the electrical conductivity of olivine. *Phys. Earth Planet. Interiors* 237, 73–79. doi:10.1016/j.pepi.2014.10.006
- Dasgupta, R., and Hirschmann, M. M. (2007). Effect of variable carbonate concentration on the solidus of mantle peridotite. *Am. Mineral.* 92, 370–379. doi:10.2138/am.2007.2201
- Dasgupta, R., and Hirschmann, M. M. (2006). Melting in the Earth's deep upper mantle caused by carbon dioxide. *Nature* 440, 659–662. doi:10.1038/nature04612
- Dasgupta, R., Hirschmann, M. M., and Withers, A. C. (2004). Deep global cycling of carbon constrained by the solidus of anhydrous, carbonated eclogite under upper mantle conditions. *Earth Planet. Sci. Lett.* 227, 73–85. doi:10.1016/j.epsl.2004.08.004
- Dubrawski, J. V. (1991). Thermal decomposition of some siderite-magnesite minerals using DSC. *J. Therm. Analysis* 37, 1213–1221. doi:10.1007/bf01913855
- Farsang, S., Louvel, M., Zhao, C., Mezouar, M., Rosa, A. D., Widmer, R. N., et al. (2021). Deep carbon cycle constrained by carbonate solubility. *Nat. Commun.* 12, 4311. doi:10.1038/s41467-021-24533-7
- Gaillard, F., Malki, M., Iacono-Marziano, G., Pichavant, M., and Scaillet, B. (2008). Carbonatite melts and electrical conductivity in the asthenosphere. *Science* 322, 1363–1365. doi:10.1126/science.1164446
- Ghosh, S., Ohtani, E., Litasov, K. D., and Terasaki, H. (2009). Solidus of carbonated peridotite from 10 to 20 GPa and origin of magnesio-carbonatite melt in the Earth's deep mantle. *Chem. Geol.* 262, 17–28. doi:10.1016/j.chemgeo.2008.12.030
- Guillot, S., Schwartz, S., Reynard, B., Agard, P., and Prigent, C. (2015). Tectonic significance of serpentinites. *Tectonophysics* 646, 1–19. doi:10.1016/j.tecto.2015.01.020
- Guo, H., and Keppler, H. (2019). Electrical conductivity of NaCl-bearing aqueous fluids to 900 °C and 5 GPa. *J. Geophys. Res. Solid Earth* 124, 1397–1411. doi:10.1029/2018JB016658
- Guo, X., Li, B., Ni, H., and Mao, Z. (2017). Electrical conductivity of hydrous andesitic melts pertinent to Subduction zones. *J. Geophys. Res. Solid Earth* 122, 1777–1788. doi:10.1002/2016JB013524
- Guo, X., Wang, Q., Li, B., Zha, X. P., Gong, B., and Ni, H. (2021). Electrical conductivity of CO_2 and H_2O -bearing nephelinitic melt. *J. Geophys. Res. Solid Earth* 126, e2020JB019569. doi:10.1029/2020JB019569
- Guo, X., Zhang, L., Su, X., Mao, Z., Gao, X., Yang, X., et al. (2018). Melting inside the Tibetan crust? Constraint from electrical conductivity of peraluminous granitic melt. *Geophys. Res. Lett.* 45, 3906–3913. doi:10.1029/2018GL077804
- Hong, M., Dai, L., Hu, H., Yang, L., and Zhang, X. (2022). Pressure-induced structural phase transitions in natural kaolinite investigated by Raman spectroscopy and electrical conductivity. *Am. Mineral.* 107, 385–394. doi:10.2138/am-2021-7863
- Hu, H., Dai, L., Li, H., Hui, K., and Sun, W. (2017). Influence of dehydration on the electrical conductivity of epidote and implications for high-conductivity anomalies in subduction zones. *J. Geophys. Res. Solid Earth* 122, 2751–2762. doi:10.1002/2016JB013767
- Hu, H., Dai, L., Li, H., Sun, W., and Li, B. (2018). Effect of dehydrogenation on the electrical conductivity of Fe-bearing amphibole: Implications for high conductivity anomalies in subduction zones and continental crust. *Earth Planet. Sci. Lett.* 498, 27–37. doi:10.1016/j.epsl.2018.06.003
- Kang, D., Schmidt, M. W., Poli, S., Franzolin, E., and Connolly, J. D. (2015). Melting of siderite to 20 GPa and thermodynamic properties of FeCO_3 -melt. *Chem. Geol.* 400, 34–43.
- Kawano, S., Yoshino, T., and Katayama, I. (2012). Electrical conductivity of magnetite-bearing serpentinite during shear deformation. *Geophys. Res. Lett.* 39, L20313. doi:10.1029/2012GL053652
- Keppler, H., Wiedenbeck, M., Shcheka, S. S., and Jons, N. (2003). Magnetite in seafloor serpentinite—Some like it hot. *Nature* 424, 414–416. doi:10.1038/nature01828
- Klein, F., Bach, W., Humphris, S. E., Kahl, W.-A., Jöns, N., Moskowicz, B., et al. (2014). Magnetite in seafloor serpentinite—Some like it hot. *Geology* 42, 135–138. doi:10.1130/G35068.1
- Klumbach, S., and Keppler, H. (2020). Electrical conductivity of HCl-bearing aqueous fluids to 700 °C and 1 GPa. *Contrib. Mineral. Petrol.* 175, 114. doi:10.1007/s00410-020-01754-5
- Kozioł, A. M. (2004). Experimental determination of siderite stability and application to Martian Meteorite ALH84001. *Am. Mineral.* 89, 294–300. doi:10.2138/am-2004-2-306
- Landauer, R. (1952). The electrical resistance of binary metallic mixtures. *J. Appl. Phys.* 23, 779–784. doi:10.1063/1.1702301
- Liu, J., Lin, J. F., and Prakapenka, V. (2015). High-pressure orthorhombic ferromagnetite as a potential deep-mantle carbon carrier. *Sci. Rep.* 5, 7640. doi:10.1038/srep07640
- Luth, R. W. (1993). Diamonds, eclogites, and the oxidation state of the earth's mantle. *Science* 261, 66–68. doi:10.1126/science.261.5117.66
- Manthilake, G., Bolfan-Casanova, N., Novella, D., Mookherjee, M., and Andraut, D. (2016). Dehydration of chlorite explains anomalously high electrical conductivity in the mantle wedges. *Sci. Adv.* 2, e1501631. doi:10.1126/sciadv.1501631
- Manthilake, G., Mookherjee, M., and Miyajima, N. (2021). Insights on the deep carbon cycle from the electrical conductivity of carbon-bearing aqueous fluids. *Sci. Rep.* 11, 3745. doi:10.1038/s41598-021-82174-8
- Maumens, J., Bagdasarov, N., and Schmeling, H. (2005). Electrical conductivity and partial melting of mafic rocks under pressure. *Geochim. Cosmochim. Acta* 69, 4703–4718. doi:10.1016/j.gca.2005.05.010
- McGary, R. S., Evans, R. L., Wannamaker, P. E., Elsenbeck, J., and Rondenay, S. (2014). Pathway from subducting slab to surface for melt and fluids beneath Mount Rainier. *Nature* 511, 338–340. doi:10.1038/nature13493
- Mibe, K., and Ono, S. (2011). Electrical conductivity of MgCO_3 at high pressures and high temperatures. *Phys. B Condens. Matter* 406, 2018–2020. doi:10.1016/j.physb.2011.03.009
- Ono, S., and Mibe, K. (2013). Electrical conductivity of aragonite in the subducted slab. *Eur. J. Mineral.* 25, 11–15. doi:10.1127/0935-1221/2013/0025-2254
- Ono, S., and Mibe, K. (2015). Influence of pressure and temperature on the electrical conductivity of dolomite. *Phys. Chem. Min.* 42, 773–779. doi:10.1007/s00269-015-0761-x
- Papathanassiou, A. N. (1998). Effect of hydrostatic pressure on the electrical conductance of polycrystalline magnesite $\text{Mg}(\text{CO}_3)$. *Phys. Rev. B* 58, 4432–4437. doi:10.1103/PhysRevB.58.4432
- Papathanassiou, A. N., and Grammatikakis, J. (1996). Pressure variation of the electrical conductivity of dolomite $[(\text{CaMg}(\text{CO}_3)_2)]$. *Phys. Rev. B* 53, 16247–16251. doi:10.1103/PhysRevB.53.16247
- Plümper, O., John, T., Podladchikov, Y. Y., Vrijmoed, J. C., and Scambelluri, M. (2017). Fluid escape from subduction zones controlled by channel-forming reactive porosity. *Nat. Geosci.* 10, 150–156. doi:10.1038/ngeo2865
- Pommier, A., Williams, Q., Evans, R. L., Pal, I., and Zhang, Z. (2019). Electrical investigation of natural lawsonite and application to subduction contexts. *J. Geophys. Res. Solid Earth* 124, 1430–1442. doi:10.1029/2018JB016899
- Romano, C., Poe, B. T., Kreidie, N., and McCammon, C. A. (2006). Electrical conductivities of pyrope-almandine garnets up to 19 GPa and 1700 °C. *Am. Mineral.* 91, 1371–1377. doi:10.2138/am.2006.1983
- Sifré, D., Hashim, L., and Gaillard, F. (2015). Effects of temperature, pressure and chemical compositions on the electrical conductivity of carbonated melts and its relationship with viscosity. *Chem. Geol.* 418, 189–197. doi:10.1016/j.chemgeo.2014.09.022

- Sinmyo, R., Pesce, G., Greenberg, E., McCammon, C., and Dubrovinsky, L. (2014). Lower mantle electrical conductivity based on measurements of Al, Fe-bearing perovskite under lower mantle conditions. *Earth Planet. Sci. Lett.* 393, 165–172. doi:10.1016/j.epsl.2014.02.049
- Stewart, E. M., and Ague, J. J. (2020). Pervasive subduction zone devolatilization recycles CO₂ into the forearc. *Nat. Commun.* 11, 6220. doi:10.1038/s41467-020-19993-2
- Sverjensky, D. A., Stagno, V., and Huang, F. (2014). Important role for organic carbon in subduction-zone fluids in the deep carbon cycle. *Nat. Geosci.* 7, 909–913. doi:10.1038/ngeo2291
- Syracuse, E. M., van Keken, P. E., and Abers, G. A. (2010). The global range of subduction zone thermal models. *Phys. Earth Planet. Interiors* 183, 73–90. doi:10.1016/j.pepi.2010.02.004
- Tao, R., Fei, Y., and Zhang, L. (2013). Experimental determination of siderite stability at high pressure. *Am. Mineral.* 98, 1565–1572. doi:10.2138/am.2013.4351
- Tao, R., Fei, Y., Zhang, L., and Liu, Q. (2014). The effect of Fe on the stability of dolomite at high pressure: Experimental study and petrological observation in eclogite from southwestern Tianshan, China. *Geochim. Cosmochim. Acta* 143, 253–267. doi:10.1016/j.gca.2014.02.031
- Ter Heege, J. H., and Renner, J. (2007). *In situ* impedance spectroscopy on pyrophyllite and CaCO₃ at high pressure and temperature: Phase transformations and kinetics of atomistic transport. *Phys. Chem. Min.* 34, 445–465. doi:10.1007/s00269-007-0162-x
- Thomson, A. R., Walter, M. J., Kohn, S. C., and Brooker, R. A. (2016). Slab melting as a barrier to deep carbon subduction. *Nature* 529, 76–79. doi:10.1038/nature16174
- Wang, D., Karato, S., and Jiang, Z. (2013). An experimental study of the influence of graphite on the electrical conductivity of olivine aggregates. *Geophys. Res. Lett.* 40, 2028–2032. doi:10.1002/grl.50471
- Wannamaker, P. E., Caldwell, T. G., Jiracek, G. R., Maris, V., Hill, G. J., Ogawa, Y., et al. (2009). Fluid and deformation regime of an advancing subduction system at Marlborough, New Zealand. *Nature* 460, 733–736. doi:10.1038/nature08204
- Weidner, J. R. (1972). Equilibria in the system Fe-C-O; Part I, Siderite-magnetite-carbon-vapor equilibrium from 500 to 10,000 bars. *Am. J. Sci.* 272, 735–751. doi:10.2475/ajs.272.8.735
- Worzewski, T., Jegen, M., Kopp, H., Brasse, H., and Castillo, W. T. (2011). Magnetotelluric image of the fluid cycle in the Costa Rican subduction zone. *Nat. Geosci.* 4, 108–111. doi:10.1038/ngeo1041
- Xu, Y., Shankland, T. J., and Duba, A. G. (2000). Pressure effect on electrical conductivity of mantle olivine. *Phys. Earth Planet. Interiors* 118, 149–161. doi:10.1016/S0031-9201(99)00135-1
- Yang, X., and Heidelbach, F. (2012). Grain size effect on the electrical conductivity of clinopyroxene. *Contrib. Mineral. Petrol.* 163, 939–947. doi:10.1007/s00410-011-0707-3
- Yoshino, T., Gruber, B., and Reinier, C. (2018). Effects of pressure and water on electrical conductivity of carbonate melt with implications for conductivity anomaly in continental mantle lithosphere. *Phys. Earth Planet. Interiors* 281, 8–16. doi:10.1016/j.pepi.2018.05.003
- Yoshino, T., and Noritake, F. (2011). Unstable graphite films on grain boundaries in crustal rocks. *Earth Planet. Sci. Lett.* 306, 186–192. doi:10.1016/j.epsl.2011.04.003
- Yui, S. (1966). Decomposition of siderite to magnetite at lower oxygen fugacities: A thermochemical interpretation and geological implications. *Econ. Geol.* 61, 768–776. doi:10.2113/gsecongeo.61.4.768
- Zhu, Y., and Ogasawara, Y. (2002). Carbon recycled into deep Earth: Evidence from dolomite dissociation in subduction-zone rocks. *Geology* 30, 947–950. doi:10.1130/0091-7613(2002)030<0947:CRIDEE>2.0.CO;2

Frontiers in Earth Science

Investigates the processes operating within the major spheres of our planet

Advances our understanding across the earth sciences, providing a theoretical background for better use of our planet's resources and equipping us to face major environmental challenges.

Discover the latest Research Topics

[See more →](#)

Frontiers

Avenue du Tribunal-Fédéral 34
1005 Lausanne, Switzerland
frontiersin.org

Contact us

+41 (0)21 510 17 00
frontiersin.org/about/contact

